

NASA Contractor Report 191464

1N-19

123049

~~402~~

402 P

Microwave Reflectometer Ionization Sensor

Joseph Seals, Jeffrey A. Fordham, Robert G. Pauley,
and Mario D. Simonutti

Electromagnetic Sciences Inc.
Norcross, Georgia

N94-17083

Unclas

G3/19 0193049

Contract NAS1-19063
October 1993



National Aeronautics and
Space Administration

Langley Research Center
Hampton, Virginia 23681-0001

(NASA-CR-191464) MICROWAVE
REFLECTOMETER IONIZATION SENSOR
(Electromagnetic Sciences) 402 P

FINAL TECHNICAL REPORT

MICROWAVE REFLECTOMETER IONIZATION SENSOR

CONTRACT NO.: NAS1-19063

**DRL 50 (FINAL TECHNICAL REPORT) and
DRL 58 (ANALYSES)**

Prepared By

ELECTROMAGNETIC SCIENCES, INC.
P. O. BOX 7700
NORCROSS, GEORGIA 30091-7700

Prepared for

NASA LANGLEY RESEARCH CENTER
ANTENNA AND MICROWAVE RESEARCH BRANCH
HAMPTON, VIRGINIA 23681-0001

TABLE OF CONTENTS

<u>SECTION</u>	<u>PAGE</u>
1.0 INTRODUCTION.....	1-1
2.0 BACKGROUND INFORMATION.....	2-1
2.1 BASIC SENSOR CONCEPT.....	2-1
2.1.1 General.....	2-1
2.1.2 Simple Reflection Model.....	2-2
2.2 SYSTEM REQUIREMENTS.....	2-4
2.2.1 Operating Frequencies.....	2-4
2.2.2 Electron Densities.....	2-5
2.2.3 Measurement Parameters.....	2-5
2.2.4 Measurement Accuracies.....	2-7
3.0 INSTRUMENT DESCRIPTION.....	3-1
3.1 OVERVIEW.....	3-1
3.1.1 Development Objectives.....	3-1
3.1.2 Description.....	3-1
3.2 TRANSMIT/RECEIVE ASSEMBLY.....	3-3
3.2.1 General.....	3-3
3.2.2 T/R Modules.....	3-3
3.2.2.1 General.....	3-3
3.2.2.2 Upconverters.....	3-4
3.2.2.3 Downconverters.....	3-9
3.2.3 IF Components.....	3-10
3.2.4 Antennas.....	3-10
3.2.5 MUX-Telemetry Board.....	3-16
3.3 DETECTOR ASSEMBLY.....	3-19
3.3.1 General.....	3-19
3.3.2 IF Subassemblies.....	3-19
3.4 GROUND SUPPORT EQUIPMENT (GSE) SUMMARY.....	3-22
3.4.1 General.....	3-22
3.4.2 Overview of Planned GSE Functions.....	3-22
3.4.3 GSE Hardware.....	3-23
3.4.4 GSE Software.....	3-27
4.0 TECHNICAL CHALLENGES AND SOLUTIONS.....	4-1
4.1 GENERAL.....	4-1
4.2 REFLECTIONS FROM TPS TILE AND ANTENNA GROUND PLANE.....	4-1
4.2.1 Interference Reflections and Multipath Reflections.....	4-1
4.2.2 Simple Interference Example.....	4-6
4.2.3 Vector Error Correction Concept.....	4-9
4.2.4 Range-Gating Concept.....	4-12

TABLE OF CONTENTS (Continued)

SECTION		PAGE
4.3	MMW INSTRUMENTATION RELIABILITY.....	4-14
4.3.1	MMW Mixers.....	4-14
4.3.2	WG Switches.....	4-18
4.4	PLASMA ATTENUATION.....	4-18
5.0	SYSTEM CONSIDERATIONS.....	5-1
5.1	SUMMARY OF SYSTEM TOPICS.....	5-1
5.2	STEPPED-FMCW DESIGN AND IMPLEMENTATION.....	5-1
5.2.1	General Description of FMCW System.....	5-1
5.2.2	Signal Processing.....	5-3
5.2.3	Frequency Sweep Parameters.....	5-4
5.2.4	Unambiguous Range.....	5-6
5.2.5	Range Resolution.....	5-8
5.2.5	Range Accuracy.....	5-10
5.3	KEY SYSTEM PARAMETERS AND DESIGN GOALS.....	5-10
5.3.1	Receiver Dynamic Range.....	5-11
5.3.2	Detector Dynamic Range.....	5-14
5.3.3	Frequency Stability.....	5-15
5.3.4	Frequency Step Accuracy.....	5-17
5.4	SYSTEM LINK BUDGET AND IF GAIN DISTRIBUTION.....	5-18
5.4.1	System Link Budget.....	5-18
5.4.2	Receiver IF Gain Distribution.....	5-25
5.5	SYSTEM CALIBRATION DISCUSSION.....	5-30
5.5.1	Summary.....	5-30
5.5.2	Monostatic and Bistatic Calibration Models.....	5-30
5.5.2.1	Monostatic Model.....	5-30
5.5.2.2	Bistatic Model.....	5-32
5.5.3	Calibrated vs Uncalibrated Performance.....	5-33
5.5.3.1	Measurements with HP8510.....	5-33
5.5.3.2	Measurements with mmW T/R Modules.....	5-37
5.5.3.3	Conclusions.....	5-46
5.5.4	Frequency Response of Error Terms.....	5-46
5.6	SYSTEM ERROR BUDGET.....	5-48
6.0	MECHANICAL DESIGN AND ANALYSIS.....	6-1
6.1	PACKAGING.....	6-1
6.2	THERMAL ANALYSIS.....	6-1
6.3	STRUCTURAL ANALYSIS AND DESIGN.....	6-5
7.0	TEST DATA AND DISCUSSION.....	7-1
7.1	SUMMARY.....	7-1

TABLE OF CONTENTS

<u>SECTION</u>	<u>PAGE</u>
7.2	DYNAMIC RANGE MEASUREMENTS.....
7.2.1	Absolute Signal Levels.....
7.2.2	Normalized Signal Levels.....
7.3	AMPLITUDE MEASUREMENT ACCURACY.....
7.3.1	Summary.....
7.3.2	Reference Signal Amplitude.....
7.3.3	Normalized Test Signal Amplitude.....
7.3.3.1	Band-A Test Signal Amplitude Results.....
7.3.3.2	Band-B Test Signal Amplitude Results.....
7.3.3.3	Band-C Test Signal Amplitude Results.....
7.3.3.4	Band-D Test Signal Amplitude Results.....
7.3.3.5	Conclusions and Recommendations.....
7.4	TARGET STANDOFF DISTANCE ACCURACY.....
7.4.1	Band-A Standoff Distance Results.....
7.4.2	Band-B Standoff Distance Results.....
7.4.3	Band-C Standoff Distance Results.....
7.4.4	Band-D Standoff Distance Results.....
7.4.5	Conclusions and Recommendations.....
8.0	CONCLUSIONS.....
9.0	REFERENCES.....

APPENDICES

APPENDIX A: T/R MODULES

- A1. T/R MODULE REPORTS
- A2. BAND-D MIXER SUMMARY
- A3. ISOCORE COAXIAL CABLE SUMMARY

APPENDIX B: SYSTEM ANALYSIS

- B1. GEORGIA TECH RESEARCH INSTITUTE REPORT
- B2. PLASMA EFFECTS
- B3. VEC ANALYSIS AND DATA SUMMARY

APPENDIX C: TEST SETUP DOCUMENTATION

APPENDIX D: LIST OF RELATED DOCUMENTS AND INTERFACE INFORMATION

- D1. PARTS LISTS FOR TRANSMIT/RECEIVE ASSEMBLY AND DETECTOR ASSEMBLY
- D2. RELATED DOCUMENTS AND INTERFACE INFORMATION

LIST OF FIGURES

<u>FIGURE</u>	<u>PAGE</u>
1-1 Block diagram of basic MRIS instrument design.....	1-3
1-2 Integrated Transmit/Receive Assembly showing T/R Modules and IF circuit.....	1-5
1-3 Integrated Transmit/Receive Assembly showing antenna subassemblies.....	1-6
1-4 Integrated Detector Assembly IF section.....	1-7
1-5 Integrated Transmit/Receive Assembly, Detector Assembly, and Ground Support Equipment used for preliminary system testing at EMS.....	1-8
2-1 Graph of Critical Electron Density versus interrogating frequency.....	2-6
3-1 Final block diagram of MRIS instrument.....	3-2
3-2a Block diagram of Band-A T/R Module ($f_c = 20$ GHz).....	3-5
3-2b Block diagram of Band-B T/R Module ($f_c = 44$ GHz).....	3-6
3-2c Block diagram of Band-C T/R Module ($f_c = 95$ GHz).....	3-7
3-2d Block diagram of Band-D T/R Module ($f_c = 140$ GHz).....	3-8
3-3a Test data for the SP4T IF switch used in the Transmit/Receive Assembly.....	3-11
3-3b Measured gain of the SP8T IF switch and IF amplifier used in the Transmit/Receive Assembly.....	3-12
3-4a Diagram of MRIS antenna subassembly (20 and 140 GHz).....	3-14
3-4b Diagram of MRIS antenna subassembly (44 and 95 GHz).....	3-15
3-5 Layout of Detector Assembly IF section.....	3-20
3-6 Block diagram of the MRIS Ground Support Equipment (GSE) hardware.....	3-24
4-1 Simplified reflection model for MRIS operation.....	4-3
4-2 Time delays for reflected signals predicted from simplified reflection model.....	4-4
4-3 Example test data demonstrating interference reflection independence from target distance of (a) 1.5 inches, (b) 6 inches, and (c) 12 inches.....	4-5

LIST OF FIGURES (Continued)

<u>FIGURE</u>		<u>PAGE</u>
4-4	Calculated values of $\delta\theta$ and δR versus the signal-to-interferer ratio.....	4-8
4-5	Example test data demonstrating ability of vector subtraction to remove close-in reflections (a) no error correction and (b) with vector subtraction.....	4-11
4-6	Vibration regimen used to test mmW mixers and Gunn Oscillators.	4-16
4-7	Depiction of alternate diode used for 140-GHz mixers.....	4-17
4-8	Predicted plasma attenuation versus distance at the center frequencies of the four MRIS operating bands.....	4-20
5-1	Generalized block diagram of stepped-FMCW approach used in the MRIS instrument.....	5-2
5-2	Example inverse-FFT showing effects of zero-filling 64-point sample to 1024 points to achieve improved interpolation in time-domain.....	5-5
5-3	Results of time delay measurements using 4032-MHz sweep bandwidth during preliminary system bistatic Band-B testing at EMS.....	5-9
5-4	Dynamic range requirements for Band-D operation.....	5-13
5-5	Calibrated Test/Reference Log Magnitude vs Distance Data for the four bands with and without the TPS tile over the antennas (a) Band-A, (b) Band-B, (c) Band-C, and (d) Band-D.....	5-21
5-6a	Final MRIS System Link Budget.....	5-22
5-6b	Notes for final MRIS System Link Budget.....	5-23
5-7	Final MRIS receiver IF gain distribution.....	5-29
5-8a	Time delays measured in Band-A using the HP8510 network analyzer: (i) with system calibration and (ii) without system calibration.....	5-34
5-8b	Time delays measured in Band-B using the HP8510 network analyzer: (i) with system calibration and (ii) without system calibration.....	5-35
5-9	Time delays measured using the Band-A T/R Module: (a) without system calibration and (b) with system calibration.....	5-38
5-10	Dispersion calculations for waveguide interconnecting lengths used in MRIS instrument.....	5-39

LIST OF FIGURES (Continued)

<u>FIGURE</u>		<u>PAGE</u>
5-11a	Uncalibrated Band-A time domain response showing significant spreading of target return due to waveguide dispersion.....	5-41
5-11b	Uncalibrated Band-B time domain response showing minimal spreading of target return due to waveguide dispersion.....	5-42
5-11c	Uncalibrated Band-C time domain response showing minimal spreading of target return due to waveguide dispersion.....	5-43
5-12	Comparison of dispersion effects for (a) short circuit directly at Band-A T/R Module waveguide port and (b) short circuit at end of Band-A module-to-antenna waveguide.....	5-44
5-13	Time domain data demonstrating (a) significant effects of dispersion in four Band-A sub-bands and (b) minimal effects of dispersion in four Band-C sub-bands.....	5-45
5-14	Example time delay plots for Band-B tests (a) without calibration and (b) with calibration.....	5-47
5-15a	Final System Error Budget for the Reference Signal Power.....	5-49
5-15b	Final System Error Budget for the Test Signal Power.....	5-50
5-15c	Final System Error Budget for the Target Standoff Distance.....	5-51
6-1a	Diagram of Transmit/Receive Assembly showing plan view of antennas.....	6-2
6-1b	Diagram of Transmit/Receive Assembly showing sectional view of Mux-Telemetry Board and IF components.....	6-3
6-1c	Diagram of Transmit/Receive Assembly showing plan sectional view of T/R Modules.....	6-4
7-1a	Maximum Test Signal and Reference Signal output voltage data for Band-A: (i) frequency domain data and (ii) time domain data.....	7-3
7-1b	Maximum Test Signal and Reference Signal output voltage data for Band-B: (i) frequency domain data and (ii) time domain data.....	7-4
7-1c	Maximum Test Signal and Reference Signal output voltage data for Band-C: (i) frequency domain data and (ii) time domain data.....	7-5
7-1d	Maximum Test Signal and Reference Signal output voltage data for Band-D: (i) frequency domain data and (ii) time domain data.....	7-6

LIST OF FIGURES (Continued)

<u>FIGURE</u>		<u>PAGE</u>
7-2a	Normalized dynamic range data for Band-A: (i) frequency domain data and (ii) time domain data.....	7-9
7-2b	Normalized dynamic range data for Band-B: (i) frequency domain data and (ii) time domain data.....	7-10
7-2c	Normalized dynamic range data for Band-C: (i) frequency domain data and (ii) time domain data.....	7-11
7-2d	Normalized dynamic range data for Band-D: (i) frequency domain data and (ii) time domain data.....	7-12
7-3	Example time domain plots showing peak target return signal for target located 4.0 inches from TPS tile surface: (a) Band-A and (b) Band-C.....	7-16
7-4a	Examples of measured test signal amplitude versus target distance data for Band-A operation without vector error correction.....	7-17
7-4b	Measured test signal amplitude versus target distance data for Band-A operation (i) with vector subtraction and (ii) with VEC-7.....	7-18
7-5a	Examples of measured test signal amplitude versus target distance data for Band-B operation without vector error correction.....	7-20
7-5b	Measured test signal amplitude versus target distance data for Band-B operation (i) with vector subtraction and (ii) with VEC-7.....	7-21
7-6a	Examples of measured test signal amplitude versus target distance data for Band-C operation without vector error correction.....	7-22
7-6b	Measured test signal amplitude versus target distance data for Band-C operation (i) with vector subtraction and (ii) with VEC-7.....	7-23
7-7a	Examples of measured test signal amplitude versus target distance data for Band-D operation without vector error correction.....	7-24
7-7b	Measured test signal amplitude versus target distance data for Band-D operation (i) with vector subtraction and (ii) with VEC-7.....	7-25

LIST OF FIGURES (Continued)

<u>FIGURE</u>		<u>PAGE</u>
7-8a	Measured time delay versus target distance for Band-A without vector error correction (i) absolute time delay versus distance and (ii) time delay deviation from ideal free-space delay.....	7-28
7-8b	Measured time delay deviations for Band-A (i) with vector subtraction and (ii) with VEC-7.....	7-29
7-9a	Measured time delay versus target distance for Band-B without vector error correction (i) absolute time delay versus distance and (ii) time delay deviation from ideal free-space delay.....	7-30
7-9b	Measured time delay deviations for Band-B (i) with vector subtraction and (ii) with VEC-7.....	7-31
7-10	Band-C measured time delay vs target distance without VEC (a) initial tests in September 1991 and (b) follow-up tests in November 1991.....	7-33
7-11a	Example Band-C test data measured without vector error correction at a target distance (i) 2.00 inches and (ii) 2.01 inches.....	7-36
7-11b	Example Band-C test data measured without vector error correction at a target distance (i) 2.02 inches and (ii) 2.03 inches.....	7-37
7-11c	Example Band-C test data measured without vector error correction at a target distance (i) 2.04 inches and (ii) 2.05 inches.....	7-38
7-11d	Example Band-C test data measured without vector error correction at a target distance (i) 2.06 inches and (ii) 2.07 inches.....	7-39
7-11e	Example Band-C test data measured without vector error correction at a target distance (i) 2.08 inches and (ii) 2.09 inches.....	7-40
7-11f	Example Band-C test data measured without vector error correction at a target distance (i) 2.10 inches and (ii) 2.11 inches.....	7-41
7-11g	Example Band-C test data measured without vector error correction at a target distance (i) 2.12 inches and (ii) 2.13 inches.....	7-42
7-11h	Example Band-C test data measured without vector error correction at a target distance (i) 2.14 inches and (ii) 2.15 inches.....	7-43

LIST OF FIGURES (Continued)

<u>FIGURE</u>	<u>PAGE</u>
7-12 Measured time delay deviations for Band-C (a) with vector subtraction and (b) with VEC-7.....	7-46
7-13a Measured time delay for Band-D without vector error correction: (i) round trip delay and (ii) time delay deviations.....	7-47
7-13b Measured time delay deviations for Band-D (i) with vector subtraction and (ii) with VEC-7.....	7-48
B1-1 MRIS delays for phase noise analysis.....	B1-2
B1-2 Block diagram for phase noise analysis.....	B1-4
B1-3 Phase noise for COHO, DTO, and mm-wave oscillators.....	B1-5
B1-4 Correlation factor for different delays.....	B1-6
B1-5 Phase noise with correlation factor weighting.....	B1-7
B2-1 Response versus range for the no-plasma case.....	B2-5
B2-2 Response versus range for the plasma case (linear profile, 0 to $6 \times 10^{12} \text{ cm}^{-3}$).....	B2-6
B2-3 Response versus range for the plasma case (linear profile, $3 \times 10^{12} \text{ cm}^{-3}$ to $6 \times 10^{12} \text{ cm}^{-3}$).....	B2-8
B2-4 Relative dielectric constant versus range for the plasma case..	B2-9
B2-5 Response versus range for different correction techniques (plasma from Figure B2-4).....	B2-10
B2-6 Indicated range versus plasma offset range for different correction techniques (plasma from Figure B2-4).....	B2-12
B2-7 Relative dielectric constant versus range of plasma case (linear profile, $3 \times 10^{12} \text{ cm}^{-3}$ to $6 \times 10^{12} \text{ cm}^{-3}$).....	B2-13
B2-8 Response versus range for different correction techniques (plasma from Figure B2-7).....	B2-14
B2-9 Indicated range versus plasma offset range for different correction techniques (plasma from Figure B2-7).....	B2-15
B3-1 Time domain plot of ρ_{LOAD} for monostatic Band-B tests.....	B3-4
B3-2 Time domain plots for monostatic Band-B tests with target located two inches from TPS tile surface (a) without vector subtraction and (b) with vector subtraction.....	B3-6

LIST OF FIGURES (Continued)

<u>FIGURE</u>		<u>PAGE</u>
B3-3	Amplitude and time delay versus distance for monostatic Band-A tests comparing performance (a) without vector error correction and (b) with vector subtraction.....	B3-8
B3-4	Dielectric-slab model used to derive basic vector error correction model used in MRIS system tests.....	B3-11
B3-5	Simulated time domain plots using dielectric slab model for target located at 10 cm (a) without vector error correction, (b) with vector subtraction, and (c) with vector error correction.....	B3-14
B3-6	Comparison of measured (simulated) target amplitudes and standoff distances versus target distance using different error correction approaches.....	B3-15
B3-7	Diagram of updated vector error correction model including lossy delay term.....	B3-17
B3-8	Comparison of time domain plots obtained in monostatic Band-B tests using (a) no error correction, (b) vector subtraction, and (c) VEC-3.....	B3-19
B3-9	Comparison of target amplitudes versus distance measured in monostatic Band-B tests using (a) no error correction, (b) vector subtraction, and (c) VEC-3.....	B3-21
B3-10	Comparison of target time delay versus distance measured in monostatic Band-B tests using (a) no error correction, (b) vector subtraction, and (c) VEC-3.....	B3-22
B3-11	Measured target amplitude and time delay versus target distance for monostatic Band-A tests using full VEC-7 model.....	B3-27
B3-12	Measured target amplitude and time delay versus target distance for bistatic Band-B tests using full VEC-7 model.....	B3-29
B3-13	Measured target amplitude and time delay versus target distance for bistatic Band-C tests using full VEC-7 model.....	B3-30
B3-14	Measured target amplitude and time delay versus target distance for bistatic Band-D tests using full VEC-7 model.....	B3-32

LIST OF TABLES

<u>TABLE</u>	<u>PAGE</u>
2-1 Measurement accuracy requirements for the MRIS instrument.....	2-8
3-1A Control commands from Detector Assembly to T/R Assembly.....	3-17
3-1B Data signals from T/R Assembly to Detector Assembly.....	3-18
5-1 Key operating parameters for the MRIS stepped-FMCW system.....	5-7
5-2 Frequency sensitivities of the MRIS T/R Modules.....	5-16
5-3 Tabulated values for range errors due to frequency step errors.	5-19
5-4 Estimated minimum and maximum signal levels at the MRIS mmW mixer input ports.....	5-24
5-5 Estimated signal-to-noise ratios for the Test Signal and Reference Signal channels.....	5-26
5-6 Estimated IF signal levels from mmW mixer outputs.....	5-27
5-7 Estimated IF levels after normalization with IF channel attenuators.....	5-28
7-1 Maximum signal level measured in each MRIS path.....	7-7
7-2 Computed delays for target returns and first multiple reflections.....	7-35
7-3 Summary of peak distance measurement errors.....	7-50
8-1A Hardware needed to configure functional MRIS test setup.....	8-2
8-1B Software needed to configure functional MRIS test setup.....	8-2
8-2A T/R assembly development status.....	8-3
8-2B Detector assembly development status.....	8-3
8-2C GSE development status.....	8-3

ACKNOWLEDGMENT

The work described in this report toward development of the Microwave Reflectometer Ionization Sensor (MRIS) was supported by personnel of (a) Electromagnetic Sciences, Inc., (b) the Millitech Corporation, (c) the Georgia Tech Research Institute, and (d) the NASA Langley Research Center. At the conclusion of the program, technical efforts at these four organizations were led by Mr. Joe Seals, Dr. Mario Simonutti, Mr. Rob Pauley, and Dr. Robert Neece, respectively. Key personnel from Electromagnetic Sciences that contributed to the MRIS effort included Mr. Jeff Fordham, Mr. Jim Gersbacher, Mr. Jim Grosch, Dr. Bill Kreutel, Mr. Jack Miller, Ms. Regina Reed, Mr. Steve Rigg, Mr. Howard Stacy, Ms. Karen Underdahl, Mr. Bill Wallace, Mr. Charles Wier, and Mr. Ron Williams. Key program personnel from Millitech were Mr. Rich Chedester and Ms. Betsy Scuderi. A key contributor from the Georgia Tech Research Institute was Mr. Jim Kurtz. Key NASA LaRC contributors included Dr. Tom Campbell, Mr. Aubrey Cross, Mr. Joe Guy (consultant), Mr. Chase Hearn, Dr. Wes Lawrence, and Dr. Rob Marshall (consultant). Valuable technical guidance and support were also received from NASA personnel of the Johnson Space Flight Center and of the Marshall Space Flight Center. Special thanks are offered to Jeff Fordham, Ron Williams, and Karen Underdahl of Electromagnetic Sciences for their dedication and hard work during the MRIS closeout effort. Great appreciation is also extended to Ms. Kathryn Franck of Electromagnetic Sciences for her efforts in preparing this report.

Respectfully Submitted,



Joe Seals

Program Manager

1.0 INTRODUCTION

This report summarizes work performed toward development of the Microwave Reflectometer Ionization Sensor during Phase 2 of NASA Contract No. NAS1-19063. The work in this report was performed for the NASA Langley Research Center in Hampton, Virginia. The primary contractor on the program was Electromagnetic Sciences, Inc. (EMS) of Norcross, Georgia. Key subcontractors on the program were the Millitech Corporation of South Deerfield, Massachusetts (millimeter-wave T/R module development) and the Georgia Tech Research Institute, a research branch of the Georgia Institute of Technology of Atlanta, Georgia (system design and analysis support).

The MRIS program began in November 1989 as a planned three-phase effort to develop a millimeter-wave instrument for evaluating the plasma field produced by the Aeroassist Flight Experiment vehicle during aerobraking. The Phase 1 design effort had been successfully completed and the Phase 2 engineering model effort was nearing completion when the MRIS development effort was halted in October 1991 due to a major de-scoping of the Aeroassist Flight Experiment. This final report focuses on providing (i) a description of the MRIS engineering model existing at the conclusion of the engineering model development effort and (ii) a review of preliminary test results obtained with the engineering model.

Prior to initiation of the MRIS contract with EMS, the concept for the MRIS instrument was investigated during a pilot study conducted by NASA personnel at the Langley Research Center. Brief summaries of this pilot study and the program phases conducted at EMS are presented below.

(a) Preliminary Phase: NASA Pilot Study

During this pilot study, theoretical analysis and laboratory investigations were conducted by NASA personnel leading to development of a double-sideband suppressed carrier (DSB-SC) approach for evaluating the plasma fields of interest. The NASA-envisioned instrument would operate at four separate frequencies within the 10 to 220 GHz millimeter-wave band. To determine the range to the target reflection, the MRIS instrument would measure the phase of the applied DSB-SC modulation. A linear sweep modulation was to be applied

during each measurement period to minimize phase errors caused by extraneous reflected signals. The design developed during this pilot study represented the starting point for efforts conducted by the MRIS development team.

(b) Phase 1: Instrument Design

Phase 1 of the contract consisted of separate Definition Study and Preliminary Design periods. The Definition Study began with the contract initiation in November 1989 and extended through the Conceptual Design Review held on NASA facilities at the Langley Research Center in Hampton, Virginia in February 1990. Key results from the Definition Study were that:

- o The three lower operating frequencies (Band-A, -B, and -C) would be 20, 44, and 95 GHz while the highest operating frequency would be 140 or 180 GHz.
- o The MRIS instrument would be divided into two separate assemblies, the Detector Assembly and the Transmit/Receive Sub-assembly. A block diagram of the basic MRIS instrument design is shown in Figure 1-1.
- o Three candidate modulation approaches were to be considered for use in the MRIS instrument (DSB-SC, stepped-FMCW, and modified stepped-FMCW).
- o A monostatic configuration was selected for the lowest operating frequency (Band-A) while bistatic configurations were selected for the three highest operating frequencies (Band-B, -C, and -D).

Following the Conceptual Design Review, the Preliminary Design period was initiated. This development period was concluded by the Preliminary Design Review held in May 1990 at facilities of Electromagnetic Sciences in Norcross, Georgia. Key results from the Preliminary Design period were that:

- o A conventional stepped-FMCW approach was selected as the baseline design based on the NASA-defined premise that plasma-induced Doppler shifts would be negligible. The sweep bandwidth for the stepped-FMCW system was established as 4 GHz.
- o The Band-D center frequency was determined to be 140 GHz based on consideration of mmW component reliability and mission science objectives.
- o The concept of vector error correction was identified as a potentially powerful tool for improving instrument performance.

(c) Phase 2: Engineering Model Development

Phase 2 of the contract focused on development of an engineering model version of the MRIS instrument. This effort ran through October 1991. Major Phase 2 accomplishments included:

MRIS BLOCK DIAGRAM

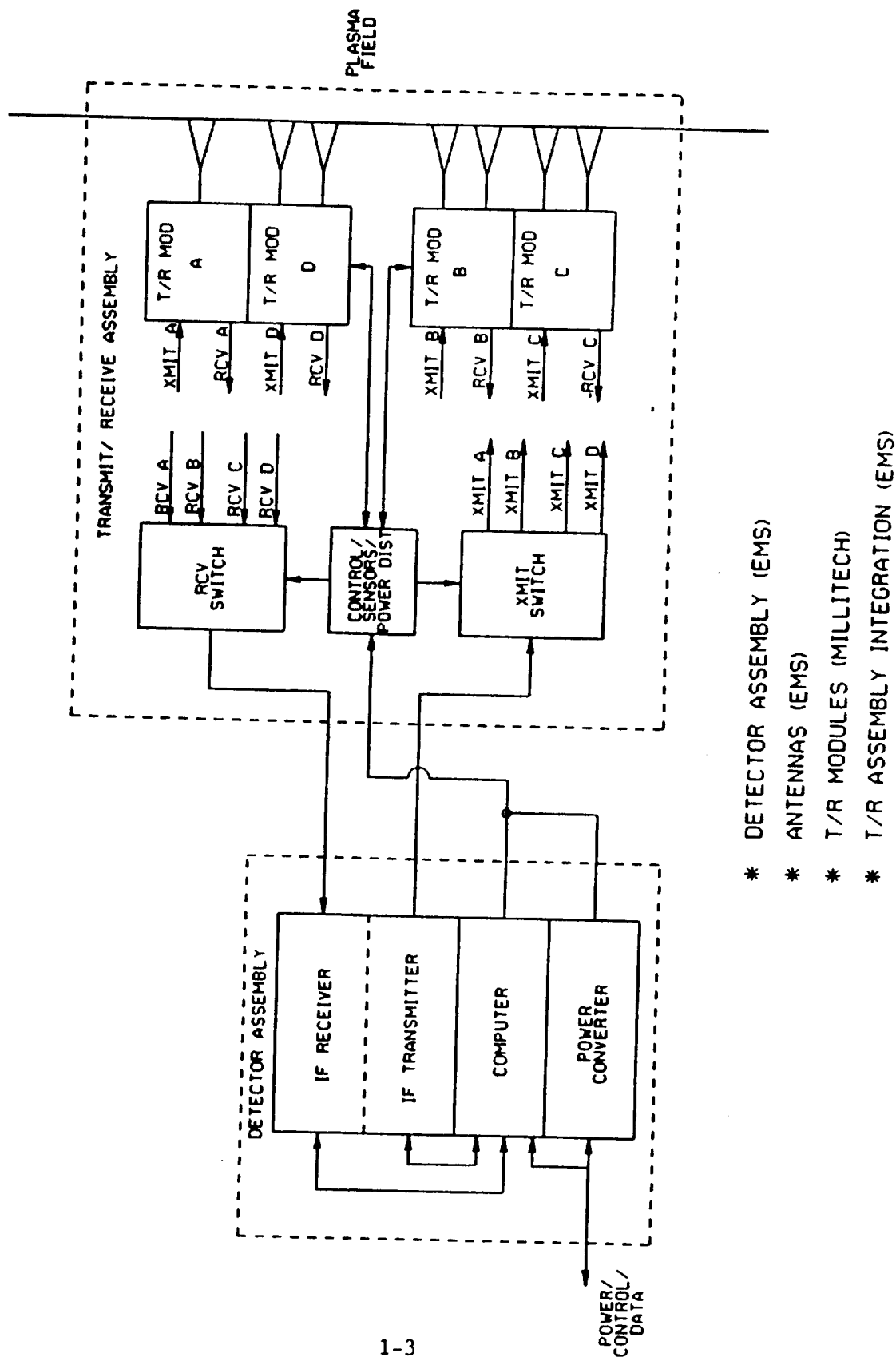


Figure 1-1. Block Diagram of Basic MRIS Instrument Design

- o Completion of the four mmW T/R modules and integration of these modules, mmW antennas, and IF circuitry into the Transmit/Receive Assembly. Photographs of the integrated Transmit/Receive Assembly are shown in Figures 1-2 and 1-3.
- o Verification of the performance of the integrated Transmit/Receive Assembly through testing with an Hewlett-Packard 8510 network analyzer system.
- o Integration and verification of the IF section of the Detector Assembly. A photograph of the completed IF section is shown in Figure 1-4.
- o Setup of a ground support equipment (GSE) test facility consisting of a stable table, motor-driven target positioner, a PC-base controller, and a NASA-furnished simulated aerobrake.
- o Integration of the Transmit/Receive Assembly with the IF section of the Detector Assembly. Preliminary testing of the integrated MRIS instrument using the GSE setup in all four operating bands. A photograph of the test setup is shown in Figure 1-5.
- o Development and implementation of several effective vector error correction approaches.

(d) Closeout Phase: Conclusion of Technical Development Effort

Beginning in October 1991, work began on closing out the MRIS program activities at EMS, Millitech, and the Georgia Tech Research Institute. Major accomplishment during this final phase included:

- o Negotiation of a contract modification for the closeout effort.
- o Delivery of all DRLs listed in the closeout contract including a complete drawing package and a GSE users manual.
- o Inventorying of all parts and equipment from EMS and Millitech. The inventoried parts were delivered to NASA LaRC in June 1992.
- o Presentation of a two-day workshop for NASA personnel at EMS to review setup and operation of the MRIS instrument in May 1992.

The closeout phase is concluded with submission of this final technical report. As noted above, this report focuses on describing the design and operation of the final instrument and on reviewing test results obtained during preliminary system testing with the final instrument.

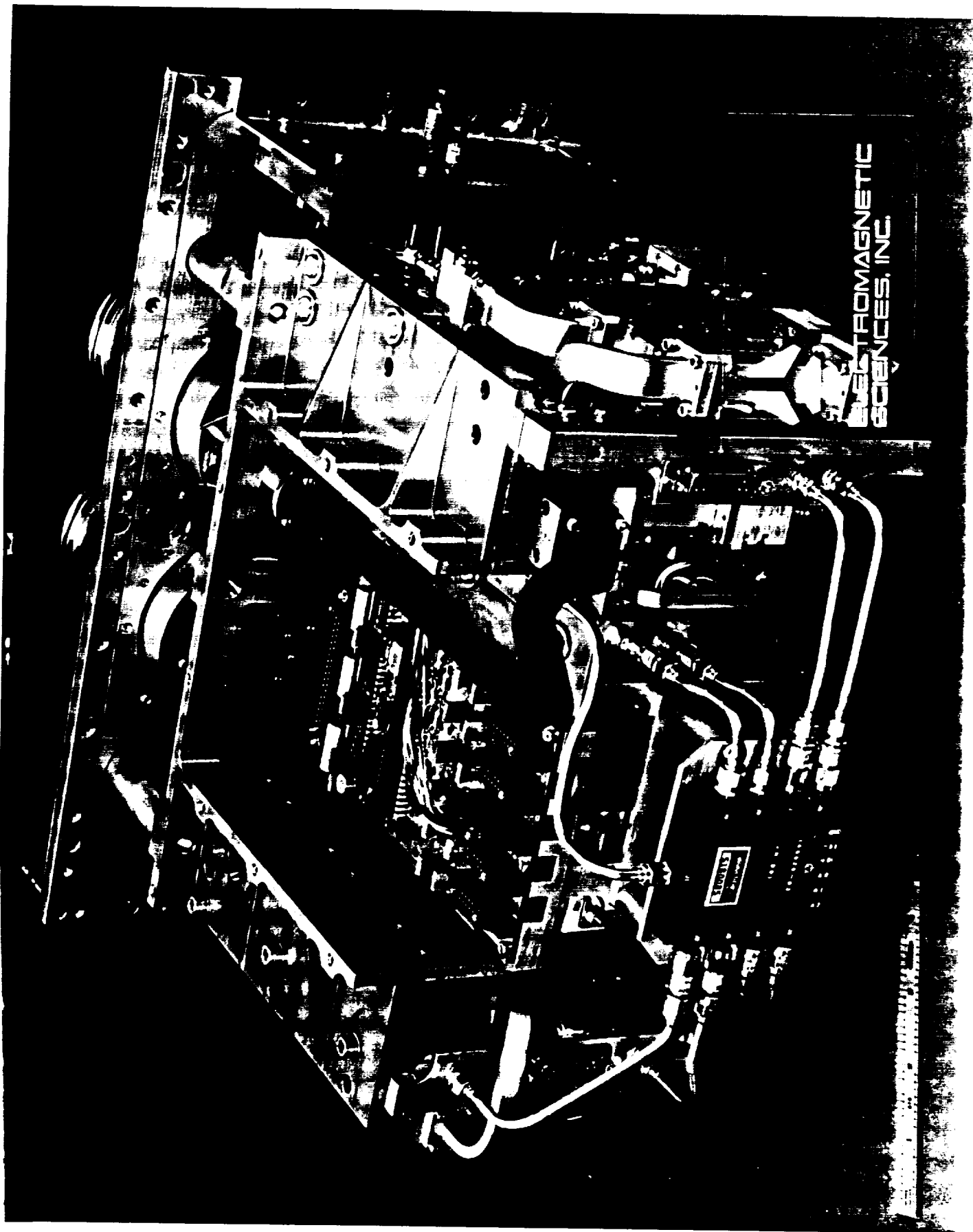


Figure 1-2. Integrated Transmit/Receive Assembly Showing T/R Modules and TP Circuit

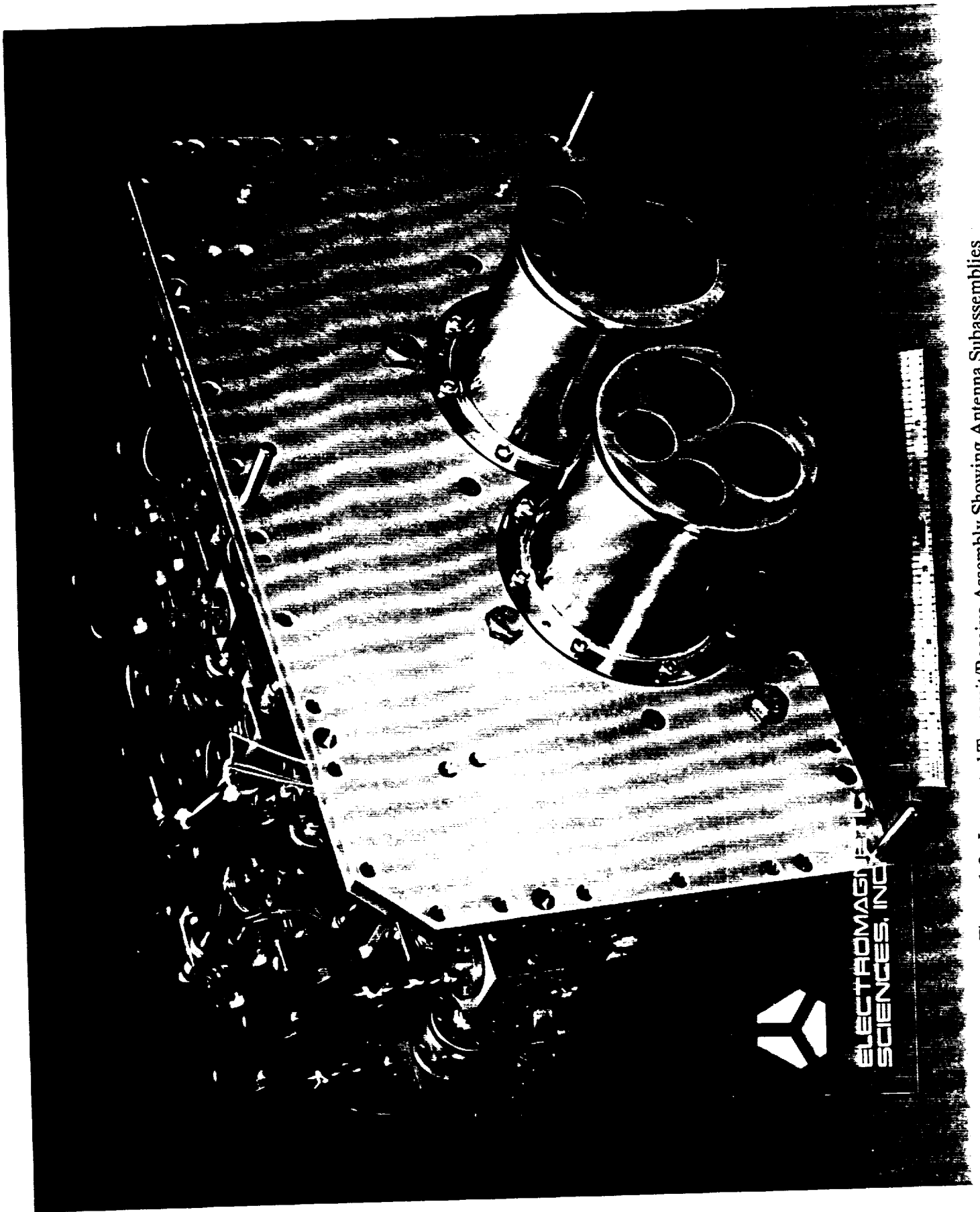


Figure 1-3. Integrated Transmit/Receive Assembly Showing Antenna Subassemblies

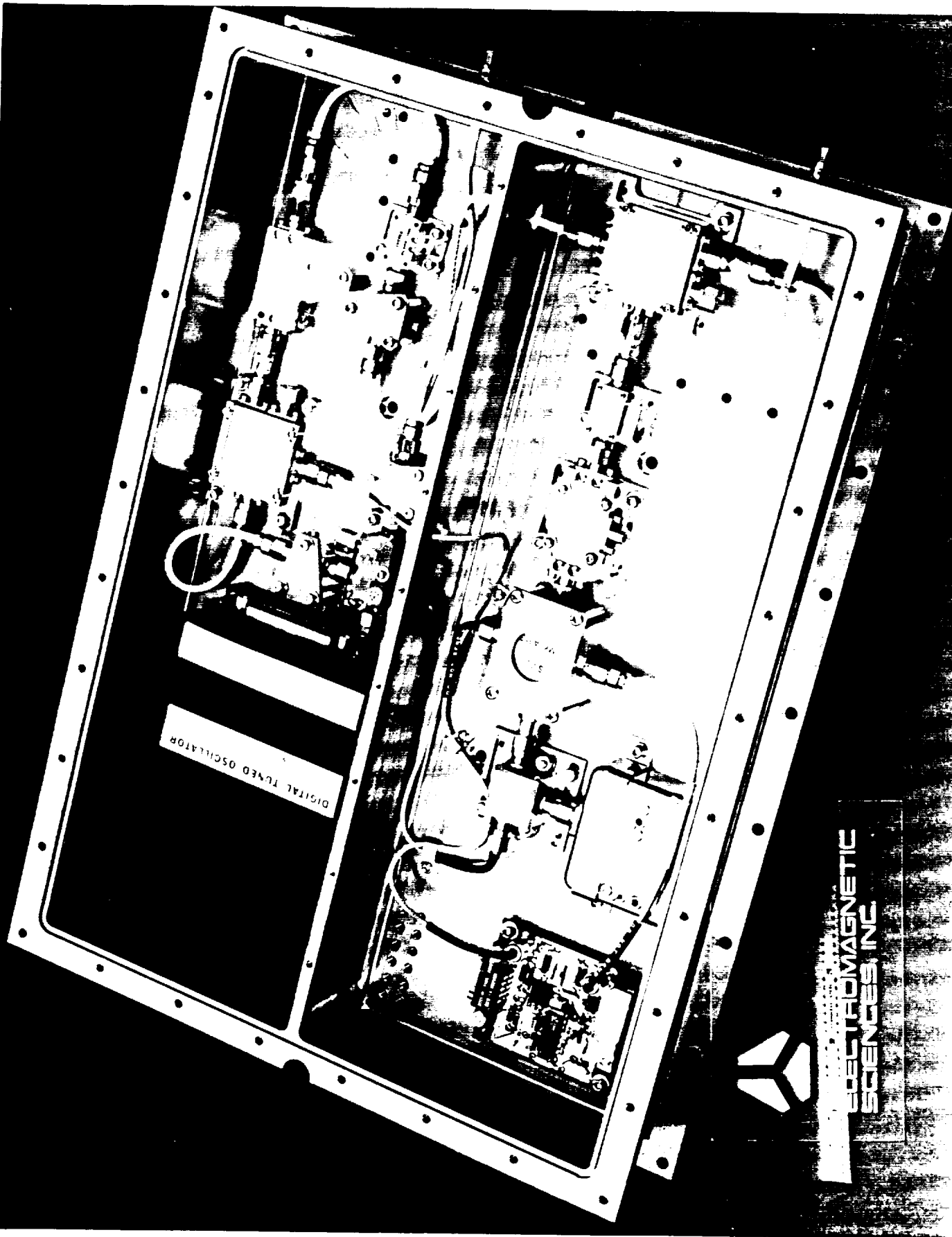


Figure 1-4. Integrated Detector Assembly IF Section

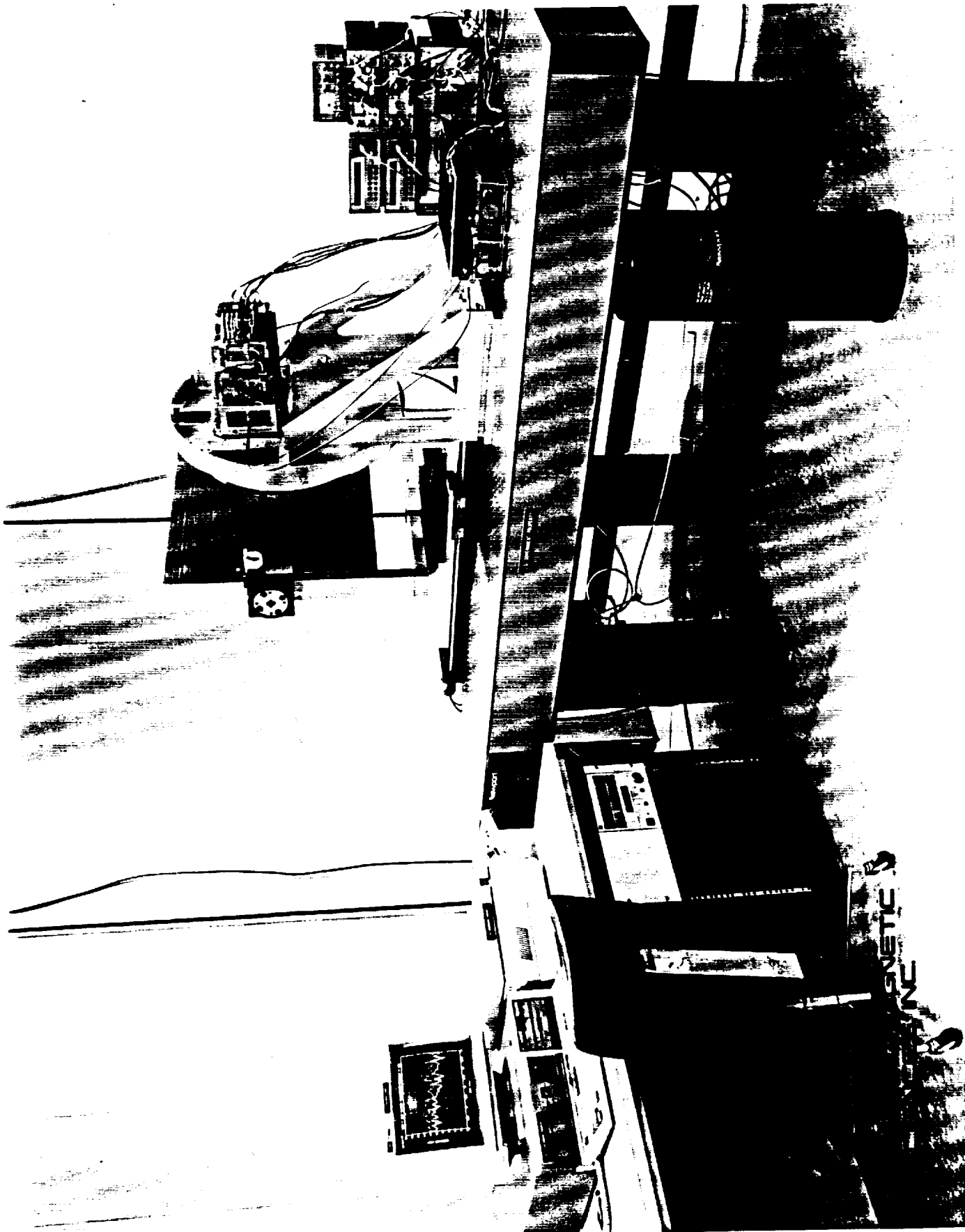


Figure 1-5. Integrated Transmit/Receive Assembly, Detector Assembly, and Ground Support Equipment used for Preliminary System Testing at EMS

2.0 BACKGROUND INFORMATION

2.1 BASIC SENSOR CONCEPT

2.1.1 General

The MRIS instrument measures data that can be used to determine the electron density profile of the plasma field that forms against the aerobrake during aeropass. To meet this objective, the instrument radiates modulated mmW signals into the plasma field then coherently detects the phase and amplitude of the reflected signals received by the instrument antennas. With appropriate ground-based signal processing, the detected phase-amplitude information can be used to estimate:

- o The onset time of the electron density producing the reflection
- o The level of the detected reflection
- o The time-delay experienced by the detected reflection during propagation to and from the reflecting plasma region.

The mmW signals propagating in the plasma field undergo near-total reflection when an electron density equal to or greater than a value denoted as the critical electron density is encountered. The critical electron density is a frequency specific effect; a mmW signal of a specific frequency will reflect at a unique electron density. Thus, the reflected signal time delay at a given mmW frequency provides a measure of the distance to a region in the plasma field having a specific electron density.

During each measurement period, the MRIS instrument operates over four separate mmW frequency bands. These bands are sufficiently narrow that reflected signals produced in each band are confined to a thin region within the plasma. This allows the distance to as many as four different electron densities to be determined during each measurement period. The resultant pairs of electron density data versus distance data represent points on the electron density profile existing during the measurement period. By taking data at designated

time intervals, a time-history of the plasma electron density profile during aeropass can be produced.

2.1.2 Simple Reflection Model

From the preceding description, it can be concluded that the MRIS instrument is a range measurement radar. In its simplest form, this type of radar consists of a continuous-wave (CW) system in which a measured phase angle (θ) is used to compute the range (R) or equivalent time delay ($\tau = 2R/v$, where $v = 3 \times 10^8$ m/s) to a single reflecting target using the relationship,

$$\theta = \omega\tau = 4\pi R/\lambda \quad (2-1)$$

The parameters λ and ω represent the wavelength of the radar signal and the angular frequency, respectively. The system output, V , is typically a phasor quantity that can be represented in the quadrature form,

$$V = \eta \cdot \exp(-j\theta) = \eta [\cos(\theta) + j\sin(\theta)] = I + jQ \quad (2-2)$$

where η accounts for cumulative losses and I and Q are DC voltages that are measured by the system processor. The desired phase angle can be obtained by computing the arctangent of the ratio Q/I . Unambiguous range measurements are possible when θ is less than 2π radians, or equivalently, when $R < \lambda/2$. This restriction is a problem at the mmW frequencies at which the MRIS instrument is to operate. This effect is shown in the table below which compares the MRIS range requirements (R_{\max}) to the unambiguous range (R_u) possible for simple CW radars.

<u>FREQ (GHz)</u>	<u>Rmax (cm)</u>	<u>Ru = $\lambda/2$ (cm)</u>
20.0	8.0	0.75
44.0	10.0	0.34
95.0	30.0	0.16
140.0	30.0	0.11

A practical method for eliminating the unambiguous range problem is to use two separate radar frequencies. If the difference between the two frequencies is

denoted Δf , a corresponding difference wavelength, $\Delta\lambda$, can be defined as $\Delta\lambda = v/\Delta f$, where v is 3×10^8 m/s. The measured phase angle is now of the form,

$$\Delta\theta = 4\pi R/\Delta\lambda \quad (2-3)$$

With appropriate demodulation, the system output using the two-frequency approach will be of the form,

$$\Delta V = \eta \cdot \exp(-j\Delta\theta) = \eta \cdot [\cos(\Delta\theta) + j\sin(\Delta\theta)] = I + jQ, \quad (2-4)$$

Unambiguous range measurements are now possible when $\Delta\theta$ is less than 2π radians or equivalently, when $R < \Delta\lambda/2$. Examples of the unambiguous range that can be achieved at several different Δf values are listed below.

<u>Δf (MHz)</u>	<u>R_{\max}</u>	<u>$R_u = \Delta\lambda/2$</u>
32.0	8.0 cm	469 cm
64.0	10.0 cm	234 cm
160.0	30.0 cm	94 cm
250.0	30.0 cm	60 cm

With this approach, the two frequencies can be transmitted sequentially or simultaneously. In the MRIS pilot study conducted at NASA, two frequencies were transmitted simultaneously using a double sideband-suppressed carrier approach. The Δf values used in the pilot studies were 160 and 250 MHz corresponding to unambiguous ranges of 94 and 60 cm, respectively. In the stepped-FMCW system developed under the current contract, multiple frequencies are transmitted serially using a frequency step size of 64 MHz. This smaller frequency step allows an unambiguous range of 234 cm to be achieved. The long unambiguous range achieved with the 64-MHz step size allows a phenomenon called multipath reflections, which are discussed later in this report, to be accommodated.

2.2 SYSTEM REQUIREMENTS

2.2.1 Operating Frequencies

The selection of operating frequencies for the MRIS instrument was impacted by several factors including (a) the electron densities of interest, (b) system considerations (surface modes at the low end of the band and plasma attenuation at the high end of the band), and (c) device reliability. Based on these factors and consultations with NASA personnel, the operating bands selected for the MRIS instrument had the following center frequencies,

- o Band-A: $f_c = 20$ GHz
- o Band-B: $f_c = 44$ GHz
- o Band-C: $f_c = 95$ GHz
- o Band-D: $f_c = 140$ GHz

The main factor impacting use of 20 GHz as the center frequency of the lowest operating band was a NASA requirement that the minimum antenna aperture be at least three wavelengths in diameter. Due to volume limitations, the largest practical antenna diameter was judged to be two inches (5.08 cm). For a two-inch aperture, the three-wavelength diameter requirement sets the lowest operating frequency at 18 GHz. Since the selected FMCW approach requires a sweep bandwidth of 4 GHz, the lowest possible operating band is 18-22 GHz, producing the center frequency of 20 GHz noted above.

The upper frequency limit was set by considerations of device reliability and receiver sensitivity. With regard to receiver sensitivity, system analysis indicated that receiver performance would become inadequate at frequencies above approximately 180 GHz, primarily due to the effects of plasma attenuation. With regard to device reliability, it was determined that the development of reliable mixers would benefit from the use of rugged beam-lead diodes. Based on previous development work at Millitech Corp., the upper frequency limit of available beam-lead diodes was estimated to be approximately 140-145 GHz. Thus, the Band-D center frequency was set to 140 GHz resulting in an operating band of 138-142 GHz. As discussed below, the

selected range of operating frequencies was found to be compatible with the science objectives of the MRIS mission.

2.2.2 Electron Densities

The selected operating bands determined the actual plasma densities that would be detected by the MRIS instrument. The NASA-provided equation describing the relationship between operating frequency and critical electron density is,

$$N_{\text{Ecr}} = 1.24 \times 10^{-8} f^2 \quad (2-5)$$

where N_{Ecr} is the critical electron density in electrons/cm³ and f is the operating frequency in Hertz.

The range of electron densities specified by NASA to be of interest for the MRIS mission was 1xE12 to 1xE15 electrons per cubic centimeter, corresponding to ideal interrogation frequencies of 8.98 to 284 GHz, respectively. A graph of N_{Ecr} versus frequency is shown in Figure 2-1. The electron density values corresponding to the actual center frequencies selected for the MRIS instrument are listed below.

- o Band-A: 4.96xE12 electrons/cm³
- o Band-B: 2.40xE13 electrons/cm³
- o Band-C: 1.12xE14 electrons/cm³
- o Band-D: 2.43xE14 electrons/cm³

Prior to the final selection of operating frequencies for the MRIS instrument, this range of electron density values were reviewed by LaRC personnel and judged to be adequate for this application.

2.2.3 Measurement Parameters

The MRIS instrument functions as a reflectometer. For each of its four operating bands, the output of the MRIS instrument at each of the 64 frequency

CRITICAL ELECTRON DENSITY VS. EM FREQUENCY

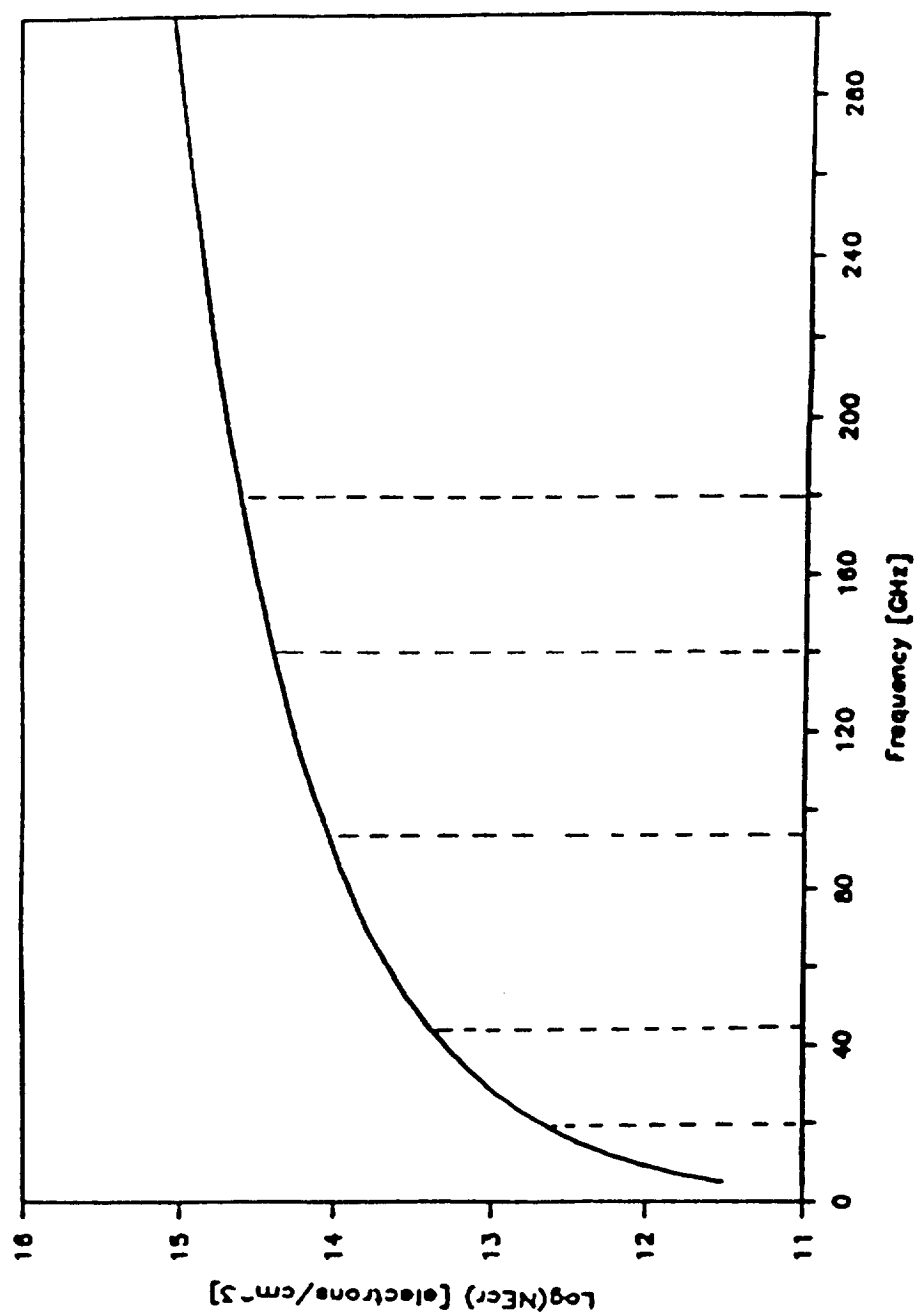


Figure 2-1. Graph of Critical Electron Density Versus Interrogating Frequency

steps consist of two In-Phase and Quadrature (I and Q) voltage pairs corresponding to a Reference Signal and Test Signal generated in each T/R module. The parameters to be determined from the measured data are listed below.

- o Transmit Signal Amplitude
- o Plasma Reflection Amplitude
- o Critical Electron Density Standoff Distance
- o Critical Electron Density Onset Time

The manner in which the MRIS instrument provides each of these parameters are as follows:

- (a) **Transmit Signal Amplitude:** The Reference Signal represents a sample of the transmit signal. Thus, the magnitude of the Reference Signal I-Q voltages can be used to determine the transmit signal amplitude noted in the parameter list above.
- (b) **Plasma Reflection Amplitude:** The Test Signal represents the summation of all reflected signals received by the T/R module. Because the various reflected signals are separated in time, the swept frequency Test Signal I-Q pairs can be inverse-FFT processed to produce a time-domain plot which permits individual reflections to be observed. Typically, the largest signal observed in the time-domain plot will correspond to the desired target reflection. The amplitude of this peak signal provides a measure of the plasma reflection amplitude. (Note: The Test Signal data is normally divided by the Reference Signal data to minimize transmitter amplitude and frequency variations.)
- (c) **Critical Electron Density Standoff Distance:** The time delay of the peak signal observed in the normalized Test Signal time-domain plot provides a measure of the standoff distance of the critical electron density producing the plasma reflection.
- (d) **Critical Electron Density Onset Time:** By logging the time at which each measurement period occurs then noting the period during which a signal peak corresponding to plasma reflection is first detected, the onset time of the critical electron density in each operating band can be determined.

2.2.4 Measurement Accuracies

During ground testing using a flat plate target, the MRIS instrument was to meet the measurement accuracies listed in Table 2-1. As discussed later in

this report, the MRIS instrument was able to meet the listed requirements during preliminary system tests performed at EMS.

TABLE 2-1
MEASUREMENT ACCURACY REQUIREMENTS FOR MRIS INSTRUMENT

DISTANCE MEASUREMENT ACCURACY

<u>BAND</u>	<u>VIRTUAL RANGE</u>	<u>ACCURACY</u>
A	0-8 cm	± 1.0 cm
B	0-5 cm	± 1.2 cm
	5-10 cm	± 1.0 cm
C	0-5 cm	± 1.5 cm
	5-30 cm	± 1.0 cm
D	4-5 cm	± 1.5 cm
	5-30 cm	± 1.0 cm

AMPLITUDE MEASUREMENT ACCURACY

<u>BAND</u>	<u>VIRTUAL RANGE</u>	<u>TEST SIGNAL</u>	<u>REFERENCE SIGNAL</u>
A	0-8 cm	± 4.0 dB	± 1.50 dB
B	0-10 cm	± 4.0 dB	± 1.50 dB
C	0-30 cm	± 4.0 dB	± 1.60 dB
D	4-10 cm	± 5.0 dB	± 1.75 dB
	10-30 cm	± 4.0 dB	± 1.75 dB

3.0 INSTRUMENT DESCRIPTION

3.1 OVERVIEW

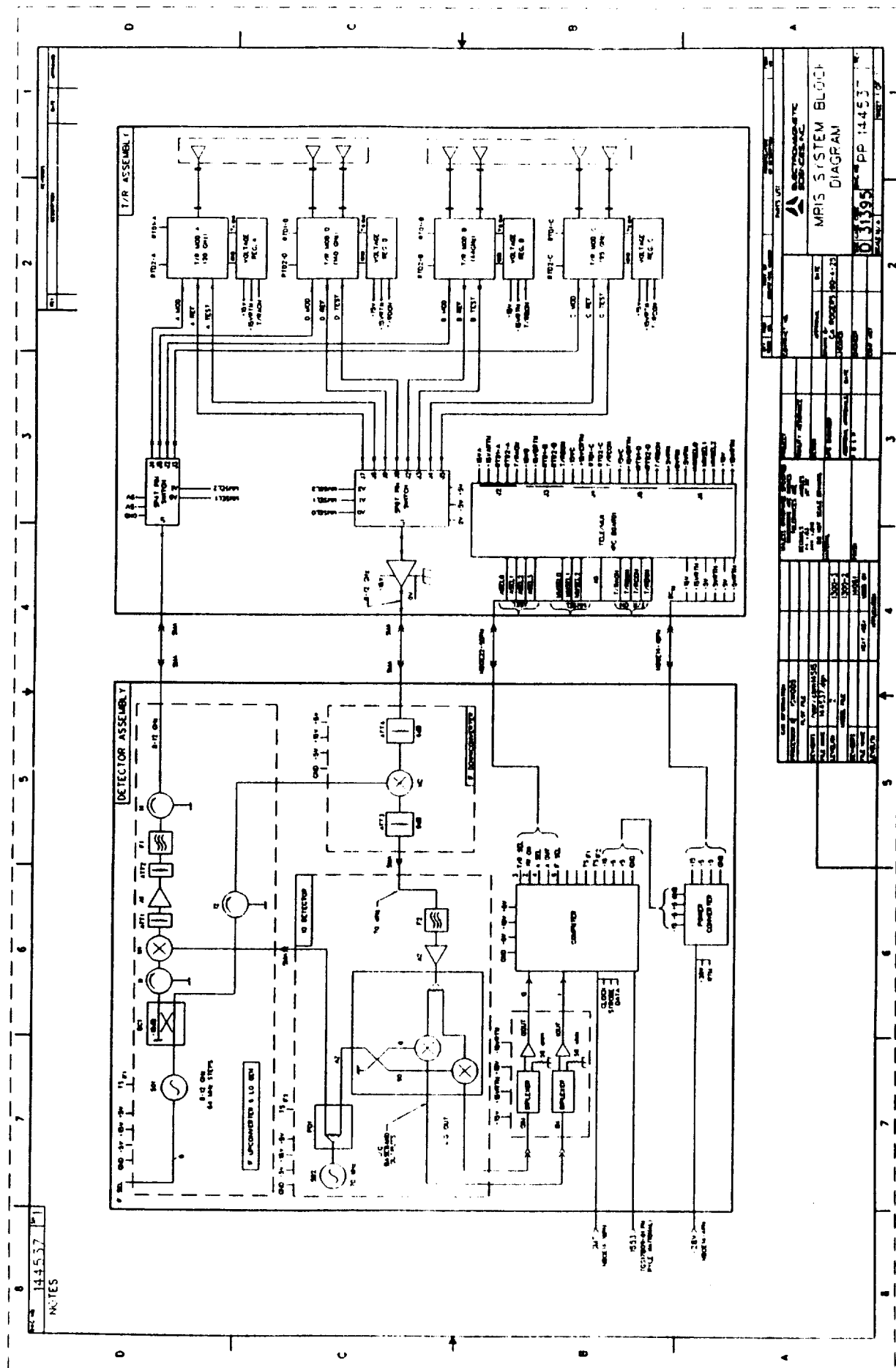
3.1.1 Development Objectives

The MRIS instrument was designed to be comprised of two assemblies, a Detector Assembly and a Transmit/Receive Assembly. A block diagram showing the internal details and interfaces of these two assemblies is shown in Figure 3-1. All mmW functions and a portion of the IF functions (switching and amplification) of the MRIS instrument are contained within the Transmit/Receive Assembly. The system processor, power converter, and remaining IF functions, including frequency sweeping, received signal amplification, and synchronous detection, are contained within the Detector Assembly. In addition to these two assemblies, EMS was tasked with developing the Ground Support Equipment (GSE) to be used to verify the performance of the completed instrument and to process data obtained during the aeropass experiment.

3.1.2 Description

In the planned design, the Detector Assembly and the Transmit/Receive Assembly are both enclosed in separate aluminum housings that mount to the aerobrake frame. The Transmit/Receive Assembly is positioned in a region behind the stagnation tile and bolts to the aluminum closeout cap. The Detector Assembly mounts approximately three feet away from the Transmit/Receive Assembly and is mounted between an intercostal and a radial stringer that are part of the aerobrake support frame.

The Detector and the Transmit/Receive Assemblies are interconnected by four cables as shown in Figure 3-1. Two of these cables are semi-rigid coaxial cables, one that carries an IF modulation signal from the Detector Assembly to the Transmit/Receive Assembly and one that carries IF output signals from the Transmit/Receive Assembly to demodulation circuitry in the Detector Assembly. The remaining two cables are multiconductor cables, one that carries DC power from the Detector Assembly to the Transmit/Receive Assembly and one that



carries commands and data between the two assemblies. To insure stable system performance, each of these four cables was to be mounted with thermally insulated brackets and shielded with appropriate thermal insulation. Details of the cable mounting and protection had not been completed when the MRIS development program was halted.

Communication and DC power was to be provided to the MRIS instrument through three multiconductor cables connected between the Detector Assembly and the AFE vehicle electronics. These cables include (a) one that provides DC power from the vehicle battery to the MRIS Instrument, (b) one that conveys commands and data via a 1533 standard interface, and (c) one that provides the MRIS instrument with a GMT clock signal for event timing.

(Note: A complete description of the connector pin-outs for the individual cables discussed above can be found in EMS Dwg. PR146623 "Detector Assembly Equipment Specification" which was delivered as part of DRL 24.)

3.2 TRANSMIT/RECEIVE ASSEMBLY

3.2.1 General

The Transmit/Receive Assembly is divided into eight subassemblies. Each subassembly mounts to a main bracket which is then enclosed by an aluminum housing. The types and quantities of the subassemblies are listed below and are discussed in the following parts of this report section.

- o T/R Modules (4)
- o Antenna Assemblies (2)
- o IF T/R Circuit (1)
- o Mux-Telemetry Board (1)

3.2.2 T/R Modules

3.2.2.1 General

There are four separate T/R Modules, one for each operating band of the MRIS

instrument. Block diagrams of the four T/R Modules, which were jointly designed by Millitech and EMS then fabricated by Millitech, are shown in Figures 3-2(a) to 3-2(d). Key functional units on each T/R Module are a single-sideband (SSB) upconverter and two downconverters. The SSB upconverters generate the mmW stepped-FMCW signals used to interrogate the plasma. The downconverters are used to produce IF signals that are detected and processed in the Detector Assembly. On each T/R Module, one downconverter produces an IF Reference signal by frequency translating a sample of the mmW transmit signal while a second downconverter produces an IF Test signal by frequency translating a sample of the received signal. The upconverter and downconverter functions are discussed in greater detail below. Each T/R Module also has its own voltage regulator. The system control electronics are designed to allow only one regulator to be activated at a time. Thus, the T/R Modules operate serially.

3.2.2.2 Upconverters

The upconverters on the T/R Modules are used to produce stepped-frequency mmW waveforms that are transmitted at the target of interest. Each upconverter has a balanced mixer which multiplies signals from a mmW local oscillator with signals from a stepped-frequency IF source. The mmW LO is provided by a fixed-frequency oscillator located onboard each T/R Module while the IF signal is provided by the companion Detector Assembly. The output of the balanced mixer contains the desired mmW transmit signal as well as an undesired image signal. The filter shown at the mixer output on each of the diagrams in Figure 3-2 is used to remove the undesired image signal. This filter also combines with the balanced operation of the mixer to suppress LO leakage.

The nominal RF, LO, and IF bands associated with the upconverter in each T/R Module are listed below. The nominal transmit power levels measured during preliminary system testing at EMS are also listed. Because the downconverters on each T/R Module use the same LO as that used in the upconverters, the frequency information listed below is also applicable to the operation of the downconverters.

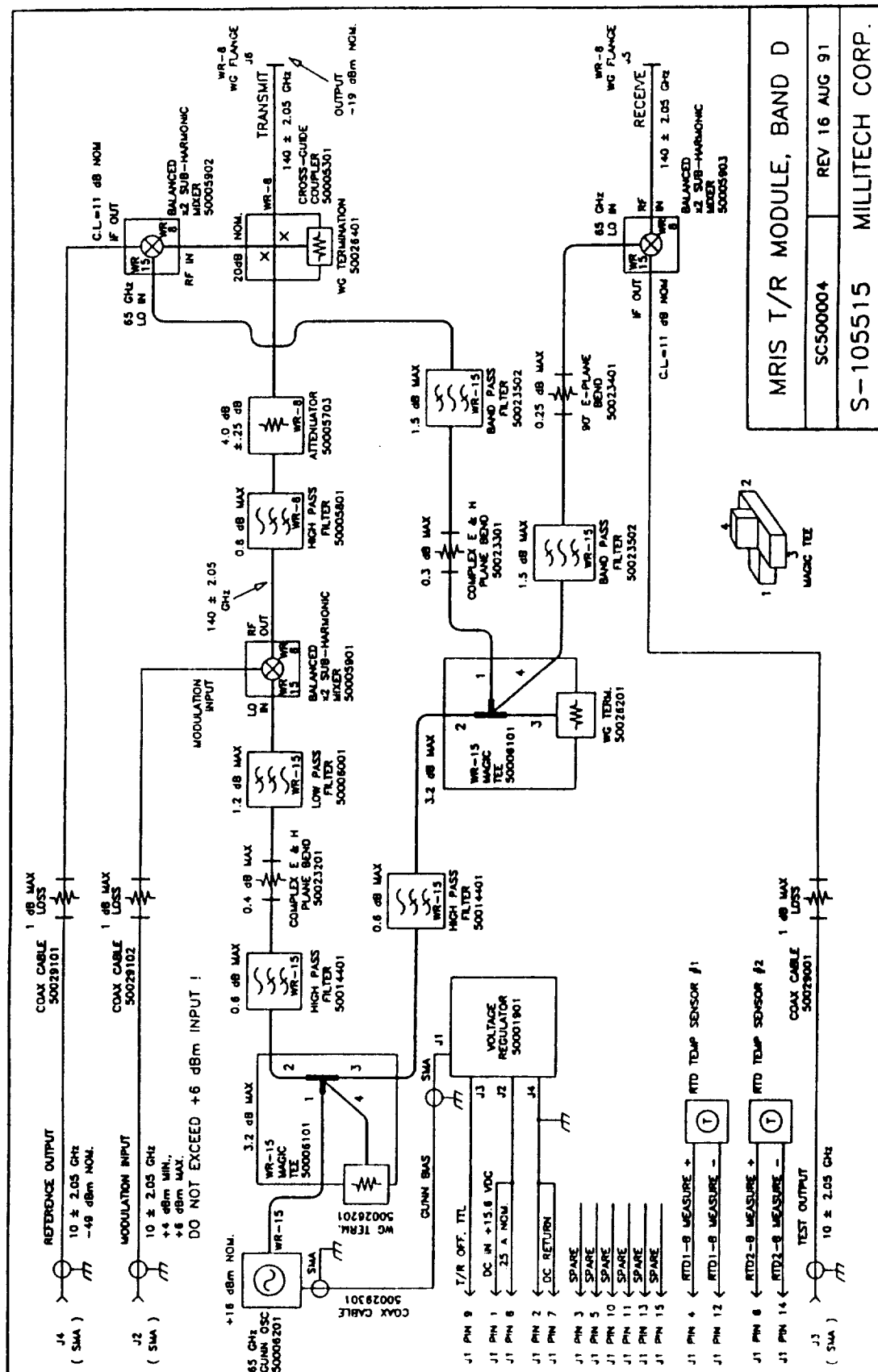


Figure 3-2(d). Block Diagram of Band-D T/R Module ($f_c = 140$ GHz)

<u>BAND</u>	<u>RF (GHz)</u>	<u>LO (GHz)</u>	<u>IF (GHz)</u>	<u>MIXING MODE</u>	<u>POUT</u>
A	20 \pm 2.016	30 GHz	10 \pm 2.016	Fund.	-22 (dBm)
B	44 \pm 2.016	34 GHz	10 \pm 2.016	Fund.	-15 (dBm)
C	95 \pm 2.016	85 GHz	10 \pm 2.016	Fund.	-11 (dBm)
D	140 \pm 2.016	65 GHz	10 \pm 2.016	Harm. (n=2)	-20 (dBm)

3.2.2.3 Downconverters

Components on each T/R Module allow the mmW transmit and receive signals to be sampled. The sampled transmit and receive signals are defined as the mmW Reference signal and mmW Test signal, respectively. The two downconverters on each T/R Module convert the mmW Reference and mmW Test signals to the required IF band. A common LO is used by the upconverters and downconverters as shown in the diagrams in Figure 3-2. In addition, de-correlation between the transmitted and received signals is negligible due to the short target distances and short interconnecting cable lengths. Therefore, the downconverted IF Reference and IF Tests signals are coherent with the IF modulation signal. This allows synchronous detection of the two IF signals to be performed in the Detector Assembly.

The noise figure of the downconverters determine the sensitivity of the individual individual Reference and Test channels. By combining the measured performances of the components in the Transmit/Receive Assembly (including the module-to-antenna waveguides), the receiver noise figure of each band can be calculated. Results from these calculations are indicated below.

<u>MRIS BAND</u>	<u>FRONT-END LOSSES (dB)</u>	<u>MIXER CONV LOSS (dB)</u>	<u>IF ATTEN (dB)</u>	<u>IF SW (dB)</u>	<u>IF AMP NF (dB)</u>	<u>RCVR NOISE FIGURE (dB)</u>
A	10.2	6.0	4.0	2.0	4.5	26.7
B	1.2	7.0	12.0	2.0	4.5	26.7
C	1.6	8.0	12.0	2.0	4.5	28.1
D	1.8	11.0	0.0	2.0	4.5	19.3

Each T/R Module has two IF output signals, an IF Reference signal and an IF Test signal. Thus, a total of eight IF signals must be transmitted to the Detector Assembly for demodulation. The IF circuitry used to perform this

task and to direct the IF modulation signal to the appropriate SSB upconverter is described in the next section of this report.

3.2.3 IF Components

IF circuitry in the Transmit/Receive Assembly includes a SP4T pin-diode switch, a SP8T pin-diode switch, and an 8-12 GHz IF amplifier. As shown in Figure 3-1, the SP4T switch is used to connect the 8-12 GHz stepped frequency signal provided by the Detector Assembly to the upconverter in the selected T/R Module. Test data for the SP4T switch installed in the MRIS instrument is shown in Figure 3-3(a). To optimize the performance of the individual upconverters, the nominal 1.5 dB loss of this switch must be accounted for in setting the IF modulation input level provided to the individual upconverters.

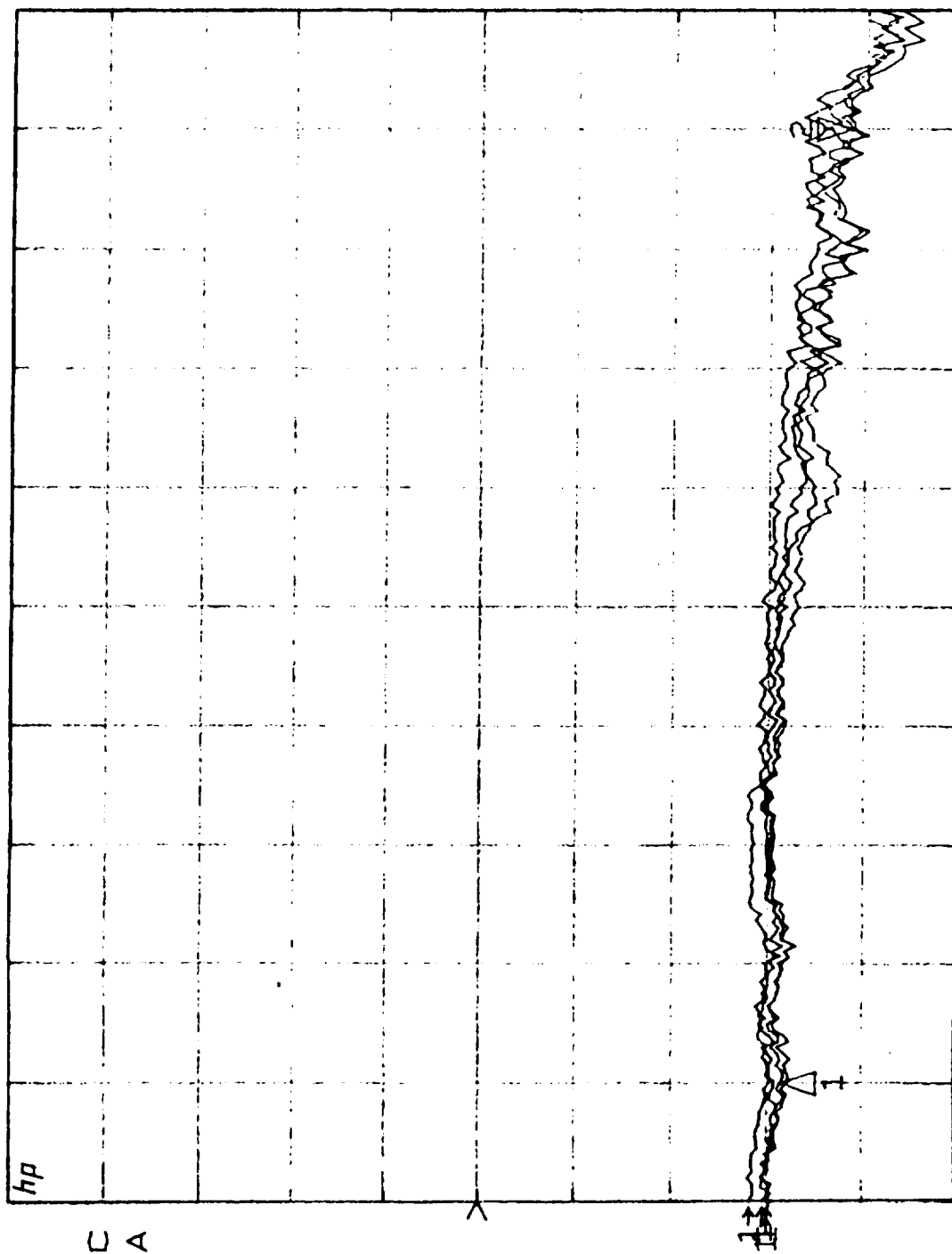
The SP8T switch is used to select either the IF Reference signal or the IF Test signal from the selected T/R Module. The nominal insertion loss through this switch is 2 dB. A 3-bit word from the MUX-Telemetry board is used to command the SP8T switch to the proper state (the upper two bits of this same word are used to command the SP4T switch to its proper state). The IF signal selected by the SP8T switch is passed to the IF amplifier which provides needed gain prior to transmission via coaxial cable to the Detector Assembly. The IF amplifier has a noise figure of 4.5 dB which contributes to the overall receiver noise figure as cited above. The gain of the IF amplifier across the 8-12 GHz band is approximately 28 dB. When combined with the 2 dB loss of the SP8T switch, the nominal loss through the switch-amplifier network should be approximately 26 dB. The measured gain through this network was found to be 26 dB as shown in Figure 3-3(b). This gain must be accounted for to properly set the IF signal level delivered to the Detector Assembly.

3.2.4 Antennas

Millimeter-wave antennas are used with each T/R Module to convert the electromagnetic energy produced by the modules from guided waves into radiated wavefronts. After reflection, the radiated wavefronts are intercepted by the antennas, converted back to guided waves, and directed to the module for down-conversion and demodulation. Each antenna is designed to perform this

S12
REF 0.0 dB
2 0.5 dB/
▽ -1.9187 dB

log MAG



START 7.500000000 GHz
STOP 12.500000000 GHz

Figure 3-3(a). Test Data for the SP4T IF Switch used in the Transmit/Receive Assembly

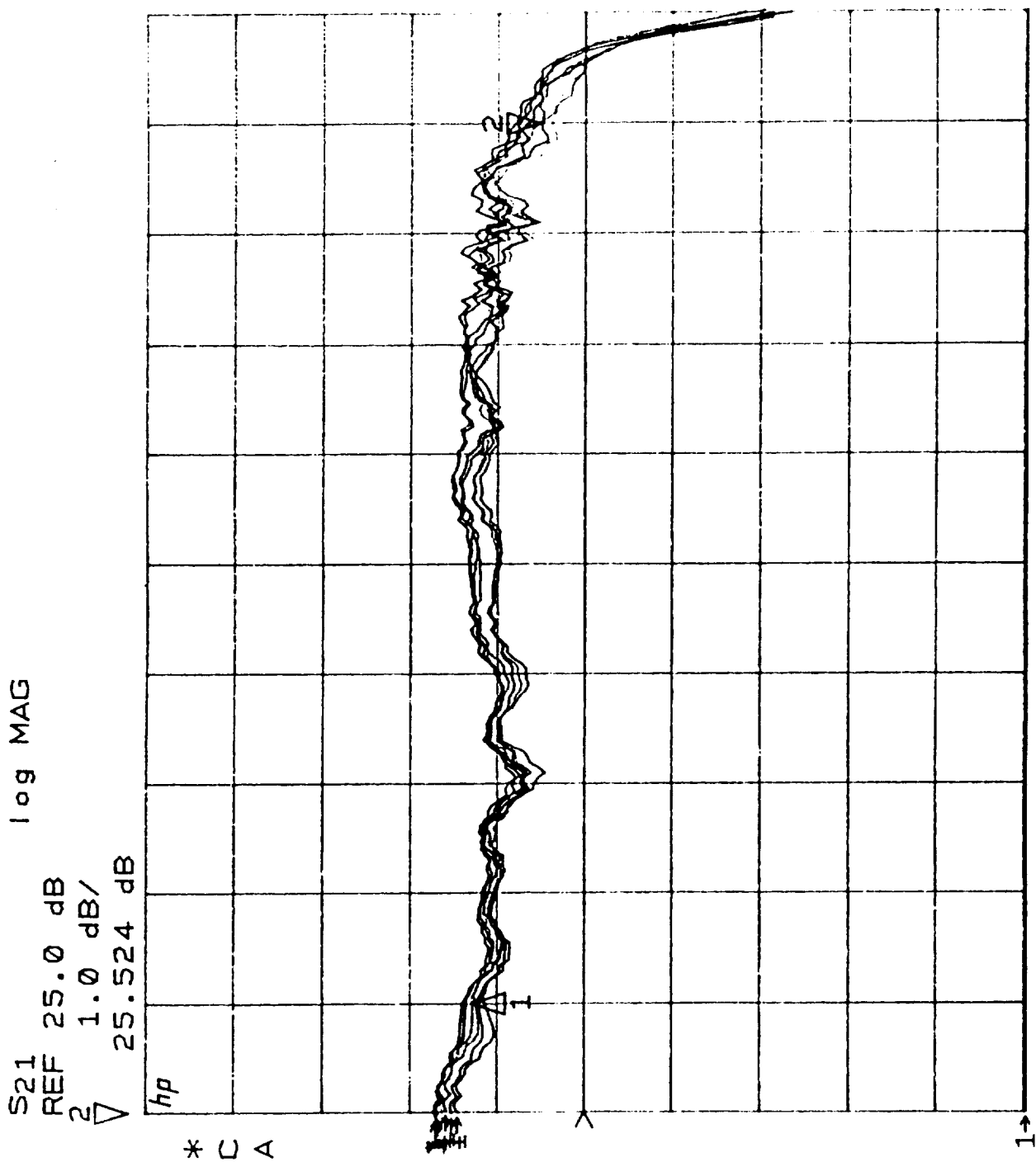


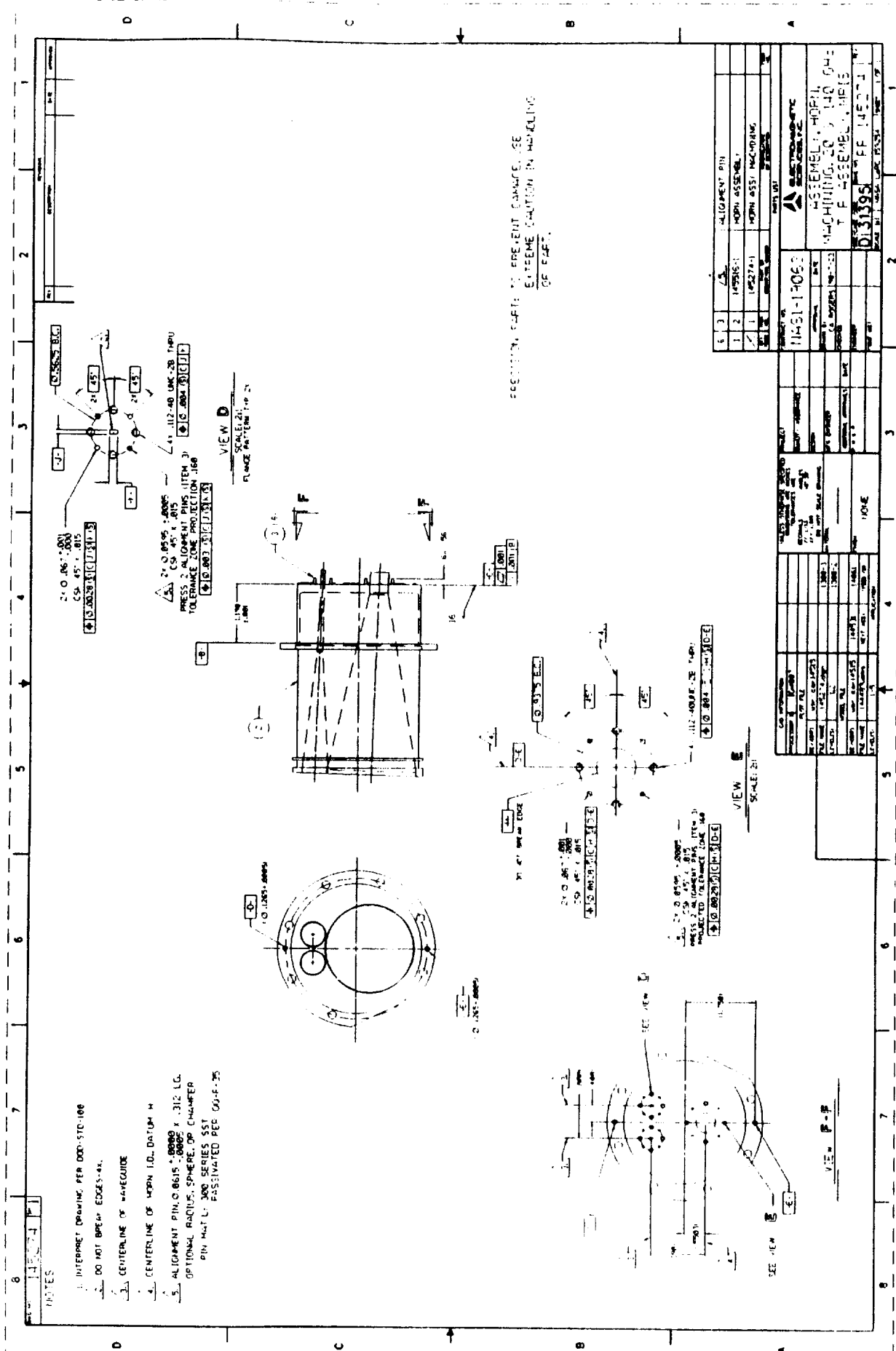
Figure 3-3(b). Measured Gain of the SP8T IP Switch and IF Amplifier used in the Transmit/Receive Assembly

function as efficiently as possible within the volume limitations of the T/R Assembly. A low phase error conical horn and a circular-to-rectangular waveguide transition is used for each antenna.

The performance of the antennas is impaired by the Thermal Protection System (TPS) tile. This tile has an outer layer of reaction cured glass (RCG) which has a moderately high dielectric constant that causes an appreciable reflected signal in all bands. In Band-B (44 GHz), -C (95 GHz), and -D (140 GHz), the tile reflection was deemed large enough to warrant using separate transmit and receive antennas (bistatic configuration) to reduce the effects of TPS tile reflections. In Band-A (20 GHz), the tile reflections were sufficiently low to allow a single antenna (monostatic configuration) to be used for both transmit and receive.

The antennas are housed in two antenna subassemblies. The Band-A antenna and the two Band-D antennas are packaged together in one antenna subassembly while the two Band-B and two Band-C antennas are packaged together in the second antenna subassembly. Each antenna subassembly consists of antennas, a lower horn support, and an upper horn support. A flange located on each lower horn support is used to attach the antenna subassemblies to the metal baseplate of the main Housing/Mounting Bracket assembly. Details of the antenna subassemblies are shown in Figures 3-4(a) and 3-4(b).

Design of the antennas requires selection of two parameters; the diameter of the antenna aperture and the antenna flare length (the length of the tapered conical section of the antenna). Design values of these parameters along with other selected information pertaining to the antennas are listed below for each of the four bands. For all bands, aperture diameters have been selected to maximize the aperture area subject to the constraints imposed by the volume available for the antennas.



<u>BAND</u>	<u>APERTURE DIAMETER</u>	<u>FLARE LENGTH</u>	<u>PHASE ERROR</u>	<u>WAVEGUIDE INTERFACE</u>
A	2.00 in. (3.4 λ)	4.2 in.	<75°	WR-42
B	1.25 in. (3.4 λ)	3.0 in.	<90°	WR-19
C	0.87 in. (3.4 λ)	3.0 in.	<90°	WR-10
D	0.70 in. (3.4 λ)	3.0 in.	<90°	WR-8

To achieve manufacturing precision, light weight, and lowered thermal conductivity, all seven antennas and associated antenna subassembly parts were manufactured from thin-walled nickel (electroforming for the antenna elements machining for the horn support elements). For the Band-B, -C and -D antennas, the required waveguide transitions were electroformed as an integral part of each antenna. The transition was manufactured as a separate assembly for the Band-A antenna. The individual parts were brazed together to form the two separate antenna subassemblies. After machining of the waveguide flange interfaces, the completed antenna subassemblies received a final gold plating.

3.2.5 MUX-Telemetry Board

The MUX-Telemetry Board provides an interface between the Transmit/Receive Assembly and the external world. As originally designed, this interface would have been to the system processor in the companion Detector Assembly. When completed, the Mux-Telemetry Board was to (a) receive and decode commands to control the T/R modules and the IF switches, (b) provide analog telemetry data, and (c) filter and distribute DC power for other components in the Transmit/Receive Assembly. The complete list of valid commands and data signals planned for the completed Mux-Telemetry Board are shown in Tables 3-1A and 3-1B. In the incomplete MRIS instrument existing when the MRIS development effort was halted, a partially completed Mux-Telemetry Board was used to control and power the two IF switches in the Transmit/Receive Assembly. The MUX/Telemetry Board was not used with the T/R Modules. Instead, the T/R Modules were directly controlled and powered from laboratory power supplies as shown in the Test Setup Documentation drawings presented in the GSE users manual (DRL 59).

TABLE 3-1A

CONTROL COMMANDS FROM DETECTOR ASSEMBLY TO T/R ASSEMBLY

T/R ON-OFF COMMAND OUTPUT FUNCTIONS

<u>T/RAON</u>	<u>T/RBON</u>	<u>T/RCON</u>	<u>T/RDON</u>	<u>FUNCTION</u>
X	X	X	0	T/R Module D Power On Command
X	X	X	1	T/R Module D Power Off Command
X	X	0	X	T/R Module C Power On Command
X	X	1	X	T/R Module C Power Off Command
X	0	X	X	T/R Module B Power On Command
X	1	X	X	T/R Module B Power Off Command
0	X	X	X	T/R Module A Power On Command
1	X	X	X	T/R Module A Power Off Command

T/R CHANNEL SELECT OUTPUT FUNCTIONS

<u>MMS2</u>	<u>MMS1</u>	<u>MMS0</u>	<u>FUNCTION</u>
0	0	0	Select Reference Channel, T/R Module B
0	0	1	Select Test Channel, T/R Module B
0	1	0	Select Reference Channel, T/R Module C
0	1	1	Select Test Channel, T/R Module C
1	0	0	Select Test Channel, T/R Module D
1	0	1	Select Reference Channel, T/R Module D
1	1	0	Select Test Channel, T/R Module A
1	1	1	Select Reference Channel, T/R Module A

TABLE 3-1B

DATA SIGNALS FROM T/R ASSEMBLY TO DETECTOR ASSEMBLY

T/R ANALOG TELEMETRY SELECT OUTPUT FUNCTIONS

AS3	AS2	AS1	AS0	FUNCTION
0	0	0	0	Select temperature sensor #1, T/R module A
0	0	0	1	Select temperature sensor #2, T/R module A
0	0	1	0	Select temperature sensor #1, T/R module B
0	0	1	1	Select temperature sensor #2, T/R module B
0	1	0	0	Select temperature sensor #1, T/R module C
0	1	0	1	Select temperature sensor #2, T/R module C
0	1	1	0	Select temperature sensor #1, T/R module D
0	1	1	1	Select temperature sensor #2, T/R module D
1	0	0	0	Select source bias voltage, T/R module A
1	0	0	1	Select source bias voltage, T/R module B
1	0	1	0	Select source bias voltage, T/R module C
1	0	1	1	Select source bias voltage, T/R module D
1	1	0	0	Spare
1	1	1	0	Spare
1	1	0	1	Spare
1	1	1	1	Spare

3.3 DETECTOR ASSEMBLY

3.3.1 General

The Detector Assembly is divided into five main subassemblies. These subassemblies are listed below.

- o IF Upconverter & LO Generator
- o IF Downconverter
- o IQ Detector & Baseband Circuit
- o Processor System Board (Computer)
- o Power Converter Board

All of these subassemblies mount into a two piece aluminum Detector Assembly housing. The IF Upconverter & LO Generator, IF Downconverter, and IQ Detector & Baseband Circuit subassemblies were completed and installed in the Detector Assembly housing and were used in system tests performed with the MRIS instrument. Summary descriptions of these three subassemblies are presented later in this section of this report. Breadboard versions of the Processor System Board and Power Converter boards were undergoing testing when the MRIS development effort was halted. However, these latter two subassemblies were never installed or operated with the remainder of the MRIS hardware. The two breadboard assemblies were included in the inventory of equipment delivered to NASA LaRC as part of the MRIS closeout effort. Specific details on these two subassemblies can be found in the Detector Assembly Equipment Specification (EMS Drawing PR146623) which was included in the drawing package delivered to NASA LaRC in fulfillment of DRL 24.

3.3.2 IF Subassemblies

The Detector Assembly portion of the MRIS block diagram in Figure 3-1 shows details of the IF Upconverter & LO Generator, IF Downconverter, and IQ Detector & Baseband Circuit subassemblies. A layout of these subassemblies in the Detector Assembly housing is shown in Figure 3-5 and a description of these subassemblies is provided below. It should be noted that the MRIS IF design allows a common IF receiver to be used to measure all the IF Reference

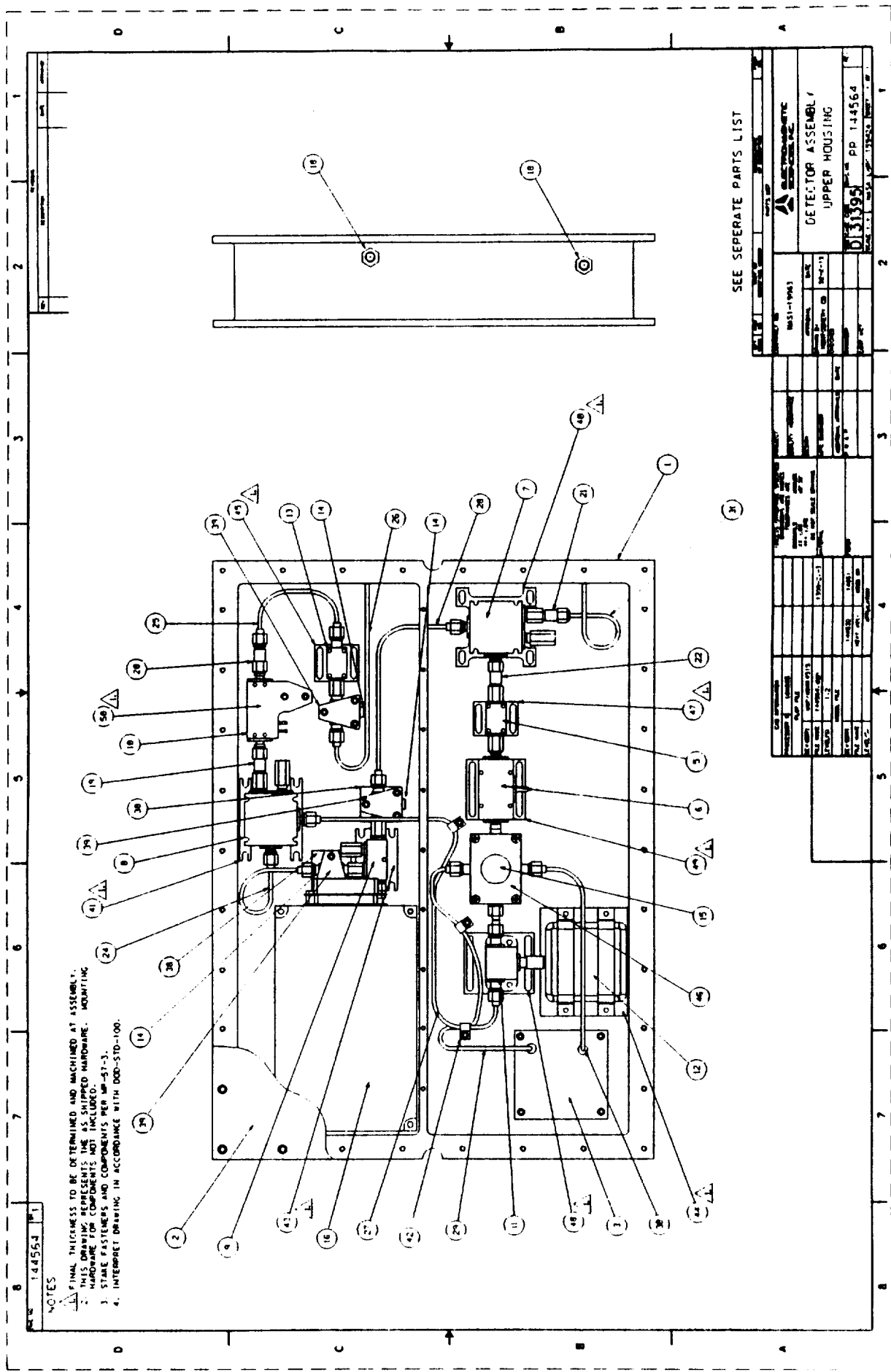


Figure 3-5. Layout of Detector Assembly IP Section

and IF Test signals produced by the T/R Modules. Specific information on the gain distribution and signal levels through the IF receiver stages is presented in Section 5 of this report.

(a) IF Upconverter & LO Generator

Two separate oscillators, an 8-12 GHz digitally tuned oscillator (DTO) and a 70-MHz crystal controlled oscillator (XCO), are used by the IF Upconverter & LO Generator subassembly. The DTO can be commanded to incrementally step from 8 to 12 GHz by appropriate commands received from the system processor while the XCO is a fixed-frequency oscillator. The output of the DTO and the XCO are both inputted into an image reject mixer which offsets the 8-12 GHz DTO signal by 70 MHz (the lower sideband was selected for this application). After appropriate filtering and amplification, the output of the image reject mixer is passed to the T/R Modules within the Transmit/Receive Assembly to permit generation of the required stepped-frequency mmW signals. A directional coupler is used to provide a portion of the DTO output to the IF Downconverter for demodulation of the IF Test and Reference signals received from the Transmit/Receive Assembly.

(b) IF Downconverter

The key component in the IF Downconverter is an image reject mixer which downconverts the received stepped-frequency IF Test and IF Reference signals. As noted above, the local oscillator used by the mixer is provided directly from the DTO. Since the frequencies of the DTO and the IF Test and Reference signals always differ by exactly 70 MHz, the mixer translates the IF input signals to a fixed frequency of 70 MHz. The 70-MHz output of the IF Downconverter is passed to the IQ Detector for amplitude-phase detection.

(c) IQ Detector & Baseband Circuit

The initial stages of this subassembly are a filter and amplifier which remove undesired mixing products and insure an adequate signal level is provided to the IQ Detector. The IQ Detector is an integrated unit that performs synchronous detection on the 70 MHz IF input signal. A coherent 70 MHz signal from the XCO is used for the local oscillator required by the IQ Detector. The output from the IQ Detector consists of two baseband DC voltages which are passed to the Baseband Circuit. The Baseband Circuit consists of a diplexor which separates the desired baseband signals from undesired mixing products from the IQ Detector. The diplexor also allows the IQ Detector to operate into a high impedance which maximizes detector sensitivity. After diplexing, the baseband signals undergo final amplification prior to being measured by an analog-to-digital converter located on the System Processor board.

3.4 GROUND SUPPORT EQUIPMENT (GSE)

3.4.1 General

Two versions of the MRIS Ground Support Equipment (GSE) should be addressed. As originally planned, the GSE was to consist of the equipment required to fully operate the completed MRIS instrument during system testing and calibration procedures. This planned version of the GSE had not been completed when the MRIS technical development effort was halted and was not completed during subsequent closeout efforts. To preserve a record of its intended design and function, this version of the GSE is described in this section of the final report. A preliminary version of the GSE was being used in system tests being performed when the MRIS technical effort was halted. This latter version of the GSE is thoroughly described in the MRIS GSE users manual (DRL 59) and is not discussed in this final report. The users manual can be consulted for further details of this version of the GSE.

3.4.2 Overview of Planned GSE Functions

When completed, the GSE was to serve as an interface to the MRIS instrument and was to perform the following functions:

- (a) Duplicate all points of electrical interface with the AFE vehicle and provide instrument power, commands, timing functions, and data transfer according to the requirements of the Interface Control Drawing ICD-02-60012.
- (b) Accept output data, monitor the status of engineering functions, and provide the means for engineering data displays, data storage and data analysis.
- (c) Provide a mobile reflective target and the associated positioning fixtures for testing the MRIS instrument's distance measurement capabilities.
- (d) Provide a stable platform for mounting and testing the MRIS instrument with the GFE.
- (e) Provide a non-contaminating, reflective target and associated fixtures for use as an effective short-circuit during ground-based calibration of the MRIS instrument.

- (f) Provide a non-contaminating, microwave absorbing target and associated fixtures for use as an effective non-reflective medium during ground-based calibration of the MRIS instrument.

To achieve the listed functions, both GSE hardware and software were to be developed by Electromagnetic Sciences, Inc. These items are discussed in the following sections.

3.4.3 GSE Hardware

The majority of the required GSE hardware was completed and delivered to NASA personnel at LaRC. A key exception is the calibration targets which were not developed. In general, the GSE hardware can be divided into two broad categories, (i) the electronic controller system and (ii) mounting/positioning hardware. The controller system consists of a PC-compatible desktop computer and its associated interface and monitoring cards. For ease of user operation and space efficiency, the controller system is designed to fit on a single work desk which was purchased for use on this program. Both the controller system and work desk were part of the overall hardware that has been delivered to NASA LaRC.

The mounting/positioning hardware consists of a stable table, a motor driven target positioner, and a mounting fixture. The mounting fixture is bolted to the stable table and accommodates mounting of the T/R Assembly and the Government furnished simulated aerobrake (GFE). The target positioner also mounts to the stable table and allows the controller system to precisely position the reflective target during system testing and calibration. The mounting/positioning hardware was also part of the overall hardware that has been delivered to NASA LaRC.

A block diagram of the GSE hardware is shown in Figure 3-6. The only power requirement for the GSE is 110 VAC with the expected AC current drain being less than 10 AMPS. Major components of the GSE hardware are described below.

(a) DC Power Supply

The GSE includes a rack mounted 200 Watt DC power supply which provides +28 VDC power to the MRIS. The power supply is current



limited and programmable from the computer for remote ON/OFF gating as well as software control of supply voltage levels. The power supply output voltage can cover the range of +24 VDC to +32 VDC required to simulate the input voltage range over which the MRIS is specified to operate.

The power supply mounts into a rack built into the lower section of the computer desk. The required 110 VAC is provided through a terminal strip built into the rack assembly. The maximum current draw of the power supply when the MRIS instrument is fully operational is three amps. The power supply contains display meters that allow the user to observe the output voltage and current levels.

(b) Computer, Monitor, and Printer

The GSE computer is a PC-compatible system with a 386DX processor and an 80387 co-processor operating at 25 MHz. Storage media consists of an 80-Megabyte hard drive, a 1.2-Megabyte 5.25-inch floppy drive, a 1.44-Megabyte 3.5-inch floppy drive, and an internal 80-Megabyte tape backup. The operating system is MS-DOS (Version 3.3) and key software packages are Turbo C++ and MATLAB (Version 3.50). Auxiliary boards in the computer include a GPIB interface card, a RS-232/RS-422 interface card, a 1553 interface board, and an eight-bit VGA graphics board. A 14-inch color monitor with 0.31-inch dot pitch and a laser printer are also part of the system. Specific functions performed by the computer include,

- o Simulating all electrical interfaces from the AFE computer via the MIL-STD-1553B serial bus.
- o Communicating with the APCU (spacecraft GSE) and the Simlab computer via the RS-422 bus.
- o Controlling the linear rail positioning table via a PC-compatible indexer.
- o Communicating with the power supply via the GPIB bus.

In addition to these communications functions, the computer performs all data analysis, data storage, and data display functions.

(c) MIL-STD-1553B Communications Card

A primary function of the GSE computer is to simulate all of the electrical interfaces from the AFE computer to the MRIS instrument. The interfaces shall satisfy the requirements of MIL-STD-1553B with all signal lines transformer isolated. To perform this serial communication from the PC to the MRIS instrument, a MIL-STD-1553B interface card was purchased and installed in the GSE computer. This card is programmed to work as an intelligent 1553B bus controller or bus monitor and provides bi-directional communication with the MRIS instrument.

As a bus controller, the 1553B interface card can command the MRIS instrument to one of several operating modes. As a bus monitor, the 1553B driver can accept both experimental and engineering data from the MRIS instrument and store this data to the GSE memory. A description of the required GSE test and calibration command modes is provided in ICD-2-60012.

Since the GSE is intended to simulate the AFE computer it was designed to accept output data from the MRIS instrument when the instrument is in its flight operating mode. A description of the output data words for the flight operating mode is provided in ICD-2-60012.

Message transmissions between the GSE and the MRIS instrument on the 1553B bus consist of one or more command, status, or data words which meet MIL-STD-1553B protocol standards.

(d) RS-422 Communications

The GSE also communicates with the APCU (spacecraft GSE) and the Simlab computer via RS-422. The format on the data transmission had not been resolved when the MRIS technical development was halted.

(e) Stable Table

A smooth surfaced, level, stable table is required for carrying the mobile positioner, MRIS fixed mount assembly, and TPS tile sample during all calibration measurements and tests. A stable table was purchased to fill this requirement. Pre-drilled holes in the stable table allow bolting on of the mounting fixture and the rail positioner.

(f) Positioner

The positioning system provides automated linear motion, as well as manual tilt adjustments in the vertical and horizontal planes. Linear motion is fully automated by means of a computer controlled stepper motor. The stepper motor is remotely controlled by the PC computer and allows the target position to be linearly varied over a range of approximately 90 cm. The positioner's minimum increment of movement is 0.00025 cm, its absolute positioning accuracy is 0.006 cm/cm, and its repeatability accuracy is 0.0005 cm. The two senses of tilt motion are controlled by manually adjusting verniers, which are connected to two independent rotary tables, to the desired setting. The vernier settings allow a minimum increment of rotation of 0.002 degrees.

(g) Target

The target is a mobile aluminum reflecting plate, 24"x24"x1/4". The reflecting surface has a flatness of 0.1 in (minimum) across the entire surface area and has a 64-microinch surface finish.

(h) MRIS Mounting Fixture and TPS Tile Fixture

A mounting fixture is required to position the MRIS instrument and TPS Tile fixture at a known location on the stable table. The TPS Tile fixture mounts to this fixture through machined angle brackets.

(i) AFE/GMT Clock Simulator

The AFE/GMT clock provides a "time-tag" for all microwave measurements taken by the MRIS instrument. The Clock Simulator duplicates this function in the GSE. The Clock Simulator was one of the hardware items that was not completed. The format of the clock output data would have been based on specifications in the MRIS ICD.

(j) Calibration Targets

Calibration targets were to be used to verify system performance during laboratory tests and after the MRIS instrument is mounted in the spacecraft. It was anticipated the calibration targets would have consisted of a family of curved reflectors that would simulate a short-circuit, offset short-circuit, and a matched load. However, requirements for the calibration targets had not been specified prior to the end of the technical development effort.

(k) Test Cables

Test cabling, necessary to join the Detector Assembly to the T/R Assembly was to be provided with the engineering model MRIS instrument. EMS personnel and personnel at the Johnson Space Center were in the process of determining specification for these cables at the time the technical development effort was halted.

3.4.4 GSE Software

The GSE software was to control the GSE equipment during all calibration and testing operations. The GSE software was to also perform all signal processing including FFT-computations and evaluation of time-domain data sets to determine target standoff distances. Completed software development was limited to that developed for the preliminary system tests performed in 1991. A complete description of the developed software can be found in the GSE users manual (DRL 59).

4.0 TECHNICAL CHALLENGES AND SOLUTIONS

4.1 GENERAL

Idealized operation of the MRIS instrument is corrupted by several factors. Based on preliminary analysis and testing performed at EMS and at LaRC, the most significant challenges facing the MRIS instrument are (a) extraneous reflected signals produced by the TPS tile and the antenna ground plane (the aluminum aerobrake skin), (b) mmW component reliability, and (c) plasma attenuation.

4.2 REFLECTIONS FROM TPS TILE AND ANTENNA GROUND PLANE

4.2.1 Interference Reflections and Multipath Reflections

The main objective of the MRIS instrument is to accurately measure the time delay experienced by the primary signal reflected by the target surface. This task is difficult because in addition to the desired target reflection, the MRIS instrument receives extraneous reflected signals caused by the Thermal Protection System (TPS) tile and the antenna ground plane formed by the aerobrake's aluminum skin. For convenience, these extraneous reflected signals, which mask the desired target reflection, have been divided into two general categories, (a) interference reflections and (b) multipath reflections.

Interference reflections are reflected signals produced solely by the TPS tile and the antenna ground plane and are considered independent of the target. Multipath reflections are portions of the primary target reflection that undergo re-reflection from some obstacle prior to being received by the MRIS instrument. Moding effects in the antennas and in the parallel plate waveguide formed between the TPS tile and the target surface, also produce additional reflected signals which can mask the primary target reflection. The levels of reflected signals due to moding are highly dependent on the characteristics of the antenna. In general, observed moding effects have been small for the low phase-error antennas used in the MRIS instrument. Therefore,

these effects are largely ignored in any analysis or modeling included in this report.

When moding effects are negligible, the simple model in Figure 4-1 can be used to conceptualize operation of the MRIS instrument. In this model, reflections occur at the following surfaces:

- o Exterior Surface of the TPS Tile (RCG Coating)
- o Target Surface (Flat Plate)
- o Antenna Ground Plane Surface (Aerobrake Skin)

There are two main time-delay periods, τ_0 and τ , in this simple model. The period τ_0 represents the round-trip delay between the antenna ground plane and the TPS tile exterior surface. The period τ represents the round-trip delay between the TPS tile surface and the target surface. When a signal is emitted from the antenna, a series of reflected signals are produced that have delays of the form,

$$\sum_{n=1}^{\infty} \sum_{m=0}^{\infty} n\tau_0 + m\tau \quad (4-1)$$

In general, the magnitude of the reflected signals is small for large m or n values. A listing of the lowest order, and hence strongest, reflected signals predicted by the model are shown in a tabular format in Figure 4-2. The following observations can be made about the individual signals listed in the table.

- (a) The signal having the time delay $\tau_0 + \tau$ makes a single round trip to and from the target and represents the primary target reflection. This is the key signal of interest to the MRIS instrument.
- (b) Signals having delays of the form $n\tau_0$ ($m=0$) represent interference reflections. Experiments indicate interference reflections are independent of the target. An example of this effect is shown in Figure 4-3 which shows nearly identical interference reflections (below 1 ns) at several different target distances.
- (c) The remaining signals represent multipath reflections and are due to target reflections which re-reflect from the TPS tile, antenna

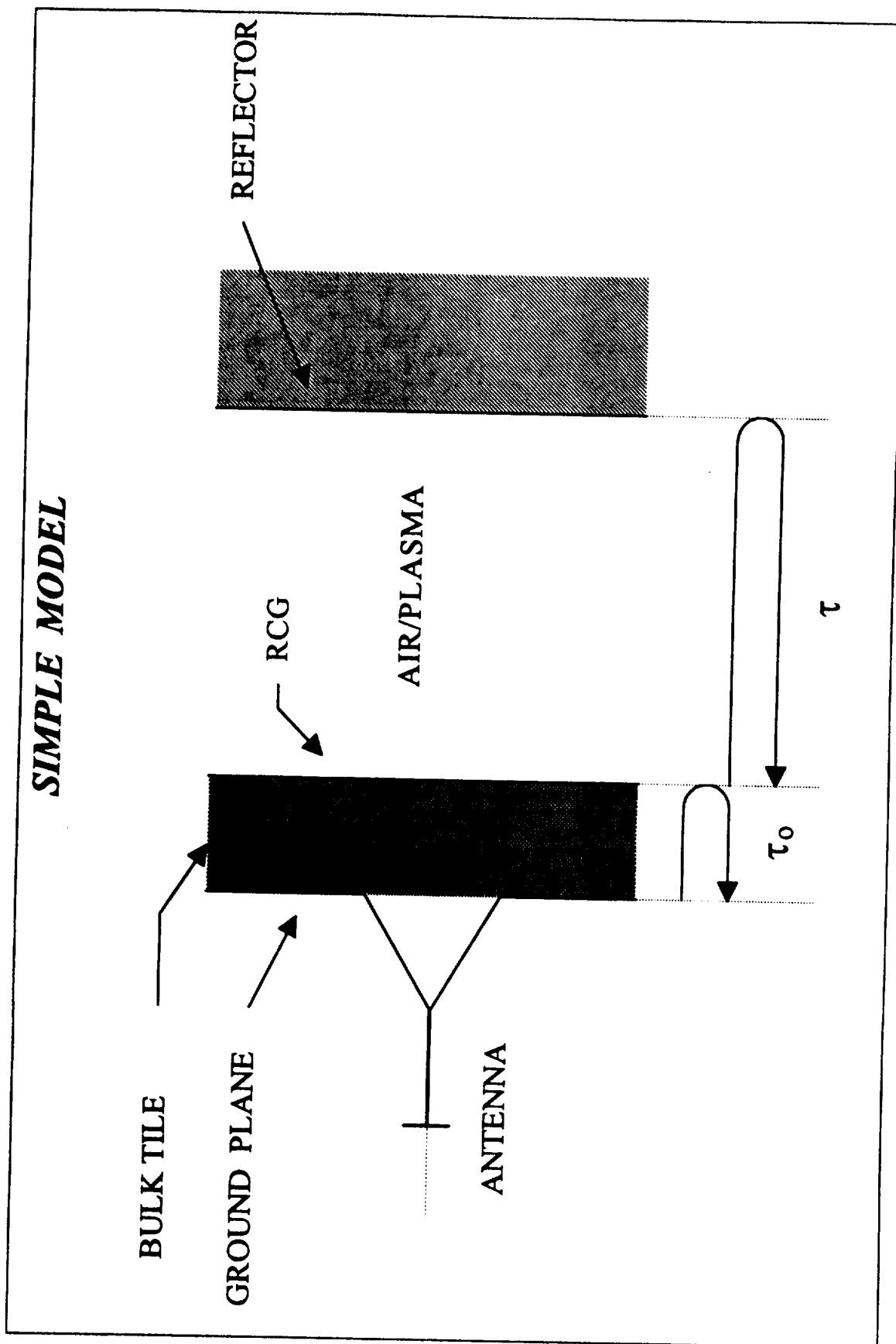


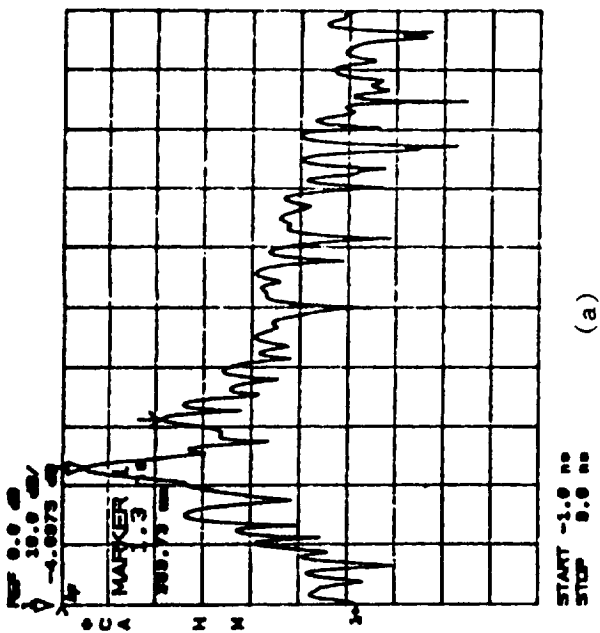
Figure 4-1. Simplified Reflection Model for MRIS Operation

TPS TILE CONSIDERATIONS

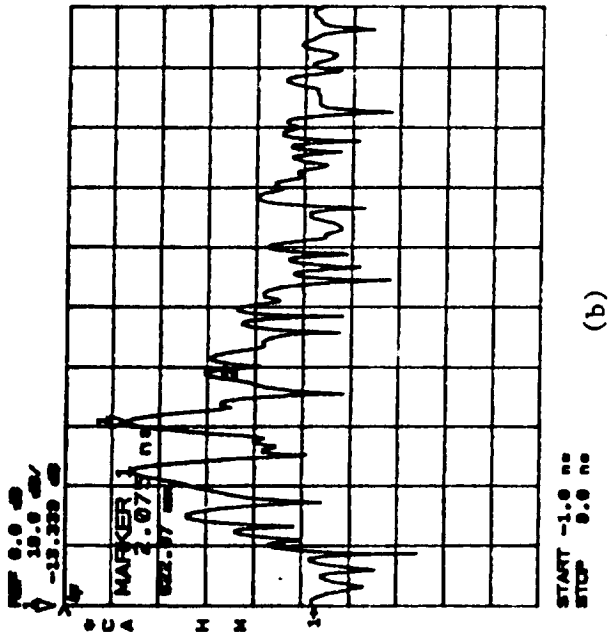
- o GOAL IS TO MEASURE THE DELAY τ DUE TO PROPAGATION THROUGH THE PLASMA
- o RETURN SIGNAL ACTUALLY IS A SUM OF MANY DELAY TERMS THAT MUST BE SORTED TO OBTAIN DESIRED INFORMATION

0	τ	2τ	3τ
τ_0	$\tau + \tau_0$	$2\tau + \tau_0$	$3\tau + \tau_0$
$2\tau_0$	$\tau + 2\tau_0$	$2\tau + 2\tau_0$	$3\tau + 2\tau_0$
$3\tau_0$	$\tau + 3\tau_0$	$2\tau + 3\tau_0$	$3\tau + 3\tau_0$

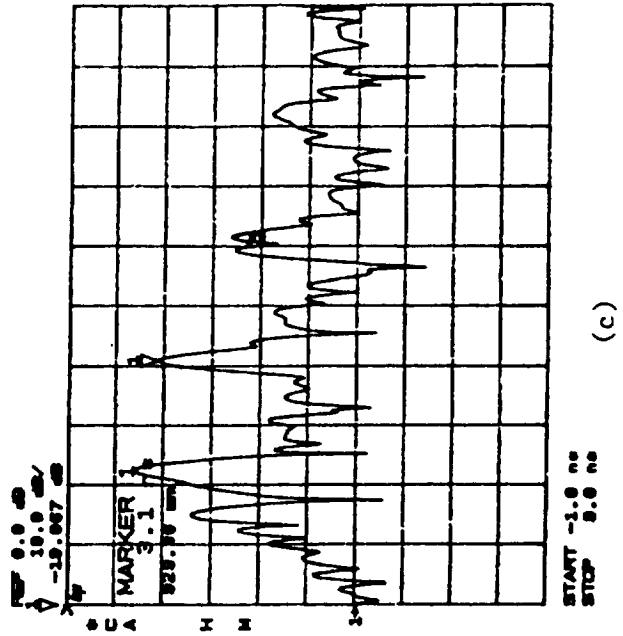
Figure 4-2. Time Delays for Reflected Signals Predicted from Simplified Reflection Model



(a)



(b)



(c)

Figure 4-3. Example Test Data Demonstrating Interference Reflection Independence from Target Distance of

- (a) 1.5 inches,
- (b) 6 inches, and
- (c) 12 inches

ground plane, and/or target surfaces before being received by the MRIS instrument.

The main task of the signal processing used with the MRIS instrument is extraction of the primary target reflection from the extraneous interference and multipath reflections. The vector error correction and range-gating features developed to combat the effects of interference and multipath reflections are discussed later in this report. In the next section of this report, example calculations are performed to analyze range-measurement inaccuracies that can be induced by unwanted reflected signals. By examining the effective levels of interference and multipath reflections that remain after range-gating and vector error correction, results from the following example calculations can be used in estimating the system accuracy that will be achieved by the MRIS instrument.

4.2.2 Simple Interference Example

In the idealized CW radar example discussed in Section 2, the reflected signal from the target was treated as a complex vector. Target range information was contained in the phase of this complex vector. In practical situations, more than one reflected signal is received by the MRIS instrument because of reflective obstacles, antenna sidelobes, and other effects. The additional reflected signals add to the receiver output forming a composite vector which is the complex sum of the individual reflected signals received by the instrument.

If the phase angle of this composite vector is used to compute the target range, the computed range will generally be in error. The range error will be small if the undesired reflected signals received by the MRIS instrument are small in comparison to the primary target reflection. In essence, the goal of the vector error correction approaches discussed later in this report is to reduce the undesired interference and multipath reflections to levels that allow the target range to be accurately estimated from the corrupted composite vector at the receiver output.

A brief analysis is now presented that quantifies the effects of various levels of extraneous reflected signals. The analysis is based on a two-frequency model by Skolnik which results in system errors comparable to those of an FM system [1]. No attempt is made to actually predict the reflected signal levels that would be produced in the actual MRIS environment.

The required analysis consists of several simple steps. Initially, an expression is derived to estimate the phase measurement error, $\delta\theta$, that can be induced by a given interfering signal (interference or multipath reflection). A corresponding range error, δR , is then estimated as a function of $\delta\theta$. These two steps allow δR to be computed as a function of the magnitude of the interfering signal. Since the system requirement for δR is known, results of this analysis can be used to estimate the allowable interfering signal levels.

For the first step indicated above, it is observed that the peak phase measurement error occurs when the interfering signal is in phase quadrature with the primary target reflection. If the ratio of the target reflection to the interfering signal is defined as the signal-to-interference ratio (or SIR), the resultant peak phase measurement error can be expressed as,

$$\delta\theta = 2 \cdot \text{ARCTAN}(\text{SIR})^{-1/2} \quad (4-2)$$

Using the two-frequency radar example discussed in Section 2, the approximate range error, δR , can be expressed as follows,

$$\delta R = \delta\theta \cdot c / (4 \cdot \pi \cdot \Delta f) \quad (4-3)$$

where, c is 3×10^{10} cm/s and Δf is the resolution determining bandwidth (4032 MHz for the MRIS application).

Calculated values of $\delta\theta$ and δR versus the SIR are shown in Figure 4-4. In general, it is desirable to limit errors due to interfering signals (i.e., interference or multipath reflections) to values less than ± 0.5 cm to insure the overall system accuracy requirements are met. Examination of Figure 4-4 indicates the minimum effective SIR must be 7 dB to meet the ± 0.5 cm objective. The overall system objective then becomes implementation of hardware

RANGE ERRORS & PHASE ERRORS VS SIR

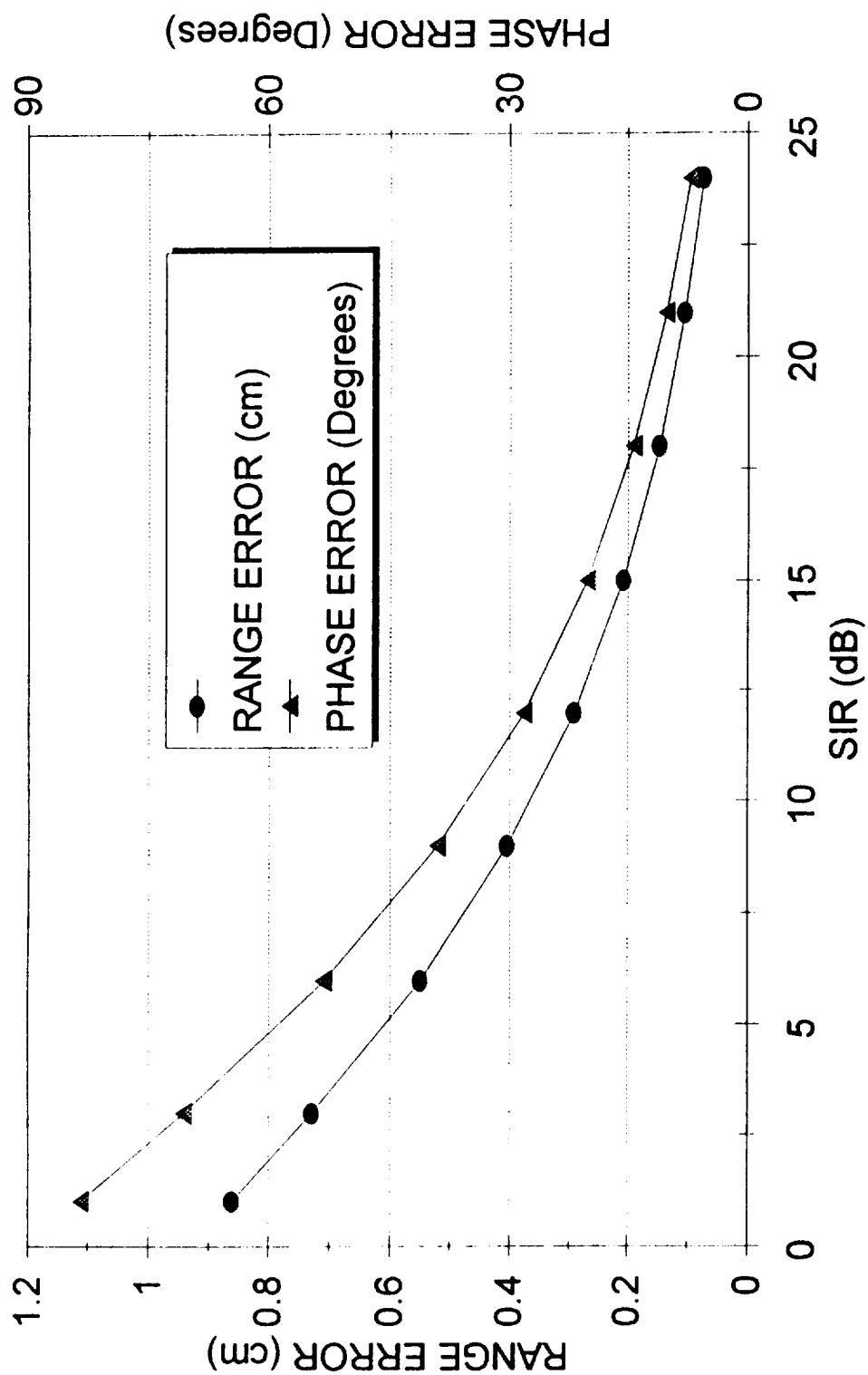


Figure 4-4. Calculated Values of $\delta\theta$ and δR Versus the Signal-to-Interferer Ratio

and software schemes that insure an effective SIR of 7 dB is met. Conceptual discussions of two techniques, vector error correction and range-gating, investigated for achieving adequate SIRs are discussed below. Further details and example data on these techniques are presented later in this report.

4.2.3 Vector Error Correction Concept

As noted in the preceding section of this report, the MRIS instrument receives interference and multipath reflections caused by the TPS tile, the antenna ground plane, and to a lesser degree, moding effects. Without appropriate signal processing, these undesired reflections can degrade system accuracy and prevent compliance with the performance requirements listed in Section 2. To aid in suppressing the effects of undesired reflected signals, vector error correction techniques similar to those used in network analyzer measurements and radar cross section measurements were investigated at EMS during the MRIS development effort.

Several different VEC approaches were investigated. Each approach is based on applying error correction to the stepped-frequency target data set in order to reduce the effects of interfering signals. The frequency-domain error correction procedure involves using data collected for a set of prescribed reference conditions to perform vector operations on data collected for the target (hence, the name vector error correction and the acronym VEC). Following error correction, an FFT algorithm is used to transform the error corrected data into the time domain where the magnitude and time-delay of the primary target reflection are estimated.

Several effective VEC procedures were developed and tested at EMS as part of the MRIS program. The simplest of these procedures, referred to as vector subtraction is briefly discussed here to introduce the vector error correction concept. A more detailed discussion of vector subtraction and other VEC procedures investigated during the MRIS development effort is presented in Appendix B of this report.

For vector subtraction, the measured reflection coefficient, $\rho_{\text{MEAS}}(f)$, at each frequency step, f , is modeled as,

$$\rho_{\text{MEAS}}(f) = \rho_{\text{LOAD}}(f) + \rho_{\text{TARGET}}(f) \quad (4-4)$$

The parameter ρ_{LOAD} represents the reflection coefficient that would be observed in the absence of a target and ρ_{TARGET} represents the reflection coefficient that would be observed if only the primary target reflection occurs. In this model, ρ_{LOAD} corrupts ρ_{MEAS} and prevents ρ_{TARGET} (and its range related phase angle) from being accurately determined. The goal of vector subtraction is to initially measure ρ_{LOAD} then use it to correct subsequent ρ_{MEAS} measurements. Implementation of vector subtraction involves initially replacing the target with a non-reflective target (e.g., a sheet of microwave absorber) so that,

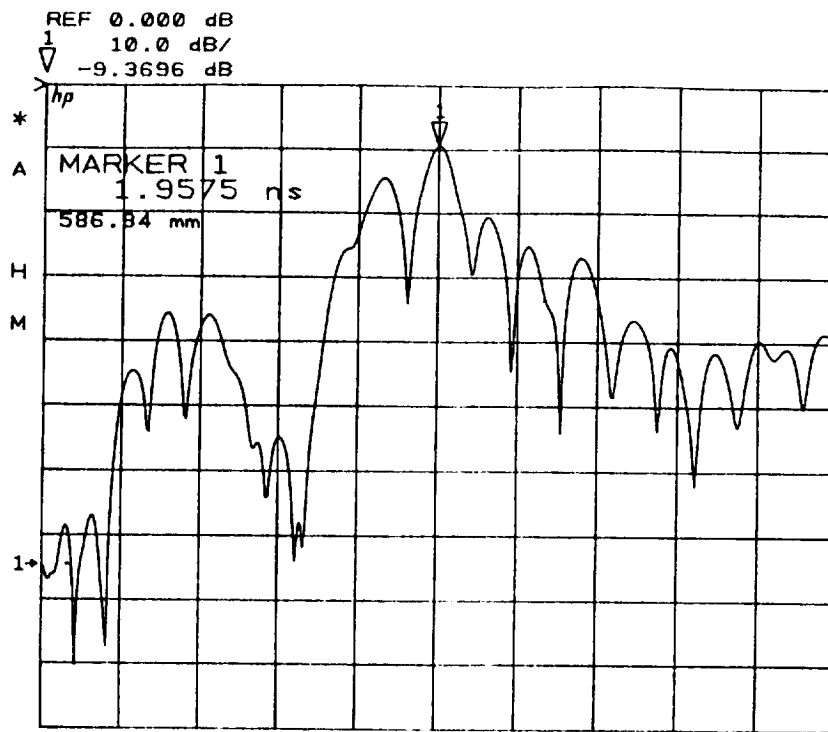
$$\rho_{\text{TARGET}}(f) = 0 \quad (4-5)$$

The measured values of ρ_{LOAD} are stored and subsequently used to correct measurements made on the target. That is, the target reflection coefficient is determined using the relationship,

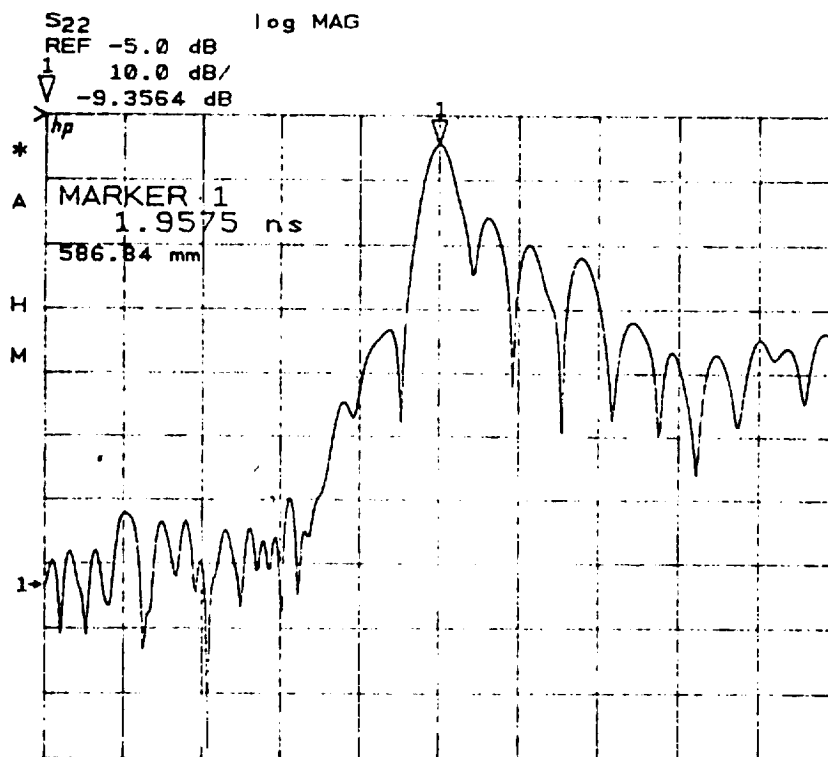
$$\rho_{\text{TARGET}}(f) = \rho_{\text{MEAS}}(f) - \rho_{\text{LOAD}}(f) \quad (4-6)$$

where, $\rho_{\text{MEAS}}(f)$ is measured with the target in place and $\rho_{\text{LOAD}}(f)$ is known from previous measurements with the target removed. An example of the effect of vector subtraction is shown in Figure 4-5. In Figure 4-5(a) vector subtraction was not applied. Two predominate reflections can be observed, an interference reflection near 1.8 ns due to the TPS tile and the target reflection near 2 ns due to the flat metal plate. In Figure 4-5(b), vector subtraction has been applied. The target reflection can still be observed near 2 ns but the interference is now substantially reduced.

Vector subtraction proved effective for the monostatic as well as bistatic configurations in the MRIS instrument. Range-measurement errors observed in uncorrected monostatic measurements were reduced by 40 to 50 percent while smaller improvements were observed in bistatic measurements (test data are



CENTER 1.9575 ns
SPAN 5.0 ns (a)



CENTER 1.9575 ns
SPAN 5.0 ns (b)

Figure 4-5. Example Test Data Demonstrating Ability of Vector Subtraction to Remove Close-in Reflections (a) No error Correction and (b) With Vector Subtraction

presented later in this report). The shortcoming of vector subtraction is that it is based on a very simple model that does not include multipath reflections. To overcome this fact, more advanced procedures were developed based on plane-wave dielectric slab models. These procedures, referred to as vector error correction or VEC, produced equations containing a larger number of unknowns than the equation produced from the simpler vector subtraction model. Hence, VEC required that preliminary measurements be performed for a larger number of reference conditions. These VEC procedures, were found to provide further performance enhancements. Data demonstrating the improvements gained from VEC are presented in Section 7 and Appendix B3.

At the time the MRIS development effort was halted, more advanced error correction procedures were being contemplated. In general, the goal of these new procedures would have been to more completely account for the effects of multipath signals resulting from the antenna ground plane (aluminum aerobrake skin). No actual work toward development of these more advanced error correction models was carried out at EMS.

4.2.4 Range-Gating Concept

The MRIS instrument possesses a range-gating capability that allows individual reflected signals to be sorted by time-delay (or equivalently, by range). The significance of range-gating was shown in Figures 4-3 and 4-4 which showed that reflected signals detected by the MRIS instrument can be FFT-processed to sort the detected signals in time. In instances where the target, interference, and multipath reflections are adequately spaced, the range of the primary target reflection can be accurately estimated by determining the position of the peak signal in the time-domain plots. If the spacing between individual reflected signals is smaller than the system range resolution, the reflected signals interfere with each other and the position of the primary target reflection can be significantly corrupted. In these instances, it is important that an effective vector error correction procedure be applied to the swept-frequency data prior to the FFT operation.

The range-gating ability of the MRIS instrument stems from its stepped-FMCW operation. In some respects, the operation of a stepped-FMCW system is an

extension of the two-frequency radar example previously discussed in Section 2. In that example it was shown that the output signal is a vector of the form,

$$V = \eta \exp(-j\Delta\theta) = \eta [\cos(\Delta\theta) + j\sin(\Delta\theta)] = I + jQ, \quad (4-7)$$

The argument $\Delta\theta$ is the difference in phase measured at the two interrogating frequencies and is related to range by the equation,

$$\Delta\theta = 4\pi R\Delta f/c \quad (4-8)$$

In a multiple stepped-frequency system such as that used for MRIS, the receiver output for a reflected signal received from an ideal point target is a vector that rotates by the angle $\Delta\theta$ as each successive frequency step is taken. Thus, for a fixed-frequency step size, the rate of rotation versus frequency is proportional to the target range.

If a total of N frequency steps is taken during each complete frequency sweep, the total sweep bandwidth is $(N-1)\Delta f$ and N pairs of I-Q data are collected. To achieve range-gating, an FFT operation can be performed to transform the N pairs of frequency domain I-Q data set into an N -element time-domain data set. The time-domain transformation will cause the energy from individual targets to appear in range bins in accordance to the rate of rotation produced in the time domain data set. For a single fixed target, all the reflected energy is in principle sorted into a single range bin. However, artifacts associated with truncated data sets will generally cause the energy to be spread in some manner over several range bins.

When multiple targets exist, each target will contribute a term to the composite output signal. However, as the frequency is stepped, each individual vector will rotate at a rate determined by the specific target range. When the composite frequency domain data is FFT'd into the time domain, the energy from the individual targets will be sorted in accordance to their rates of rotation which, as previously noted is equivalent to range.

Key factors associated with range-gating systems are unambiguous range (R_u), range resolution (ΔR), and range accuracy (δR). The significance of each of these factors along with further discussion of the range-gating concept is presented in the system discussion in Section 5 of this report.

4.3 MILLIMETER-WAVE INSTRUMENTATION RELIABILITY

At the beginning of the MRIS program, a major system concern was the reliability of the mmW modules used in the MRIS instrument. In the initial design, there were two component types that were of particular concern, (a) mixers fabricated using whisker-contact diodes and (b) mechanical waveguide switches that used solenoid-driven rotating or sliding waveguide switching sections. To minimize the risk of potential problems with these components, two key decisions were made. The upper frequency for the MRIS instrument was limited to 140 GHz which allowed the whisker-contact mixers to be replaced with beam-lead diode mixers. In addition, the mechanical switches were eliminated by modifying the system design to provide separate Reference and Test channels that did not require switching. Further discussion on these two decisions are presented below.

4.3.1 MMW Mixers

Whisker-contact mixers use a thin, pointed metal wire (the whisker) to make contact to a single diode in a multi-diode wafer. The metal-semiconductor junction formed between the metal whisker tip and the doped semiconductor region forms the required rectifying diode junction. The whisker is slightly spring loaded and the associated mechanical force is relied upon to maintain the integrity of the diode junction. Typically, the other end of the whisker is electrically connected through a transmission line (e.g., PC-board) to the mixer's IF connector. Because of its mechanical design, whisker-contact mixers can be sensitive to mechanical forces that degrade the metal-semiconductor junction. Problems can arise from vibration and shock as well as from torque transmitted through the coaxial connector used for the mixer IF port.

To eliminate potential problems with whisker-contact mixers, a decision was made to use beam lead diodes in the mmW mixers used in the MRIS instrument. Beam-lead diodes have the required rectifying junction formed directly onto a semiconductor substrate. A metallized anode and cathode can then be grown or sputtered onto the substrate. Finally, terminals in the form of rugged metal tabs can be attached to the metallized terminals. Unlike point-contact diodes which depend on simple mechanical pressure to maintain electrical integrity, beam-lead diodes can be securely attached using solder, metallized epoxy, or welding.

For MRIS, two types of beam-lead diodes were employed. For the 20, 44, and 95 GHz mixers, a pair of standard beam-lead diodes manufactured by Marconi were used in each of the nine mixers (three mixers per band). The diodes were attached by welding the diode leads to the mixer IF center-pin and to the mixer body. Following fabrication of the required mixers at Millitech, the units were delivered to EMS where they underwent the vibration regimen outlined in Figure 4-6. All nine mixers tested successfully passed the vibration test verifying the ruggedness of the beam-lead diode based mixers.

For the 140 GHz modules, it was determined that the capacitance of the standard beam lead diodes resulted in excessive conversion losses and limited operating bandwidth. In this case, an alternative non-whisker diode referred to as a flip-chip diode was used. This diode, which was developed and manufactured by the University of Virginia, actually contains a pair of anti-parallel diodes. As with the standard diode, the flip-chip diode has two permanently attached metallized contacts. One of the leads is attached to the anode of the first diode and the cathode of the second diode. Conversely, the second metallized lead is attached to the cathode of the first diode and the anode of the second diode.

The contacts of the flip-chip diodes do not extend from the diode body as shown in Figure 4-7. Thus, these diodes are best suited for attachment through soldering or epoxying. For the MRIS application, silver epoxy was used to attach the two contacts of the diode to the mixer center-pin and body. In general, the 140 GHz mixers constructed in this manner worked well. For example, the mixers successfully survived vibration testing performed at EMS.

Vibration, Non-operating

The random vibration loads acting on the T/R Modules result from the resonant structural response of the Module Assemblies to random vibration input from the rocket engine mechanically and acoustically induced vibrations during launch.

Random vibration test for the T/R Module Assemblies are required to show the component will survive and operate after exposure to the required test criteria. This test criteria is as shown below.

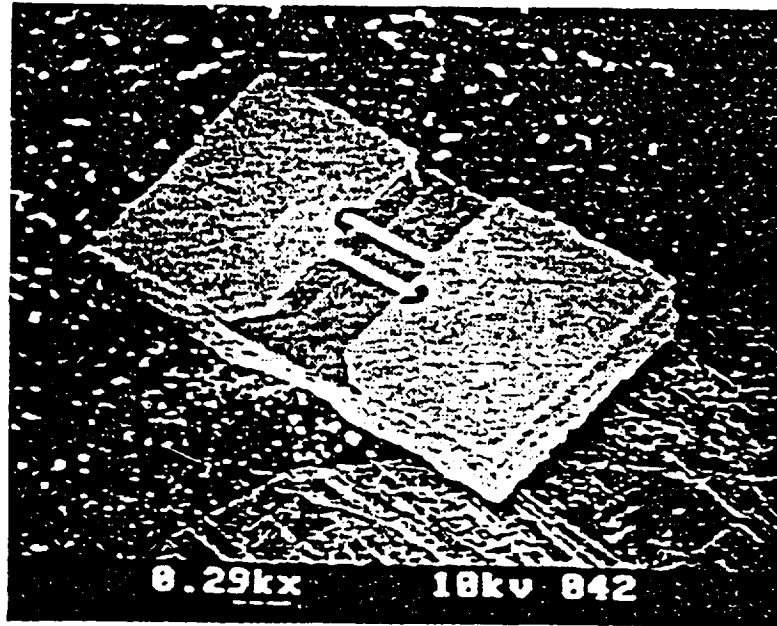
20 Hz @ $.003g^2/\text{Hz}$
20-140 Hz @ +9 dB/Octave
140-320 Hz @ $1.0g^2/\text{Hz}$
320-2000 Hz @ -12 dB/Octave
2000 Hz @ $.00066g^2/\text{Hz}$

Composite = 17.9 G-rms

Duration: Engineering Model: 120 Sec Per Axis
 Flight Model 60 Sec Per Axis.

The test spectra shall be verified by narrow band spectral analysis using an analysis system that is independent from the analyzer/equalizer used to control the test. The acceptable tolerances are given in Table 9.0-1 of MSFC-DOC-1774.

Figure 4-6. Vibration Regimen used to Test mmW Mixers and Gunn Oscillators



Scanning Electron Micrograph of an integrated pair of anti-parallel Schottky barrier diodes on GaAs.

Figure 4-7. Depiction of Alternate Diode used for 140-GHz Mixers

However, several failures did occur during assembly and laboratory testing of the 140-GHz mixers. The cause of these failures was under investigation at the time the MRIS development effort was halted. The status of the 140 GHz mixer development is discussed in Appendix A2 of this report. In general, it appeared the failures were not directly due to the flip-chip diodes but to a flaw in the design of the mixer housing and to the use of a silver epoxy that was not adequately flexible for this application. Each of these problems is easily corrected.

4.3.2 WG Switches

The initial module design included waveguide switches that would select either the reference channel or test channel for measurement. The reliability of the mechanical switches available for Band-A, Band-B, and Band-C was a concern because of the significant number of times these units would be switched during instrument development and during the AFE mission. For Band-D, available switch designs had not been extended to 140 GHz and development of suitable units was considered a high-risk area. Because of these potential problems, the decision was made to eliminate the switches from the system design.

In each T/R Module, the purpose of the waveguide switches was to switch the receiver between the reference and test channels. As noted in Section 3 of this report, the need for the switches was eliminated by configuring the T/R Modules and IF front-end to provide separate Reference and Test channels.

4.4 PLASMA ATTENUATION

A final challenge facing the MRIS instrument was the mmW signal attenuation produced by the plasma, particularly at higher frequencies. The plasma attenuation significantly increased the dynamic range requirements for the MRIS instrument and limited the highest practical frequency to approximately 140 GHz. All plasma loss estimates were based on the following equation which was provided to EMS by LaRC.

$$\text{LOSS (dB/cm)} = 0.141 + 1.56\text{E-}3 * \text{FREQ (GHz)} \quad (4-9)$$

Use of the above equation yields the attenuation versus distance and frequency graphs depicted in Figure 4-8. At the longest required MRIS operating range of 30 cm, early analysis indicated plasma attenuation would cause the signal-to-noise ratio to degrade to 0 dB at 180 GHz and this was considered the highest possible operating frequency for the MRIS instrument.

PLASMA ATTENUATION ESTIMATES

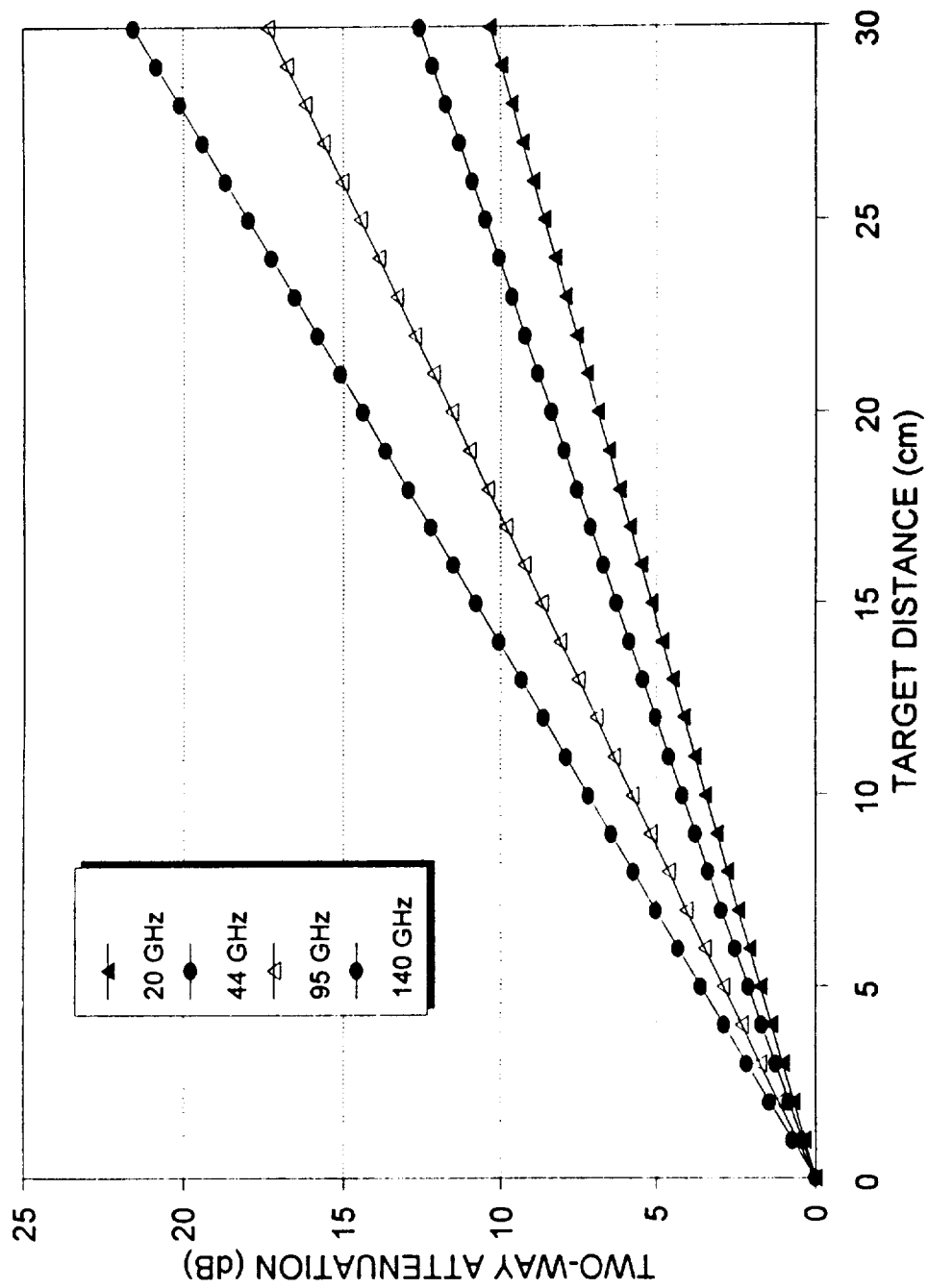


Figure 4-8. Predicted Plasma Attenuation Versus Distance at the Center Frequencies of the Four MRIS Operating Bands

5.0 SYSTEM CONSIDERATIONS

5.1 SUMMARY OF SYSTEM TOPICS

System issues considered in designing and developing the MRIS instrument are summarized in this section of the final report. Specific topics addressed include, (a) stepped-FMCW operation, (b) key system design parameters, (c) the system link budget, (d) system calibration, and (e) the system error budget.

5.2 STEPPED-FMCW DESIGN AND IMPLEMENTATION

5.2.1 General Description of Stepped-FMCW System

The MRIS instrument uses a stepped-FMCW approach to discriminate between the primary target reflection and undesired interference and multipath reflections. Discrimination is achieved by evaluating time-domain data sets in which energy from individual reflected signals is sorted into specific range bins determined by the time delay experienced by the signals. Since the time delay of the primary target reflection, interference reflections, and multipath reflections will generally differ, time-domain sorting allows selectivity in locating and evaluating the target reflection.

Investigations during the MRIS development effort indicated that range discrimination is very effective when individual reflections are adequately spread in time. If the separation between reflections is comparable to or less than the resolution of the FMCW system, additional techniques must be employed to obtain suitable range measurement accuracy.

A block diagram of the basic approach used in the MRIS instrument is shown in Figure 5-1. As discussed in Section 3, a stepped-frequency transmit signal (f_{RF}) is produced in each of the four operating bands by mixing a fixed-frequency mmW signal (f_{LO}) and a stepped-frequency microwave signal (f_{IF}). Two mmW signals, the Reference Signal (a_1) and the Test Signal (b_1), are produced by the instrument at each step frequency. These signals can be represented as,

MRIS STEPPED -FMCW SYSTEM

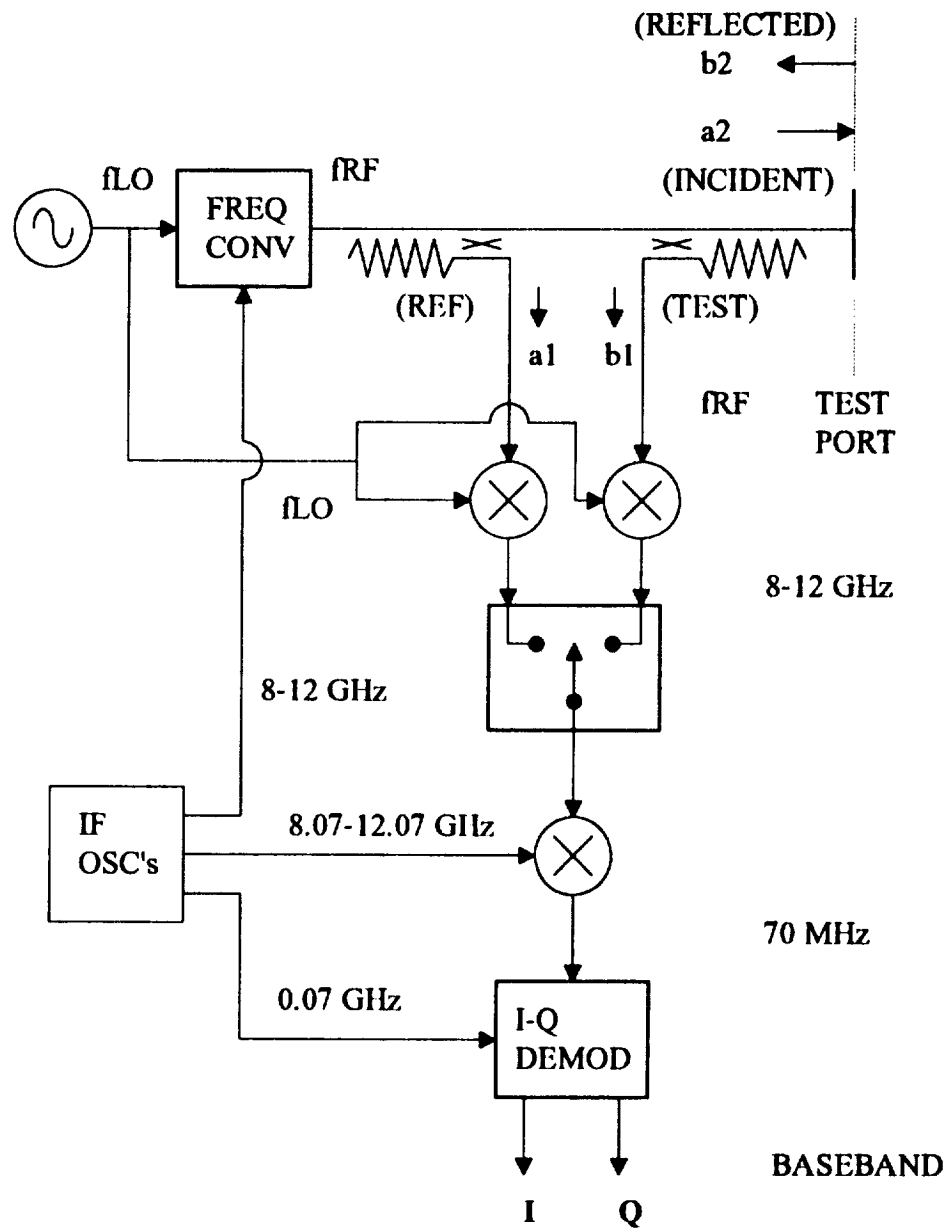


Figure 5-1. Generalized Block Diagram of Stepped-FMCW Approach used in the MRIS Instrument

$$a_1(f_1) = A_1 \cos(2\pi f_1 + \phi_1) \quad (5-1a)$$

$$b_1(f_1) = B_1 \cos(2\pi f_1 + \psi_1) \quad (5-1b)$$

where f_1 represents the individual stepped frequencies. The amplitude and phase of these two signals represent the information of interest for the MRIS instrument.

The signals a_1 and b_1 , undergo several demodulation steps. Initially, the signals are mixed with a portion of the fixed-frequency mmW LO as shown in Figure 5-1. This downconverts the signals from stepped-frequency mmW signals to stepped-frequency IF signals in the 8-12 GHz band. At each frequency step, the down-converted a_1 and b_1 signals are alternately routed through an IF switch to an additional mixer. The LO input to this mixer is a stepped-frequency IF signal offset from a_1 and b_1 by exactly 70 MHz. The output of this mixer is therefore a 70 MHz signal.

The 70-MHz signal from the mixer is inputted to the I-Q Demodulator where final amplitude-phase detection is performed. The outputs of the I-Q Demodulator are two voltages, I and Q, that represent the desired amplitude and phase information in a rectangular format. Since the Reference Signal and Test Signal are alternated, a pair of I-Q voltages corresponding to the Reference and Test Signals are produced at each frequency step. For the 64 frequencies used in each frequency sweep, a total of 128 I-Q voltage pairs is produced.

5.2.2 Signal Processing

At each frequency step, the measured I-Q pairs are normalized by dividing the measured Test Signal I-Q voltages by the measured Reference Signal I-Q voltages. After normalization, a total of 64 normalized complex voltages are obtained. These normalized voltages can be represented as,

$$\begin{aligned} V(f_1) &= [I_T(f_1) + jQ_T(f_1)] / [I_R(f_1) + jQ_R(f_1)] \\ &= M_1 \cdot \exp(-j\theta_1), \quad 1 = 1, 2, 3, \dots, 64 \end{aligned} \quad (5-2)$$

This 64-element set of normalized complex voltages is the frequency domain representation of the reflected signals received by the MRIS instrument in a given operating band. With appropriate processing, this frequency domain data set can be transformed to an equivalent time domain representation that allows individual reflected signals to be sorted by range. For the MRIS application, the familiar inverse-FFT of the form shown below is used to perform the required transformation.

$$T(k) = \sum_{n=0}^{N-1} [V(n) \cdot \exp(+j2\pi nk/N)] \quad k = 0, 1, 2, \dots, N-1 \quad (5-3)$$

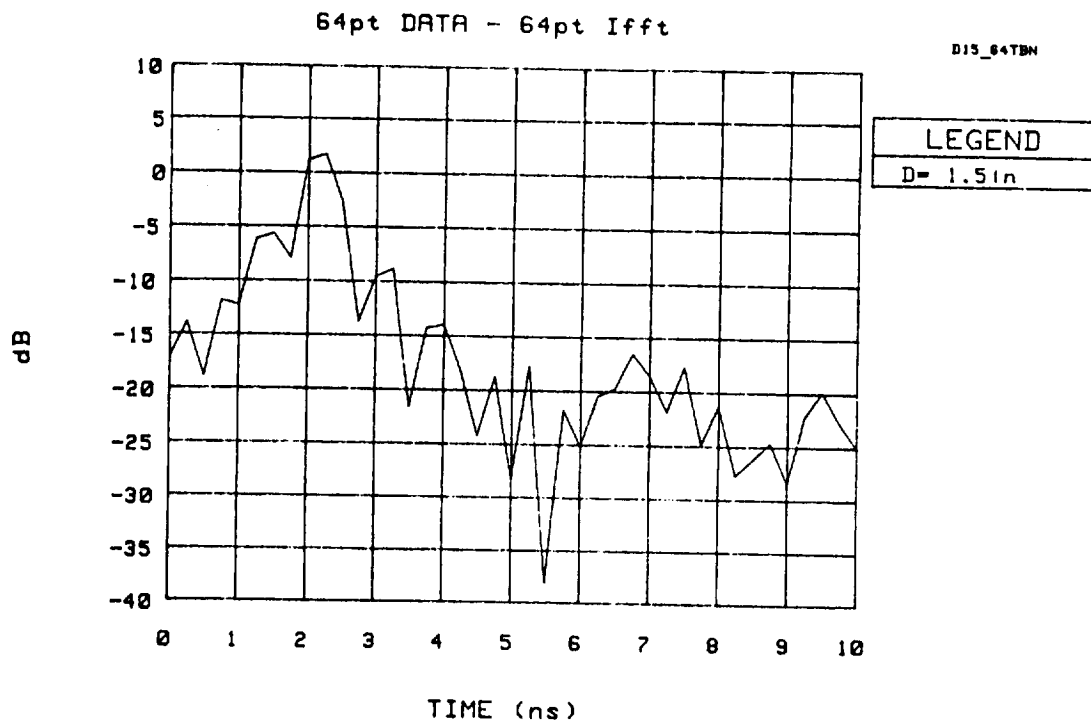
where,

- k = Array element of time domain data
- n = Array element of frequency domain data
- T(k) = Array of time domain values
- V(n) = Array of frequency domain values
- N = No. of FFT points

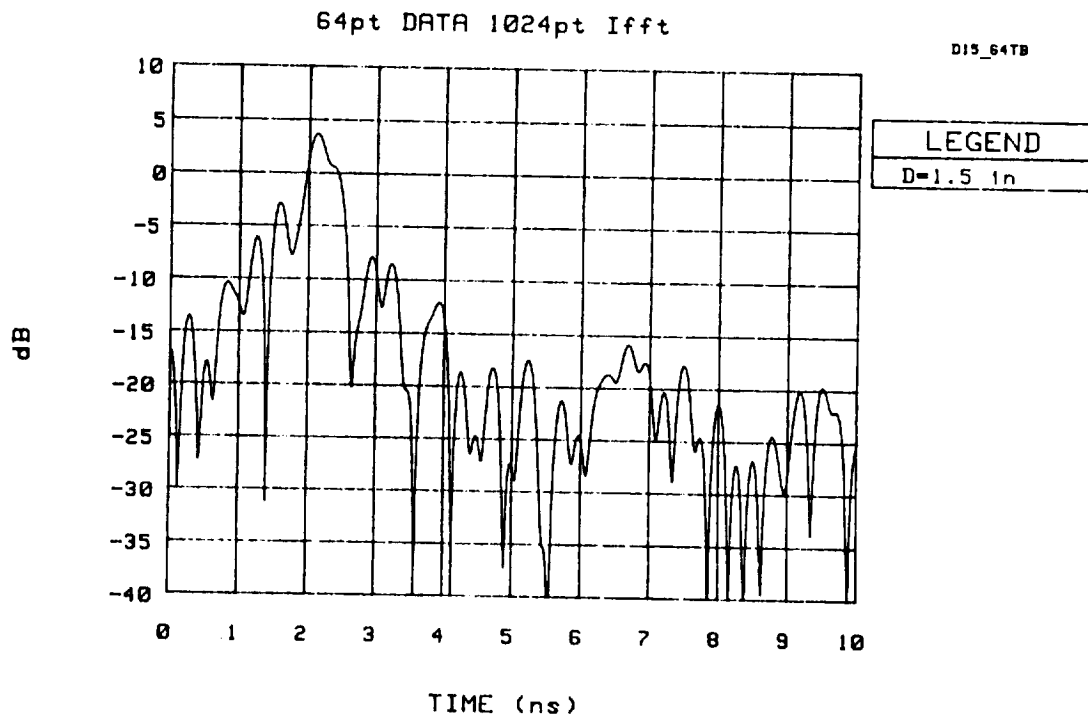
The required FFT operation was implemented using MatLab 3.0 software on the PC computer included in the MRIS Ground Support Equipment. This software allowed convenient implementation of windowing and zero-filling functions. In practice, windowing with anything other than a uniform window was found to be of little benefit. However, zero-filling proved to be useful for interpolation purposes and was used for the bulk of the data described in this report. Typically, zero-filling was used to increase the FFT size to 1024 or 2048. An example showing the improved interpolation achieved with zero-filling is shown in Figure 5-2. In this case, a 64-point frequency domain data set was zero-filled to allow a 1024-point inverse-FFT to be performed.

5.2.3 Frequency Sweep Parameters

Key parameters describing the range-gating capability of a stepped-FMCW system are the unambiguous range (R_u), the range resolution (ΔR), and the range accuracy (δR). These parameters are defined by the operating characteristics of the instrument including the sweep bandwidth (BW), the frequency step-size



10:12:00 12 Jul 1991



17:43:24 12 Jul 1991

Figure 5-2. Example Inverse-FFT Showing Effects of Zero-filling 64-point Sample to 1024 points to Achieve Improved Interpolation in Time-domain

(Δf), and the system signal-to-noise ratio (SNR). Specific operating parameters for the MRIS instrument are shown in Table 5-1. Discussions pertaining to these parameters are presented below.

5.2.4 Unambiguous Range

The unambiguous range, R_u , is the distance at which a range-gating system ceases being able to unambiguously determine target range. A target located at R_u will be sorted into the same range bin as a target located at zero range, creating a range ambiguity. Similarly, a target located beyond R_u will "fold over" and appear to lie in a range bin between zero and R_u , again creating a range ambiguity. As shown in the following example, R_u for a stepped-FMCW system is determined by the frequency step size, Δf .

For a reflected signal from a fixed point target at a range, R , the phase change during a single frequency step, Δf , is defined as,

$$\Delta\theta = 4\pi R\Delta f/c \quad (5-4)$$

where, $c = 3 \times 10^{10}$ cm/s and R is expressed in centimeters. R_u results from the fact that the maximum value of $\Delta\theta$ for a single frequency step must be less than 2π radians if the phase measurement is to be unambiguous. Therefore,

$$R_u = c/(2\Delta f) \quad (5-5)$$

For the MRIS application, it is important that R_u be sufficient to insure that desired targets can be unambiguously detected up to the maximum target range of 30 cm-virtual. It is also important that multiple reflections do not fold over and appear in the range bin containing the target reflection. The MRIS instrument uses a frequency step-size of 64 MHz which produces an R_u of 234 cm. At the maximum MRIS range of 30 cm, an R_u of 234 cm is sufficient to accommodate the target range as well as multipath signals that bounce as many as eight times between the target and TPS tile surfaces. Preliminary system tests indicate an R_u of 234 cm is adequate in air. The demands in plasma should be less stringent since multipath signals will undergo added attenuation due to excess plasma losses.

TABLE 5-1

KEY OPERATING PARAMETERS FOR THE STEPPED-FMCW SYSTEM

$$\Delta f = 64 \text{ MHz}$$

$$N = 64 \text{ (Number of measurement frequencies)}$$

$$BW = (N-1)\Delta f = 4032 \text{ MHz}$$

$$R_u = c/(2\Delta f) = 234 \text{ cm}$$

$$\Delta R = c/(2BW) = 3.72 \text{ cm}$$

$$\delta R = \Delta R/(\text{SNR})^{1/2} = 0.23 \text{ cm}$$

5.2.5 Range Resolution

The range resolution, ΔR , represents the separation between adjacent range bins and is a measure of the ability of a stepped-FMCW system to resolve closely spaced targets. As discussed below, ΔR is set by the total sweep bandwidth of the stepped-FMCW system.

The total unambiguous range was previously defined to be,

$$R_u = c/(2\Delta f) \quad (5-6)$$

Since there are N frequency steps, there will also be N points in the time domain data set and the total unambiguous range is divided into $N-1$ range bins. Therefore the resultant range bin size or range resolution can be defined as,

$$\Delta R = R_u/(N-1) = c/[2\Delta f(N-1)] \quad (5-7)$$

The quantity $\Delta f(N-1)$ is simply the total sweep bandwidth, BW . Therefore, the range resolution is set by the bandwidth and can be expressed as,

$$\Delta R = c/(2BW) \quad (5-8)$$

The MRIS instrument uses a total bandwidth of 4032 MHz. The corresponding range resolution is,

$$\Delta R = 3 \times 10^{10} / (2 \cdot 4032 \times 10^6) = 3.72 \text{ cm} \quad (5-9)$$

Experiments during the MRIS instrument development indicated that adequate discrimination between the target reflection and undesired interference and/or multipath reflections can be achieved when the reflections are separated by a distance greater than approximately 1.3 times the range resolution. This is demonstrated by the example data in Figure 5-3 which shows the variations in measured time delay as the range to a flat plate target was varied in a linear manner. Ideally, the time delay versus distance graph will produce a straight line of the form,

22-Nov-91

BAND B CALIBRATED TST/REF ROUND-TRIP TIME DELAY

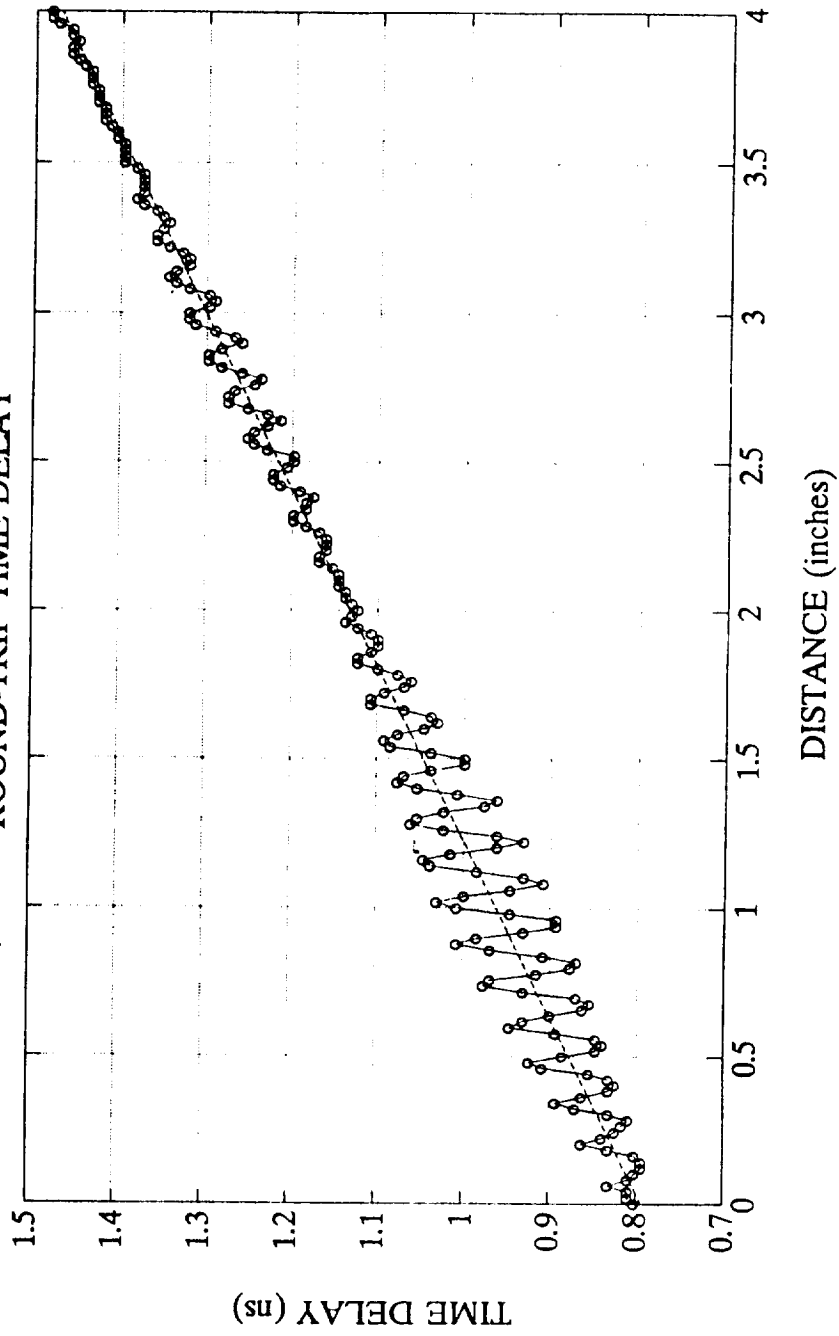


Figure 5-3. Results of Time Delay Measurements using 4032-MHz sweep Bandwidth during Preliminary System Bistatic Band-B Testing at EMS

$$\tau = m*d + \tau_0 \quad (5-10)$$

where, τ is the two-way time delay in seconds, d is the one-way distance to the target in centimeters, m is the time-delay slope through vacuum of $6.667\text{E-}11$ sec/cm, and τ_0 is an offset due to delays through the measurement hardware.

Examination of Figure 5-3 reveals that deviations from the ideal straight line are small for target distances greater than 1.9 inches (approximately 1.3 times ΔR) but can be large at smaller target distances. This example demonstrates the limitations of range-gating using a finite bandwidth and shows the need for further processing to aid the performance of the MRIS instrument for small target distances.

5.2.6 Range Accuracy

The final parameter considered for stepped-FMCW operation is the range accuracy, δR . The range accuracy provides a measure of the ability of a system to determine the location of a single target when the only interference is system noise. The range accuracy is determined by the range resolution and the system signal-to-noise ratio (SNR). Using the previous definition for range resolution, the range accuracy can be approximated as,

$$\delta R = \Delta R / (\text{SNR})^{1/2} \quad (5-11)$$

For the MRIS application, a minimum acceptable SNR of 24 dB was used in all system design and analysis effort. This results in a range accuracy of 0.23 cm which is reflected in the overall system error budget presented in Section 5.6 of this report.

5.3 KEY SYSTEM PARAMETERS AND DESIGN GOALS

Key system parameters considered in designing the MRIS instrument were (a) receiver dynamic range, (b) detector dynamic range, (c) frequency step accuracy, and (d) frequency step stability. These parameters and associated system design goals are discussed through the remainder of this subsection.

5.3.1 Receiver Dynamic Range

The difference between the minimum and maximum mmW signal levels appearing at the receiver inputs determine the receiver dynamic range required in each of the four MRIS operating bands. The minimum received signal level must be greater than the average noise floor of the receiver by an appropriate margin; the required margin being dependent on the required system performance. Similarly, the maximum received signal level must be lower than the compression point of the receiver; the required margin again being dependent on the required system performance.

In the following example, the Band-D Test Channel receiver dynamic range requirements are analyzed since the most severe requirements occur in this channel (primarily because of the effects of plasma attenuation). The dynamic range requirements of the remaining MRIS bands were determined using similar analysis and are summarized in the system link budget presented in Section 5.4 of this report.

Estimates of the minimum and maximum received signal levels occurring in Band-D can be made from considerations of transmit power level, antenna responses, TPS tile characteristics, and plasma attenuation as summarized in the system link budget. From the system link budget, the estimated maximum and minimum received signal levels for the Band-D Test signal channel when viewing plasma are -48 dBm and -72 dBm, respectively. By subtracting the desired SNR from the latter of these two levels, the lower end of the required receiver dynamic range can be determined. For the MRIS application, a margin of 14 dB between the minimum received signal and the receiver noise peaks is considered adequate based on the accuracy calculations such as those discussed in Section 3. Since receiver noise peaks are typically 10 dB higher than the receiver average noise floor, a margin of 24 dB is needed between the minimum received signal and the receiver average noise floor. This requires that the receiver average noise floor correspond to a level of -96 dBm or lower.

The difference between the estimated maximum received signal of -48 dBm and the required receiver average noise floor of -96 dBm defines the required

receiver dynamic range when operation in plasma is considered. The overall requirements are summarized in Figure 5-4. To allow for device limitations, component degradation, and other factors, a design goal for the MRIS receivers was to exceed the required system dynamic range by 6 dB at the high end and 3 dB at the low end.

For the mixers in the MRIS instrument, minimal signal compression occurs if the input signal level is 20 dB below the applied local oscillator (LO) power. A local oscillator power of +5 dBm is employed in Band-D. This makes the maximum allowed signal level -15 dBm; providing a 33 dB margin over the estimated maximum received signal level of -48 dBm. As discussed later in this report, this margin was needed to accommodate measurements for a candidate calibration step involving a "THRU" measurement in which a short waveguide is directly connected between the module transmit and receive ports.

(Note: An LO power of +10 dBm is employed in Band-A, -B, and -C. This makes the maximum allowed input signal level approximately -10 dBm in these bands.)

The receiver average noise floor can be computed to estimate the lower end of the receiver dynamic range. Based on a noise figure of 20 dB and the baseband bandwidth of 130 kHz used in the final detector stage, the computed receiver average noise floor is -101 dBm. With the desired 3-dB margin, the minimum signal at the receiver input must be -98 dBm or greater. Thus, the theoretical receiver dynamic range in Band-D extends from -15 to -98 dBm. This range accommodates the minimum to maximum received signal range of -48 to -96 dBm estimated for Band-D.

In practice, the usable receiver dynamic range is normally less than the theoretical receiver dynamic range due to limits in subsequent sections of the receiver. A key receiver engineering task is insuring the usable portion of the theoretical receiver dynamic range is adequate to fulfill system requirements. For the MRIS application, an important factor that limits the theoretical receiver performance is the the detector stage. It is imperative that the gain of the receiver front-end be carefully set to make optimum use of the available detector stage dynamic range as discussed below.

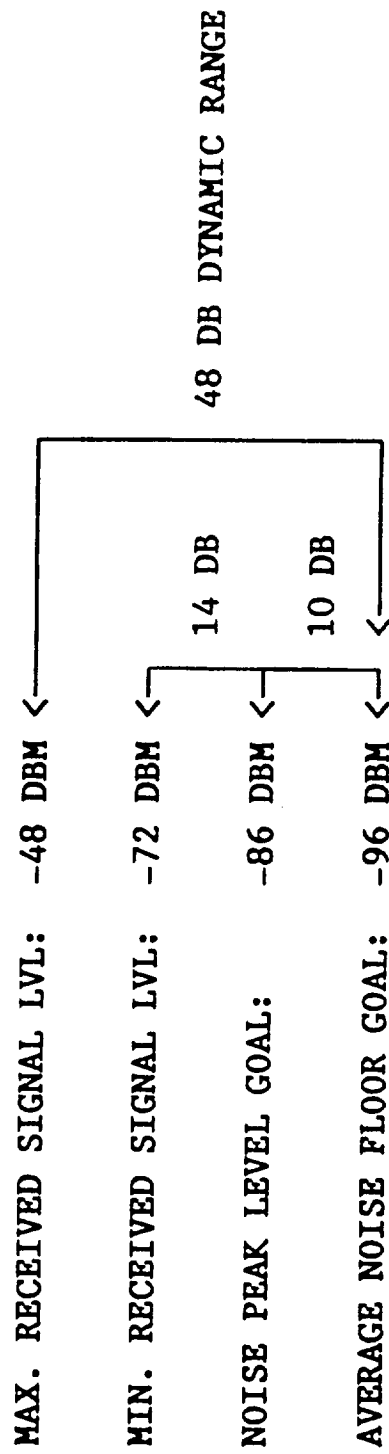


Figure 5-4. Dynamic Range Requirements for Band-D Operation

5.3.2 Detector Dynamic Range

The detector stage of the MRIS receiver consists of a mixer-based IQ detector, two baseband amplifiers, and a 12-bit analog-to-digital detector (ADC). With the exception of the ADC, the detector stage had been implemented and tested when the MRIS development effort was halted. A pair of laboratory digital voltmeters were used in place of the ADC during all preliminary system tests as described in the MRIS users manual.

The overall function of the detector stage is to measure the amplitude and phase of an IF input signal using synchronous demodulation. The primary demodulation operation is performed in the IQ detector. The input signal into the IQ detector is a time varying voltage of the form,

$$V = A \cos(\omega_{IF} t + \phi) \quad (5-12)$$

where, the parameters A and ϕ are the amplitude and phase, respectively of the IF input signal. The parameter ω_{IF} represents the angular frequency and equals the product $2\pi f_{IF}$. For the MRIS receiver, f_{IF} is 70 MHz. A coherent 70 MHz local oscillator is also provided to the IQ detector. Quadrature mixing of the input signal and local oscillator signal result in the IQ detector outputting two analog voltages of the form,

$$I = dA/\sqrt{2} \cos(\phi) \quad (5-13a)$$

$$Q = dA/\sqrt{2} \sin(\phi) \quad (5-13b)$$

where the constant, d, represents the gain of the detector. During system operation, a pair of I-Q values corresponding to the Reference and Test signal channels are measured at each frequency step. Although not shown in the preceding equations, the I and Q voltages typically include DC offset terms due to imperfections in the IQ detector and to leakage signals in the mmW T/R modules. For the MRIS instrument, the baseband amplifiers in the detector include nulling circuits which significantly reduce any DC offset terms output by the IQ detector. Offset voltages not compensated for by the nulling circuit can be simply measured then subtracted from subsequent measurements.

In the completed MRIS instrument, the I-Q signals were to be measured by a 12-bit ADC. This ADC is capable of indicating 4096 possible states. If the ADC achieves a resolution of ± 1 LSB, the dynamic range of the ADC and of the overall detector stage is 72 dB. It was noted previously that the required receiver dynamic range in Band-D is 57 dB (48 dB signal dynamic range + 6 dB margin at top + 3 dB margin at bottom). Thus, the planned detector stage should have proved adequate. To insure good performance, the IF gain between the front-end section and the detector stage had to be carefully set to insure that the input signal levels into the detector stage were appropriate. This procedure is described in greater detail later in this report.

5.3.3 Frequency Stability

For the MRIS application, frequency stability is used to describe any long-term drift in the nominal operating frequencies of the MRIS instrument. Frequency drift in the MRIS instrument is caused by the mmW local oscillators (one per T/R module) and the digitally-tuned IF oscillator (DTO). The main part of the frequency drift of these components is thermally related. The specified thermal sensitivity of the DTO is 0.5 MHz/°C. The specified thermal sensitivities of the mmW LOs are significantly greater and largely determine the overall frequency stability of the MRIS instrument, particularly in Bands-B, -C, and -D. The specified thermal sensitivities of the mmW LOs used in the T/R modules as well as the rms values obtained by combining the DTO and LO stabilities are listed in Table 5-2.

Thermal analysis performed during the development effort indicated the thermal gradient experienced by the internal hardware of the MRIS subassemblies will be less than 10°C during aeropass operation. Thus, the worst-case frequency drift should be limited to approximately 9 MHz in Band-A and 40 MHz in Band-D. In general, this frequency drift does not appear to be a problem except for possible degradation of stored calibration data sets and small errors in the calculated critical electron density values. However, preliminary system tests (see Section 5.5) indicate that system calibration is not critical and the errors in critical electron density values are small compared to the uncertainty associated with the 4 GHz sweep bandwidths.

TABLE 5-2

FREQUENCY SENSITIVITIES OF THE MRIS T/R MODULES

<u>BAND</u>	<u>LOCAL OSC. SENSITIVITY</u>	<u>RMS DTO & LO SENSITIVITY</u>
Band-A	0.75 MHz/°C	0.90 MHz/°C
Band-B	1.50 MHz/°C	1.58 MHz/°C
Band-C	3.00 MHz/°C	3.04 MHz/°C
Band-D	4.00 MHz/°C	4.03 MHz/°C

NOTE

Specified sensitivity of the DTO is 0.5 MHz/°C

5.3.4 Frequency Step Accuracy

Achieving good frequency step accuracy is important to achieving good distance measurement accuracy. There are numerous types of frequency step errors that can occur. For example, random errors can occur in the individual frequency steps or the overall frequency step progression can be non-linear. The worst case error appears to occur when the individual frequency steps are in error by a fixed amount producing a corresponding error in the overall sweep bandwidth. This worst case condition can be evaluated using the results from the two-frequency radar example introduced earlier in this report.

For this example case, the overall phase change, θ , across the sweep band can be expressed as,

$$\theta = 2\pi \cdot BW(T_1 - T_0 - \Delta T) \quad (5-14)$$

where,

BW = Total Sweep Bandwidth
 T_0 = Residual Test Channel Delay
 T_1 = Residual Reference Channel Delay
 ΔT = Round Trip Delay to Target

The target range, R, can be found by noting that

$$R = c \cdot \Delta T / 2 = (c/2)(T_1 - T_0 - \theta/[2\pi \cdot BW]) \quad (5-15)$$

where,

$$c = 3 \times 10^8 \text{ m/s.}$$

Using a Taylor Series expansion, the range error, δR , resulting from a frequency error, δf , can be approximated as,

$$\delta R = (\delta f) \left(c[T_1 - T_0 - \Delta T] / [2BW] \right) \quad (5-16)$$

The quantity $c(T_1 - T_0 - \Delta T)/2$ corresponds to a worst path difference of approximately 100 cm (this includes a 60-cm round-trip to the target and the 40-cm length of the receive path waveguide and antenna). Thus, the range error can be rewritten as,

$$\delta R = 100(\delta f/BW) \text{ cm} \quad (5-17)$$

Tabulated values for δR are shown in Table 5-3. The DTO used in the MRIS instrument was specified to have a total frequency sweep error of no more than ± 10 MHz. This corresponds to a possible range error of ± 0.248 cm from Table 5-3. This range error value was used in the system error budget presented in Section 5.6.

5.4 SYSTEM LINK BUDGET AND IF STAGE GAIN DISTRIBUTION

An early step in the MRIS design was development of a system link budget for estimating the mmW and IF signal levels generated in the Test and Reference signal channels in each of the four operating bands. This guided the design of the mmW T/R modules and also defined the requirements for the single IF amplification and detection stage used to process the IF signals generated by the T/R modules. The system link budget and the IF stage gain distribution are discussed in the following subsections.

5.4.1 System Link Budget

The system link budget was developed by identifying individual factors that could influence the signal levels in each operating band. The cumulative effects of the individual factors were tabulated on a spread sheet format to estimate the mmW and IF signal levels at different points of the receiver chain. Factors considered in the system link budget include,

- o Transmit Power Levels
- o MMW Transmit Path Losses
- o Antenna Response
- o Plasma Attenuation

TABLE 5-3

**TABULATED VALUES FOR RANGE ERRORS
DUE TO FREQUENCY STEP ERRORS**

<u>δf (MHz)</u>	<u>δR (cm)</u>
± 5	± 0.124
± 10	± 0.248
± 20	± 0.496
± 40	± 0.992

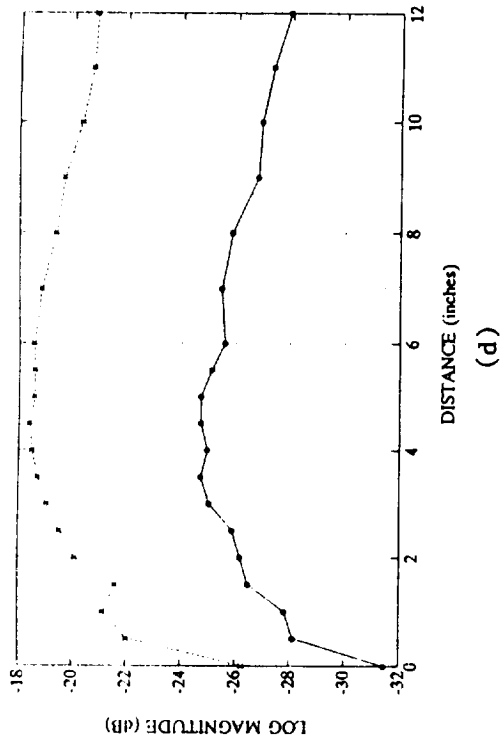
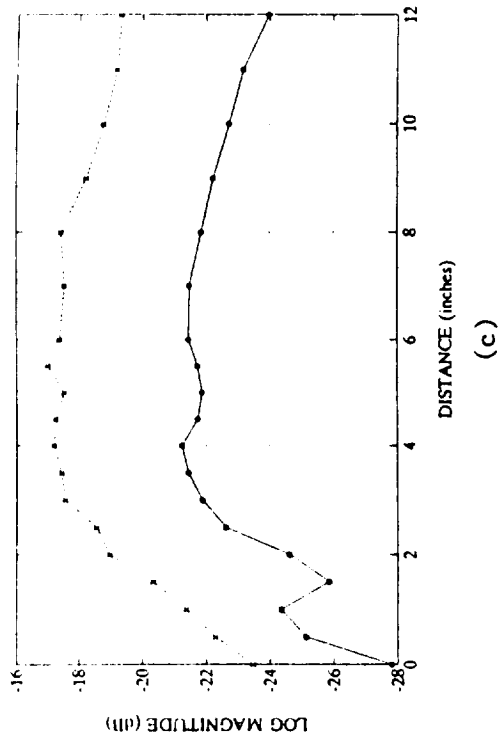
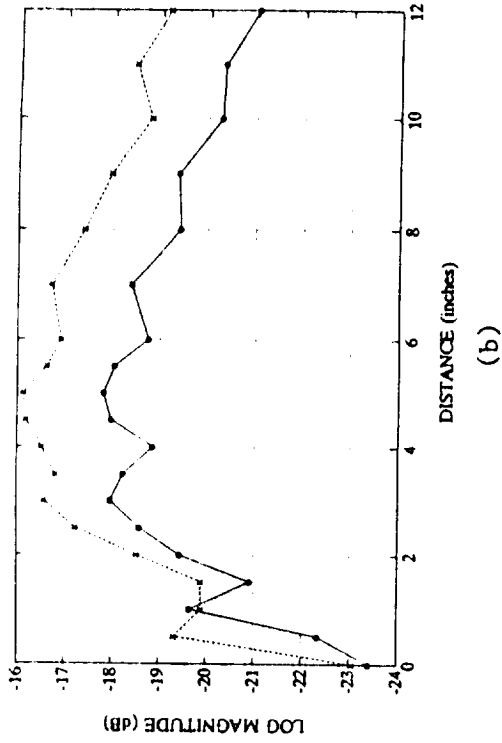
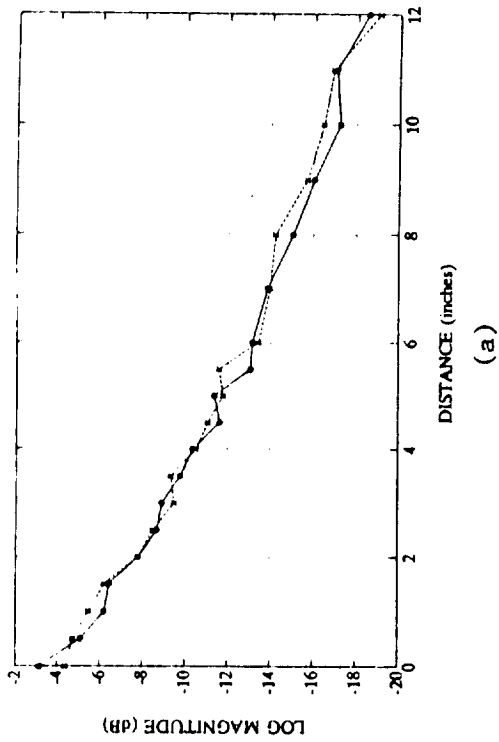
- o Tile Losses
- o MMW Receive Path Losses
- o IF Receive Gain

Initial evaluation of these factors was based on engineering estimates. In most cases, test data was subsequently used to refine the initial estimates as the instrument development advanced. One exception was the plasma attenuation estimates. In this case, NASA informed EMS that the initial engineering estimates were accurate and these values were maintained in the final system link budget. In making the transition from engineering estimates to measured test data, only one significant deviation was found. This occurred in Band-D where the transmit power level was initially estimated to be -8 dBm while the measured transmit power was found to be -20 dBm. This caused some adjustment of the IF gain distribution but did not have a significant impact on system performance.

A key step in development of the system link budget was estimating the response of the antennas and the losses induced by the TPS tile. Initial estimates from the report by Kreutel proved very accurate [2]. The actual antenna coupling and TPS tile losses measured during system testing for each of the four operating bands are shown in Figure 5-5 (the curved GFE tile was used for these measurements).

A summary of the system link budget is presented in Figure 5-6(a). An accompanying set of explanatory notes is presented Figure 5-6(b). A key purpose of the link budget was to estimate the minimum and maximum mmW signal levels that could appear at any mixer input port. The minimum and maximum mmW levels for the four operating bands are listed in Table 5-4. It was previously shown that the acceptable input range for Band-A, Band-B, and Band-C is -10 dBm to -72 dBm and that the acceptable range for Band-D is -15 dBm to -72 dBm. Thus, the estimated maximum and minimum mmW signal levels shown in Table 5-4 are compatible with the MRIS receiver input requirements.

It was also noted earlier that the minimum signal level to be measured in any band should be at least 24 dB above the receiver average noise. At the estimated average receiver noise floor of -98 dBm, the minimum (worst-case) SNR



o - With Tile
x - No Tile

Figure 5-5. Calibrated Test/Reference Log Magnitude vs Distance Data for the Four Bands With and Without the TPS Tile Over the Antennas (a) Band-A, (b) Band-B, (c) Band-C, and (d) Band-D

MRIS SYSTEM LINK BUDGET

	Band-A			Band-B			Band-C			Band-D		
	Ro	Rmax		Ro	Rinterm	Rmax	Ro	Rinterm	Rmax	Ro	Rinterm	Rmax
1. Standoff Distance												
2. PR @ PT = 0 dBm	0.0	-12.0		-24.0	-16.0	-20.0	-28.0	-16.0	-20.0	-28.0	-16.0	-21.0
3. Excess Plasma Loss	0.0	-2.8		0.0	-2.0	-5.0	0.0	-3.0	-18.0	0.0	-3.0	-22.0
4. PT (Actual)	-22.0	-22.0		-15.0	-15.0	-15.0	-11.0	-11.0	-11.0	-20.0	-20.0	-20.0
5. XMIT Loss	-1.0	-1.0		-1.2	-1.2	-1.2	-1.6	-1.6	-1.6	-1.8	-1.8	-1.8
6. Tile Loss (2-Way)	-1.0	-1.0		-2.0	-2.0	-2.0	-5.0	-5.0	-5.0	-5.1	-5.1	-5.1
7. Receive Loss	-10.2	-10.2		-1.2	-1.2	-1.2	-1.6	-1.6	-1.6	-1.8	-1.8	-1.8
8. PR @ mmW Mixer Input	-34.2	-49.0		-43.4	-37.4	-44.4	-47.2	-38.2	-57.2	-56.7	-47.7	-71.7
9a. Req'd Margin @ Max PR	0.0				6.0			6.0			6.0	
9b. Req'd SNR @ Min PR		-24.0				-24.0			-24.0			-24.0
10a. Test Sig Max & Min	-34.2	-73.0			-31.4	-68.4		-32.2	-81.2		-41.7	-95.7
10b. Ref Sig Lvl	-42.2				-35.0			-30.0			-40.0	
10c. SHCKT or THRU Lvl	-31.6				-15.8			-13.0			-22.0	
10d. mmW Dynamic Range	-31.6	-73.0			-15.8	-68.4		-13.0	-81.2		-22.0	-95.7
11. Mixer Conv. Loss	-5.5	-5.5			-7.0	-7.0		-8.0	-8.0		-11.0	-11.0
12a. IF Test Sig Max & Min	-39.7	-78.5			-38.4	-75.4		-40.2	-89.2		-52.7	-106.7
12b. IF Ref Sig Lvl	-47.7				-42.0			-38.0			-51.0	
12c. IF SHCKT or THRU	-37.1				-22.8			-21.0			-33.0	
12d. IF Dynamic Range	-37.1	-78.5			-22.8	-75.4		-21.0	-89.2		-33.0	-106.7

All Table Units are dB or dBm.

Figure 5-6(a). Final MRIS System Link Budget

NOTES FOR SYSTEM LINK BUDGET

- (1) STANDOFF DISTANCE: These values indicate the specific distances used to calculate the values listed in the budget.
- (2) PR @ PT = 0dBm: Indicates the received power for a transmit power of 0 dBm based on the antenna model developed by Kreutel [2]. Does not include the effects of the TPS tile or tile attenuation.
- (3) EXCESS PLASMA LOSS: Calculated from plasma attenuation equation provided by NASA.
- (4) PT (ACTUAL): Transmit power at output of T/R module.
- (5) XMIT LOSS: Attenuation in transmit path including antenna and module-to-antenna waveguide.
- (6) TILE LOSS (2-WAY): Reflection and attenuation loss of TPS tile.
- (7) RECEIVE LOSS: Attenuation in receive path including antennas, module-to-antenna waveguide, and front-end components.
- (8) PT @ mmW MIXER INPUT: Estimated mmW input power at each mixer input vs target range.
- (9a) REQ'D MARGIN @ MAX PR: Margin required to accomodate peaks in frequency domain response.
- (9b) REQ'D SNR @ MIN PR: Margin required above estimated noise peaks.
- (10a) TEST SIGNAL MAX & MIN: Dynamic range required for Test Signal levels.
- (10b) REF SIG LEVEL: Estimated Reference Signal level.
- (10c) SHCKT OR THRU LVL: Estimated short-circuit and THRU levels during calibration.
- (10d) DYNAMIC RANGE (mmW): The estimated dynamic range required at the input of the mmW mixers.
- (11) MIXER CON. LOSS: Estimated conversion loss for the mmW mixers.
- (12a) IF TEST SIGNAL MAX & MIN: Dynamic range required for IF Test Signal levels.
- (12b) IF REF SIG LEVEL: Estimated IF Reference Signal level.
- (12c) IF SHCKT OR THRU LVL: Estimated short-circuit and THRU levels during calibration.
- (12d) IF DYNAMIC RANGE (mmW): The estimated IF dynamic range required at the IF output of the mmW mixers.

Figure 5-6(b). Notes for Final MRIS System Link Budget

TABLE 5-4

**ESTIMATED MINIMUM AND MAXIMUM
SIGNAL LEVELS AT MIXER INPUT PORTS**

<u>BAND</u>	<u>CHAN</u>	<u>MAXIMUM (mmW)</u>	<u>MINIMUM (mmW)</u>
A	TEST	-31.6 dBm	-49.0 dBm
	REF	-42.2 dBm	-----
B	TEST	-15.8 dBm	-44.4 dBm
	REF	-35.0 dBm	-----
C	TEST	-13.0 dBm	-57.2 dBm
	REF	-29.0 dBm	-----
D	TEST	-22.0 dBm	-71.7 dBm
	REF	-40.0 dBm	-----

for the Test and Reference channel signal levels in Table 5-4 are listed Table 5-5. From the listed values, it may be observed that the required 24-dB SNR is achieved in all bands. The SNR in the Band-D Test channel just meets the requirement but this shouldn't be considered a problem since the design includes a margin of 3 dB. Also, if the SNR falls below 24 dB, system performance will degrade gracefully.

The system link budget also shows the expected minimum and maximum signal levels directly after IF down conversion (Row 12a, 12b, and 12c). These values and the associated mixer conversion loss in each band are listed in Table 5-6. From the values in Table 5-6, it may be noted that the largest and smallest IF signals to be measured by the IF chain are -21.0 and -82.7 dBm, respectively. The difference between these two values corresponds to a dynamic range of 61.7 dB. The required IF dynamic range can be reduced by using IF attenuators to normalize the IF signal levels to that of the maximum signal in the Band-D Test Channel as discussed in the next section.

5.4.2 Receiver IF Gain Distribution

Attenuators can be placed in the various IF channels to normalize the signal levels in each channel. This normalization process reduces the overall dynamic range requirements on the IF chain. The normalization scheme currently in place in the MRIS instrument is shown in Table 5-7. This scheme was based on conveniently available attenuator values and is not necessarily optimum. After normalization, the largest and smallest IF signals to be measured by the IF chain are -33.0 and -85.7 dBm, respectively. This difference between these two values corresponds to a dynamic range of 52.7 dB, an improvement over the 61.7 dB required before normalization.

The overall receiver IF gain distribution, including the normalization attenuators, is summarized in Figure 5-7. This summary uses the results from the system link budget and evaluates the signal level at different points in the IF chain. The purpose of this evaluation is to verify that receiver does not go into compression because of excessively high signal levels and that receiver noise floor is always lower than the weakest signal level. Examination

TABLE 5-5

**ESTIMATED SNR FOR THE TEST
AND REFERENCE SIGNAL CHANNELS**

BAND	CHAN	MINIMUM SNR
A	TEST	48 dB
	REF	55 dB
B	TEST	53 dB
	REF	62 dB
C	TEST	40 dB
	REF	61 dB
D	TEST	25 dB
	REF	57 dB

TABLE 5-6

ESTIMATED IF SIGNAL LEVELS DIRECTLY FROM MIXERS

BAND	C.LOSS	CHAN	MAXIMUM (IF)	MINIMUM (IF)
A	5.5 dB	TEST	-37.1 dBm	-54.5 dBm
		REF	-47.7 dBm	-----
B	7.0 dB	TEST	-22.8 dBm	-51.4 dBm
		REF	-42.0 dBm	-----
C	8.0 dB	TEST	-21.0 dBm	-65.2 dBm
		REF	-37.0 dBm	-----
D	11.0 dB	TEST	-33.0 dBm	-82.7 dBm
		REF	-51.0 dBm	-----

NOTE:

Total IF dynamic range requirement without normalization is:

$$-21.0 \text{ dBm} - (-82.7 \text{ dBm}) = 61.7 \text{ dB}$$

TABLE 5-7

IF LEVELS AFTER NORMALIZATION WITH ATTENUATORS

BAND	CHAN	ATTEN	MAXIMUM (IF)	MINIMUM (IF)
A	TEST	4 dB	-41.1 dBm	-58.5 dBm
	REF	3 dB	-50.7 dBm	-----
B	TEST	12 dB	-34.8 dBm	-64.4 dBm
	REF	2 dB	-44.0 dBm	-----
C	TEST	12 dB	-33.0 dBm	-77.2 dBm
	REF	3 dB	-40.0 dBm	-----
D	TEST	3 dB	-36.0 dBm	-85.7 dBm
	REF	2 dB	-54.0 dBm	-----

NOTE:

Total IF dynamic range requirement after normalization is:

$$-33.0 \text{ dBm} - (-85.7 \text{ dBm}) = 52.7 \text{ dB}$$

MRIS RECEIVER IF GAIN DISTRIBUTION

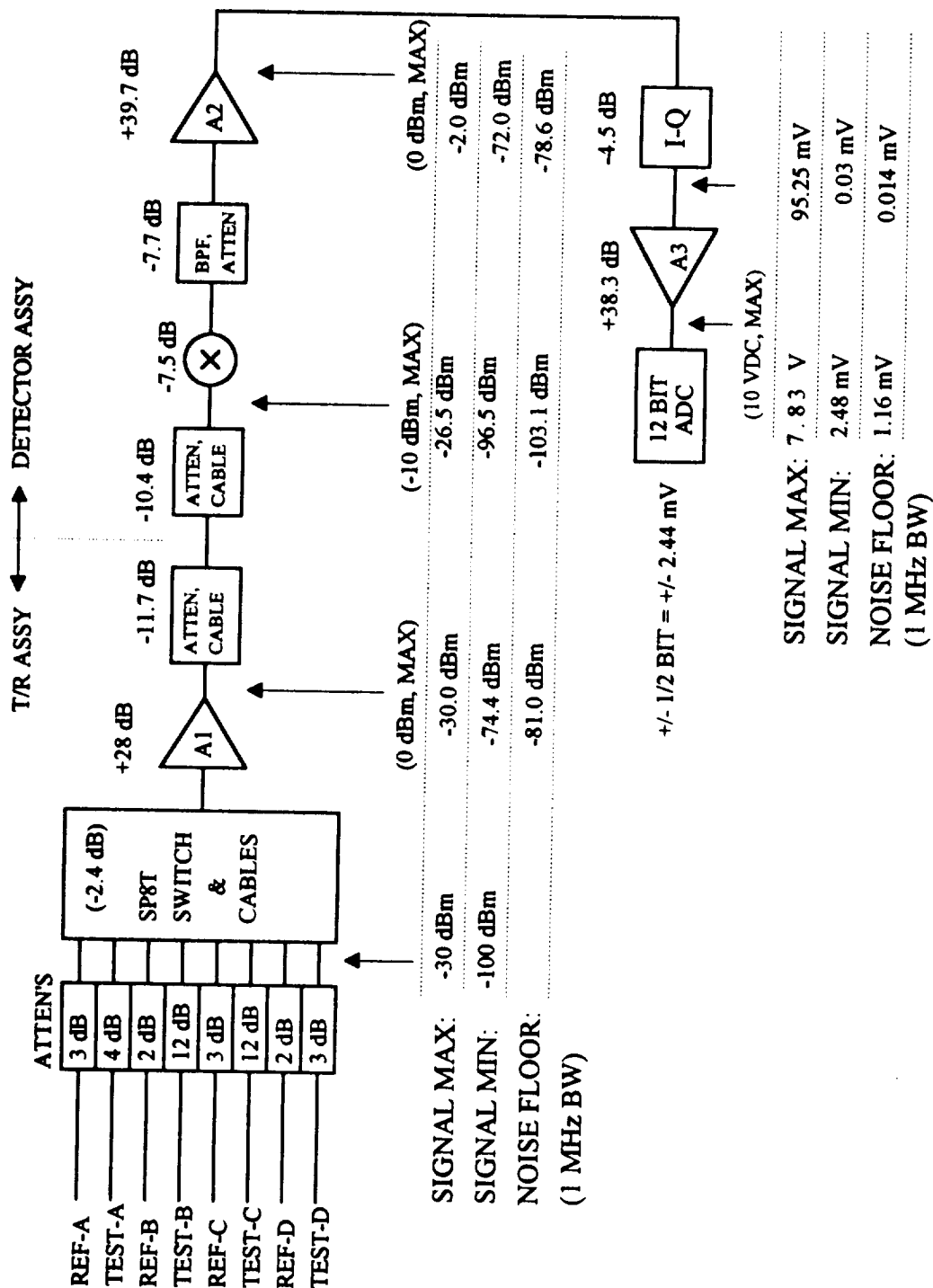


Figure 5-7. Final MRIS Receiver IF Gain Distribution

of the figure shows that this objective is met at all points in the receiver chain.

5.5 SYSTEM CALIBRATION DISCUSSION

5.5.1 Summary

System calibration is the procedure used to account for systemic errors that corrupt measurement accuracy and degrade the performance of the MRIS instrument. For the MRIS instrument, the systemic errors in question are caused by imperfections in components preceding the antennas. Therefore, the system calibration procedure does not account for errors caused by the antennas and TPS tiles. Errors due to these sources are accounted for by the Vector Error Correction procedures discussed in Appendix B of this report.

For monostatic operation, the initial system calibration goal was to implement a full one-port error model that accounted for Directivity, Source Match, and Frequency Tracking errors. Subsequent testing indicated that a simplified model based on determining only the Directivity and Frequency Tracking errors was adequate. For bistatic operation, the system calibration goal was implementation of a response/isolation model that accounted for Isolation and Frequency Tracking errors.

Following implementation of the error correction models, investigations were conducted to determine the magnitude of the performance improvements offered by system calibration. In general, it was determined that system calibration was worthwhile for Band-A operation but did not significantly improve performance in Band-B, -C, or -D. A more detailed description of the error correction models and a discussion of test results are presented below.

5.5.2 Monostatic and Bistatic Calibration Models

5.5.2.1 Monostatic Model

System calibration models used in the MRIS instrument were based on simplified versions of the familiar error models used for error correction of laboratory

network analyzers such as the HP8510 [3]. For the monostatic operation used in Band-A, the one-port correction model is represented as,

$$S_{11M} = E_{DF} + (S_{11A} \cdot E_{RF}) / (1 - S_{11A} \cdot E_{SF}) \quad (5-18)$$

where,

S_{11M} = "Measured" Reflection Coefficient

S_{11A} = "Actual" Reflection Coefficient

E_{DF} = Directivity Error

E_{SF} = Source Match Error

E_{RF} = Frequency Tracking Error

During testing of the MRIS instrument, a simplified model in which E_{SF} was assumed to be zero, proved very effective. With this simplification, the error correction model can be rewritten as,

$$S_{11M} = E_{DF} + E_{RF} \cdot S_{11A} \quad (5-19)$$

Calibration for the monostatic case consists of initially measuring a matched load for which S_{11A} is theoretically zero (a load with a measured S_{11A} of -40 dB was used in practice). This measurement allows the Directivity Error to be computed as,

$$E_{DF} = LD \quad (5-20)$$

where the parameter LD represents the complex quantity measured with the system terminated with the matched load. With E_{DF} known, a measurement is performed on a short-circuit for which S_{11A} is theoretically -1. This measurement allows the Frequency Tracking Error to be computed as,

$$E_{RF} = -(SC - LD) \quad (5-21)$$

where SC represents the complex quantity measured with the system terminated by a short-circuit. With E_{DF} and E_{RF} known, the actual reflection coefficient

(S_{11_A}) corresponding to the error contaminated measured reflection coefficient (S_{11_M}) can be computed as,

$$S_{11_A} = -(S_{11_M} - LD)/(SC - LD) \quad (5-22)$$

5.5.2.2 Bistatic Model

The equation describing the response-isolation model used for the bistatic system calibration can be written as,

$$S_{21_M} = E_{XF} + E_{TF} \cdot S_{11_A} \quad (5-23)$$

where,

S_{21_M} = "Measured" Transmission Coefficient
 S_{11_A} = "Actual" Transmission Coefficient
 E_{XF} = Isolation Error
 E_{TF} = Frequency Tracking Error

This equation has the exact same form as the simplified monostatic model. The calibration process is therefore similar. Calibration consists of initially performing a measurement with the transmit and receive ports completely isolated from each other. This is accomplished by terminating both ports with matched loads. This measurement allows the Isolation Error to be computed as,

$$E_{XF} = ISOL \quad (5-24)$$

where the parameter ISOL represents the complex quantity measured with the system terminated with the matched load. With E_{XF} known, a measurement is performed with the transmit and receive ports connected directly together. In this case, S_{21_A} is theoretically +1 (a delay term can be used to account for waveguide length if a finite waveguide length is used to make the connection). This measurement allows the Frequency Tracking Error to be computed as,

$$E_{TF} = (THRU - ISOL) \quad (5-25)$$

where the parameter THRU represents the complex quantity measured with the transmit and receive ports connected. With E_{XF} and E_{TF} known, the actual transmission coefficient ($S21_A$) corresponding to the error contaminated measured transmission coefficient ($S21_M$) can be computed as,

$$S21_A = (S21_M - ISOL)/(THRU - ISOL) \quad (5-26)$$

Test results obtained with these two error correction models are discussed in the next subsection.

5.5.3 Calibrated vs Uncalibrated Performance

5.5.3.1 Measurements with HP8510

Prior to completion of the T/R modules by Millitech, system testing was performed at EMS using an existing HP8510B system. Because of hardware availability, system testing was limited to Band-A and Band-B. One goal of these early tests was to determine if system calibration would have a significant impact on the performance of the MRIS instrument. The basic test performed consisted of measuring the time-delay of the return from a flat-plate target as the target was stepped through standoff distances from 0 to 2 inches. As noted previously, a graph of measured time delay versus standoff distance should consist of a straight line of the form,

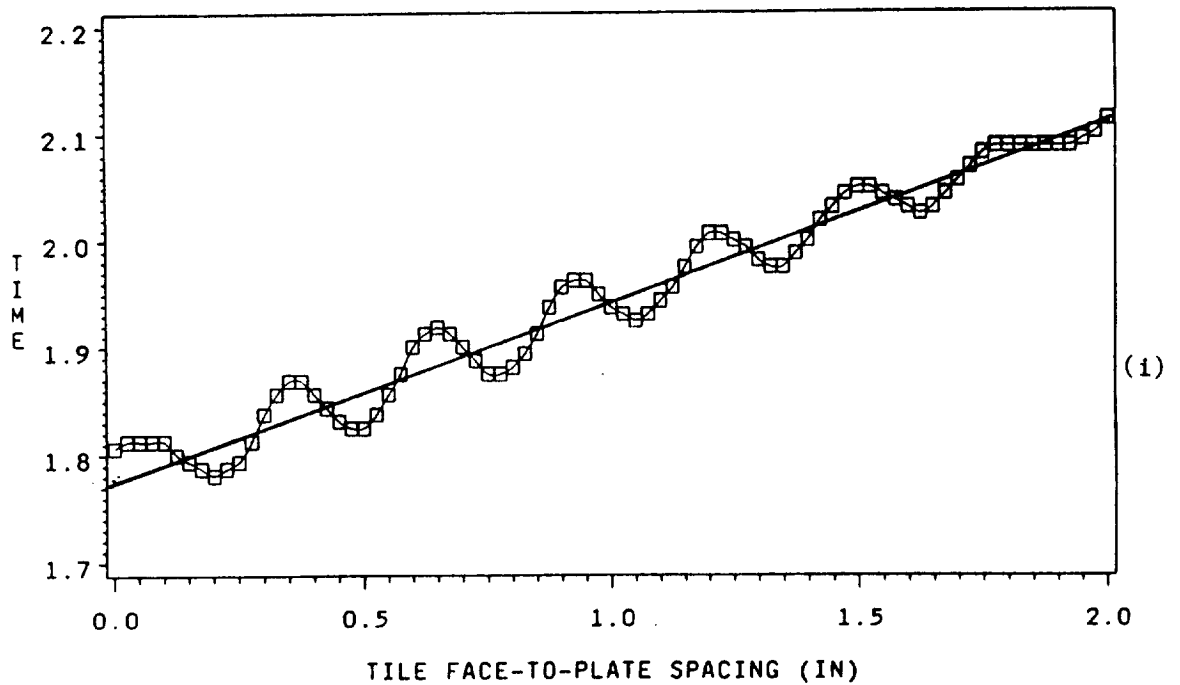
$$\tau = m*d + \tau_0 \quad (5-27)$$

where the slope m has a value of $6.667E-11$ sec/cm (or $1.6934E-10$ sec/inch).

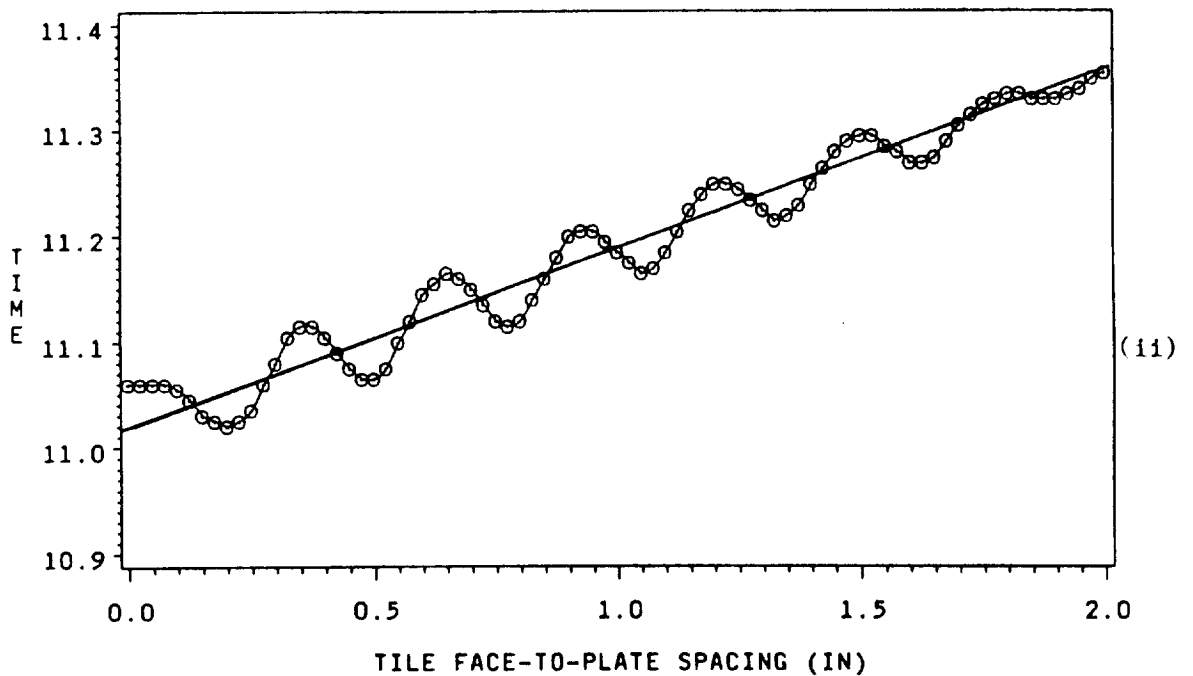
Graphs of data measured with and without system calibration in Band-A are shown in Figure 5-8(a). A straight line of slope m is shown superimposed on the data in these graphs. For the graph of the data taken using calibration, the τ_0 value is 1.8 ns which corresponds to a free-space distance of 10.6 inches. Since this offset is measured relative to the calibration plane, it corresponds to the approximate length of the antenna, circular-to-rectangular waveguide transition, and interconnecting waveguide.

MRIS

BAND-A HP8510 DATA

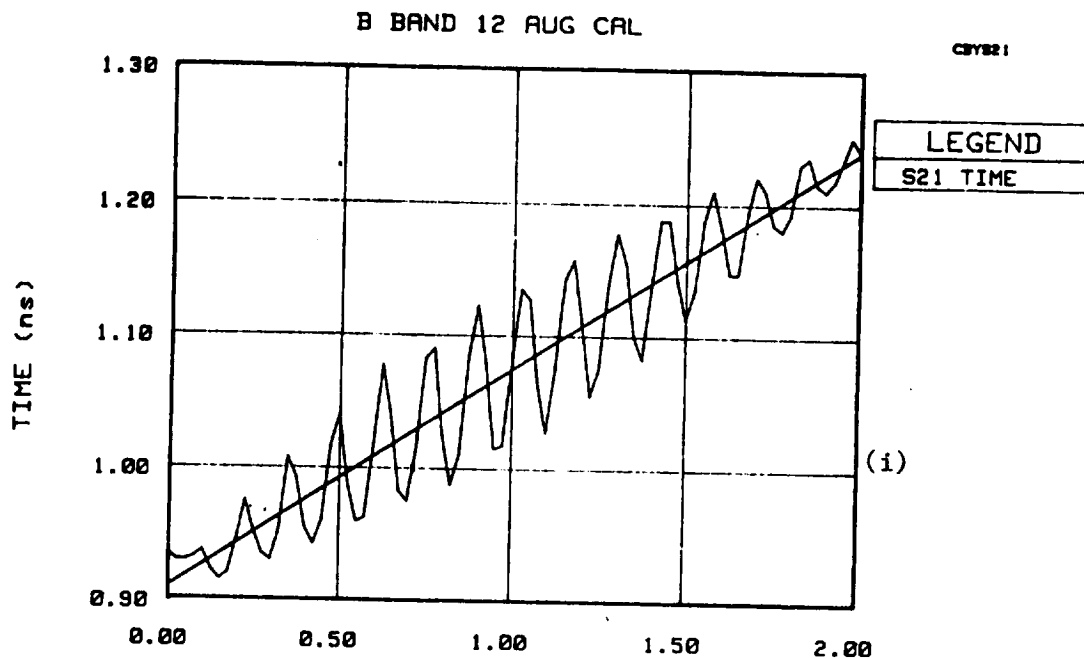


SQUARE=WITH CAL MIN WINDOW

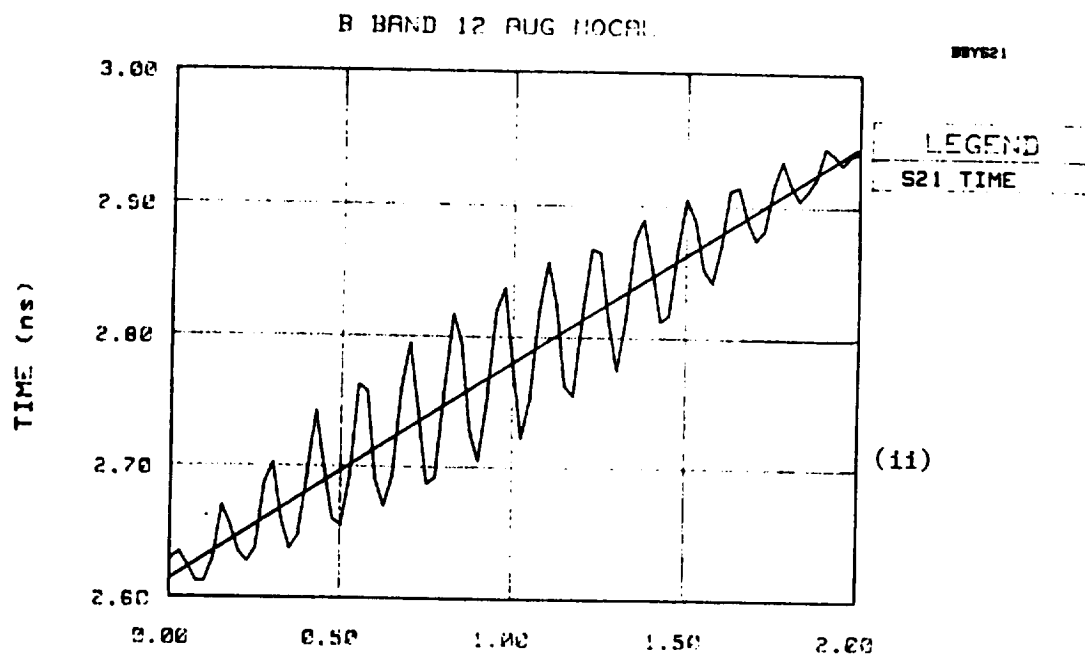


CIRCLE=NO CAL MIN WINDOW

Figure 5-8(a). Time Delays Measured in Band-A using the HP8510 Network Analyzer: (i) With System Calibration and (ii) Without System Calibration



01:00:25 1 Mar 1980



14:21:51 12 Aug 1981

Figure 5-8(b). Time Delays Measured in Band-B using the HP8510 Network Analyzer: (i) With System Calibration and (ii) Without System Calibration

For the graph of the data taken without calibration, the τ_0 value is approximately 11.06 ns. This offset corresponds to a free-space distance of 65 inches. However, because a calibration plane was not established, this latter offset value cannot be associated with a useful reference plane. The lack of a defined reference plane does not pose a problem since all target measurements can be referenced to measurements on a target at a known distance.

In both cases shown in Figure 5-8(a), it may be observed that the measured time delay deviates from the ideal straight line by a maximum value of ± 0.06 ns. This deviation corresponds to a distance measurement error of ± 0.9 cm. Since the deviation is the same in both graphs, it may be concluded that calibration did not improve the performance of the HP8510 Band-A measurements.

Similar results were observed for the Band-B measurements made with the HP8510 system. Graphs of data measured with and without system calibration in Band-B are shown in Figure 5-8(b). A straight line of slope m is again shown superimposed on the data in these graphs. For the graph of the data taken using calibration, the τ_0 value is 0.94 ns which corresponds to a free-space distance of 5.6 inches. As before, this offset corresponds to the approximate length of the antenna, circular-to-rectangular waveguide transition, and interconnecting waveguide.

In both cases shown in Figure 5-8(b), the measured time delay deviates from the ideal straight line by a maximum value of ± 0.06 ns, corresponding to a distance measurement error of ± 0.9 cm. Since the deviation is the same in both graphs, it may again be concluded that calibration did not improve the performance of the HP8510 Band-B measurements.

Based on the data in the preceding discussion, it was concluded that system calibration was not a critical issue for either monostatic or bistatic operation. In subsequent measurements performed with the mmW T/R Modules, it was confirmed that calibration did not have a profound effect on the bistatic operation used in Band-B, -C, or -D. However, it was determined that some

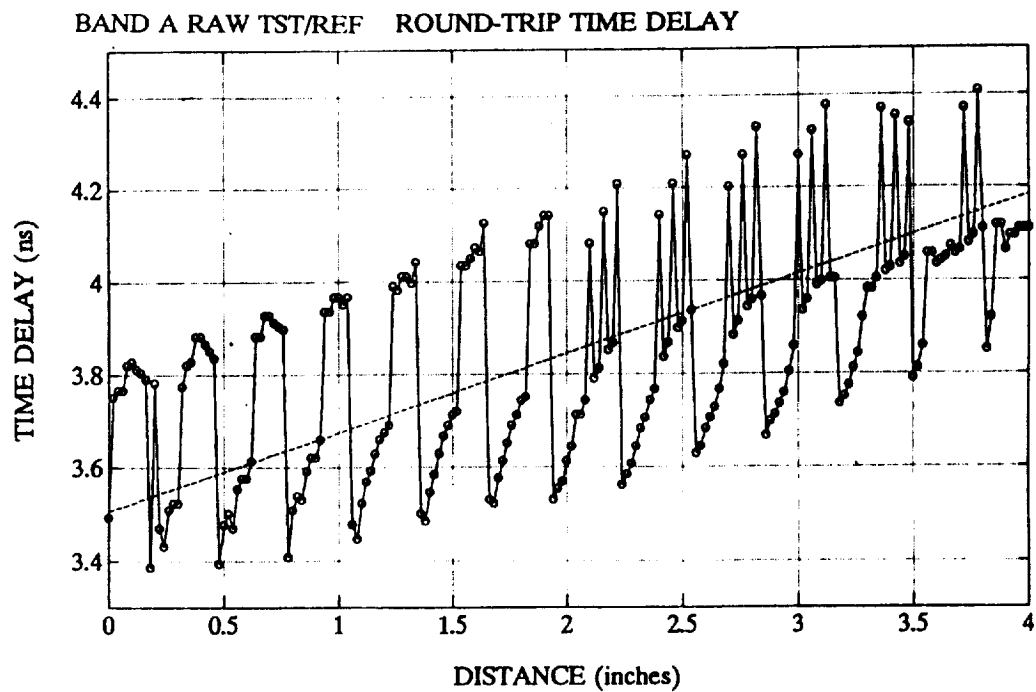
form of system calibration should be used for Band-A. These results are discussed below.

5.5.3.2 Measurements with mmW T/R Modules

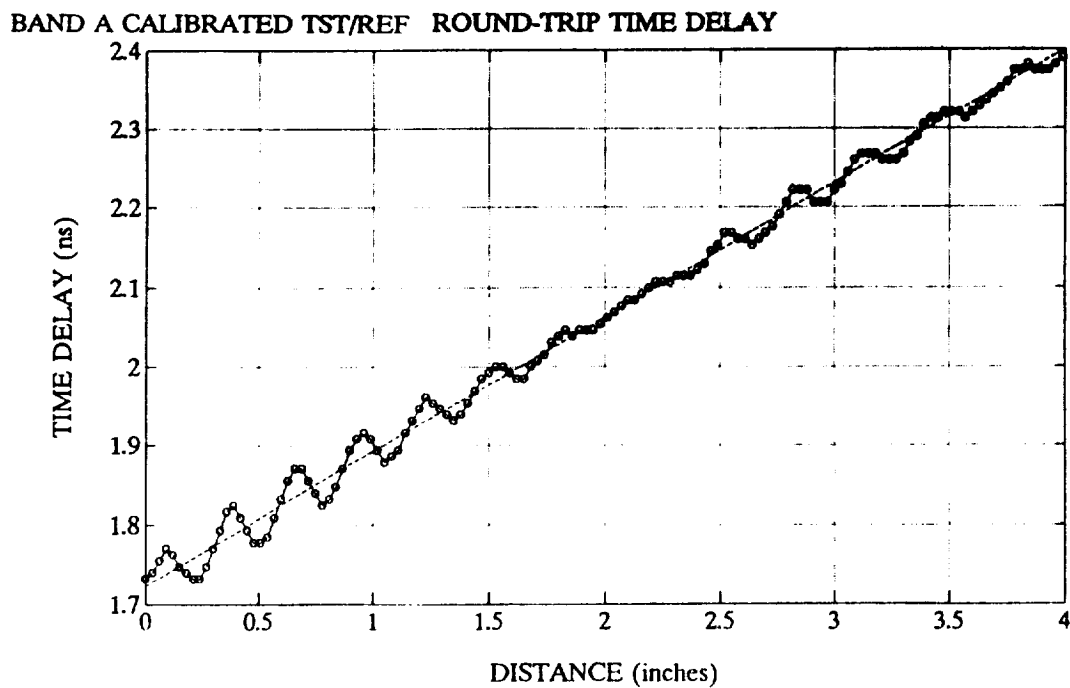
Comparison of time delay measurements performed with and without calibration using the Band-A T/R Module are depicted in Figure 5-9. A significant difference can be observed in the two cases. For data taken without calibration, the worst case deviation from the ideal straight line is ± 0.3 ns or ± 4.5 cm. This error is significantly larger than the system specification of ± 1.0 cm. With system calibration applied, a significant improvement is observed. In this example, the worst case deviation from the ideal straight line is only ± 0.04 ns or ± 0.6 cm with calibration applied (slightly better than that observed using the HP8510).

Initially, it was believed that the poor performance observed without calibration was due to VSWR problems that might be occurring because of several sharp bends in the waveguide used between the Band-A T/R Module and antenna. However, testing indicated that the waveguide did not have significant VSWR problems. In subsequent discussions with NASA personnel, it was theorized that the problem might be due to waveguide dispersion. In principle, waveguide dispersion causes the time-delay to a fixed-range target to vary with frequency. Thus, a fixed-range target will appear to be distributed in range as the sweep frequency is varied. To achieve low waveguide dispersion, the time delay difference across each frequency sweep band must be small.

To determine if dispersion was possibly a problem, the time delay through waveguide lengths matching those used with each T/R module were calculated for each of the four MRIS operating bands. Results of the calculations are summarized in Figure 5-10. The calculated values show that the time delay deltas across the sweep bandwidths of Band-B, -C, and -D are small. However, a very large time delay delta of 0.587 ns (8.8 cm in air) was observed for Band-A. This amount of dispersion would cause the target to appear to be at different ranges as the operating frequency is swept from 18-22 GHz.



(a)



(b)

Figure 5-9. Time Delays Measured using the Band-A T/R Module: (a) Without System Calibration and (b) With System Calibration

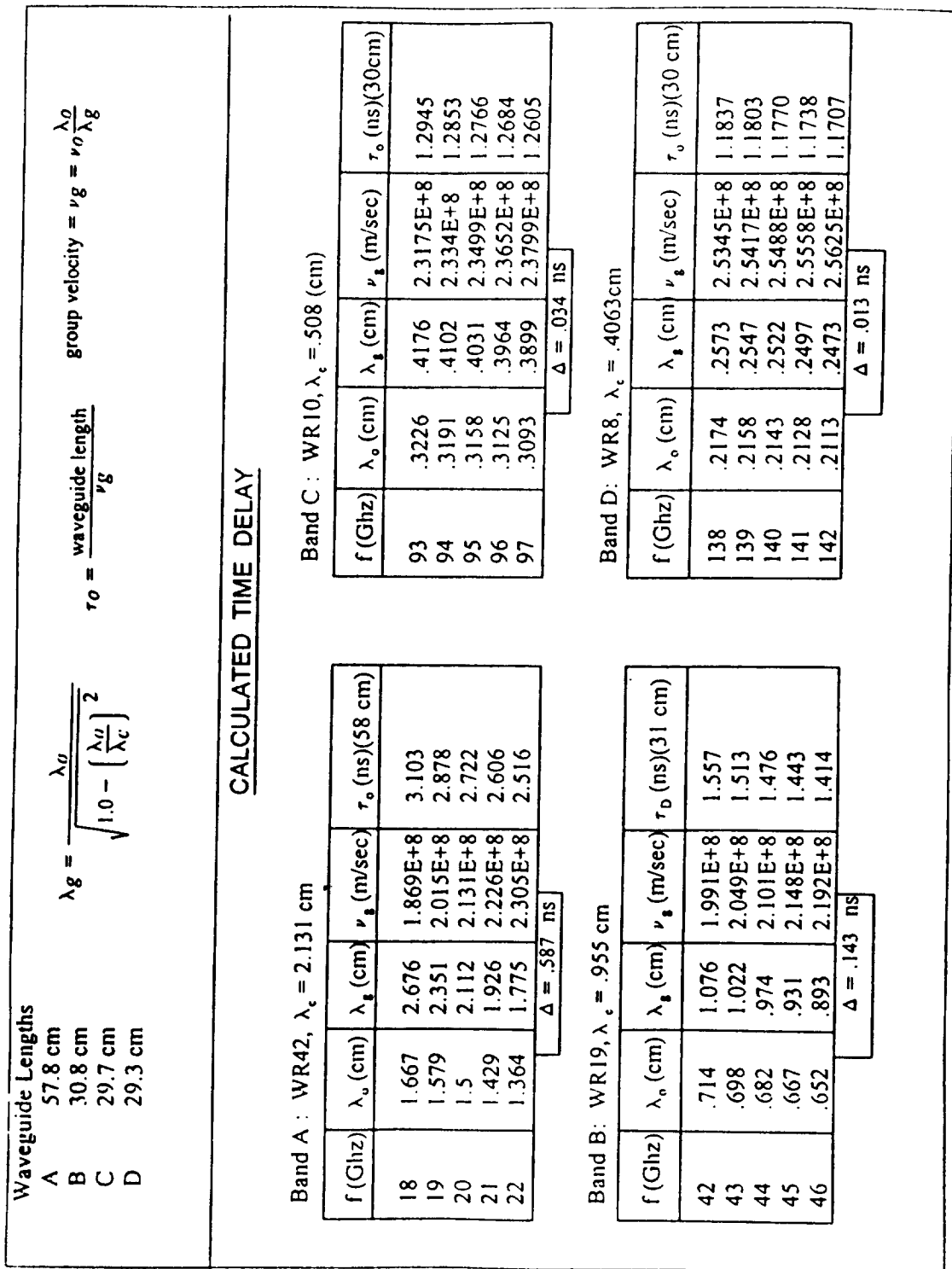


Figure 5-10. Dispersion Calculations for Waveguide Interconnecting Lengths used in MRIS Instrument

The effects of dispersion can be observed in Figure 5-11(a) which shows the time domain response obtained for a fixed-position flat plate target when uncalibrated measurements were made with the Band-A module. As predicted, it can be observed that the target return is smeared, making determination of the target location difficult. Results from similar uncalibrated measurements with the Band-B and -C modules are depicted in Figures 5-11(b) and -11(c) (uncalibrated data was not available for Band-D). In these time domain plots, low dispersion allows a distinct target signal to be observed which enhances the ability to determine the target location.

Subsequent tests with the Band-A T/R Module confirmed that dispersion in the module-to-antenna waveguide was a problem. In one test, uncalibrated measurements were compared for a short-circuit placed directly at the module T/R port versus a short-circuit placed at the end of the module-to-antenna waveguide. The resulting data is shown in Figure 5-12. Several observations can be made.

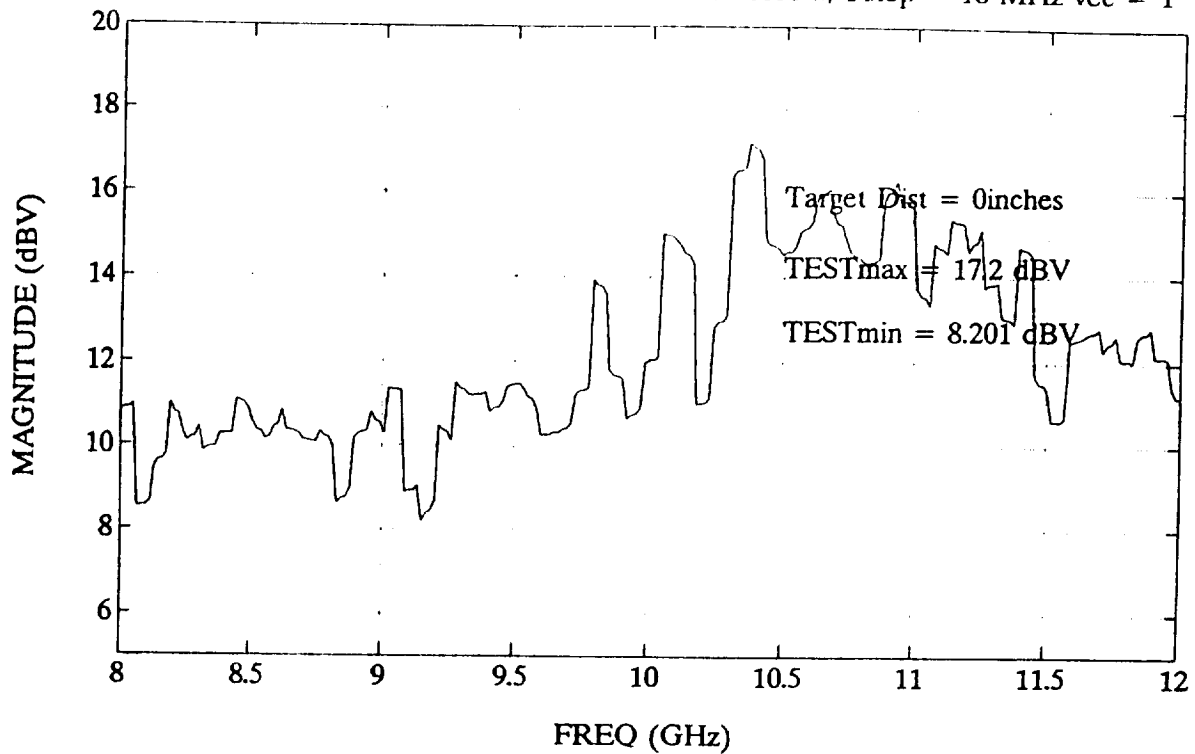
The time-domain plot for the short-circuited module shows a relatively distinct return signal. The corresponding plot for the short-circuited waveguide shows a smeared return signal, indicating the effects of dispersion. For the short-circuited module data in Figure 5-12(a), the amplitude of the return signal observed in the time-domain data is 12.04 dBV. For the short-circuited waveguide data in Figure 5-12(b), the amplitude of the return signal observed in the time-domain data has a peak value of only 10.87 dBV. Thus, the spreading due to dispersion also influences the peak amplitude observed for the return signal.

As a final test, Band-A data was taken for the short-circuited waveguide across four 1 GHz bandwidths, 18-19 GHz, 19-20 GHz, 20-21 GHz, 21-22 GHz. Because of dispersion, the target return signal should appear to be at a different range for each of the four measurements. Results of this test are shown in Figure 5-13(a). As predicted, the target appeared to move from 2.55 ns for the 18-19 GHz measurements to 2.977 ns for the 21-22 GHz measurements. The 0.427 ns difference between these two values represents a distance of 6.4 cm and indicates significant effects of dispersion in Band-A. Results for a similar set of measurements performed with the Band-C module are shown

WAVEGUIDE SHORT CIRCUIT

5-Mar-92

MRIS BAND A LOG MAGNITUDE RAW DATA w/ Fstep = 16 MHz vec = 1



TIME RESPONSE w/ 2048 point FFT

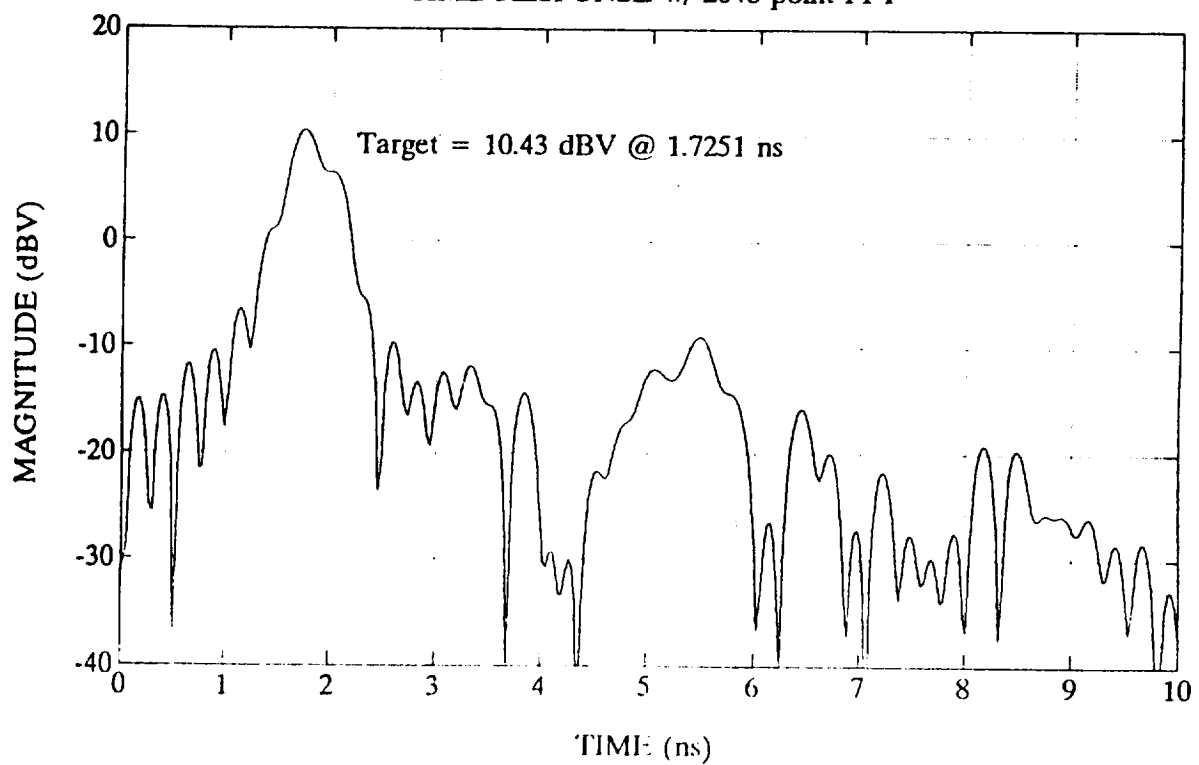
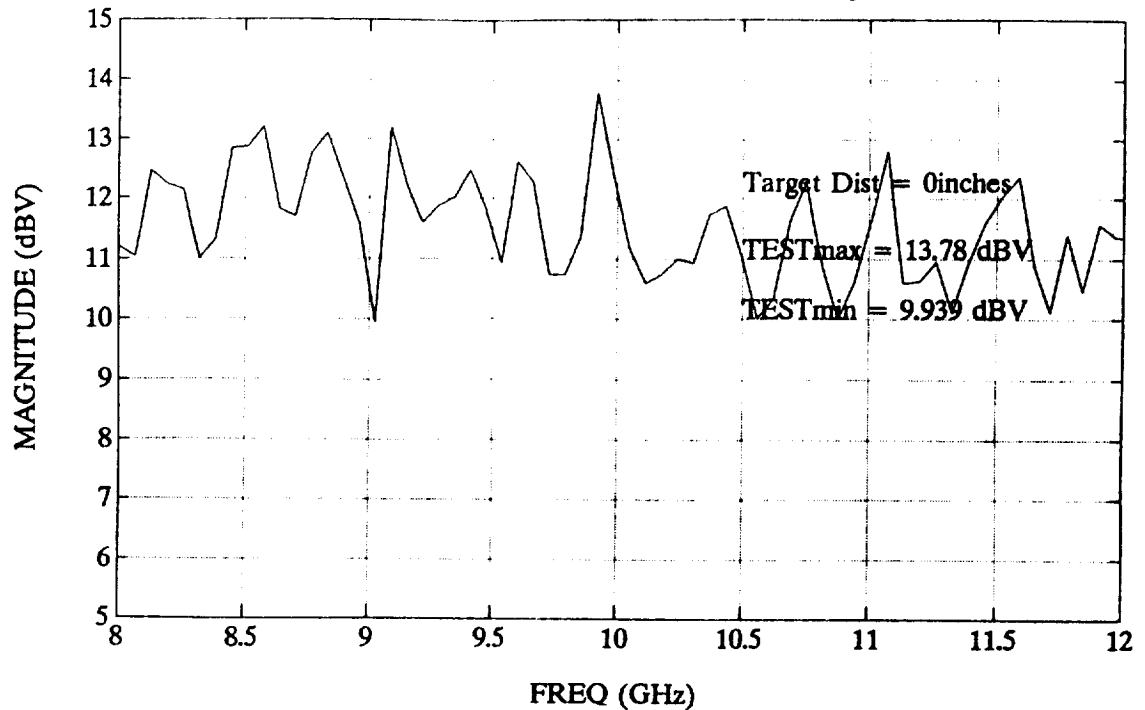


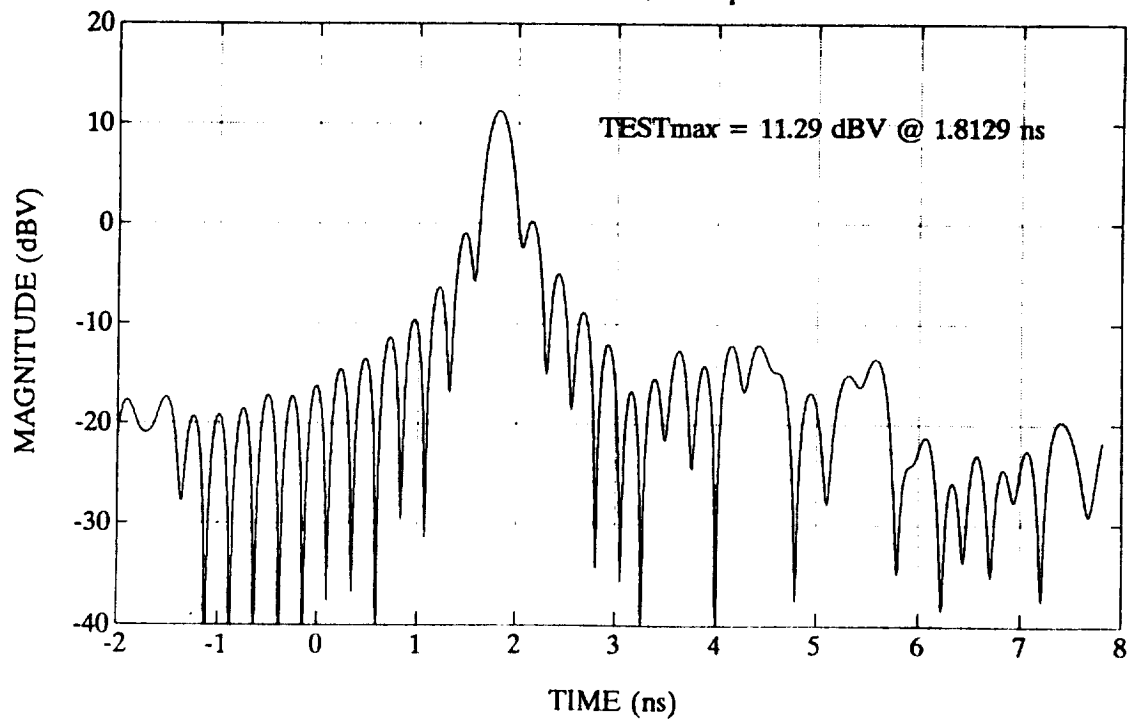
Figure 5-11(a). Uncalibrated Band-A Time Domain Response Showing Significant Spreading of Target Return due to Waveguide Dispersion

29-Dec-91

MRIS BAND B LOG MAGNITUDE RAW DATA w/ Fstep = 64 MHz vec = 1



TIME RESPONSE w/ 2048 point FFT



FILE NAMES: TEST CHANNEL- btwg_sc
REFERENCE CHANNEL- brwg_sc

Figure 5-11(b). Uncalibrated Band-B Time Domain Response Showing Minimal Spreading of Target Return due to Waveguide Dispersion

6-Mar-92

MRIS BAND C LOG MAGNITUDE RAW DATA w/ Fstep = 16 MHz vec = 1

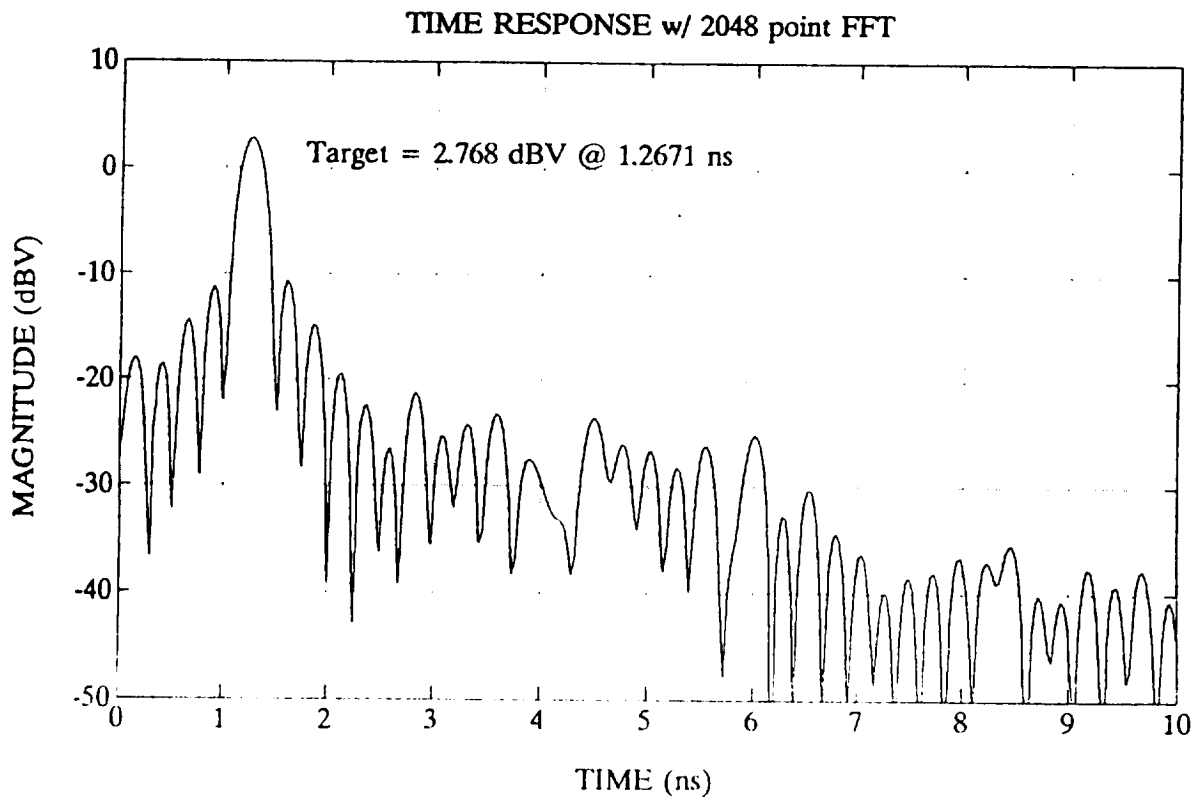
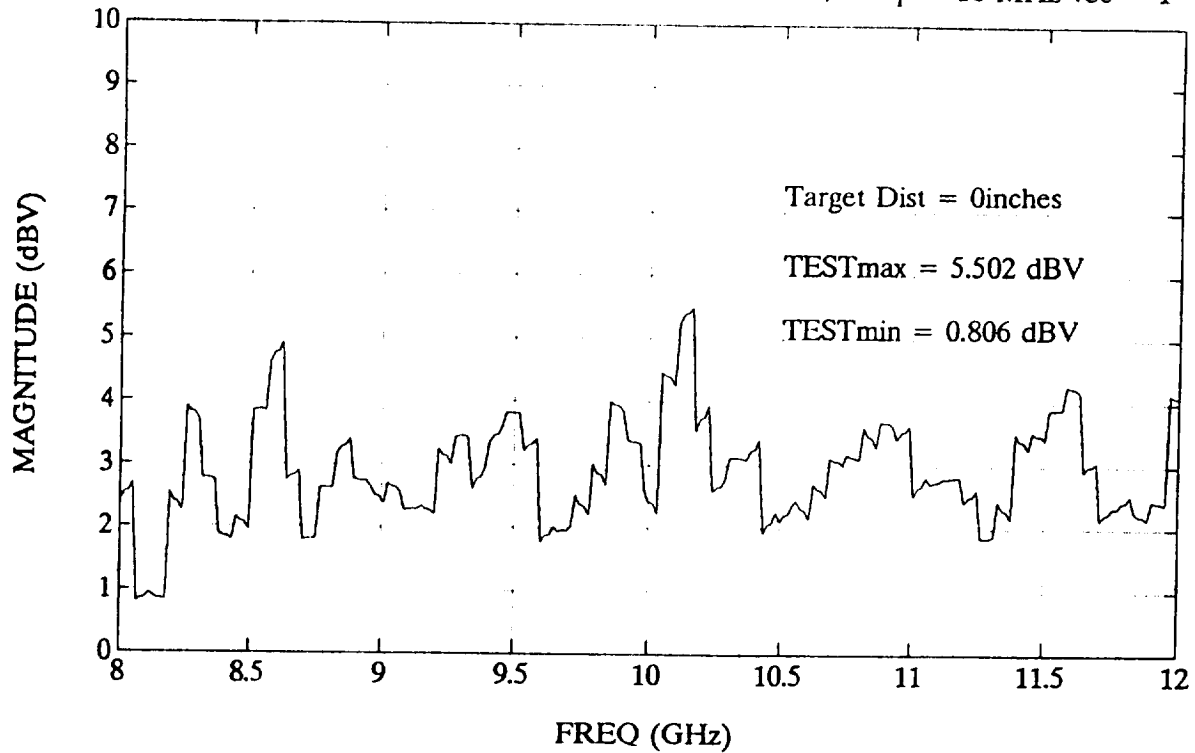


Figure 5-11(c). Uncalibrated Band-C Time Domain Response Showing Minimal Spreading of Target Return due to Waveguide Dispersion

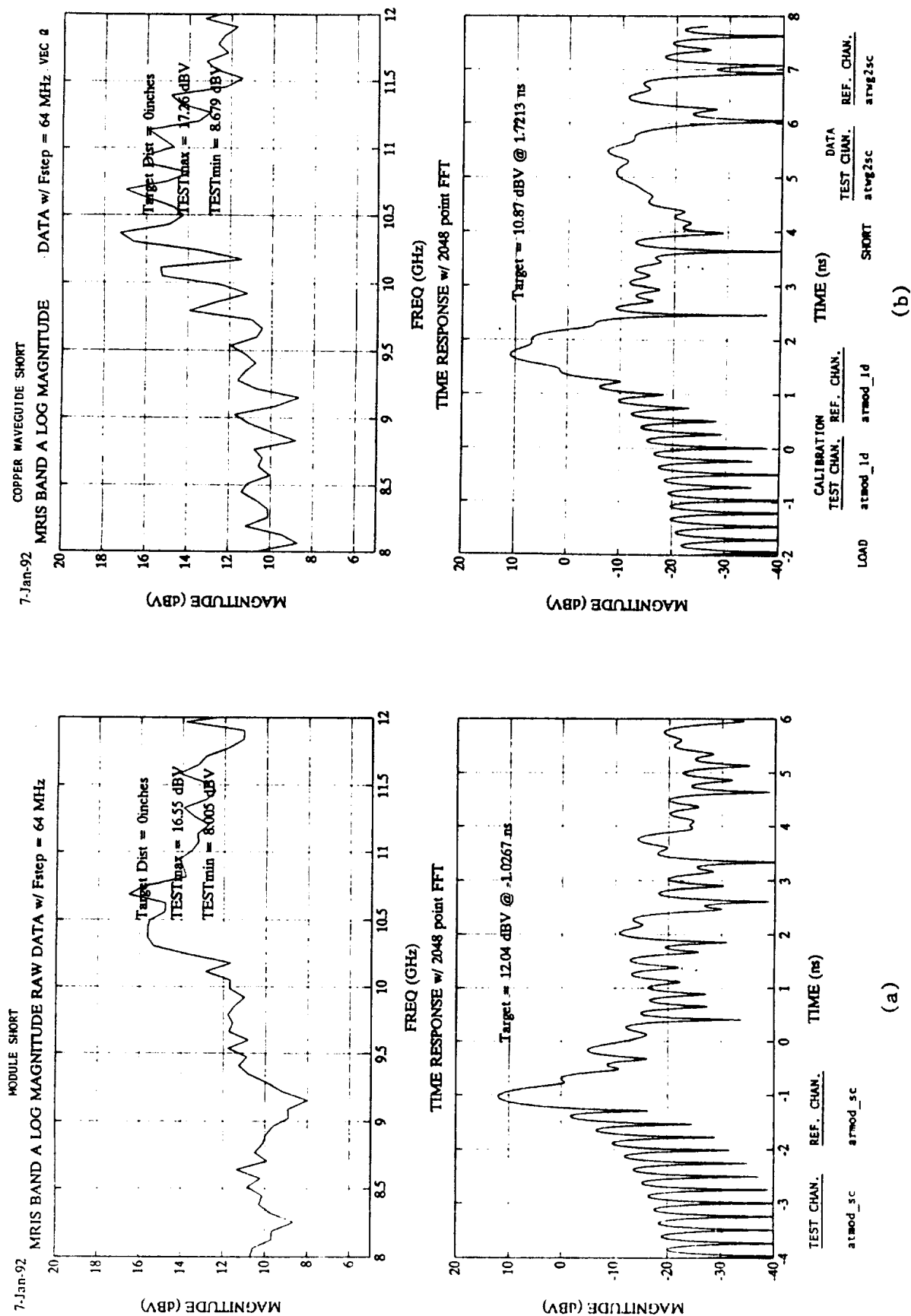


Figure 5-12. Comparison of Dispersion Effects for (a) Short Circuit Directly at Band-A T/R Module Waveguide Port and (b) Short Circuit at End of Band-A Module-to-Antenna Waveguide

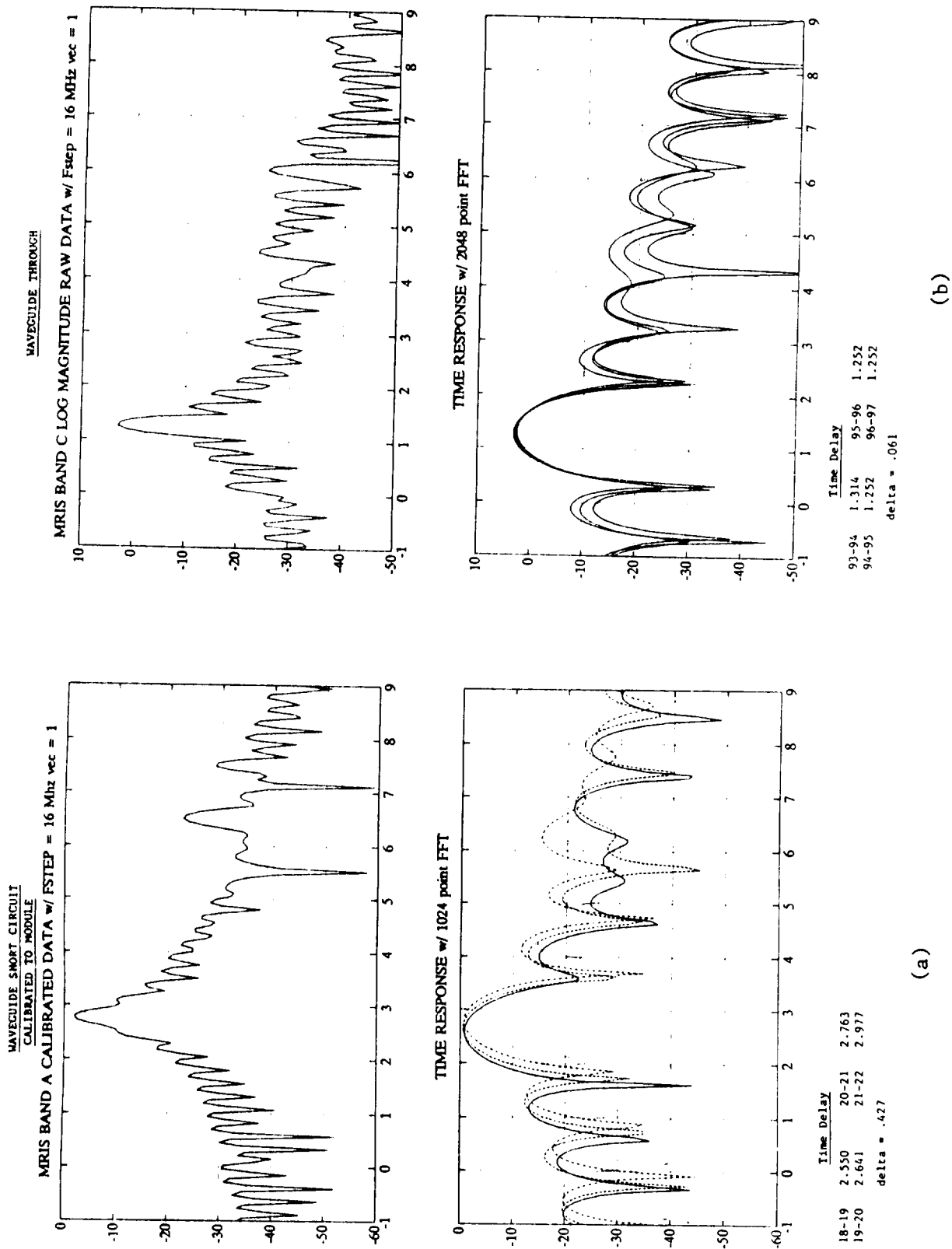


Figure 5-13. Time Domain Data Demonstrating (a) Significant Effects of Dispersion in four Band-A Sub-bands and (b) Minimal Effects of Dispersion in four Band-C Sub-bands

in Figure 5-13(b). In this case, only minimal spreading due to dispersion can be observed.

5.5.3.3 Conclusions

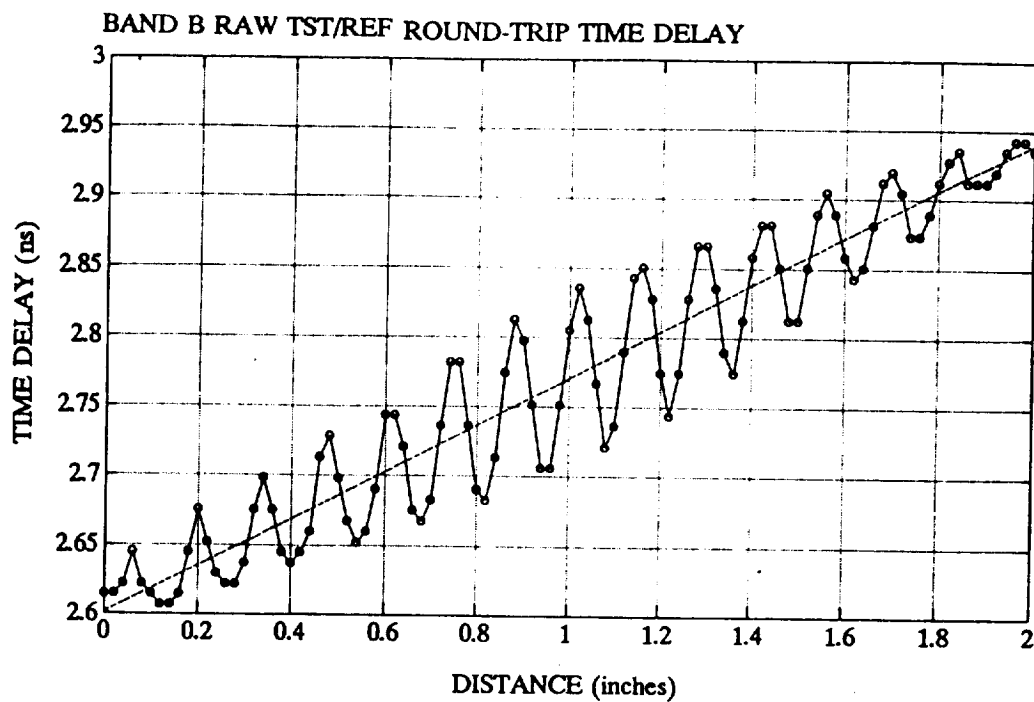
System calibration did not have a significant effect for measurements made in the three higher frequency bands. Example time delay plots of calibrated and uncalibrated data for Band-B are shown in Figures 5-14 (similar results were obtained in Band-C and -D). Examination of this graph shows that comparable accuracy is achieved with or without system calibration.

System calibration clearly had a significant effect on operation with the Band-A module. However, it appears the primary benefit of system calibration in Band-A is to simply correct the effects of waveguide dispersion. This correction is primarily achieved through the Frequency Tracking Error term, E_{RF} . The Directivity Error term, E_{DF} does not appear to be critical since it precedes the target return in time and for all practical purposes is gated out.

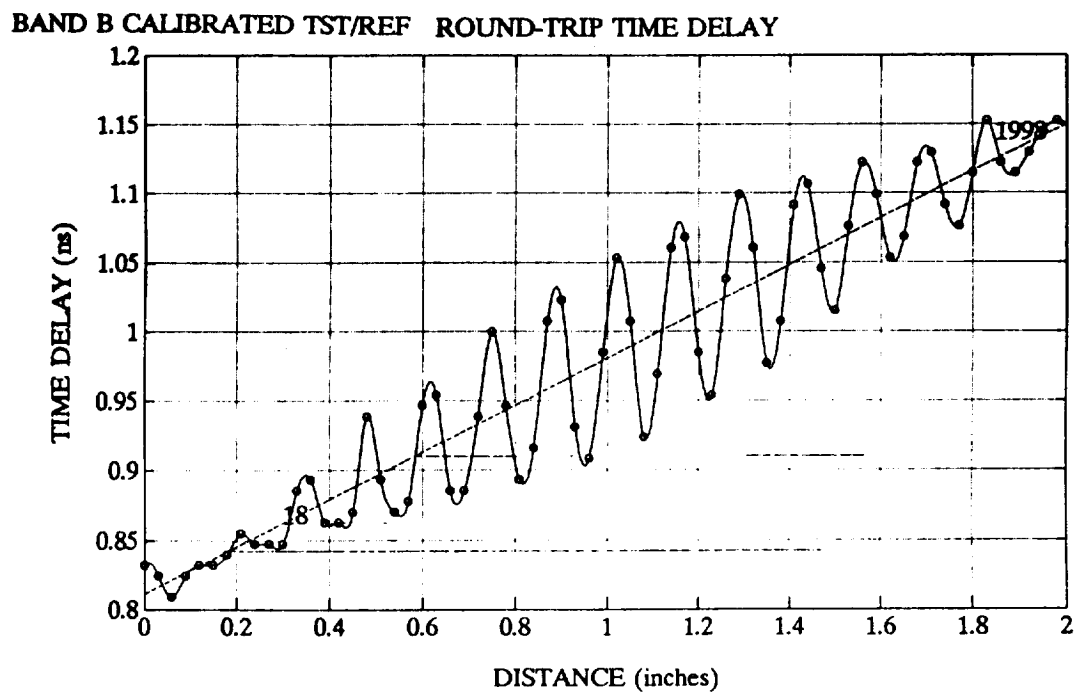
Once the Frequency Tracking Errors are established, it is probable that system accuracy will not be strongly influenced by any drift that may occur in the system calibration. That is, since the main influence of the calibration is to correct for waveguide dispersion, any drift in the calibration terms will not result in target smearing and will simply cause the absolute target position in the time domain outputs to drift. Any apparent problems can be routinely handled by performing a measurement on a target with a known position to establish a measurement reference point. In most cases, it appears the return signal received from the TPS tile can serve as the required reference position.

5.5.4 Frequency Response of Error Terms

Investigations were planned to evaluate the behavior of the system calibration error terms versus frequency. The motivation for these investigations was to verify that the error correction terms did not behave in a manner that necessitated placing stringent frequency stability requirements on the mmW local



(a)



(b)

Figure 5-14. Example Time Delay Plots for Band-B Tests (a) Without Calibration and (b) With Calibration

oscillators used in the T/R modules or on the swept frequency DT0. These investigations had not been initiated when the technical development effort was halted and therefore were not carried out.

5.6 SYSTEM ERROR BUDGET

A system error budget was used to tabulate the effects of predicted error sources and to predict the measurement accuracy expected for the MRIS instrument. Separate tables were established for three parameters, the Reference Signal Power Level, the Test Signal Power Level, and the Standoff Distance. Summaries of the error budget existing at the conclusion of the MRIS development effort are presented in Figure 5-15(a) to -15(c). The final three columns in each summary represent (i) the predicted rms error based on estimated individual error terms, (ii) recommended system specification that had been accepted by NASA at the end of the MRIS technical development effort, and (iii) the specification called out in the original NASA MRIS Statement of Work. In general, results from the preliminary system tests described in Section 7 of this report indicate that the recommended system specifications would have been met.

MRUS SYSTEM ERROR BUDGET

Date: 10/24/91

Page 1 of 3

PARAMETER-1: REFERENCE (TRANSMIT) SIGNAL POWER LEVEL ACCURACY

FREQ BAND	STANDOFF DISTANCE (cm)	CAL ERR (+/-dB)	DET ERR (+/-dB)	DIR ERR (+/-dB)	TOTAL RMS ERROR (+/-dB)	SOW SPEC (+/-dB)
A (20 GHz)	0 - 8	0.20	1.00	0.05	1.02	1.50
B (44GHz)	0 - 10	0.20	1.00	0.10	1.02	1.50
C (95 GHz)	0 - 30	0.50	1.00	0.15	1.10	1.60
D (140 GHz)	4 - 30	0.80	1.00	0.15	1.24	1.75

NOTES

1. CAL ERR is the sum of errors occurring during calibration of the amplitude detection system. Primary contributors to this error are the directional coupler and power meter used to measure the Reference Signal power level during calibration of the MRUS instrument.
2. DET ERR is the sum of errors in the amplitude detection system. The dominant source of this type of error is IF gain instability due to thermal variations. Other contributors to this type of error include (a) system noise, (b) RF gain instability, (c) I-Q Detector accuracy, and (d) A-D quantization errors.
3. DIR ERR is the error due to Test Signal (reflected signal) leakage into the Reference Signal measurement channel. This error is mainly determined by the directivity of the directional coupler used to sample the transmit signal.

Figure 5-15(a). Final System Error Budget for the Reference Signal Power

RTIS SYSTEM ERROR BUDGET

Page 2 of 3

PARAMETER-2: NORMALIZED TEST SIGNAL AMPLITUDE ACCURACY

FREQ BAND	STANDOFF DISTANCE (cm)	REFLECTED POWER (dB)	CAL ERR (+/-dB)	DET ERR (+/-dB)	SIR ERR (+/-dB)	TOTAL RMS ERROR (+/-dB)	SOW SPEC (+/-dB)
A (20 GHz)	0 - 8	0 to -15	0.50	0.15	1.0	1.2	1.5
B (44GHz)	0 - 10	-10 to -30	0.50	0.10	1.5	1.6	4.0
C (95 GHz)	0 - 10	-10 to -35	0.50	0.15	2.5	2.6	4.0
	10 - 30	-10 TO -45	0.50	0.50	0.50	0.9	4.0
D (140 GHz)	4 - 10	-10 to -30	0.50	0.10	3.5	3.6	5.0
	10 - 30	-10 to -50	0.50	1.00	0.5	1.30	4.0

NOTES

1. Since the Test Channel is normalized to the Reference Channel, the CAL ERROR is essentially due to post calibration drift in the portions of the RF-IF receiver chains that are not common to both measurement channels.
2. DET ERR is the sum of errors in the IF amplitude detection system. Contributors to this error include (a) system noise, (b) I-Q Detector errors, and (c) A-D quantization errors. Analysis indicates A-D quantization errors is the main source of this type of error and this analysis assumed an A-D error of +/- 3 LSB's.
3. SIR ERR is the error due to interference signal leakage into the Test Signal measurement channel. Sources of this interference include (a) coupler directivity and antenna reflections (monostatic configuration), (b) antenna-antenna coupling (bistatic configuration), and (c) tile reflections (including multiple reflections). The error levels carried in this budget are based on the the effective interference levels after vector-error correction and range-gating.

Figure 5-15(b). Final System Error Budget for the Test Signal Power

PARAMETER-3: STANDOFF DISTANCE (RANGE) MEASUREMENT ACCURACY

FREQ BAND	STANDOFF DISTANCE (cm)	CAL ERR (+/-cm)	PHASE DET ERR (+/-cm)	SIR ERR (+/-cm)	FREQ ERR (+/-cm)	SIG PROC ERR (+/-cm)	TOTAL RMS ERR (+/-cm)	SOW SPEC (+/-cm)
A (20 GHz)	0 - 8	0.02	0.20	0.45	0.15	0.12	0.53	1.0
B (44GHz)	0 - 5	0.02	0.20	0.70	0.15	0.12	0.76	1.2
	5 - 10	0.02	0.20	0.25	0.20	0.12	0.40	1.0
C (95 GHz)	0 - 5	0.02	0.20	0.75	0.15	0.12	0.80	1.5
	5 - 20	0.02	0.20	0.25	0.20	0.12	0.40	1.0
	20 - 30	0.02	0.20	0.25	0.30	0.12	0.46	1.0
D (140 GHz)	4 - 5	0.02	0.20	0.75	0.15	0.12	0.80	1.5
	5 - 20	0.02	0.20	0.25	0.20	0.12	0.40	1.0
	20 - 30	0.02	0.20	0.25	0.30	0.12	0.46	1.0

NOTES

1. CAL ERR is the sum of errors from (a) calibration of the phase detection system and (b) post calibration drift.
2. PHASE DET ERR is the sum of errors in the IF phase detection system. Contributors to this error include (a) system noise, (b) I-Q Detector accuracy, and (c) A-D quantization errors.
3. SIR ERR is the error due to interference signal leakage into the Test Signal measurement channel. Sources of this interference signal include (a) coupler directivity and antenna reflections (monostatic configuration), (b) antenna-antenna coupling (bistatic configuration), and (c) tile reflections. The error levels carried in this budget are based on the effective interference levels after vector-error correction and range-gating.
4. FREQ ERR is the range error due to frequency step errors in the interrogating signal and to drift in the average transmit frequency.
5. SIG PROC ERR is the range error due to the interpolation resolution of the signal processor.
6. Specifications are listed in virtual distance units.

Figure 5-15(c). Final System Error Budget for the Target Standoff Distance

6.0 MECHANICAL DESIGN AND ANALYSIS

6.1 PACKAGING

The Detector Assembly and the Transmit/Receive Assembly were designed for survival in a space environment. Conditions considered during the mechanical design included (a) launch shock, (b) vibration, and (c) deep space vacuum. In addition, the size, weight, and power consumption of the two assemblies had to be minimized.

A major concern in designing the MRIS hardware was limiting the maximum component operating and non-operating temperatures while simultaneously minimizing weight. To minimize the component temperatures, mycalex insulating washers were used between the aerobrake structure and the MRIS assemblies. Additionally, for the Transmit/Receive Assembly, the horn antennas and horn supports were electroformed from thin walled nickel to provide a high impedance thermal path.

Housings and mounting brackets for both assemblies were fabricated from aluminum. Weight relief machining was used in all areas where this did not jeopardize the structural integrity of the assemblies. The four T/R Modules were designed as light-weight, individual modules, thus simplifying the final assembly and testing of the Transmit/Receive Assembly. Diagrams of the Transmit/Receive Assembly are shown in Figures 6-1(a) to 6-1(c). A diagram of the IF section of the Detector Assembly (the only portion of this assembly that was completed) is shown in Figure 3-5. Parts lists for these figures can be found in Appendix D of this report.

6.2 THERMAL ANALYSIS

Thermal analysis was performed for the Transmit/Receive Assembly and the Detector Assembly to determine if the units met the operational and non-operational thermal requirements defined in the MRIS Statement of Work. The thermal environment used in the analysis was transient and defined in the Aeroassist Flight Experiment Interface Control Document (ICD-2-60012).

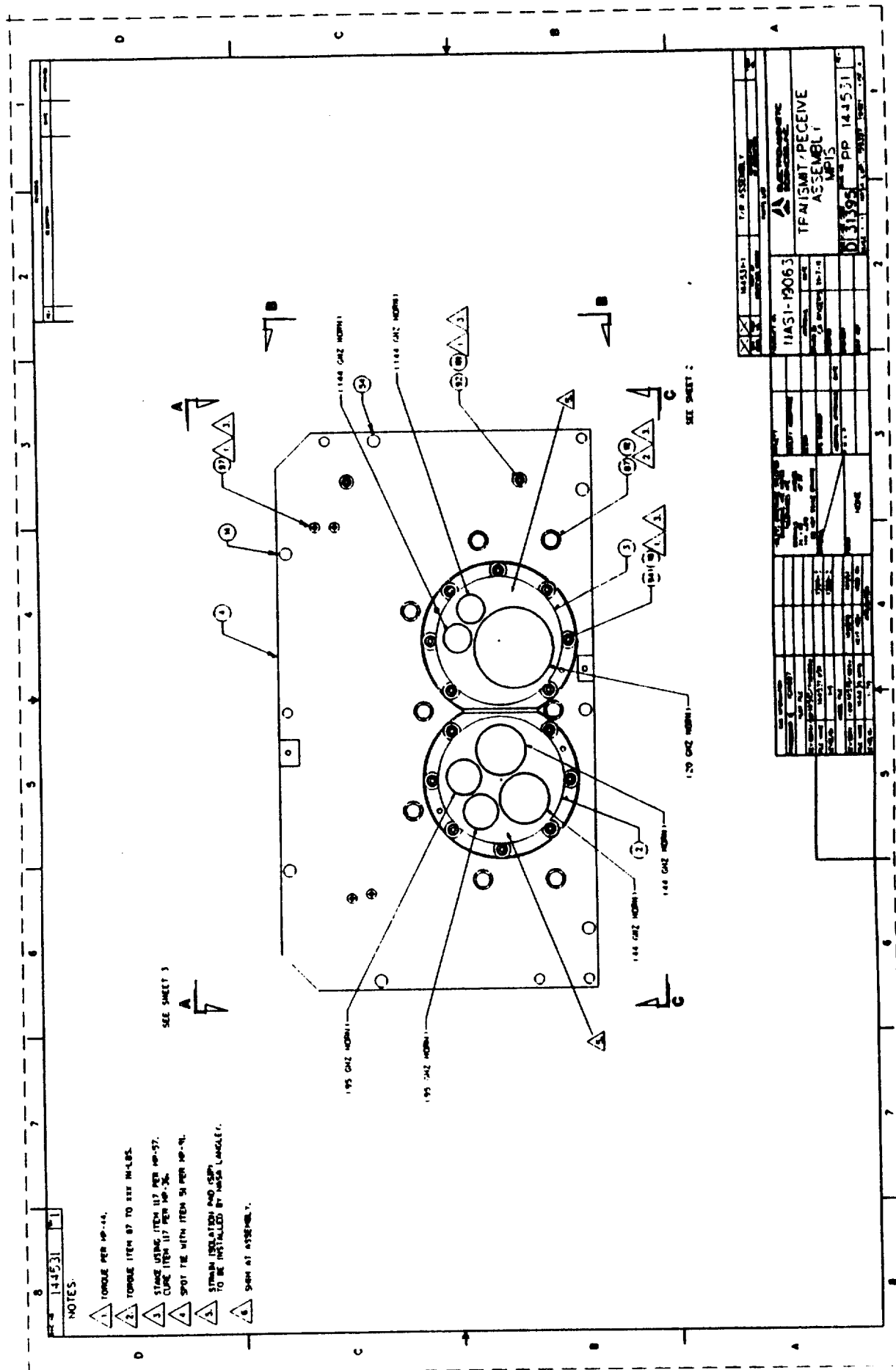


Figure 6-1(a). Diagram of Transmit/Receive Assembly Showing Plan View of Antennas

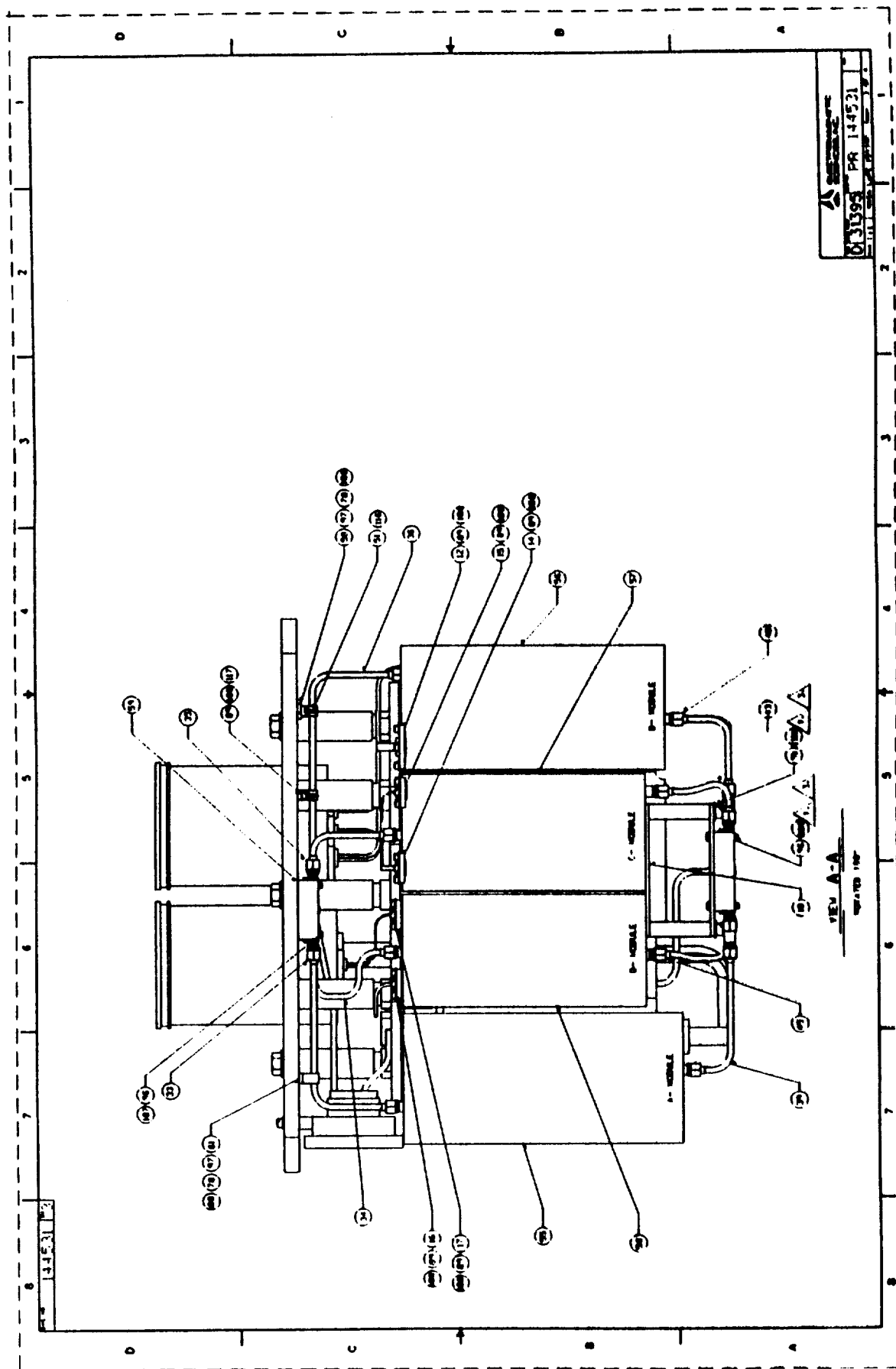


Figure 6-1(c). Diagram of Transmit/Receive Assembly Showing Plan Sectional View of T/R Modules

To determine the component temperature profiles of the two assemblies, a thermal model was made of each unit using SINDA (Systems Improved Numerical Differencing Analyzer) software program. Arrays were used to correct thermal conductivity and specific heat of aluminum verses time and to input the temperature verses time values for the mounting surfaces of the units. A detailed discussion of the thermal analyses and results are not addressed in this report, but can be found in the preliminary mechanical design report for the Transmit/Receive Assembly and Detector Assembly that was submitted to NASA LaRC in February 1991 (reference Letter No. N14061-910218-074).

6.3 STRUCTURAL ANALYSIS AND DESIGN

Both the Transmit/Receive Assembly and the Detector Assembly consisted of machined aluminum housings and support bracketry for the microwave components and printed circuit boards. To evaluate the integrity of the assemblies, finite element computer models and manual calculations were used to analyze each assembly. Eight finite element models were made for the T/R Assembly and one was made for the Detector Assembly. All models were constructed using Intergraph-Rand Micas software.

Results from these models were used to evaluate resonance frequencies and the internal stresses of the horns, structural bracketry, printed circuit boards, and electroformed waveguide. The dynamic loads used in the analysis for the MRIS hardware was derived from the NASA document "Aeroassist Flight Experiment Dynamic Loads and Criteria Databook" (MSFC-DOC-1774). Results of this analysis verified the adequacy of the MRIS assembly designs. A detailed discussion of the structural analysis and results can also be found in the preliminary mechanical design report submitted to NASA LaRC in February 1991.

7.0 TEST DATA AND DISCUSSION

7.1 SUMMARY

A variety of measurements were performed with the MRIS instrument during preliminary system tests performed at Electromagnetic Sciences. Initial tests were aimed at measuring the dynamic range in each operating band and verifying the design objectives discussed had been met. Results of these measurements indicated the required dynamic range was achieved in all four operating bands. Results of the dynamic range measurements are described in Section 7.2.

Tests were then performed to evaluate the ability of the MRIS instrument to accurately measure the Reference Signal Amplitude, the Normalized Test Signal Amplitude, and the target Standoff Distance. The amplitude measurement results are discussed in Section 7.3. The Standoff Distance measurement results are discussed in Section 7.4. Where applicable, results with and without vector error correction are discussed.

Satisfactory amplitude measurement accuracy could be achieved with and without vector error correction in all four bands. Satisfactory Standoff Distance measurement accuracy could be achieved with or without vector error correction in Band-A and Band-B. In Band-C and Band-D, satisfactory Standoff Distance accuracy generally could be achieved with or without vector error correction for target ranges greater than 5 cm. For target ranges less than 5 cm, some form of vector error correction was generally required to insure instrument specifications were met.

In an additional test performed with the MRIS instrument, limited data was collected over temperature and compared to reference values established at room temperature. These measurements, not included in this report, indicated the individual Test Signal and Reference Signal levels were impacted by temperature. However, the practice of normalizing Test Signal data by dividing it by the corresponding Reference Signal data (a key design goal) effectively neutralized the effects of temperature.

7.2 DYNAMIC RANGE VERIFICATION

Dynamic range estimates and requirements for the four MRIS operating bands were presented in Section 5. The measurements discussed below were performed to determine the actual level of performance achieved by the completed hardware. Both the absolute and normalized values of the Reference Signal and Test Signal levels were of interest during this evaluation.

7.2.1 Absolute Signal Levels

The MRIS receiver chain was designed to produce an output voltage of +20 dBV at the maximum allowable signal level. An objective of the preliminary system tests was to verify this +20 dBV limit was not exceeded under maximum signal conditions. For the monostatic Band-A module, the maximum signal level occurs when the module transmit/receive port is terminated with a short circuit. For the bistatic Band-B -C, and -D modules, the maximum signal occurs when a direct connection is made between each pair of transmit and receive ports.

Graphs of the swept-frequency Reference Signal and Test Signal data for all four bands under maximum signal conditions are shown in Figures 7-1(a) to 7-1(d). The peak signal levels measured from each of these graphs are summarized in Table 7-1. It may be observed that the maximum output voltage measured for each signal path was lower than the +20 dBV limit. The smallest margin of 2.3 dB (i.e., 20.0 dBV minus 17.7 dBV) occurs in the Band-B Test Signal channel. The IF attenuator used in this channel could be increased by 1 to 2 dB to provide a more comfortable margin.

7.2.2 Normalized Signal Levels

To help minimize the effects of variations in the transmit signal amplitude and/or frequency, the Test Signal measured at each step frequency is normalized by dividing it by the Reference Signal measured at that step frequency. The difference between the maximum normalized Test Signal level and normalized noise floor measured for each module represents the dynamic range available in each of the four MRIS operating bands.

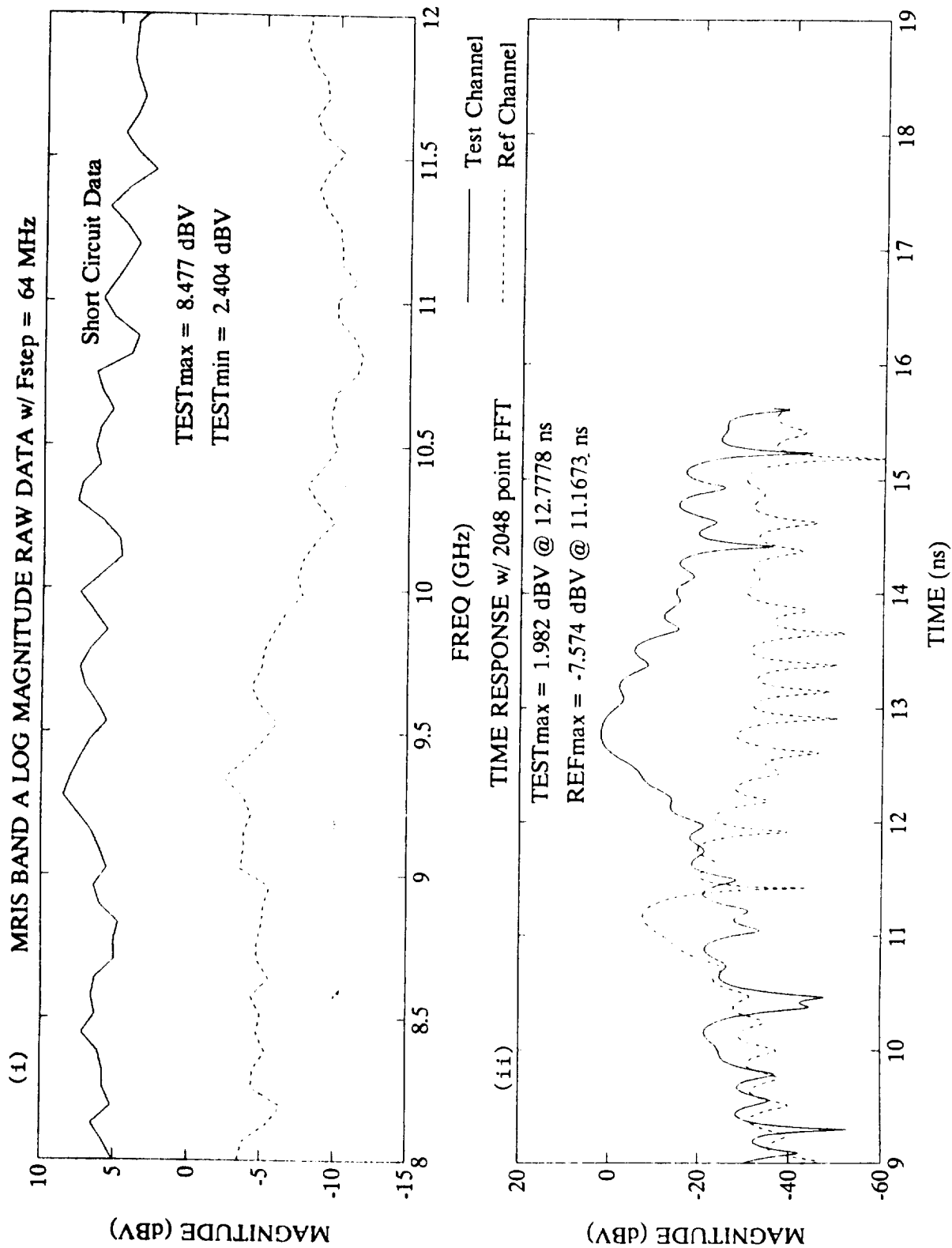


Figure 7-1(a). Maximum Test Signal and Reference Signal Output Voltage Data for Band-A: (i) Frequency Domain Data and (ii) Time Domain Data

3-Sep-91

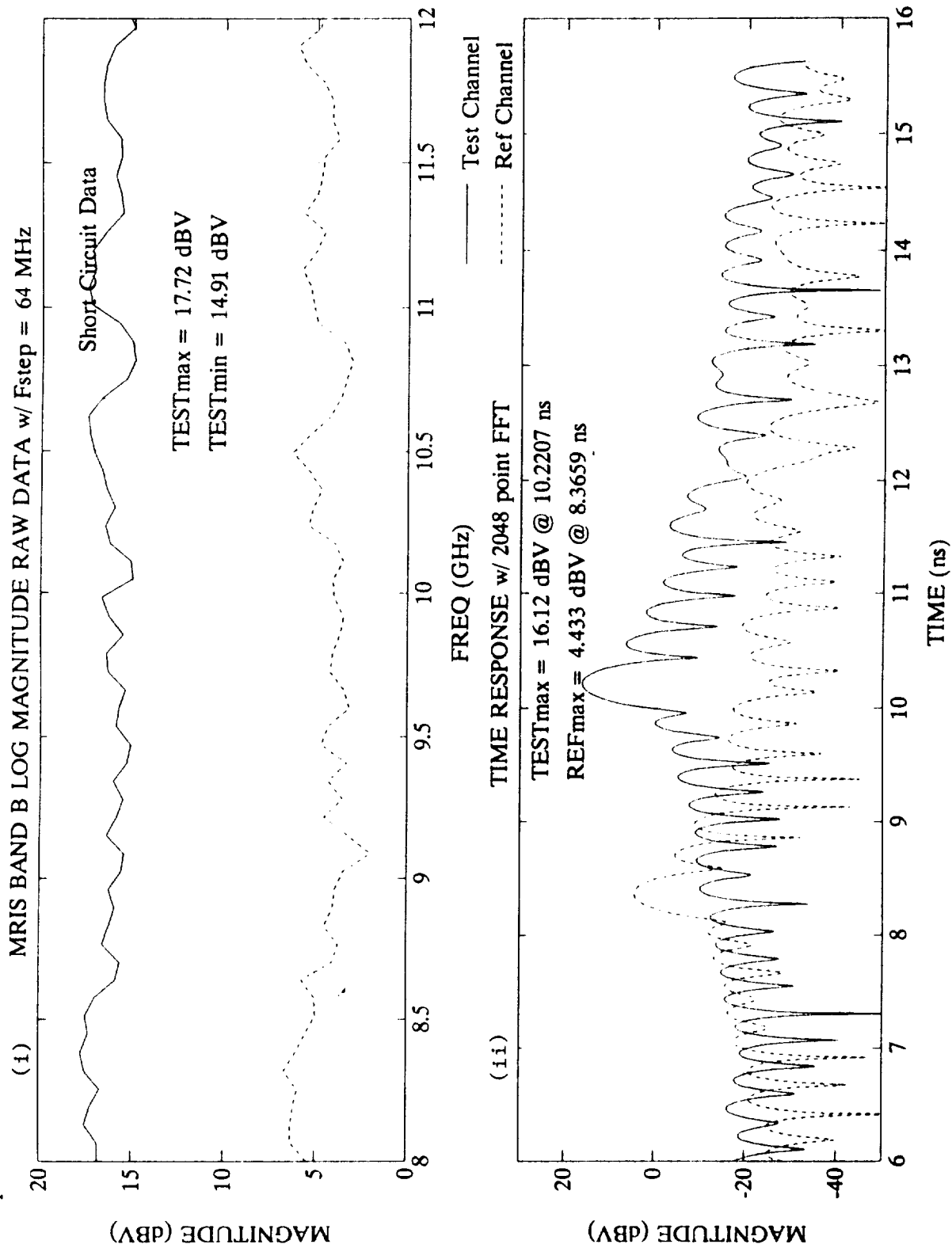


Figure 7-1(b). Maximum Test Signal and Reference Signal Output Voltage Data for Band-B: (i) Frequency Domain Data and (ii) Time Domain Data

3-Sep-91

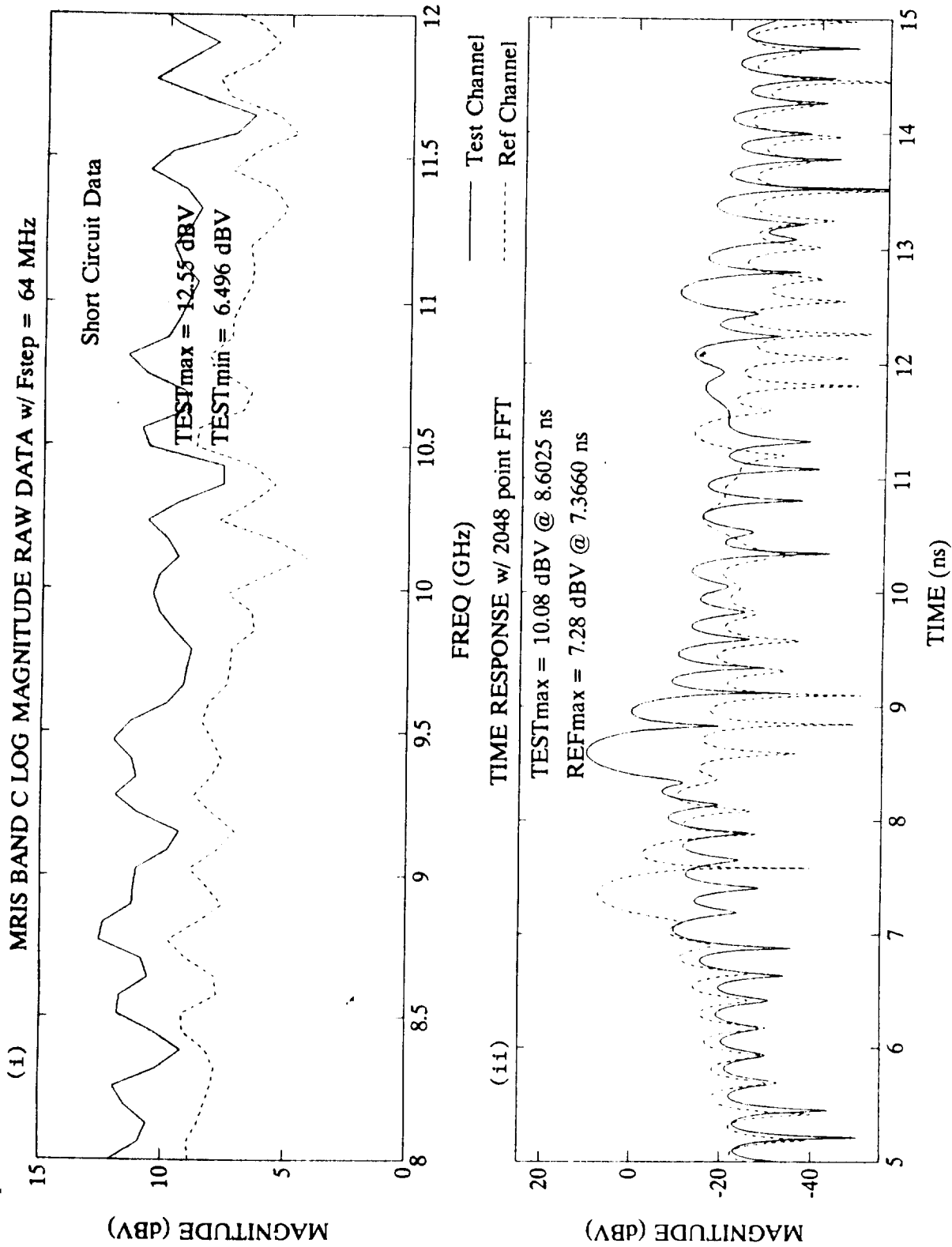


Figure 7-1(c). Maximum Test Signal and Reference Signal Output Voltage Data for Band-C: (i) Frequency Domain Data and (ii) Time Domain Data

3-Sep-91

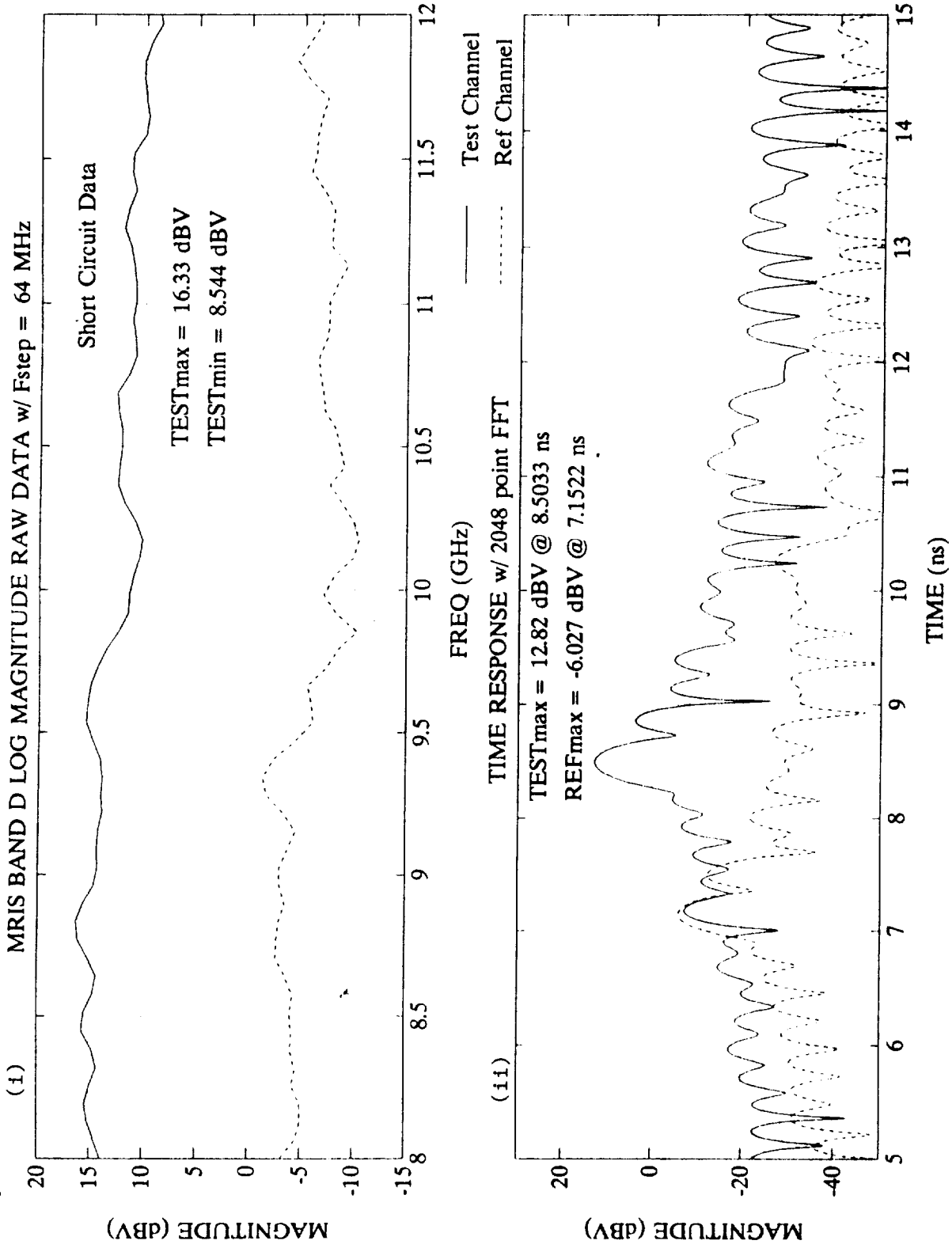


Figure 7-1(d). Maximum Test Signal and Reference Signal Output Voltage Data for Band-D: (1) Frequency Domain Data and (11) Time Domain Data

TABLE 7-1

MAXIMUM SIGNAL LEVEL MEASURED IN EACH PATH

<u>BAND</u>	<u>CHAN</u>	<u>MEASURED MAX (DBV)</u>
A	TEST	+ 8.5
	REF	- 2.5
B	TEST	+17.7
	REF	+ 6.7
C	TEST	+12.6
	REF	+ 9.8
D	TEST	+16.3
	REF	- 1.2

NOTE: Maximum allowed signal level is +20 dBV

The maximum normalized signal level can be produced by terminating the Band-A module with a short circuit and by directly connecting the transmit and receive ports of the Band-B, Band-C, and Band-D modules. The normalized noise floor can be estimated by two means, (i) the modules can be terminated with matched loads to minimize reflected signals in the Test Signal path or (ii) the input to the receiver IF chain can be deactivated. This latter procedure is accomplished by simply disconnecting the IF receive signal path between the Detector Assembly and the T/R modules.

Graphs of the normalized swept frequency and normalized time-domain data taken to evaluate the dynamic range in Band-A are shown in the graphs in Figure 7-2(a). Three different traces are shown in these graphs. The traces marked "SHORT (RESPONSE)" and "ISOLATION (LOAD)" correspond to the short-circuit and load conditions described above. The trace marked "OFFSET VOLTAGE" was taken with the T/R module output disabled and the IF receiver input terminated with a 50-ohm load and represents imperfections in the IF receiver.

The SHORT (RESPONSE) swept frequency data in Figure 7-2(a) shows the Band-A frequency response varies by ± 4.5 dB across the operating band, slightly exceeding the EMS-imposed design requirement of ± 3 dB. No detrimental effects were observed due to this frequency response but methods for improving the T/R Module to reduce the frequency response variations would have been recommended had the program continued.

The Band-A swept frequency ISOLATION (LOAD) data in Figure 7-2(a) is 20-25 dB below the corresponding SHORT (RESPONSE) data. Since the load used in these tests had a measured return loss of 40 dB, it can be reasonably assumed the ISOLATION (LOAD) data represents the directivity of the Band-A T/R Module. This performance meets the EMS-imposed directivity requirement of 20 dB. The OFFSET VOLTAGE swept frequency data in Figure 7-2(a) is typically 50-55 dB below the SHORT (RESPONSE) data and 10-30 dB lower than the ISOLATION (LOAD) data. The fact that the OFFSET VOLTAGE data is small indicates the system is capable of accurately measuring the module directivity. This allows the module directivity to be measured then subtracted from subsequent measurements.

2-Sep-91

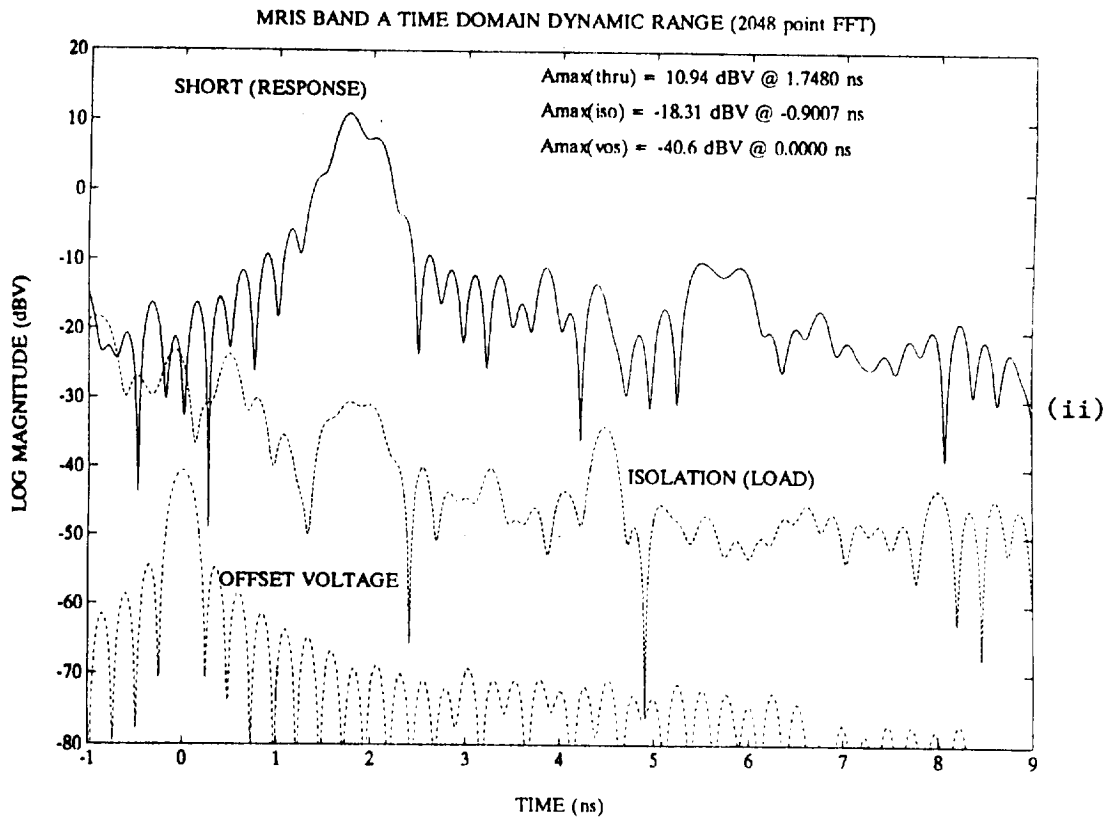
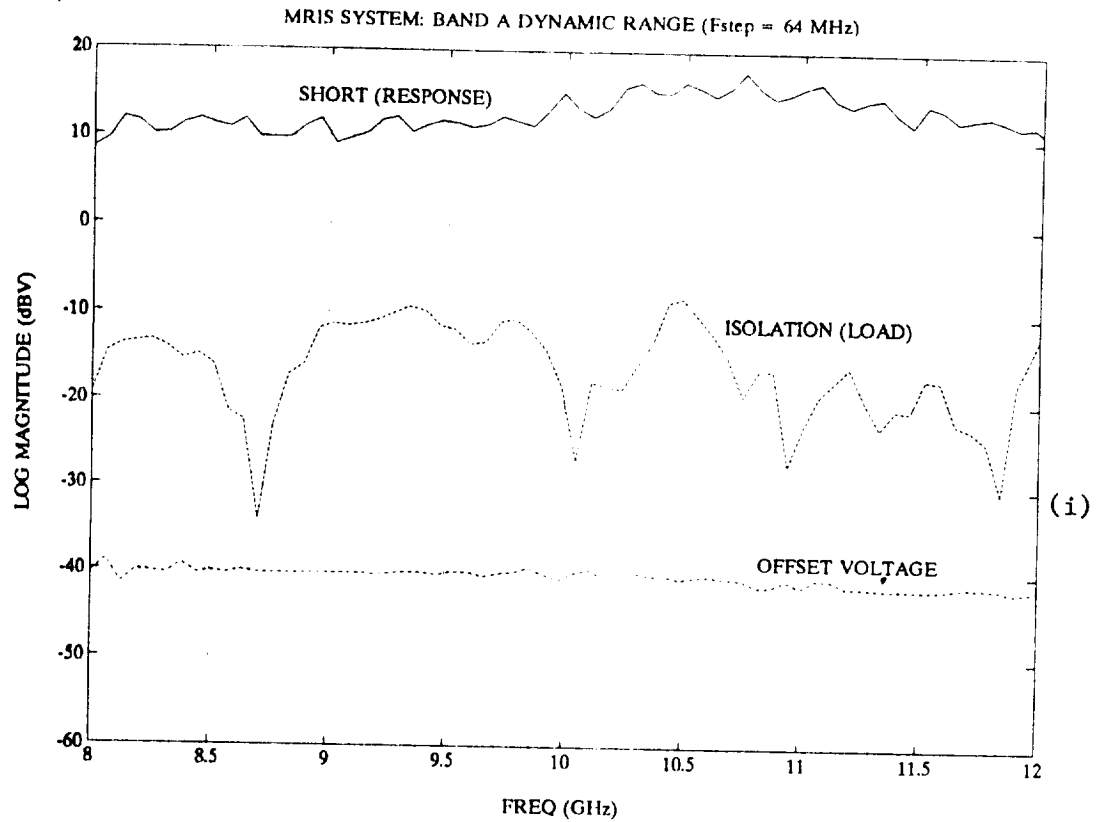


Figure 7-2(a). Normalized Dynamic Range Data for Band-A: (i) Frequency Domain Data and (ii) Time Domain Data

2-Sep-91

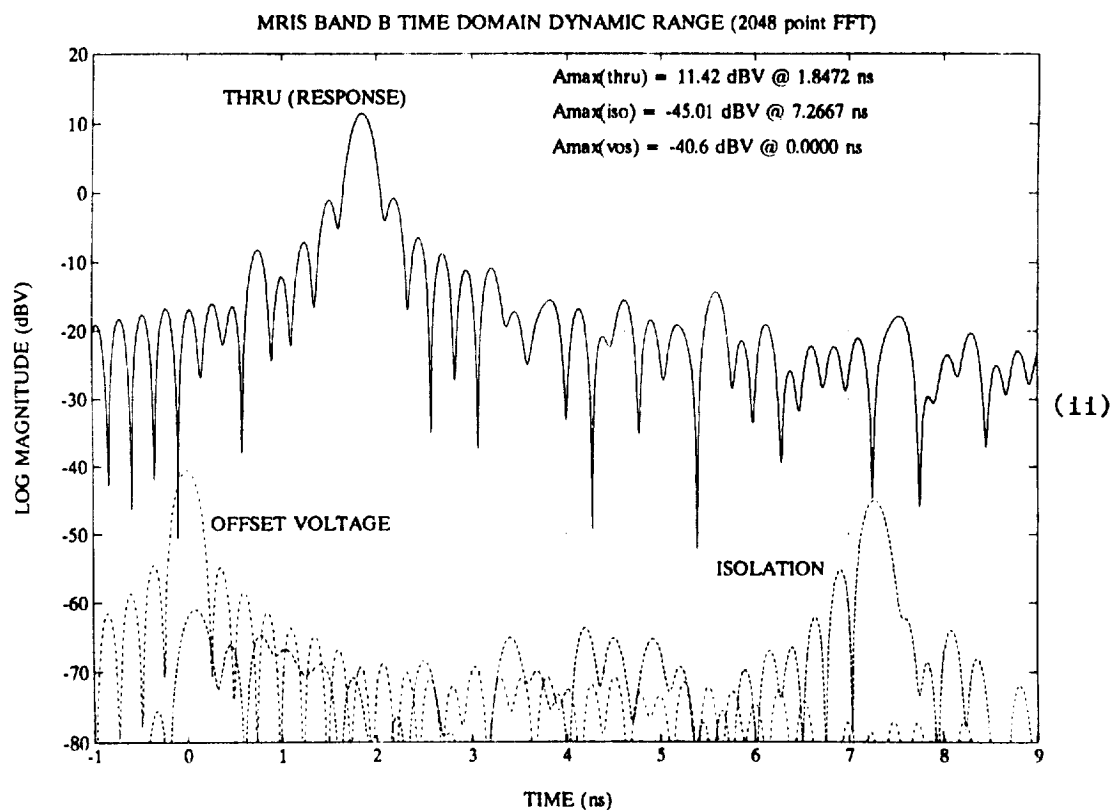
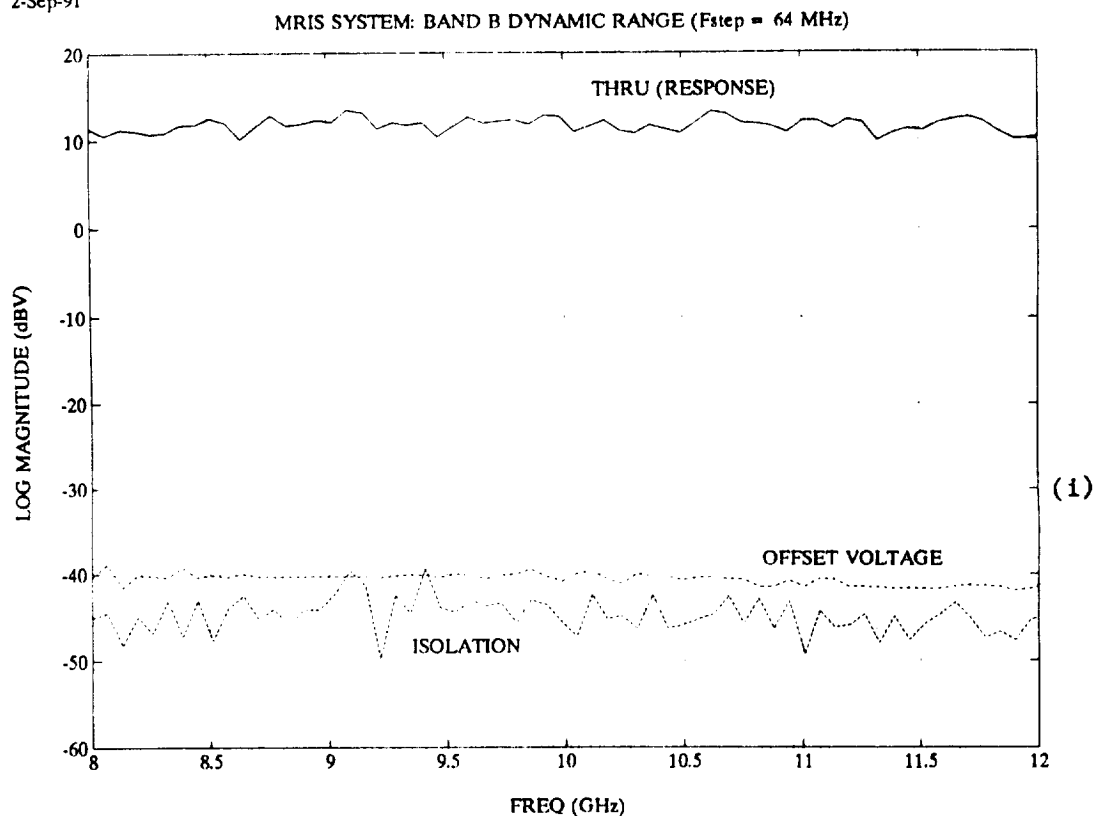


Figure 7-2(b). Normalized Dynamic Range Data for Band-B: (i) Frequency Domain Data and (ii) Time Domain Data

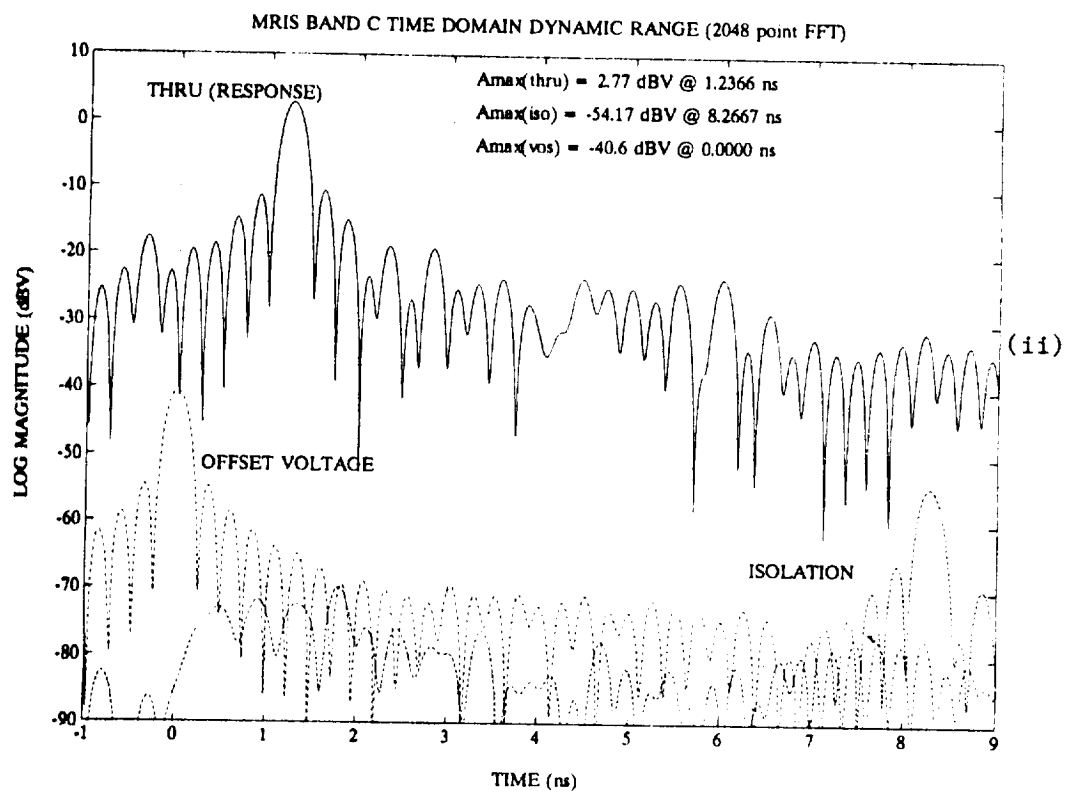
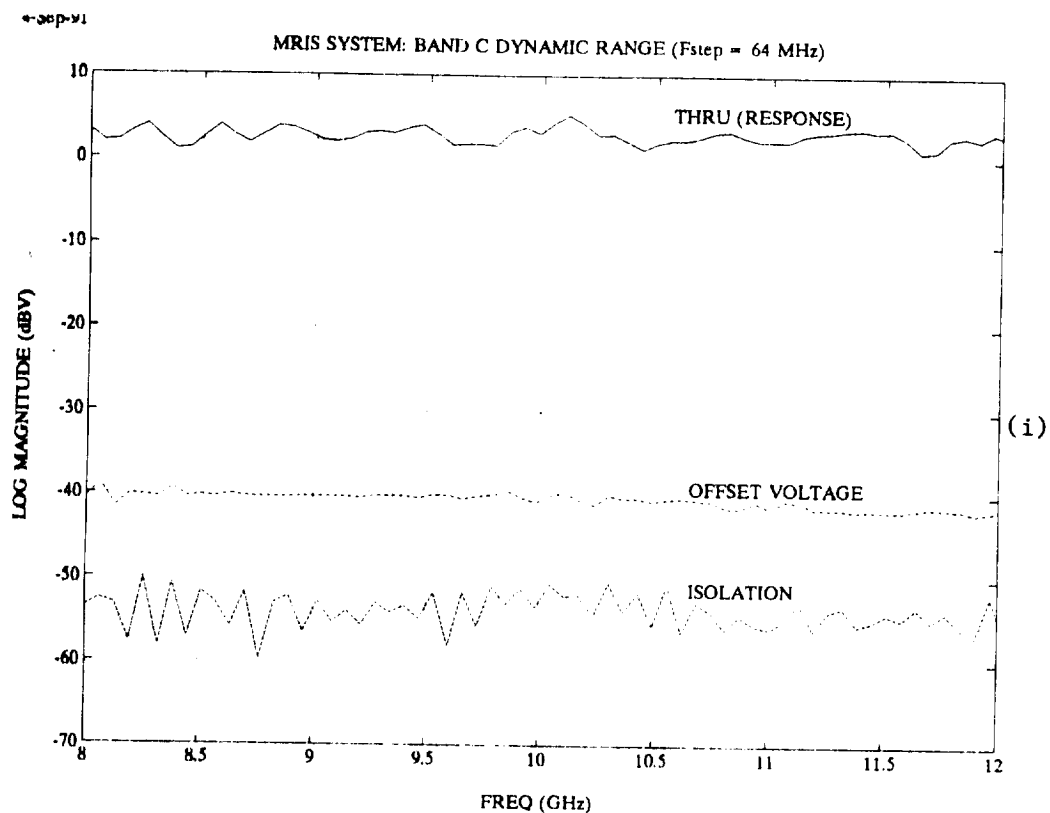


Figure 7-2(c). Normalized Dynamic Range Data for Band-C: (i) Frequency Domain Data and (ii) Time Domain Data

6-Sep-91

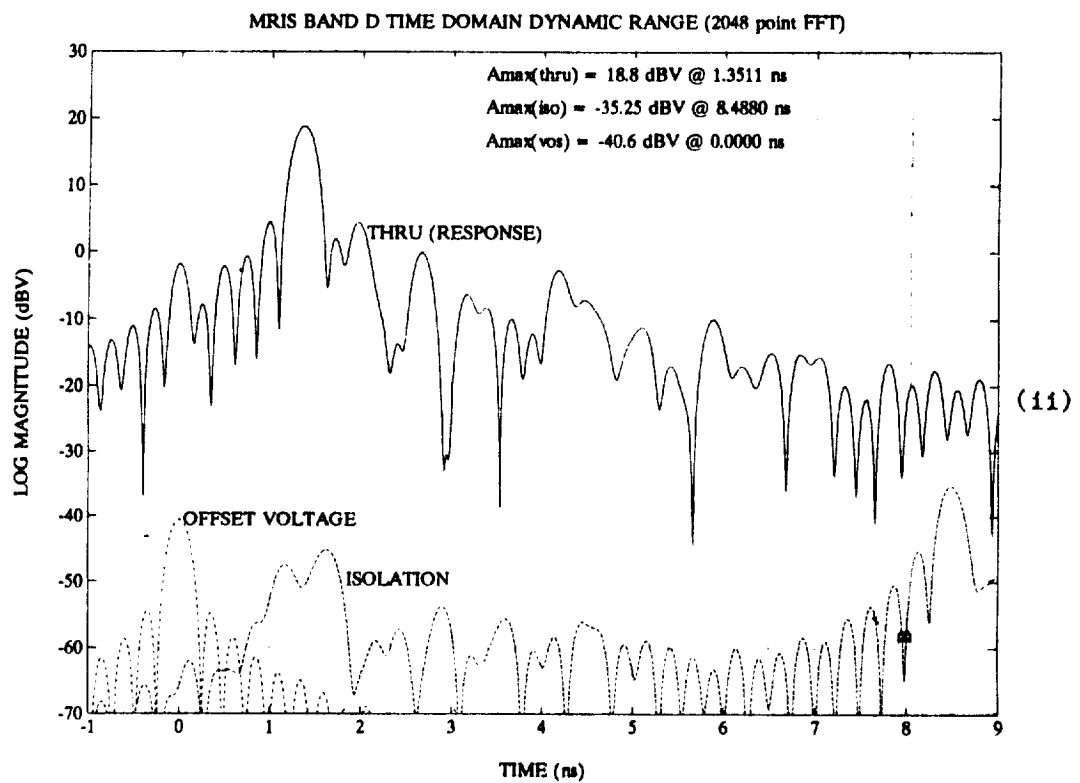
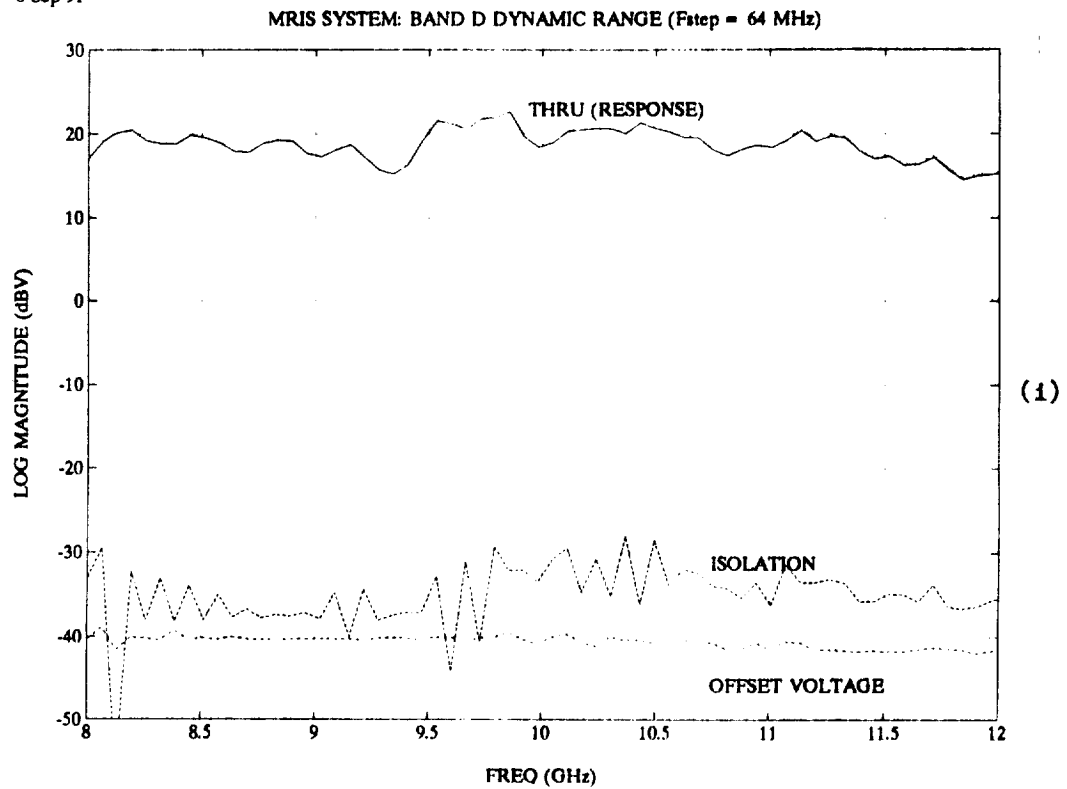


Figure 7-2(d). Normalized Dynamic Range Data for Band-D: (i) Frequency Domain Data and (ii) Time Domain Data

The 50-55 dB difference between the Band-A OFFSET VOLTAGE AND SHORT (RESPONSE) swept-frequency data normally would be defined as the available dynamic range. However, the time domain capability of the MRIS instrument actually enhances the dynamic range performance as is evident from the Band-A time domain plots at the bottom of Figure 7-2(a). These time domain plot show that most of the ISOLATION (LOAD) and OFFSET VOLTAGE energy occurs prior to 1 ns. Since the target information of interest will all be occurring from 2 to 5 ns, the true dynamic range in Band-A is represented by the difference between the maximum normalized signal level of 10.94 dBV (see legend on graph) and the noise floor maximum between 2 and 5 ns (in this example, the exterior TPS tile surface is located at approximately 2 ns).

The time domain data in Figure 7-2(a) shows a noise floor peak of -31 dBV near 2 ns due to a peak in the ISOLATION (LOAD) data. The resulting dynamic range is approximately 42 dB. If calibration is used, the ISOLATION (LOAD) trace will be reduced by a minimum of 20 dB, increasing the usable dynamic range to approximately 62 dB. Either of these values would meet the Band-A dynamic range requirement of approximately 41 dB.

Similar results for the Band-B, -C, and, -D modules are shown in Figures 7-2(b) to 7-2(d). The swept frequency THRU (RESPONSE) data in these graphs shows the frequency ripple in these three bands is ± 2 dB, ± 1.5 dB, and ± 3.5 dB, respectively. A small improvement would have been recommended for the Band-D module although no evidence was found of problems due to excessive ripple. The swept-frequency ISOLATION (LOAD) data in these graphs is also very low, indicating there is very low internal leakage within the T/R modules. The ISOLATION (LOAD) and OFFSET VOLTAGE data are in fact, comparable. There even appears to be some beneficial vector cancellation in Band-C as evidenced by the ISOLATION (LOAD) data appearing to be smaller than the OFFSET VOLTAGE data.

The time domain plots for the Band-B, Band-C, and Band-D data can similarly be used to determine the dynamic range for each of these bands. The maximum normalized Test Signal levels in these bands are 11.42 dBV (Band-B), 2.77 dBV (Band-C), and 18.8 dBV (Band-D). The normalized noise floors observed from 2 to 5 ns for these bands is approximately -66 dBV. The differences between

this noise floor and the maximum normalized Test Signal levels listed above can be considered as the useful dynamic range in band. The resulting dynamic ranges for Band-B, Band-C, and Band-D are 77 dB, 69 dB, and 85 dB, respectively. As required, these values are better than the minimum dynamic range requirements for these bands of approximately 52.6 dB, 68.2 dB, and 73.7 dB, respectively (from Row 12d of Figure 5-6(a)).

It should be noted that precision digital voltmeters were used for these measurements. In the completed system, the DVMs would have been replaced by a 12-bit analog-to-digital converter. Assuming ± 1 -bit accuracy the ADC would have limited the achievable dynamic range to approximately 72 dB or 78 dB if $\pm 1/2$ -bit accuracy is achieved.

7.3 AMPLITUDE MEASUREMENT ACCURACY

7.3.1 Summary

The MRIS instrument is required to estimate the transmit power level and the target return signal level. The transmit power level is estimated by measuring the amplitude of the Reference Signal then dividing the measured value by the receiver gain. The target return signal level is determined from the peak value of the time domain data set obtained by taking the inverse-FFT of the normalized swept-frequency Test Signal. Efforts to measure these two parameters during the MRIS preliminary system tests are discussed below.

7.3.2 Reference Signal Amplitude

Trigonometric identities can be used to calculate the Reference Signal Amplitude levels from the I-Q voltages measured by the receiver. Graphs showing the Reference Signal Amplitude levels measured for the four MRIS bands were shown in Figures 7-1(a) to 7-1(d). The swept frequency plots shown in these figures can be used to estimate the Reference Signal Amplitude levels on a frequency-by-frequency basis. Optionally, the time-domain plots shown in these figures can be used to determine a nominal Reference Signal level. In both cases, the measured values must be divided by the total receiver gain to estimate the actual mmW signal level. Because the total receiver gains in

each Reference Signal path were not measured during preliminary system testing, the required calculations are not presented in this report.

7.3.3 Normalized Test Signal Amplitude

Time domain plots of the normalized Test Signal were used to determine the amplitude of the target return signal. Generally, the peak response appearing in the time domain plots was defined as the target return signal. Examples of time domain plots showing target return peaks are shown in Figure 7-3. By retrieving the level of the peak signal in the time domain plot corresponding to a specific target distance, Target Return Level versus Distance plots can be produced. In general, it is believed these plots should appear as smooth curves that decay monotonically for the monostatic case and are parabolic for the bistatic case.

7.3.3.1 Band-A Test Signal Amplitude Results

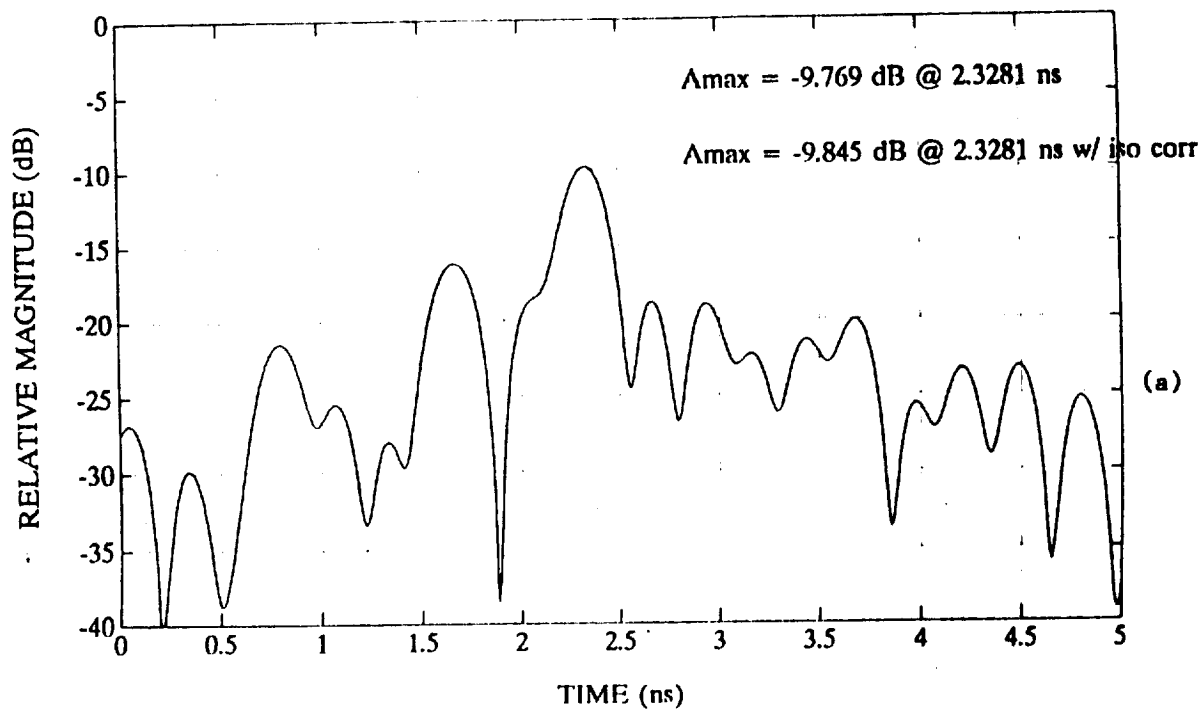
Examples of two test runs made for Band-A are shown in Figure 7-4(a). The upper graph is from tests made from 0-4 inches in 0.03-inch steps. A maximum signal level of approximately -3 dB occurs at a range of zero inches then decays with distance. The nearly periodic variations observed in the data are measurement errors believed to be caused by interference and multipath reflections. The period between successive peaks was found to correspond to a distance of one-half the wavelength at the sweep center frequency of 20 GHz. This phenomena was found to be consistent in all four operating bands. The worst-case amplitude errors is ± 0.8 dB, well within the instrument accuracy specification of ± 1.5 dB. Results from a similar set of measurements made from 0-12 inches is shown in the lower graph. The measured amplitudes continue to decay and the periodic variations observed at closer ranges can also be observed at longer ranges.

Although the system specification could be adequately met in Band-A without imposing vector error correction (VEC), tests were performed using different forms of VEC. When vector subtraction (VEC-2) was applied, significant reductions were observed in the amplitude variations observed beyond approximately 1 inch as shown in the upper part of Figure 7-4(b). Curiously, vector

5-Sep-91

MRIS BAND A CALIBRATED TST/REF LOG MAGNITUDE w/ Fstep = 64 MHz

TIME RESPONSE w/ 2048 point FFT



4-Sep-91

MRIS BAND C CALIBRATED TST/REF LOG MAGNITUDE w/ Fstep = 64 MHz

TIME RESPONSE w/ 2048 point FFT

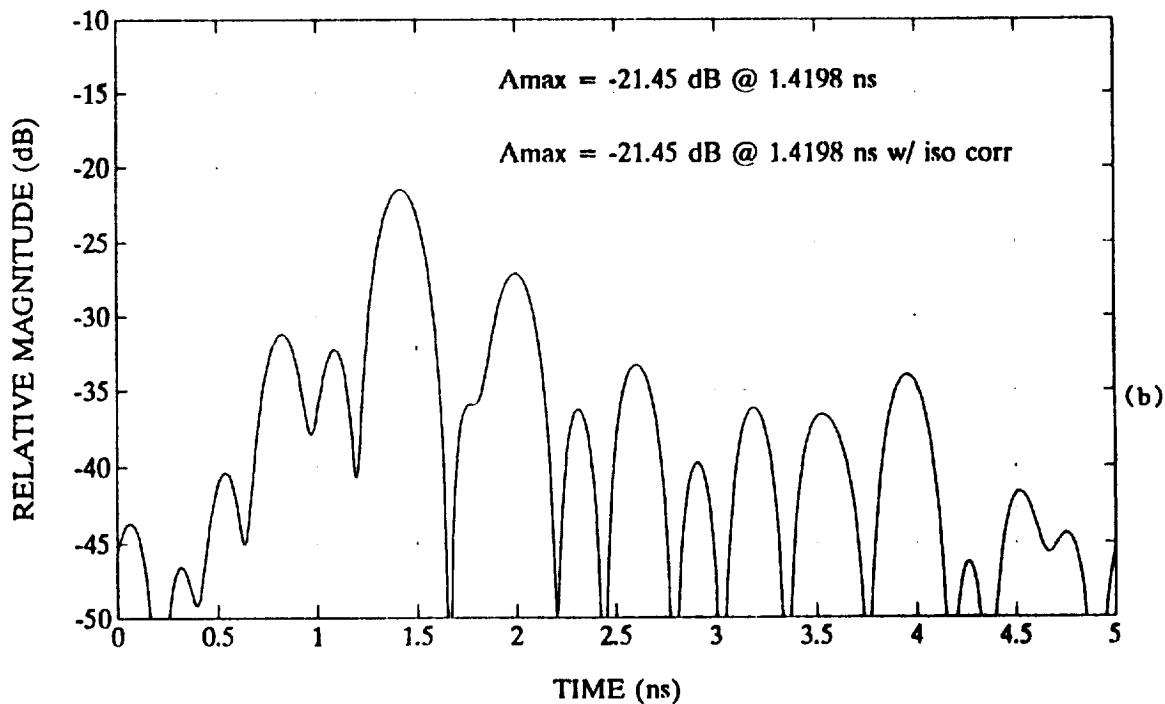
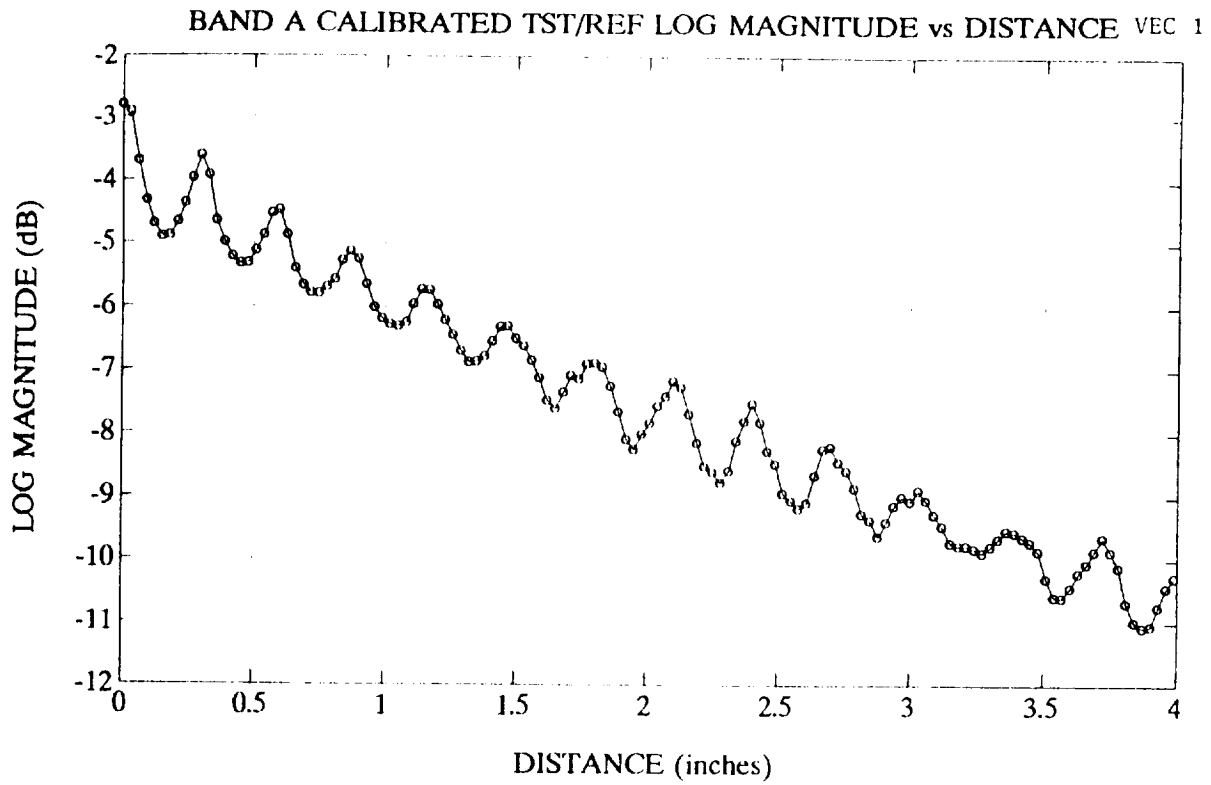


Figure 7-3. Example Time Domain Plots Showing Peak Target Return Signal for Target Located 4.0 inches from TPS Tile Surface: (a) Band-A and (b) Band-C

18-Nov-91



17-Sep-91

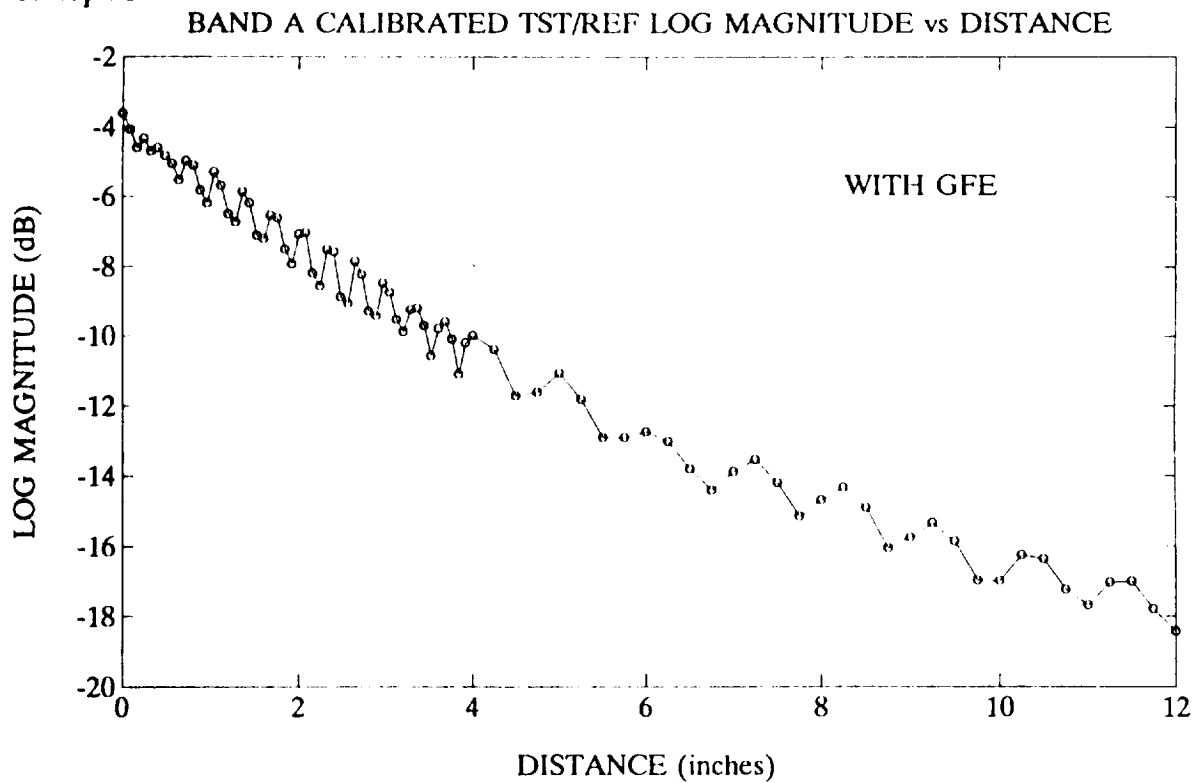
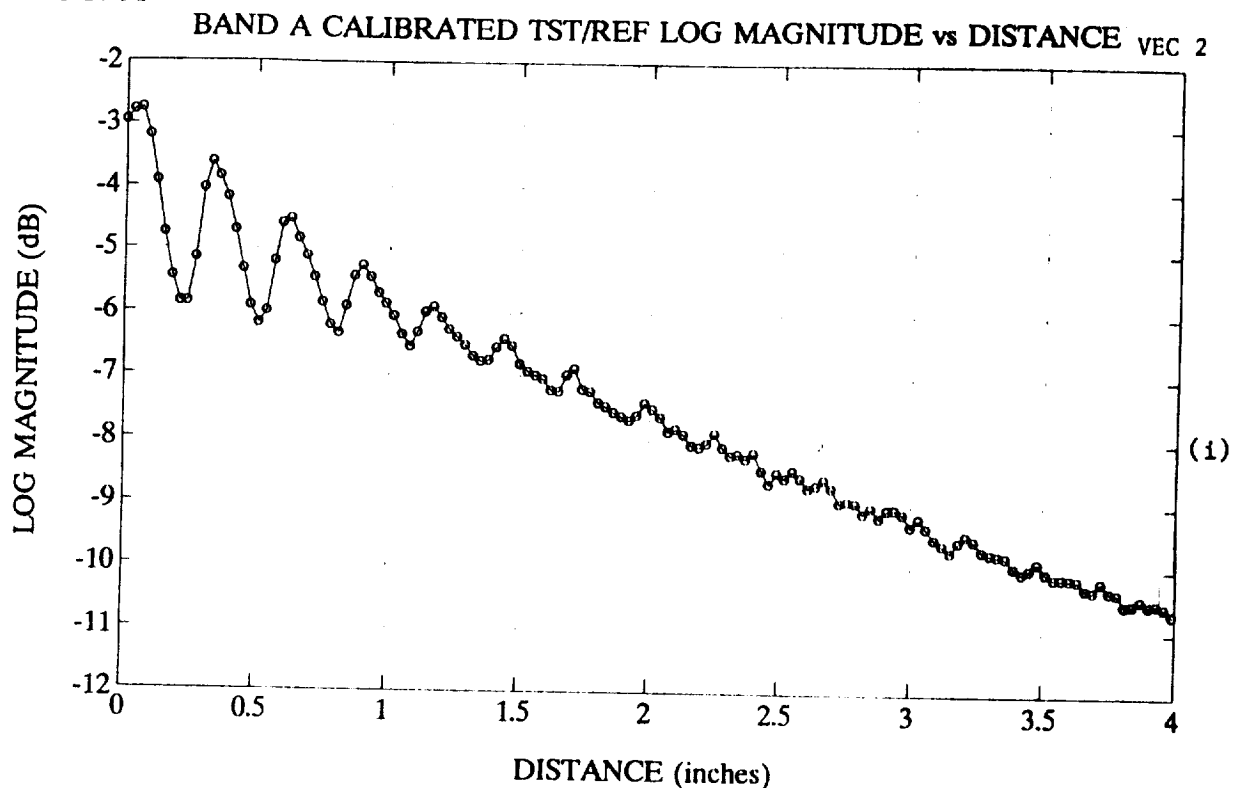


Figure 7-4(a). Examples of Measured Test Signal Amplitude Versus Target Distance Data for Band-A Operation Without Vector Error Correction

19-Nov-91



2-Jan-92

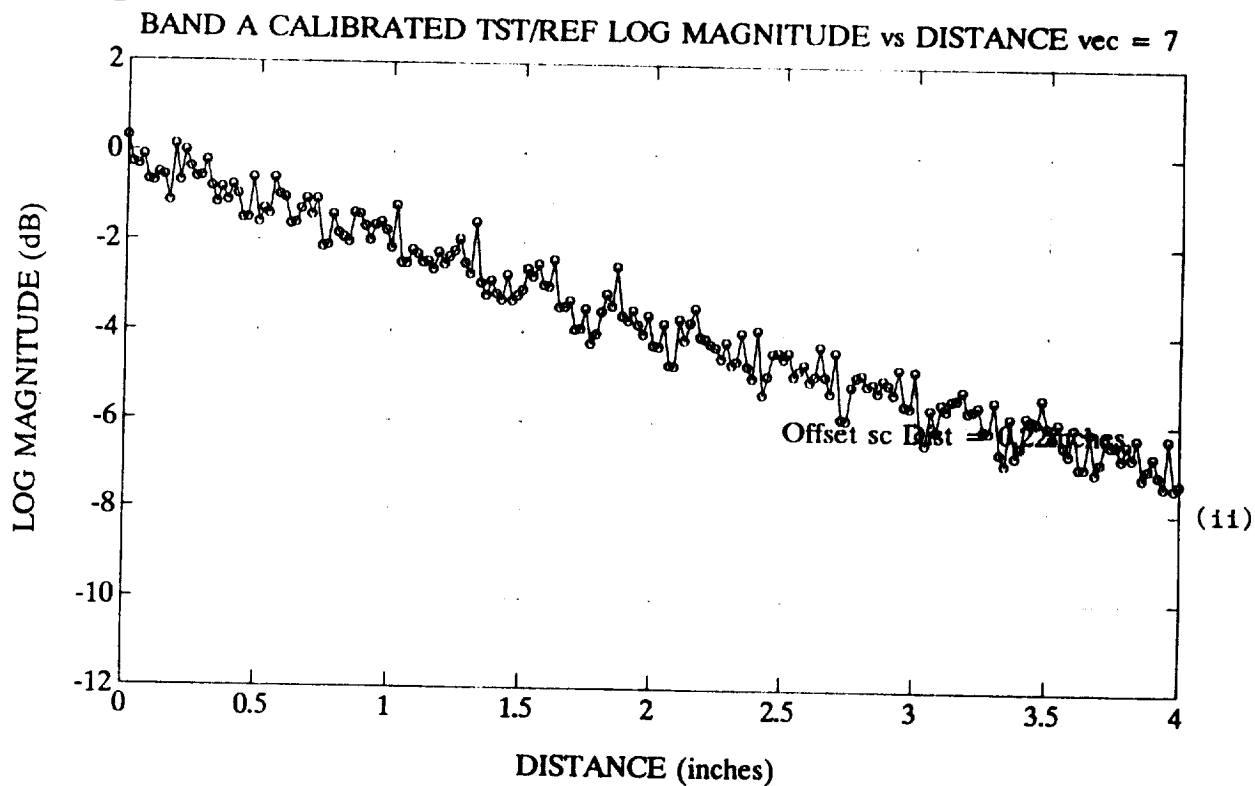


Figure 7-4(b). Measured Test Signal Amplitude Versus Target Distance Data for Band-A Operation (1) With Vector Subtraction and (11) With VEC-7

subtraction appeared to worsen the observed amplitude fluctuations at target ranges less than one inch. When VEC-7 was applied, the amplitude fluctuations decreased to a worse case of ± 0.5 dB as shown in the lower part of Figure 7-4(b). Since this particular VEC involved using a close-range target as one of the VEC reference points, the 0-inch data in this case is automatically normalized to have an amplitude 0-dB.

7.3.3.2 Band-B Test Signal Amplitude Results

Two examples of results obtained in Band-B are shown in Figure 7-5(a). This data displays the parabolic shape expected for the bistatic Band-B module and has a peak response near a target range of five inches. This data verifies that the coupling of the bistatic horn arrangement is in fact low at close-in distances. The deviations observed in the graphs have a worse case value of ± 1.5 dB, well within the instrument specification of ± 4.0 dB. Vector subtraction appeared to degrade performance for distances less than two inches while performance from 2-4 inches appeared unaffected as shown in the upper part of Figure 7-5(b). VEC-7 also did not provide any significant improvements as shown in the lower part of Figure 7-5(c).

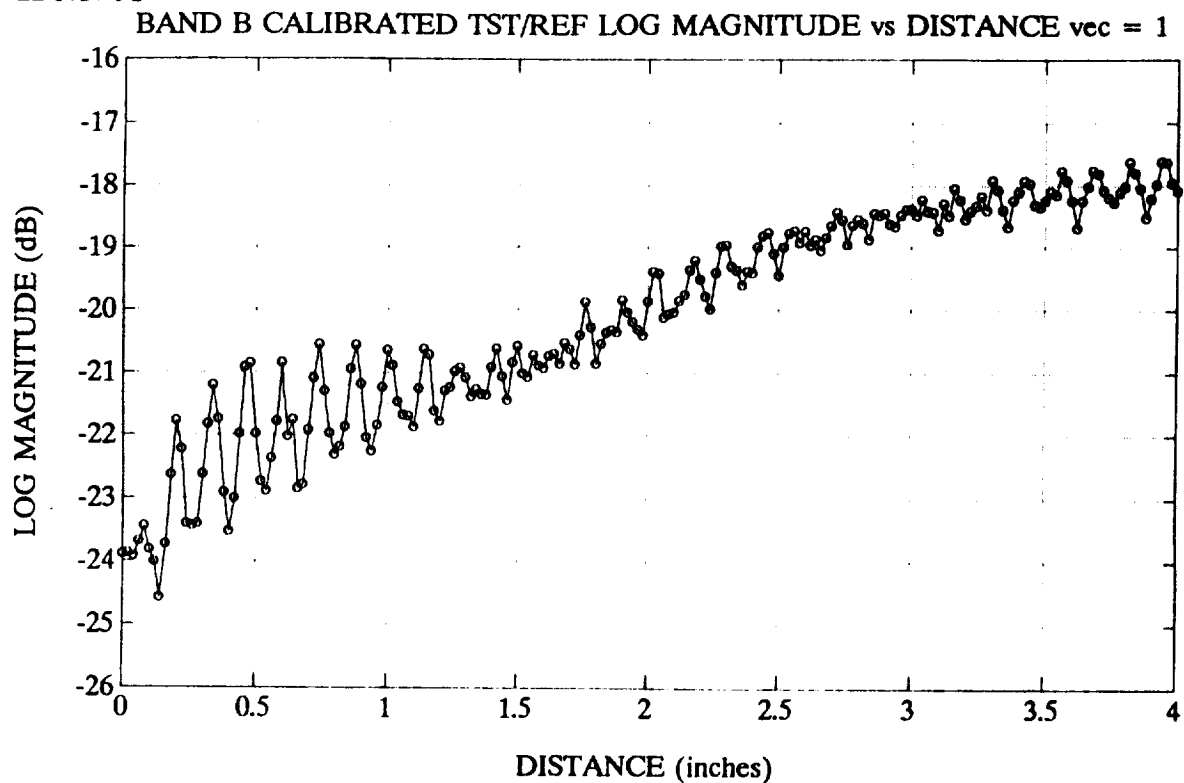
7.3.3.3 Band-C Test Signal Amplitude Results

Two examples of data collected in Band-C are shown in Figure 7-6(a). The data displays the expected parabolic shape with a peak response near a target range of five inches. The deviations observed in the graphs have worst case value of ± 2.0 dB, well within the instrument specification of ± 4.0 dB. Vector subtraction appeared to degrade performance for distances less than 2.5 inches while performance from 2.5 to 4.0 inches appeared unaffected as shown in the upper part of Figure 7-6(b). VEC-7 also did not provide any significant improvements as shown in the lower part of Figure 7-6(b).

7.3.3.4 Band-D Test Signal Amplitude Results

Two examples of data collected in Band-D are shown in Figure 7-7(a). The data displays the expected parabolic shape with a peak response near a target range of five inches. The variations observed in the graphs have a worst case value

22-Nov-91



17-Sep-91

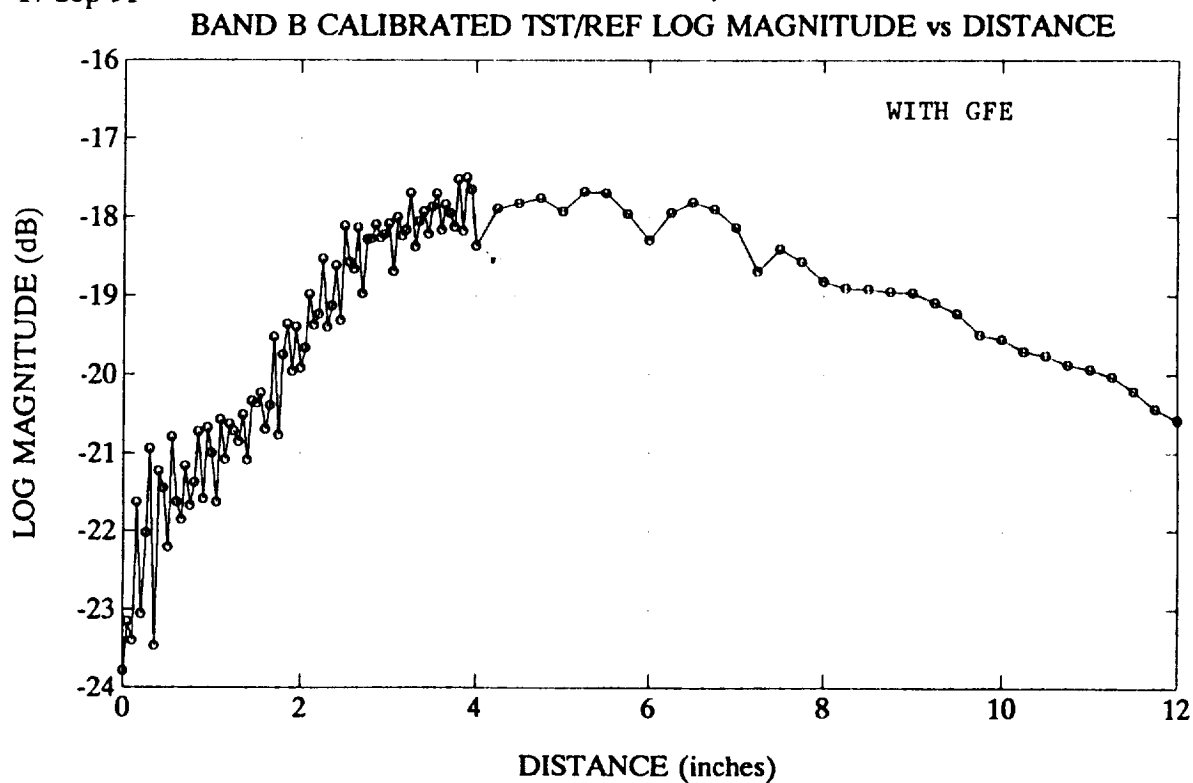
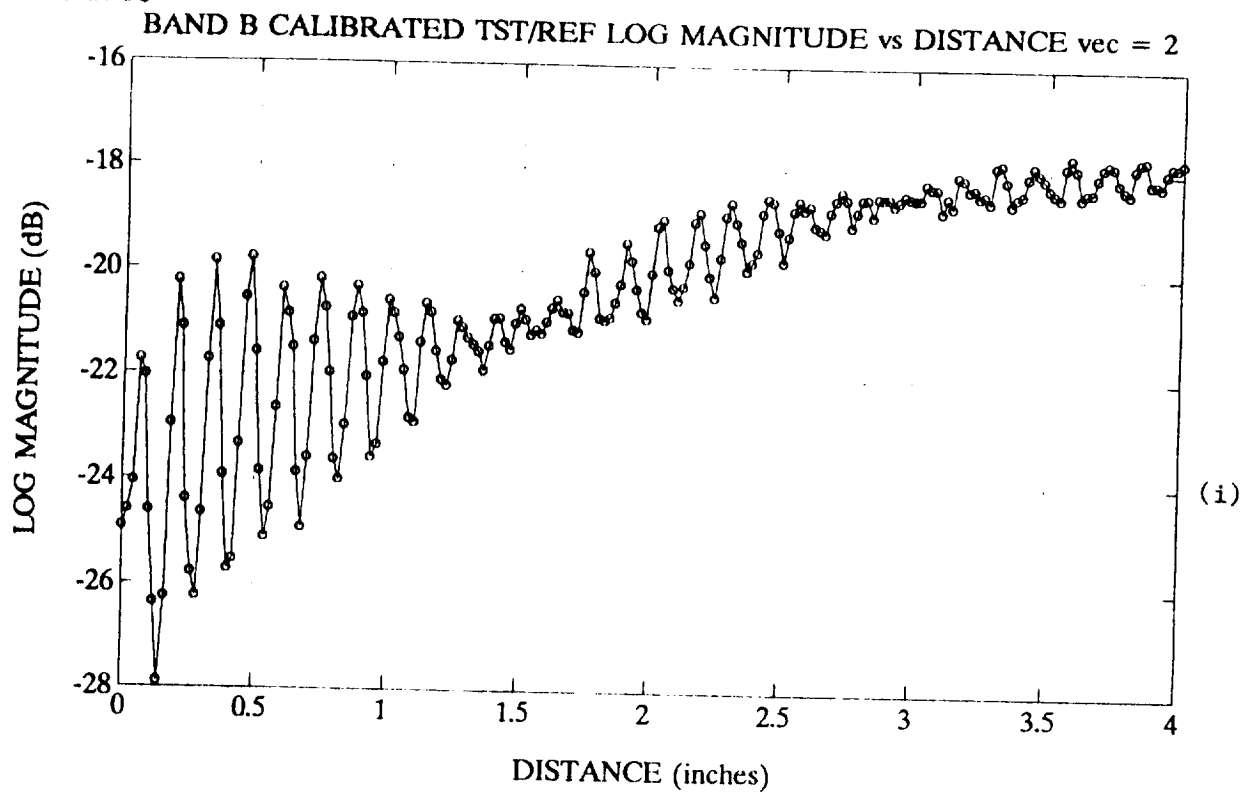


Figure 7-5(a). Examples of Measured Test Signal Amplitude Versus Target Distance Data for Band-B Operation Without Vector Error Correction

22-Nov-91



20-Dec-91

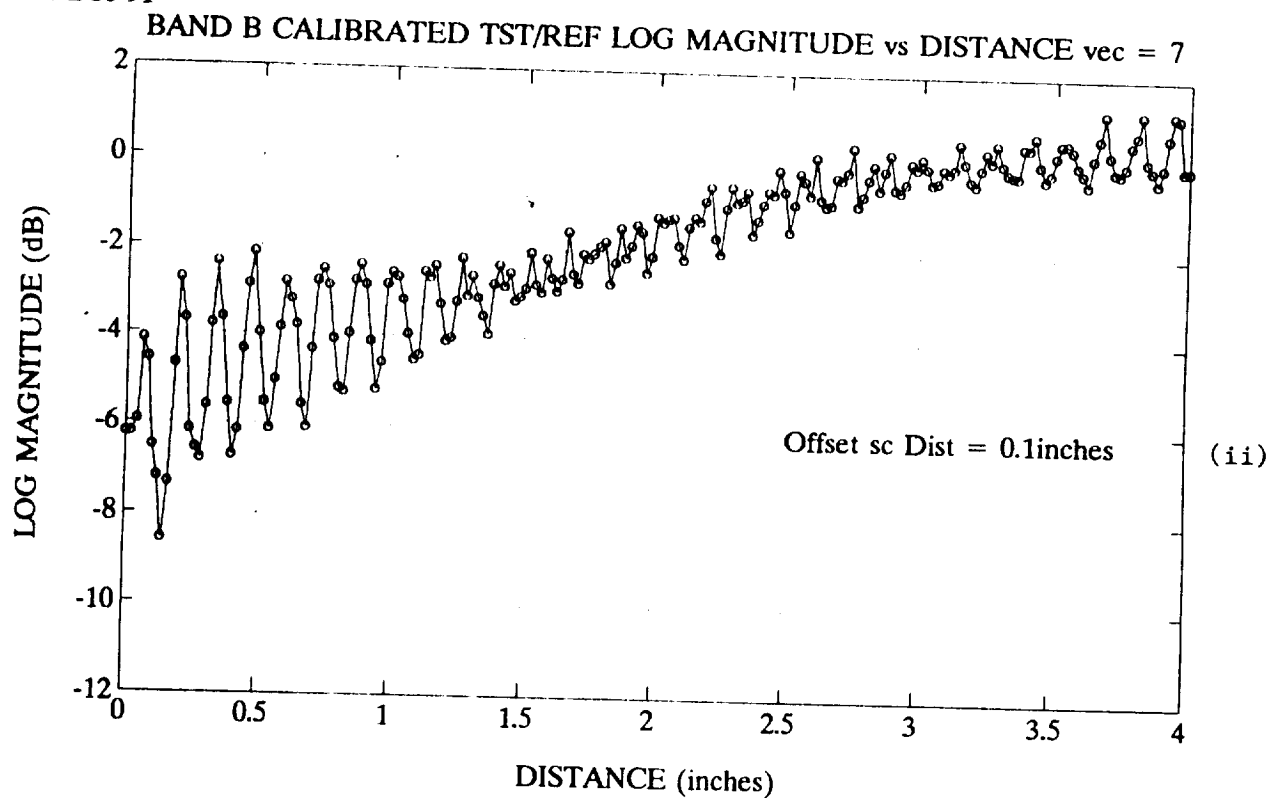
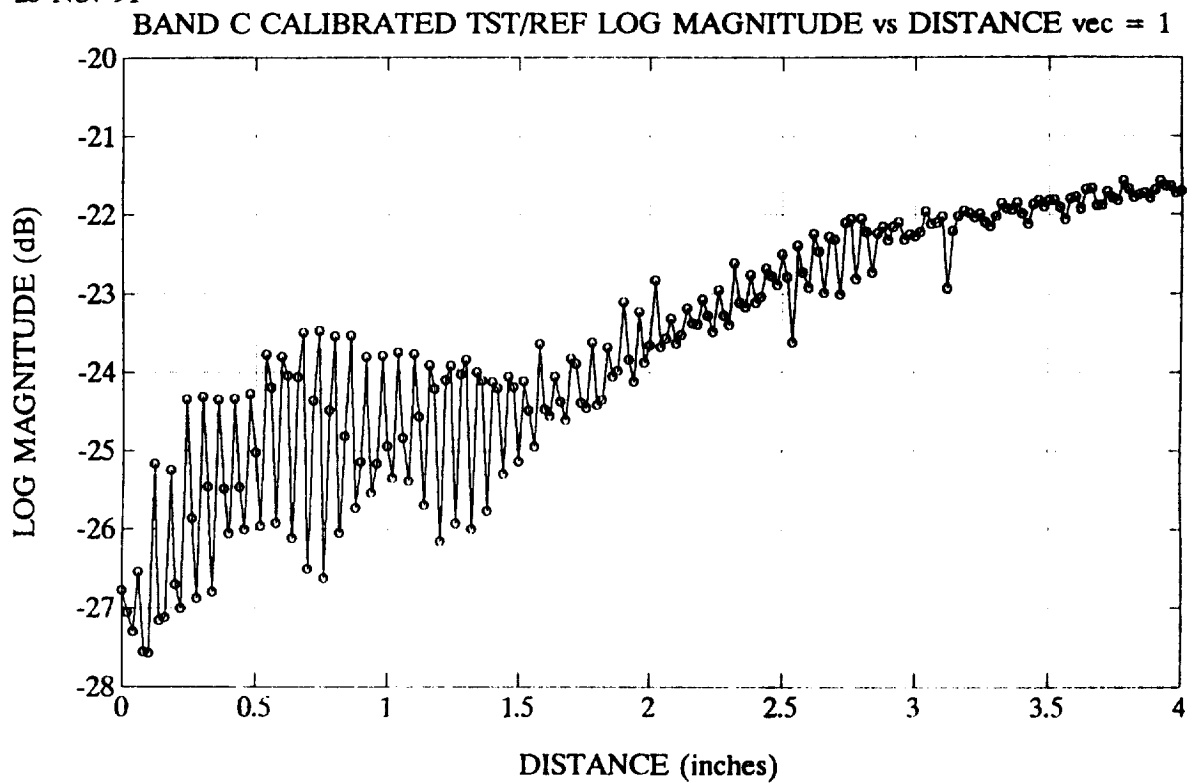


Figure 7-5(b). Measured Test Signal Amplitude Versus Target Distance Data for Band-B Operation (i) With Vector Subtraction and (ii) With VEC-7

25-Nov-91



17-Sep-91

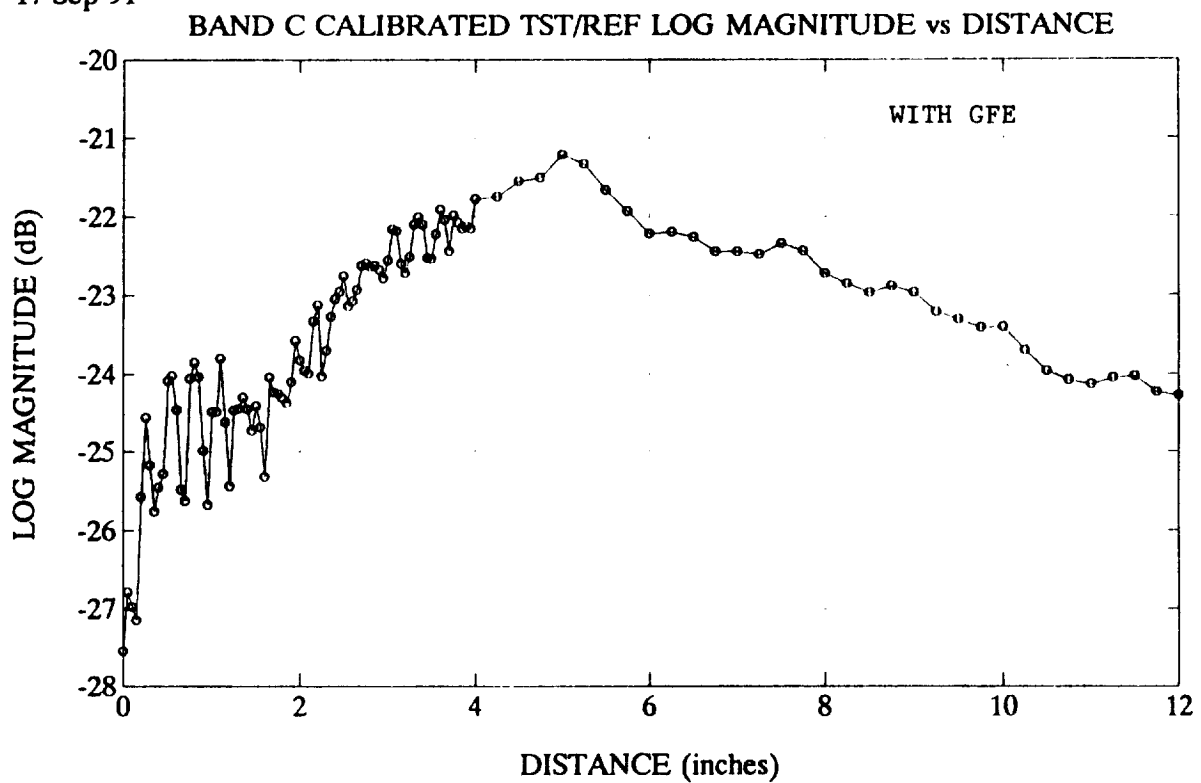
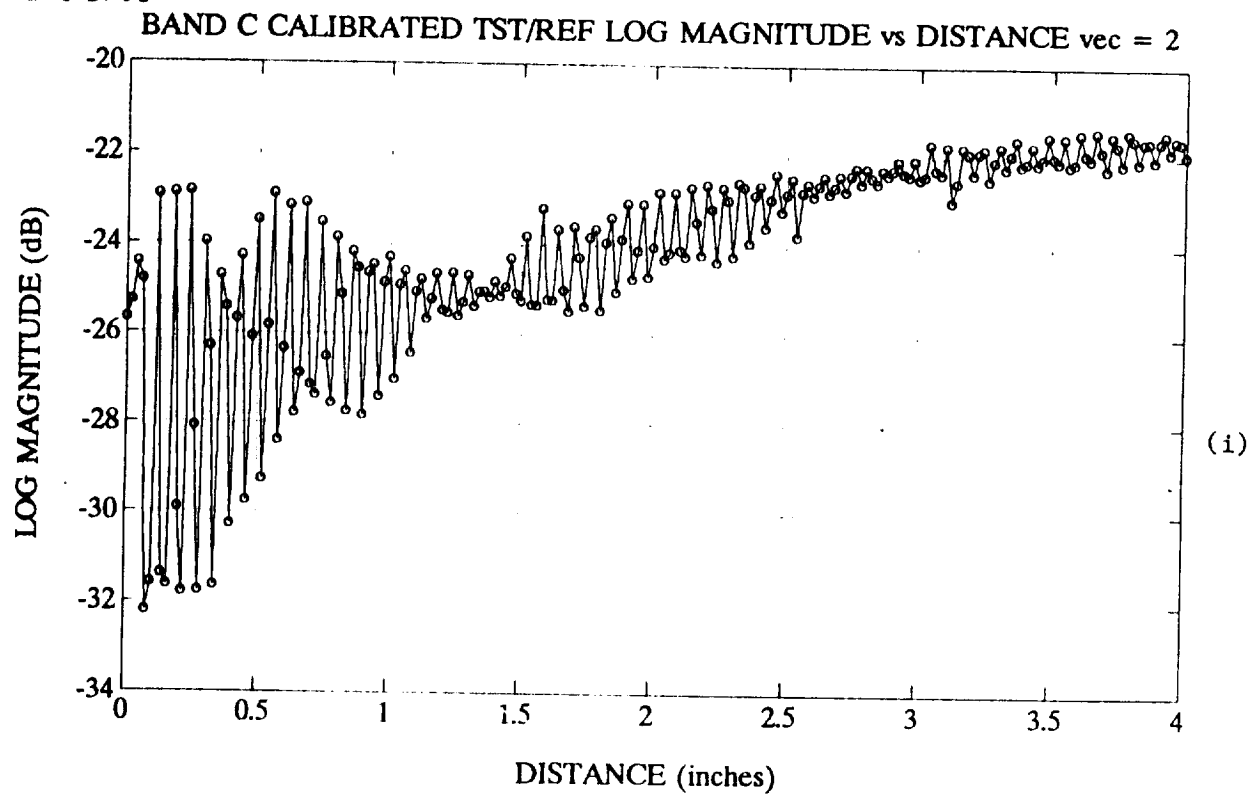


Figure 7-6(a). Examples of Measured Test Signal Amplitude Versus Target Distance Data for Band-C Operation Without Vector Error Correction

25-Nov-91



20-Dec-91

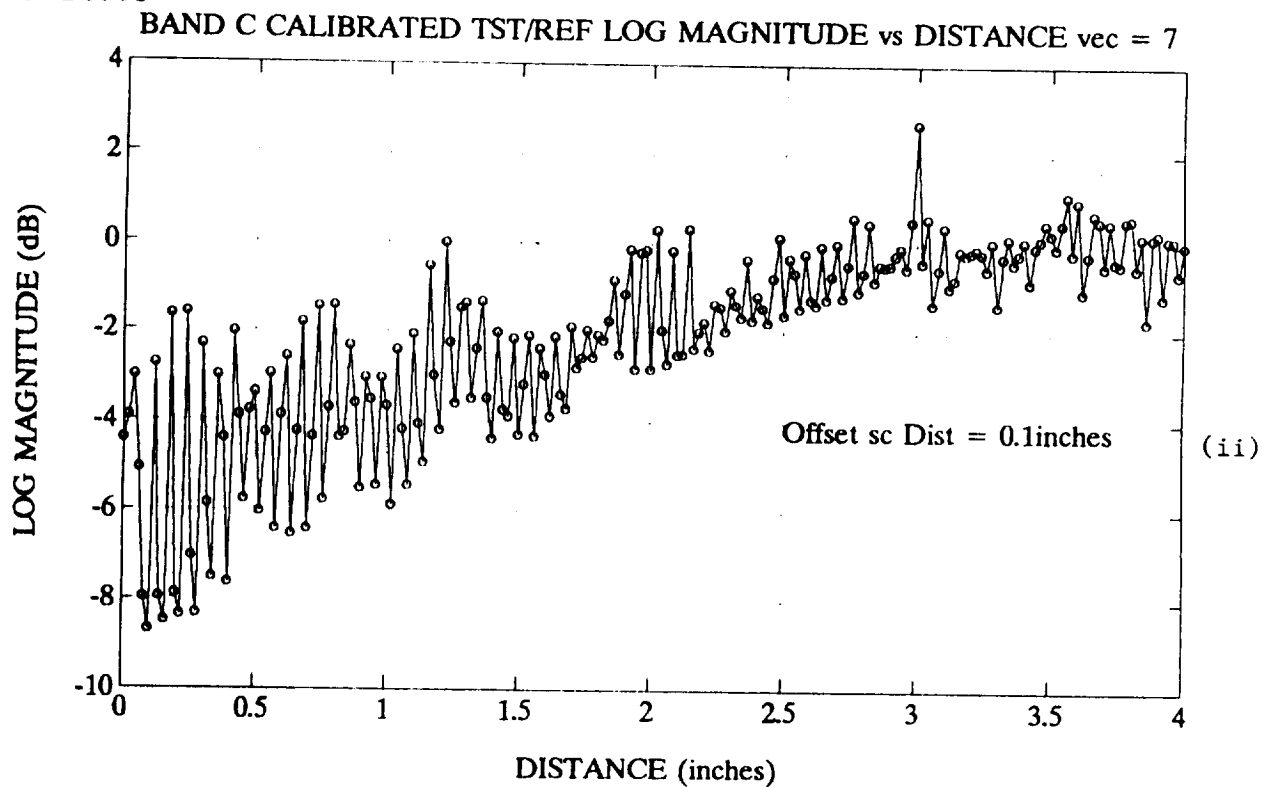
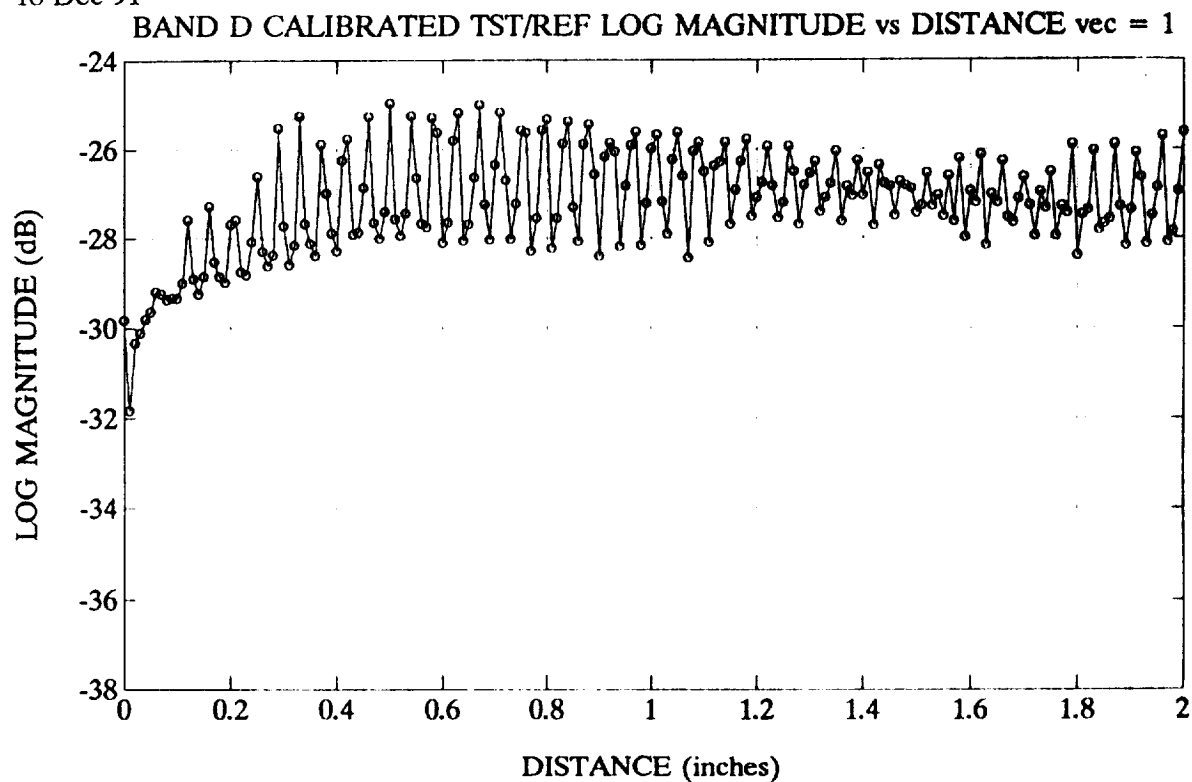


Figure 7-6(b). Measured Test Signal Amplitude Versus Target Distance Data for Band-C Operation (i) With Vector Subtraction and (ii) ith VEC-7

18-Dec-91



16-Sep-91

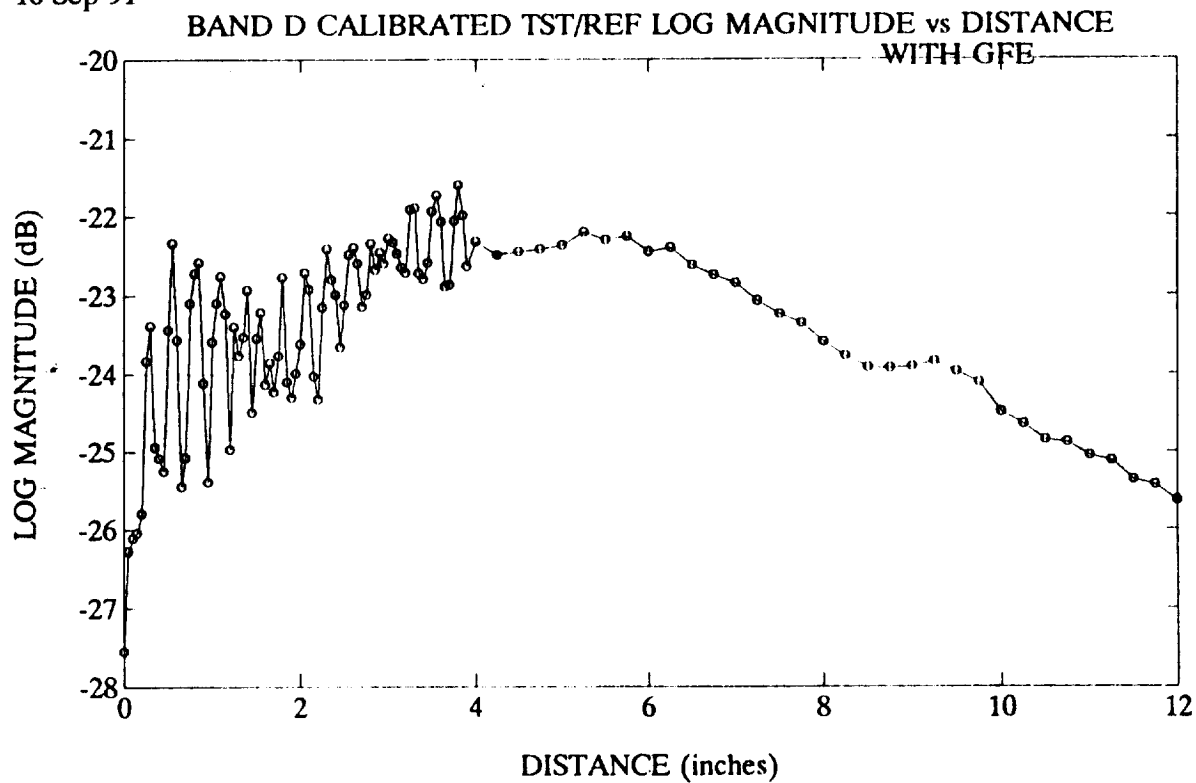
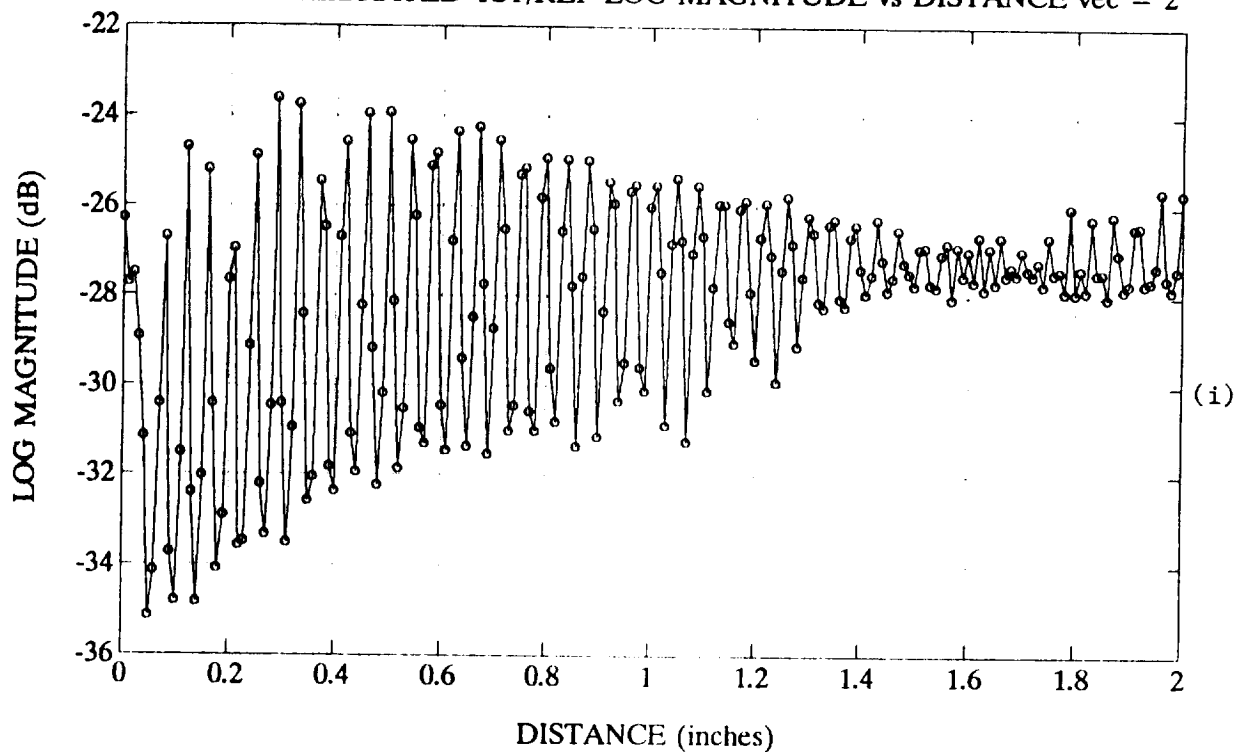


Figure 7-7(a). Examples of Measured Test Signal Amplitude Versus Target Distance Data for Band-D Operation Without Vector Error Correction

18-Dec-91

BAND D CALIBRATED TST/REF LOG MAGNITUDE vs DISTANCE vec = 2



21-Dec-91

BAND D CALIBRATED TST/REF LOG MAGNITUDE vs DISTANCE vec = 7

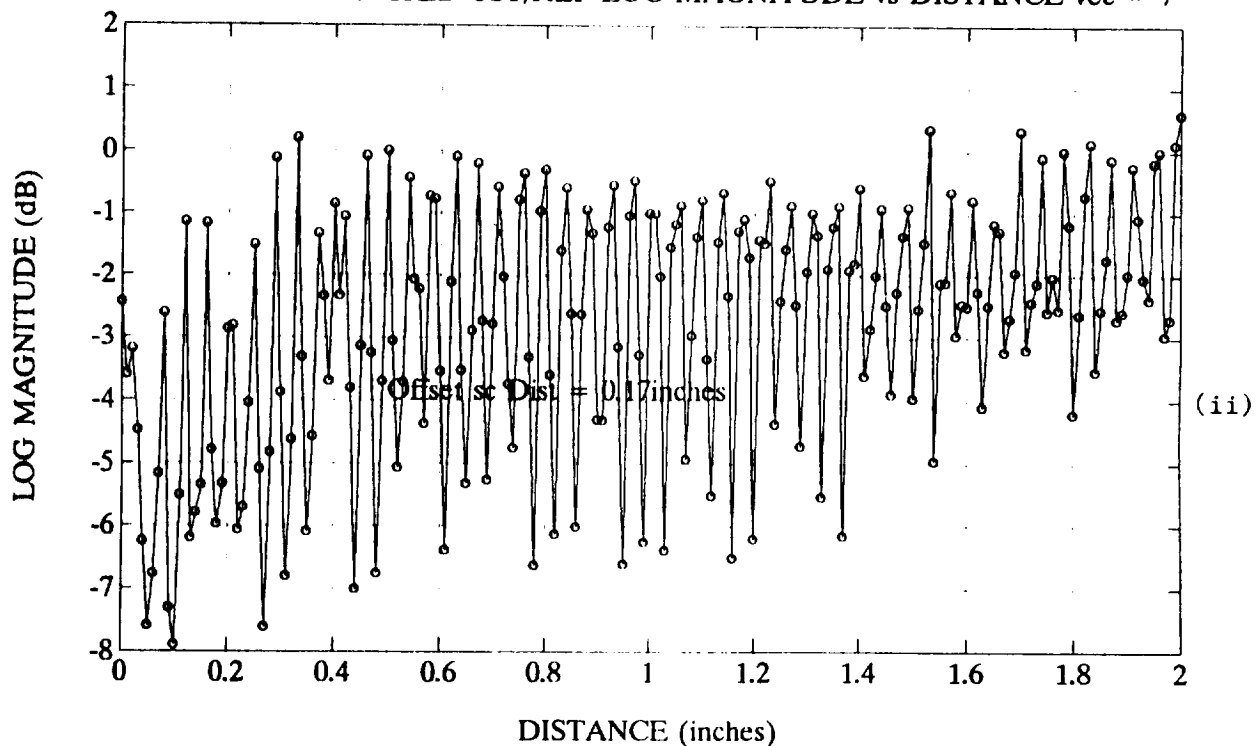


Figure 7-7(b). Measured Test Signal Amplitude Versus Target Distance Data for Band-D Operation (i) With Vector Subtraction and (ii) With VEC-7

of ± 1.7 dB, well within the instrument specification of ± 4.0 dB for 10-30 cm and ± 5 dB for 4-10 cm. Both vector subtraction and VEC-7 appeared to degrade overall performance as shown in Figures 7-7(b).

7.3.3.5 Conclusions and Recommendations

In all bands, adequate Test Signal Amplitude measurement accuracy was obtained without imposing any form of vector error correction. In Band-A, slight improvements could be obtained by using VEC-7 at close ranges and VEC-2 (simple vector subtraction) at long ranges. In Band-B, moderate improvements were obtained using vector subtraction at distances greater than two inches. Vector error correction did not offer significant performance improvements in either Band-C or Band-D.

7.4 TARGET STANDOFF DISTANCE ACCURACY

Time domain plots of the normalized Test Signal were also used to determine the time delay of the target return signal. The simple target detection algorithm implemented on the GSE computer defined the peak response appearing in the time domain plots as the target and the corresponding time delay was equated to the target distance. This procedure worked well in all bands except Band-C where large multiple reflection appeared to be present at times. Some specific examples of problems encountered in Band-C are presented later in this section of the report.

By retrieving the time delay of the peak return in the time domain plots of data taken at varying target distances, plots can be produced of Target Return Time Delay versus Distance. As noted earlier in this report, the time delay versus distance graphs should be a straight line of the form

$$\tau = m \cdot d + \tau_0 \quad (7-1)$$

Without VEC, the MRIS instrument met specifications in Band-A and Band-B and slightly exceeded the specification at close distances in Band-C and Band-D. With some form of VEC, data in all four bands generally met the instrument specification.

7.4.1 Band-A Standoff Distance Results

A graph of the measured time delay versus target distance is shown in the upper part of Figure 7-8(a). The measured data generally has the proper average slope of $1.693\text{E-}10$ sec/inch. The τ_0 value of 1.7 ns is referenced to the end of the antenna-to-module waveguide where the response-isolation type system calibration was performed. Variations from the ideal straight line can be observed, particularly at target distances below one inch. To better examine these deviations, the difference between the measured data and an ideal straight line are plotted on a more useful scale in the bottom part of Figure 7-8(a). This graph shows the worst case deviation at target ranges below two inches is ± 0.035 ns (± 0.52 cm in free-space). At target ranges greater than two inches, the worse case deviation is ± 0.02 ns (± 0.30 cm in free-space). Both of these values meet the instrument accuracy specification of ± 1.0 cm.

The time-delay measurement accuracy in Band-A was affected by vector correction. Example data with vector subtraction (VEC-2) applied is shown in Figure 7-8(b). In this case, the worst case error at target ranges less than 2 inches is ± 0.02 ns (± 0.30 cm). The maximum error is ± 0.01 ns (± 0.15 cm) at target ranges greater than two inches. Thus, nearly a factor of two reduction of the observed errors is obtained with use of vector subtraction.

Tests were also performed with other forms of vector error correction. The observed deviations varied from ± 0.02 ns (± 0.30 cm) to ± 0.05 ns (± 0.75 cm). An example of data taken using VEC-7 is shown in the lower part of Figure 7-8(b). Although the VEC-7 data doesn't exhibit the smallest error, it does have several beneficial effects. As noted in the previous subsection, VEC-7 does a reasonably good job of correcting the amplitude data. Also, VEC-7 establishes the time reference plane at the surface of the tile. Thus, the zero-inch time delay is normalized to 0 ns.

7.4.2 Band-B Standoff Distance Results

A graph of the measured time delay versus target distance is shown in the upper part of Figure 7-9(a). The measured data generally has the proper

BAND A CALIBRATED TST/REF

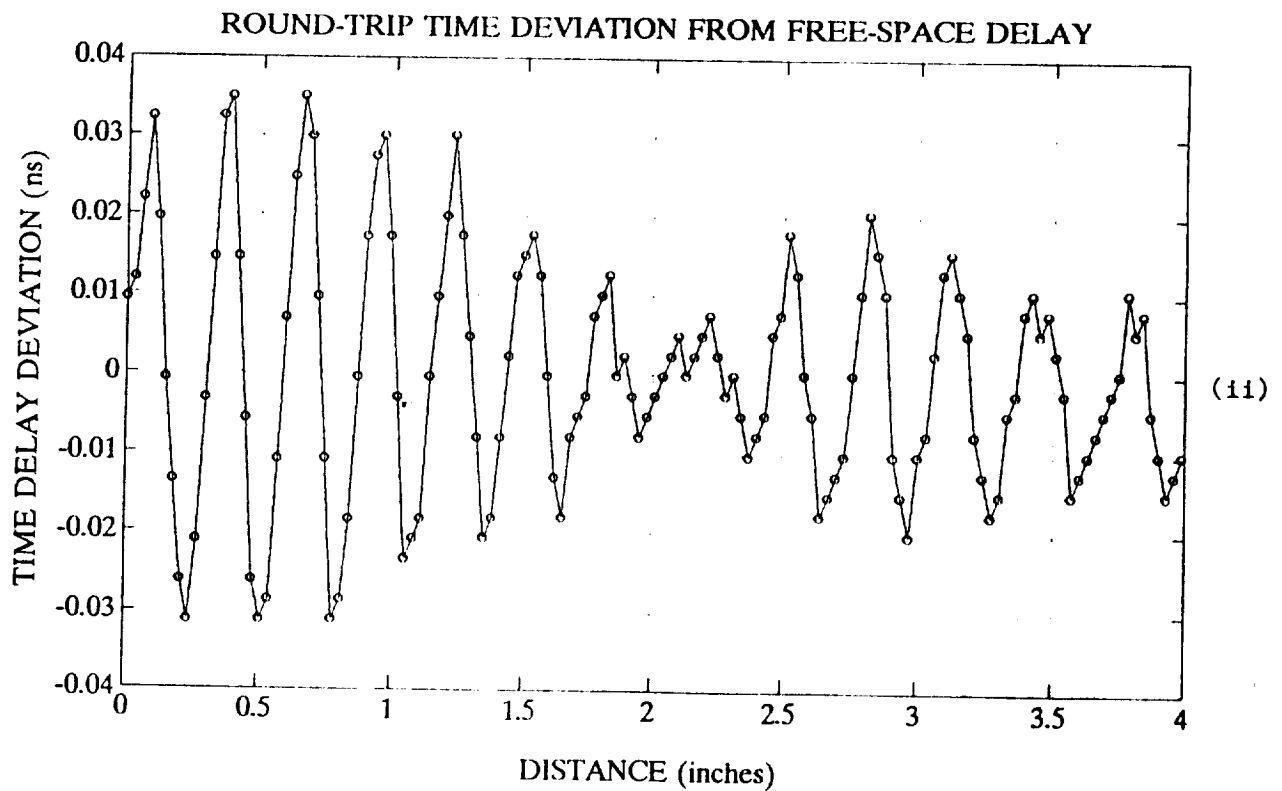
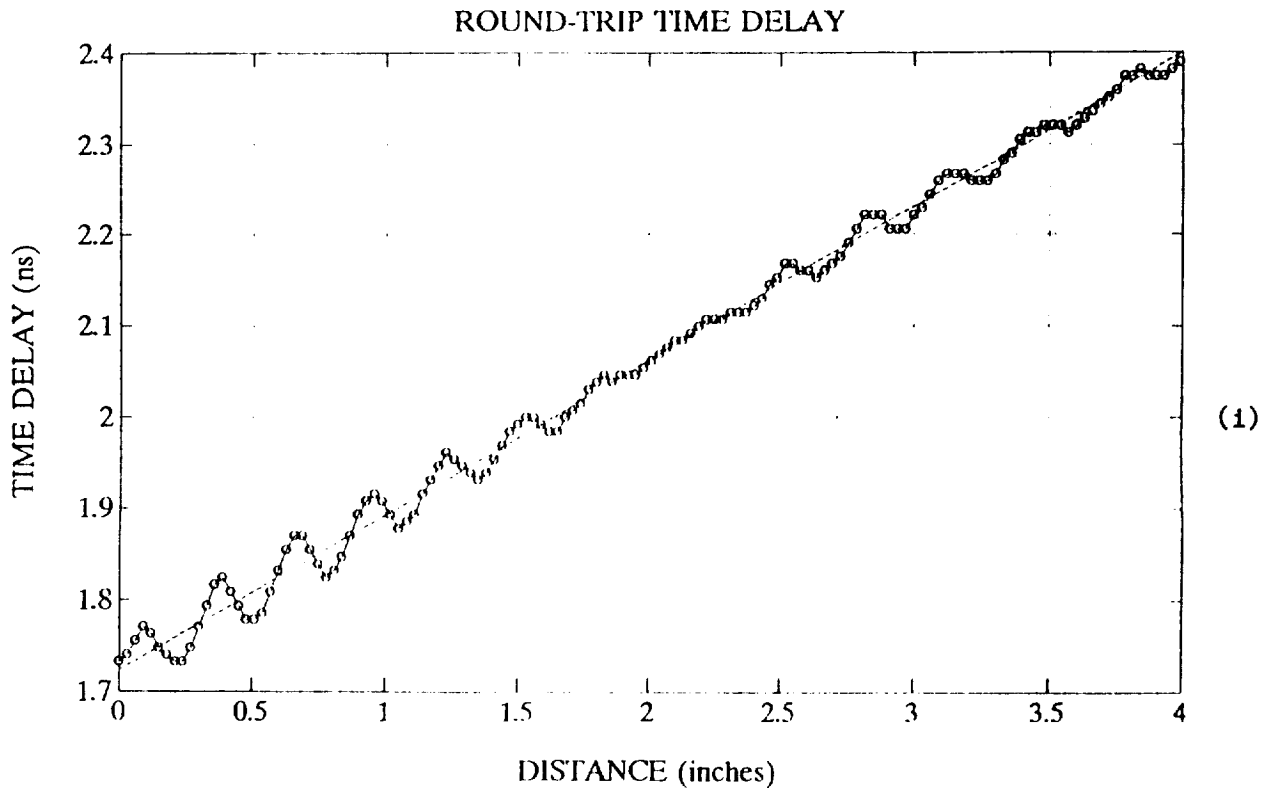
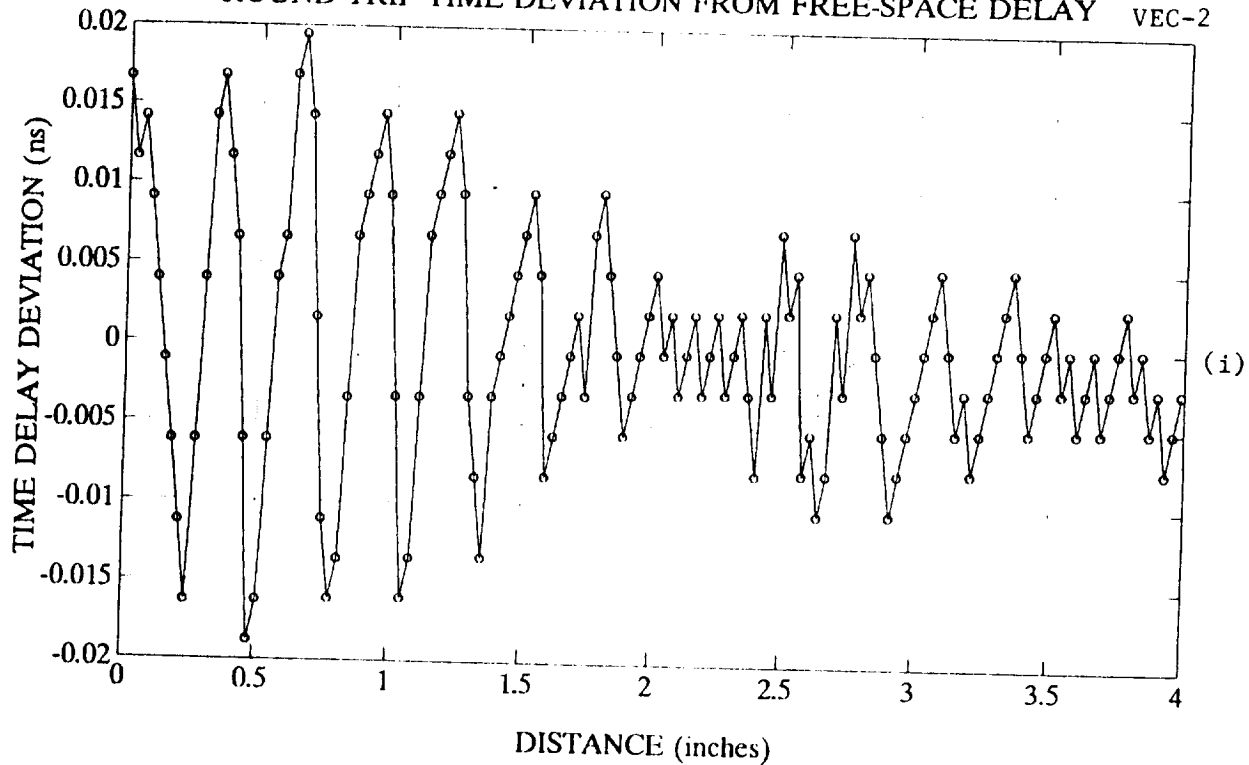


Figure 7-8(a). Measured Time Delay Versus Target Distance for Band-A Without Vector Error Correction (i) Absolute Time Delay Versus Distance and (ii) Time Delay Deviation from Ideal Free-space Delay

19-Nov-91

BAND A CALIBRATED TST/REF

ROUND-TRIP TIME DELAY DEVIATION FROM FREE-SPACE DELAY VEC-2



ROUND-TRIP TIME DELAY DEVIATION FROM FREE-SPACE DELAY VEC-7

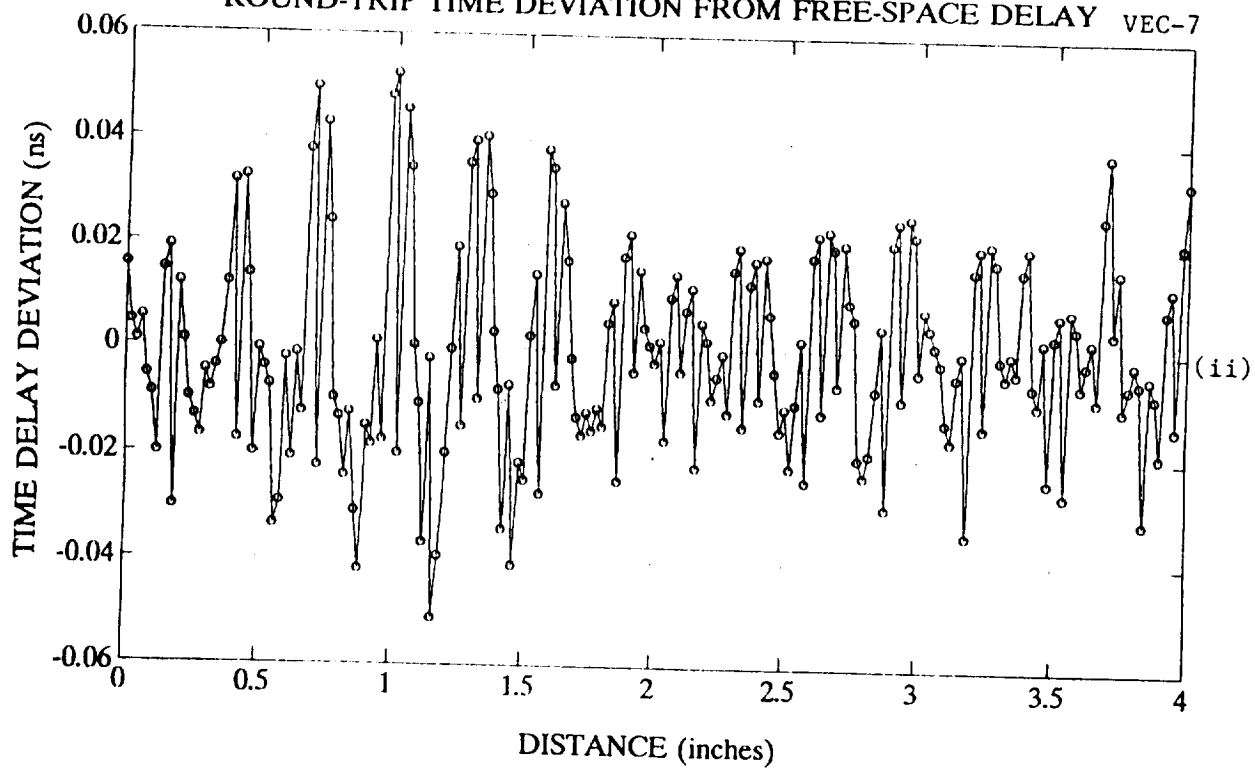


Figure 7-8(b). Measured Time Delay Deviations for Band-A (i) With Vector Subtraction and (ii) With VEC-7

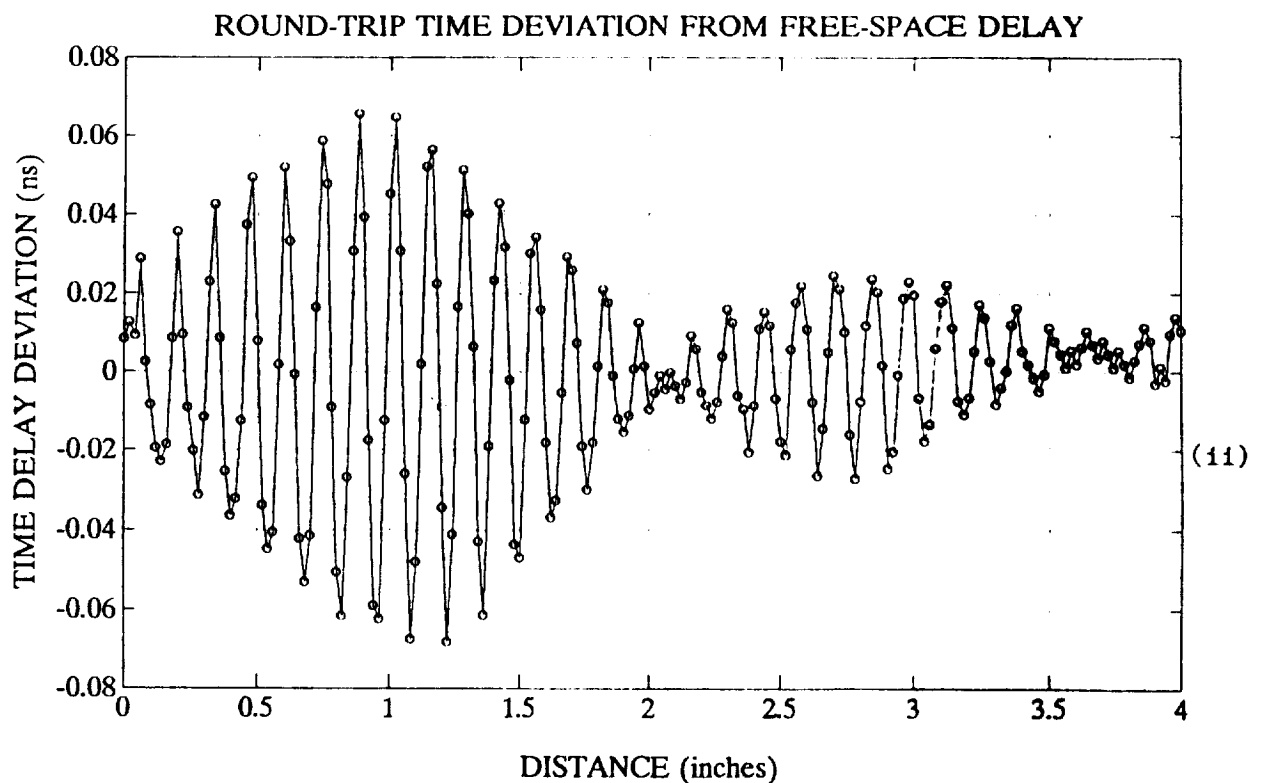
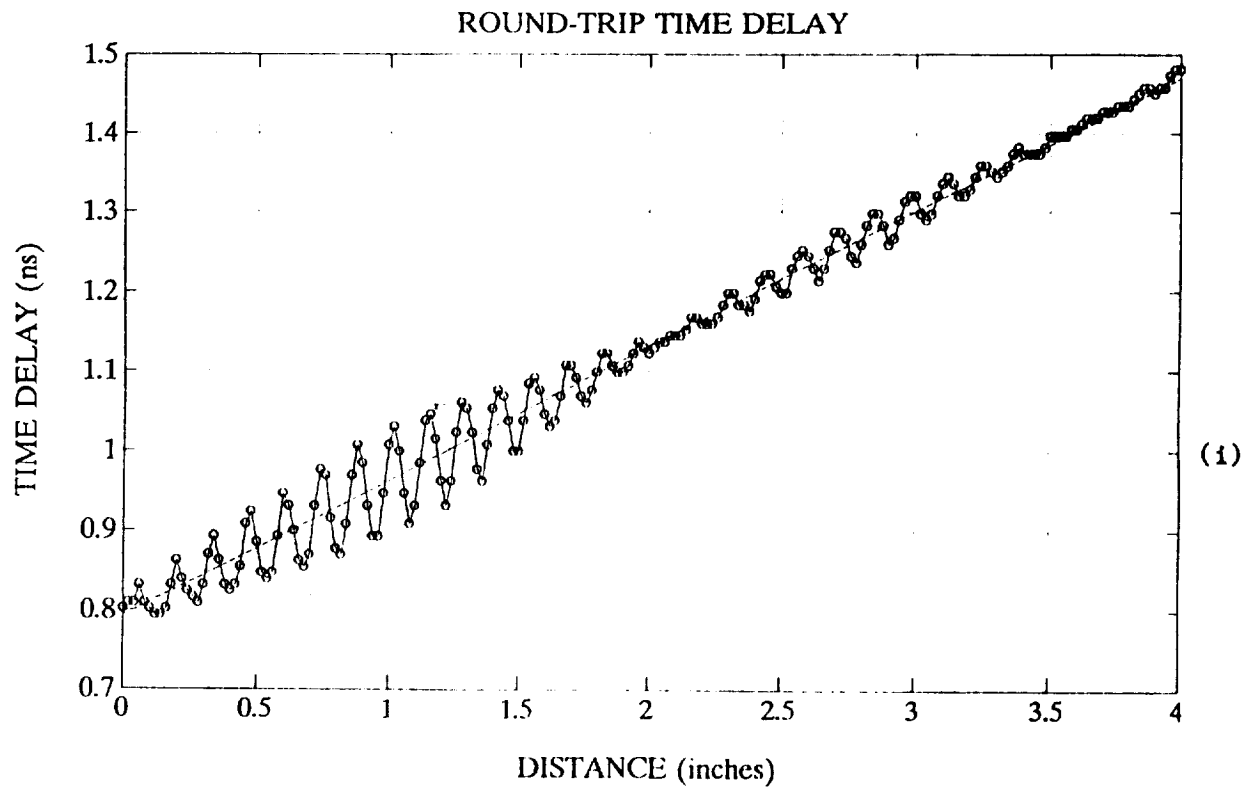
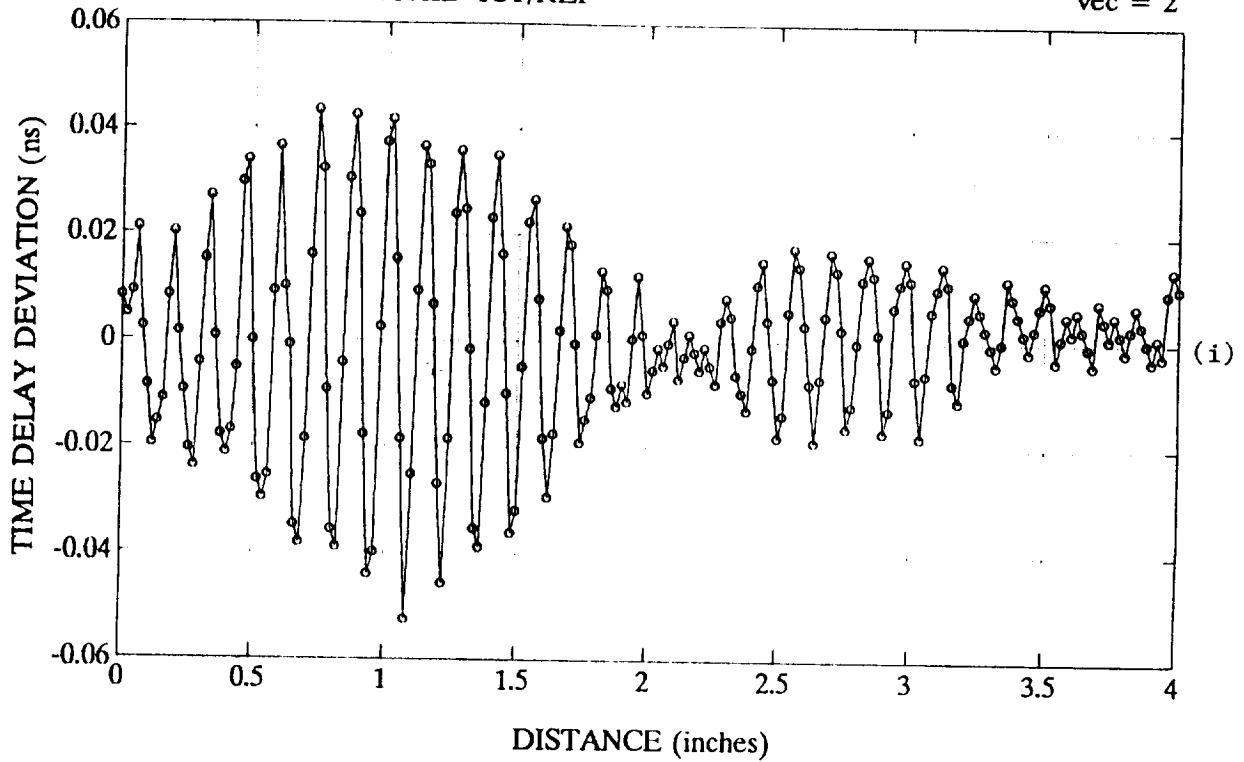


Figure 7-9(a). Measured Time Delay Versus Target Distance for Band-B Without Vector Error Correction (i) Absolute Time Delay Versus Distance and (ii) Time Delay Deviation from Ideal Free-space Delay

22-Nov-91

BAND B CALIBRATED TST/REF

vec = 2



20-Dec-91

BAND B CALIBRATED TST/REF

vec = 7

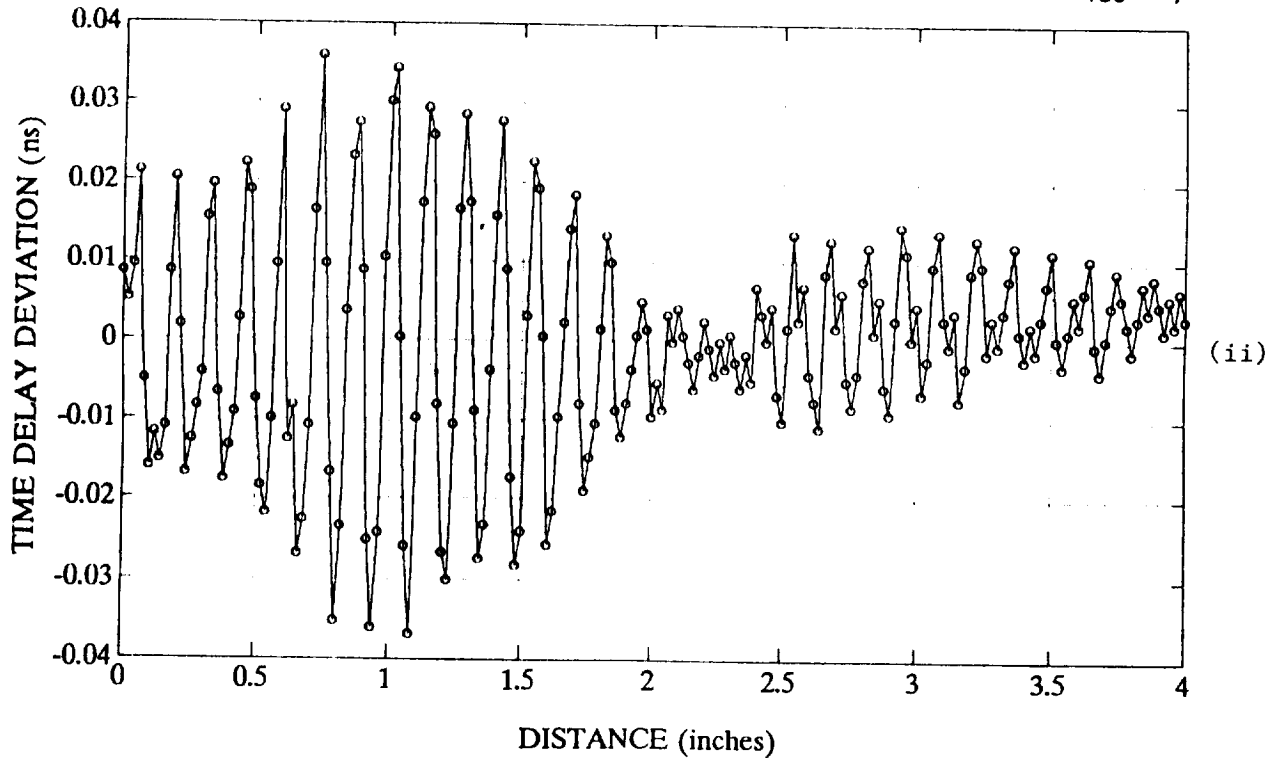


Figure 7-9(b). Measured Time Delay Deviations for Band-B (i) With Vector Subtraction and (ii) With VEC-7

average slope of $1.693\text{E-}10$ sec/inch and has a τ_0 value of 0.8 ns referenced to the ends of the antenna-to-module waveguides where the response-isolation type system calibration was performed. Some variations from the ideal straight line can be observed, particularly at target distances below 2 inches. The difference between the measured data and a ideal straight line are plotted in the bottom part of Figure 7-9(a). This graph shows the worst error at target ranges below two inches is ± 0.07 ns (± 1.05 cm in free-space), meeting the instrument specification of ± 1.2 cm in this range. At target ranges greater than two inches, the worst case error is ± 0.03 ns (± 0.45 cm), again meeting the instrument specification of ± 1.0 cm in this range.

The time-delay measurement accuracy obtained in Band-B was improved when vector subtraction (VEC-2) was applied. Example data with vector subtraction applied is shown in Figure 7-9(b). In this case, the worst case error at target ranges less than two inches was ± 0.045 ns (± 0.67 cm), a significant improvement over the uncorrected error of ± 0.07 ns (± 1.05 cm). The maximum error is ± 0.02 ns (± 0.30 cm) at target ranges greater than two inches, slightly better than the ± 0.03 ns (± 0.45 cm) error observed without error correction.

Very good results were also obtained with other vector error correction. The observed errors varied from ± 0.035 ns (± 0.52 cm) to ± 0.05 ns (± 0.75 cm). An example of data taken using VEC-7 is shown in the lower part of Figure 7-9(b). In this case, the time delay variations were reduced to ± 0.035 ns (± 0.52 cm).

7.4.3 Band-C Standoff Distance Results

The largest time delay errors as well as the most difficult target identification occurred in Band-C. Results from an early set of Band-C measurements are shown in Figure 7-10(a). In this case, the maximum delay errors occurred below one inch. The worst case errors were ± 0.07 ns (± 1.05 cm), meeting the instrument specification of ± 1.5 cm in this target range. For target ranges greater than two inches, the worst case errors were ± 0.03 ns (± 0.45 cm), again meeting the instrument specification of ± 1.0 cm for target ranges from 5-30 cm.

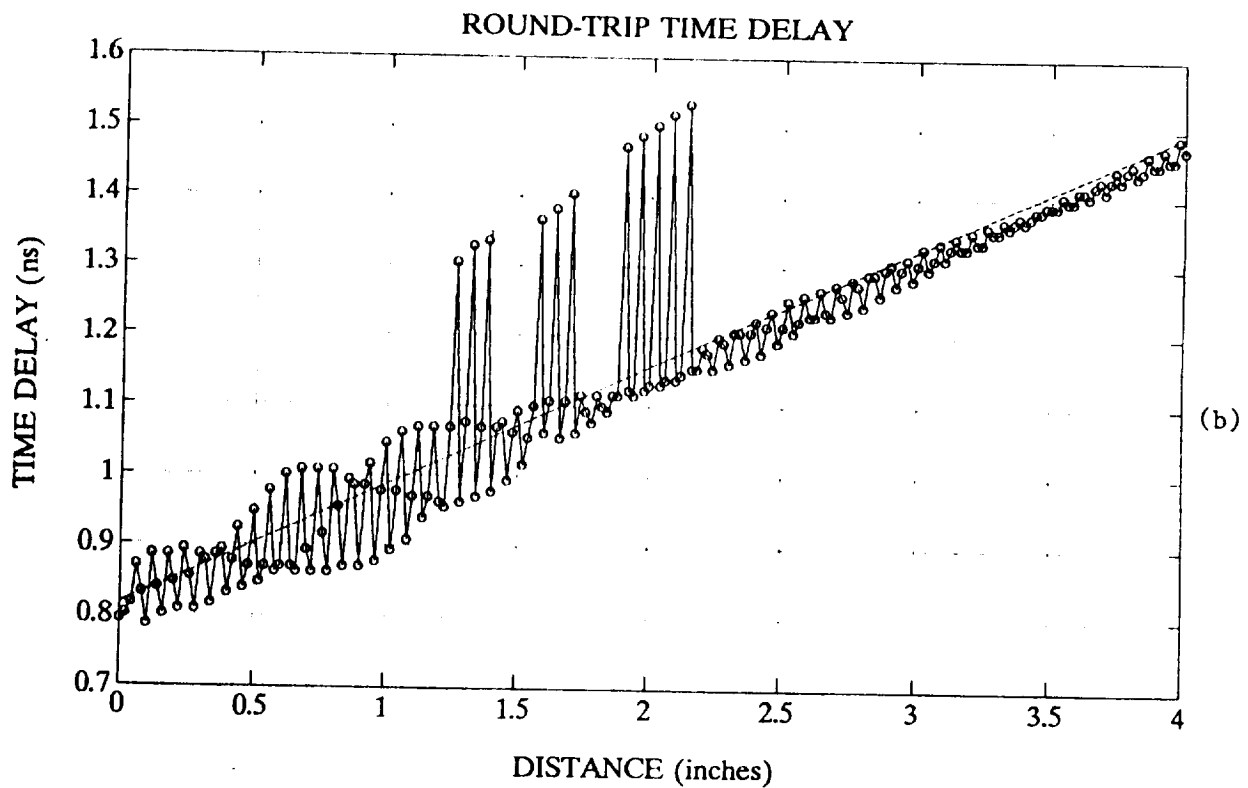
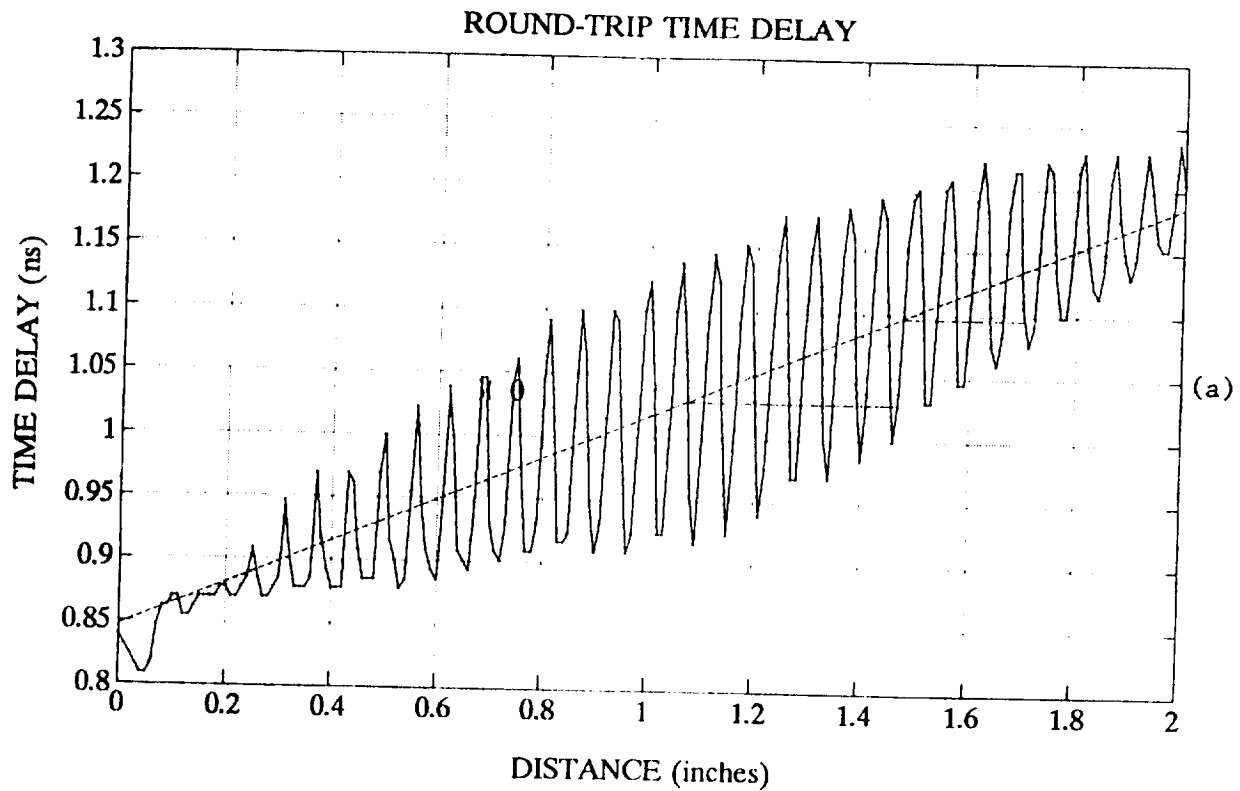


Figure 7-10. Band-C Measured Time Delay vs Target Distance Without VEC
(a) Initial Tests in September 1991 and (b) Follow-up Tests in November 1991

Data was collected at steps of 0.05 inches in this initial test. In a subsequent test, data was collected at smaller steps of 0.02 inches to insure adequate sampling was being achieved in view of the short free-space wavelength of 0.124 inches at 94 GHz. In these tests, problems with correct identification of the target return signal was encountered for the first time. Results from these tests are shown in Figure 7-10(b). This data shows that large errors occurred at several points for target ranges between 1.25 and 2.25 inches. It was suspected the target selection algorithm, which automatically selected the largest target return as the desired target, was being defeated. Also, since the observed errors appeared to consistently indicate a target range that was greater than the actual target location, it appeared a large multiple reflection was being falsely identified as the target.

To investigate this idea, a series of measurements were performed for target distances from 2.00 to 2.15 inches in small steps of 0.01 inches. These results are shown in Figures 7-11(a) to 7-11(h). From Figure 7-10(b) it may be noted the measured time-delay is ideally represented by an equation of the form

$$\tau = 1.6934\text{E-}10 \text{ (sec/inch)} \cdot d \text{ (inch)} + 0.82\text{E-}9 \text{ (sec)} \quad (7-2)$$

The calculated time delay for the main target return as well as the first multiple reflection due to tile effects are tabulated in Table 7-2. At 2.00 inches, Table 7-2 indicates a target return should be observed at 1.1587 ns and the first multiple reflection should be observed at 1.4974 ns. The time domain plot obtained at 2.00 inches is shown in Figure 7-11(a)(i). In this case, the peak return occurs at 1.1379 ns, corresponding to an error of 0.31 cm from the calculated value of 1.1587 ns. As suspected, a fairly large signal can be observed at approximately 1.50 ns corresponding to the first multiple reflection. Since this multiple reflection is 4 to 5 dB lower than the peak return, no problems were encountered in correctly identifying the target return.

At 2.01 inches, Table 7-2 indicates a target return should be observed at 1.1604 ns and a multiple reflection should be observed at 1.5007 ns. The time domain plot obtained at 2.01 inches is shown in Figure 7-11(a)(ii). In this

TABLE 7-2

COMPUTED DELAYS FOR TARGET AND MULTIPLE REFLECTION RETURNS

TARGET DISTANCE	TARGET DELAY	MULTIPLE REFLECTION DISTANCE	MULTIPLE REFLECTION DELAY
2.00 inches	1.1587 ns	4.00 inches	1.4974 ns
2.01	1.1604	4.02	1.5007
2.02	1.1621	4.04	1.5041
2.03	1.1638	4.06	1.5075
2.04	1.1655	4.08	1.5109
2.05	1.1671	4.10	1.5143
2.06	1.1688	4.12	1.5177
2.07	1.1705	4.14	1.5211
2.08	1.1722	4.16	1.5245
2.09	1.1739	4.18	1.5278
2.10	1.1756	4.20	1.5312
2.11	1.1773	4.22	1.5346
2.12	1.1790	4.24	1.5380
2.13	1.1807	4.26	1.5414
2.14	1.1824	4.28	1.5448
2.15	1.1841	4.30	1.5482

NOTE:

$$\text{TARGET DELAY} = m \cdot d + \tau_0$$

$$\text{MULT. REFLECTION DELAY} = m \cdot (2d) + \tau_0$$

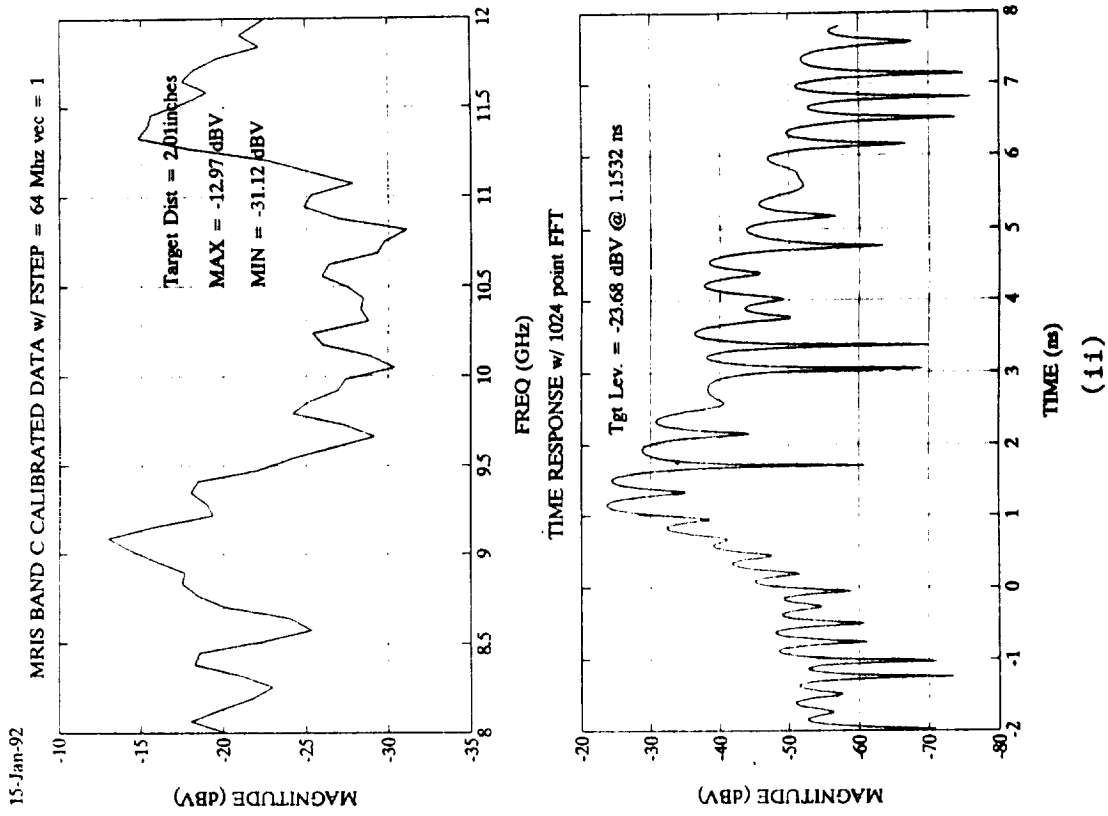
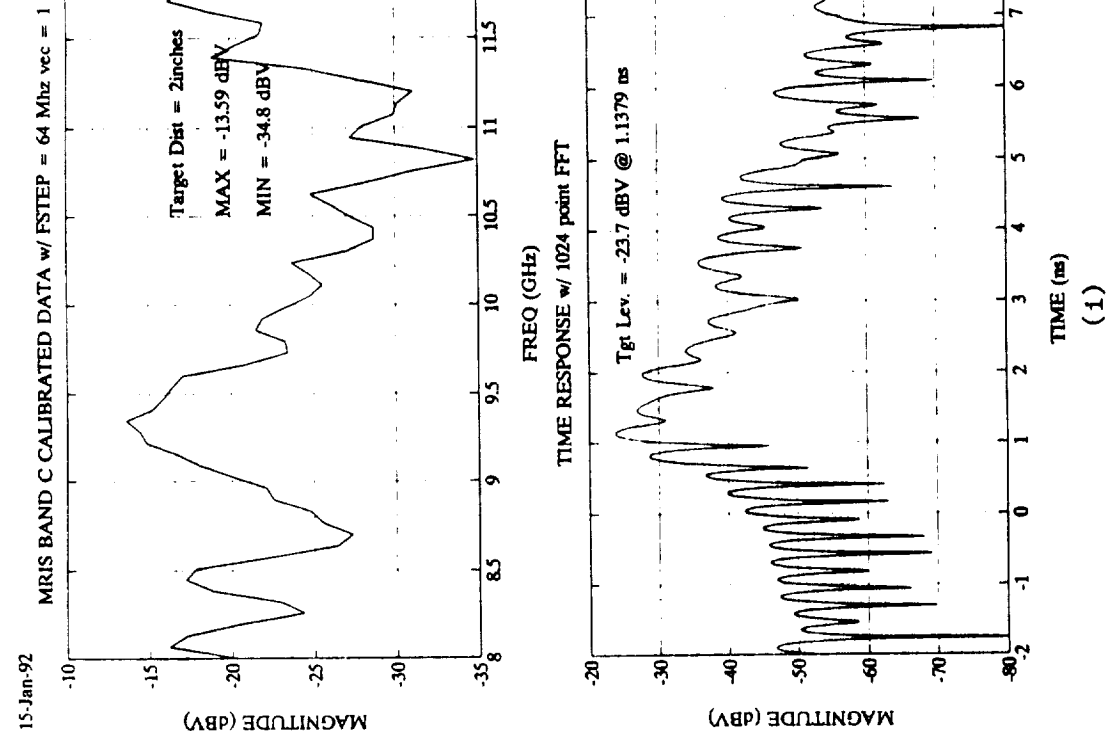


Figure 7-11(a). Example Band-C Test Data Measured Without Vector Error Correction at a Target Distance (i) 2.00 inches and (ii) 2.01 inches

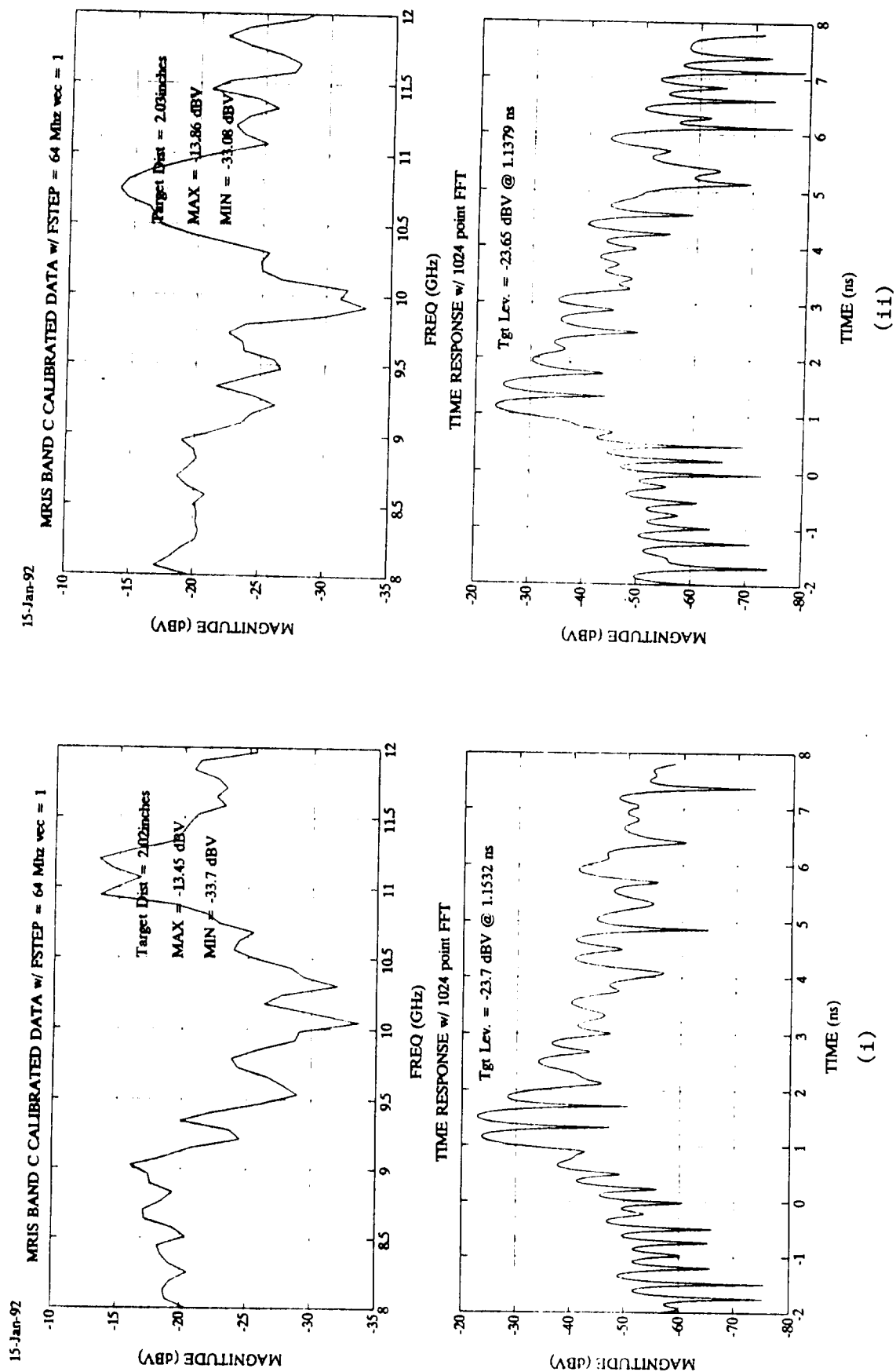


Figure 7-11(b). Example Band-C Test Data Measured Without Vector Error Correction at a Target Distance (i) 2.02 inches and (ii) 2.03 inches

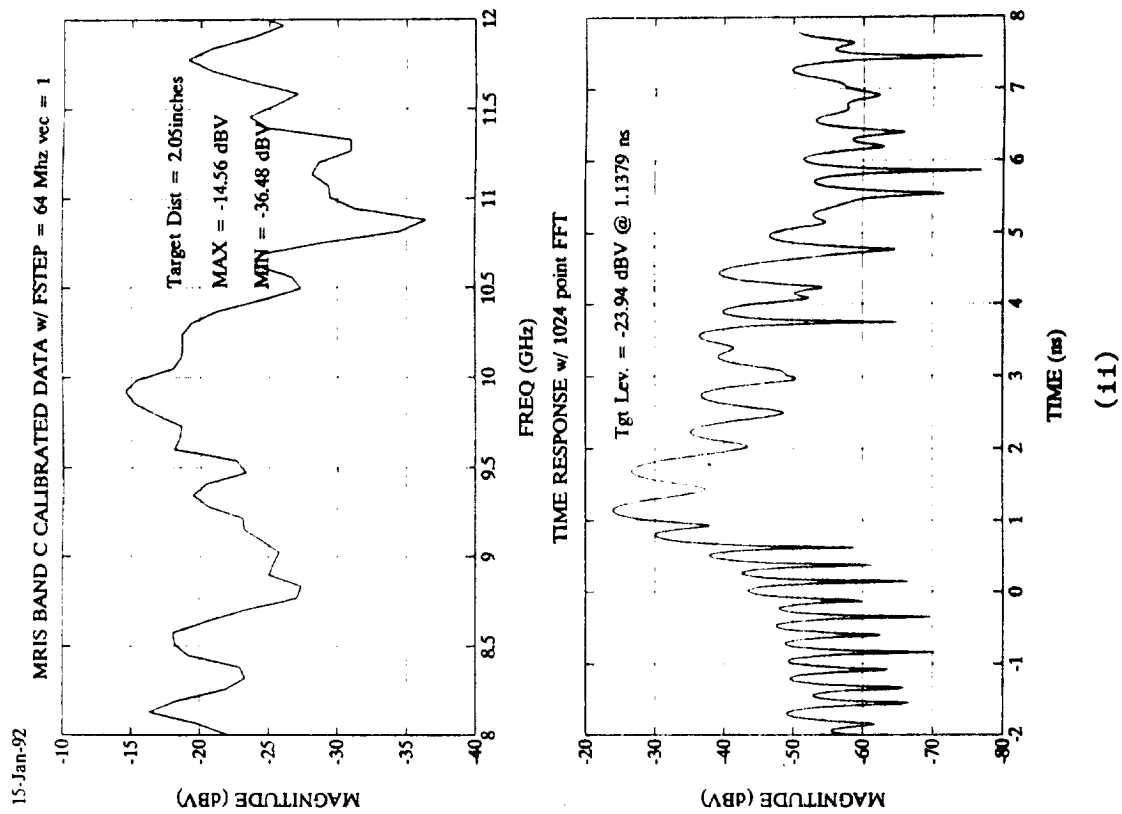
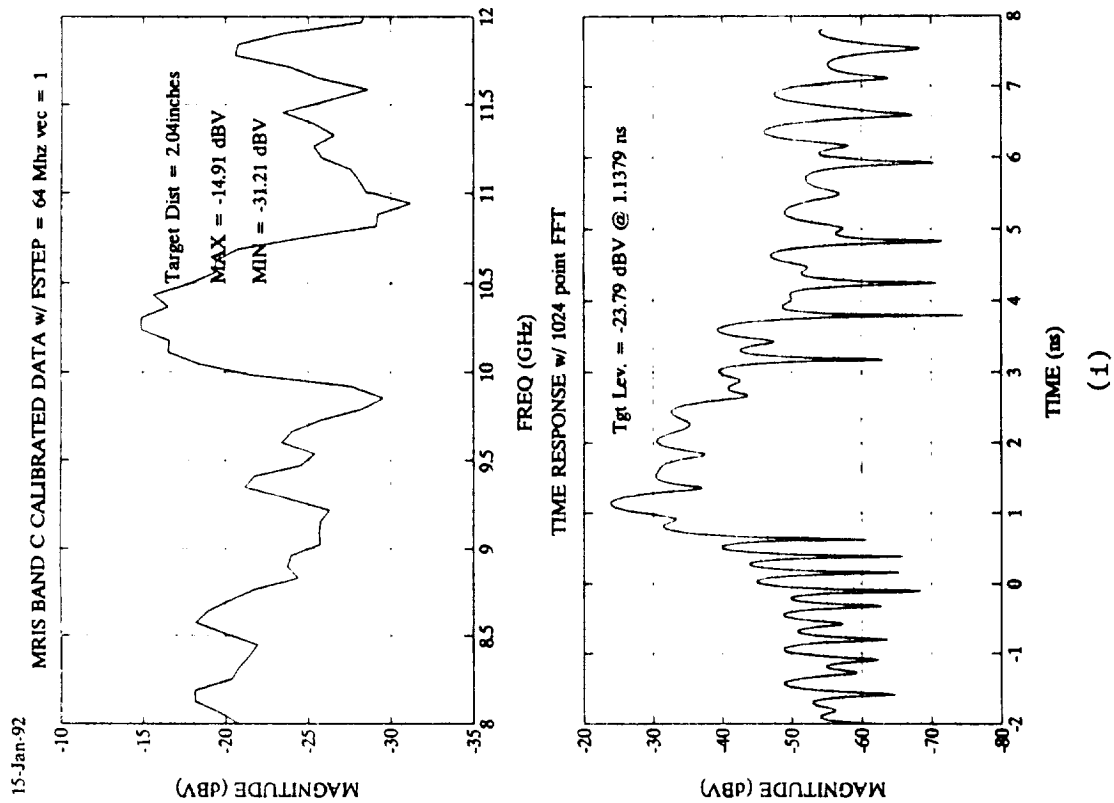


Figure 7-11(c). Example Band-C Test Data Measured Without Vector Error Correction at a Target Distance (i) 2.04 inches and (ii) 2.05 inches

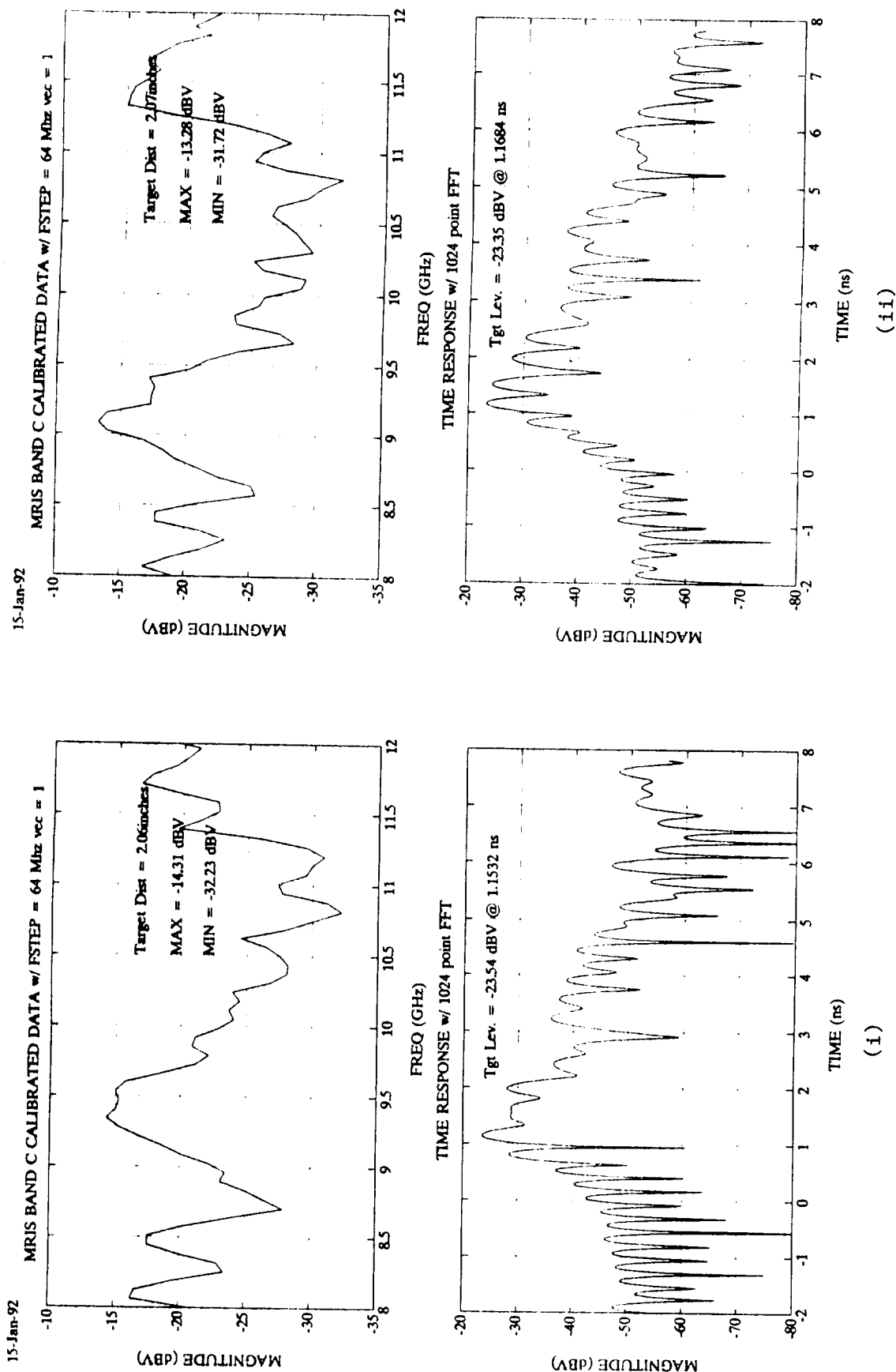


Figure 7-11(d). Example Band-C Test Data Measured Without Vector Error Correction at a Target Distance (i) 2.06 inches and (ii) 2.07 inches

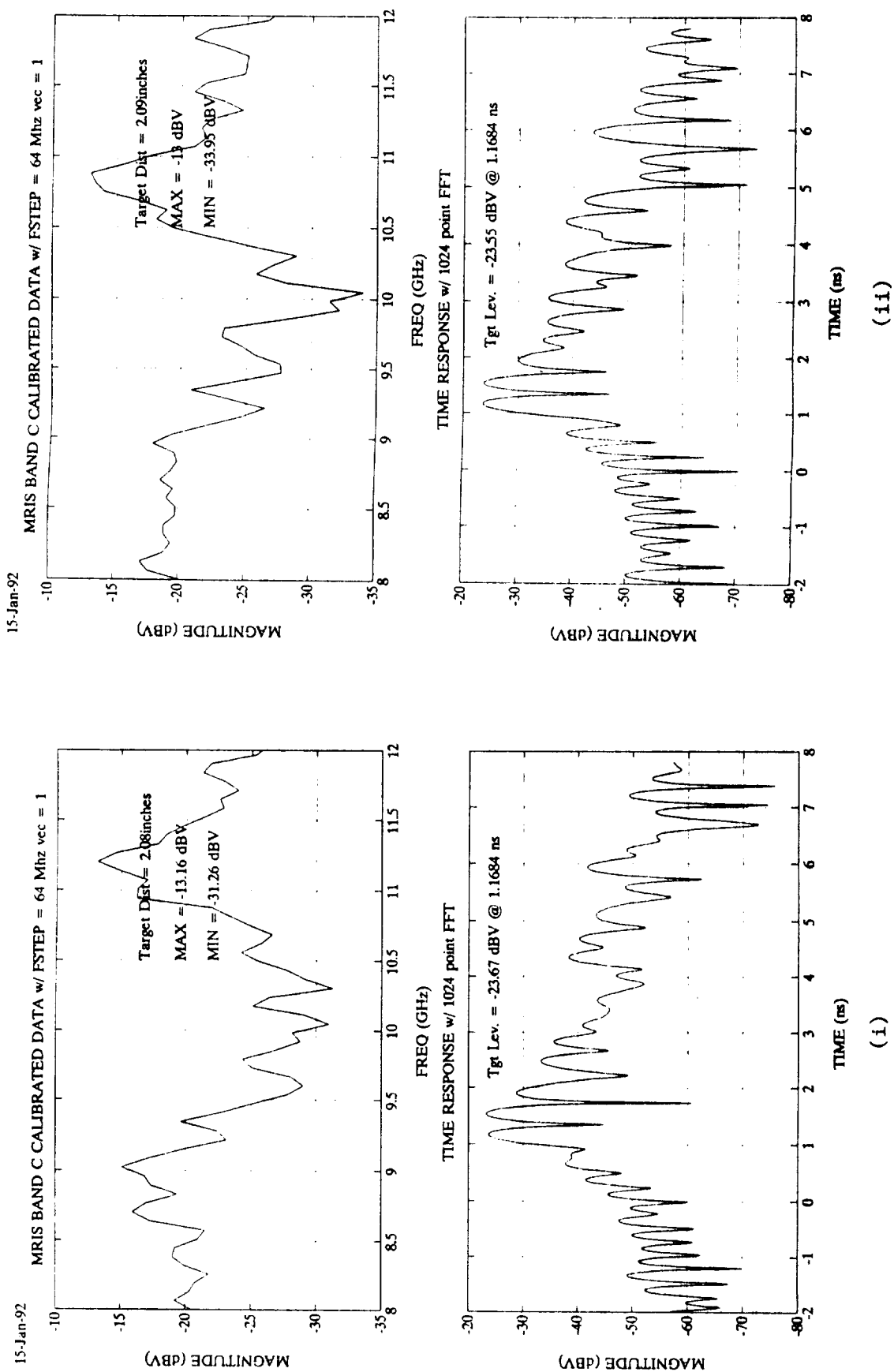


Figure 7-11(e). Example Band-C Test Data Measured Without Vector Error Correction at a Target Distance (i) 2.08 inches and (ii) 2.09 inches

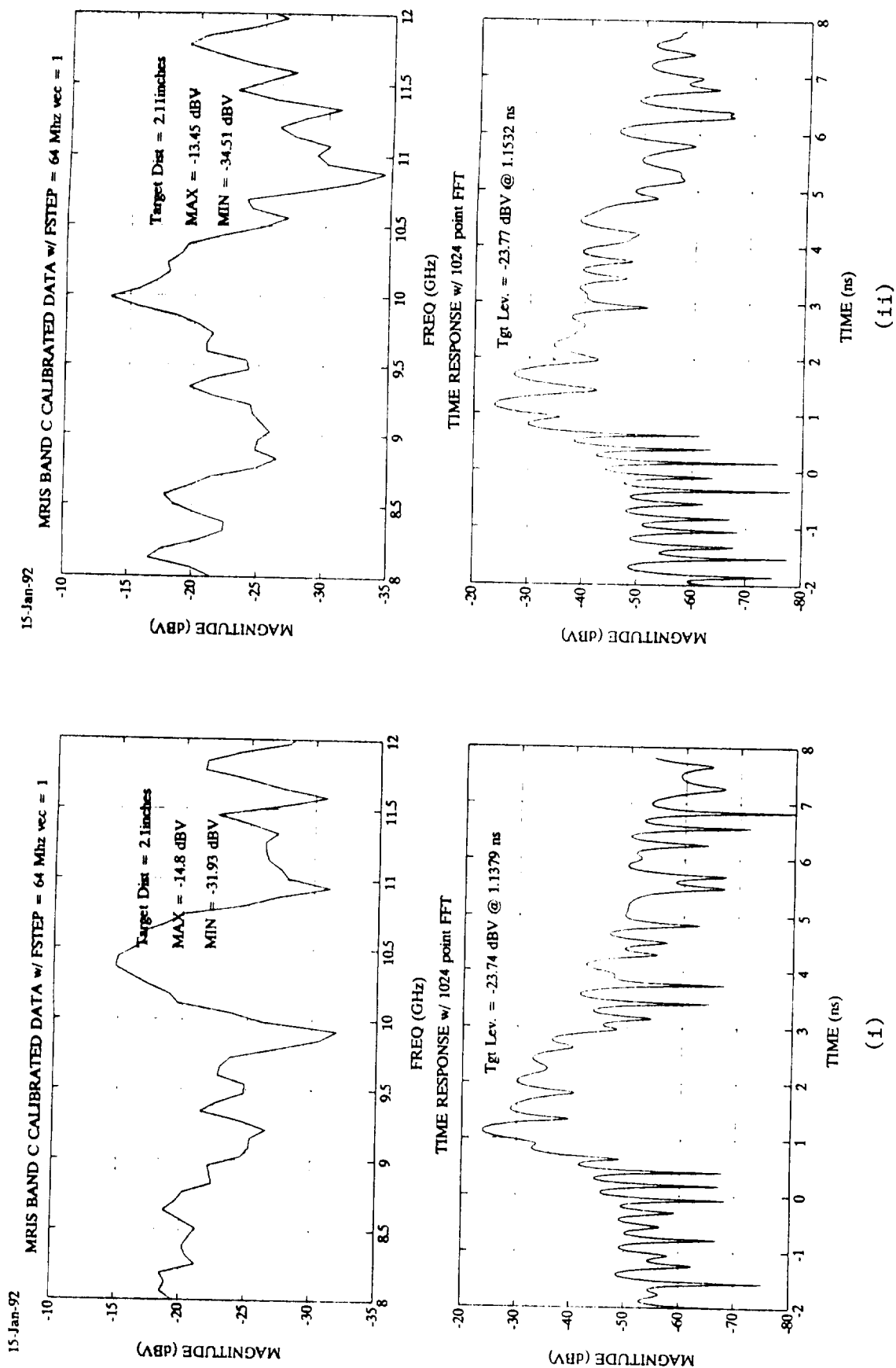


Figure 7-11(f). Example Band-C Test Data Measured Without Vector Error Correction at a Target Distance (i) 2.10 inches and (ii) 2.11 inches

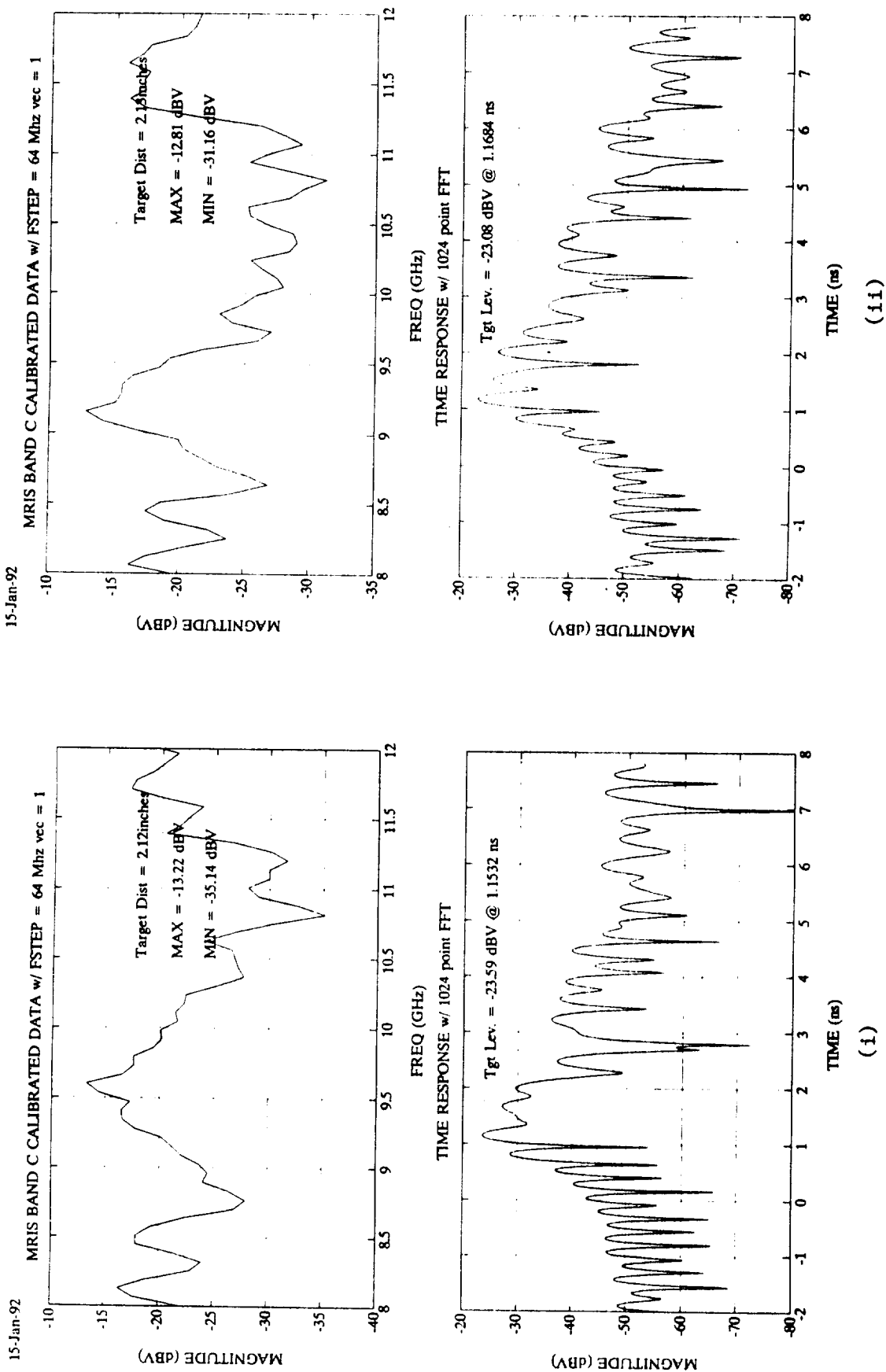


Figure 7-11(g). Example Band-C Test Data Measured Without Vector Error Correction at a Target Distance (i) 2.12 inches and (ii) 2.13 inches

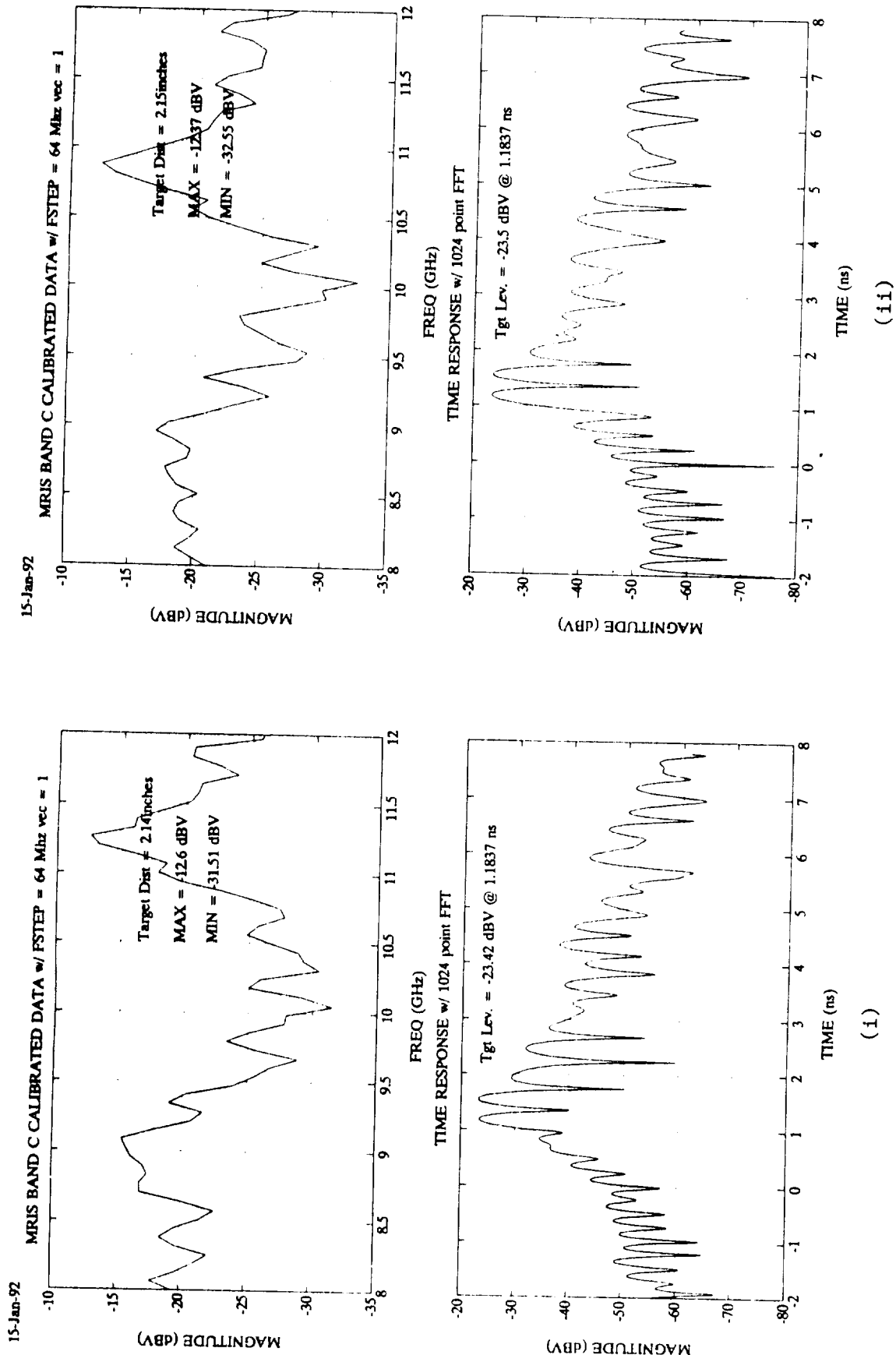


Figure 7-11(h). Example Band-C Test Data Measured Without Vector Error Correction at a Target Distance (i) 2.14 inches and (ii) 2.15 inches

case, the peak return occurs at 1.1532 ns, corresponding to an error of 0.11 cm from the calculated delay of 1.1604 ns. As suspected, a large signal can also be observed at approximately 1.50 ns corresponding to the first multiple reflection. Since this multiple reflection is lower than the peak return, the target return was again correctly identified. However, the multiple reflection is only 1 to 2 dB lower than the target return. This result hinted that at certain target distances, problems might be encountered in determining whether the target return or the first multipath return represented the desired target information.

At 2.02 inches, Table 7-2 indicates a target return should be observed at 1.1621 ns and a multiple reflection should be observed at 1.5041 ns. The time domain plot obtained at 2.02 inches is shown in Figure 7-11(b)(i). In this case, a large signal can be observed at 1.1532 ns, only 0.13 cm from the predicted target location. However, the largest return signal occurs near 1.50 ns, the predicted location of the first multiple reflection from the tile. In this case, the peak detection algorithm would have selected the wrong return signal as the target.

As the target location was increased from 2.02 to 2.06 inches, the level of the first multiple reflection decreased and it was again possible to correctly locate the target by simply noting the time delay of the peak signal in the time domain response. At 2.07 inches, the level of the first multiple reflection began increasing and at 2.08 inches, the first multiple reflection again became the largest signal in the time domain plot as shown in Figure-11(e)(i). This pattern continued and the first multiple reflection would have been incorrectly identified as the target return at 2.02, 2.08, and 2.14 inches. Since the free-space wavelength at 95 GHz is 0.124 inches, the observed peaks in the first multiple reflection appear to occur at one-half wavelength intervals.

The problem discussed above is a detection issue and would benefit from use of a more sophisticated detection algorithm. This algorithm might be as simple as detecting the location of the largest two or three peaks that meet a pre-defined detection criterion then selecting the one with the smallest time delay (i.e., the one closest to the instrument) as the correct target. Although

such an algorithm was not implemented under this contract, a visual evaluation of the data in Figure 7-11 indicates the correct target location would have been correctly determined with this scheme.

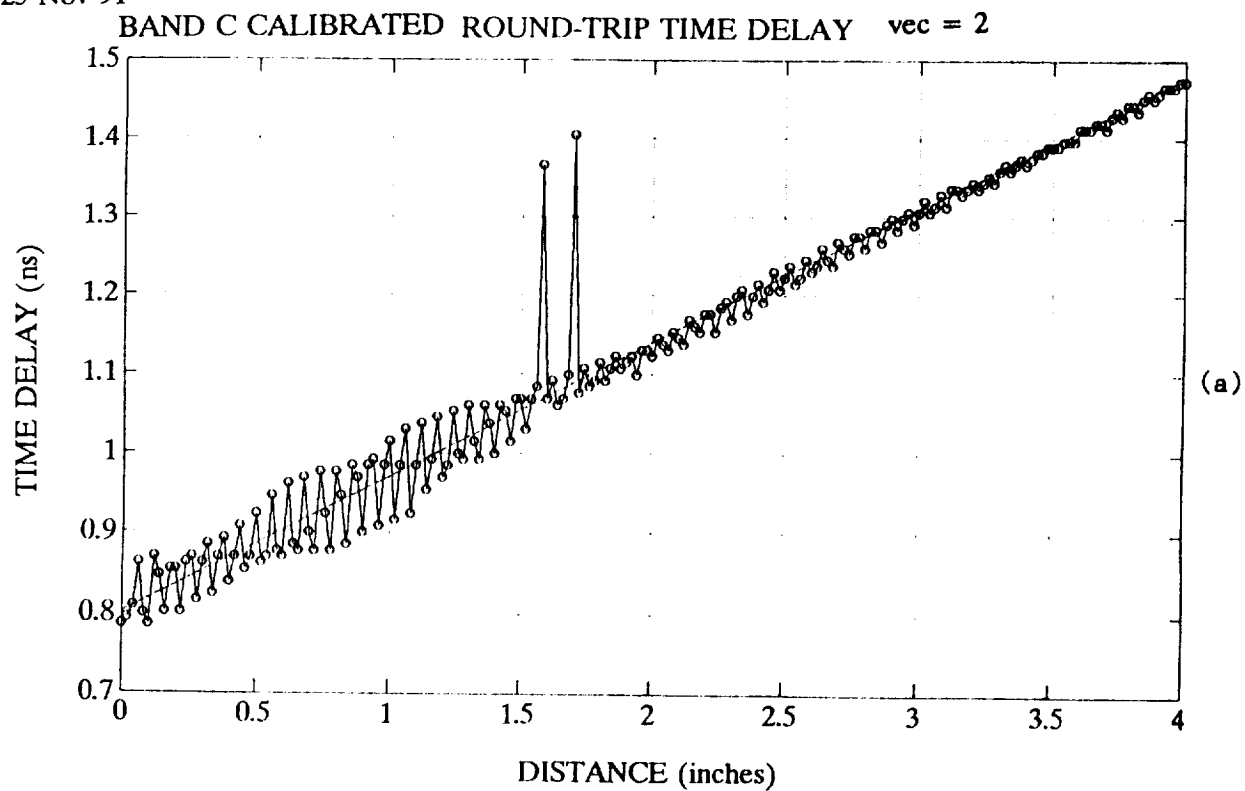
Several of the vector error correction procedures developed during the MRIS program schemes were evaluated to determine their effectiveness in Band-C. Results with vector subtraction (VEC-2) are shown in Figure 7-12. Curiously, even though vector subtraction does not account for multiple reflection effects, fewer cases of incorrect target selection were observed when vector subtraction was used. Reasonably good results were also obtained with VEC-7 which does attempt to account for multiple reflections. Example results with VEC-7 are also shown in Figure 7-12. In this case, it does not appear a multiple reflection was ever erroneously selected as the target, and the worst case errors are ± 0.06 ns (± 0.9 cm). No detailed time domain plots of the the performance with either the VEC-2 or VEC-7 were available for inclusion in this report. The data files necessary to produce these plots are available within the data files provided to NASA.

7.4.4 Band-D Standoff Distance Results

A graph of the time delay measured versus target distance in Band-D is shown in the upper part of Figure 7-13(a). The measured data has the expected average slope of $1.693\text{E-}10$ sec/inch but deviations from the ideal straight line are evident. The lower graph in this figure shows the difference between the measured data and an ideal straight line. The worst error for target ranges from 0 to 2 inches is ± 0.11 ns (± 1.65 cm), exceeding the instrument specification of ± 1.5 cm in this range. At target ranges greater than 2 inches, the worst case error is ± 0.03 ns (± 0.45 cm), meeting the instrument specification of ± 1.0 cm in this range.

The time-delay measurement accuracy obtained was improved when vector subtraction (VEC-2) was applied. Example data with vector subtraction applied is shown in Figure 7-13(b). In this case, the worst case error for target ranges between 0 and 2 inches is ± 0.08 ns (± 1.2 cm). This represents a significant improvement over the uncorrected error of ± 0.11 ns (± 1.65 cm) and also meets the instrument specification of ± 1.5 cm.

25-Nov-91



20-Dec-91

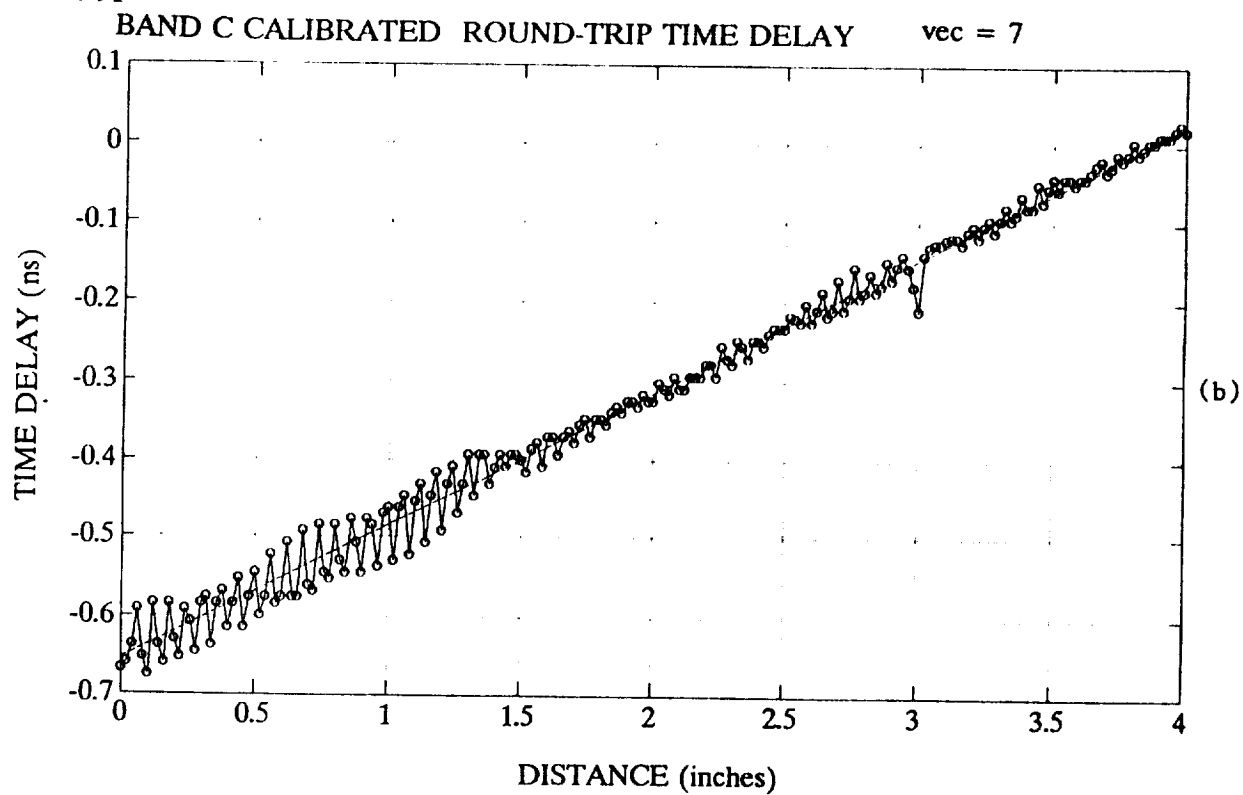


Figure 7-12. Measured Time Delay Deviations for Band-C (a) With Vector Subtraction and (b) With VEC-7

18-Dec-91

BAND D CALIBRATED TST/REF

vec = 1

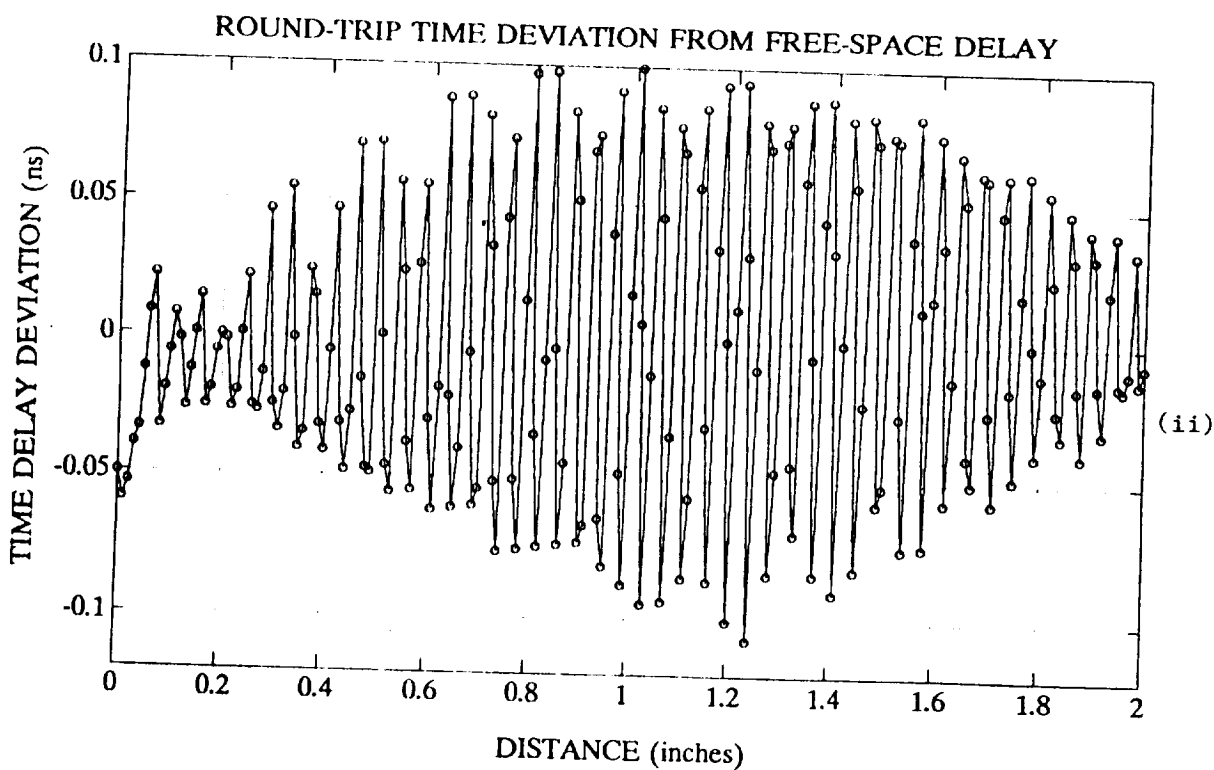
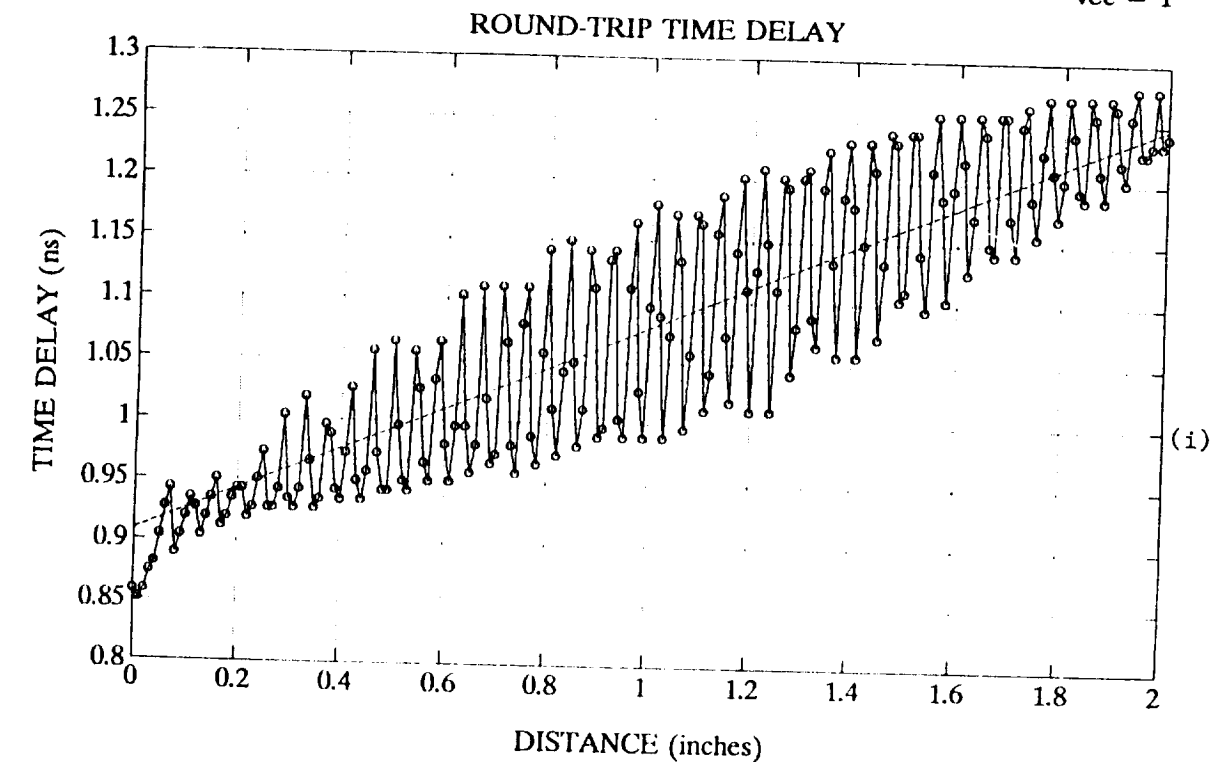
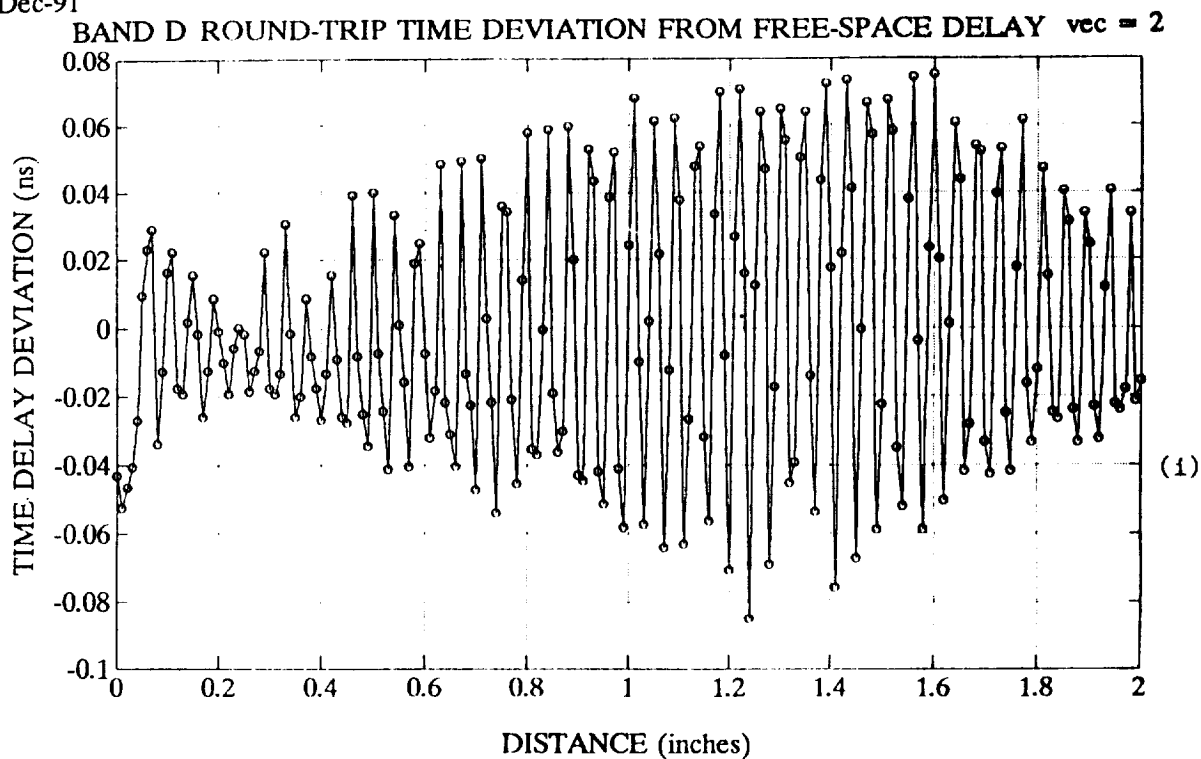


Figure 7-13(a). Measured Time Delay for Band-D Without Vector Error Correction: (i) Round Trip Delay and (ii) Time Delay Deviations

18-Dec-91



21-Dec-91

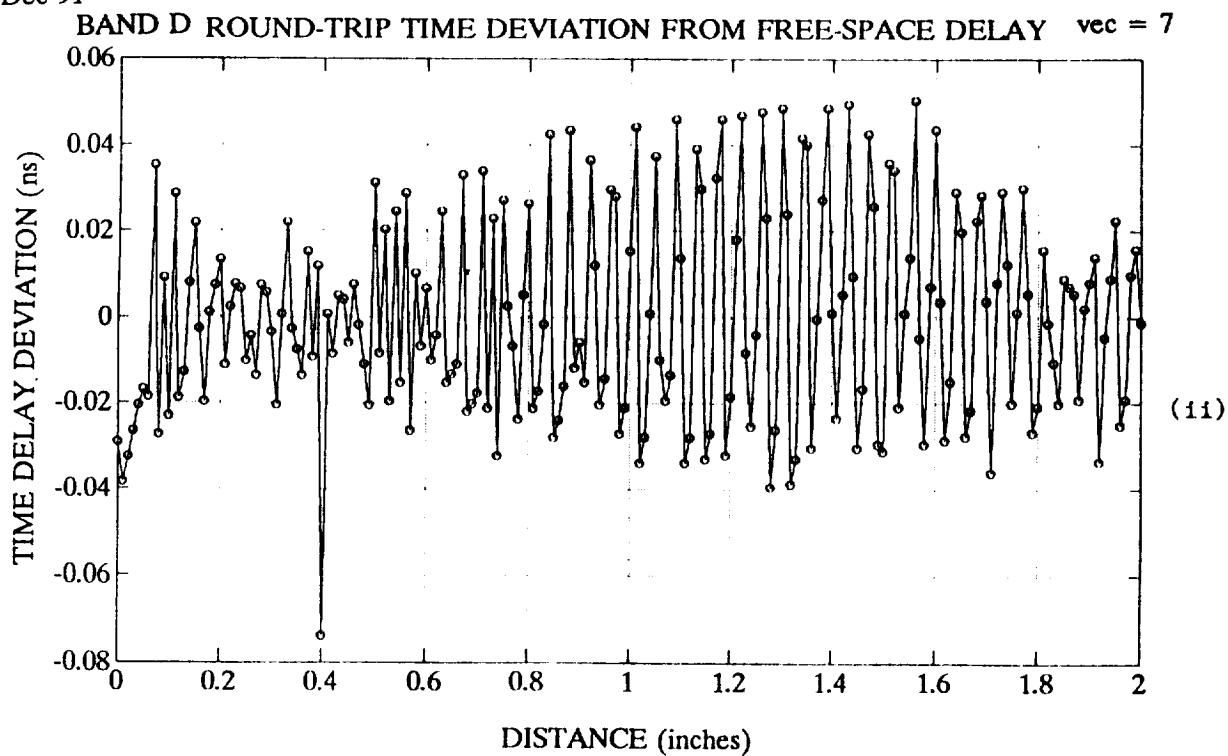


Figure 7-13(b). Measured Time Delay Deviations for Band-D (i) With Vector Subtraction and (ii) With VEC-7

Mixed results were obtained with other vector error correction procedures applied in Band-D. An example of data obtained using VEC-7 is shown in the lower part of Figure 7-13(b). In most cases, the error in this figure is limited to ± 0.05 ns (± 0.75 cm). However, at a target distance of 0.4 inches, an error of 0.07 ns (1.05 cm) can be observed. The specific cause of this anomaly was not determined.

7.4.5 Conclusions and Recommendations

A summary of the measurement accuracy observed in the standoff distance tests is shown in Table 7-3. The instrument specifications could be met in all bands for target ranges beyond two inches without having to apply any form of vector error correction. However, vector subtraction improved measurement accuracy in this range. For target distances less than two inches, vector error correction was required in Band-C and Band-D to meet the instrument specification. Vector subtraction was again very effective for correcting these close in measurements. The most significant problems were found in Band-C where it was difficult to use simple detection algorithms to identify the main target return. As noted above, implementation of more sophisticated detection algorithms appears very practical.

TABLE 7-3

SUMMARY OF PEAK DISTANCE MEASUREMENT ERRORS

<u>BAND</u>	<u>VEC-1</u>	<u>VEC-2</u>	<u>VEC-7</u>
A	± 0.52 cm	± 0.30 cm	± 0.75 cm
B	± 1.05 cm	± 0.67 cm	± 0.52 cm
C	± 1.05 cm	± 0.90 cm	± 0.75 cm
D	± 1.65 cm	± 1.20 cm	± 0.75 cm

NOTES

1. VEC-1 denotes no error correction.
2. VEC-2 denotes vector subtraction.
3. VEC-7 denotes full vector error correction model.
4. Not including anomalies in Band-C and Band-D data.

8.0 CONCLUSIONS

This report and accompanying appendices have reviewed the design, operation, and performance of the MRIS instrument developed during this contract. The information presented demonstrates that a functional model of the MRIS instrument capable of meeting the basic system performance requirements had been completed when the development effort was concluded. The successful operation of this functional model verified the suitability of the system design concepts and specifications recommended during the Preliminary Design Review in 1990 and provided a clear indication that development of a fully compliant engineering model was well underway.

The functional model noted above consisted of a combination of deliverable hardware/software and EMS laboratory equipment. A complete list of the items needed to configure a functional instrument is provided in Table 8-1. The majority of listed items was included in the inventory of equipment that was delivered to NASA LaRC in June 1992. Laboratory-type items that will have to be provided by NASA are marked with an asterisk. General purpose power supplies with adequate current capacity (see GSE users manual for specifications) can be used. However, the EMS-provided software for the GSE computer requires that the specified multimeters and driver control system be used. As noted in the GSE users manual, appropriate software modifications must be made if alternate multimeters or driver control systems are employed.

Although a functional model of the MRIS instrument was configured, several significant development tasks were in progress when the development effort was concluded. In general, efforts at the conclusion of the contract focused on final modifications to (a) electronic hardware associated with the system processor, Mux-Telemetry Board, and power converter and (b) software for the system processor and the Ground Support Equipment computer. An overall status summary of development efforts associated with the T/R Assembly, Detector Assembly, and the Ground Support Equipment is presented in Table 8-2. The information in this table can be used to determine specific tasks to be completed in the event the MRIS development effort is re-initiated.

TABLE 8-1A

HARDWARE NEEDED TO CONFIGURE FUNCTIONAL MRIS TEST SETUP

- o T/R ASSEMBLY
- o DETECTOR ASSEMBLY
- o GSE CONTROLLER CONSISTING OF
 - AST 386/25 COMPUTER WITH 387/25 COPROCESSOR
 - PARADISE VGA VIDEO CARD
 - VGA MONITOR
 - HP82335A GPIB INTERFACE CARD
 - COMPUMOTOR PC21 INDEXER CARD
- o MOUNTING STAND AND FIXTURES
- o STABLE TABLE
- o TARGET/TARGET POSITIONER
- o RAIL/MOTOR DRIVE
- o HP3478A MULTIMETERS (2) *
- o CURRENT LIMITING POWER SUPPLIES (3) *
- o EMS DRIVER CONTROL SYSTEM *

NOTE: Items with an asterisk represent EMS laboratory equipment and were not included in deliverable hardware.

TABLE 8-1B

SOFTWARE NEEDED TO CONFIGURE FUNCTIONAL MRIS TEST SETUP

- o MS-DOS 3.3 (OR HIGHER)
- o ASTSETUP SOFTWARE
- o PC-MATLAB
- o TURBO C++ (OPTIONAL)
- o MRIS TEST SOFTWARE PROGRAM

TABLE 8-2A
T/R ASSEMBLY DEVELOPMENT STATUS

o T/R MODULES (BAND-A, B, C):	COMPLETED
o T/R MODULE (BAND-D):	MIXER FAILURE
o ANTENNAS:	COMPLETED
o IF SUBSYSTEM:	COMPLETED
o MUX-TELEMETRY CIRCUIT BOARD:	PARTIALLY TESTED
o MAIN BRACKET ASSEMBLY:	COMPLETED
o COVER:	DESIGN COMPLETED

TABLE 8-2B
DETECTOR ASSEMBLY DEVELOPMENT STATUS

o IF SUBSYSTEM:	COMPLETED
o BASEBAND CIRCUIT BOARD:	COMPLETED
o POWER CONVERTER BOARD:	TESTED; NOT INSTALLED
o PROCESSOR BOARD:	BREADBOARD COMPLETED
o UPPER/LOWER HOUSINGS:	COMPLETED

TABLE 8-2C
GSE DEVELOPMENT STATUS

o GSE COMPUTER:	COMPLETED
o FLAT-PLATE TARGET/POSITIONER:	COMPLETED
o STABLE TABLE/MOUNTING FIXTURES:	COMPLETED
o AFE/GMT CLOCK:	REQ'S PARTIALLY DEFINED
o CALIBRATION TARGETS:	REQ'S PARTIALLY DEFINED
o GSE SOFTWARE:	PREL. TEST SOFTWARE COMPLETED

9.0 REFERENCES

1. Merrill I. Skolnik, Introduction to Radar Systems, McGraw-Hill Book Company, New York, pp. 68-98, 1980.
2. R. William Kreutel, MRIS Antenna Design: A Status Report, EMS Report on NASA Contract No. NAS1-19063, pp. 26-39, 16 July 1990.
3. HP 8510 Network Analyzer Operating and Programming Manual, Manual Part No. 08510-90005, Hewlett-Packard Company, Santa Rosa, CA, 1984, pp. 69-90, 1984.

APPENDIX A: T/R MODULES

- A1. T/R Module Reports
- A2. Band-D Mixer Summary
- A3. Isocore Coaxial Cable Summary

APPENDIX A1. T/R MODULE REPORTS

Prepared By: brady Sarker
Approved By: M. Dimonetti
Date Prepared: 17 June 91

INTRODUCTION

This report describes initial testing of the Engineering Model Band A T/R Module. The Band A module operates over an output frequency band of 18 to 22 GHz and utilizes WR-42 waveguide at the output port. The preliminary testing reported herein was performed according to a test plan agreed to by EMS and Millitech. This test plan is described in the memo dated 20 February 91 prepared by Joe Seals of EMS. This preliminary testing does not replace the more extensive testing which will be performed at a later date per the complete Acceptance Test Procedure (ATP). ATP be performed when the Engineering Model T/R Modules are returned by EMS to Millitech around September 1991.

Prior to performing the testing on the Band A module as described in this report, the fully assembled module was put through temperature cycling pre-conditioning in a programmable laboratory temperature test chamber. Unit was non-operating during this temperature cycling. Cycling schedule was three complete cycles between -53°C and +140°C with a one-hour soak time at the upper and lower temperature extremes.

A. CHECK OF LO POWER DISTRIBUTION TO THE THREE MIXER LO PORTS.

The LO distribution network of the T/R Modules consists of the WR-28 waveguide components starting from the Gunn oscillator and ending at those three waveguide interfaces which, in normal operation, are connected to the LO ports of each of the three mixers. Figure 1 shows the Band A Block Diagram.

First, we measured the power directly at the 30 GHz Gunn oscillator, before the LO distribution network. In its final configuration, the Band A Gunn had an output power of +16.7 dBm.

When the Band A Gunn oscillator was originally fabricated, it passed an extensive checkout on one of Millitech's standard Gunn fabrication test setups. Later, after the unit was initially integrated into the Band A module, we found a problem of moding of this Gunn oscillator when operated on the module. Moding is a term describing a condition, commonly observed with Gunn oscillators, in which, following the application of DC power, the unit either fails to produce oscillation altogether or produces oscillation at a frequency significantly different from the desired one. This type of behavior is generally load dependent.

We eliminated this moding problem on the Band A Gunn by installing a rectangular piece of Eccosorb MF-124 microwave absorber material .082" x .0925" x .266" bonded into the WR-28 output port of the Gunn. This material was located entirely within the outline of the unit. There was no protrusion of material beyond the waveguide interface port. This retrofit of Eccosorb material into the Gunn resulted in an output power reduction of approximately 2 dB to the final +16.7 dBm level as indicated above.

This modification had only slight effect on the oscillation frequency, and the mechanical tuner on the Gunn oscillator allowed us to adjust out any frequency shift. Test B, described below in this report, verified that, following this modification, the temperature coefficient of frequency drift of the Gunn remained within the specified limit. A similar technique of retrofit of a piece of Eccosorb MF-124 was used on the T/R Module B Gunn oscillator. However, for the Band B Gunn, moding was not a problem. It was necessary only to reduce the output power of the Gunn for optimization of the overall performance of the module.

The measurement of LO power distribution was made using a WR-28 waveguide thermistor mount power sensor and associated power meter. The thermistor mount was placed successively on each of the three ports to be measured. Waveguide terminations, instead of the actual mixers of the T/R Module, were placed on the remaining two WR-28 ports not connected to the power meter. With the actual mixers installed, reflections at the LO ports of each mixer causes some redistribution of the Gunn LO power among the three mixers. Because of the extreme difficulty which would be encountered in performing such a measurement with useful accuracy, we did not attempt to characterize this redistribution of LO power. Table 1 lists the LO distribution power levels. By design, the upconverter mixer receives about 3 dB greater LO power than the two downconverter mixers.

During hardware integration of the Band A module, we found that we could obtain improved flatness in the RF performance of the mixers by improving the LO port match on the mixers. We accomplished this by installing alumina matching chips, bonded with Scotchweld 2216 B/A epoxy, into appropriate locations within the WR-28 waveguide LO ports of the three mixers such that the LO power reflected would be reduced.

Table 1 Band A Gunn LO Power Distribution	
MIXER	LO POWER
Receive Mixer (Test)	+ 10.81 dBm
Reference Mixer	+ 10.91 dBm
Upconverter Mixer	+ 13.91 dBm

B. GUNN OSCILLATOR FREQUENCY VS TEMPERATURE DRIFT WITH GUNN INSTALLED ON COMPLETE MODULE.

Prior to running the test described in this section, a final trimming of the frequency of the 30 GHz Band A Gunn oscillator was performed. At the time of this adjustment, the Gunn was integrated into the complete T/R Module. This final trimming corrects for frequency shifts due to load pulling effects caused by multiple reflections of the Gunn oscillator signal within the LO distribution network.

For this test, the Band A T/R Module was installed in a laboratory temperature chamber. To monitor the Gunn frequency, we used an EIP millimeter wave frequency counter connected directly to the coaxial IF port of the upconverter mixer. The in-place upconverter mixer on the T/R Module serves as the external harmonic mixer for the operation of the millimeter wave frequency counter. The Gunn voltage regulator was in place and operational on the module. Therefore, effects of the Gunn voltage regulator are included in the measurement of frequency versus temperature. During this test, the WR-42 transmit-receive output port of the T/R Module was terminated with a laboratory waveguide termination. In this manner, we could measure with high precision the frequency of the Gunn oscillator over temperature with the Gunn in its exact operating environment.

With the complete Module A assembly placed in the temperature chamber, we measured Gunn oscillator frequency vs. baseplate temperature for a temperature range of -28°C to $+85^{\circ}\text{C}$. Baseplate temperature was measured with a thermocouple whose junction was located directly in contact with the mounting plate of the T/R Module, and in the vicinity of the Gunn oscillator. Figure 2 is a plot of measured data.

As indicated in Figure 2, the Gunn Oscillator frequency at 17.5°C is 29.997 GHz, and the temperature drift coefficient is approximately $-0.73\text{ MHz}/^{\circ}\text{C}$ over the operating range of -20°C to $+70^{\circ}\text{C}$. The Equipment Specification requires the frequency of the Gunn oscillator to be $30.000 \pm .020\text{ GHz}$ at a baseplate temperature of 17.5°C . Maximum allowable drift is $0.75\text{ MHz}/^{\circ}\text{C}$. This test verifies that the unit meets these requirements.

C. CHECK OF TRANSMIT RF OUTPUT POWER LEVEL ACROSS BAND.

For this test, as well as for the testing in Sections D and E of this report, we set up the sweep generator to deliver IF Modulation Input signal at the levels of +13 dBm, +14 dBm, and +15 dBm, as required, over the 8 to 12 GHz IF frequency band. Plots of power levels versus frequency for the resulting 8 to 12 GHz swept Modulation Input signal obtained from the sweep generator, as well as plots for the 18 to 22 GHz RF output and for both 8 to 12 GHz IF outputs, were obtained using a calibrated HP Model 8592B microwave spectrum analyzer operating in its "max hold" mode. This method of using repetitive scans in "max hold" produces output similar to what would be produced with a tracking generator in place of the free-running sweep generator. All of the described signals are within the direct, pre-selected input frequency band of the microwave spectrum analyzer. Generally, we did not utilize power meters for these measuring the power levels of these signals.

For each measurement, the power versus frequency display of the spectrum analyzer was recorded on a digital plotter. Figure 3 shows the amplitude of the swept IF Modulation Input signal. This plot indicates a small degree of slope in the amplitude of the output of our sweeper over the 8 to 12 GHz band. Modulation Input power decreases slightly at the high end of this band. The variation displayed in the plot of Figure 3 should be used to normalize the swept output signals in the plots of the RF Transmit Output, and the Reference and Test IF outputs of the T/R Module. Direct dB for dB normalization is applicable since, for the Band A module, the upconverter mixer operates in its linear range.

Note that, because the Band A module, upconversion uses the lower sideband of the upconverter mixer. Therefore, for a given upward frequency sweep of RF Transmit output frequency over the 18 to 22 GHz band, the corresponding IF frequency sweeps downward. In effect, frequencies are determined by $IF = 30 \text{ GHz} - RF$. This must be accounted for in comparison between RF and IF responses.

Note that the +13 to +15 dBm range which we selected for Modulation Input power levels in this testing of the Band A Module spans a 2 dB total range of power, consistent with the present revision of the Equipment Specification. However these levels are not consistent with the +14 to +16 dBm range indicated in the present revision of the Equipment Specification. In our comprehensive evaluation of the Band A T/R Module, we found that overall performance is optimized for this +13 to +15 dBm range of Modulation Input.

The issue has not yet been resolved on how to eliminate this discrepancy in Modulation Input power levels. One option is to revise the Equipment Specification to reflect these lower input power levels. The other option is to change the configuration of the Band A T/R Module to include a 1 dB coaxial attenuator to provide this reduced input power level to the upconverter mixer while retaining the original +14 to +16 dBm level at the Modulation Input interface of module.

Using the test setup shown in Figure 4, we measured the swept response of the RF transmit output power versus RF output frequency over the specified 18 to 22 GHz band for the three fixed modulation input power levels of +13 dBm, +14 dBm, and +15 dBm. Figure 5 contains plots of the three power output sweeps.

D. CHECK OF REFERENCE IF OUTPUT POWER LEVEL ACROSS BAND **ALSO**

E. CHECK OF TEST IF OUTPUT SENSITIVITY TO RF INPUT POWER.

We used the same microwave spectrum analyzer for measurement of power level versus frequency at both the Reference IF Output and at the Test IF Output ports. A block diagram of this test setup is shown in Figure 4. IF Modulation Input power levels were set, sequentially, to the values of +13 dBm, +14 dBm and +15 dBm and swept over the IF frequency band. The swept response of the Reference IF output is shown in Figure 6 for the case where the WR-42 waveguide output/input port of the T/R Module is shorted, while Figure 7 shows the swept response for the case with the waveguide output/input port terminated with a laboratory waveguide termination.

Swept response of the Test IF output is shown in Figure 8. This plot includes both conditions when the WR-42 waveguide output/input T/R port is shorted and terminated, and for the three values of IF modulation input power. The level of Test IF output signal obtained when the T/R port is terminated determines the isolation between the IF Modulation Input signal and the Test IF output port. This performance parameter is discussed in more detail in Section I.

F. CHECK OF REFERENCE IF AND TEST IF OUTPUT SPECTRUM.

We did a general search for spurious output signals across the entire 8 to 12 GHz output frequency band. As predicted the only significant spurious occurs around 10.0 GHz input frequency. This spurious occurs at a frequency of two times the Modulation Input frequency. We found that the spur level varied between -28 dBc and -35 dBc at the Test IF Output and between -25 dBc and -35 dBc on the Reference IF Output. See Figure 9. We also took a close look around 10.0 GHz where the spur crosses the carrier signal as the Modulation Input frequency is swept. We found that, at the crossover point, the spur level is approximately -30 dBc on the Test IF output, as shown in Figure 10, and the spur level is around -28 dBc on the Reference IF output, as shown in Figure 11.

G. CHECK OF BAND A TEST IF OUTPUT POWER LEVEL ACROSS BAND.

This is a measurement of the Test IF output power for the condition where a waveguide short is placed on the RF Transmit/Receive WR-42 waveguide output/input port. Swept response data was presented in Figure 8. This response is to be compared with the RF Transmit Output shown in Figure 5. This indicates approximately 16 dB conversion loss for the Test IF channel. This meets the Equipment Specification requirement of 19.5 dB max., and the variation across the band is within ± 2.0 dB, also within the requirements of the Equipment Specification.

H. MEASURE SPECTRUM OF TRANSMIT RF OUTPUT.

Test deleted. This performance characteristic is effectively covered in Section F, evaluation of IF output spectrum.

I. ISOLATION, IF MODULATION INPUT TO TEST IF OUTPUT PORT.

With the WR-42 RF Transmit/Receive waveguide output/input port terminated with a laboratory grade waveguide termination, the residual signal at the IF Test output was measured using a spectrum analyzer. Results are shown in Figure 8 where data is plotted on the same plot as the results of Section E, Test IF Output versus frequency with a waveguide short, instead of a termination, placed on the WR-42 waveguide output/input port. This plot shows worst case isolation of approximately 22 dB. This is consistent with the -35 dBm maximum signal out of the Test IF Output port as called for in the Equipment Specification.

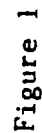
WEIGHT

This Band A Module Engineering Model was weighed in its fully assembled configuration. The actual weight was 62.6 oz (1.78 Kg). This is below the 64 oz. maximum allowable weight indicated in the Equipment Specification.

MECHANICAL ALIGNMENT PER ICD

The critical positioning of the WR-42 RF Transmit/Receive waveguide port interface of the Band A module was accomplished using a "Microhite" precision measuring system. For most dimensions, we were able to achieve positioning within the tolerances specified in the ICD. Figures 12 and 13 are the two sheets of the EMS ICD, Drawing No. PR145213, for the Band A module. We include on these figures our handwritten markups indicating actual measurements of the respective dimensions as we were able to, on a best effort basis, align the module at this time.

We plan to align the module once again when it is returned to Millitech for full acceptance testing. At that time, we will have available a set of custom alignment fixtures which we have designed, but not yet fabricated, for this task. These fixtures will allow more accurate positioning of the interfaces with respect to the mounting structure of the module.



MODULE A INTEGRATION 7 JUNE 91

GUNN OSCILLATOR FREQUENCY VS. TEMPERATURE, MODULE FULLY ASSEMBLED, INCLUDING REGULATOR

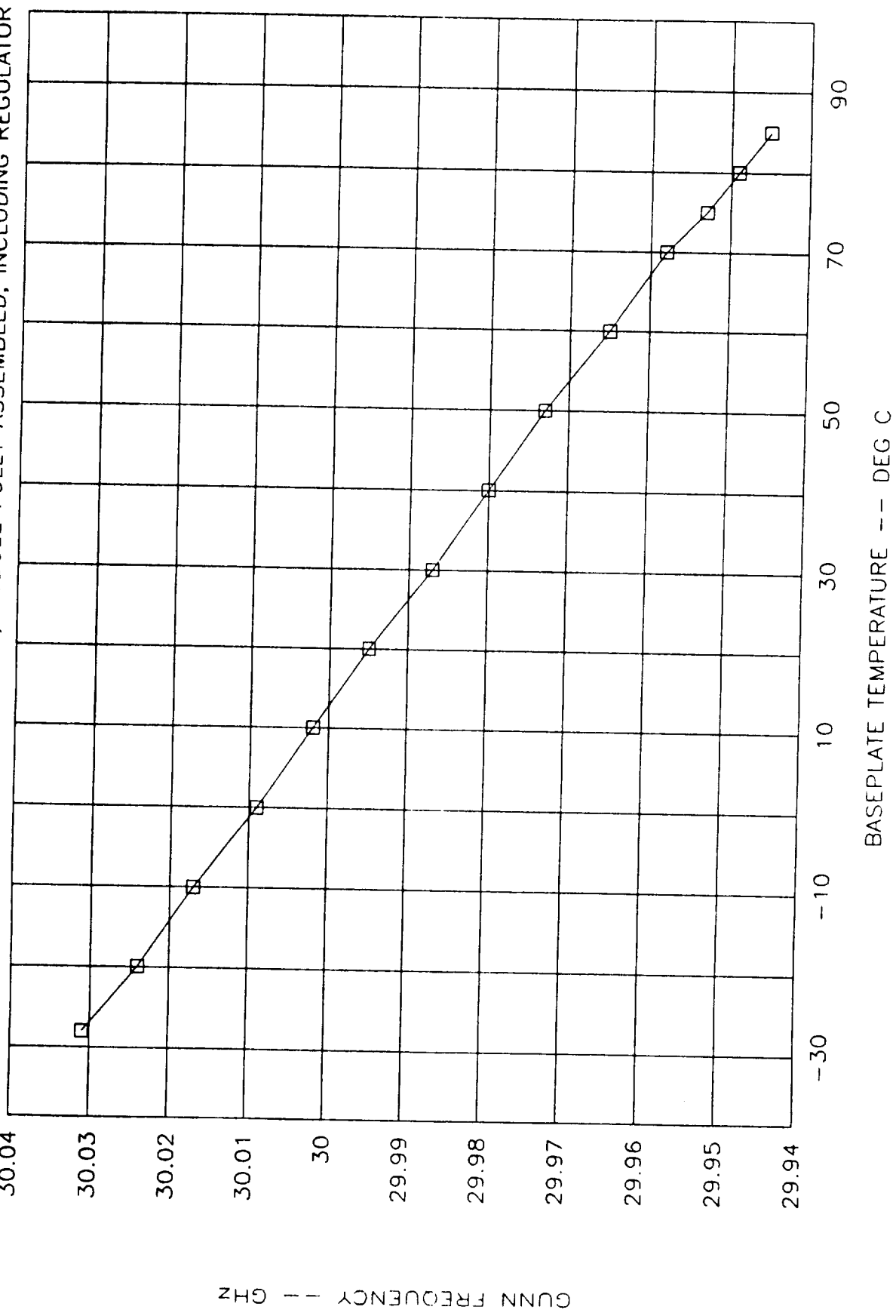


Figure 2

15:57:18 JUN 10, 1991 MODULE A - IF MODULATION INPUT

REF 20.0 dBm ATTEN 30 dB SWEEP SET TO +10.1, +15.1, +14.1

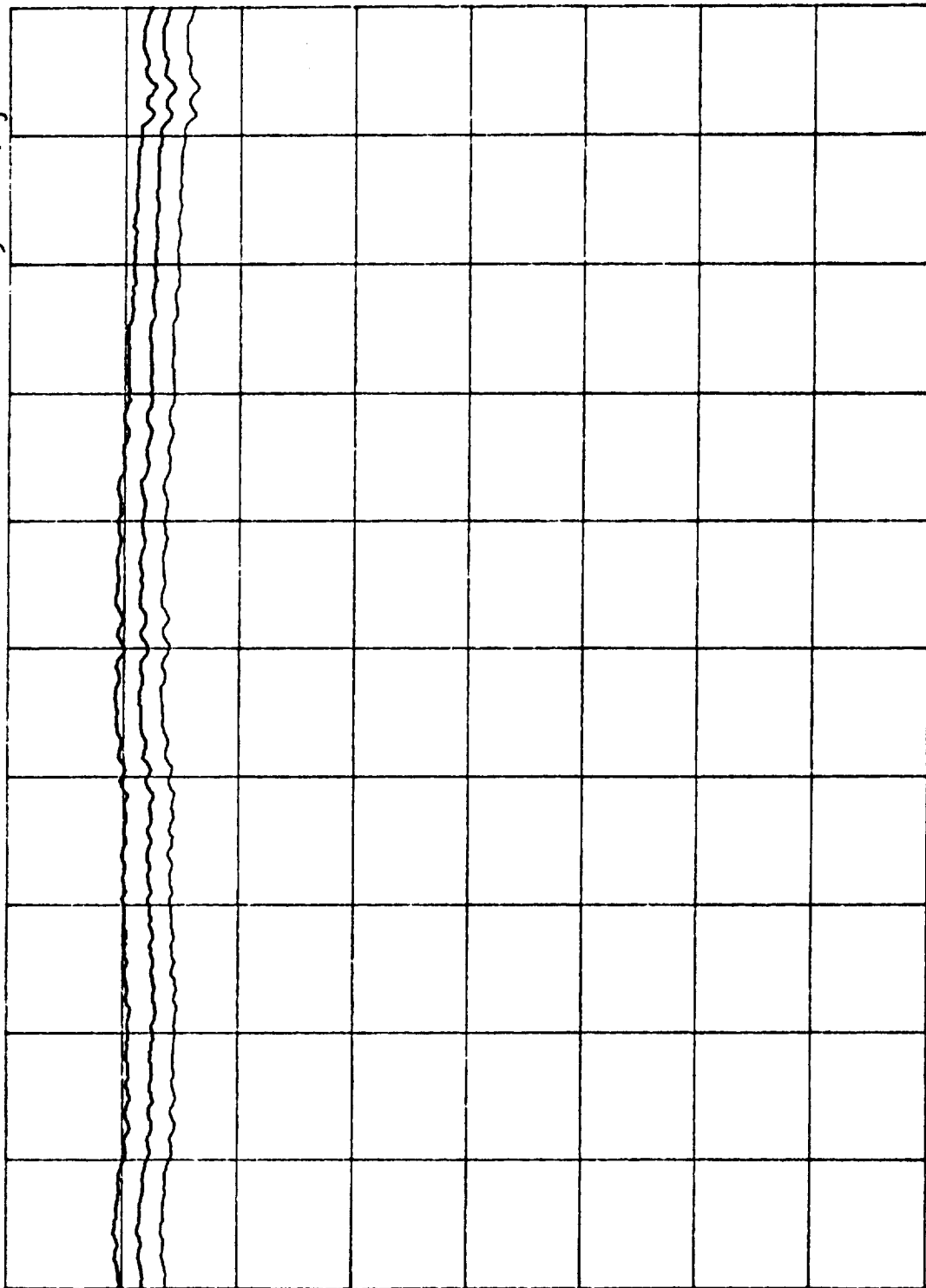
PEAK

LOG

5

dB/

+15 dBm
+14 dBm
+13 dBm

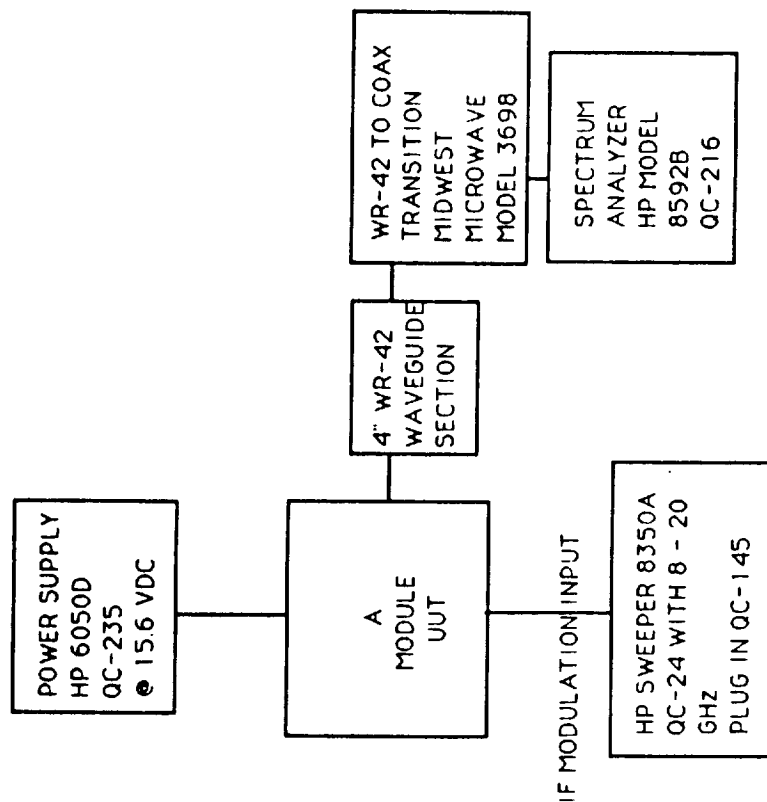


VA MB
SC FC
CORR

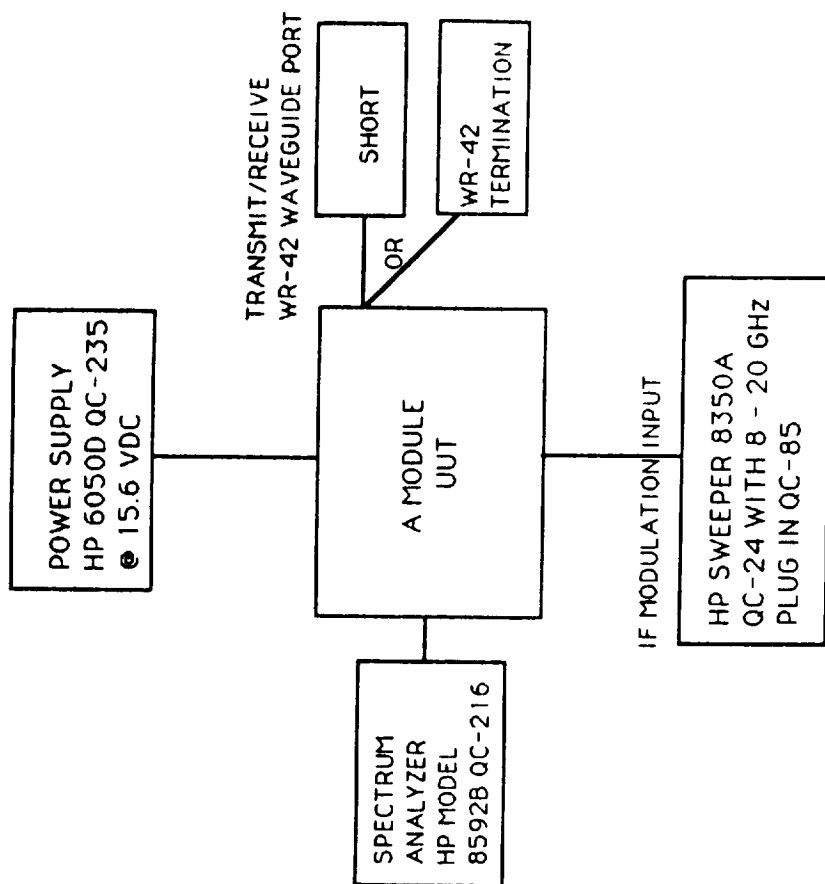
START 8.000 GHZ
RES BW 3 MHz

STOP 12.000 GHZ
VBW 1 MHz
SWP 80 msec

Figure 3



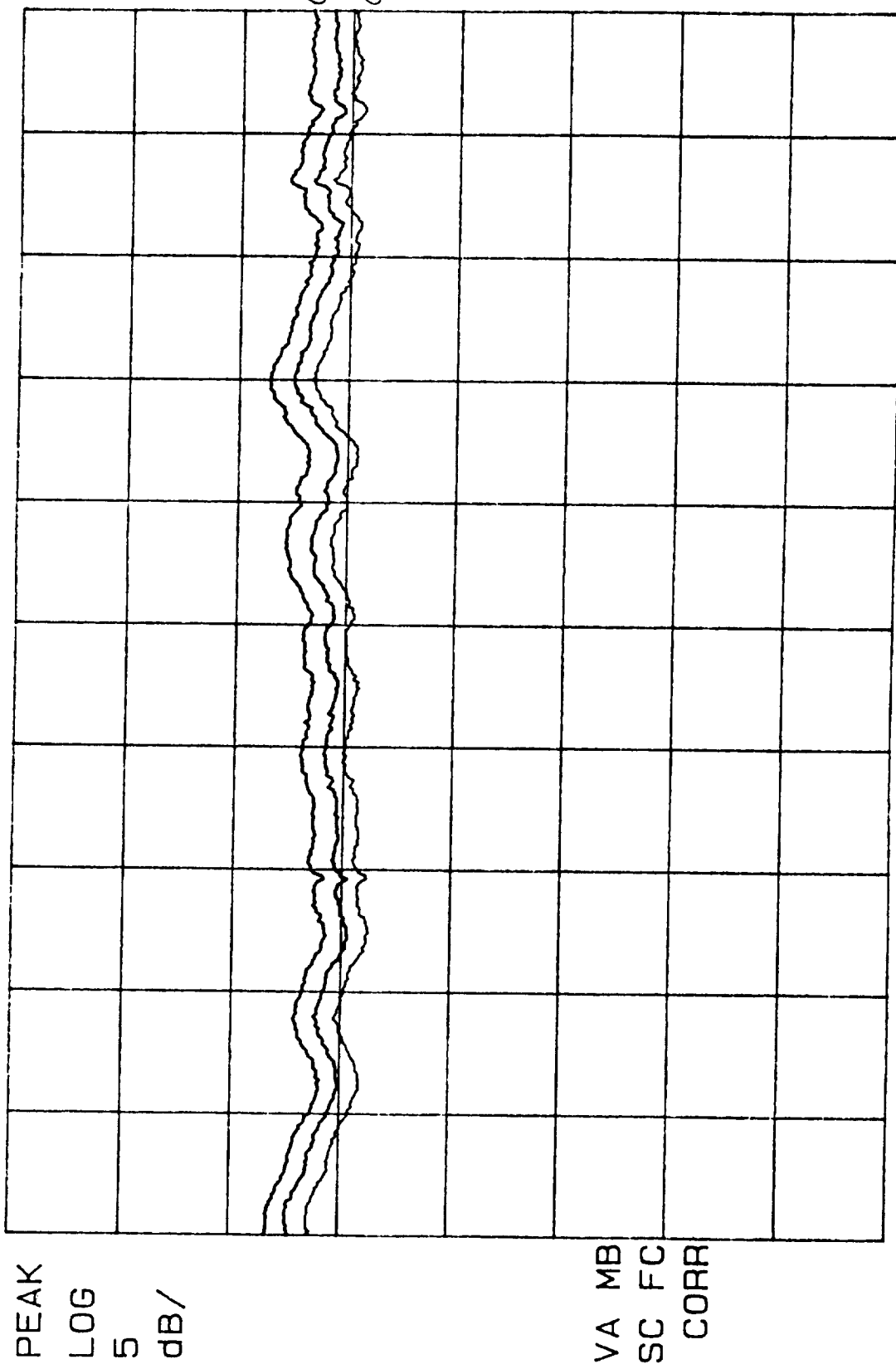
TRANSMIT RF OUTPUT TEST SET-UP



REFERENCE IF AND TEST IF OUTPUT TEST SET-UP

FIGURE 4

16:07:53 JUN 10, 1991 MODULE A - RF TRANSMIT OUTPUT
 REF .0 dBm WITH VARYING IF MODULATION INPUT POWER LEVEL
 ATTEN 10 dB



-13.13m WPM
 -14.13m WPM
 -13.13m WPM

VA MB
 SC FC
 CORR

START 18.000 GHZ STOP 22.000 GHZ
 RES BW 3 MHz SWP 80 msec

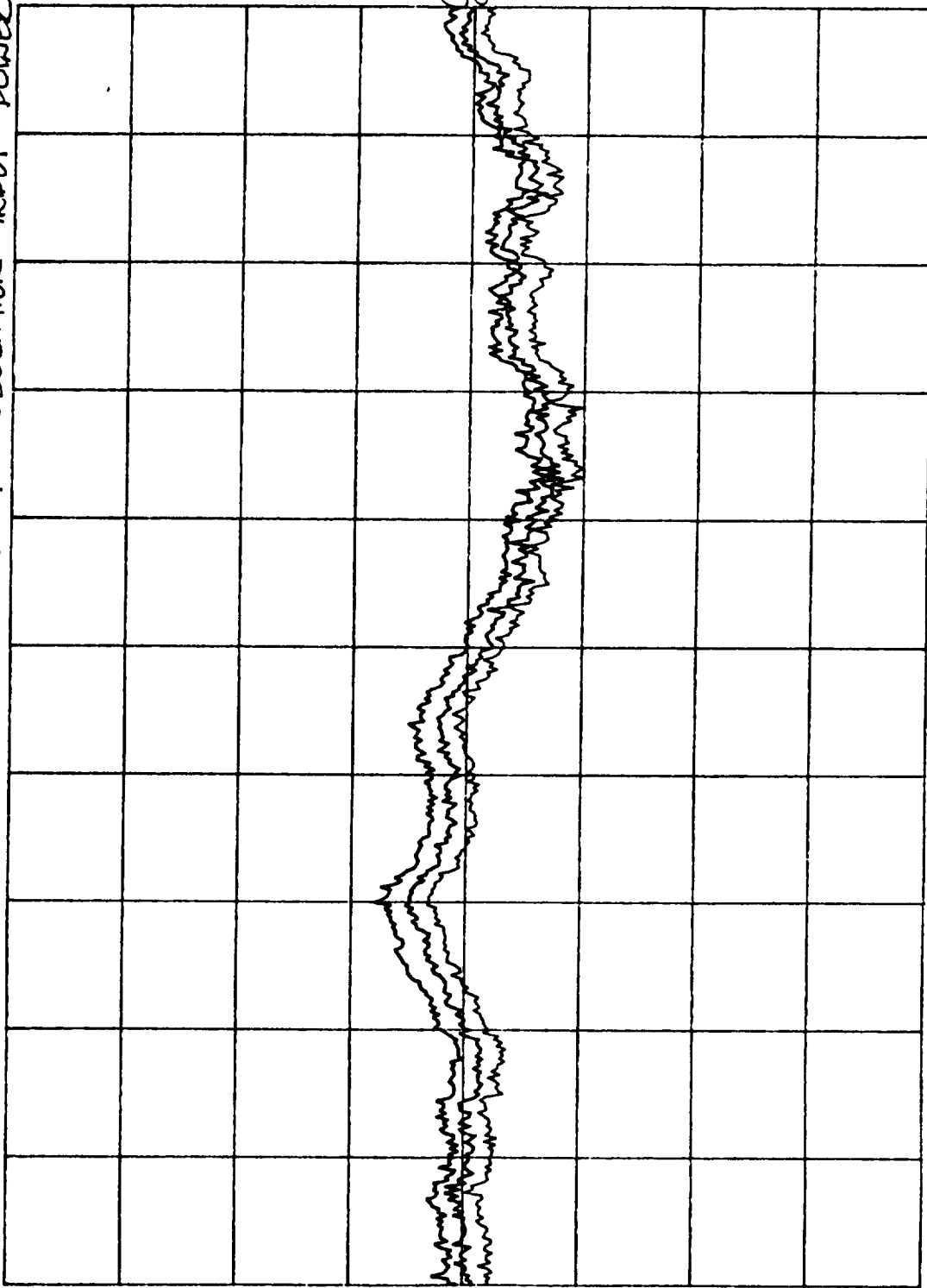
Figure 5

16:21:36 JUN 10, 1991 MODULE A - REFERENCE OUTPUT

WITH A SHORT ON T/R PORT

REF -20.0 dBm ATTEN 10 dB FOR VARYING IF MODULATION INPUT POWER LEVELS

PEAK
LOG
5
dB/



VA MB
SC FC
CORR

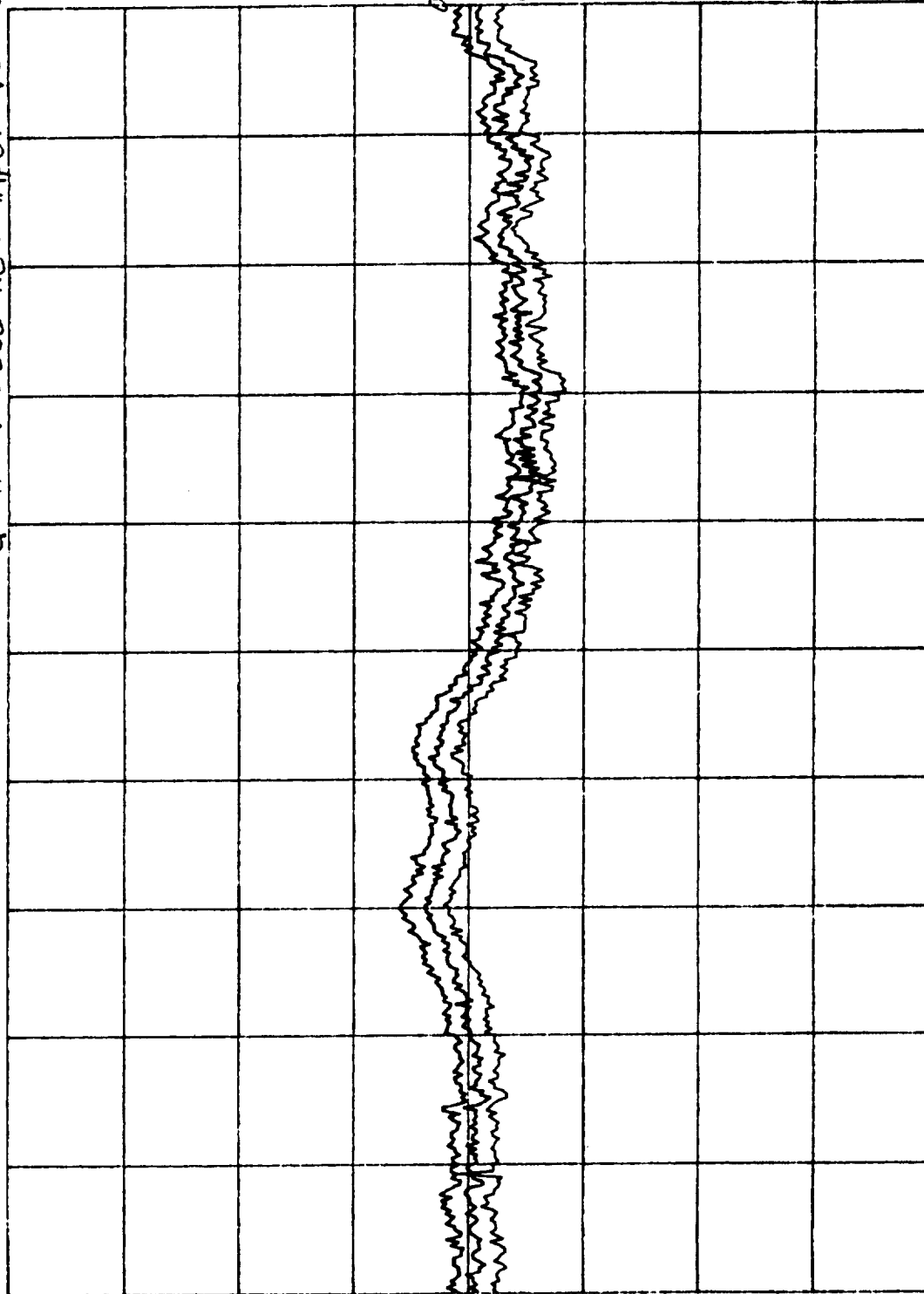
START 8.000 GHz STOP 12.000 GHz
RES BW 3 MHz SWP 80 msec
VBW 1 MHz

Figure 6

16:36:24 JUN 10, 1991 MODULE A - REFERENCE OUTPUT
WITH A TERMINATION ON THE PORT

REF -20.0 dBm ATTEN 10 dB FOR VARYING IF MODULATION INPUT POWER LEVELS

PEAK
LOG
5
dB/



VA MB
SC FC
CORR

START 8.000 GHZ STOP 12.000 GHZ
RES BW 3 MHZ VBW 1 MHZ SWP 80 msec

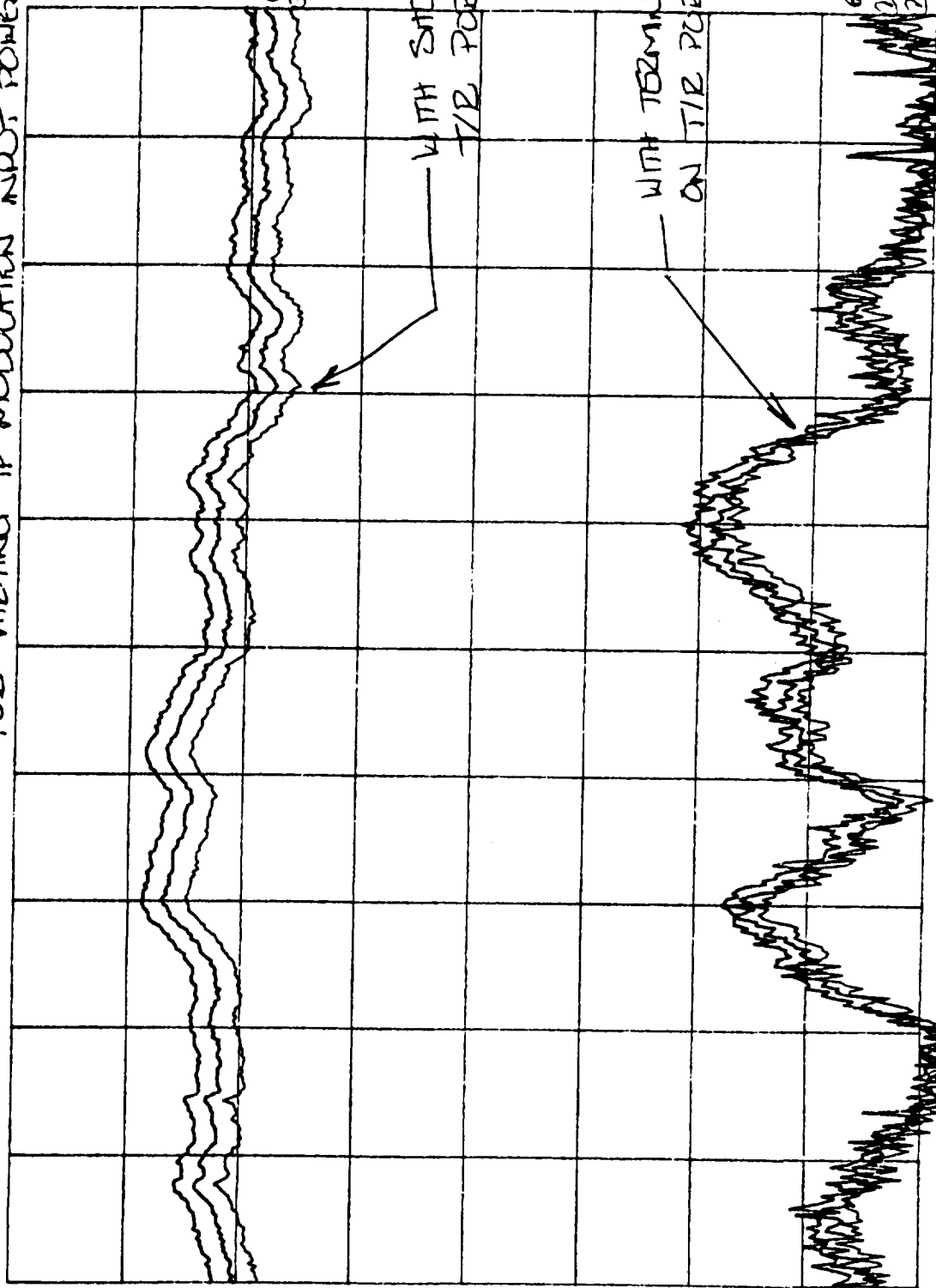
Figure 7

16: 47: 10 JUN 10, 1991 MODULE A - TEST OUTPUT

WITH SHORT & TERMINATION ON T/R PORT

REF -20.0 dBm ATTEN 10 dB FOR VARYING IF MODULATION INPUT POWER LEVELS

PEAK
LOG
5
dB/



VA MB
SC FC
CORR

START 8.000 GHz
#RES BW 1 MHz
STOP 12.000 GHz
VBW 300 KHZ
SWP 80 msec

Figure 8

MODULE A INTEGRATION 11 JUNE 91

SPUR LEVELS VS. FREQUENCY, IF MODULATION INPUT = +14 dBm

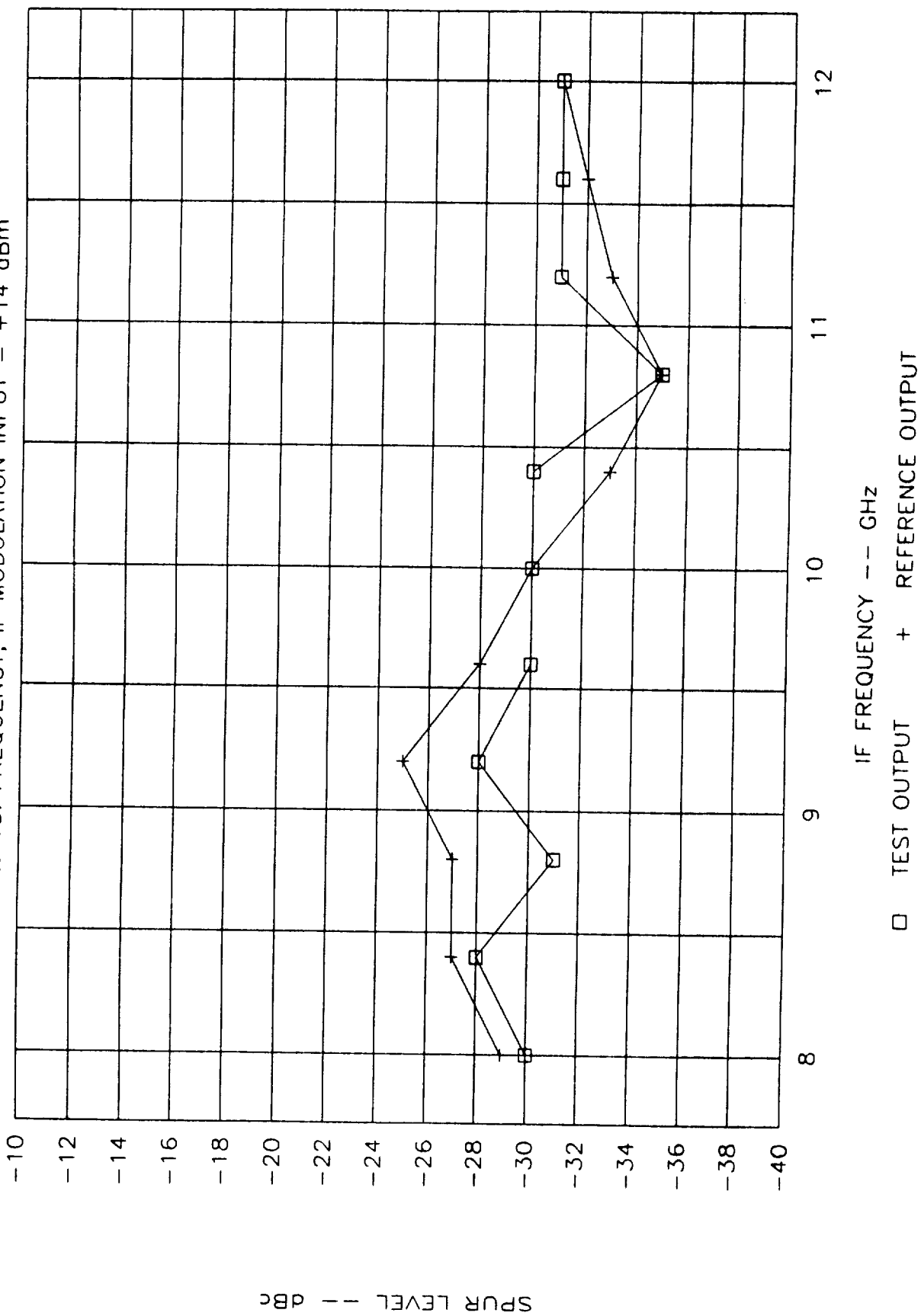
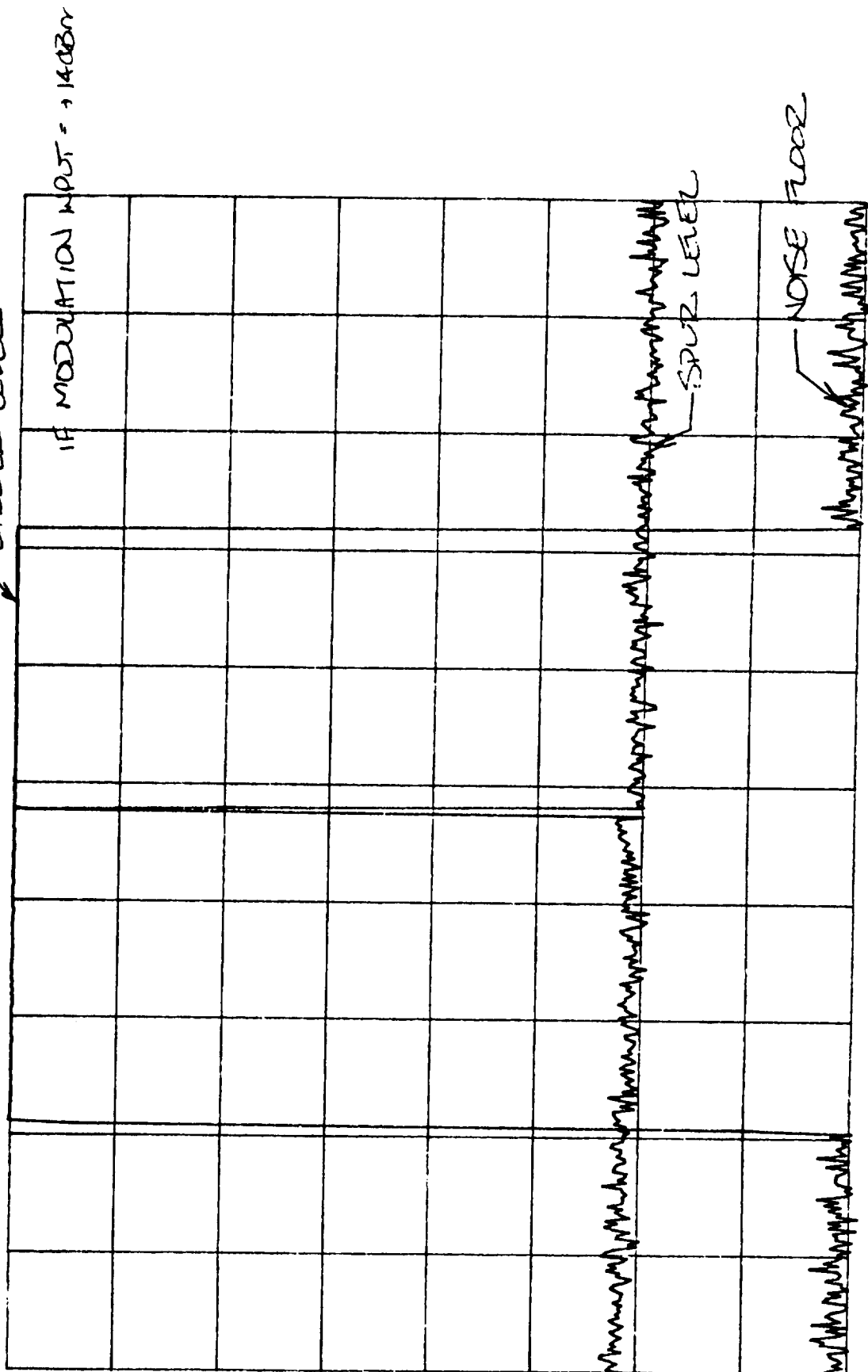


Figure 9

11:12:22 JUN 11, 1991 MODULE A - SPURIOUS ANALYSIS

REF -29.5 dBm ATTEN 10 dB TEST START PORT WITH SHORT ON THE PORT
← CARRIER LEVEL

PEAK
LOG
5
dB/



MA SB
SC FC
CORR

CENTER 10.0000 GHz
#RES BW 100 KHz

VBW 30 KHz

SPAN 100.0 MHz
SWP 100 msec

Figure 10

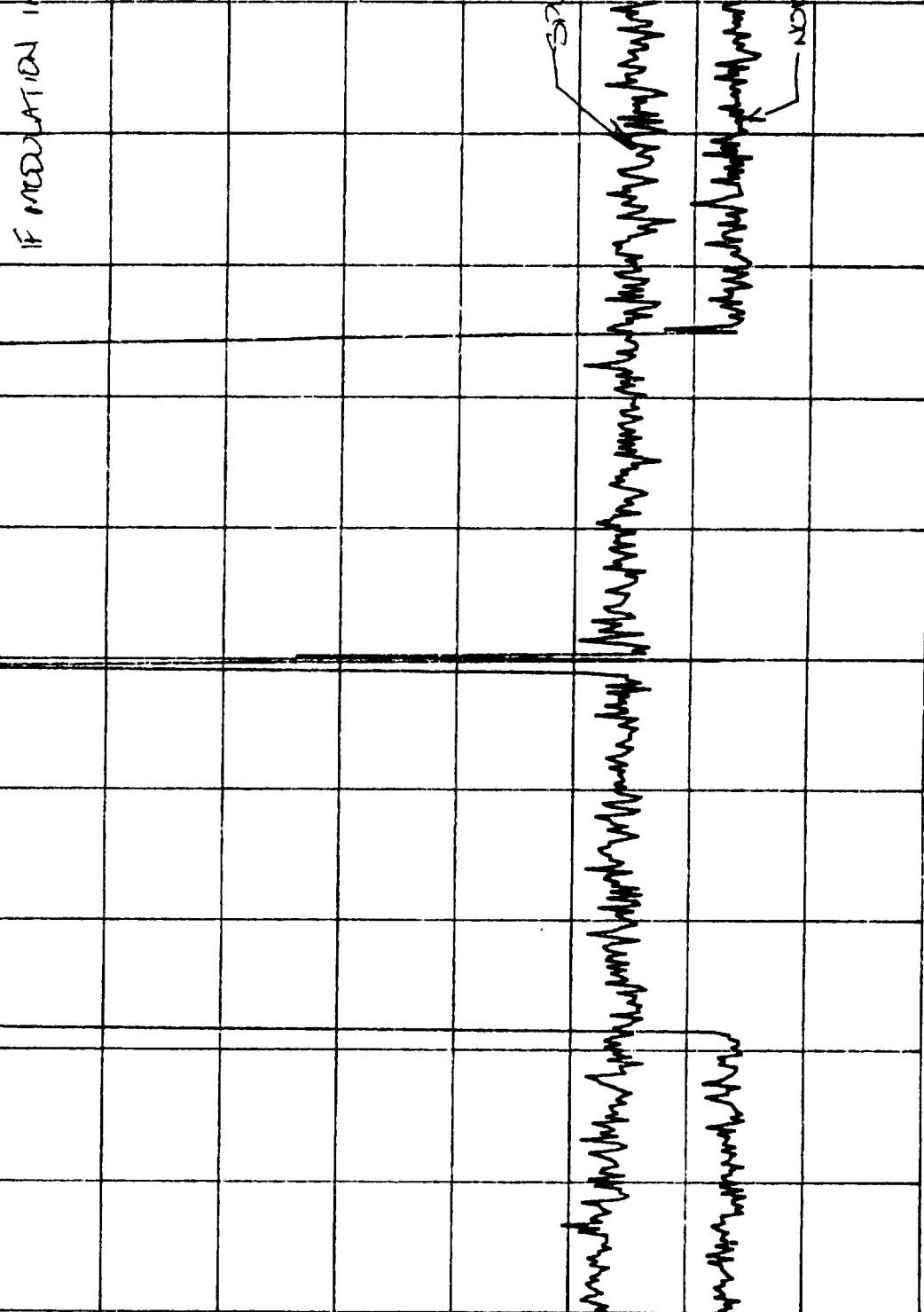
14:56:39 JUN 07, 1991 MODULE A - SPECTRUM ANALYSIS

REFERENCE OUTPUT PORT WITH SHIELD ON T/R PORT

REF -42.0 dBm ATTEN 10 dB

CARRIER LEVEL

PEAK
LOG
5
dB/



DL
-67.0
dBm

MA SB
SC FC
CORR

CENTER 10.0000 GHz

#RES BW 30 KHZ

SPAN 100.0 MHz

VBW 30 KHZ

SWP 333 msec

Figure 11

Prepared By: Betsy Scuderi

Approved By: M. J. Smith

Date Prepared: 29 April 91

INTRODUCTION

This test report incorporates the preliminary tests agreed to by EMS and Millitech as described in the memo dated 20 February 91 written by Joe Seals of EMS. This testing does not replace the complete Acceptance Test Procedure (ATP) which will be performed when the Engineering Model T/R Modules are returned to Millitech in September 1991.

A. CHECK OF LO POWER DISTRIBUTION TO THE THREE MIXER LO PORTS.

The LO distribution network on the T/R Modules consists of all components and waveguide sections from the Gunn oscillator to the three waveguide ports which are to be later connected to the LO ports of the three mixers. See Block Diagram attached. The Gunn oscillator output power initially measured was +23 dBm. This was the power level which we originally estimated would be necessary to drive all three mixers, the upconverter mixer and two downconverters. This was based upon an originally estimated LO power requirement of about +13 dBm for mixers operated as downconverters. However, performance data taken on 11 JAN 91 on the three actual mixers designed and fabricated for the Band B module indicated that when the mixer is used in the downconverter mode, their performance is optimized for LO input power in the range of +6 to +7 dBm. It was also found that the spurious performance of the mixer operated as the upconverter on the Band B module improved with the reduced LO power level.

In order to provide local oscillator power at levels closer to what our evaluation of the Band B mixers determined was optimum for these mixers, we reduced the Gunn oscillator power level from its initial +23 dBm level to +11.3 dBm. This was accomplished by inserting three small rectangular pieces of Eccosorb MF-124 into the WR-28 waveguide portion of the Gunn oscillator. The Eccosorb did not extend outside of the unit beyond the face of the waveguide flange. The size of these pieces of Eccosorb necessary to produce the desired power reduction was determined through experimentation. We bonded the Eccosorb MF-124 in place using Scotchweld 2216 B/A epoxy and cured the assembly at 90°C for approximately 1 hour. Frequency set-point and drift of frequency with temperature were checked on the Gunn oscillator following this modification. These characteristics displayed little change following the addition of the Eccosorb.

The measurements of LO power distribution were made directly with a waveguide power meter placed successively on each of the three ports to be measured, and with waveguide terminations in place of the actual mixers on the remaining two ports not being measured. With the actual mixers installed, the reflections at the LO port of each mixer causes some redistribution of LO power among the three mixers. We did not attempt to characterize this redistribution of LO power.

Table 1 shows the results of the measurement of LO power distribution to the three mixer LO ports, as determined with waveguide terminations in place of the mixers.

Table 1 Band B Gunn Power Distribution	
MIXER	LO POWER
Receive Mixer (Test)	+ 6.3 dBm
Reference Mixer	+ 6.7 dBm
Upconverter Mixer	+ 9.0 dBm

B. CHECK/ADJUST GUNN OSCILLATOR FREQUENCY WHEN GUNN OSCILLATOR IS INSTALLED ON COMPLETE MODULE

A final setting of the Gunn oscillator frequency was performed after the Gunn was integrated into the complete T/R Module. This final check in this configuration is necessary to account for effects of multiple reflections of the Gunn oscillator signal within the LO distribution network. To monitor the Gunn frequency, we used an EIP millimeter wave frequency counter connected directly to the IF coaxial output port of the upconverter mixer. Waveguide terminations were placed on the transmit and receive ports of the T/R Module. In this convenient manner, we measured the frequency of the Gunn oscillator with the Gunn in its precise operating environment. This requires only a single coaxial cable connected between the upconverter mixer and the EIP frequency counter which was located external to the temperature chamber.

The Equipment Specification specifies the nominal frequency of the Gunn at a baseplate temperature of 17°C. It is most convenient to adjust the frequency with the unit out on the bench at room ambient temperature. Previously, the Gunn oscillator was characterized in detail at the component level both pre- and post-vibration (See data taken 31 Jan 91 and 6 Feb 91). From this data it was determined that the frequency change with temperature for this Gunn is approx. -1.0 MHz/°C. Using the miniature precision screw tuner assembly on the Module B Gunn oscillator, the frequency was adjusted to 33.994 GHz while the baseplate temperature was 23°C so that at 17°C the frequency would be a nominal 34.000 GHz per the equipment specification.

Following this tuning of the Gunn oscillator frequency, the entire Module B assembly was then placed into the temperature chamber and the Gunn oscillator frequency vs. baseplate temperature data was taken for a temperature range of -30°C to +75°C. See Figure 1.

C. CHECK OF TRANSMIT RF OUTPUT POWER LEVEL ACROSS BAND

For measurement of RF transmit output power on the T/R Module, we set up the sweep generator to deliver IF modulation input power at the levels of +9 dBm, +10 dBm, and +11 dBm at 0.5 GHz frequency increments over the 8 to 12 GHz IF frequency band. An HP coaxial power meter was used for this setup of modulation input power. We saved these settings on the HP sweeper using its built-in store settings capability. Note that these three power levels which we selected for final testing of the Band B Module span a ± 1 dB range of power, as is shown in the Equipment Specification, but are otherwise lower than the +14 to +16 dBm range indicated in the specification. As a part of our comprehensive evaluation of the T/R Module during integration testing, we found that overall performance is optimized for this +9 to +11 dBm input power range. The issue has not yet been resolved whether to change the Equipment Specification to reflect this reduced input power level range, or to change the configuration of the Band B T/R Module to include a coaxial attenuator to provide this reduced effective input power level while maintaining the +14 to +16 dBm level at the Modulation Input interface connector of module.

Using the test setup shown in Figure 2, RF transmit output power vs. RF output frequency data was taken for the three fixed modulation input power levels of +9 dBm, +10 dBm, and +11 dBm. See Figure 3.

When the IF power is turned off and the LO power is left on, we should see, per the Equipment Specification, an LO leakage below -20 dBc. We found however, that the power level indicated on our power meter, calibrated for measurements over the WR-19 band (40 to 60 GHz) only, was significantly higher, approximately -15 dBc. We then added a lab WR-19 low-pass filter at the output. The filter passes below 61 GHz and rejects all higher frequencies. The measured output power indication then went under range on the meter. We concluded from this that the spurious out of the transmit port is at a frequency of 2 times the LO (68 GHz). It is generated in the upconverter mixer and is an out-of-band spurious signal. A possible change in the design of this T/R Module consisting of adding a low pass waveguide filter before the transmit output port would effectively eliminate this 2 times LO spurious output.

- D. CHECK OF REFERENCE IF OUTPUT POWER LEVEL ACROSS BAND AND ALSO
- E. CHECK OF TEST IF OUTPUT SENSITIVITY TO RF INPUT POWER.

We used an HP Model 8592B microwave spectrum analyzer for measurement of power level versus frequency at both the Reference IF Output and at the Test IF

Output. IF Modulation Input power levels were accurately controlled to the precise value of +10 dBm over the IF frequency band. To measure the Test IF Output response, a custom WR-19 waveguide test loop and a Hughes WR-19 precision variable attenuator were installed to provide a direct, controlled path to direct the RF transmit output power into the receive waveguide port. For the data shown in Figure 4 the variable attenuator was set to 20 dB. In addition to this attenuation, there is an estimated 1.0 dB insertion loss of the custom WR-19 waveguide loop section.

F. CHECK OF REFERENCE IF AND TEST IF OUTPUT SPECTRUM.

While we did a general search for spurious output signals across the entire 8 to 12 GHz output frequency band, spurious levels were carefully characterized around predicted problem frequencies of 8.50 GHz and 11.33 GHz. The spur at 8.50 GHz was found to be approximately -28 dBc from the carrier and therefore not a problem. The level of the spur at 11.33, on the other hand, was found to vary significantly with frequency. Figures 5 and 6 show spur level vs. frequency for an IF modulation input of +10 dBm. It was found that at the frequency at which the spur crosses the carrier the upper and lower side band are -27 dBc and -22 dBc respectively. The final nominal power level selected for the Modulation Input signal, and the final +11.3 dBm power level set on the Gunn oscillator, were determined during the process of obtaining acceptable spurious levels while maintaining other performance parameters

G. CHECK OF BAND A TEST IF OUTPUT POWER LEVEL ACROSS BAND

This test is only applicable to the Band A T/R Module.

H. MEASURE SPECTRUM OF TRANSMIT RF OUTPUT.

Deleted. This performance characteristic is covered in F, evaluation of IF output spectrum.

I. CHECK ISOLATION OF IF MODULATION INPUT TO TEST IF OUTPUT PORT.

With the transmit output and receive input waveguide ports terminated to prevent direct coupling of the RF transmit output signal into the RF receive port, the IF test output signal level was measured using a spectrum analyzer. The results are shown in Table 2. The measured power at the carrier frequency represents a leakage signal. Note that in the design of the T/R Modules, we made a tradeoff of transmit signal-to-Test IF output leakage performance for symmetry in the LO distribution network to the Reference and Test mixers. One bandpass filter in each of the two LO distribution waveguides were selected, therefore. While this approach insures a high degree of symmetry, the E-plane bandpass filters have limited rejection for frequencies far above the pass band. Improved isolation could have been obtained through an approach which uses a high-pass waveguide filter in one arm and a low-pass waveguide filter in the other, but this approach lacks the channel-to-channel symmetry offered by the pair of E plane bandpass filters.

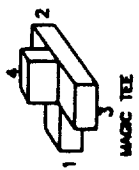
Table 2 Isolation, Modulation Input to Test IF Out	
IF FREQUENCY GHz @ +12 dBm MODULATION INPUT	TEST IF OUTPUT SIGNAL LEVEL dBm (LEAKAGE)
8	-85
8.5	-75
9	-67
9.5	-71
10	-90
10.5	-90
11	-85
11.5	-81
12	-87

WEIGHT

The B Module was weighed in its final configuration. It was found to be within the 50 oz. maximum required by the equipment specification. The actual weight was 45 oz.

MECHANICAL ALIGNMENT PER ICD

The mechanical alignment was performed using a "Microhite" to locate the transmit and receive ports of the module in the position and tolerance as specified in the ICD. We were able to achieve the required position within a tolerance of $\pm .002$ " in most cases, whereas the tolerance presently specified in the ICD is $\pm .001$ ". We plan to align these modules again when they are returned to Millitech for final testing. At that time we plan to have alignment fixtures available for more accurate positioning.



BAND B T/R MODULE, GUNN OSC CHECK

FULLY ASSEMBLED MODULE EXC. VOLTAGE REG, GUNN=11.00V, 2-3 MAR 91

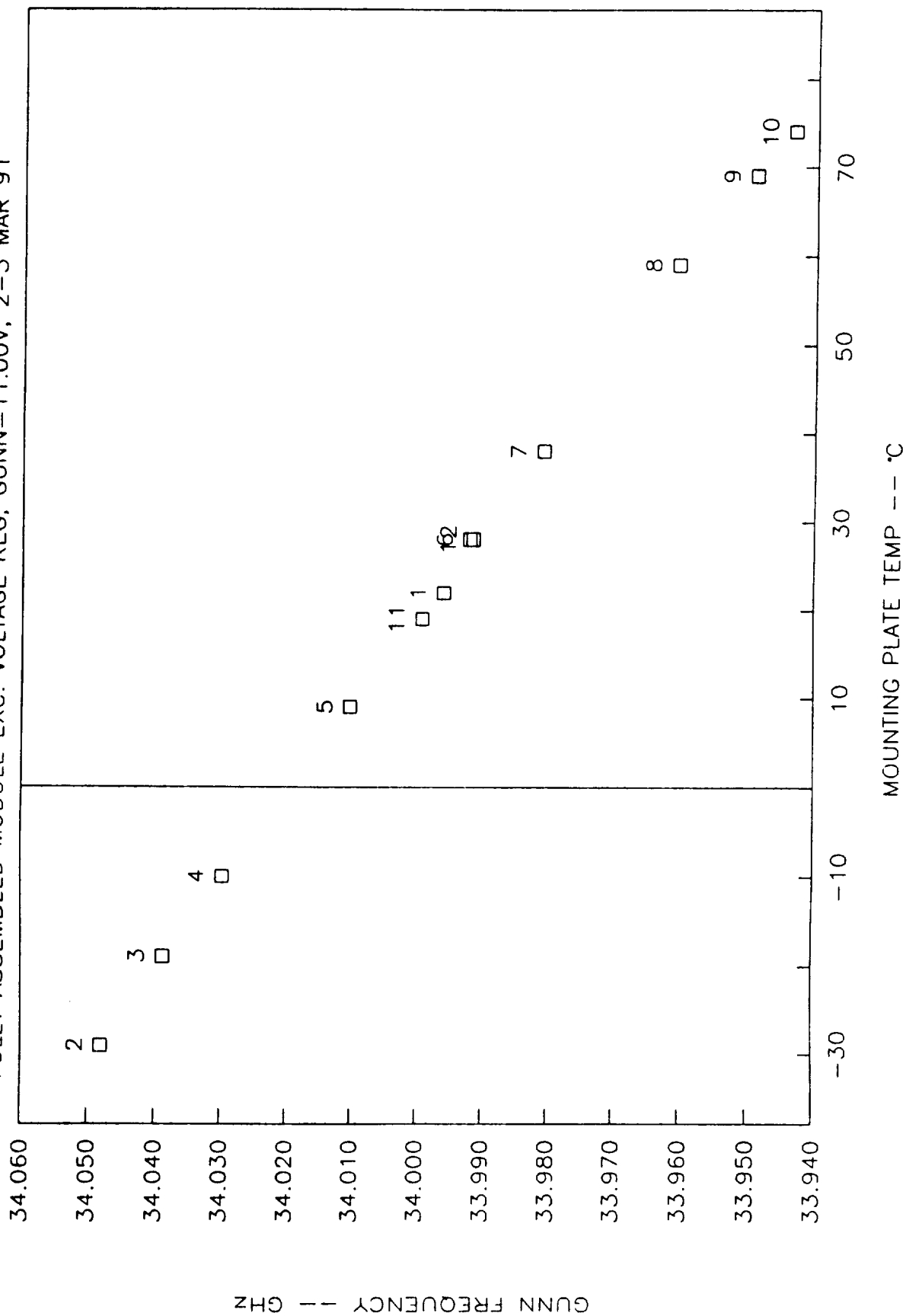
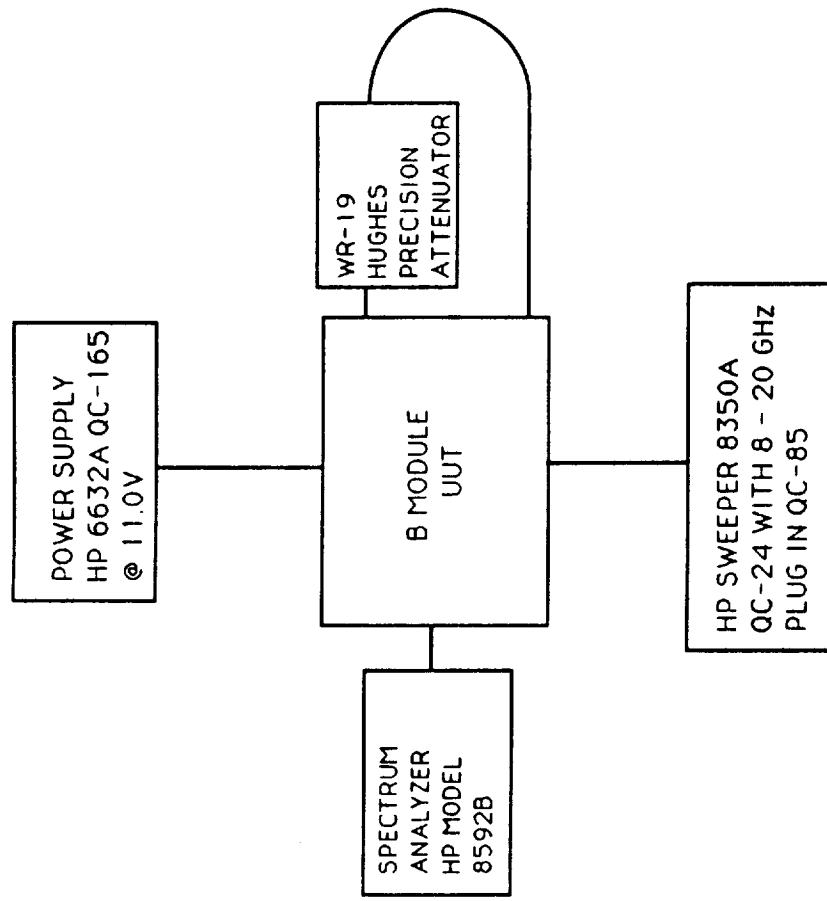
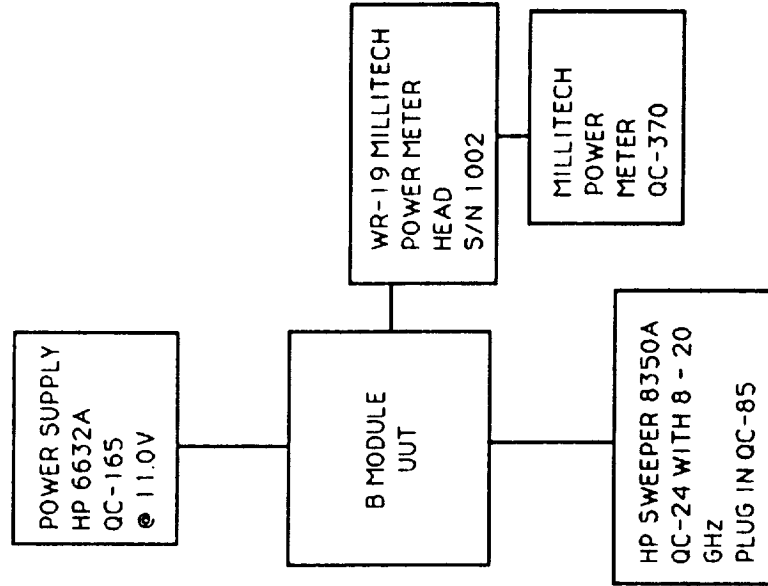


Figure 1



REFERENCE IF AND TEST IF OUTPUT TEST SET-UP



TRANSMIT RF OUTPUT TEST SET-UP

FIGURE 2

MODULE B INTEGRATION 3 APRIL 91

RF OUTPUT POWER VS. RF FREQUENCY, VARYING IF MODULATION INPUT POWER LEVEL

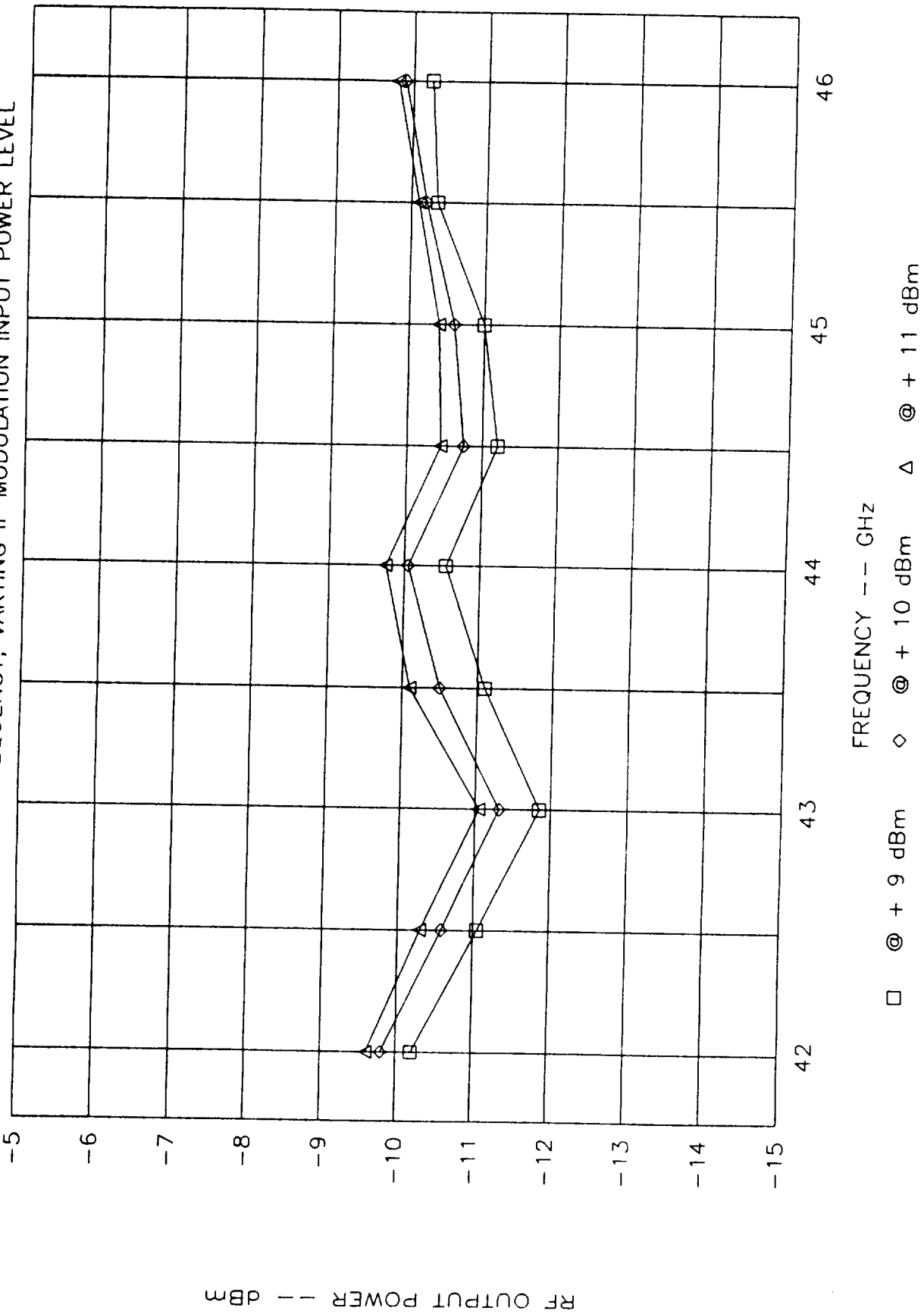


Figure 3

MODULE B INTEGRATION 3 APRIL 91

REFERENCE AND TEST IF OUTPUT POWER VS. FREQUENCY, IF MODULATION INPUT POWER = +10 dBm

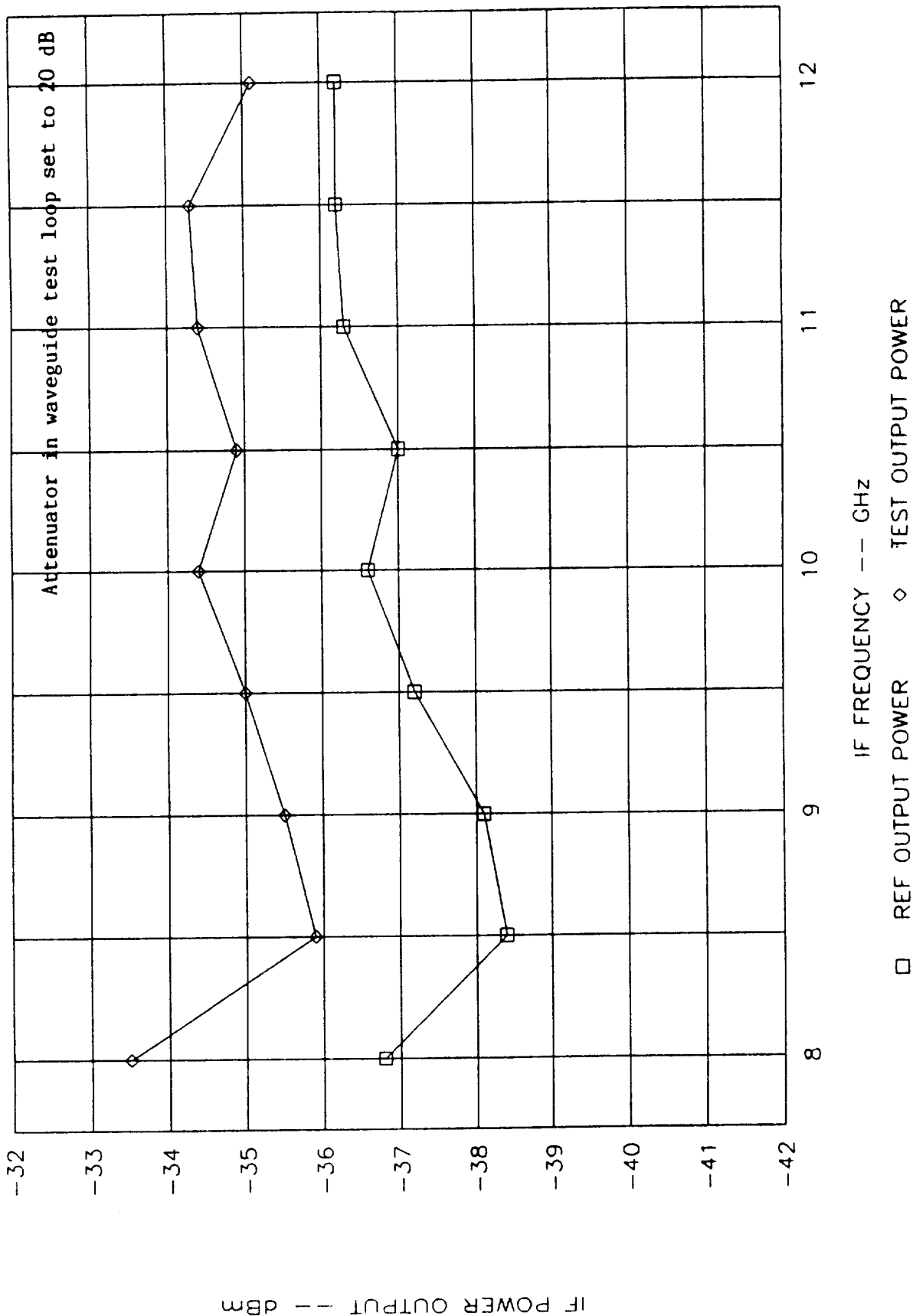


Figure 4

MODULE B INTEGRATION 3 APRIL 91

SPUR LEVELS VS. FREQUENCY, IF MOD INPUT = +10 dBm

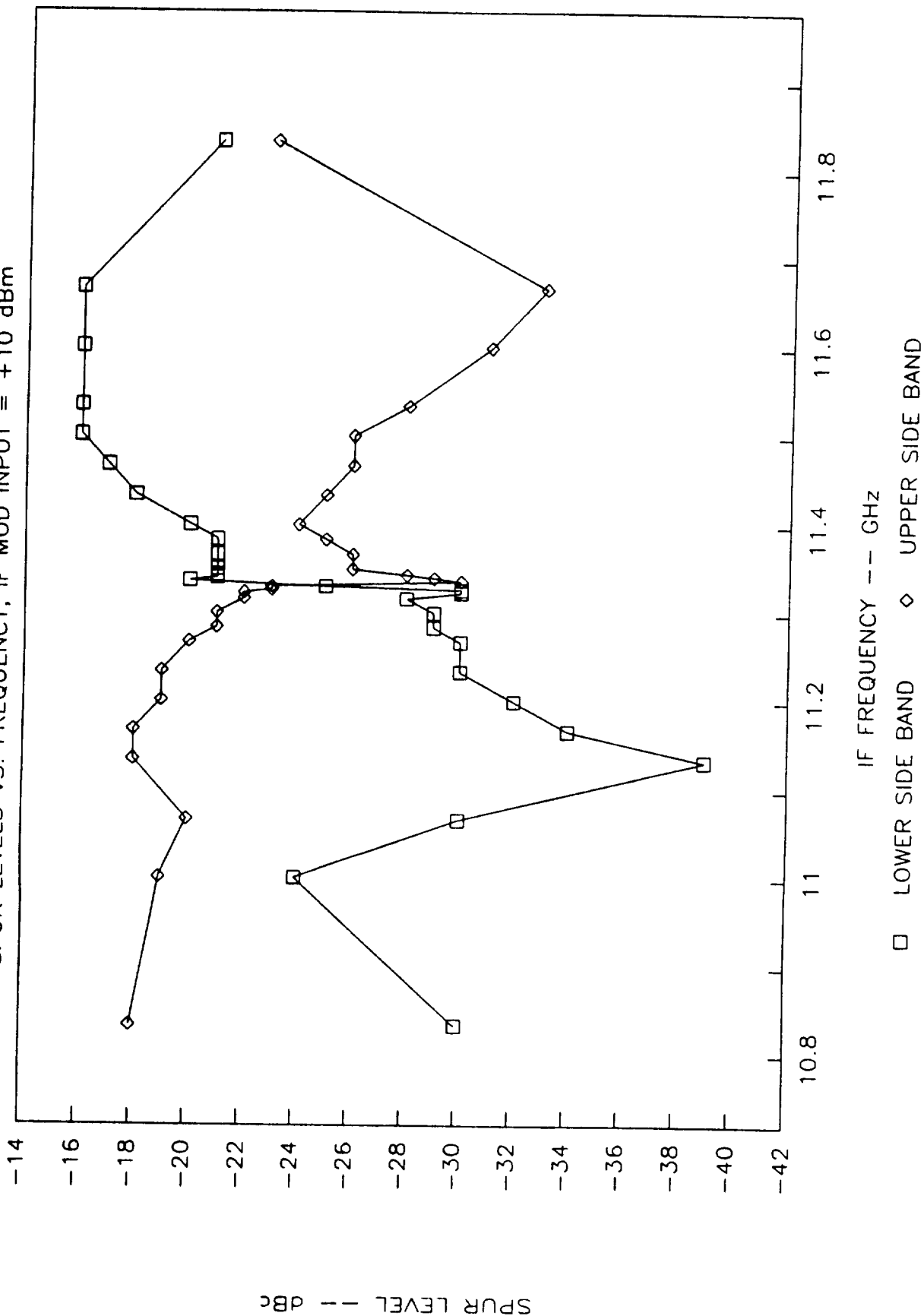


Figure 5

MODULE B INTEGRATION 3 APRIL 91

SPUR LEVELS VS. FREQUENCY, IF MOD INPUT = +10 dBm

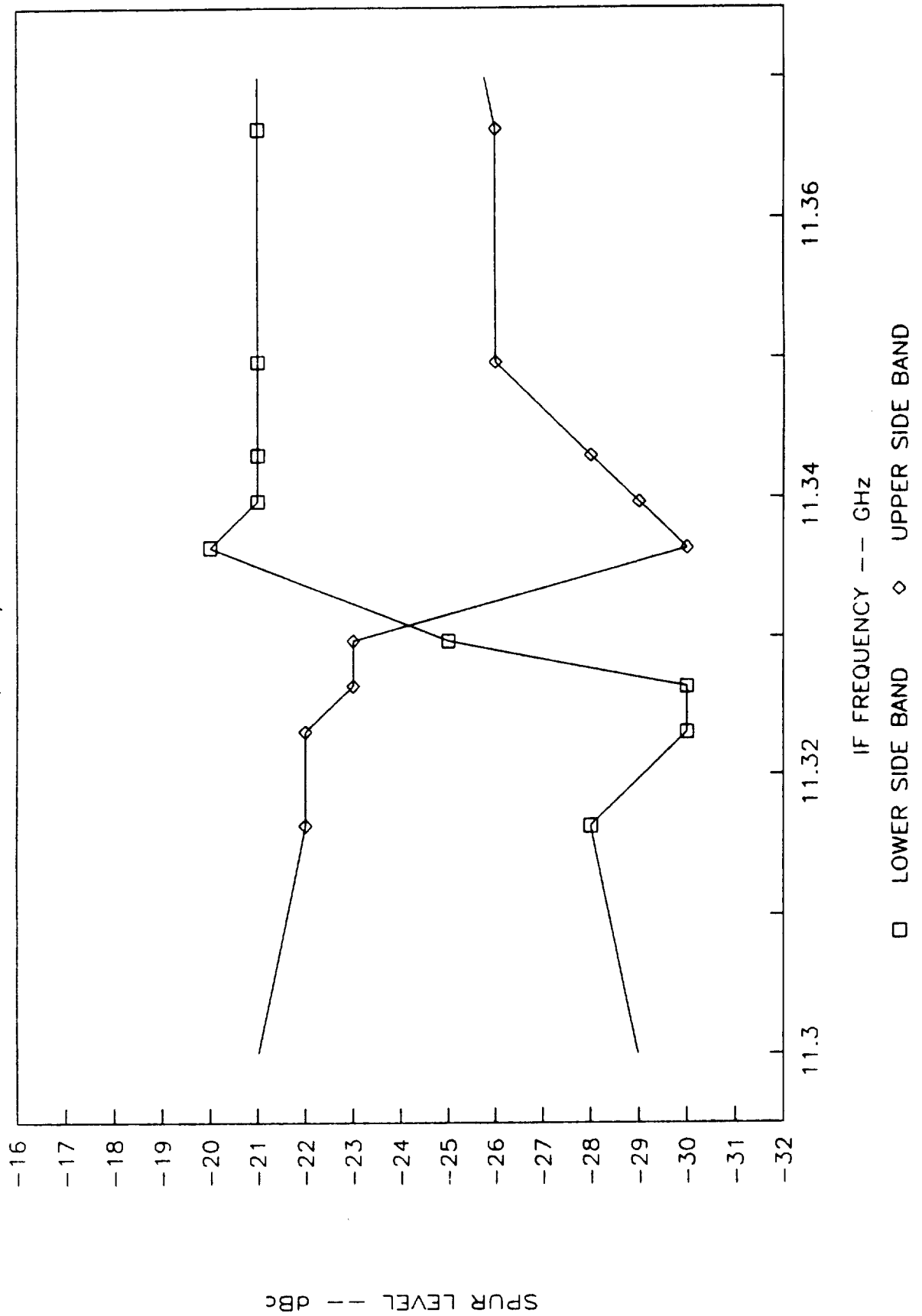


Figure 6

Prepared By: Betsy Scuteri
Approved By: M. J. J. J. J.
Date Prepared: 13 May 91

INTRODUCTION

This report describes initial testing of the Engineering Model Band C T/R Module which operates over an output frequency band of 93 to 97 GHz. The preliminary testing reported herein was performed according to a test plan agreed to by EMS and Millitech and described in the memo of Joe Seals of EMS dated 20 February 91. This testing does not replace testing per the complete Acceptance Test Procedure (ATP) which will be performed when the Engineering Model T/R Modules are returned to Millitech on or about September 1991.

A. CHECK OF LO POWER DISTRIBUTION TO THE THREE MIXER LO PORTS. The LO distribution network on the T/R Modules consists of those components and waveguide sections starting from the Gunn oscillator and ending at the three waveguide ports which are to be later connected to the LO ports of each of the three mixers. See Block Diagram in Figure 1. First we measured output power directly at the Gunn oscillator output port. +18 dBm was indicated. This is approximately the power level which was originally estimated would be necessary to drive all three mixers, the upconverter mixer and two downconverters. This original design value was based on an estimated LO power requirement of about +10.7 dBm for those mixers operated as downconverters, and about 3 dB greater for the upconverter mixer.

Performance data taken on 15 JAN 91 on the three actual mixers designed and fabricated for the Band C module confirmed that when these mixers are used in the downconverter mode, their performance is optimum for LO input power in the range of +10 to +12 dBm. Therefore, we did not adjust the output power of the Gunn oscillator for this Band C module, whereas, as described in the report for the B Module, some adjustment of the Gunn oscillator for that module was required at integration testing.

The measurement of LO power distribution was made using a waveguide power meter head placed successively on each of the three ports to be measured. Waveguide terminations, instead of the actual mixers of the T/R Module, were placed on the remaining two ports not connected to the power meter. With the actual mixers installed, the reflections at the LO port of each mixer causes some redistribution of the Gunn LO power among the three mixers. Because of the extreme difficulty which would be encountered in performing such a measurement with useful accuracy, we did not attempt to characterize this redistribution of LO power. Table 1 summarizes the results of this measurement.

Table 1 Band C Gunn Power Distribution	
MIXER	LO POWER
Receive Mixer (Test)	+ 11.03 dBm
Reference Mixer	+ 10.58 dBm
Upconverter Mixer	+ 13.62 dBm

B. CHECK/ADJUST GUNN OSCILLATOR FREQUENCY WHEN GUNN OSCILLATOR IS INSTALLED ON COMPLETE MODULE. A final check of the Gunn oscillator frequency was performed after the Gunn was integrated into the complete T/R Module. This final check in this configuration is necessary to account for any possible changes in loading caused by multiple reflections of the Gunn oscillator signal within the LO distribution network.

To monitor the Gunn frequency, we used an EIP millimeter frequency counter connected directly to the coaxial IF port of the upconverter mixer. We placed waveguide terminations on the transmit and receive ports of the T/R Module. In this convenient manner, we could measure with high precision the frequency of the Gunn oscillator with the Gunn in its exact operating environment. This requires only a single coaxial cable connected between the upconverter mixer and the EIP frequency counter which, during testing, is located external to the temperature test chamber which was used in this test.

The entire Module C assembly was then placed into the temperature chamber and Gunn oscillator frequency vs. baseplate temperature data was taken for a temperature range of -30°C to +75°C, as measured directly at the mounting plate of the T/R Module. See Figure 2.

As indicated in Figure 2, the Gunn Oscillator frequency at 17.5 °C is 85.030 GHz, and the temperature drift coefficient is approximately -2.07 MHz/°C. The Equipment Specification specifies the nominal frequency of the Gunn oscillator to be $85.0 \pm .095$ GHz at a baseplate temperature of 17.5°C with a maximum allowable drift of 3 MHz/°C. The unit meets these requirements.

C. CHECK OF TRANSMIT RF OUTPUT POWER LEVEL ACROSS BAND. For measurement of RF transmit output power on the T/R Module, we set up the sweep generator to deliver IF Modulation Input power at the levels of +9 dBm, +10 dBm, and +11 dBm at discrete 0.5 GHz frequency increments over the 8 to 12 GHz IF frequency band. An HP coaxial power meter was used for this setup of Modulation Input power. We saved these settings on the HP sweeper using its built-in store settings capability.

Note that +9 to +11 dBm range which we selected for Modulation Input in this testing of the Band C Module spans a ± 1 dB range of power, consistent with the present revision of the Equipment Specification. However these levels are otherwise lower than

the +14 to +16 dBm range indicated in the Specification. In our comprehensive evaluation of the T/R Module during integration testing, we found that overall performance is optimized for this +9 to +11 dBm input power range. The issue has not yet been resolved whether to revise the Equipment Specification to reflect this reduced input power level range for operation, or to change the configuration of the Band C T/R Module to include a coaxial attenuator to provide this reduced effective input power level to the upconverter mixer while retaining the original +14 to +16 dBm level at the Modulation Input interface of module.

Using the test setup shown in Figure 3, RF transmit output power vs. RF output frequency data was taken for the three fixed modulation input power levels of +9 dBm, +10 dBm, and +11 dBm. See Figure 4.

When the IF power is turned off and the LO power is left on, we should see, per the Equipment Specification, an LO leakage below -20 dBc. We found however, that the power level indicated on our power meter, calibrated for measurements over the WR-10 band (75 to 110 GHz) only, was significantly higher, approximately -13 dBc. We then added a lab WR-10 low-pass filter on the output. This filter passes below 114 GHz and rejects higher frequencies. The measured output power indication then went under range on the meter. We concluded from this check that the spurious out of the RF Transmit Output port is at a frequency of 2 times the LO (170 GHz). It is generated in the upconverter mixer and is an out-of-band spurious signal. This x2 LO output frequency component is typical for the mixers used on the T/R Module.

When the IF Modulation Input power is on and the LO power is off, the measured RF Transmit Output power indication was under range (<-25 dBm) for all frequencies of IF modulation input between 8 and 12 GHz. The transmit output power was also measured without the lab low-pass filter on the transmit output port. See Figure 5. This data is approximately 1.5 dB higher as a result of the 2 times LO spur leakage.

D. CHECK OF REFERENCE IF OUTPUT POWER LEVEL ACROSS BAND ALSO

E. CHECK OF TEST IF OUTPUT SENSITIVITY TO RF INPUT POWER. We used an HP Model 8592B microwave spectrum analyzer for measurement of power level versus frequency at both the Reference IF Output and at the Test IF Output ports. IF Modulation Input power levels were accurately controlled to the values of +9 dBm, +10 dBm and +11 dBm at the discrete measurement frequencies over the IF frequency band. To measure the Test IF Output response, a custom WR-10 waveguide test loop and a Hughes WR-10 precision variable attenuator were installed to provide a controlled path to direct the RF transmit output power into the RF Receive waveguide port. For the plots shown in Figures 6 and 7, the variable attenuator was set to 20 dB. In addition to this attenuation, there is an estimated 1.0 dB insertion loss of the custom WR-10 waveguide loop section.

F. CHECK OF REFERENCE IF AND TEST IF OUTPUT SPECTRUM. We did a general search for spurious output signals across the entire 8 to 12 GHz output frequency band first on the Test mixer using an IF Modulation Input power level of +10 dBm. We did not find any spurs above approximately -80 dBm, i.e., -40 dBc. Also, the spurious analysis performed during the design effort relating to these mixers did not predict in-band spurious. Next in this test, IF modulation input power level was increased so that any problem frequencies could be located. We found a spur at approximately 9.449 GHz. Figure 8 shows this spur at a level of -40 dBc with an IF Modulation Input power level of +12 dBm. When the IF modulation was decreased to +10 dBm, which is the nominal operating level for this module, the spur drops below -45 dBc as shown in Figure 9.

This procedure was repeated for the Reference mixer. Figure 10 shows this spurious signal at -54 dBc for an IF modulation input power level of +10 dBm. These levels meet the requirements of the T/R Module Equipment Specification.

G. CHECK OF BAND A TEST IF OUTPUT POWER LEVEL ACROSS BAND. This test is only applicable to the Band A T/R Module.

H. MEASURE SPECTRUM OF TRANSMIT RF OUTPUT. Deleted. This performance characteristic is covered in F, evaluation of IF output spectrum.

I. CHECK ISOLATION OF IF MODULATION INPUT TO TEST IF OUTPUT PORT. With the RF Transmit output and RF Receive input waveguide ports terminated to prevent direct coupling of the RF transmit output signal into the RF receive port, the residual signal at the IF test output was measured using a spectrum analyzer. See Table 2.

This measured power at the carrier frequency represents a leakage signal. The primary path of this leakage is the local oscillator distribution waveguide network between the Test and Reference mixers. Note that in the design of the T/R Modules, we made a tradeoff of transmit signal-to-Test IF output leakage performance for symmetry in the LO distribution network to the Reference and Test mixers. A configuration using one bandpass filter in each of the two LO distribution waveguide arms was selected. While this approach insures a high degree of symmetry, the E-plane bandpass filters have limited rejection for frequencies far above the pass band. Improved isolation performance could have been achieved through an approach which uses a high pass waveguide filter in one arm and a low pass waveguide filter in the other, but this approach lacks channel-to-channel symmetry.

TABLE 2 ISOLATION, IF MODULATION INPUT TO TEST IF OUTPUT			
IF FREQUENCY GHz	TEST IF OUT SIGNAL LEVEL dBm (LEAKAGE) @ +9 dBm IN	TEST IF OUT SIGNAL LEVEL dBm (LEAKAGE) @ +10 dBm IN	TEST IF OUT SIGNAL LEVEL dBm (LEAKAGE) @ +11 dBm IN
8.0	<-90	<-90	<-90
8.5	<-90	<-90	<-90
9.0	-87	-86	-85
9.5	-80	-78	-78
10.0	-81	-81	-80
10.5	-82	-80	-80
11.0	<-90	<-90	<-90
11.5	<-90	<-90	<-90
12.0	<-90	<-90	<-90

WEIGHT

The C Module was weighed in its final configuration. It was found to be within the 39 oz. maximum required by the equipment specification. The actual weight was 32.4 oz.

MECHANICAL ALIGNMENT PER ICD

Critical positioning of the RF Transmit and RF Receive waveguide port interfaces of the module was accomplished using a "Microhite". We were able to achieve positioning within a tolerance of $\pm .001$ " in most cases, except for the two dimensions shown in Figures 11 and 12, where we were within $\pm .0025$ ". The tolerance presently specified in the ICD is $\pm .001$ ". We plan to align these modules again when they are returned to Millitech for final testing. At that time, we will have available a set of custom alignment fixtures which we have designed, but not yet fabricated, for this task. These fixtures will allow more accurate positioning.

CHECK OF SWEPT RESPONSE

As a final check on the overall RF performance, we produced a plot showing the swept response of the IF outputs of the module over its operating band. The IF Modulation Input signal applied to the upconverter was swept between 8 and 12 GHz. This input signal as well as the response from the IF Reference and the IF Test outputs were recorded on the spectrum analyzer using its "Max Hold" mode. Figure 13 shows the amplitude of the swept IF Modulation Input signal. This plot indicates the small variations in the amplitude of our signal generator when swept for a nominal +10 dBm level. Output power decreases slightly at the higher end of the 8 to 12 GHz band. This variation should be used to normalize the swept output signals obtained from the Reference and Test ports of the T/R Module.

Figure 14 shows the IF Reference and the IF Test outputs. Note that they display the same general shape of the plot of swept Modulation Input signal.

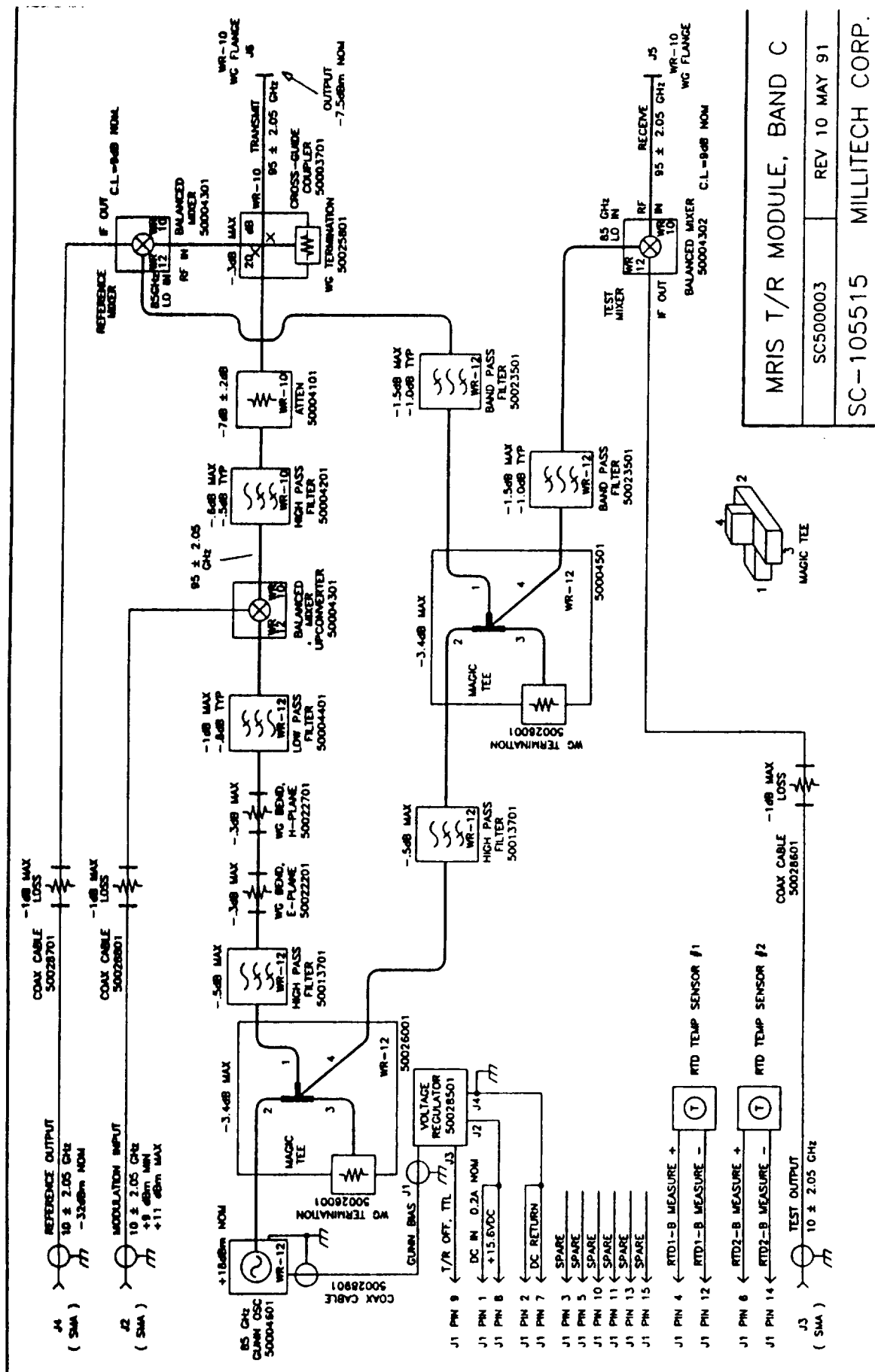


Figure 1

MODULE C INTEGRATION 26 APRIL 91

GUNN OSCILLATOR FREQUENCY VS. TEMPERATURE, MODULE FULLY ASSEMBLED, VOLTAGE = 9.5V

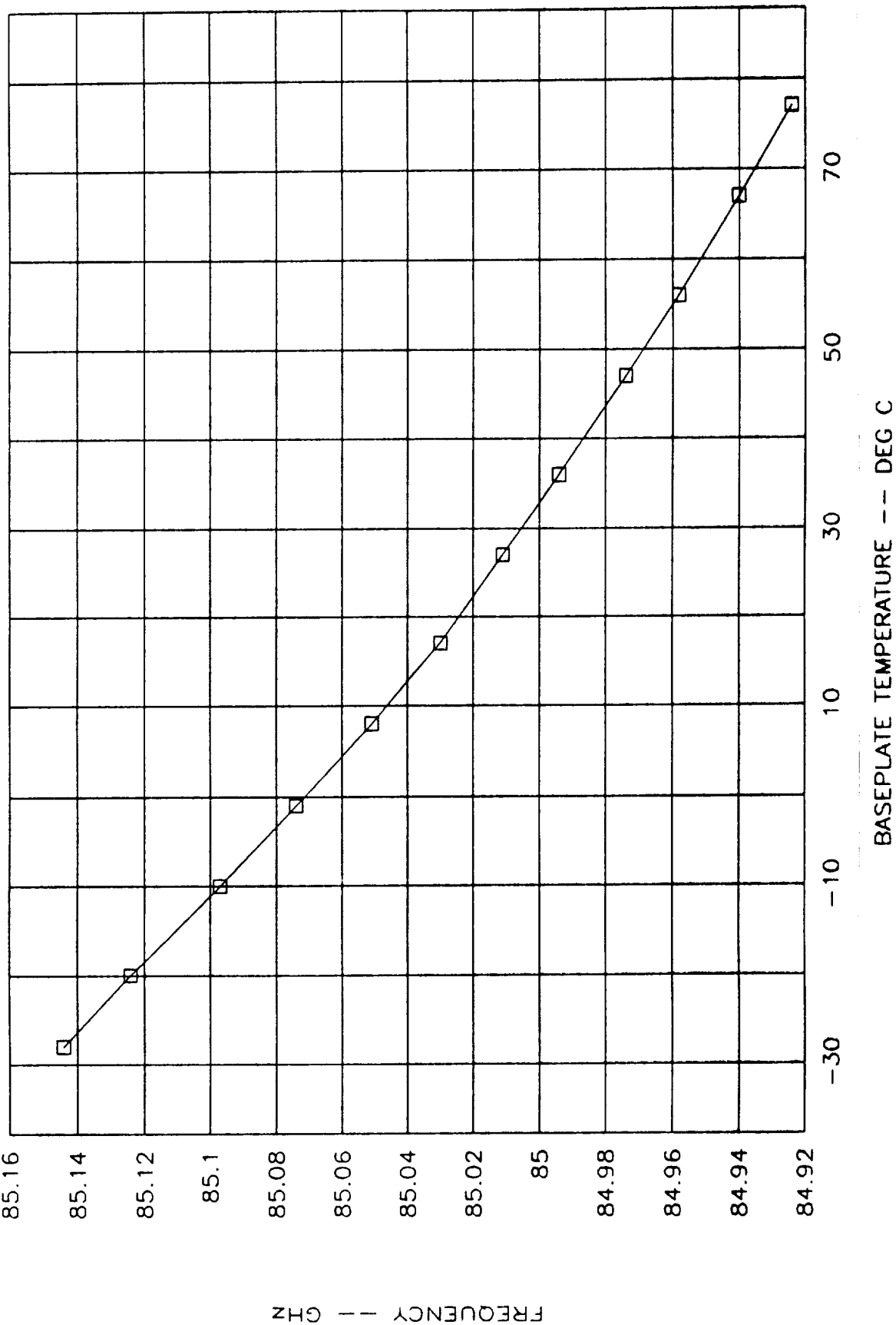
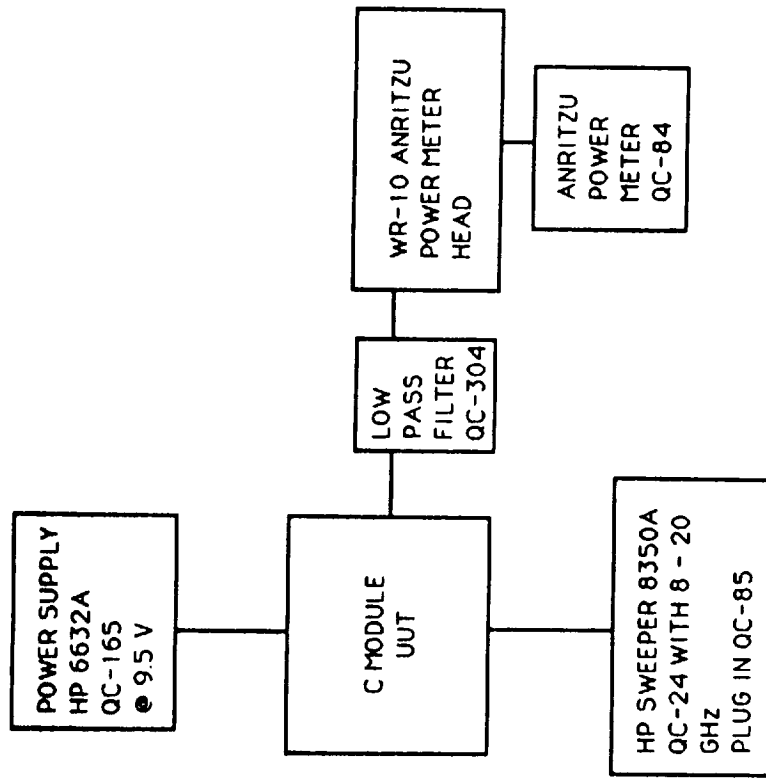
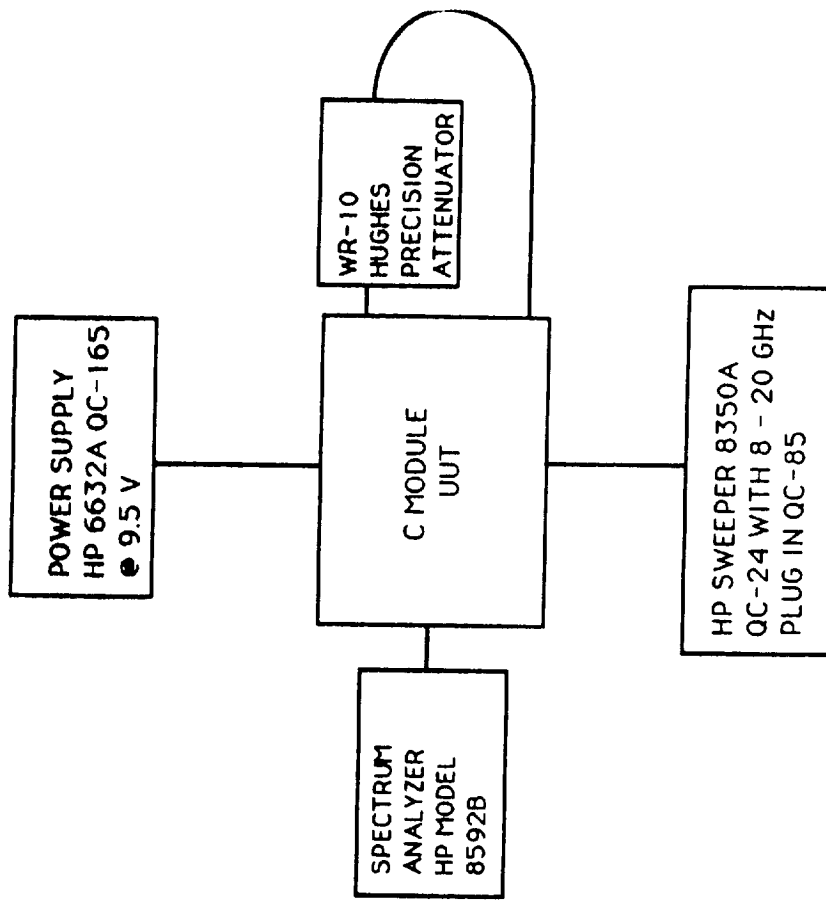


Figure 2



TRANSMIT RF OUTPUT TEST SET-UP

REFERENCE IF AND TEST IF OUTPUT TEST SET-UP

FIGURE 3

MODULE C INTEGRATION 26 APRIL 91

RF OUTPUT POWER VS. RF FREQUENCY, VARYING IF MODULATION INPUT POWER LEVEL

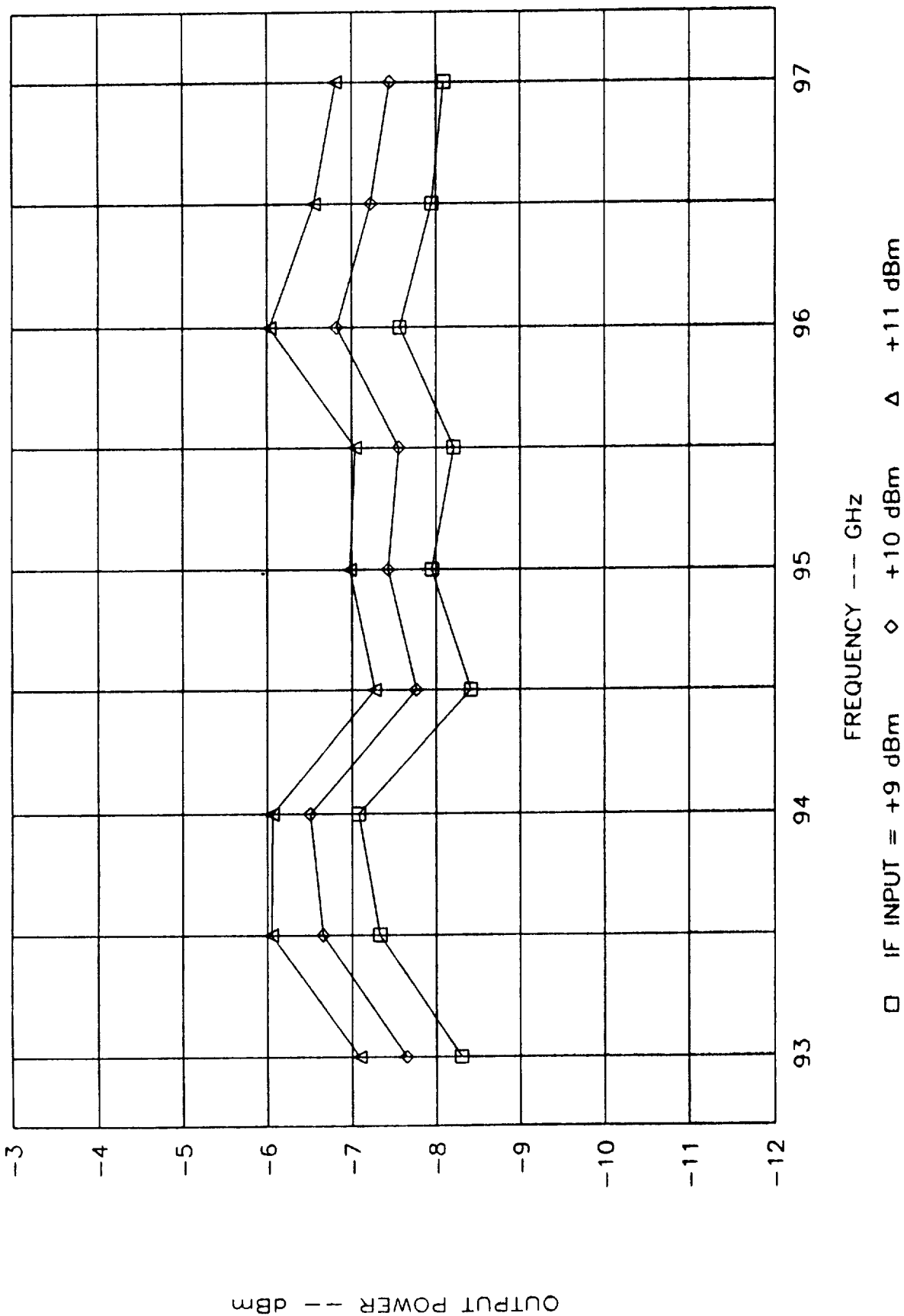


Figure 4

MODULE C INTEGRATION 26 APRIL 91

RF OUTPUT POWER VS. FREQUENCY, NO LAB WR-10 LOW PASS FILTER ON TRANSMIT PORT, MOD INPUT = +10 dBm

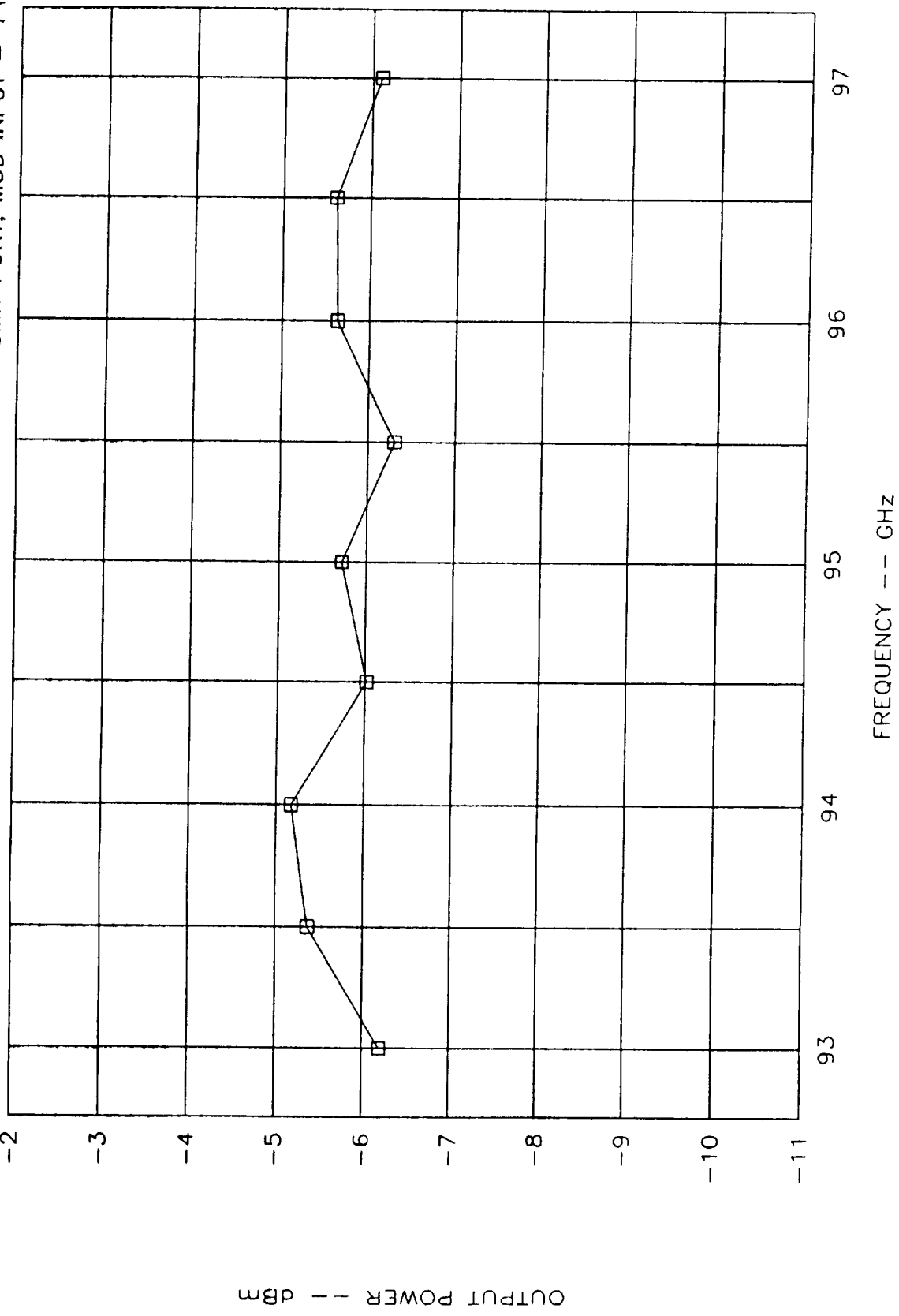


Figure 5

MODULE C INTEGRATION 26 APRIL 91

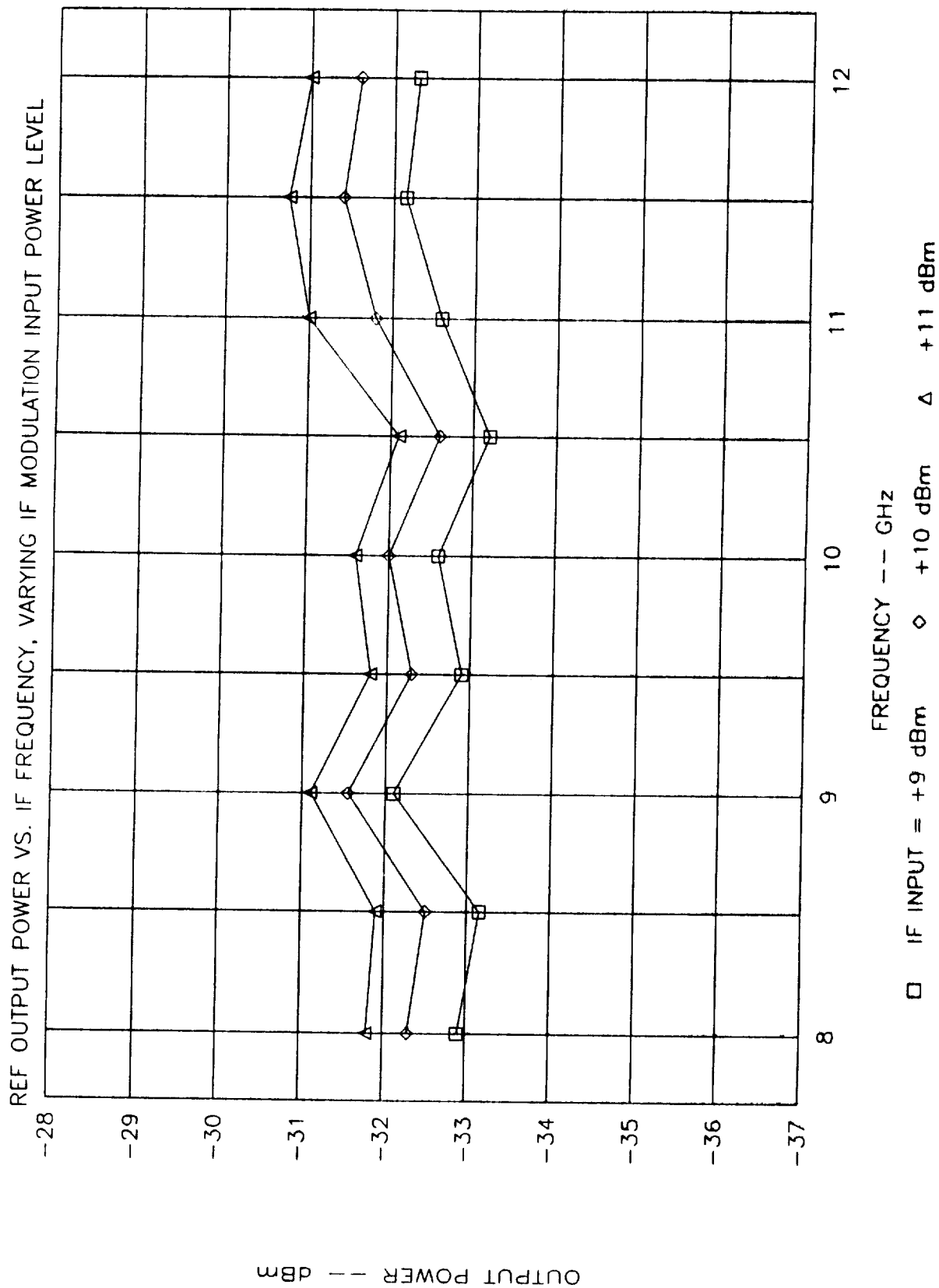


Figure 6

MODULE C INTEGRATION 26 APRIL 91

TEST OUTPUT POWER VS. IF FREQUENCY, VARYING IF MODULATION INPUT POWER LEVEL

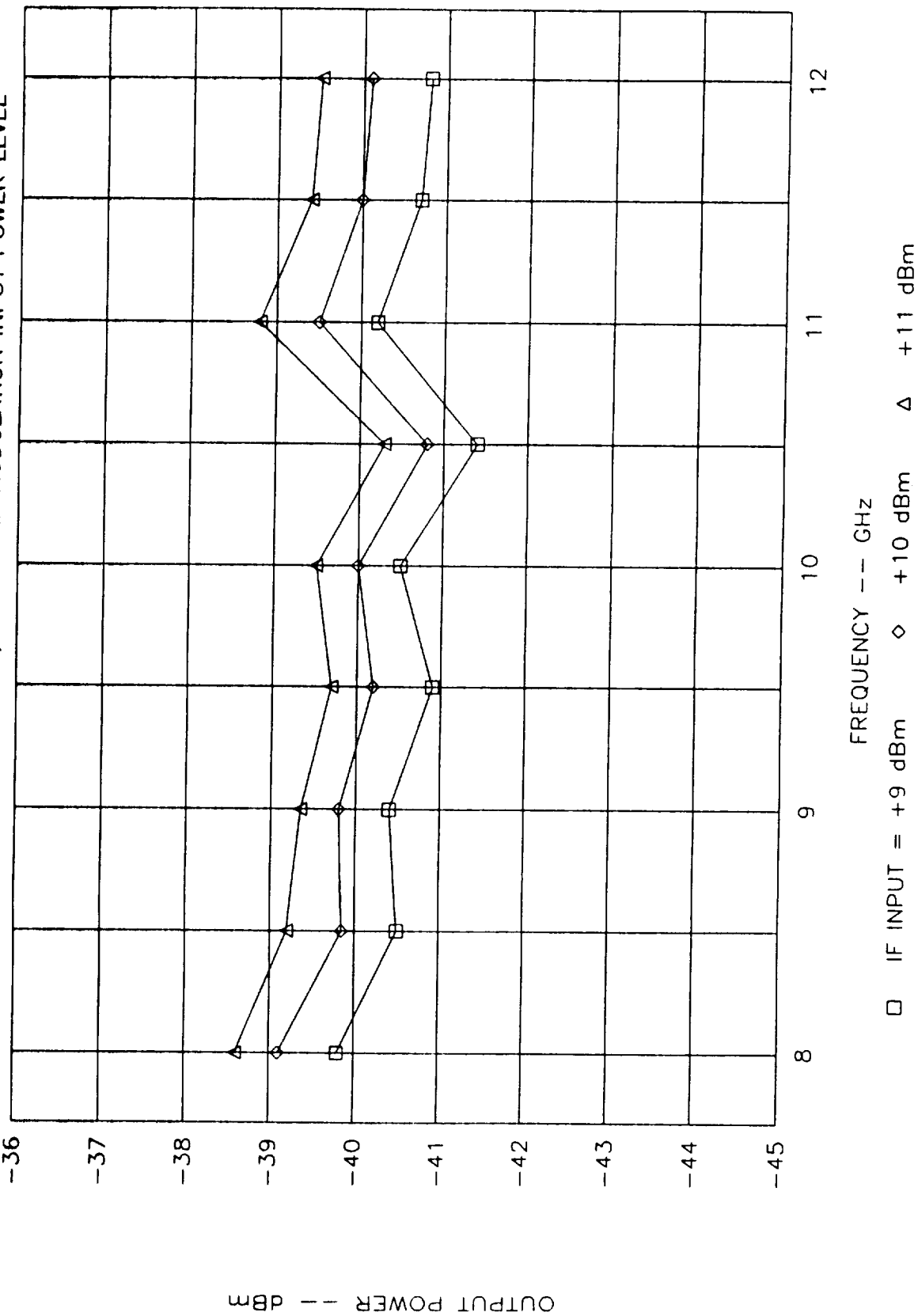
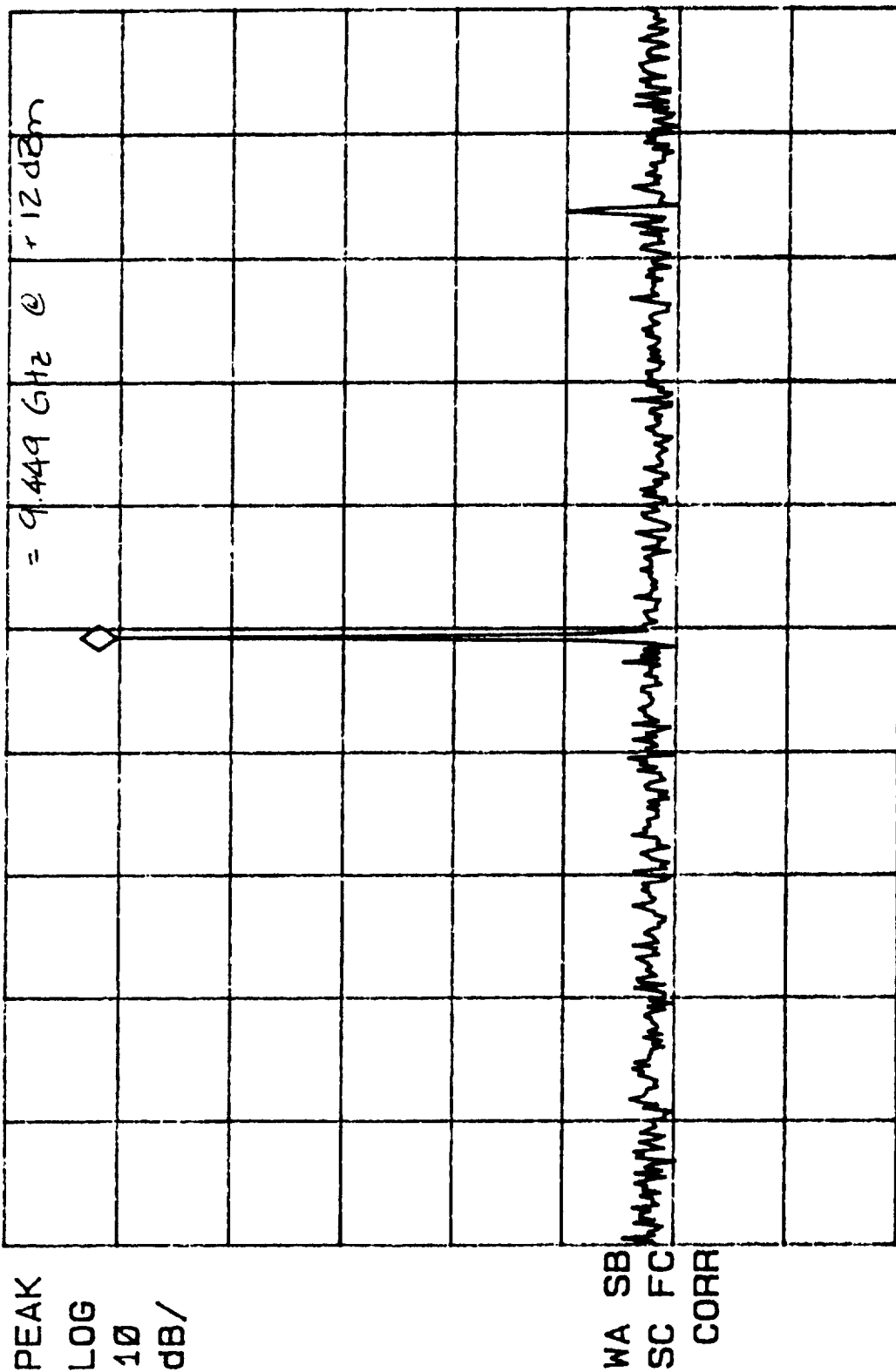


Figure 7

10:38:46 APR 25, 1991 MODULE C INTEGRATION TESTING
 SPURIOUS ANALYSIS
 TEST OUTPUT MKR-TAK 9.45000 GHz
 REF -30.0 dBm ATTEN 10 dB IF MODULATION INPT -39.78 dBm

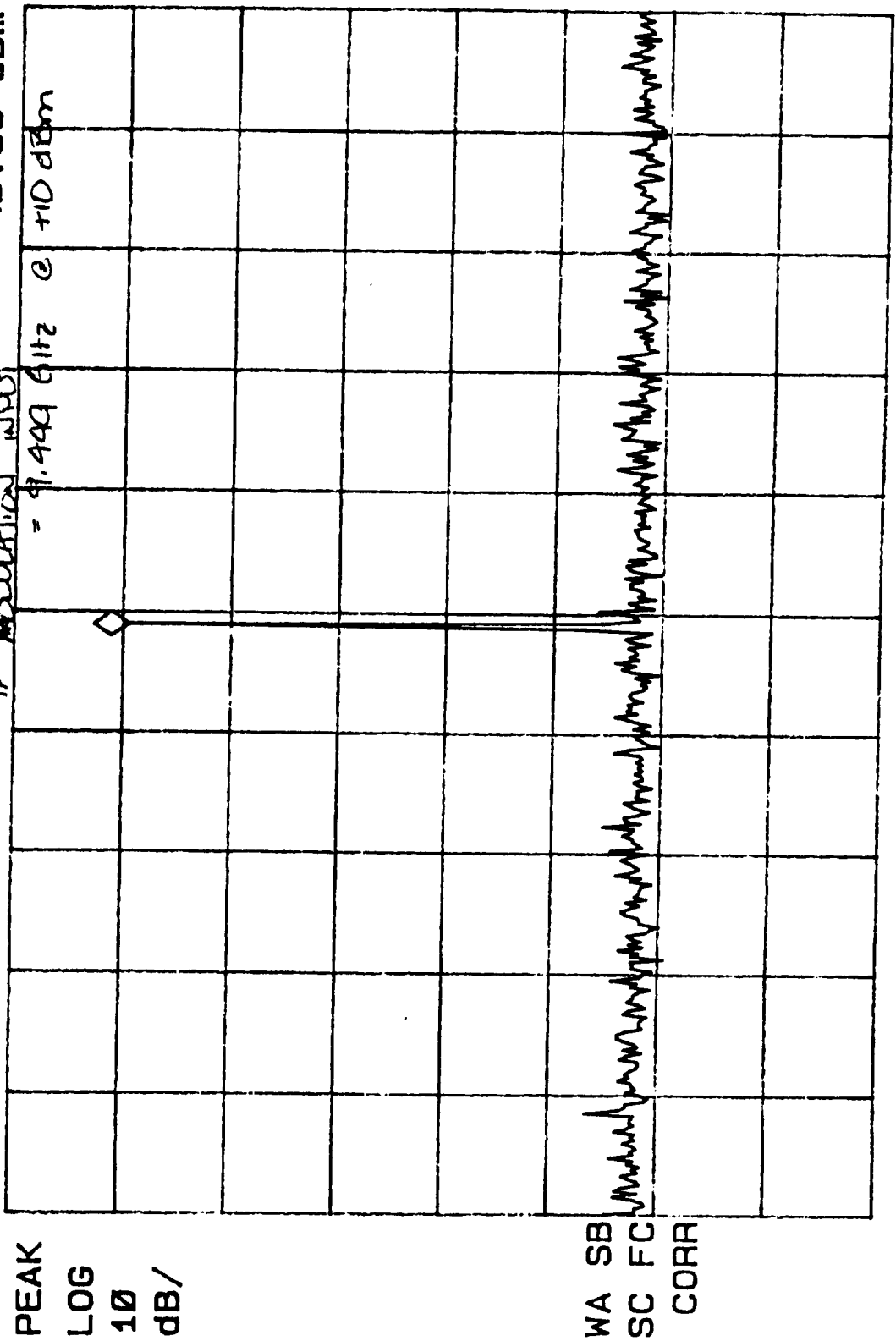


CENTER 9.45015 GHz
 #RES BW 3 KHZ
 VBW 3 KHZ
 SPAN 20.00 MHz
 SWP 6.7 sec

Figure 8

10:41:28 APR 25, 1991 MODULE C INTEGRATION TESTING
 SPURS ANALYSIS

TEST OUTPUT MKR-TRK 9.44995 GHz
 REF -30.0 dBm ATTN 10 dB IF MODULATION INPUT -40.56 dBm



CENTER 9.45015 GHz
 #RES BW 3 KHZ

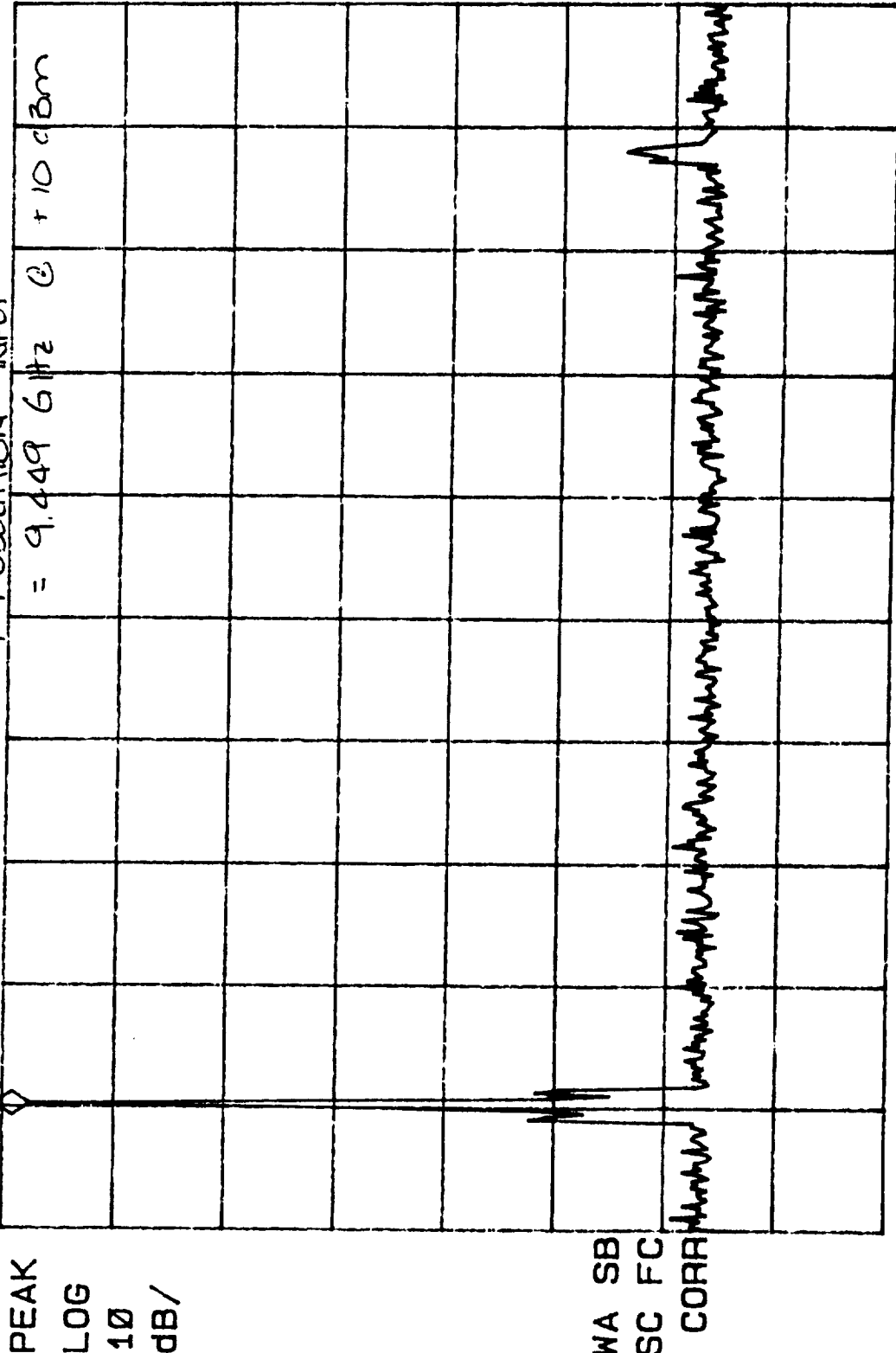
SPAN 20.00 MHz
 SWP 6.7 sec

Figure 9

11: 17: 56 APR 25, 1991 MODULE C INTEGRATION TESTING

SPURIOUS ANALYSIS MKR 9.449675 GHZ
REFERENCE OUT -32.52 dBm

REF -30.0 dBm ATTEN 10 dB IF MODULATION WPT



WA SB
SC FC
CORR

-54.12C

CENTER 9.451662 GHz
#RES BW 1 KHZ
#VBW 1 KHZ
SPAN 5.000 MHz
SWP 15 SEC

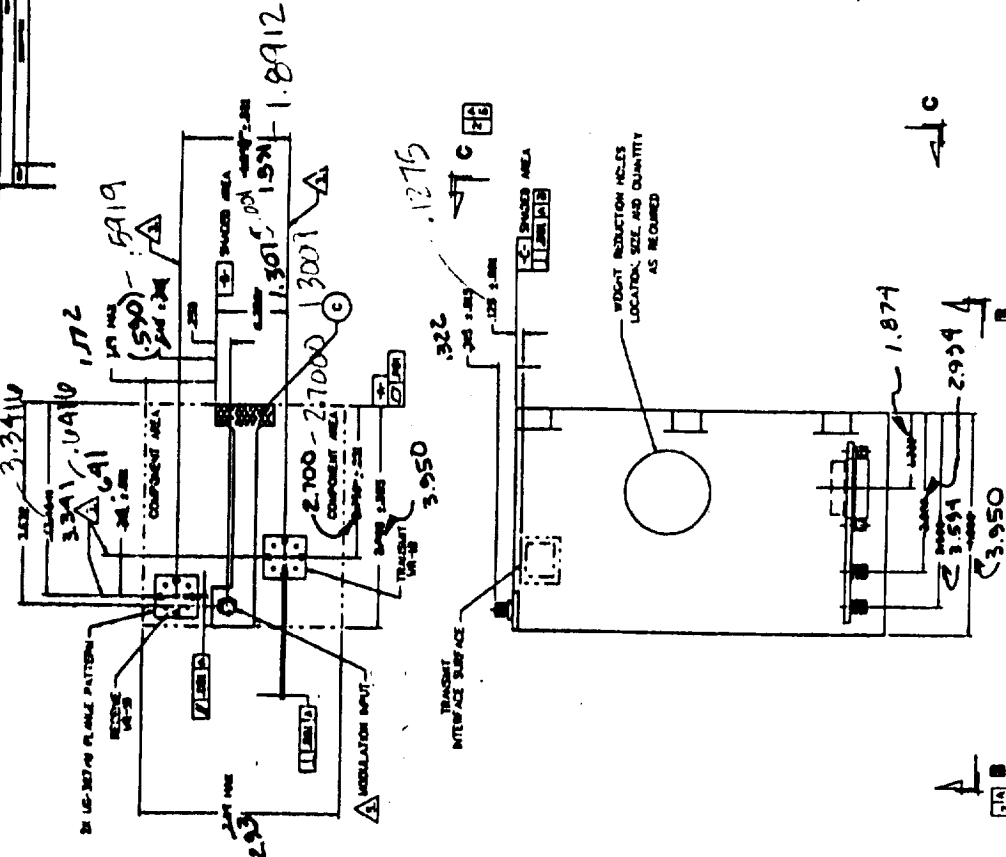
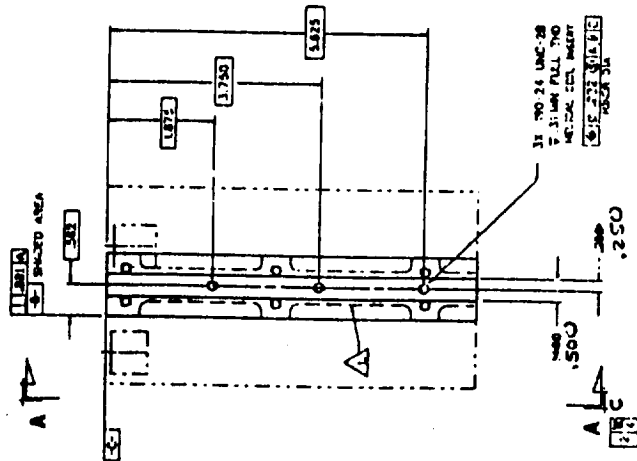
Figure 10

145273

NOTES

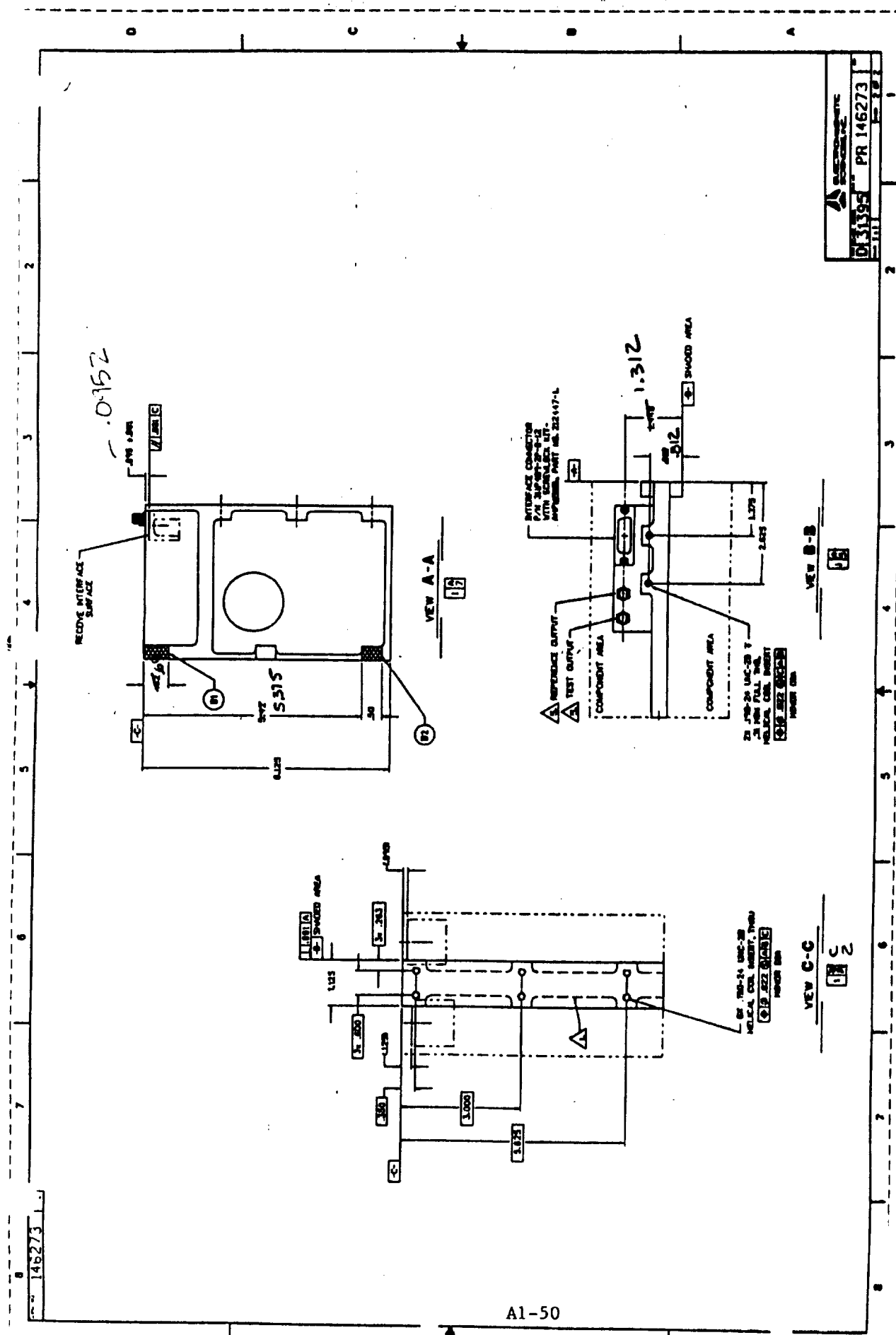
- 1. FOR LIGHT REDUCTION MEASURING RANGE MAY BE RELATED BETWEEN SCREENS
- 2. UNIT SHALL MEET ALL REQUIREMENTS OF DAS SPEC - 145273
- 3. CENTERLINE OF ANCHORAGE
- 4. INTERFERENCE TO ANYTHING ELSE SHALL BE MINIMUM
- 5. CONNECTION PART NO. 145273/145273

ITEM	DESCRIPTION	UNIT	QTY
1	SPARE	EA	1
2	SPARE	EA	1
3	SPARE	EA	1
4	SPARE	EA	1
5	SPARE	EA	1
6	SPARE	EA	1
7	SPARE	EA	1
8	SPARE	EA	1
9	SPARE	EA	1
10	SPARE	EA	1
11	SPARE	EA	1
12	SPARE	EA	1
13	SPARE	EA	1
14	SPARE	EA	1
15	SPARE	EA	1



ITEM	DESCRIPTION	UNIT	QTY
1	SPARE	EA	1
2	SPARE	EA	1
3	SPARE	EA	1
4	SPARE	EA	1
5	SPARE	EA	1
6	SPARE	EA	1
7	SPARE	EA	1
8	SPARE	EA	1
9	SPARE	EA	1
10	SPARE	EA	1
11	SPARE	EA	1
12	SPARE	EA	1
13	SPARE	EA	1
14	SPARE	EA	1
15	SPARE	EA	1

Actual Dimensions Measured
Figure 11



Actual Dimensions Measured

Figure 12

09: 17: 57 MAY 06, 1991 Module C
 IF MODULATION INPUT WITH SWEET SET
 REF 20.0 dBm ATTEN 30 dB TO 12.4 dBm

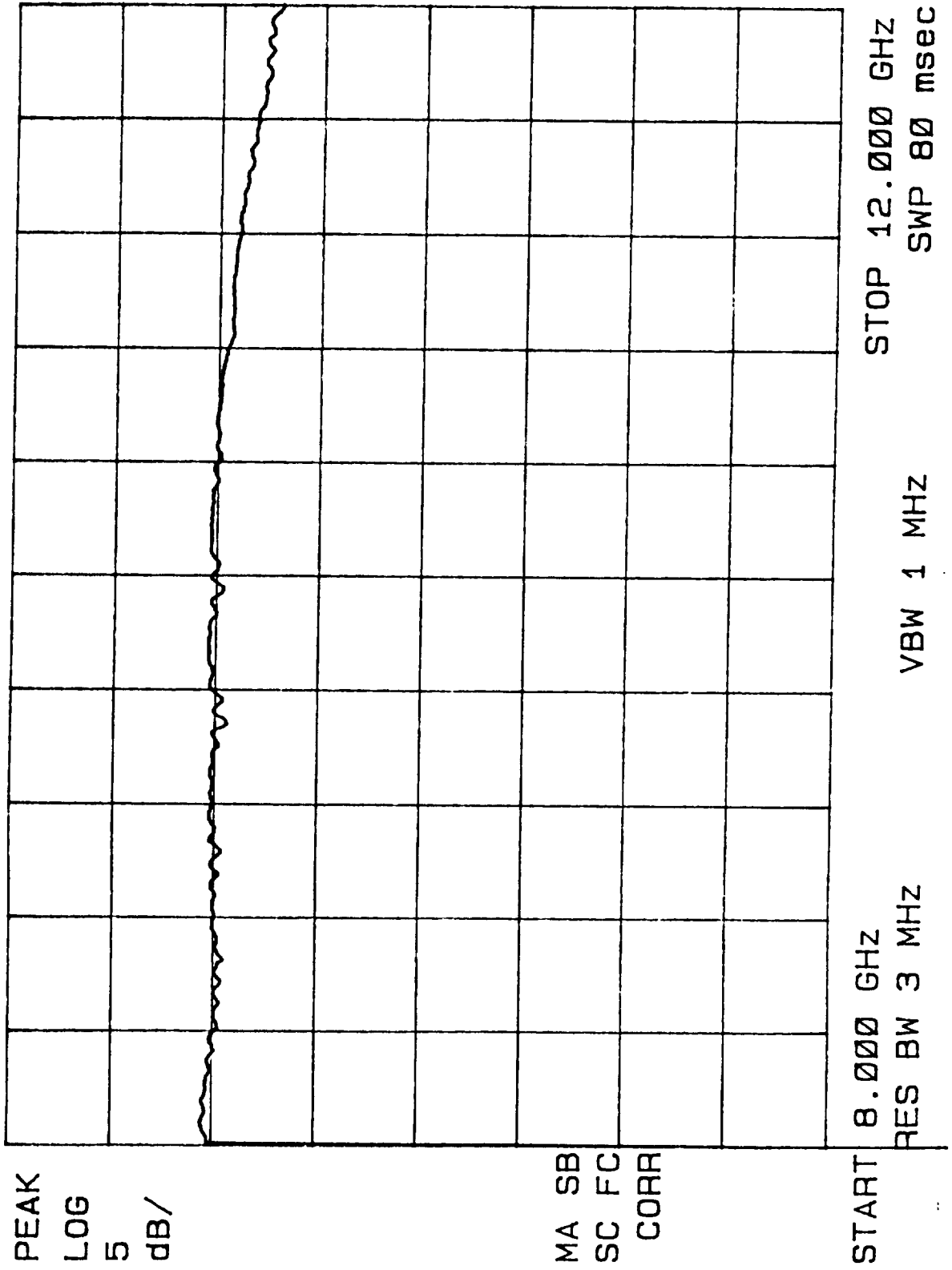


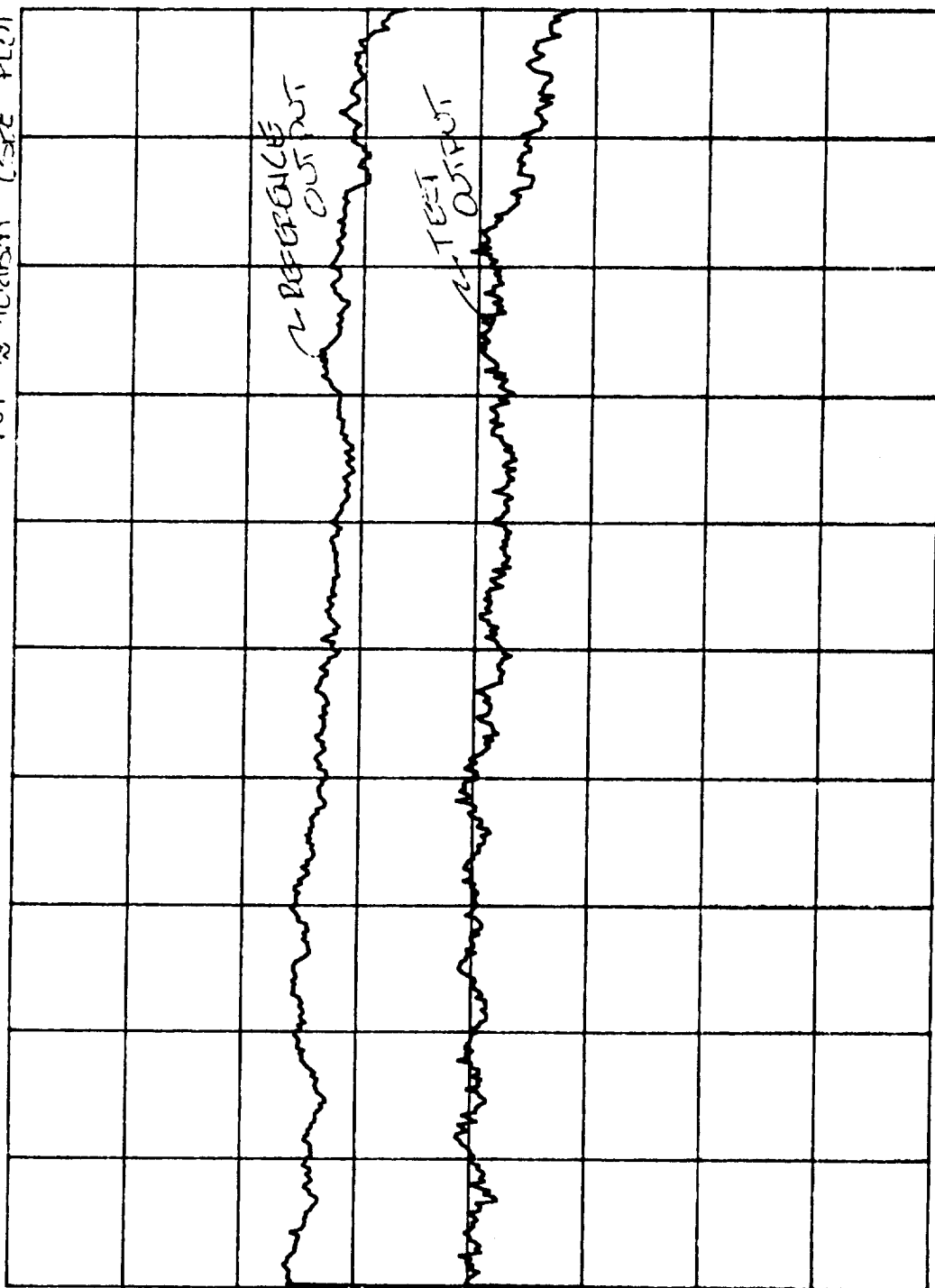
Figure 13

09:24:57 MAY 06, 1991 MODULE C INTEGRATION TESTING

FINAL DATA

REF -20.0 dBm ATTEN 10 dB IF MODULATION INPUT ~10dBm (SEE PLOT)

PEAK
LOG
5
dB/



MA SB
SC FC
CORR

START 8.000 GHz STOP 12.000 GHz
RES BW 3 MHz SWP 80 msec
VBW 1 MHz

Figure 14

SUBCONTRACT S-105515

Prepared By: baby SuderiApproved By: M. AmirthiDate Prepared: 20 August 91

INTRODUCTION

This report describes the initial testing of the Engineering Model Band D T/R Module. The Band D module operates over an output frequency band of 138 to 142 GHz and utilizes WR-8 waveguide at the input and output ports. The preliminary testing reported herein was performed according to a Test Plan agreed to by EMS and Millitech and described in the memo of Joe Seals of EMS dated 20 February 91. This testing does not replace the more extensive testing which will be performed at a later date per the complete Acceptance Test Procedure (ATP). ATP will be performed when the Engineering Model T/R Modules are returned to Millitech around September 1991.

PRECAUTIONS FOR HANDLING AND OPERATING HARDWARE

To help to prevent damage to the hardware through improper handling or operation, we have prepared, and include as Figure 12 of this report, a one-page document entitled "Precautions for Handling and Operating MRIS T/R Modules." This document applies to all of the T/R Modules. It should be read and understood by all personnel handling and/or operating the equipment.

TEMPERATURE CYCLING/PRE-CONDITIONING

Prior to performing the testing on the Band D module as described in this report, the fully assembled module was put through temperature cycling pre-conditioning in a programmable laboratory temperature test chamber. Unit was non-operating during this temperature cycling. Cycling schedule was three complete cycles between -53°C and +140°C, with a minimum one-hour soak time at the upper and lower temperature extremes.

Following this non-operating temperature cycling on the Band D engineering model, we proceeded to perform the precision mechanical alignment of the input and output

waveguide ports relative to the mounting structure of the module per the ICD. Some difficulty was experienced in this operation and it was necessary to remove and re-install various components from and to the module repeatedly. We became concerned that the stress from this repeated handling of the components could have degraded performance. We ran a brief performance check before completing the mechanical alignment.

This performance check indicated a failure of the Test Mixer on this Band D module. Testing of this mixer indicated a good I-V characteristic of the mixer diode, but that LO power was not turning on the diodes of this mixer sufficiently to allow normal mixer operation. On close mechanical inspection of the mixer, no mechanical anomalies were evident. We found that replacing the diode in this mixer returned it to operation. We cannot determine conclusively the cause of this failure of the Band D Test Mixer. We identify two possible causes: temperature cycling pre-conditioning at +140°C, and stresses induced during the mechanical alignment process.

As part of the diode installation procedure, the entire mixer is baked at 100°C for two hours. Therefore this re-built Test Mixer received this high temperature exposure, but we did not repeat the -53°C to +140°C pre-conditioning of this Band D T/R Module. We proceeded with completion of mechanical alignment, then on to the Preliminary Testing procedure.

A. CHECK OF LO POWER DISTRIBUTION TO THE THREE MIXER LO PORTS.

The LO distribution network on the T/R Modules consists of the WR-15 waveguide components and waveguide sections starting from the Gunn oscillator and ending at the three waveguide ports which, in normal operation, are connected to the LO ports of each of the three mixers. Refer to Figure 1, Band D Block Diagram.

With it removed from the module, we measured output power directly at the 65 GHz Gunn oscillator, before the LO distribution network. In its final configuration, the Band D Gunn had an output power of +16.4 dBm.

During our testing of the 65 GHz Gunn oscillator we found that the frequency was about 70 MHz high. Since this Gunn oscillator design does not have a screw tuner for mechanical fine tuning adjustment that the Band A and Band B Gunn oscillators have, it was necessary to tune the oscillator frequency with a small alumina chip inserted into the cavity region of the oscillator. The tuning chip was bonded with Scotchweld 2216 B/A, into the appropriate location.

This frequency tuning process lowered slightly the Gunn oscillator output power, by approximately 1.3 dB. However, during our evaluation of the module, we found that the RF Transmit output power is optimized with this lower level of Gunn power. We originally installed a small chip of Eccosorb microwave absorber material in the Gunn to reduce the power by approximately this 1.3 dB. Following frequency adjust with the alumina chip, this absorber was no longer necessary and it was removed.

The measurement of LO power distribution was made using a WR-15 waveguide thermistor mount power sensor and associated power meter. The thermistor mount was placed successively on each of the three ports to be measured. Waveguide terminations, instead of the actual mixers of the T/R Module, were placed on the remaining two ports not connected to the power meter. With the actual mixers installed, the reflections at the LO port of each mixer causes slight redistribution of the Gunn LO power among the three mixers. Because of the extreme difficulty which would be encountered in performing such a measurement with useful accuracy, we did not attempt to characterize this redistribution of LO power. However, the LO ports on each of the three mixers were matched to better than 8 dB return loss, so this redistribution of LO power is probably insignificant. Table 1 summarizes the results of this measurement.

During hardware integration of the Band D module, we found that we could obtain improved flatness in the RF performance of the mixers by improving the LO port match on the mixers. We accomplished this by, again, using a reflection test setup and installing alumina matching chips of the appropriate size and in the appropriate locations within the WR-15 waveguide LO ports of the mixers. Chips were bonded in place with Scotchweld 2216 B/A epoxy. With the matching chips in place, power reflected at the LO ports is reduced.

Table 1 Band D Gunn Power Distribution	
MIXER	LO POWER
Receive Mixer (Test)	+ 8.6 dBm
Reference Mixer	+ 8.5 dBm
Upconverter Mixer	+ 11.6 dBm

B. CHECK/ADJUST GUNN OSCILLATOR FREQUENCY WHEN GUNN OSCILLATOR IS INSTALLED ON COMPLETE MODULE. A final check of the Gunn oscillator frequency was performed after the Gunn was integrated into the complete T/R Module. This final check in this configuration is necessary to account for any possible changes in loading caused by multiple reflections of the Gunn oscillator signal within the LO distribution network.

For this test, the Band D T/R Module was installed in a laboratory temperature chamber. To monitor the Gunn frequency, we used an EIP direct reading millimeter wave frequency counter connected directly to the coaxial IF port of the Test (Receive) mixer. The in-place Test mixer on the T/R Module serves as the external harmonic mixer for the operation of the millimeter wave frequency counter. The Gunn voltage regulator was in place and operational on the module during this temperature test. Therefore, effects of the Gunn voltage regulator are included in the measurement of Gunn frequency versus temperature. In this manner, we could measure with high precision the frequency of the Gunn oscillator over temperature with the Gunn in its exact operating environment.

With the complete Module D assembly placed into the temperature chamber, we measured Gunn oscillator frequency vs. baseplate temperature for a temperature range of -28°C to +85°C. Baseplate temperature was measured with a thermocouple whose junction was located directly in contact with the mounting plate of the T/R Module, and in the vicinity of the Gunn oscillator. Figure 2 is a plot of measured data.

As indicated in Figure 2, the Gunn Oscillator frequency at 17.5 °C is 65.032 GHz, and the temperature drift coefficient is approximately -1.64 MHz/°C. The Equipment Specification specifies the nominal frequency of the Gunn oscillator to be $65.0 \pm .070$ GHz at a baseplate temperature of 17.5°C with a maximum allowable drift of 2 MHz/°C. This test verifies that the unit meets these requirements.

C. CHECK OF TRANSMIT RF OUTPUT POWER LEVEL ACROSS BAND.

For this test, as well as for the testing described in Sections D and E of this report, we set up the sweep generator to deliver IF Modulation Input signal at the nominal levels of +4 dBm, +5 dBm, and +6 dBm, as required, over the 8 to 12 GHz IF frequency band. Plots of the actual power levels versus frequency for the resulting 8 to 12 GHz swept Modulation Input signal obtained from the sweep generator, as well as plots for both 8 to 12 GHz IF outputs, were obtained using a calibrated HP Model 8592B microwave spectrum analyzer operating in its "max hold" mode. This method of using repetitive scans in "max hold" on our spectrum analyzer produces output similar to what would be produced with a tracking generator in place of the free-running sweep generator. All

of the described signals are within the direct, pre-selected input frequency band of the microwave spectrum analyzer. We only used power meters for measuring the power levels of the RF Transmit Output signal.

For each swept measurement, the power versus frequency display of the spectrum analyzer was recorded on a digital plotter. Figure 3 shows the amplitude of the swept IF Modulation Input signal. A worst case power flatness of about ± 0.5 dB is indicated for the Input signal provided by the sweep generator. This data is included for reference. Since the upconverter mixer on the Band D module is operated in a saturated condition, the IF modulation input variations cannot be directly normalized out over the output signal band.

Note that the +4 to +6 dBm range which we selected for Modulation Input power levels in this testing of the Band D Module spans a 2 dB total range of power, consistent with the present revision of the Equipment Specification. However these absolute levels are not consistent with the +14 to +16 dBm range indicated in the present revision of the Equipment Specification. In our comprehensive evaluation of the Band D T/R Module, we found that overall performance is optimized for this +4 to +6 dBm range of Modulation Input.

The issue has not yet been resolved on how to eliminate this discrepancy in Modulation Input power levels. One option is to revise the Equipment Specification to reflect these lower input power levels. The other option is to change the configuration of the Band D T/R Module to include a 10 dB coaxial attenuator to provide this reduced input power level to the upconverter mixer while retaining the original +14 to +16 dBm level at the Modulation Input interface of module.

Using the test setup shown in Figure 4, we measured the response of the RF transmit output power versus RF output frequency over the specified 138 to 142 GHz band, taking data every 0.1 GHz, for the three fixed modulation input power levels of +4 dBm, +5 dBm, and +6 dBm. Figure 5 shows plots of the three power output sweeps.

D. CHECK OF REFERENCE IF OUTPUT POWER LEVEL ACROSS BAND
ALSO

E. CHECK OF TEST IF OUTPUT SENSITIVITY TO RF INPUT POWER.

We used the same microwave spectrum analyzer for measurement of IF output power level versus frequency at both the Reference IF Output and at the Test IF Output ports. A block diagram of this test setup is also shown in Figure 4. IF Modulation Input power levels were set, sequentially, to the values of +4 dBm, +5 dBm and +6 dBm and

swept over the IF frequency band. The swept response of the Reference IF output is shown in Figure 6 where the WR-8 waveguide output port of the T/R Module is terminated with a laboratory waveguide termination.

Swept response of the Test IF output is also shown in Figure 6. A custom WR-8 waveguide test loop and a WR-8 straight section were installed between the Transmit and Receive ports to provide a controlled path to direct the RF transmit output power into the RF Receive waveguide port. The estimated loss in this WR-8 waveguide loop is approximately 2 dB.

F. CHECK OF REFERENCE IF AND TEST IF OUTPUT SPECTRUM. We did a general search for spurious output signals across the entire 8 to 12 GHz output frequency band on the Test mixer using an IF Modulation Input power level of +5 dBm. We did not locate any spurs. Our system sensitivity threshold level in this measurement was approximately -75 dBm, i.e., -45 dBc. Note that a spurious analysis performed during the design effort relating to the Band D module did not predict any in-band spurious.

G. CHECK OF BAND A TEST IF OUTPUT POWER LEVEL ACROSS BAND. This test is only applicable to the Band A T/R Module.

H. MEASURE SPECTRUM OF TRANSMIT RF OUTPUT. Deleted. This performance characteristic is covered in F, evaluation of IF output spectrum.

I. CHECK ISOLATION OF IF MODULATION INPUT TO TEST IF OUTPUT PORT. With the RF Transmit output and RF Receive input waveguide ports terminated to prevent direct coupling of the RF transmit output signal into the RF receive port, the residual signal at the IF test output was measured using a spectrum analyzer. See Table 2.

This measured power at the carrier frequency represents a leakage signal. The primary path of this leakage is the local oscillator distribution waveguide network between the Test and Reference mixers. Note that in the design of the T/R Modules, we made a tradeoff of transmit signal-to-Test IF output leakage performance for symmetry in the LO distribution network to the Reference and Test mixers. A configuration using one band-pass filter in each of the two LO distribution waveguide arms was selected. While this approach insures a high degree of symmetry, the E-plane bandpass filters have limited rejection for frequencies far above the pass band. Improved isolation performance could

have been achieved through an approach which uses a high pass waveguide filter in one arm and a low pass waveguide filter in the other, but this approach lacks channel-to-channel symmetry.

TABLE 2 ISOLATION, IF MODULATION INPUT TO TEST IF OUTPUT	
IF FREQUENCY GHz	TEST IF OUT SIGNAL LEVEL dBm (LEAKAGE) @ +5 dBm INPUT
8.0	<-82
8.5	<-82
9.0	<-82
9.5	-81
10.0	<-82
10.5	<-82
11.0	<-82
11.5	-81
12.0	<-82

WEIGHT

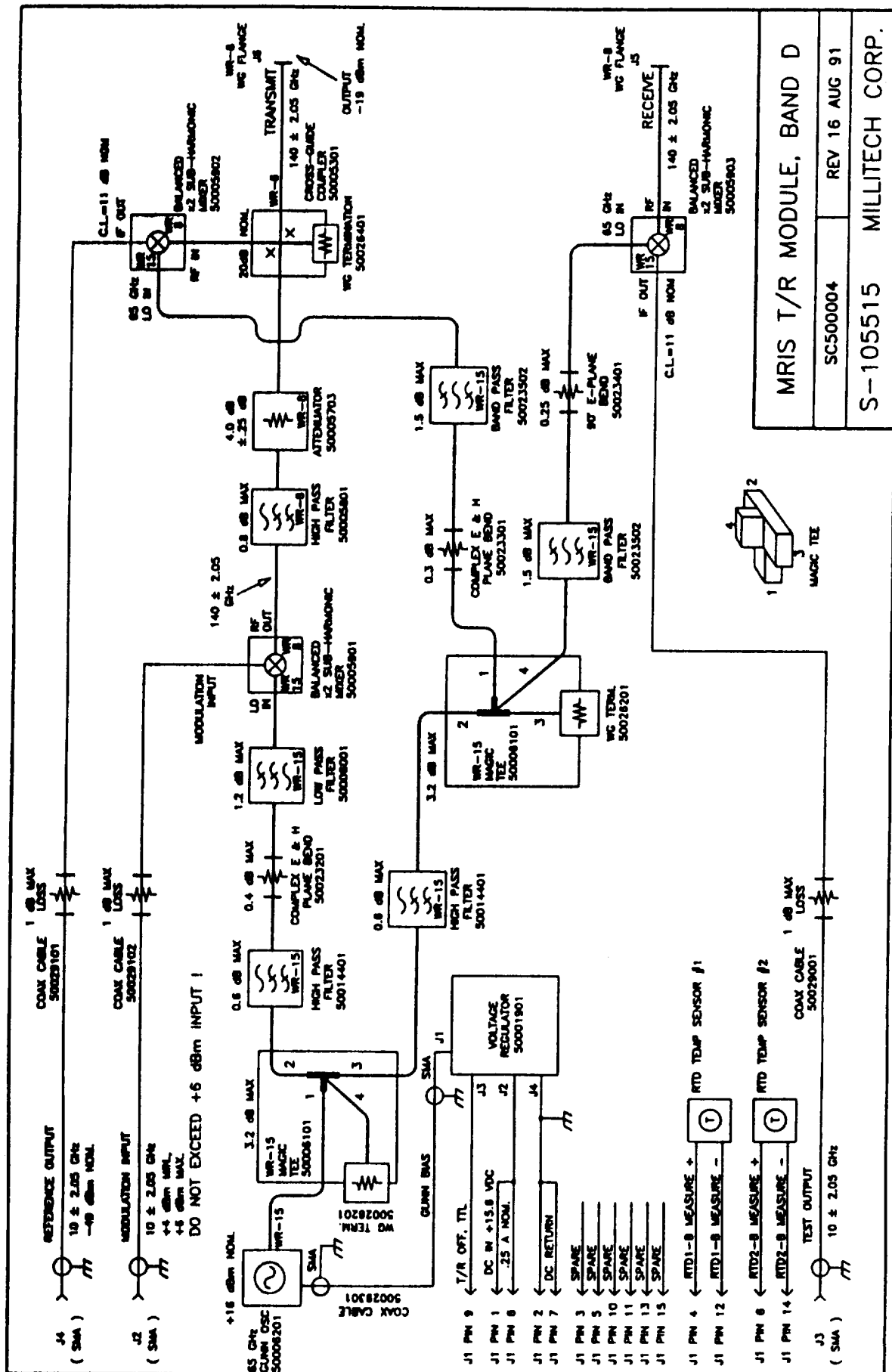
The D Module was weighed in its final configuration. It was found to be within the 43 oz. maximum required by the equipment specification. The actual weight of the fully assembled module was 36.4 oz.

MECHANICAL ALIGNMENT PER ICD

Critical positioning of the RF Transmit and RF Receive waveguide port interfaces of the module was accomplished using a "Microhite" measuring instrument. We were able to achieve positioning within a tolerance of $\pm .001$ " in most cases, except for the receive port perpendicularity shown in the marked-up ICD of Figures 7 and 8.

MIXER IF RETURN LOSS MEASUREMENTS

During the integration of the D Module we spent considerable time and effort on the development of the Band D sub-harmonic mixers to obtain good conversion loss performance. We found that we could improve the performance by matching the LO port, and in one case match the RF port, of the mixers using alumina matching chips. Since the LO and RF matching improved the performance of the mixers we theorized that matching the IF port could also improve the performance, although we made no attempts to design IF matching networks. However, we did measure the IF Port Return Loss on the three Module D mixers. Plots are shown in Figures 9, 10 and 11. Note that IF Return Loss measurement is a requirement for the ATP.



MODULE D GUNN OSC FREQUENCY VS. TEMP

15 AUG 91, V TO REGULATOR = 15.6V, COUNTER CONNECTED TO TEST MIXER

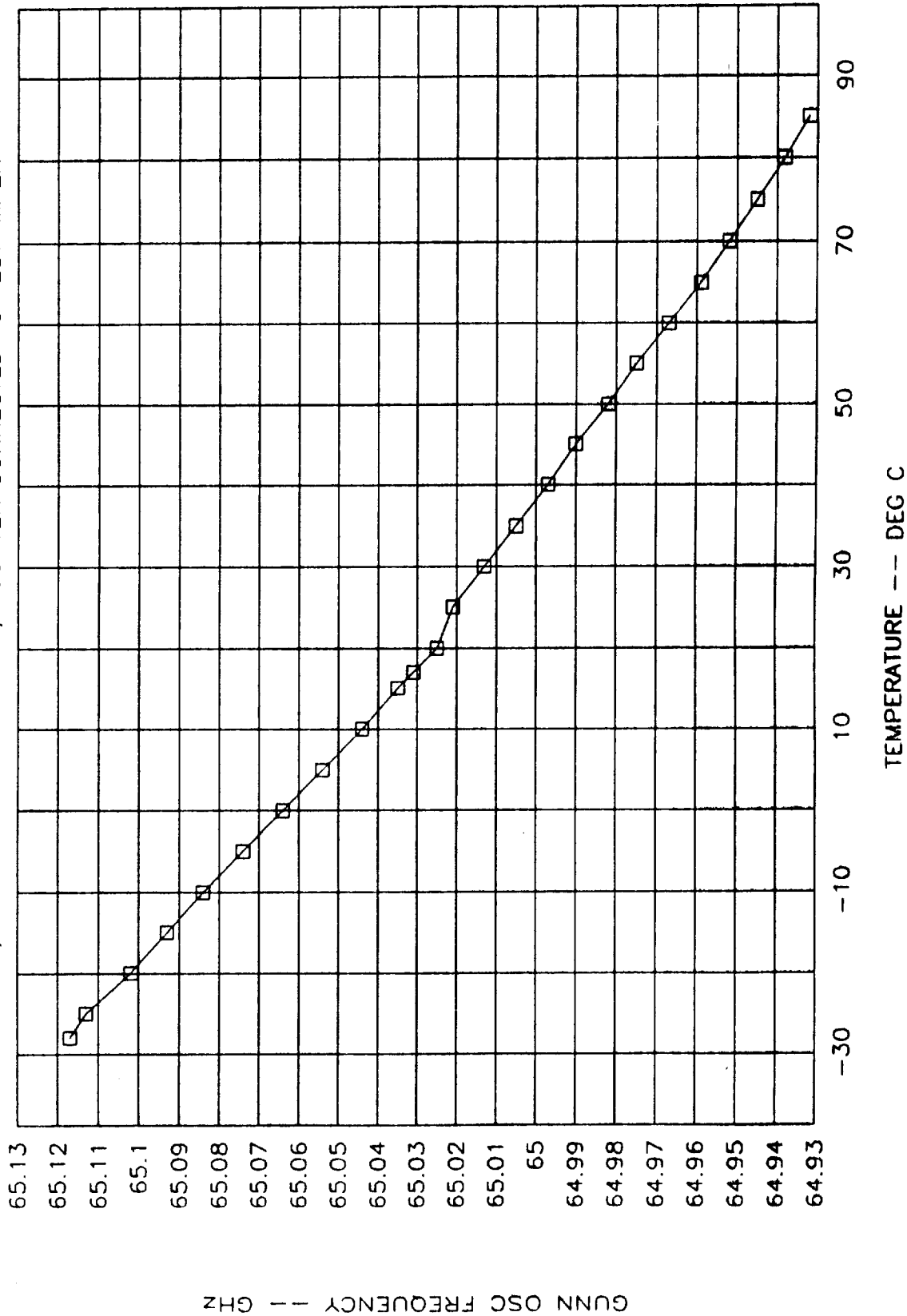
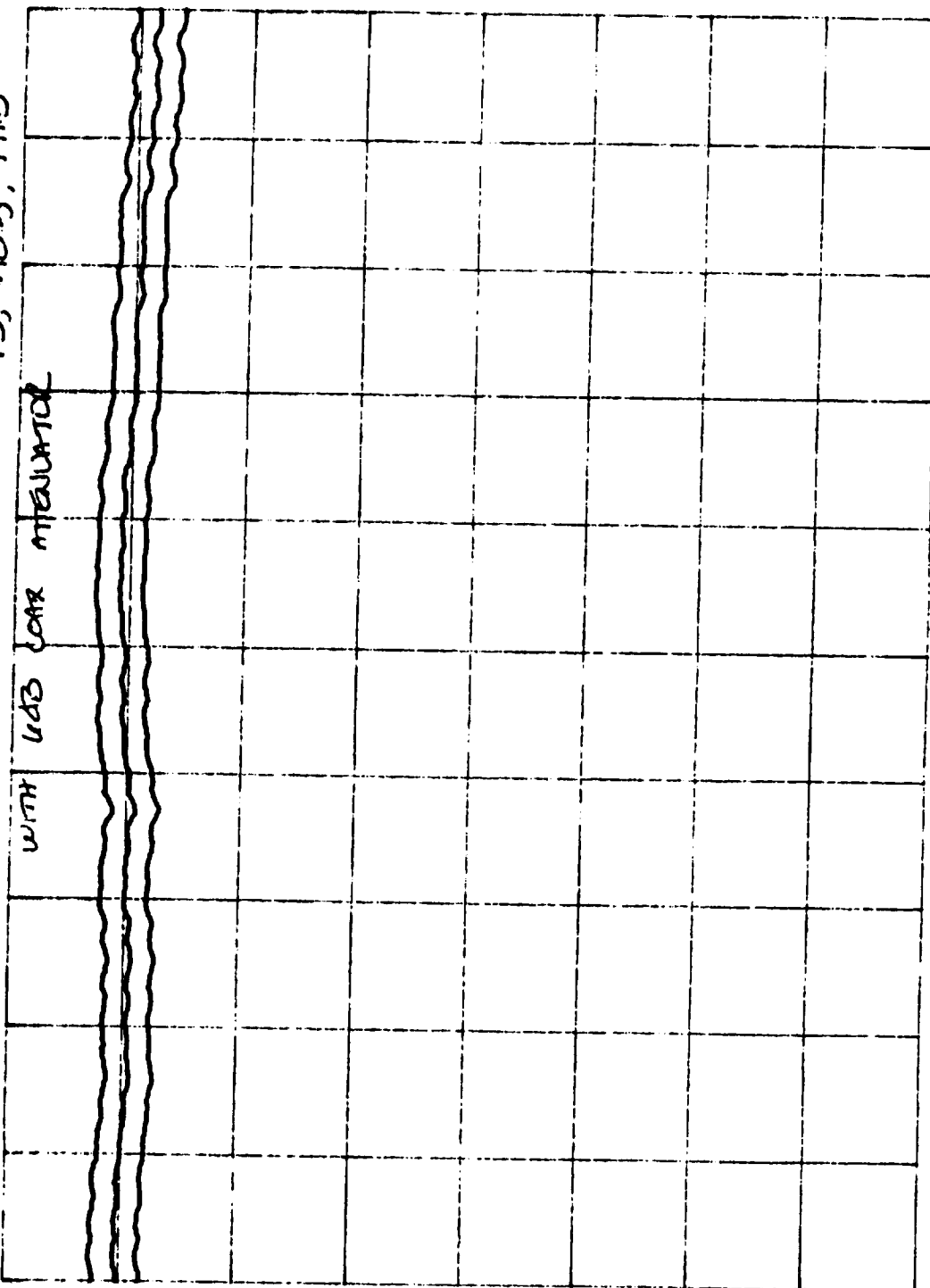


Figure 2

13: 28: 39 AUG 16, 1991 MODULE D TESTING

REF 10.0 dBm ATTEN 20 dB SWEEPER SET TO +9.5, +10.5, +11.5



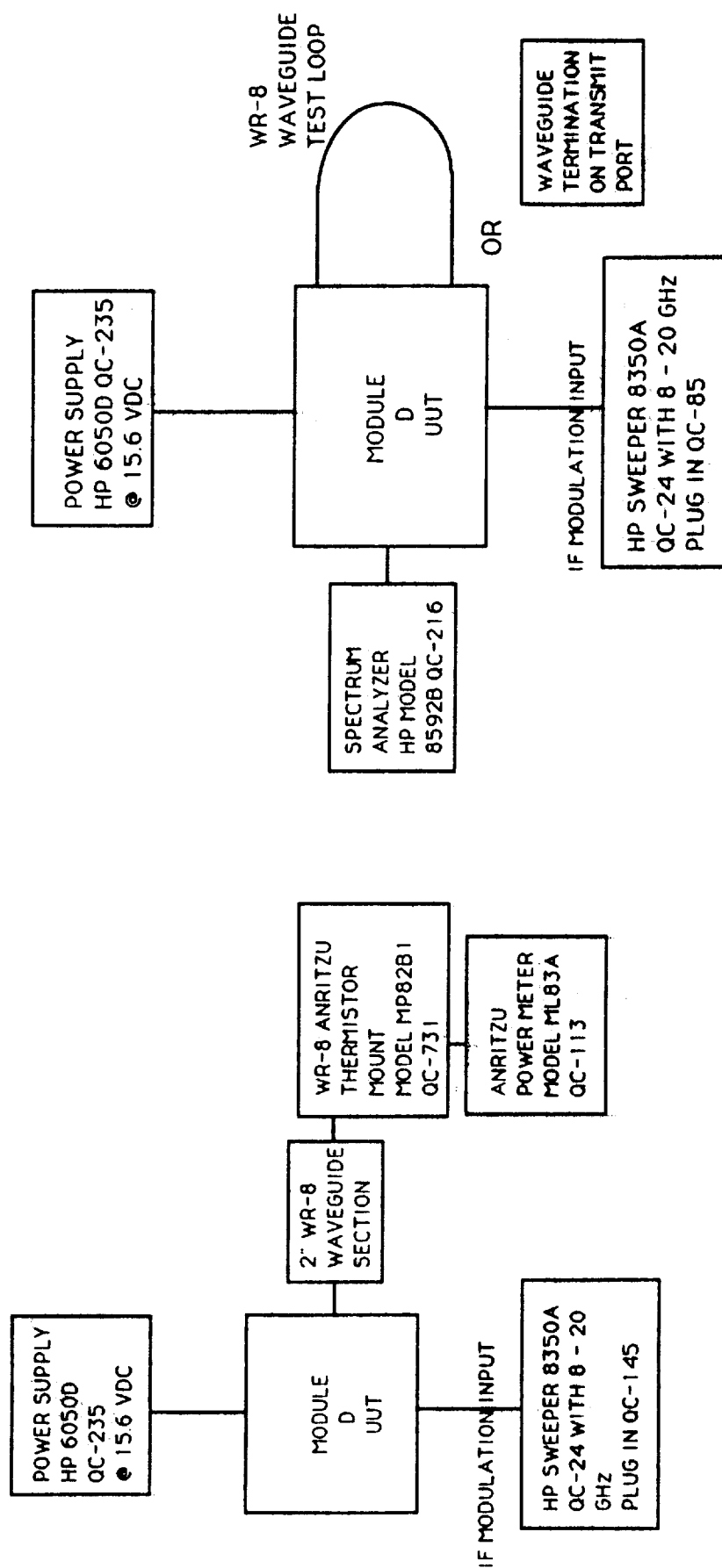
WITH 40dB LOSS ATTENUATOR

PEAK
LOG
5
dB/

MA SB
SC FC
CORR

START 8.000 GHZ
RES BW 3 MHz
STOP 12.000 GHZ
SWP 80 msec

Figure 3



TRANSMIT RF OUTPUT TEST SET-UP

REFERENCE IF AND TEST IF OUTPUT TEST SET-UP

FIGURE 4

MODULE D INTEGRATION TESTING 16 AUGUST 91

RF TRANSMIT OUTPUT POWER VS. RF FREQUENCY, MODULE IN FINAL CONFIGURATION

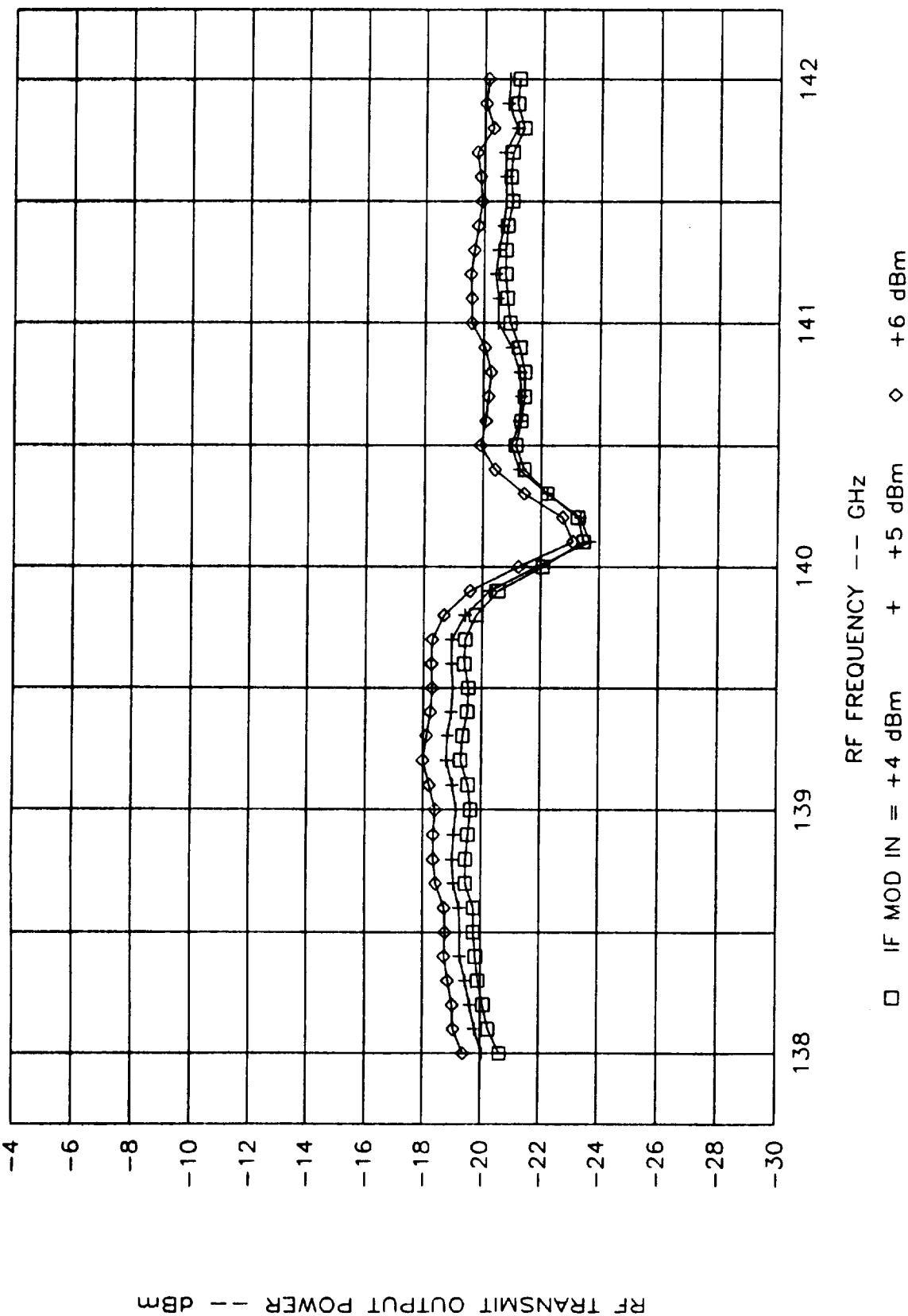
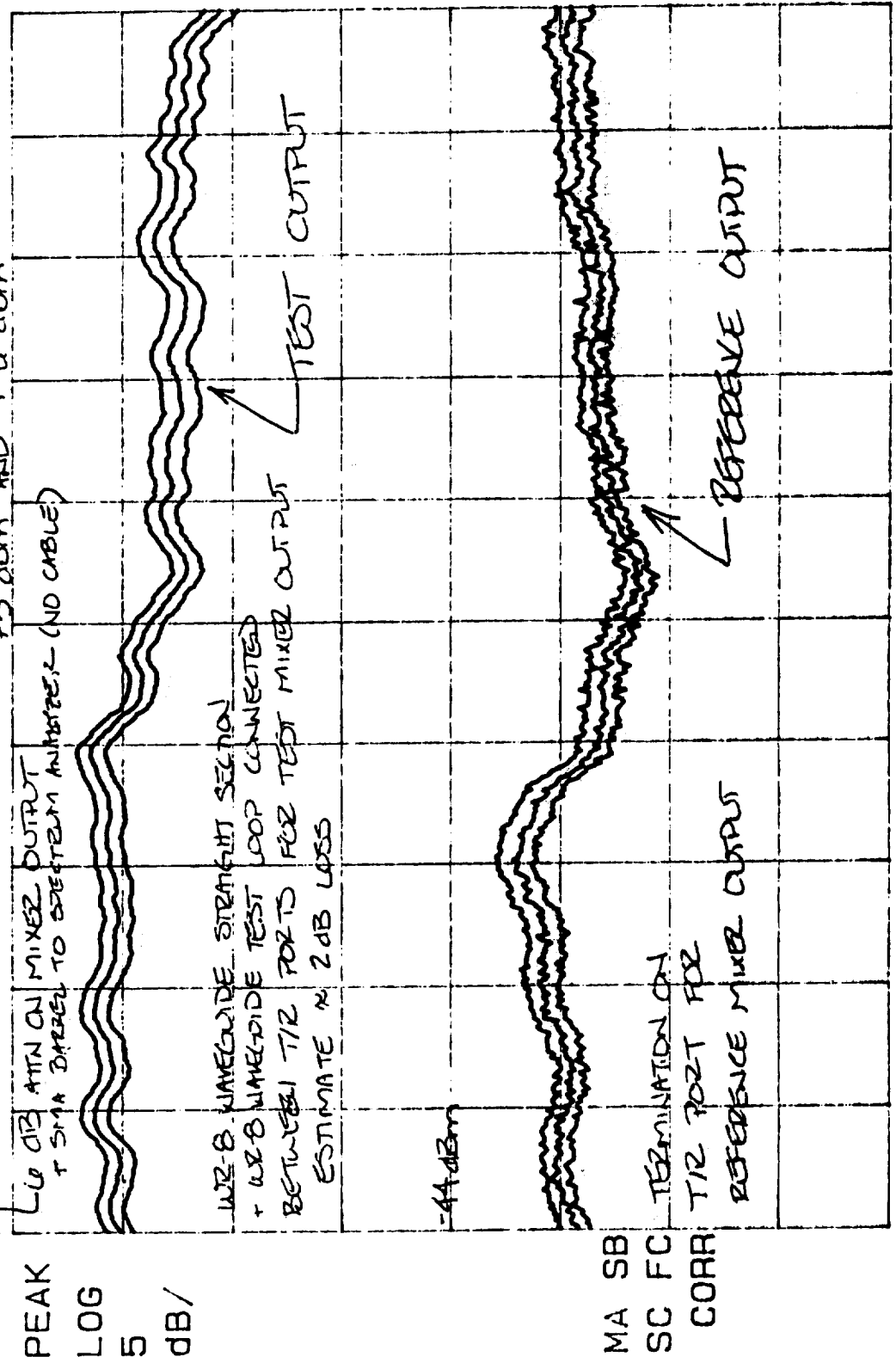


Figure 5

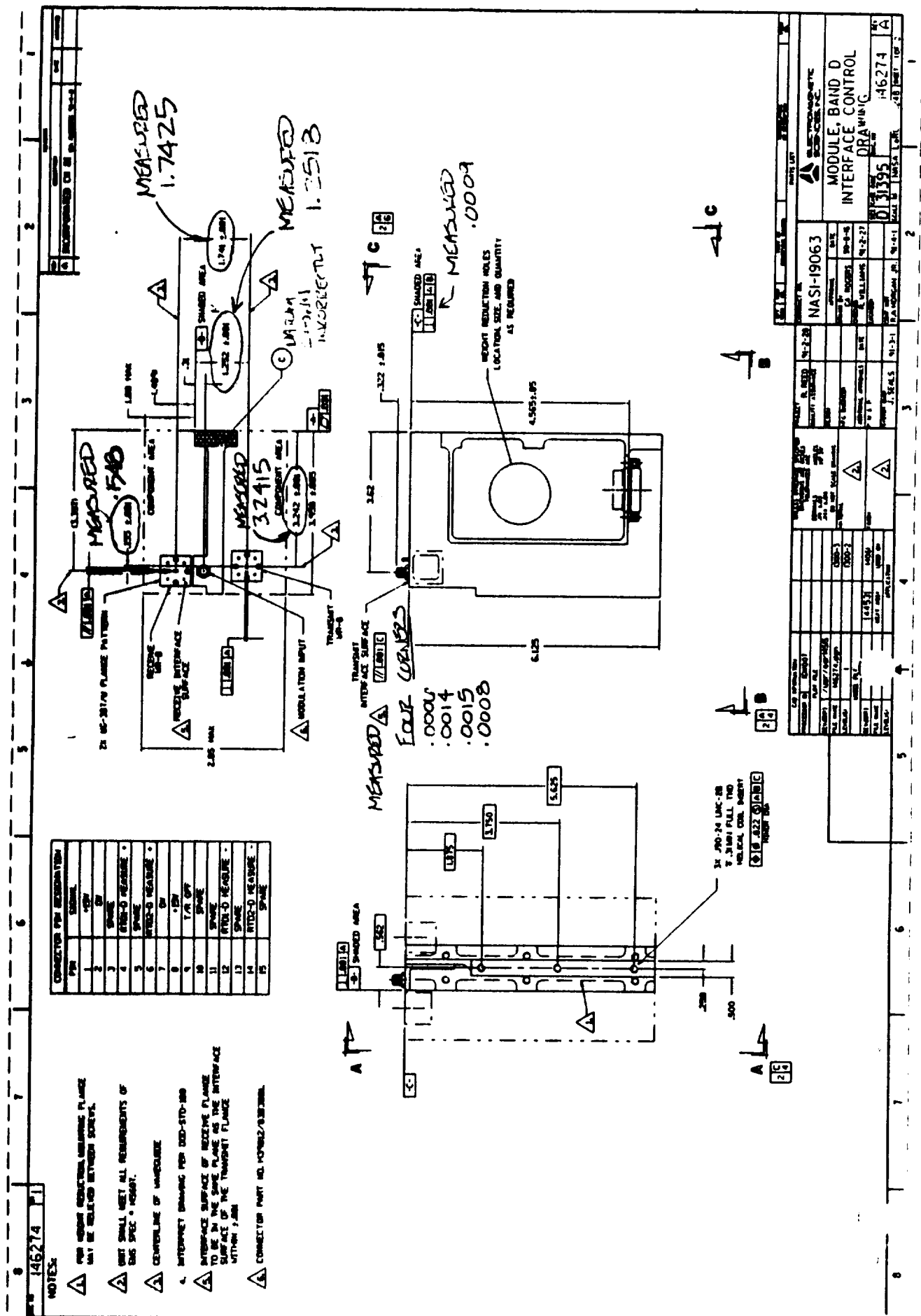
14:20:22 AUG 16. 1991 MODULE D TESTING
 REF -30.0 dBm ATTN 10 dB WITH IF MODULATION INPUT = +4 dBm,
 -24



START 8.000 GHZ STOP 12.000 GHZ
 #RES BW 5 MHZ #VBW 10 KHZ SWP 240 msec

Figure 6

Figure 7



[illegible]

8/19/91

JA - REFERENCE MIXER - IF IMPEDANCE

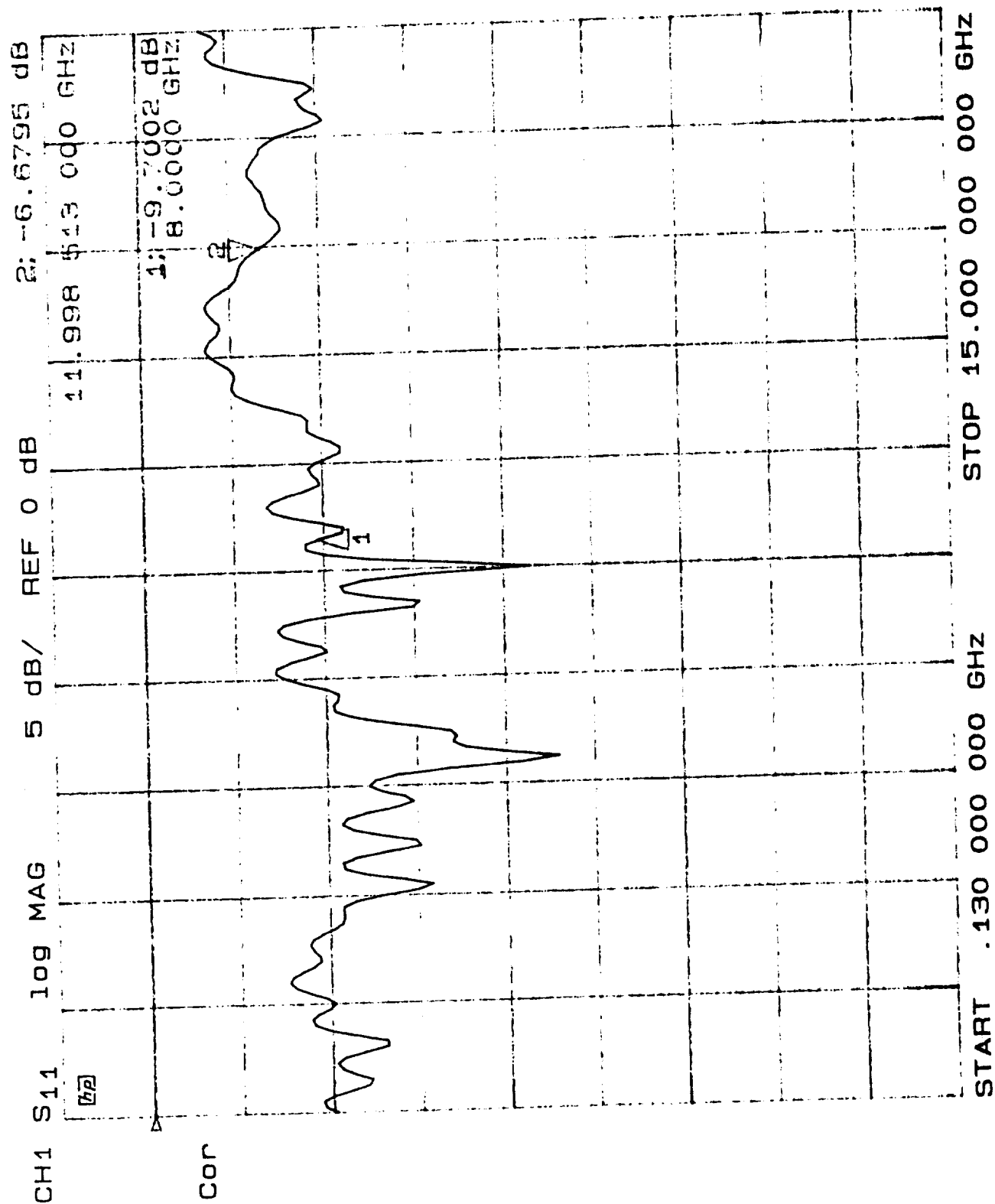


Figure 10

8/19/9

JB - TEST MUEZ - IF IMPEDANCE

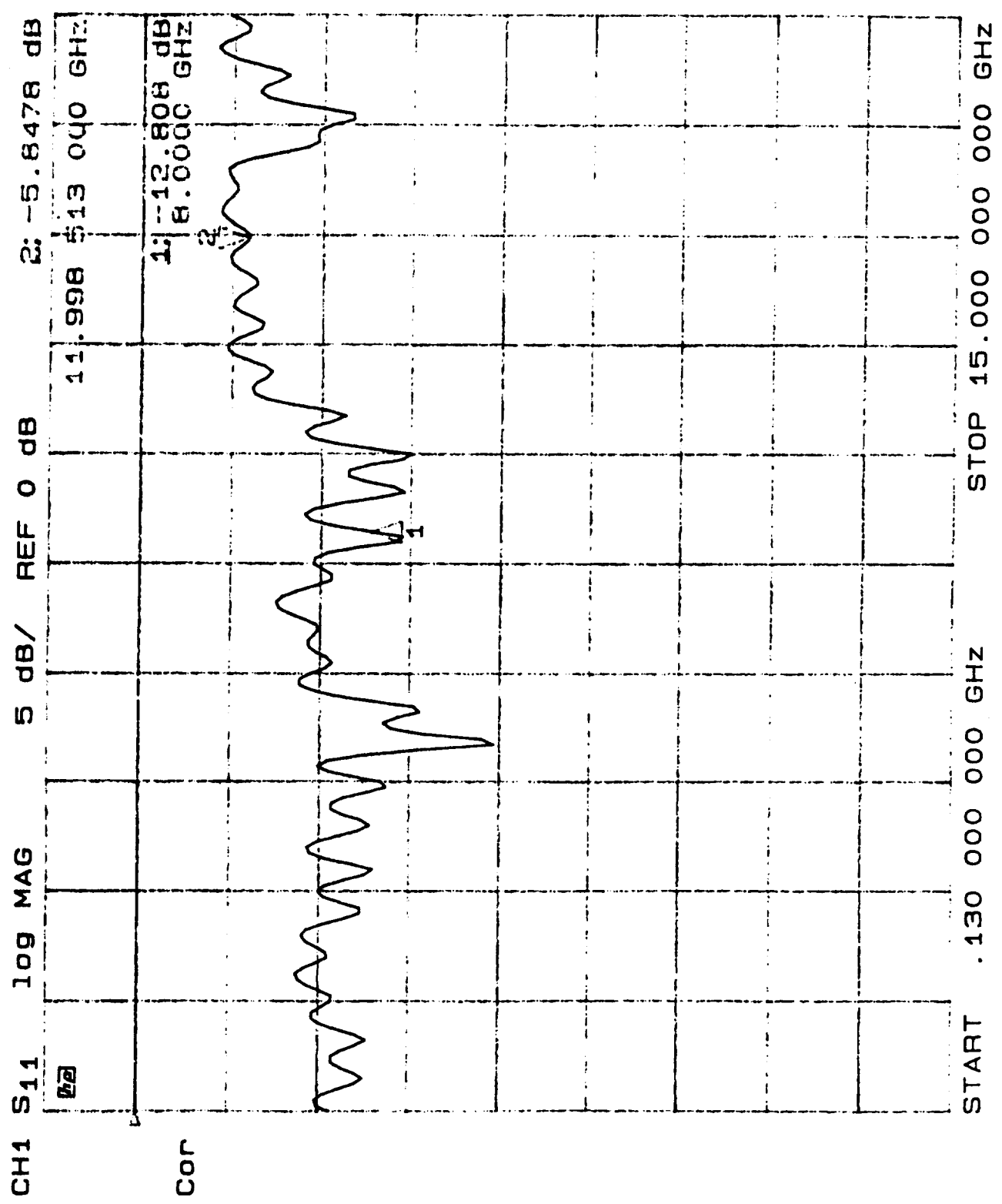


Figure 11

**PRECAUTIONS FOR HANDLING AND OPERATING
MRIS T/R MODULES**

1. **HARDWARE IS STATIC SENSITIVE. USE ESTABLISHED PROCEDURES FOR HANDLING.**

DISCHARGE AND GROUND INTERCONNECTING COAXIAL CABLES BEFORE INSTALLATION TO T/R MODULES.

INSTALL SHORTING CAPS ON THREE SMA CONNECTOR INTERFACES WHEN THESE INTERFACES ARE NOT USED.

2. **DO NOT BEND, DEFORM, NICK, OR SCRATCH SEMI-RIGID COAXIAL CABLING ON T/R MODULES.**
3. **KEEP TRANSMIT AND RECEIVE WAVEGUIDE PORTS COVERED TO PROTECT AGAINST DUST, DEBRIS, AND OTHER CONTAMINATION.**
4. **TO PREVENT DAMAGE TO THREADS ON MECHANICAL INTERFACES, USE CARE IN INSTALLING SCREWS INTO ALUMINUM THREADS ON WAVEGUIDE PORTS OF THE T/R MODULE.**
5. **OBSERVE CORRECT POLARITY AND VOLTAGE LEVELS FOR DC INPUT POWER. CONSULT THE ICD AND/OR THE BLOCK DIAGRAM FOR THE T/R MODULE.**
6. **MAXIMIM SAFE MODULATION INPUT POWER LEVELS. DO NOT EXCEED THE FOLLOWING MAXIMUM RF INPUT POWER LEVELS:**

BAND A MODULE	+ 15 dBm (31 MILLIWATTS) MAX
BAND A MODULE	+ 13 dBm (20 MILLIWATTS) MAX
BAND C MODULE	+ 13 dBm (20 MILLIWATTS) MAX
BAND D MODULE	+ 6 dBm (4 MILLIWATTS) MAX

APPENDIX A2. BAND-D MIXER SUMMARY

**DEVELOPMENT OF MIXERS
FOR BAND D T/R MODULE**

DATE PREPARED: JUNE 9, 1992

SUBCONTRACT NO. S-105515

PREPARED BY

MILLITECH CORPORATION

P.O. BOX 109

SOUTH DEERFIELD RESEARCH PARK

SOUTH DEERFIELD, MA 01373

PREPARED FOR

ELECTROMAGNETIC SCIENCES, INC.

NORCROSS, GA

PREPARED BY: M. Simonutti

M. Simonutti

1. Selection of Operating Center Frequency for Band D T/R Module

Prior to the formal start of the EMS/Millitech portion of the MRIS program, the center frequency of the Band D T/R Module operating band had been tentatively specified as 220 GHz. However, as part of the actual MRIS program effort by these two participants, an analysis for the selection of the optimum frequency for Band D was to be performed. For the Band D module, a frequency as high as 220 GHz was desirable from a science point of view. However, analysis of cost and schedule risk for development of the hardware would be a major factor concerning the final selection of the center frequency. From the outset of the project, it was recognized that the critical item for the Band D module would be the development of a suitable mixer.

For the frequencies of the Band A, B, and C modules, centered at 20, 45, and 94 GHz, respectively, waveguide component technology needed for these modules was already existing prior to the beginning of the project. Development of these three lower frequency modules would consist almost exclusively of frequency scaling of some component designs and packaging and mounting of the set of integrated components within individual T/R Module assemblies.

The situation was different for development of the Band D T/R Module, since waveguide component technology for frequencies above 100 GHz was significantly less mature, particularly with respect to high performance mixers. However, waveguide components other than the mixer could be designed through a relatively straightforward scaling of the dimensions of the components developed for the lower frequency bands. Fabrication of the high frequency waveguide components would be somewhat more costly, however, because the relatively small dimensions, typical of millimeter wave waveguide components in this frequency range, require holding relatively high precision tolerances.

There would be little problem in producing a suitable local oscillator for the Band D module, as long as the operating frequency of the module was kept below the 200 GHz range. This is a consequence of the fact that we planned to develop a mixer for Band D which would be of a X2 sub-harmonically pumped design. For this type of mixer, a relatively conventional Gunn oscillator would suffice since the required output frequency would be below 95 GHz.

Therefore, development of new technology for the Band D module was limited to development of the mixers for the module. Otherwise, the design of the Band D module consisted largely of frequency scaling of designs of conventional millimeter wave components already developed at Millitech, and the task of mechanical packaging of the integrated assembly as be performed for the Band A through C T/R Modules.

2. Selection of Design Approach for the Band D Mixer

The selection of operating frequency for Band D would be a direct and major driving factor on the development of mixer technology for the Band D module. Therefore, the process of selection of operating frequency for the Band D module and the selection of the design approach for the Band D mixer became closely related.

The primary area of business at Millitech is in the design and manufacture of components and systems for the millimeter wave and sub-millimeter wave bands. One of Millitech's areas of specialization in this field is the design and manufacture of mixers for the high frequency portion of the millimeter wave band and beyond to the submillimeter wave range. Millitech has experience in development and manufacture of various types of high frequency mixers.

For the frequency range between 100 and 200 GHz, there are several candidate technologies for development of the Band D mixer. Because of packaging and interface constraints, and the extreme operating environment for the MRIS T/R Modules, we can exclude certain types of mixers which have been demonstrated for this frequency range. Also, we exclude mixers such as quasi-optical designs which are open structures which cannot be readily configured with waveguide ports and in a compact package. We exclude mixers requiring cryogenic cooling.

What remains are essentially three candidate mixer types the Band D module of MRIS:

- 1) Mixers with whisker contacts to a honeycomb diode array chip.
- 2) Mixers using beam-lead diodes.
- 3) Mixers based upon a relatively new, dual-diode array integrated circuit chip developed within a laboratory at the University of Virginia.

A. Candidate 1), Mixers with Whisker Contacted Diodes

Whisker-contacted mixers are widely used for many specialized millimeter wave and sub-millimeter wave applications. This configuration offers lowest parasitic reactances. Consequently, for applications above 100 GHz, this configuration is generally capable of superior performance over all other mixer configurations.

Millitech produces whisker contacted mixers routinely for frequencies from 100 GHz to beyond 500 GHz. With this approach, a 180 GHz mixer with excellent electrical performance could have been produced for the MRIS Band D module. However, whisker contact technology was ruled out for application on MRIS based upon questionable reliability of the exposed, unprotected whisker contacted semiconductor device within the relatively extreme MRIS environmental conditions of high temperature, shock and vibration.

B. Candidate 2), Mixers Using Beam-Lead Diodes.

Waveguide mixers utilizing beam-lead diodes are commonly employed for millimeter wave frequencies up to about 100 GHz. Beam-lead diode mixers, in various design implementations, are fabricated at many laboratories throughout the world. A critical component of this type of mixer, the beam-lead diode semiconductor devices, are available commercially from several companies for application up to about 100 GHz.

Beam-lead diode mixers for the millimeter wave range have become one of Millitech's most popular products. Millitech has a unique design for its beam-lead diode mixers. This design offers what is probably the best electrical performance among beam-lead diode mixers within the industry. It is also one of the most rugged under conditions of shock, vibration, and temperature. This excellent performance under environmental conditions is a consequence of a simple, highly functional mechanical design which employs no soft dielectrics, and no epoxies or other organic materials. In these mixers, Millitech generally employs beam-lead diodes procured from Marconi, since those devices offer best electrical performance, as well as best reliability and ruggedness. To date, Millitech has delivered approximately one thousand such mixers for frequencies between 20 and 100 GHz.

We selected the general beam-lead diode mixer configuration for the initial development of the Band D mixer. Our approach was to extend, through a

development effort on MRIS, the upper frequency range of our design to approximately 140 GHz. The Marconi beam-lead diode which we proposed to use was physically the same device used for most of Millitech's beam lead diode mixers, but for flight hardware we would employ the high-rel screened version offered by Marconi.

We considered development of a 140 GHz beam-lead mixer for Band D a reasonable objective consistent with the budget and schedule constraints of the MRIS project. This implied the selection of a center frequency of 140 GHz for the Band D module. This frequency would provide useful science data for the mission.

C. Candidate 3), Mixers Based Upon New U of Va Mixer Diode IC

At the beginning of the MRIS project, we ruled out developing a mixer based upon a relatively new, dual-diode array integrated circuit chip developed by the University of Virginia. Although reports of its performance were highly favorable, the device was relatively new, and expensive. We wished to avoid development of an approach based upon a semiconductor device which was relatively unproven in field applications.

For the MRIS Band D mixer, we began development of a unit which was to be based upon Millitech's rugged design utilizing beam-lead diodes. We selected an RF center frequency for the mixer, and therefore for the Band D module, of 140 GHz. 140 GHz represented a reasonable limit to extend this basic beam-lead diode approach from the previous limit of approximately 100 GHz. The significant factor limiting the upper frequency range of this type of configuration is the parasitic resistance and capacitance of the beam-lead mixer diodes. We utilize, in our mixers at Millitech, those beam-lead diodes which are generally available in the industry and which have the highest cutoff frequency, i.e., minimum parasitics. These same diodes were identified for the 140 GHz unit which we would develop.

While Millitech's standard beam-lead diode mixers for the millimeter wave frequencies up to 100 GHz operate in a fundamental mode, for the Band D mixer to be developed, we proposed X2 sub-harmonic operation. In this case, the applied local oscillator signal would be at precisely one-half the effective local oscillator frequency. The nonlinear response of the mixer diodes would create an effective doubling of the local oscillator input signal frequency. This sub-harmonic approach is commonly utilized

in high frequency mixer design. For MRIS, it facilitates the realization of a local oscillator signal source, and little would be sacrificed in terms of mixer conversion loss.

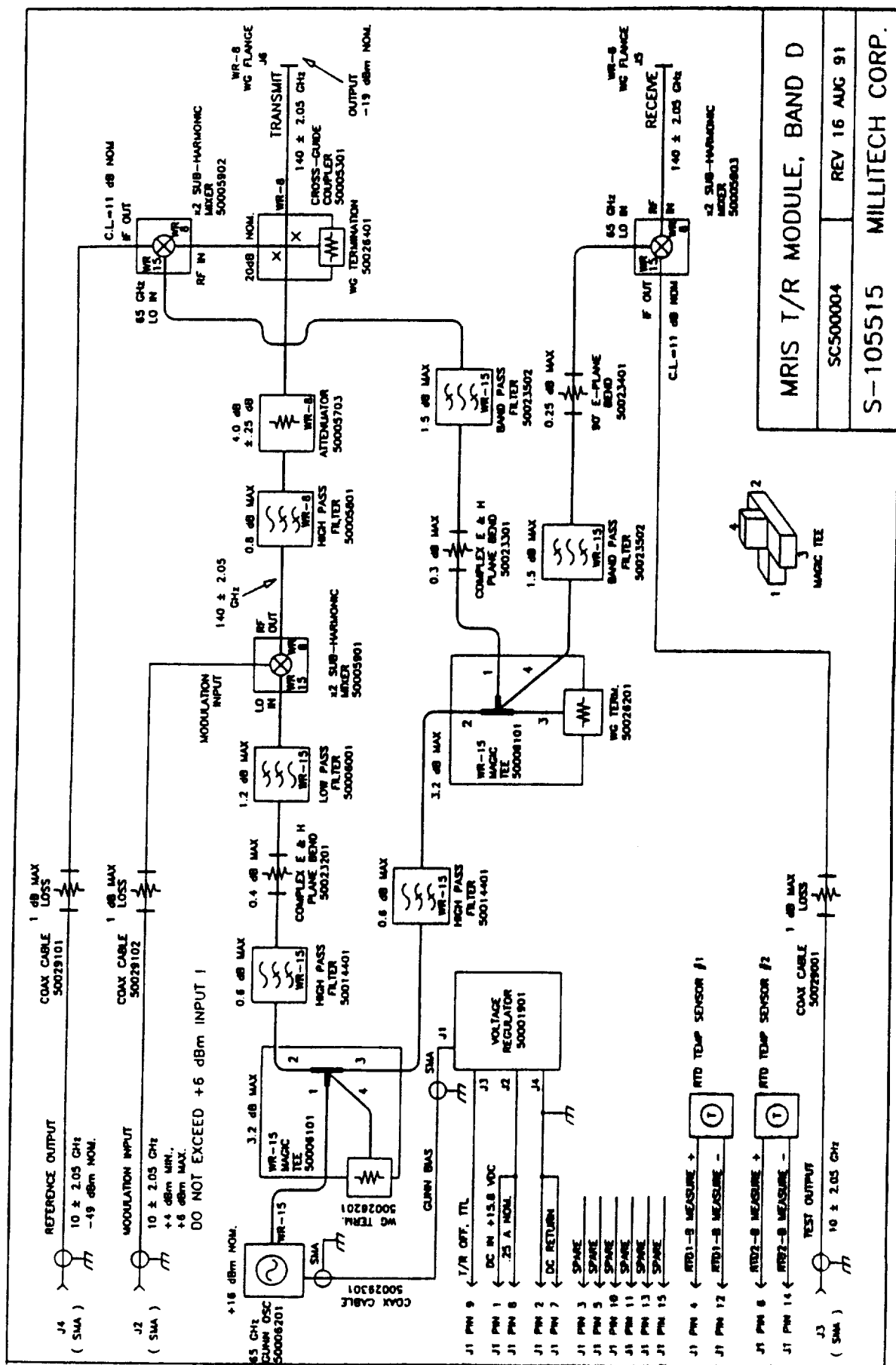
For a 140 GHz center frequency fundamental mode mixer on MRIS, instead of a sub-harmonic design, we would require, an effective local oscillator (LO) frequency of 130 GHz. The tens of milliwatts power level which would be required to drive the three mixers is beyond the capability of a conventional Gunn oscillator, and out of range for essentially any other practical solid state local oscillator power source which would be sufficiently compact and of sufficiently low power consumption for MRIS. However, the 65 GHz LO frequency requirement for a 140 GHz mixer of sub-harmonic design is well within the range of indium phosphide Gunn oscillator technology. We utilize, also, Indium phosphide gunn local oscillators on the Band A through C T/R Modules on MRIS.

3. Application of Mixers on the Band D T/R Module

The configuration of the mixers and the local oscillator on the Band D module is indicated in Figure 1, the block diagram for the Band D T/R Module. Overall, the T/R Module consists of a somewhat complex configuration of millimeter wave waveguide components integrated and mounted on a lightweight, rugged mounting structure.

For the Band D module, two different waveguide band sizes are employed. WR-15 size waveguide is utilized for the generation and distribution of the fixed frequency 65 GHz local oscillator signal. WR-8 size waveguide is utilized for the processing of the RF transmit and receive signals which extend over the 138 to 142 GHz band. Note that the mixers have one waveguide port at each of these two waveguide bands, plus a coax port for the 8 to 12 GHz modulation input and IF output frequency band. The various low-pass, band-pass, and high-pass waveguide filters are included to suppress spurious responses within the transmit/receive function of the complete module.

In their mode of operation on the Band D T/R Module, one of the three mixers is used for the generation of the transmit signal through the conventional up-conversion application of a mixer, while the other two mixers are operated as receivers, functioning in the down-conversion mode. In general, the same mixer hardware can



serve both functions of up-conversion and down-conversion. Except for the sub-harmonic mode of operation of the mixers instead of the fundamental mode, this general block diagram design of the Band D T/R Module is identical on the Bands B and C T/R Modules for MRIS.

4. Analytical Design for the Sub-Harmonic Beam-Lead Diode Mixer for 140 GHz

Our approach for development of the Band D mixer for MRIS was to use as a starting point our 94 GHz beam-lead diode mixer which is of a mature design. We would perform analytical design work to extend this design to 140 GHz. This effort would be more than a simple scaling of dimensions of the 94 GHz design to 140 GHz. The circuit model for the diode is relatively complex and is frequency dependent in a manner which demands careful analytical modeling. Therefore, the details of the waveguide and coaxial matching sections within the mixer will differ from a simple scaling of dimensions from a lower frequency design. The sub-harmonic LO feature of the mixer requires slightly different analytical treatment from our standard beam-lead diode fundamental mode mixers.

This analytical design effort for the MRIS Band D mixer was performed utilizing microwave circuit design software as an important design tool. We utilized the Touchstone software package from EEsof Corporation. This is the same basic design approach used on essentially all of Millitech's millimeter wave and sub-millimeter wave mixers. We enter within our computer model of the mixer our lumped element models for the mixer diode, coupled with detailed modeling of various coaxial and waveguide matching sections within the mixer. A considerable level of iteration is employed, along with optimization routines contained within the microwave design analysis software package. The objective in this design effort is to produce an appropriate set of physical dimensions for the mixer features which provides suitable impedance match at the RF and LO waveguide ports of the mixer, over the required frequency bandwidth.

From the analytical design effort, we obtained the dimensions of the various waveguide and coaxial section electrical features of the mixer. In general, waveguide and coax sections included stepped transformer sections, with each step approximately one-quarter wavelength in length. These steps provide impedance matching and/or filtering in different regions of the mixer.

5. Mechanical Design of Band D Mixer

Those dimensions related to electrical performance which were obtained from this analytical design effort were then taken and incorporated in to a complete set of detailed mechanical design drawings which would be used for fabrication of the actual mixer component hardware. This hardware includes integral waveguide flanges for the RF and LO ports, and coaxial connector for the IF port. Figure 2 is a photographs of the hardware parts of the Band D mixer. This photo also shows hardware, which is similar appearance, for the mixers of the Band A through C modules.

The mixer housing was designed from aluminum as the basic material. Gold plating, with zinc and nickel underplate over the aluminum base material, was the finish selected for corrosion resistance and good conductivity. The complex machined-in waveguide and coaxial section features are realized using Millitech's standard split-block construction. The mixer housing is actually machined in separate halves from two blocks to allow machining of complex internal details by conventional machining methods. Then the two blocks are clamped together with screws, and the final external features of the mixer are machined in. The general external appearance of this mixer is similar to that of most of Millitech's beam lead mixer designs for the lower frequency waveguide bands.

6. Unacceptable Performance of Beam Lead Mixer Design for Band D

At Millitech we fabricated a complete set of hardware for a prototype unit for the Band D mixer. We assembled the parts and bonded in the pair of high frequency beam-lead diodes procured from Marconi. These diodes are of the same part number as used in the mixers for the three lower frequency T/R Modules. For the flight hardware, we would procure these devices to a specification requiring screening for hi-rel.

We obtained consistently poor performance from this design configuration based on the beam-lead diode approach. We focused on studying various sections of the mixer, and it appeared that matching of the LO port was a significant problem. Also, conversion loss was always high, greater than 20 dB. It seemed that there were several problems present together, and our efforts at identifying and isolating each were generally unsuccessful. Possibly, our analytic circuit model for the mixer diode used in the computer design task was inadequate.

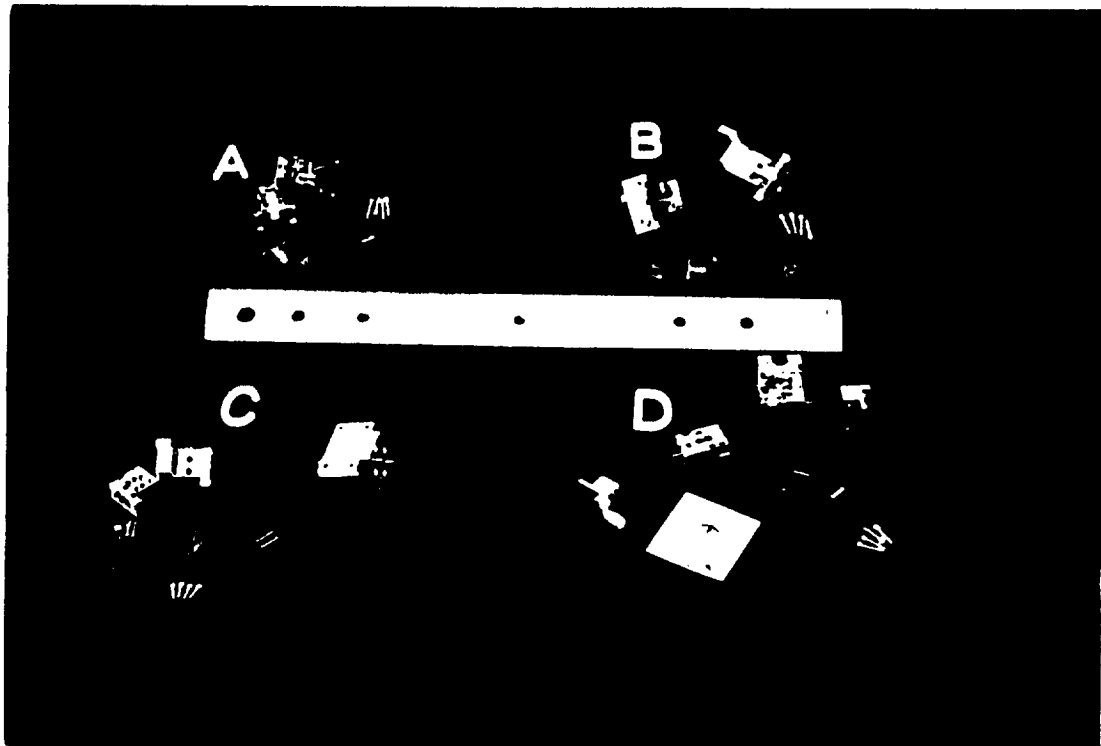


Figure 2
Dis-assembled Housings for Mixers,
Bands A through D

At Millitech, we decided that the beam lead diode approach for the MRIS Band D mixer should be abandoned, based upon our inability to achieve indication of achieving useable performance from that design approach.

7. Concept for Adaptation of Band D Mixer Hardware for the U of Va Dual Diode Chip

Considering the schedule delay encountered from the unsuccessful initial development effort for the Band D mixer, we sought a solution by which, ideally, we could utilize the existing mixer housing hardware with minimal modification, but by which we could replace the beam-lead diode pair with an alternate semiconductor device. Fortunately, we identified an approach which could potentially satisfy these requirements.

Millitech engineering personnel were aware of a highly specialized mixer diode device which was developed within a laboratory at the University of Virginia. This was an integrated circuit, anti-parallel pair dual-diode leadless chip developed especially for mixers which are to operate at the higher end of the millimeter wave band, that is, above about 100 GHz. Figure 3 is a scale dimensioned drawing of this semiconductor device. Note that a relatively large portion of the top surface area of this chip consists of the two gold bonding pads, one toward each of the two ends of the chip.

An important factor concerning this dual-diode IC chip is cost. For the standard unit, which is supplied with essentially no screening other than one-time evaluation of basic DC parameters by the supplier, University of Virginia, the price to Millitech was \$2000 each.

Note the extremely small size of this dual diode chip as indicated by the dimensions in the figure. Small size, along the absence of any packaging or glass passivation which is an integral part of a beam-lead device, and the absence of leads, results in extremely low parasitic reactances. Also, the two mixer diodes included on this chip are designed for small cross-sectional area, and therefore, low capacitance. These properties are well suited for our application at 140 GHz, and we believed that there would be low technical risk with a new approach based upon use of this two-diode array chip.

We implemented a very simple approach for mounting this leadless mixer diode chip into our existing mixer housing hardware which was previously designed for the beam-

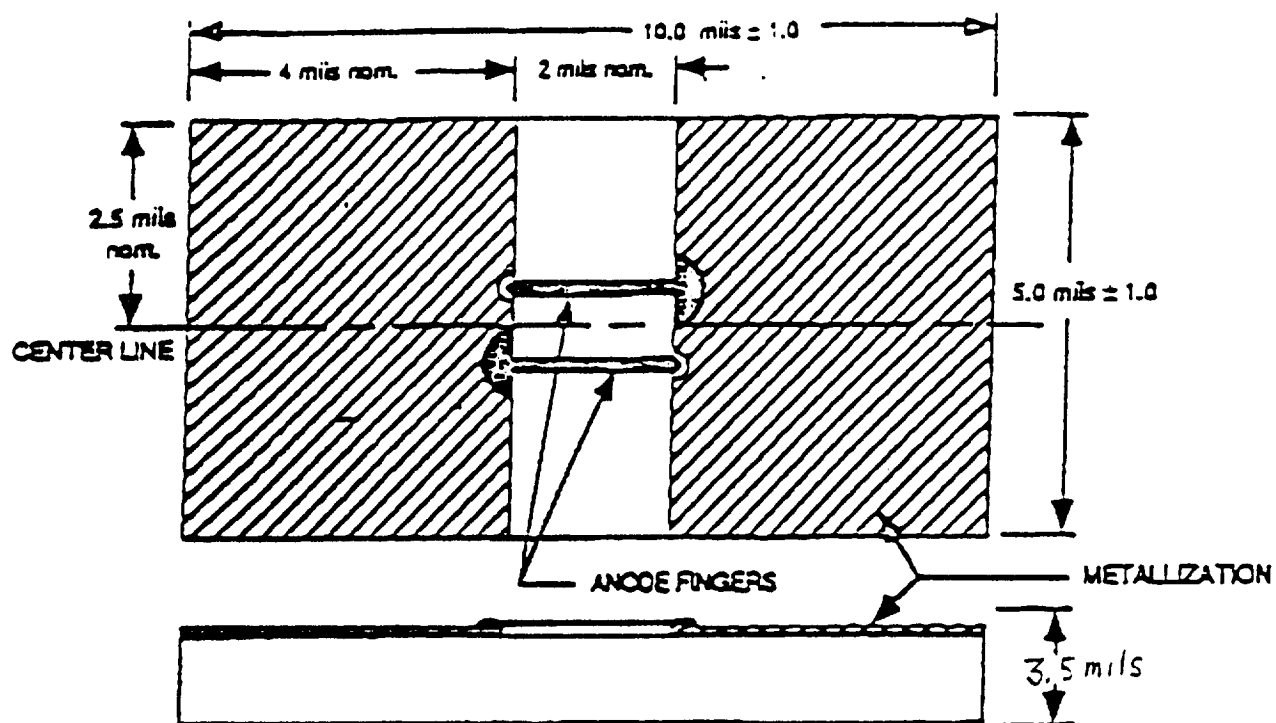


Figure 3
 Scale Drawing
 U. of Va Dual Diode Array Mixer IC

lead diode pair. Using conducting epoxy we would bond the two electrode pads, which are located at opposite ends of the diode chip, to the two metallic regions of the mixer where previously one of the two beam-lead mixer diodes would be mounted. The central portion of the diode chip in which the active devices are located would be suspended within the air gap in the mixer between the two electrodes. This configuration is illustrated in Figure 4. Note that a moderate curve was added to the center conductor pin to provide optimum spacing.

With this mounting scheme for the diode chip, the position where the other beam-lead mixer diode would have been located would be left vacant. We anticipated that this design should provide the required electrical performance while requiring minimal changes to existing hardware previously designed and fabricated for the beam-lead diode approach. We found it necessary to machine a small notch for height clearance of the 4-mil thick dual-diode chip which was bonded into a region originally dimensioned to clear the 1-mil thick gold beam leads of the beam-lead mixer diodes.

An initial order for several of these dual-diode mixer chips was placed with University of Virginia, and the first device was installed into one set of mixer hardware for initial evaluation. As with any significantly new mixer design, it was necessary with this initial assembly unit to perform the usual optimization of local oscillator power level and of tuning of a sliding waveguide backshort designed into the RF signal waveguide within the mixer body. Also, a level of development, including debugging, optimization, and calibration was required to assemble a test station to allow for meaningful comprehensive testing of the Band D mixer.

8. Test Setup for Characterization and Development Testing of Band D Mixer

Figure 5 is a block diagram describing the setup developed for most of the RF testing performed in development of the Band D mixer. As the diagram indicates, the setup includes various components of waveguide hardware for the WR-15 and WR-8 bands, millimeter wave power meters with power sensor heads for the WR-15 and WR-8 bands, a microwave power meter with coax head for measuring the 8-12 GHz IF signal levels, a microwave spectrum analyzer for characterizing the 8-12 GHz IF signals including the desired signal and spurious products, and a sweep generator for producing an 8-12 GHz modulation input signal for tests where the mixer was to be evaluated as an up-converter.

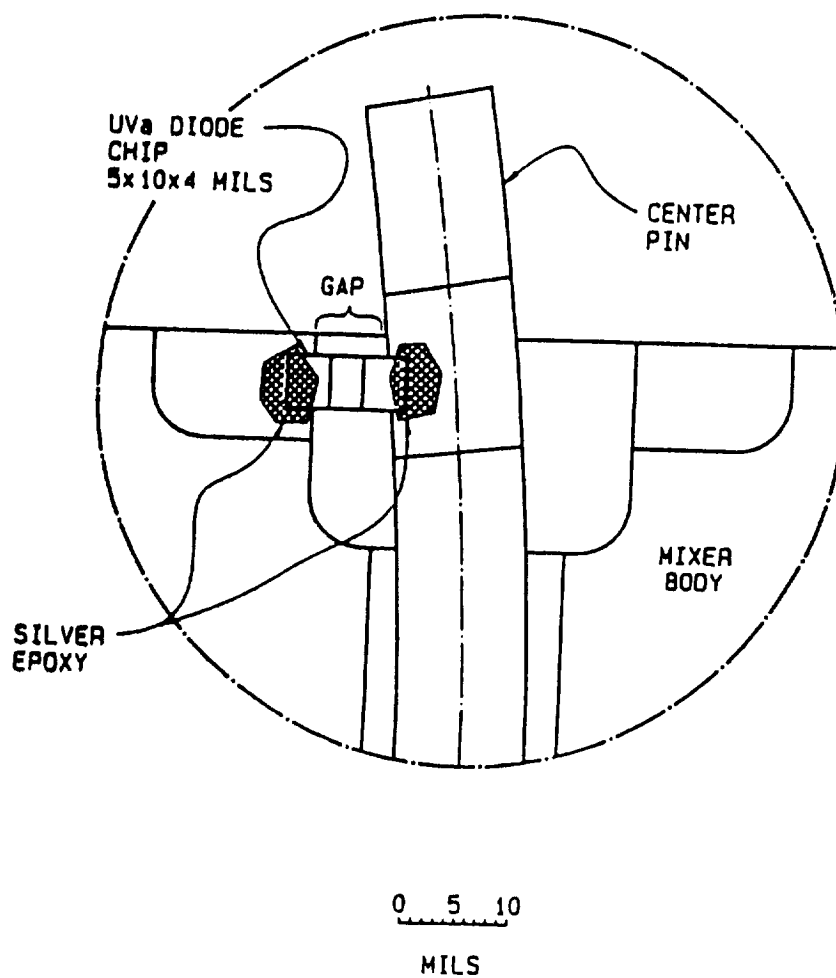
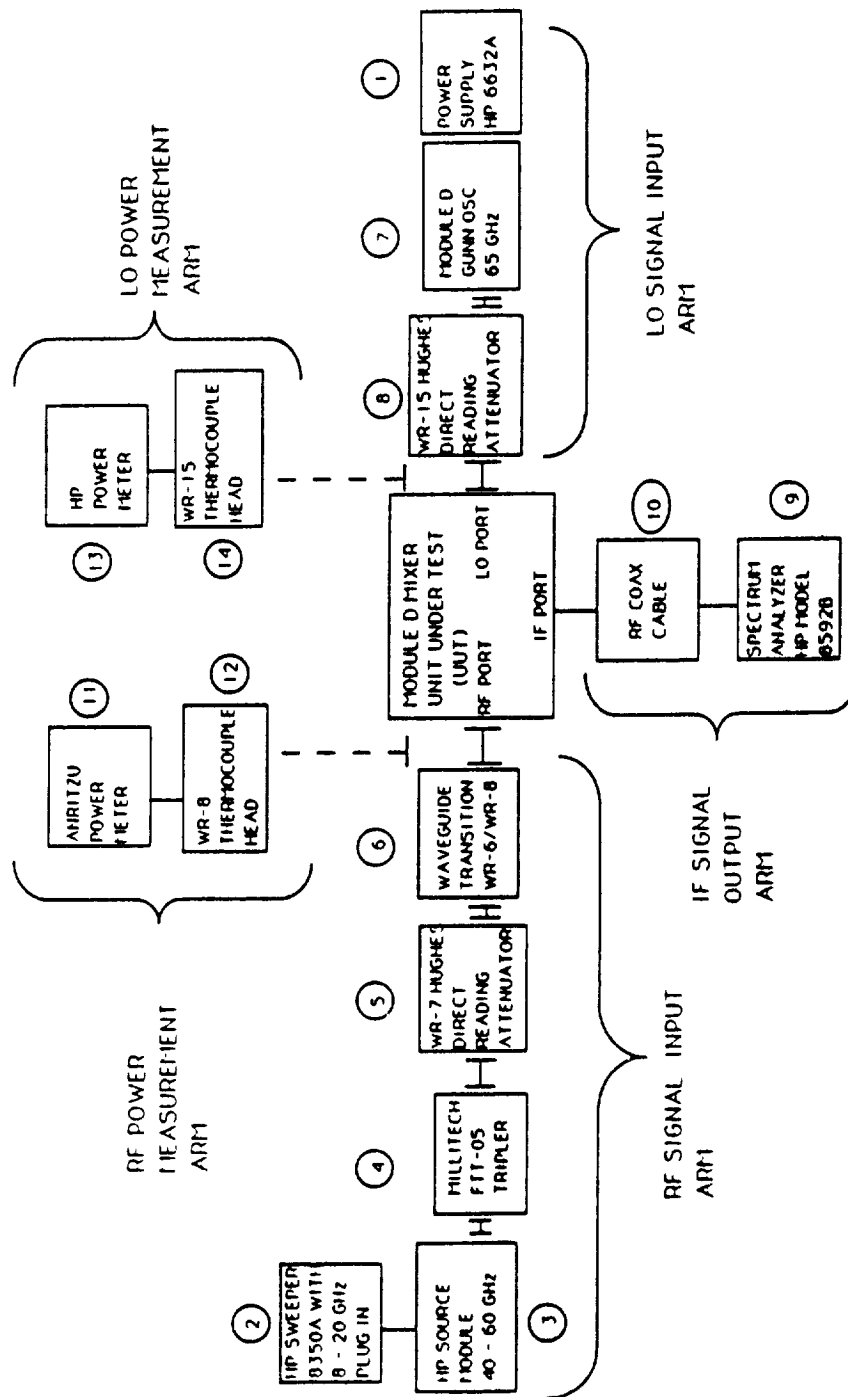


Figure 4
Method of Mounting U. of Va Dual Diode
Array Chip into Mixer



TEST CONFIGURATION FOR BAND D MIXER
DOWNCONVERTER/UPCONVERTER EVALUATION

Figure 5

Our source for the 65 GHz LO signal into the Band D mixer was the 65 GHz Gunn oscillator which we developed for the Band D module. For purposes of mixer development, we used a variable lab attenuator between this Gunn oscillator and the mixer under test to allow a means adjusting the level of LO input power to the mixer LO port. This configuration limited our LO signal to a single frequency, that for which the T/R Module is designed.

For evaluation of the Band D mixer in the down-converter or receiver mode, we step the RF input frequency manually in 0.5 GHz steps from 138 to 142 GHz. This RF input signal was derived beginning with a 2 to 20 GHz Hewlett Packard microwave sweep generator driving a Hewlett Packard millimeter wave multiplier head capable of covering the 40 to 60 GHz band. The output from this unit was then followed by a frequency tripler of Millitech standard design to generate the 138 to 142 GHz range RF input signal for mixer testing.

Generally, for best accuracy, data was taken manually and point-by-point. In the case of down-converter, or receiver, mode of operation of the mixer, for each frequency step, IF power levels were read off of the display of a calibrated 0 to 20 GHz microwave spectrum analyzer. In the case of up-converter mode operation, RF output power levels were read point-by-point from a WR-8 waveguide band thermocouple based power meter with high resolution digital readout. In either case, input frequency was stepped in fixed frequency increments over the 4 GHz operating band. This provides us with point-by-point data from which we produced plots of conversion loss versus RF frequency. Generally, we would enter sets of point-by-point data into a computer for data analysis and graphic plotting.

This mixer, like other x2 sub-harmonic mixers of this type, produces a relatively high level of spurious output signal which is a x3 multiplication of the local oscillator input power signal. This 195 GHz output would have essentially no impact on the functioning of the T/R Module. For the nominal LO drive level which produces best conversion loss in this mixer, we determined through measurement that this Band D mixer configuration produces a x3 LO frequency component, at 195 GHz in our case, of approximately 6 micro-watts, or -22 dBm power level. This spurious signal power, if left unaccounted for, would add a large error term in the measurement of RF output power generated by the mixer in the up-converter mode of operation, since the thermocouple power meter responds to this frequency.

This same 195 GHz signal is present emanating from this port in the down-converter mode, but output power is generally not measured from that port when the mixer is operated in the down-converter mode. We did not have available a waveguide low-pass filter for this waveguide band and frequency range. Therefore, this offset power level was subtracted out from the raw data when making measurements of conversion loss in the up-converter mode.

With this test configuration, we were able to make an accurate initial assessment of the potential performance of this revised configuration for the Band D mixer, that is, with the U of Va dual diode array chip installed to replace the beam-lead diode pair.

9. Favorable Initial Performance Achieved with Mixer Operated in Down-Conv. Mode

Initial performance achieved, as evaluated through measurement of conversion loss of the mixer in the down-convert mode, was favorable. Approximately 11 dB maximum conversion loss with ± 0.5 dB flatness across the 138 to 142 GHz frequency band was achieved initially. Figure 6 shows the conversion loss versus frequency, for several LO power levels, for one of the early mixer assemblies using the new U of Va diodes. Two additional mixers were assembled with these diode chips, and their initial performance was comparable. This demonstrated performance of the mixers in the down-converter mode was acceptable for MRIS. Of particular note was that this favorable and repeatable performance was achieved early on in our effort based on using this new mixer diode.

The optimum LO and modulation input power levels to this mixer were determined. For down-converter operation, +10 dBm 65 GHz LO drive was optimum. For up-converter operation, +12.9 dBm 65 GHz LO drive was optimum. Also, in the up-converter mode, +5 dBm of 8 to 12 GHz modulation input power level is optimum.

10. Deficiency in Performance of Initial Config. of Mixer when Run as Up-Converter

While the performance of the mixer, as initially evaluated as a down-converter, was highly encouraging, when the mixer was evaluated for operation in the up-converter mode, a significant problem was indicated. A lack of flatness in the plot of conversion loss versus frequency was displayed. This was in the form of a pair of narrow dips near the center of the operating band. The plot shown in Figure 7 is an example of

BAND D MIXER T/R MODULES MILLITECH

S/N 168. W/UV α 2-DIODE CHIP ARRAY. PRE-VIB, NEW DIODE 20 APR 91, RF TEST 22 APR 91, -17dBm RF IN

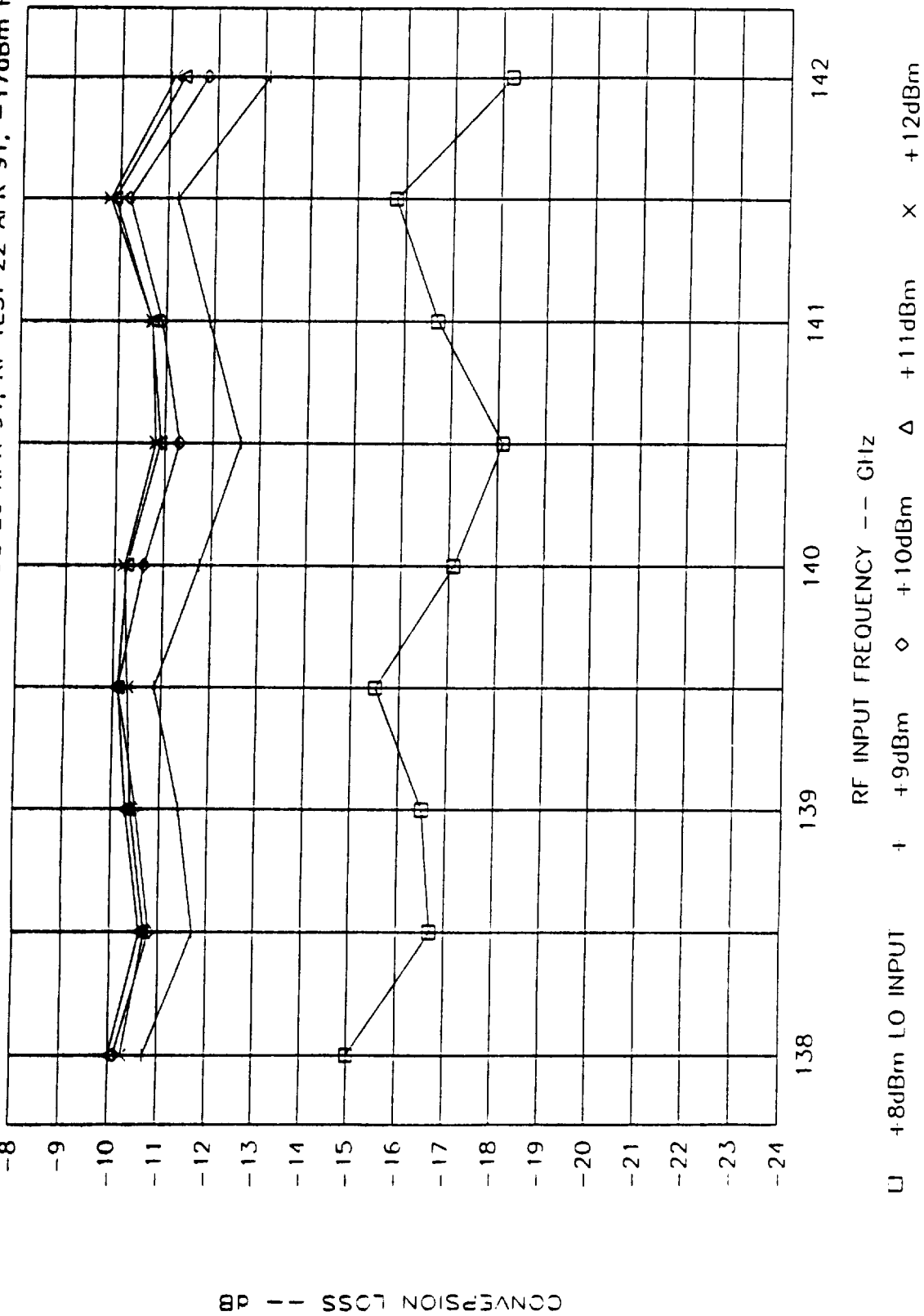


Figure 6
Band D Mixer Performance,
Down-converter Mode

MODULE D INTEGRATION TESTING 3 JULY 91

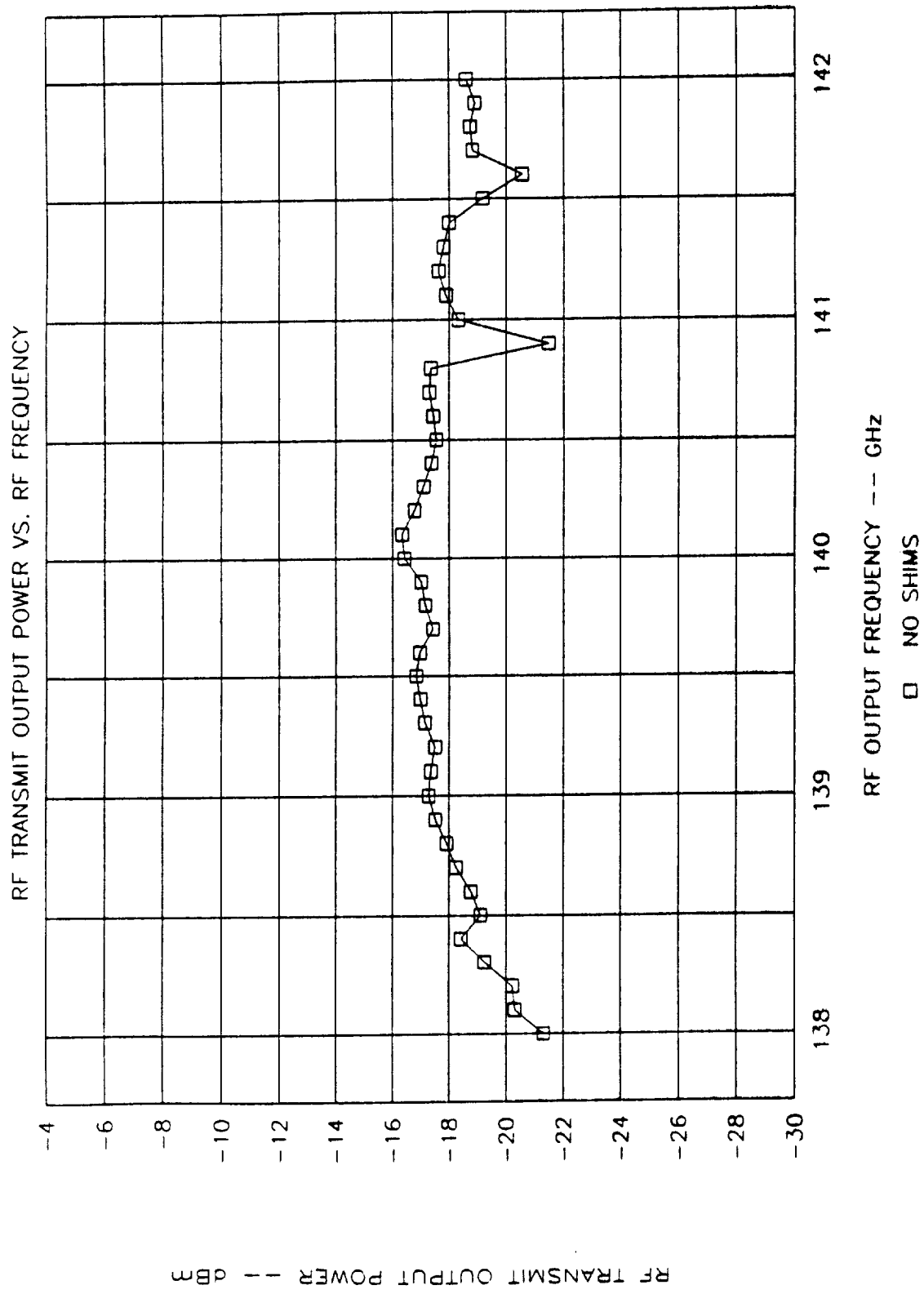


Figure 7
Performance of Band D Mixer Operated as an Up-converter,
Pre-mode Suppression Filter

this characteristic in the up-converter performance of the initial configuration of the mixer using the new U of Va diode approach.

While the nominal 11 dB conversion loss for the down-converter mode of operation of this mixer was quite favorable, the narrow dips in the mixer response displayed when the mixer operated in the up-converter mode were not acceptable in terms of their impact upon the mission planned for this hardware. Therefore, we proceeded with an effort to correct the problem. We formed theories which might explain this feature in the response, and we performed various tests on this mixer within the laboratory to prove or disprove these theories. This procedure led us to positively identify the mechanism causing this response characteristic.

Our conclusions were as follows: As intended, a 138 to 142 GHz RF signal is produced within the mixer through up-conversion by mixing of the two signals, a times 2 component of the 65 GHz local oscillator input which is directed into the WR-15 LO input port of the mixer, and the 8 to 12 GHz modulation input signal directed into the coaxial IF port of the mixer. Ideally, all of the desired 138 to 142 GHz up-converter product is directed out of the WR-8 waveguide port, designated the RF port, of the mixer.

As the block diagram for the Band D T/R Module indicates, the WR-15 LO input port of the up-converter mixer connects to a waveguide low-pass filter. The purpose of this filter is to prevent the leakage of the up-converted RF output signal through the LO waveguide distribution network, and into the two receive mixers of the T/R Module. In our actual hardware, any leakage component of the 138 to 142 GHz RF signal out of the LO waveguide port of the up-converter mixer is very efficiently reflected by this waveguide low-pass filter and directed back into the LO waveguide port of the mixer. However, we demonstrated that this reflected back signal causes an interference with the original RF output signal within the mixer and, consequently, the two sharp dips appear in the passband response of up-converter operation of the mixer.

The presence of this feature of two relatively sharp dips in the up-converter response was not acceptable in terms of the performance of the T/R Module. We proceeded to develop some modification of the mixer which would reduce or eliminate this problem.

11. Mode Suppression Filter to Eliminate Problem of Notches in Up-Conv. Response

Our objective was to develop a modification of the mixer which would sufficiently reduce the RF-to-LO leakage out of the mixer. This would then reduce the effect of the standing wave between the mixer LO port and the WR-15 low pass filter. We previously demonstrated that this standing wave was the cause of the sharp dips in the bandpass response of the up-converter.

We developed a mode suppression filter by which we effectively accomplished the objective of reducing the standing wave. This filter was realized by placing a resistive film card horizontally within the LO waveguide section of the mixer. The length of the card was somewhat critical, while its width extended between the two side walls of the waveguide. Also critical was the ohms per square resistance of the card material. We used material consisting of a 5-mil thick Kapton substrate with a metal film of 377 ohms per square. We had available for evaluation of this concept, this type of resistive card material in two different resistivities, 377 and 200 ohms per square. We found the 377 ohm per square material adequate.

This resistive attenuator card placed horizontally across the waveguide has minimal effect on the 65 GHz LO input signal of the mixer. This frequency can propagate in the WR-15 size waveguide only in the dominant mode of propagation which has its electric field normal to the plane in which the card is oriented. However, leakage of up-converter generated RF signal into this waveguide, which would be in the 138 to 142 GHz range, can propagate in the dominant mode, as well as in several higher order modes. Some of these modes have a component of electric field in the plane of the resistive card. For those modes, the card should provide significant attenuation of the RF leakage signal.

Our design for this modification of the mixer included a simple and effective means of constraining this mode suppressor card suspended across the WR-15 waveguide portion of the mixer. A pair of grooves 5 mils deep by 5 mils wide were machined along the center of the side walls of the WR-15 waveguide section of the mixer. The mode suppressor card was cut to a rectangular shape having a width to fit within this groove without binding, and with no side play. The card was slid along this pair of grooves, and epoxy was used to hold the card from sliding in this groove. The card 5-mil thick material itself was sufficiently rigid to allow this configuration to readily withstand the environmental conditions of the unit.

Figure 8 is a plot of the response of the mixer as an up-converter after the mode conversion filter was installed as just described. Only a wide, shallow, smooth dip now appears in the frequency region where the pair of sharp dips formerly existed. The system application of this mixer could readily accept this shallow, broad dip in the response.

Millitech has prepared a source control drawing for procurement of the U of Va mixer dual-diode array chip IC's for use on flight hardware.

12. Mixer Failure Caused by Differential Thermal Expansion in Temperature Cycling

At this point in the development, we had a mixer configuration for the Band D T/R Module which demonstrated excellent flatness and good 10 to 11 dB conversion loss performance for this frequency range operating as a down-converter. In the up-converter mode, our mode suppression filter provided good output power flatness, and power output level was adequate, although marginal.

A new problem was uncovered when the mixers were tested under temperature cycling. All three mixers were assembled into the complete Band D T/R Module, and the complete assembly was tested in a temperature test chamber where temperature of the ambient air was cycled between the temperature range of -20°C and $+85^{\circ}\text{C}$. Intermittent degradation of performance was displayed as the module was cycled over temperature. Generally, good performance was displayed at room temperature and above, but the transmit/receive characteristics of the module would degrade substantially below about $+15^{\circ}\text{C}$.

We set up a simple test to allow us to monitor, using a curve tracer, the I-V characteristic of each of the mixer diodes while the fully assembled T/R Module was cycled over temperature. This would allow us to determine readily if there were any abnormality in any of the mixers as temperature was varied. The T/R Module was installed within in a temperature test chamber, and we made DC electrical connections to the coaxial IF ports of each of the mixers. As temperature was cycled we determined that the electrical continuity to the diode chips in two of the three mixers opened as temperature was reduced. One mixer opened at $+14^{\circ}\text{C}$ and remained open for temperatures below this, while a second one opened at approximately -10°C air and remained open for lower temperatures. When temperature was raised above

MODULE D INTEGRATION TESTING 8 JULY 91

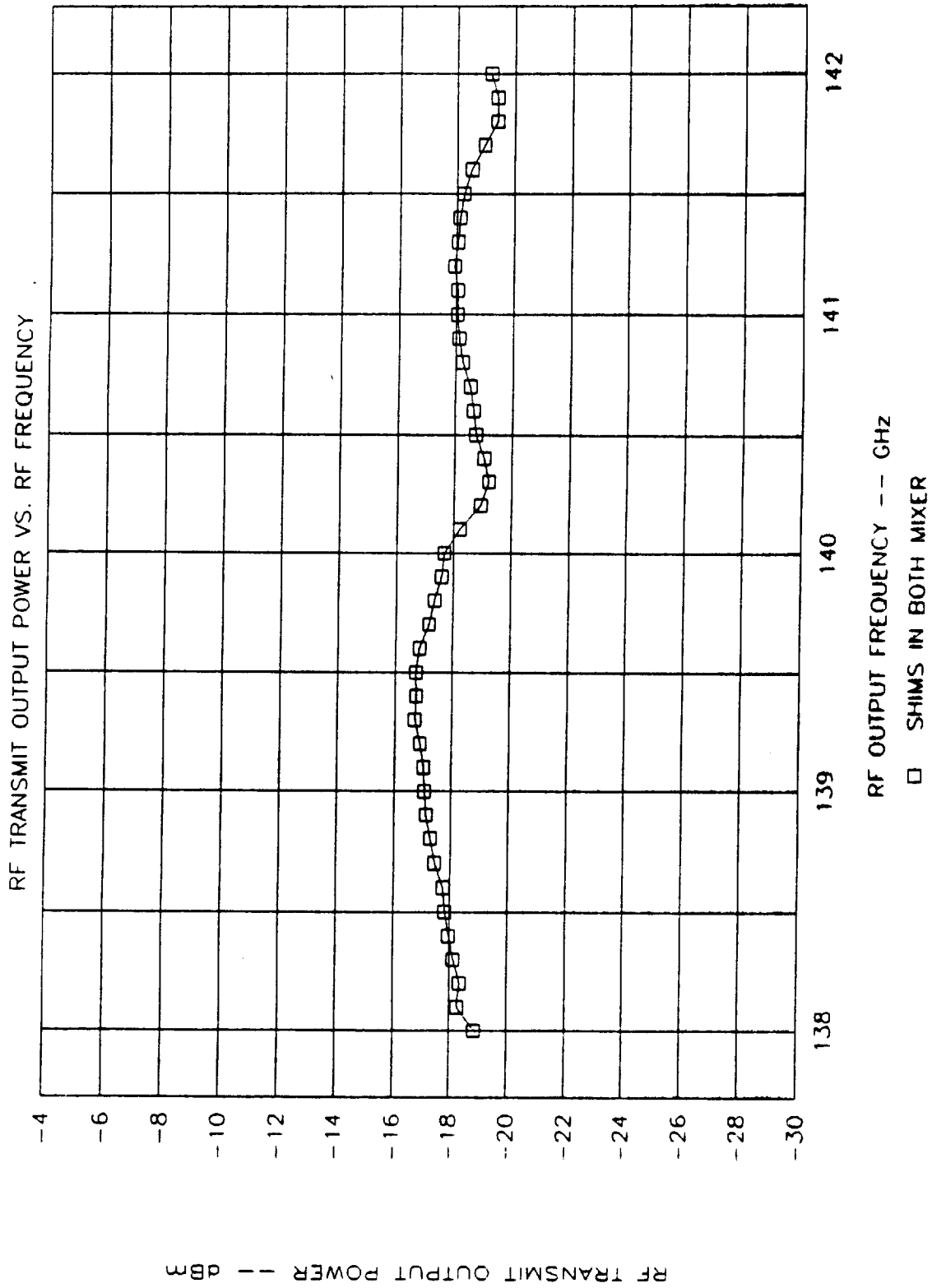


Figure 8
Performance of Band D Mixer Operated as an Up-converter,
After Mode Suppression Filter was Installed

room temperature, both mixers returned to good continuity, and to good RF performance. The third mixer displayed no anomaly under this test.

Simple continuity checks indicated that the cable and connectors on the module were not the cause of the intermittent open circuit conditions, and that the faults were located internal to the mixers. We proceeded to remove the three mixers from the Band D T/R Module. This would allow us to analyze the mixers for the precise location and nature of the intermittent open circuit conditions within the mixers. We disassembled the mixers by separating the two block halves of the mixer split-block bodies. This allowed access for us to inspect visually under a microscope the bonds of conductive epoxy joining each of the two electrodes of the mixer diode chip to the mounting surfaces of the mixer body.

Using a standard stereo zoom microscope of about 25 X power, we were able to identify conclusively the area of failure of the two mixers for which contact to the mixer diodes failed to an open circuit condition at low temperatures. For one of the mixers we found failure of the epoxy bond joining one mixer electrode pad to the coaxial center pin conductor of the mixer. The hardened epoxy separated from the mixer gold electrode pad at the end of the mixer diode chip. For the other mixer, the mixer diode chip itself fractured in the form of a hair-line crack in the chip. For both units, electrical contact would re-establish at elevated temperatures by mechanical contact of conducting surfaces.

We performed analysis of our structure and concluded that these failures were a result of differential thermal expansion between the two surfaces to which the ends of the mixer diodes were bonded with the conductive epoxy. The design of the mixer includes the coaxial center conductor pin mounted rigidly to the mixer body at the far end of the pin from which the mixer diode is bonded. Also, the pin is of a different material, gold plated kovar, than the mixer body which is aluminum. The relatively long working distance, approximately 0.15 inches, and the difference in materials sets up relative motion with temperature changes of the bonding locations for the mixer diode. The bonds of conductive epoxy did not offer sufficient strain relief for this motion, and the failures occurred.

To correct this problem, it is necessary to prepare an additional design modification to the mixer. We propose adding for strain relief a short length of gold ribbon to one end contact of the mixer diode chip. The gold ribbon can be attached to the diode either by thermo-compression bonding, or possible by epoxy bonding with conductive

epoxy. This concept is illustrated in Figure 9. We did not have opportunity to follow through in solving this problem with the Band D mixer on the MRIS program.

13. Practical Difficulties in Working with U of Va Dual-Diode Array Chip

In our work with the U of Va mixer diode chips to develop and produce the three mixers for the Band D T/R Module, we had a problem of failure of a substantial number of the diode chips. This problem was primarily a result mis-handling of the mixer diodes. This mis-handling was part of the learning process in working with these unique semiconductor devices. Because of their microscopic size, several diodes were physically lost in the assembly process. Their small size implies lower RF power handling capability. Until this was recognized, several failed through application of RF power over-stress through LO as well as modulation input RF power. Devices also were degraded from improper practice in I-V curve tracer testing. Table I is a listing of the history of each of the diodes purchased under the MRIS T/R Modules program. The table describes failures where encountered, and it identifies which diodes were successfully installed into completed mixers.

These problems proved costly, at \$2000 per mixer diode. However, they can be avoided with education on application of these specialty devices. Millitech has prepared a detailed assembly procedure for the Band D mixer as it has been developed to date. This procedure incorporates all of the significant information which we have compiled concerning the handling and operation of the mixer diode chips.

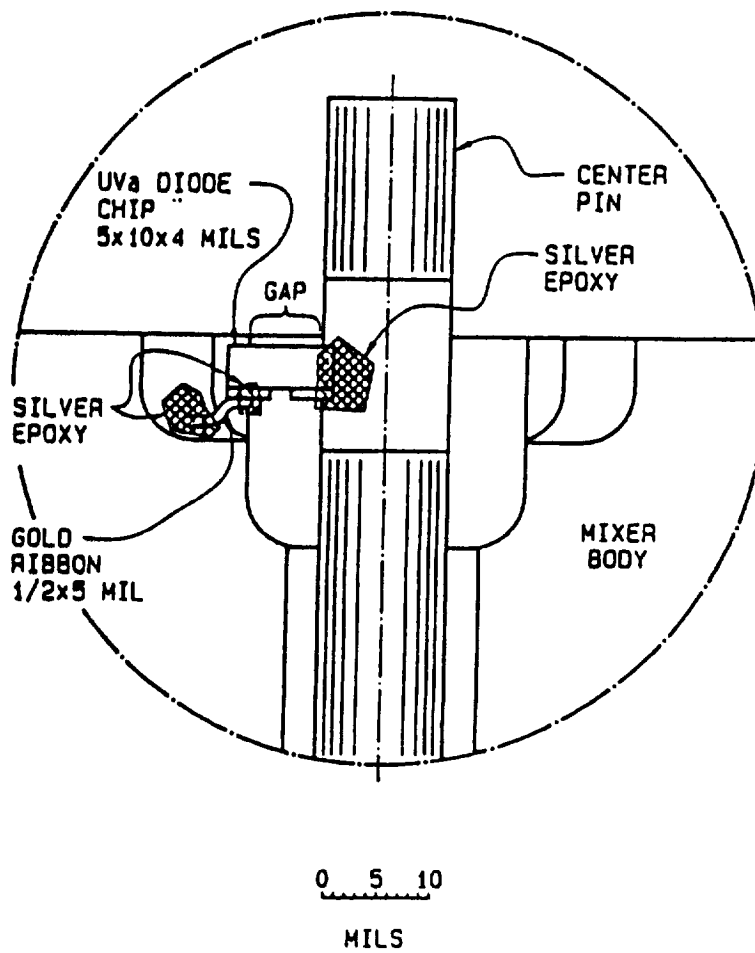


Figure 9
Concept for Adding Gold Ribbon Strain Relief
to Diode Contact on Band D Mixer

Table 1

MILLITECH CORP.

22 AUGUST 91

STATUS OF UNIVERSITY OF VIRGINIA DIODES PROCURED FOR MRIS T/R MODULES PROGRAM
SUBCONTRACT S105515

P.O. 16953 Lot Number SD2T3, Qty = 1, Received 5 March 1991

1) Unit failed at EMS in mixer component only, modules not integrated at that time. Diode checked bad prior to their running vibration testing on the individual mixer component. Diode tested tests open. Possible cause was electrical overstress induced during pre-vib I-V check of diode.

Note: Shipment from UVa included 5 mechanical samples, practice diodes, at no charge. One remains.

P.O. 17092 Lot Number SD1T1, Qty = 5, Received 4 April 1991

- 1) Installed into S/N 170, Reference mixer. Presently on Band D Module Engineering Model.
- 2) Originally installed into S/N 168, Test mixer. Degraded from electrical overstress in the form of application of excessive IF modulation input power. This diode was physically lost during the process of removing it from the mixer.
- 3) Originally installed into S/N 167, Upconverter mixer. Degraded from electrical overstress in the form of application of excessive IF modulation input power. Diode was removed from mixer and is available.
- 4) One damaged when conductive epoxy, used for bonding diode into the mixer, inadvertently shorted the two contact electrodes.
- 5) This diode was physically lost in handling during process of installing it into S/N 168 mixer.

P.O. 17579 Lot Number SD1T1, Qty = 2

- 1) Installed into S/N 167, Upconverter mixer. Presently on Band D Module Engineering Model.
- 2) Initially installed into S/N 168, Test mixer. Later removed and replaced. Although I-V characteristics looks OK, suspected, but not confirmed, poor RF performance characteristic.

P.O. 17839 Lot Number SD1T1, Qty = 3

- 1) Initially installed in S/N 168, Test mixer. Later removed and replaced. Although initially tested good in mixer RF performance, mixer later degraded in performance. I-V characteristics still look good. Suspect degraded RF characteristic. Possible causes: temperature cycling to +140°C, or mechanical overstress from excessive handling of component.
- 2) Physically lost during process of installing it into S/N 168.
- 3) Installed into S/N 168, Test mixer. Presently on Band D T/R Module Engineering Model.

APPENDIX A3. ISOCORE COAXIAL CABLE SUMMARY

**SEMI-RIGID COAXIAL CABLE ASSEMBLIES
FOR MRIS T/R MODULES**

DATE PREPARED: REVISED MARCH 13, 1992

SUBCONTRACT NO. S-105515

PREPARED BY

MILLITECH CORPORATION

P.O. BOX 109

SOUTH DEERFIELD RESEARCH PARK

SOUTH DEERFIELD, MA 01373

PREPARED FOR

ELECTROMAGNETIC SCIENCES, INC.

NORCROSS, GA

PREPARED BY: M. Simonutti

A handwritten signature in dark ink, appearing to read 'M. Simonutti', is written over the printed name.

**SEMI-RIGID COAXIAL CABLE ASSEMBLIES
FOR MRIS T/R MODULES**

TABLE OF CONTENTS

- I. INTRODUCTION AND SUMMARY**
 - A. Scope**
 - B. Four Cable Assemblies per T/R Module**
 - C. Performance Defects in Cable Assemblies**
 - D. Highlights of Corrective Action**
 - E. Cable Assemblies for Flight Hardware**
- II. SELECTION OF MATERIAL FOR SEMI-RIGID COAX ASSEMBLIES**
 - A. Isocore Semi-Rigid Coax Material for High Temperature**
 - B. MIL-C-39012 SMA Style Connectors**
- III. HISTORY OF PROBLEMS**
 - A. Summary of Factors Leading to Actual or Potential Defects**
 - B. Evidence of Possible Defects in Isocore Cable Material**
 - C. First Occurrence of Performance Problem -- Sharp Dip in Transmission Response**
 - D. Defective T/R Module Band C Cable Detected During Testing at EMS**
 - E. Problem of Excessive Ripple**
- IV. ELECTRICAL REQUIREMENTS AND ACTUAL PERFORMANCE**
 - A. Basic Performance Requirements for Cables**
 - B. Measurements from Acceptable and Defective Cable Assemblies**

V. CORRECTIVE ACTION

A. Summary of Early Oversights

B. Key Items in Corrective Action

- 1. Utilize Supplementary Assembly Procedures and Special Tooling**
- 2. 100 Percent Temperature Cycling and Electrical Testing at Fabrication.**
- 3. Re-design Cable Runs to Reduce Amount of Bending.**
- 4. Perform Incoming Inspection of Dielectric on Isocore Cable Stock.**
- 5. Insure Adequate Strain Relief Designed into Cable Assemblies.**
- 6. Fabricate Replacement Cables for Modules Bands A, B, and C.**

VI. STRAIN RELIEF REQUIREMENT FOR CABLE ASSEMBLIES

VII. SMA CONNECTORS USED AND PROBLEMS IN ASSEMBLY

A. Four types of MIL-C-39012 SMA-Style Connectors Used

B. Performance Defects Caused by Improper Installation of Connectors

VIII. SUPPLEMENTARY INSTRUCTIONS FOR FABRICATING ISOCORE CABLE ASSEMBLIES

I. INTRODUCTION AND SUMMARY

A. Scope

This report documents the application of semi-rigid coaxial cable assemblies fabricated for the Engineering Model units of the four MRIS T/R Modules, Bands A through D. These T/R Modules have been designed and fabricated at Millitech under sub-contract from Electromagnetic Sciences, Inc., as part of the MRIS program. Included in this report is an analysis of the defects found in the early cable assemblies fabricated at Millitech for the T/R Modules. We describe our various measures for corrective action.

B. Four Cable Assemblies per T/R Module

Each of the four T/R Modules, Band A through Band D, utilizes four individual coaxial cable assemblies. Three of the four cables on each module are used for RF signals, all of which cover the same 8 to 12 GHz frequency band. The specific assignments of the three RF cables on each module are as follows:

Modulation Input to the Upconverter Mixer

Test IF Output from Test Mixer

Reference IF Output from Reference Mixer

In addition to these three cables which carry RF signals, each module has a fourth coaxial cable assembly used for the DC bias voltage. This cable runs from the DC voltage regulator to the Gunn oscillator. Each of the four cables per module is formed to a custom shape as specified on the drawing for each, and each cable has two of any of four different types of SMA connectors installed at each end. These four SMA connector styles will be described later in this report.

C. Performance Defects in Cable Assemblies

We initially attributed the defects in the electrical performance of our cable assemblies to our lack of familiarity with assembly procedures for working with the Isocore cable material, a specialty style of semi-rigid coax cable. After some analysis, we determined, however, that this was only partially correct. We identified two major causes for problems. Both were associated with the assembly and soldering two particular types of SMA connectors onto the semi-rigid cable. One of the two types of defects in our assemblies would likely have occurred even with the standard type of semi-rigid cable material. For corrective action relating to these problems, we

found it necessary to take measures in the installation of connectors beyond those indicated in the assembly procedures supplied by the manufacturer of the connectors.

D. Highlights of Corrective Action

We developed a set of supplementary assembly operations and notes for producing these cable assemblies. These include special steps for the installation of the two particular types of SMA connectors which caused problems. One of these two types of connectors requires an operation which we developed exclusively to accommodate the properties of Isocore. For the other connector, we supplied additional notes to avoid a problem which could go unnoticed. This relates to the soldering of the cable to the connector.

Our procedures include special techniques for the formation of bends in the Isocore semi-rigid coaxial cable material. Also, temperature cycling of the cable assemblies and swept measurements for complete electrical performance evaluation of the cable assemblies are essential.

E. Cable Assemblies for Flight Hardware

This report was prepared primarily to document the performance defects which were exhibited in the early cable assemblies fabricated at Millitech for the Engineering Model T/R Modules. As this report demonstrates, Millitech is now in a position to produce high-quality, reliable cable assemblies for the T/R Modules. While we are making the cable assemblies for the Engineering Model units in house, our plans for obtaining the cable assemblies for the Flight Model units are not yet set. The option which is the likely one for Millitech, is to procure the assemblies from an outside vendor experienced in producing cable assemblies made with Isocore. Our other option is to fabricate the assemblies in-house at Millitech. Millitech and our prime contractor for this project, EMS, will be involved in selecting from these two options.

II. SELECTION OF MATERIAL FOR SEMI-RIGID COAX ASSEMBLIES

A. Isocore Semi-Rigid Coax Material for High Temperature

A major decision in the engineering design of the T/R Modules has been the selection of the type of coaxial cable to be used in the various coaxial cable assemblies on the

T/R Modules. To obtain low RF insertion loss and low VSWR over the 8-12 GHz band, we selected semi-rigid coaxial cable instead of flexible style coaxial cable.

A high-temperature environmental requirement for the T/R modules was a key driver in our selection of a particular style of semi-rigid coax. The T/R Modules must withstand a temperature of up to 140°C in a non-operating mode, without suffering degradation. MIL-C-17 is the specification controlling MIL-spec standard semi-rigid coaxial cables. Semi-rigid coaxial cables of this standard style utilize solid PTFE teflon dielectric, and this standard style of cable is rated for a temperature range of up to 125°C. Above this temperature, solid PTFE dielectric has a tendency to expand excessively. This expansion leads to failure of the semi-rigid cable by bursting of the outside copper jacket of the cable. The widely used MIL-C-17 cable material was, therefore, not an option for the T/R Modules.

The industry offers a variety of alternate, non-MIL-spec, semi-rigid cable types which are designed to withstand higher temperatures. This is accomplished primarily by application of different dielectric materials other than solid PTFE. Most employ teflon in the dielectric, but not simply solid teflon. Most common are teflon foam or a matrix of teflon with a filler material. Such compositions have a greatly reduced tendency to expand at high temperatures and consequently burst the copper outer conductor. A consequence of its crystalline properties, the dielectric constant of solid PTFE, which is used in MIL-spec cable, has a relatively high variation with temperature compared with the dielectric materials used in these specialty cables. As a result, these specialty cables offer greater phase stability over temperature compared with MIL-C-17 cable. However, while good phase stability with temperature is a desirable electrical performance property for the cables, it was not a primary factor in our selection of Isocore.

Another characteristic of these alternate semi-rigid cable types, particularly Isocore, is that their dielectric has considerably less firmness than the solid PTFE dielectric of the MIL-spec style cable. This mechanical property is not a desired one. It is a consequence of tradeoffs made in the development of the dielectric for the improved temperature performance. As we emphasize in this report, this property of reduced firmness makes it necessary to employ special assembly procedures.

For application on the T/R Modules, Millitech selected Isocore semi-rigid coaxial cable material, in the .086-inch OD configuration, and with silver plated beryllium copper center conductor. The dielectric of Isocore consists of a matrix of a teflon base with a ceramic powder filler. Isocore was developed by, and is manufactured by, the

Rogers Corporation, specialists in teflon based dielectric products for the microwave industry. Their Part Number for this material is IA-086NB. The manufacturer rates this material for a temperature range of -100°C to +250°C.

B. MIL-C-39012 SMA Style Connectors

Besides its high temperature performance, an important factor in our selection of Isocore for the T/R Modules is its compatibility with standard, MIL-C-39012 style SMA coaxial connectors intended for standard MIL-C-17 semi-rigid coaxial cable. All other special high-temperature semi-rigid coaxial cable types require special SMA connectors, and such connectors are not controlled by widely applied government specifications. Note that MIL-C-39012 rates the SMA style coaxial connectors specified therein for the temperature range of -65°C to +165°C. Of the many types of SMA connectors offered in MIL-C-39012, we use four different types on the T/R Modules. These are described in Section VII-B.

III. HISTORY OF PROBLEMS

A. Summary of Factors Leading to Actual or Potential Defects

As we describe in this report, several factors contributed directly to the occurrence of performance defects and failures in the early Isocore cable assemblies produced at Millitech for the T/R Modules. In addition, we found items which, without the corrective action which we have implemented, could potentially lead to other defects. These various factors are listed here in order, from most critical to least:

1. Failure to perform electrical acceptance testing on the first sets of cable assemblies before they were integrated in the first Engineering Model T/R Modules. Generally, a schedule of temperature cycling should be included with pre- and post-electrical testing of the cables.
2. The need for special procedures, not peculiar to Isocore, for installing a certain style of SMA connector, M39012/83B3001, Bulkhead Feedthrough Cable Jack.
3. The need for special procedures unique to Isocore for installing another style of SMA connector, M39012/80B3001, Right Angle Cable Plug.

4. The reduced level of firmness property of Isocore's dielectric material, and the consequent need for special techniques, of which we were not previously knowledgeable, for forming bends in the cables.
5. Failure to perform incoming inspection on the Isocore, or to control it by imposing procurement requirements on the vendor. Of particular concern is the absence of voids in the dielectric and concentricity of inner and outer conductors.
6. Inadequate attention to the cosmetic appearance of the completed cable assemblies. Nicks and scratches were apparent on our earlier cable assemblies, some as a result of the necessary repeated assembly and disassembly of the T/R Modules during module integration. While these appearance items may or may not directly affect performance, they are not representative of flight-grade hardware.

We have subsequently compiled an extensive amount of information on procedures for fabricating cable assemblies for the requirements of the T/R Modules. The vendor of the cable material supplied us with the limited applications information they had available. Of greatest significance, we have performed a program of analysis and troubleshooting of the defective cable assemblies. Based on this, we developed, where necessary, special supplementary assembly techniques. We understand the causes for the defects which have previously occurred. We have developed, demonstrated, and gained sufficient experience in applying the necessary controls to insure that Millitech can fabricate, in a reproducible manner, high performance, reliable cable assemblies for the T/R Modules.

B. Evidence of Possible Defects in Isocore Cable Material at Initial Assembly

Our first exposure at Millitech to application of Isocore was in the fabrication of the initial set of four cable assemblies for the Band B T/R Module. While examining the Isocore material during installation of connectors, the assembler found evidence of possible defects in the cable material.

The process of preparing each end of a section of the cable for the installation of connectors involves the following operations:

1. Trimming back the solid copper jacket outer conductor of the cable.
2. Trimming back the dielectric.
3. Trimming the exposed center conductor to extend a precisely specified length beyond the trimmed outer jacket.
4. Scraping the exposed portion of the center conductor to remove a thin teflon coating deposited over the center conductor during the manufacture of the Isocore. This scraping prepares the center conductor for soldering.

These operations require close inspection of the inner and outer conductors, as well as of the dielectric. During this, the assembler noted and reported two apparent anomalies with the Isocore cable material on some of the lengths of cable being prepared:

1. The center conductor on some sections appeared noticeably off-center with respect to the outer conductor.
2. The dielectric displayed the presence of voids. These voids had roughly spherical shape, their diameter extending from the center conductor to the outer conductor.

The assembler also called attention to the almost paste-like consistency of the dielectric material of the cable. However, this particular characteristic is understood to be normal for Isocore. We performed some simple tests involving the application of heat to the material. We were very impressed with the mechanical stability at high temperatures of the Isocore dielectric material relative to that of standard MIL-spec semi rigid cable.

We performed an electrical test with the specific goal of characterizing the electrical effect of these voids. We installed connectors on each end of a full-length five-foot section of 0.086" O.D. Isocore and performed a time domain reflectometry check on it using our vector network analyzer. The presence of the voids in the dielectric might result in measurable reflections from the material. However, we could not identify any responses in the time domain measurement which suggested the presence of such discontinuities in the dielectric.

At the time that we initially observed the two anomalies, we proceeded to build our cable assemblies with this lot of material. We did not reject the lot entirely. Instead, we scrapped those sections where the anomalies were evident based upon an inspection of the exposed ends of the cable. In our haste to deliver the first completed T/R Module, Band B, we chose not to suspend our use of this material and investigate the situation further to determine whether these observed anomalies were sufficient grounds to impact the electrical performance of the cables. In the future, we will perform an incoming inspection on new lots of Isocore material received, and we will reject material which displays obvious voids in the dielectric or poor concentricity of the center and outer conductors.

C. First Occurrence of Performance Problem -- Sharp Dip in Transmission Response

For integration testing of the first engineering model T/R Module which we completed, Band B, we employed microwave power meters for the measurement of signals for the 8 to 12 GHz IF band, and for the 43 to 45 GHz RF band of the module. Compared with other methods of signal measurement, microwave power meters generally provide the highest accuracy of power measurement. However, without specialized instrumentation which Millitech did not have available, this high-accuracy approach limits our measurements to point-by-point data across the band of interest. It does not allow plotting of a continuous swept response. In any case, initial testing at Millitech of the Band B T/R Module showed no apparent problems with the first set of cable assemblies. Also, this Band B module was delivered to EMS where swept testing was performed by EMS project personnel. EMS obtained overall acceptable performance from this first T/R Module. No obvious performance problems were evident in the cable assemblies on this first module.

For the major part of integration testing on the second T/R Module, Band C, we also utilized power meters, as we did exclusively on the first module. Our point-by-point evaluation data indicated no significant anomalies in the Band B module. However, just prior to release of this module for shipment, we added to our integration testing sequence, for the first time, a pair of swept measurement checks for the IF output signals. These tests would verify the overall swept response of the Upconverter Mixer-Test Mixer combination, and the Upconverter Mixer-Reference Mixer combination.

This check at Millitech of sweep testing of the Band C module indicated a problem which the previous point-by-point testing failed to uncover:

The swept measurement check of the Band C T/R Module indicated, for both the Reference IF Output and the Test IF Output, a narrowband dip of about 3 dB amplitude. For both IF outputs, these dips appeared at the same location at the upper end of the 8 to 12 GHz IF band. Through a simple check consisting of bypassing the cable assemblies on the T/R Module, we identified the source of the problem as a defective semi-rigid coax cable assembly carrying the Modulation Input signal to the upconverter mixer. A subsequent swept measurement of the transmission response of this cable assembly on a microwave vector network analyzer verified the presence of a defect in the cable.

A narrowband dip in the swept transmission measurement of the cable assembly was evident. The location of this narrowband response defect was such that it occurred in between a pair of our previous point-by-point measurements taken at 0.5 GHz intervals on the module, and the defect was therefore missed in the previous point-by-point testing.

With the occurrence of this first problem of a defective coaxial cable on the T/R Modules, our corrective action was limited to fabrication of a replacement cable. We then repeated the swept measurement check of the IF signals output on the module. Following the replacement of this first defective cable, the swept response check of the module was acceptable.

Initially, we suspected that the cause was related to some characteristic of the Isocore cable, either to the lack of firmness inherent in its dielectric, or to the voids in the dielectric which we observed during assembly. This problem of narrowband dips in the transmission characteristic of the cable assembly later appeared, very similar in nature, in other assemblies which we fabricated. Ultimately, we found, as we will explain, that these defects were a result of improper soldering of a particular type of connector used on the cables, and not caused by any specific property of the Isocore.

As described in the next section, the new cable assembly which was fabricated to replace the original defective one, itself later developed a defect similar that just described, i.e., a narrowband dip in the bandpass response. This new defect did not become evident until this Band C Module was delivered to EMS and was tested by EMS personnel. In retrospect, we realize a key point in the sequence of events. The swept measurement performed at Millitech on the Band C module replacement of the cable was performed with all cable assemblies installed on the module. However, the

testing was performed prior to our installing the tie-downs to secure the cables in place. The probable explanation of the later failure is that the defect, which as we describe later was inadequate soldering of the SMA bulkhead connector, was latent prior to cable tie-down. During cable tie-down, sufficient mechanical stress was imparted to the defective solder joint to make the defect evident in a performance check.

D. Defective T/R Module Band C Cable Detected During Testing at EMS

The Band C module was received and processed by EMS receiving personnel, inspected by their QA, and delivered to MRIS project personnel. EMS project test personnel performed an initial evaluation of the unit. This initial evaluation consisted of a swept measurement check of the IF signals. An anomaly was detected during this sweep testing of the Band C module at EMS.

EMS informed Millitech that their measurements on the Band C module indicated a pronounced, sharp dip, several dB in depth, in the upper frequency end of the passband response of the Reference and Test IF outputs. EMS performed checks to localize the cause of the problem. A swept transmission measurement on the Modulation Input semi-rigid coax cable assembly disconnected from the module indicated that the problem was due to a defect in the electrical performance of this cable assembly.

This failed cable assembly is in the identical position as the defective one reported in Section III-C. above. However, it was a physically different cable assembly.

This Band C module was returned to Millitech. We performed a swept measurement check of cable assembly in question and we confirmed the defect reported by EMS. Since the module previously tested acceptable under swept testing at Millitech, the defect in the cable must have become established between the time that it was tested at Millitech and the time that it was tested at EMS. As explained above, we believe the defect of the cable assembly was most likely induced at Millitech during the process of tying down the cable assemblies to the T/R Module mounting plate, an operation which was performed following RF testing at Millitech. The underlying cause was faulty soldering of an SMA connector to the cable.

E. Problem of Excessive Ripple

During our effort of determining the cause of the sharp dip in the transmission response in some cable assemblies, we also were in the position to detect and determine the cause of other possible problems. In the process, we uncovered and corrected a less extreme, but still significant, electrical performance defect in the cable assemblies. We found that those cables which utilized the right-angle cable plug displayed noticeably higher ripple in their swept transmission response than those cables not using the right-angle connector. Our corrective action for this problem is described in Section VII-B.

IV. ELECTRICAL REQUIREMENTS AND ACTUAL PERFORMANCE

A. Basic Performance Requirements for Cables

There are two general requirements on the electrical performance for the coaxial cables: low transmission loss and low ripple in the transmission across the frequency band. A third parameter is VSWR, or return loss, to be measured looking into each of the two ends of the cable. We have not previously set actual performance requirements on these cables. In this section we will present an initial set of requirements which will be incorporated as a specification for the cable assemblies on the T/R Modules.

Maximum Insertion Loss. The manufacturer's data for Isocore indicates, for 0.086" O.D. material, an insertion loss of 1.2 dB per foot at 12 GHz, the upper frequency of operation for the IF signals on the T/R Modules. The actual loss which we have measured on cables was slightly less than this published value. The overall lengths of the individual semi-rigid cables on the T/R Modules are all under 8-inches. We shall set a maximum insertion loss of 0.8 dB for these cables, for frequencies from 0 to 12 GHz.

Maximum Ripple in Insertion Loss. Ripple is the variation in the curve of insertion loss versus frequency. Generally, the response of the cable material alone, if free of defects, will produce negligible ripple. Connectors add some degree of ripple, and if they are incorrectly installed, could produce a substantial amount of ripple. Ripple in the swept response of the T/R Modules must be controlled. Any present in the insertion loss characteristic of the cables adds to that resulting from the remaining portions of the module. Based upon a review of all of our measurements performed on the cables of the T/R Modules, we shall set a maximum of 0.3 dB peak-to-peak allowable ripple.

VSWR or Return Loss. Normally, low ripple in the insertion loss characteristic is an indication of low return loss for the cable assembly. Consequently, we did not perform consistent measurements of return loss of the cables. However, for future work, we shall set maximum allowable return loss of 17 dB.

B. Measurements from Acceptable and Defective Cable Assemblies

Plots of measured data which we present were taken using an integrated microwave vector network analyzer, Hewlett Packard Model 8720. The plots presented are produced directly by this instrument writing to an external printer.

Measurement on Good Cable Assembly. Figure 1 is a plot of the swept measurement of one of the cable assemblies made for the T/R Modules. We consider this cable free of performance defects. Note that for up to 12 GHz, the insertion loss is better than about 0.7 dB and the maximum peak-to-peak ripple about 0.2 dB.

Measurement on Cable with Sharp Dip in Transmission Characteristic. Figure 2 is a plot typical of a cable in which the Bulkhead Feedthrough Cable Jack SMA connector is improperly installed with insufficient solder flow into the connector around the O.D. of the cable. Note the sharp dip, about 2 dB in depth, and appearing around 6.4 GHz. We have observed this type of dip occurring in such cables anywhere in the range from about 6 to 18 GHz, depending on the precise distribution of the inadequate solder flow. A detailed discussion of this problem is presented in Section VII-B.

Measurement on Cable with High Ripple. Figure 3 is a plot of a typical cable in which the Right Angle Cable Plug SMA connector is installed without the special procedure we developed for using this connector with Isocore. Note the relatively high ripple with a somewhat periodic nature across the entire plot. This is typical of a cable with a localized discontinuity in impedance. In this case that discontinuity is within the Right Angle Cable Plug SMA connector when installed on Isocore where the dielectric cable dielectric is trimmed back flush with the outer conductor. Our special procedure which we describe in this report, reduces this discontinuity to an acceptable level. A detailed discussion of this problem presented in Section VII-B.

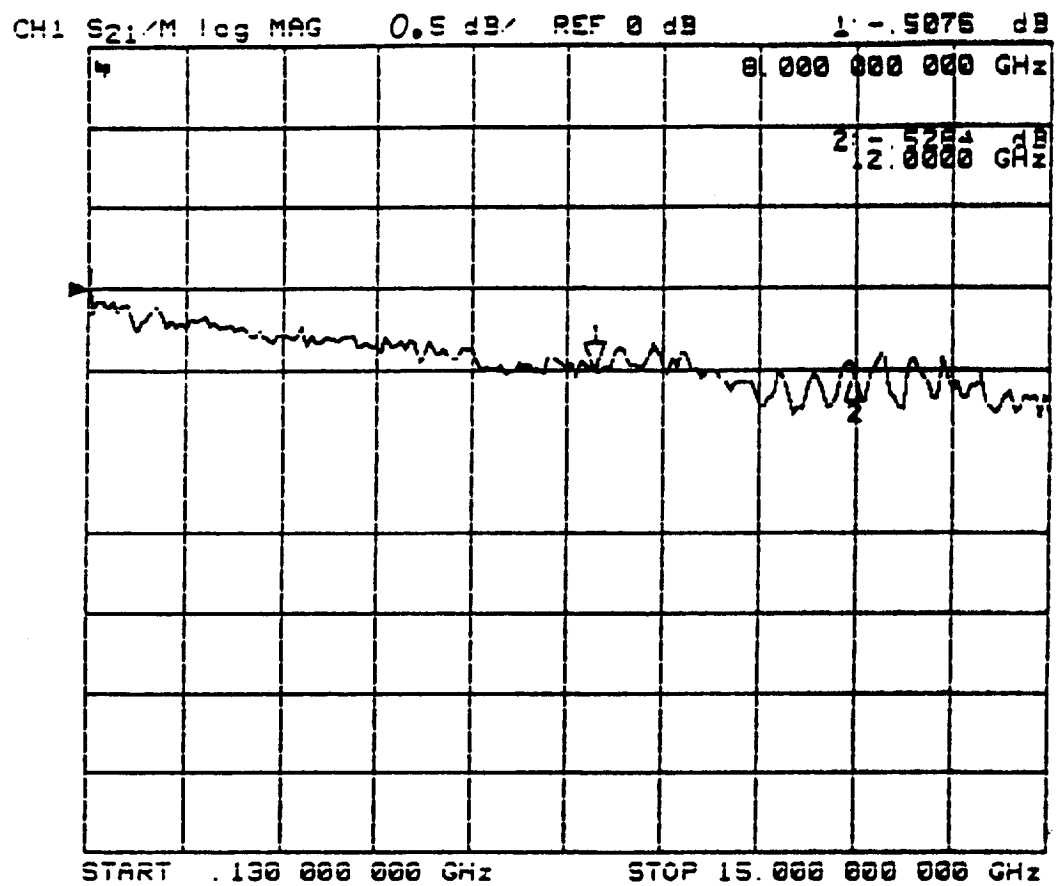


Figure 1. Swept insertion loss of typical isocore semi-rigid cable assembly approximately 6-inches in length.

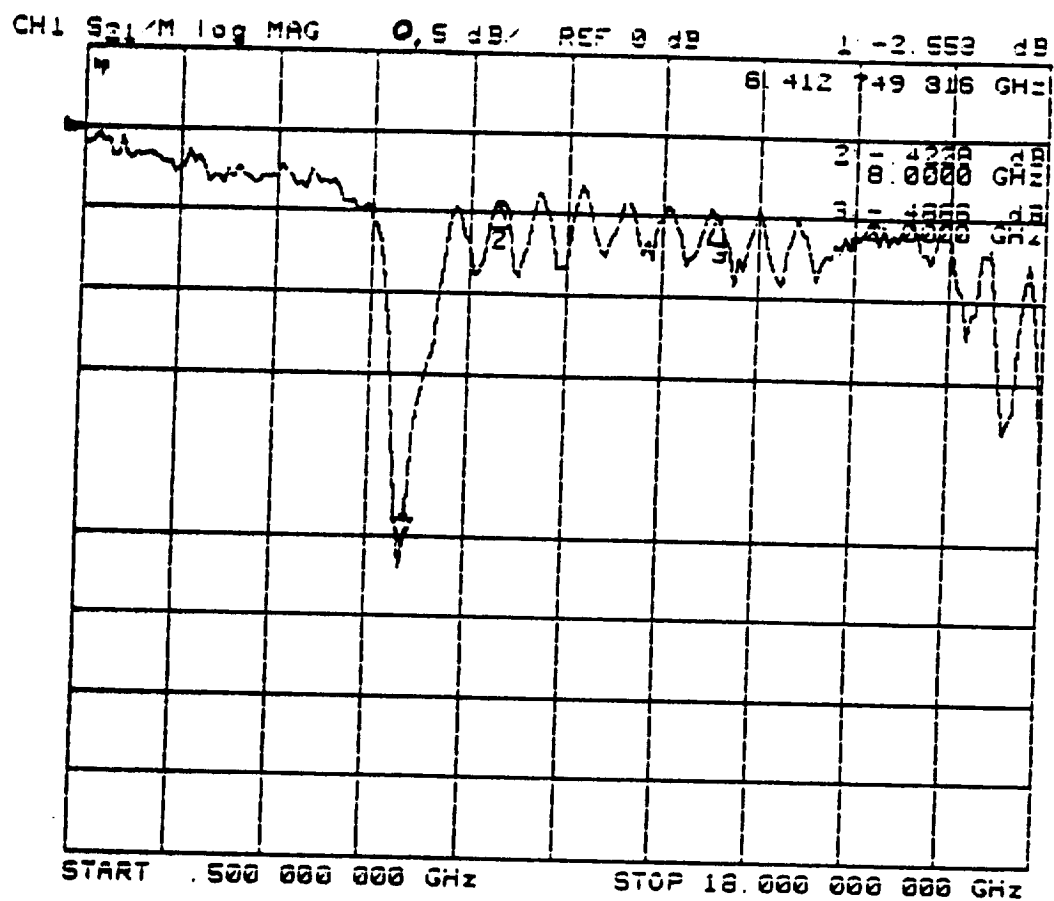


Figure 2. Swept insertion loss measurement of cable with Bulkhead Feedthrough Cable Jack SMA connector Improperly installed. Sharp dip resonant-like response results.

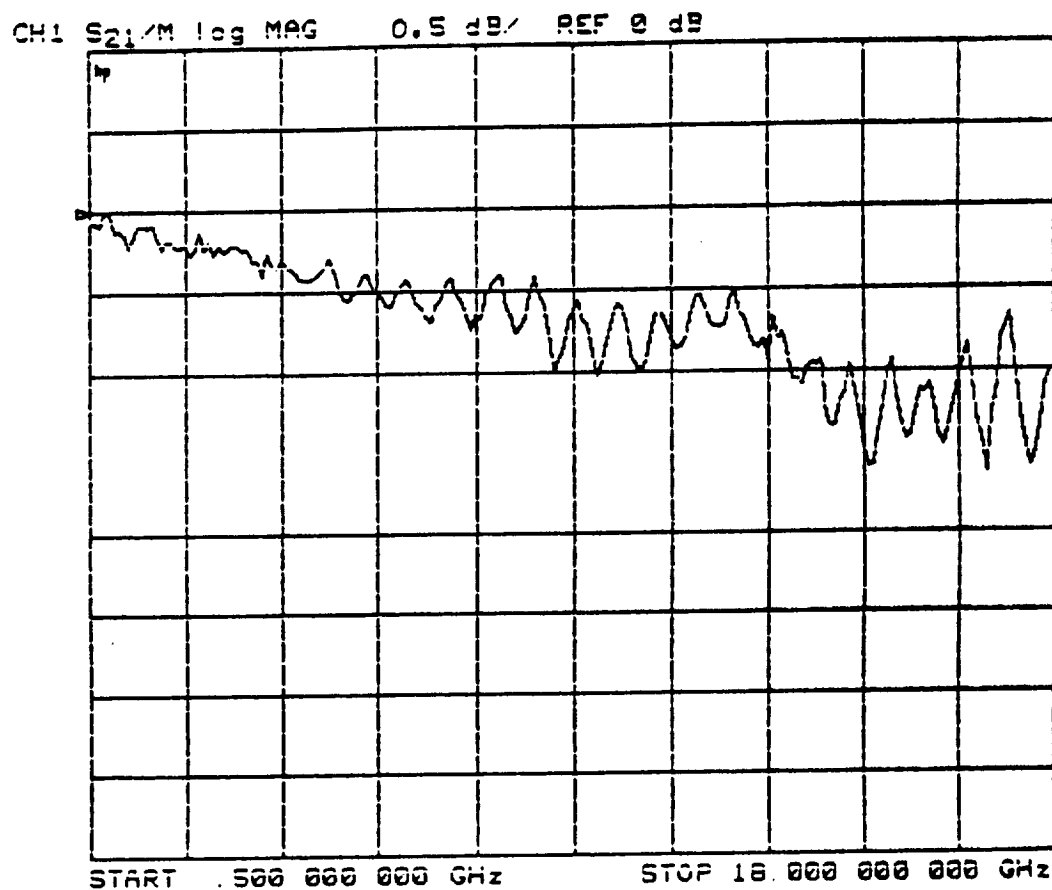


Figure 3. Swept insertion loss measurement of cable with Right Angle Cable Plug SMA connector installed without added teflon bead. High ripple results.

V. CORRECTIVE ACTION

A. Summary of Early Oversights

First we list three items which were overlooked during Millitech's fabrication of the initial cable assemblies. If these items were not missed at the outset, the defects in our cable assemblies would have been caught early on and corrected. Most, if not all, of the problems which have resulted could have been avoided.

1. Microwave cable assemblies should be subjected to thorough electrical sweep testing before being installed into any system. Millitech did not perform electrical tests on the individual completed cable assemblies initially fabricated for Bands A, B, and C Engineering Model T/R Modules.
2. Final sweep testing of the Band C module should have been performed following, not prior to, the installation the tie-downs to the coaxial cable runs.
3. Prior to the emergence of any of these problems, and prior to fabrication of any of the cable assemblies at Millitech, we did not consult the manufacturer of Isocore for information on any special procedures which might be recommended or required for the fabrication of cable assemblies with Isocore. We fabricated the assemblies using our methods which we use with standard solid PTFE dielectric semi-rigid cable assemblies.

One other item was overlooked, but this probably had no significant impact on the assemblies:

1. The apparent defects in the semi-rigid coax material, as described in Section III-B, should have been grounds for rejection of the lot and the findings brought to the immediate attention of the vendor.

B. Key Items In Corrective Action

We have identified and corrected for the causes of the defects present in the early cable assemblies we produced for the T/R Modules. We conclude that these problems were primarily related to the improper installation of connectors. For the most part,

the problems were not directly related to any inherent limitation of Isocore, although we did develop a special technique for installing one particular type connector on Isocore to obtain somewhat improved electrical performance in terms of reduced ripple. We also fabricated a simple tool, based upon applications information from the manufacturer of Isocore, for forming bends in the cable. This tool insures that minimum distortion of the cross-section of the cable is imparted in the bending process.

Following are the key design and procedural changes which we have developed to insure against similar problems, as well as to prevent other potential problems, in the future.

1. Utilize Supplementary Assembly Procedures and Special Tooling. We have held discussions with, and obtained applications literature from, the manufacturer of Isocore and vendors of cable assemblies. Our in-house effort in failure analysis and in developing assembly procedures for the specific connectors which we use on the T/R Modules has been especially productive. From these areas, we have now developed highly effective procedures for installing connectors, and we have fabricated the simple tooling we require to form bends in the Isocore cable assemblies. We are in the process of completing the formal written procedure which we will apply. The key points are listed in Section III of this report.
2. 100 Percent Temperature Cycling and Electrical Testing at Fabrication. We will perform 100 percent electrical testing of all Isocore coaxial cable assemblies according to a test procedure which we will establish as part of the T/R Modules program. Pass/Fail conditions will be determined from the specifications on electrical performance presented in Section IV-A. In event that we obtain assemblies fabricated from outside vendors, as is likely for flight hardware, we will include swept testing of the cable assemblies as part of incoming inspection at Millitech. Electrical testing is to consist of swept transmission testing over a 0 to 15 GHz band, temperature cycling between -53°C and +140°C, and a repeat of swept transmission testing.
3. Re-Design Cable Runs to Reduce Amount of Bending. We have been informed by the manufacturer of Isocore that use of correct procedures in the forming of bends in the material is critical. In addition to applying

recommended procedures for forming the bends, we will perform a minor re-design effort to reduce the total number of bends on our assemblies. This involves applying these design guidelines: 1) employ an SMA right-angle cable connector in place of one of the straight connectors to eliminate a 180-degree bend in one of the assemblies, 2) employ SMA right-angle cable connectors in place of some of the straight connectors to eliminate some of the 90-degree bends in the cable assemblies, 3) change the routing of some of the cable runs to eliminate some bends and/or to allow a larger bend radius.

4. Perform Incoming Inspection of Dielectric on Isocore Cable Stock. The presence of what appeared to be manufacturing defects on the Isocore cable stock, as noted in Section III-B, may not have been the cause of any of the performance problems we encountered. However, we believe that these manufacturing defects are not normal, and a discussion by Millitech with the manufacturer indicated that this is true. Therefore, incoming inspection specifically for these potential problems could prevent new types of problems, and possibly prevent new types of failures, from occurring in the future. This inspection will consist of, at a minimum, taking several cross-sectional cuts in on or more lengths of the Isocore stock, and examining the condition of the dielectric under magnification.
5. Insure Adequate Strain Relief Designed into Cable Assemblies. This issue is described in detail in Section VI.
6. Fabricate Replacement Cables for Bands A, B, and C Modules. Our controls for the fabrication of cables were effectively fully developed in time for the Band D module, the last of the four Engineering Model units which we fabricated. We had the opportunity to rework or replace the cable assemblies on the Band C modules. This was necessary for reasons not due to any causes related to the cables themselves. To insure against any latent defects in those first cable assemblies produced, those on Bands A and B, we will fabricate and replace the cables on those two Engineering Model modules, sometime around September 1991 before we perform the complete ATP on those Engineering Model T/R Modules.

VI. STRAIN RELIEF REQUIREMENT FOR CABLE ASSEMBLIES

We had previously considered another form of corrective action intended to eliminate potential causes of failure of the cable assemblies. This was to change from 0.086" O.D. semi-rigid cable material to the next larger standard diameter, 0.141" O.D. Justification for this proposed design change was based upon our early, and what proved to be erroneous, belief that one cause of our cable failures was lateral displacement of the center conductor relative to the outer conductor of the Isocore cable material when forming bends.

Our concern over this problem was based upon the reduced firmness property of the dielectric of the Isocore material. We believed that larger diameter Isocore cable material would be less susceptible to degradation of performance from this effect. However, we subsequently concluded that lateral displacement of the center conductor during bending of the cable was not a significant problem, and was not the cause of any of the defects which we experienced. Also, this sort of displacement could be minimized by application of bending techniques recommended by the manufacturer of the cable. This includes use of a simple bending fixture which we fabricated and now employ at Millitech.

We later determined that, because of the relatively short lengths of the cable runs, as short as three inches for one of the cables, the larger diameter 0.141" O.D. cable must, in fact, be avoided for application on the T/R Modules. Cable assemblies based upon 0.141" O.D. cable would be much stiffer relative to those fabricated from 0.086" O.D. The stiffer material would not offer the strain relief provided by the more flexible 0.086" O.D. material. A minimum degree of strain relief against stresses along the axis of the cable is essential, especially on the short, relatively straight cable sections. Such stresses would be induced by differential thermal expansion and vibration in our configuration where the mating connectors to which the ends of the cables attach are rigidly fixed relative to the mounting structure of the modules. We depend upon the curves in the cable runs to provide this needed axial strain relief, and for this to be effective, we require the more flexible 0.086" O.D. material. In at least one assembly, which for the purposes of cable layout could have been a short, straight run of cable, we added a jog in the cable just to provide this strain relief.

VII. SMA CONNECTORS USED AND APPLICABLE ASSEMBLY PROCEDURES

As we explain in this report, the sole source of all of the performance defects we found in the cable assemblies fabricated at Millitech was eventually determined to be the installation of the SMA connectors on to the Isocore cable material. In this section, we describe the SMA-style RF connectors used on the cable assemblies of the T/R Modules, and we present the special steps which we developed and added to the standard assembly procedures for the installation of two of these connectors to insure quality, high performance, Isocore cable assemblies.

A. Four types of MIL-C-39012 SMA-Style Connectors Used on the T/R Modules

Four different part numbers controlled under the MIL-C-39012 specification for SMA-style connectors are utilized among the 16 different Isocore cable assemblies for the four T/R Modules. These four connector types are listed in Table 1. Also listed along with each connector is the identification number of the associated assembly procedure published by Omni-Spectra Corp, a QPL manufacturer of MIL-C-39012 connectors. Note that the MIL-C-39012 specification rates the connectors for a temperature range of -65°C to +165°C, well within the range of the requirement of the T/R Modules.

TABLE 1. SMA CONNECTORS USED IN SEMI-RIGID COAXIAL CABLE ASSEMBLIES		
PART NUMBER FROM MIL-C-39012	DESCRIPTION	OMNI SPECTRA ASSY PROCEDURE NO.
M39012/79B3001	Straight Cable Plug	20-543
M39012/80B3001	Right Angle Cable Plug	20-547
M39012/81B3001	Straight Cable Jack	20-549
M39012/83B3001	Bulkhead Feedthrough Cable Jack	20-557

B. Performance Defects Caused by Improper Installation of Connectors

One type of defect displayed in the electrical performance of one group of the cable assemblies which we fabricated was the presence of a dip, or notch, of between 2 to 5 dB depth, in the plots from the measurement of swept insertion loss. This notch would have a typical width of about 0.5 to 1 GHz and would be located somewhere within the band of about 6 to 15 GHz. Figure 2 in Section IV-B shows the response of one of the early cable assemblies fabricated for the T/R Modules and which displays this type of defect in its swept response. The presence of a notch of this type suggests a parasitic resonance condition within the cable assembly. When we positively identified the cause of this problem in our cable assemblies, such was found to be the case.

We noticed that those cable assemblies which displayed this characteristic resonance all utilized a particular SMA connector type on one of the two ends. This connector was the Bulkhead Feedthrough Cable Jack, one of the four connectors listed in Table 1. We found that the problem of the resonance in the response stems from the outer sleeve, approximately 0.25" in length, on this connector into which the end of the cable, previously prepared for the connector, is inserted. Following insertion, the copper outside jacket of the cable is soldered to this sleeve. Solder is flowed in from the outside end of the sleeve, and it flows into the narrow cylindrical gap between the inside surface of the sleeve and the outside surface of the outer conductor of the cable.

We found that the cause of the resonance notch was incomplete solder flow into this cylindrical gap. As a result, a cylindrical resonant cavity region was formed. We eliminate this defect by taking appropriate measures to insure the complete flow of solder into the sleeve. Also, to insure consistency from unit-to-unit, we measure a fixed volume of solder in advance for this operation. This requirement is addressed in the procedures in Section VIII.

A second defect which was displayed in the electrical performance of another group of our early cable assemblies was the presence of relatively high level of ripple extending across the entire 0 to 15 GHz span of the swept insertion loss plots. The cable assemblies displaying this characteristic ripple have in common another type of connector, the Right Angle Plug connector listed in Table 1. Figure 3 in Section IV-B is a plot of performance of one of the cables displaying this characteristic.

This problem of high ripple across a wide band was traced to a property of the dielectric material of the Isocore cable. The assembly procedure which the manufacturer provides for this type of connector was intended for installing the connector on MIL-standard semi-rigid cable which uses solid PTFE teflon dielectric. That procedure for this connector calls for a short length of exposed cable dielectric to extend beyond the stripped-back outer conductor of the cable.

We found that, because of its soft consistency preventing it from maintaining its cylindrical shape when the outer conductor is stripped away, the dielectric for the Isocore cable could not be made to extend in the manner called for in the vendor-supplied assembly procedure for the connector. In our first cable assemblies, we simply cut the dielectric off flush with the stripped back outer conductor. This, we later realized, resulted in the high ripple characteristic. We found that the length of exposed dielectric was critical to the proper impedance matching of the right-angle plug connector, and that eliminating it results in the ripples we observed.

We solved this problem by trimming the dielectric of the Isocore flush as we did previously, but then we installed, over the center conductor of the Isocore cable, a bead of solid PTFE dielectric having the same inside and outside diameter of the dielectric of Isocore. This bead can be most readily obtained from a section of PTFE dielectric taken from 0.086" O.D. MIL-SPEC cable. This bead serves the role of the length of exposed dielectric which the Omni-Spectra Assembly Procedure 20-547 specifies for the MIL-SPEC Right Angle Cable Plug. This assembly procedure is described in Section VIII of this report.

VIII. SUPPLEMENTARY INSTRUCTIONS FOR FABRICATING ISOCORE CABLE ASSEMBLIES

A. General Notes

- 1. Nicks, scratches, solder splashes, uncontrolled solder flow, etc., on the finished cable assemblies are to be avoided. These appearance items could have associated with them actual or latent performance defects in the cable assembly. Use adequate care in application of tools, vices, and other assembly fixtures, and apply protective surfaces to these items where necessary to prevent marking of assemblies.**
- 2. Follow assembly procedures in Omni-Spectra Assembly Procedures manual. These procedures specify which special tools are to be employed. These procedures are to be supplemented by the notes listed herein.**
- 3. Use a resistive heater soldering tool for all operations of soldering of outer conductors to connectors body.**
- 4. Do not immerse cable material at any time into liquid solvents. Dielectric of Isocore is extremely porous and such immersion could entrap solvents and affect electrical properties.**

B. Preparing cable ends for connectors:

- 1. Do as much bending of the cable material as possible in advance before preparing cable ends for installation of connectors. This insures that any axial displacement of the center conductor that might occur during bending will not create stress on the solder joints of the connectors.**
- 2. Use tools in Omni-Spectra tool kit for sawing cable to length and for dressing ends of outer conductor flat and free of burrs.**
- 3. To prepare cable outer conductor for soldering, polish the outside surface of the copper outer conductor with Scotch Brite abrasive pad to a distance of at least 1-inch back from each end. Then clean any residue from polished surface with trichloroethylene solvent and paper wiper. Do not allow solvent to contact dielectric of cable.**

4. In all cases, trim dielectric material flush with copper outer jacket. Make sure end surface of dielectric is trimmed clean and flush. This takes exception to the assembly for the right angle plug connector which specifies leaving a length of dielectric exposed.
5. Isocore semi-rigid cable material is fabricated with a thin teflon coating over its center conductor. This must be removed from the exposed portion of the center conductor to allow solder to bond to the connectors. Use a sharp blade and lightly scrape off this coating from the exposed center conductor. Avoid nicking or scratching center conductor while removing this coating. Note: .086 O.D. standard MIL-spec semi rigid coax does not have this coating of the center conductor.
6. Inspect prepared copper outer conductor for clean edges and absence of burrs. If any burrs are observed, use blade with scraping motion in a direction outward from the cable center to remove these burrs.
7. Before attachment of connector to prepared end of cable, inspect prepared cable end under stereo zoom microscope to check for absence of debris and burrs, check for clean face of dielectric.
8. Tin exposed center conductor of cable before soldering center conductor to connector parts.
9. Soldering flux and solder: Use 63/37 Sn/Pb solder with RMA rosin core flux.
10. Except where specified herein, do not use additional flux for soldering. Where use of additional flux is specified herein, it is exclusively for soldering of outer conductor of coax to connector. Do not use additional flux for soldering of center conductors.

C. Procedures for Specific Connectors

1. For all connectors except right angle plug:

Soldering of Center Conductor to Connector:

Tin center conductor of cable. Using small-diameter solder w/rosin core tin ID of center pin. Use center contact holder and heat pin. Slide pin over center

conductor and gauge its position per standard assembly procedure provided for connector. If excess solder on shoulder of pin, scrape it off OD of pin using blade. Avoid solder flow to contact portions of pin. If excess flux remains on assembly wipe it off with small quantity of alcohol using paper wipe or swab. Minimize amount of solvent used in wiping.

2. For right angle connector:

Soldering of Center Conductor to Connector:

For right angle connector, modification to AP 20-305: Use PTFE teflon bead, from MIL-spec .086" semi rigid cable, to substitute for .055" extension of dielectric in step 1.0.

Tin center conductor of cable. Tin center contact slot of connector. Using Scotch Brite and trichloroethylene solvent, clean outer conductor surface to be soldered. Place connector body in position per AP, solder center conductor to contact slot in connector. Note: center conductor should extend between 0.000" and 0.005" beyond outer face of contact slot. Wrap two complete turns of 0.025" diameter rosin core solder around cable at end of connector and cut off remaining solder. Have cable pointed upward to allow solder to flow in a downward direction. Use resistance solder tool to apply heat connector body, apply heat at bottom and watch for complete flow of solder into gap. Wipe off flux from external surfaces of assembly, inspect inside of connector under microscope. If flux or contaminants are observed on the interior, clean out with thin swab and slightly wetted with solvent. Do not immerse in ultrasonic cleaner. Do not solder in cap until entire assembly has been had a swept measurement electrical test.

3. For straight bulkhead connector:

Install center conductor per AP. Wrap three complete turns of 0.025" diameter rosin core solder around cable at end of connector and cut off remaining solder. Have cable pointed upward to allow solder to flow in a downward direction. Use resistance solder tool to apply heat connector body, apply heat at bottom and watch for complete flow of solder into gap. Wipe off flux from external surfaces of assembly.

4. For straight cable plug and straight cable jack connectors:

Install center conductor per AP. Wrap two complete turns of 0.025" diameter rosin core solder around cable at end of connector and cut off remaining solder. Have cable pointed upward to allow solder to flow in a downward direction. Use resistance solder tool to apply heat connector body, apply heat at bottom and watch for complete flow of solder into gap. Wipe off flux from external surfaces of assembly.

D. Forming Bends in Isocore Semi-Rigid Cable Material

Use Millitech plastic mandrel tool No. TBD for forming all bends. Install cable in groove of tool. Apply uniform pressure to straight portions of cable ahead of tool to bend cable around mandrel.

APPENDIX B: SYSTEM ANALYSIS

- B1. GEORGIA TECH RESEARCH INSTITUTE REPORT**
- B2. PLASMA EFFECTS**
- B3. VEC ANALYSIS AND DATA SUMMARY**

B1. PHASE NOISE ANALYSIS

The phase noise of the oscillators used in the MRIS system will have an affect on the system performance. In the worst case, phase noise could limit the detection of a small amplitude plasma return, while, in the best case, phase noise adds another error term to the amplitude and distance measurement. In general, the participants in the MRIS design have believed that phase noise effects will be insignificant. This analysis confirms that belief.

The MRIS system employs three oscillators for the frequency conversions and coherent detection. They consist of a 70 MHz oscillator (Coho) for coherent detection, a 8-12 GHz digitally-tuned oscillator (DTO) to generate the stepped-frequency waveform and a millimeter wave local oscillator (LO) for conversion to and from the transmitted band. A simplified diagram of the frequency conversions is shown in Figure B1-1. The diagram indicates time delay associated with the circuitry at the different frequencies. The delay of interest is the differential time delay between the two signals appearing at the downconversion mixers, D1-3. These are denoted as T1, T2, T3 for the Coho, DTO, and millimeter-wave LO respectively.

Each oscillator together with its associated differential time delay and receiver mixer forms a frequency discriminator. The discriminator has a sensitivity to the oscillator's frequency determined by the differential time delay. If, for example, the differential time delay were zero, then the output of the receiver mixer (a phase detector) connected to that source would be fixed regardless of the oscillator's frequency. For a given differential time delay, the sensitivity of the mixer's output or Correlation Factor is given by the following equation, from a paper by Goldman [1],

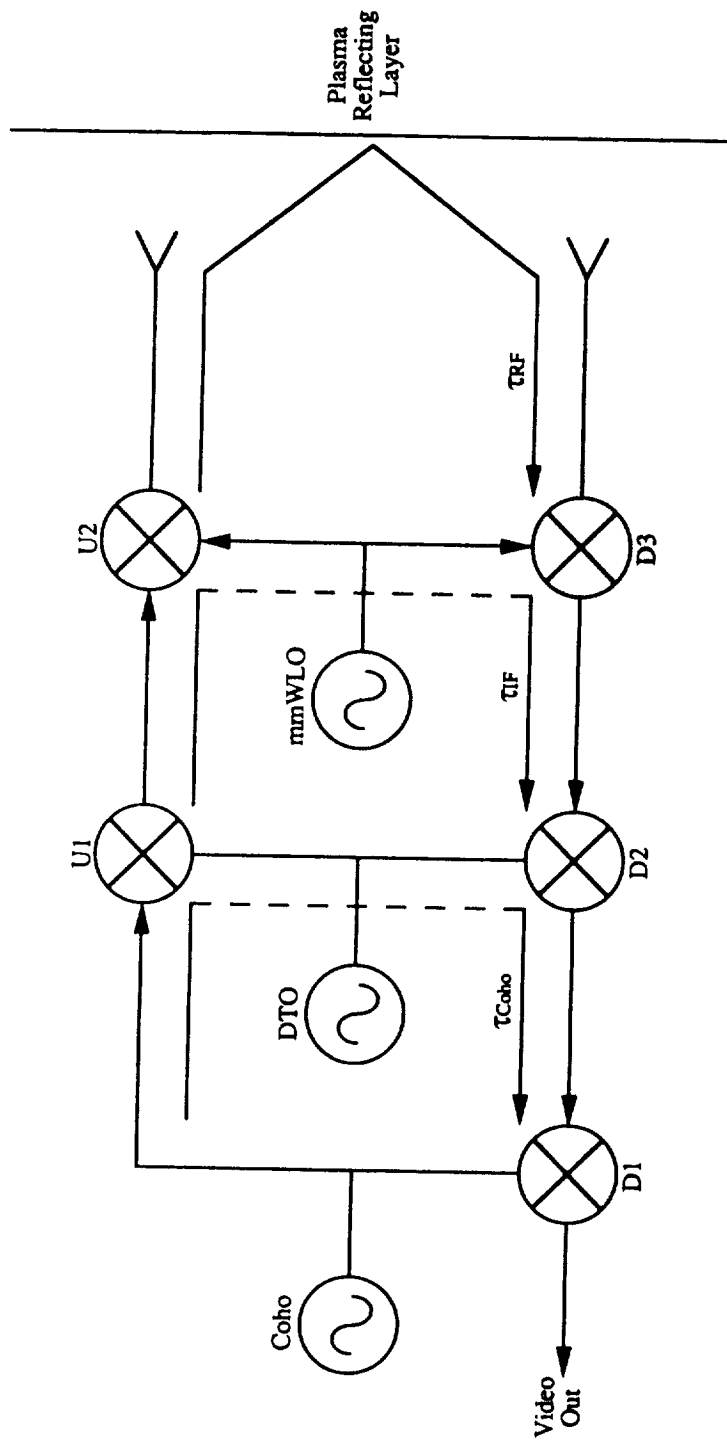
$$K = 2 (1 - \cos(2 \pi f_m t))$$

where

f_m is the offset frequency

¹ Goldman, Stan, "Oscillator Phase Noise Proves Important to Pulse-Doppler Radars," Microwave Systems News, February 1984.

MRIS Delays for Phase Noise Analysis



$$\text{Delay (Coho)} = \tau_{\text{Coho}} + \tau_{\text{IF}} + \tau_{\text{RF}} = T_1$$

$$\text{Delay (DTO)} = \tau_{\text{IF}} + \tau_{\text{RF}} = T_2$$

$$\text{Delay (mmWLO)} = \tau_{\text{RF}} = T_3$$

Figure B1-1. MRIS delays for phase noise analysis.

and t is the time delay.

The general procedure for analyzing the effects of phase noise is to take the appropriate correlation factor and apply it to the source's phase noise spectrum as shown in Figure B1-2. The resulting spectrum is passed through the video filter and then sampled, which is exactly what happens in the MRIS system. The sampling frequency F_s is assumed to 12.8 kHz and the bandwidth of the video filter is 100 kHz. The video filter simply cuts off the phase noise spectrum, while the sampling will fold all of the phase noise into the 12.8 kHz processing bandwidth due to aliasing.

To perform the calculation, we have assumed some realistic phase noise spectra and differential time delays. Figure B1-3 shows the phase noise for the three oscillators. The differential time delays are assumed to be

20 ns (T1: Coho)

20 ns (T2: DTO)

2 ns (T3: millimeter wave LO).

Figure B1-4 is a plot of the correlation factor for the different delays. After the spectrum has been multiplied by the correlation factor, the resulting phase noise is shown in Figure B1-5. The sum of these resulting spectra is dominated by the contribution from the MMW LO. Its peak level is less than -80 dBc after sampling at 12.8 kHz (which causes the effective noise floor at frequencies higher than 12.8 kHz to foldover into the 12.8 kHz region). The dynamic range between the thermal protection system (TPS) and plasma responses is expected to be less than 50 dB (usually no more than 40 dB, except at band D), so the phase noise from a large response will still be far below any weak returns from the plasma.

LOCAL OSCILLATOR PHASE NOISE ANALYSIS

The above analysis primarily addresses the effects of oscillator phase noise on return signals, i. e., return signals from desired reflections such as plasma boundary

Block Diagram for Phase Noise Analysis

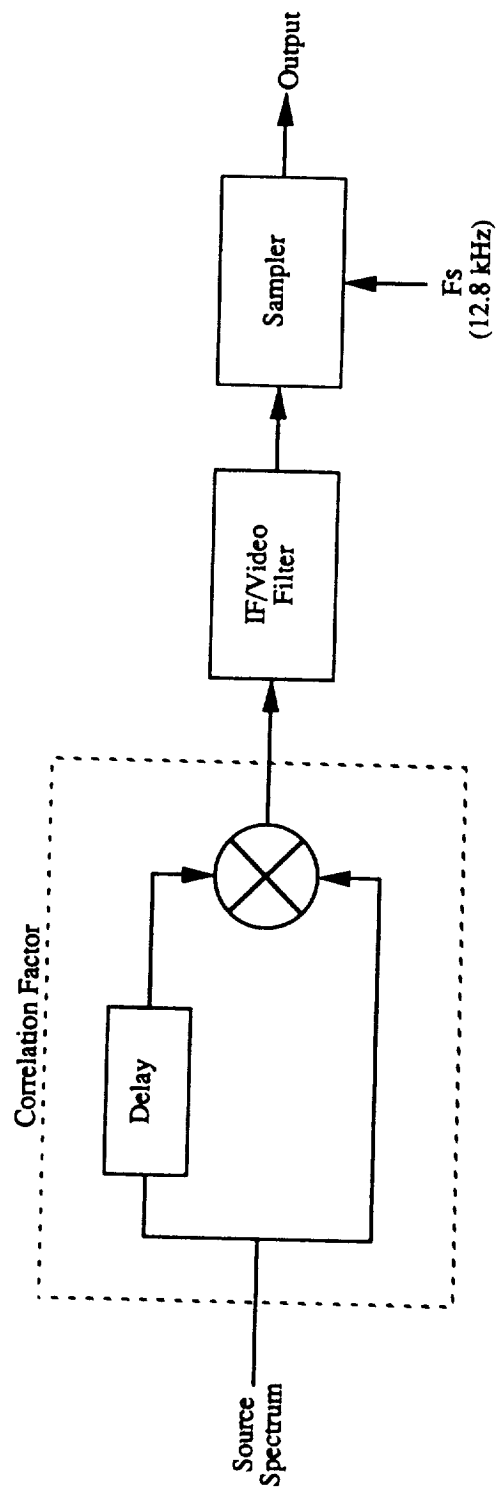


Figure B1-2. Block Diagram for phase noise analysis.

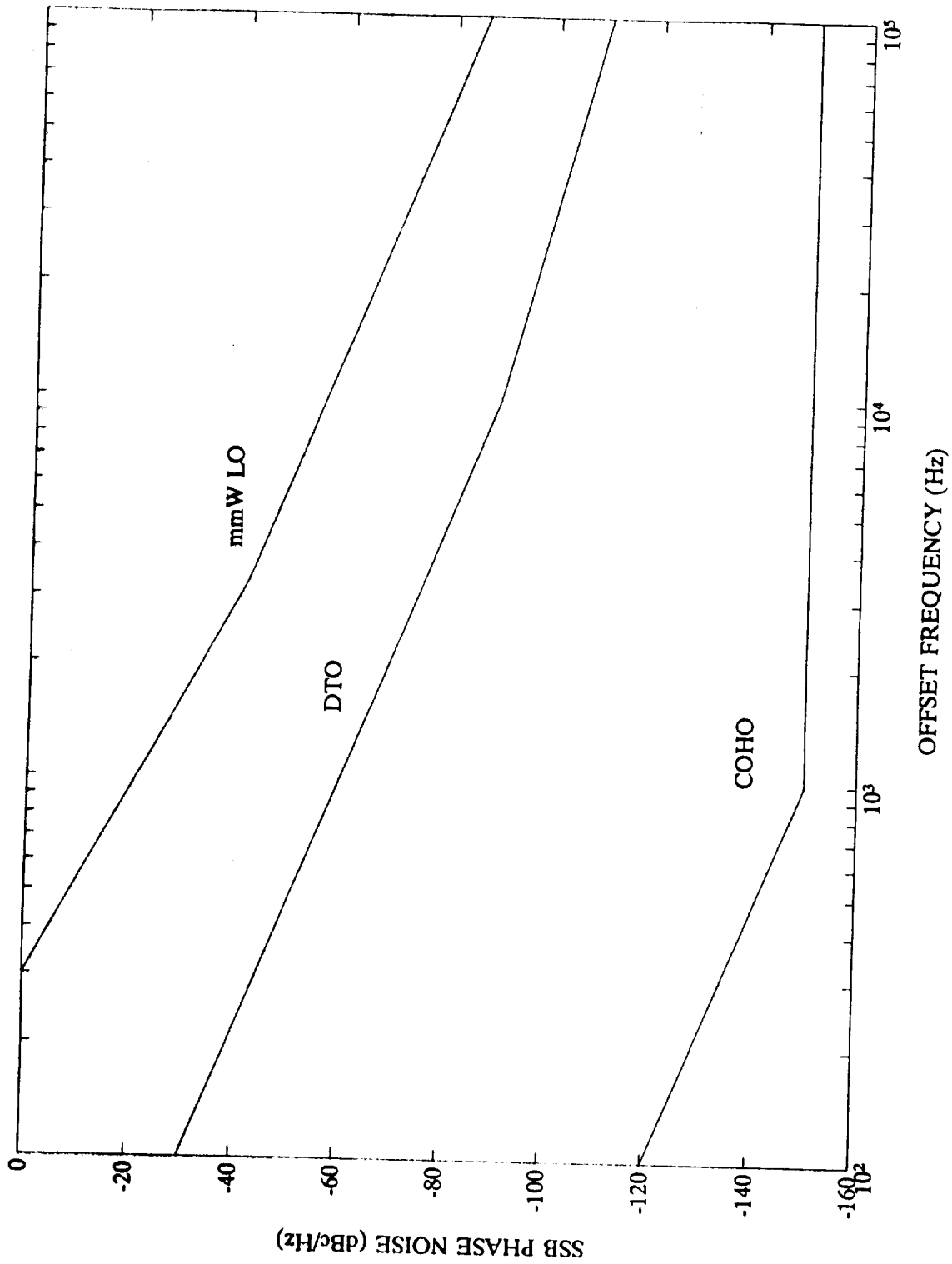


Figure B1-3. Phase noise for COHO, DTO, and mm-wave oscillators.

Correlation Factor for Different Delays

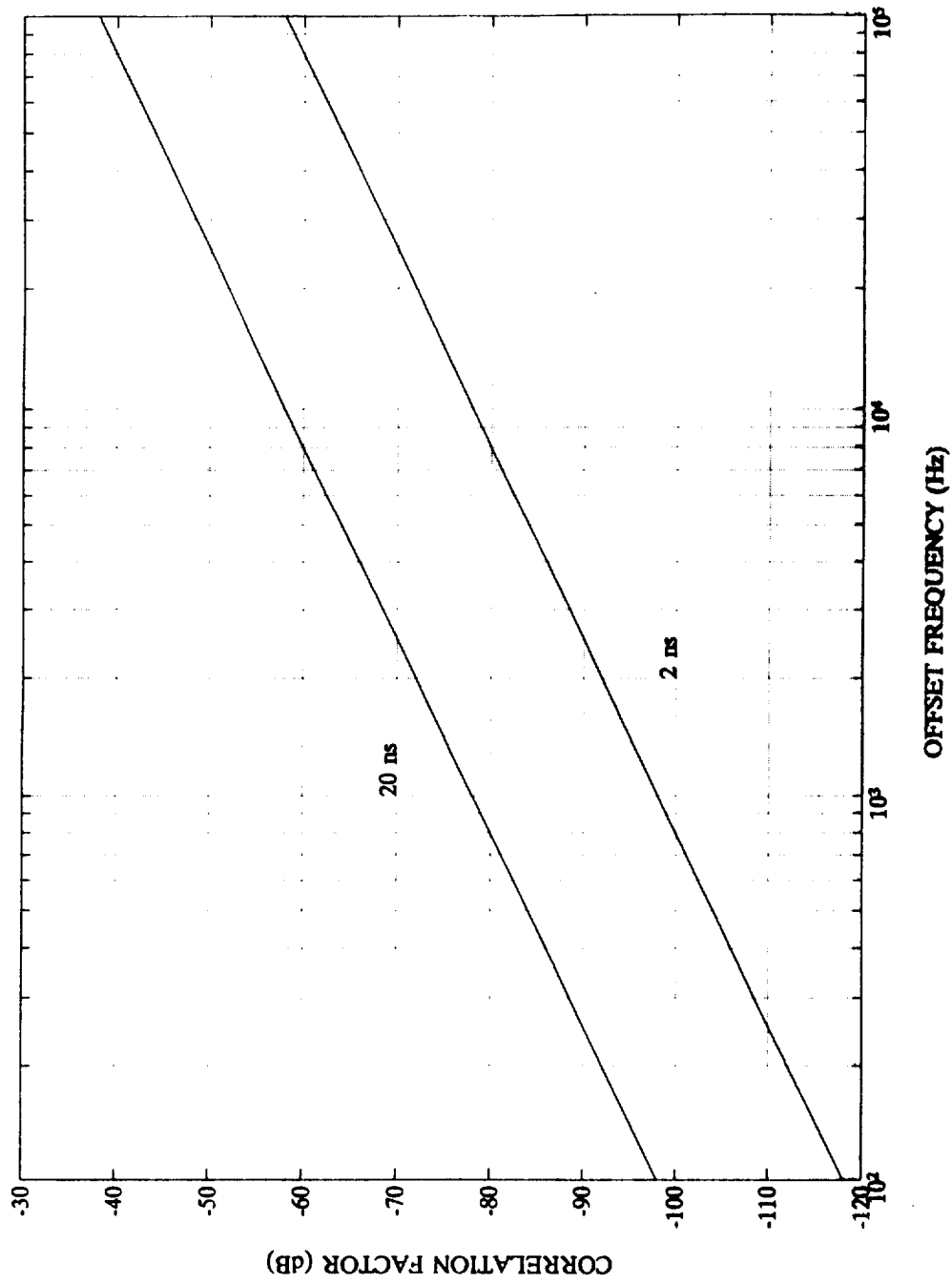


Figure B1-4. Correlation factor for different delays.

Phase Noise with Correlation Factor Weighting

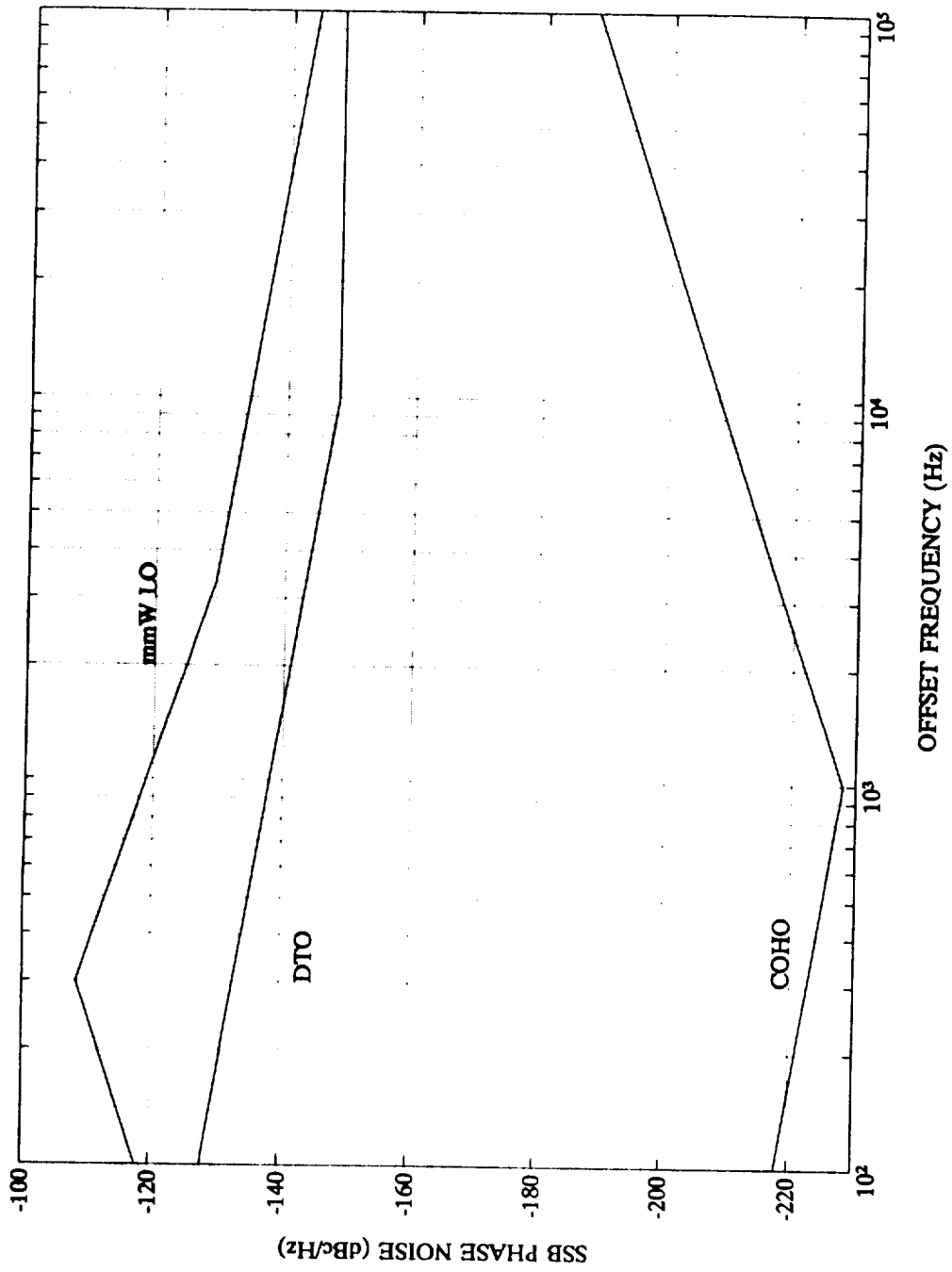


Figure B1-5. Phase noise with correlation factor weighting.

layers, and undesired returned signals such as those from the tile and multiple reflections. The effects of phase noise on these return signals was shown not to be a serious problem, based on the expected phase noise characteristics for the millimeter wave oscillator, the digitally tuned oscillator, and the coherent local oscillator.

A second phase noise effect is that due to phase noise on the mixer local oscillators themselves, and the amount of that noise that contaminates or interferes with the desired target signal. To analyze this effect, some assumptions about the phase noise characteristics of the oscillators must be assumed. Phase noise on the local oscillator signal will create noise around the target signal in a frequency band offset from the local oscillator by the amount of the intermediate frequency. For example, the first IF frequency will be 8-12 GHz, after mixing of the return signal with the MMW local oscillator. Consequently, phase noise on the MMW local oscillator, in a band 8-12 GHz away from the MMW local oscillator frequency, will interfere with the signal. For purposes of analysis, it has been assumed that the phase noise on the MMW oscillator will reach an ultimate (minimum) level of -120 dBc/Hz. The validity of this assumption is based on preliminary discussions with oscillator manufacturers, however, it is not expected to be much in error for the MRIS local oscillators. Given this phase noise spectral density, it is desirable to know the effective noise power at the input to the mixer. If +10 dBm LO power, 10 dB LO to RF port isolation, and an effective RF port return loss of -10 dB is assumed, the effective LO level at the input is -10 dBm. This implies the phase noise spectral density is -130 dBm/Hz at the mixer input. Utilizing 32 frequency bins for stepped frequency processing implies

$$\text{Bandwidth/bin} = 100 \text{ kHz}/32 = 4 \text{ kHz} = 36 \text{ dBHz},$$

where 100 kHz is the video bandwidth. Therefore, the noise power in any bin will be -130 + 36 = -94 dBm/bin. This assumes that there is no appreciable leakage of the LO into the IF, which is a reasonable assumption in most cases, since this mixer port will be a waveguide below cutoff for those frequencies.

From previous work the minimum expected signal level at the RF test mixer input is approximately -61 dBm for band D. A signal-to-noise (thermal noise) ratio of 30 dB has been assumed in previous error budgets and error analyses. Therefore, the above phase noise analysis indicates that the LO phase noise will not further degrade either the amplitude or distance measurements (compared to thermal noise), provided the

phase noise level does not exceed the estimated level. Consequently, the MMW LO phase noise will not present a significant problem if the phase noise at 8-12 GHz away from the RF carrier is at a level no higher than -120 dBc/Hz.

The other local oscillators will also have phase noise components at frequency offsets equal to the IF. However, the phase noise contributions from these sources will be at levels at least as low as for the MMW local oscillator and therefore should not create a problem.

B2-2. PLASMA EFFECTS

GENERAL EFFECTS

The plasma which the MRIS should encounter will constitute a dispersive medium through which the sensor's transmitted signal will travel. This dispersion is caused by the plasma exhibiting a dielectric constant which is a function of frequency. The dielectric constant will also be a function of offset distance from the TPS, since the plasma free electron density is a function of this offset distance. The dielectric constant of the plasma is less than one and goes to zero at the critical electron density. At this point, the transmitted wave is completely reflected. Since the plasma is dispersive, the equivalent pulse width of the system (determined by the transmit bandwidth) is widened and, therefore, system resolution is degraded. The plasma's dielectric constant being less than one results in an increased measured time delay for the reflection. The gradation of the plasma (density is a function of offset distance) can reduce system resolution by producing spurious reflections at intermediate points between the TPS and the critical electron density offset distance.

Some of the possible effects of the plasma on the measurement system, as compared to the laboratory setup with air and a metal reflecting plate, were analyzed. The analysis was done for a TEM propagation mode only. The analysis program was written in MATLAB and the listing is included at the end of this section.

ANALYSIS OF PLASMA GROUP DELAY

In order to analyze the effects of a graded dielectric transmission medium on the proposed system and its vector error correction (VEC) techniques, an analytical expression for the group delay, τ_{group} , was derived for a carrier frequency, ω_c . Start with the definition for group delay,

$$\tau_{group} = \frac{d\phi}{d\omega_c} ,$$

where ϕ is the carrier phase. The incremental phase shift, $d\phi$, of the carrier is related to the incremental distance, dz , along the direction of travel by,

$$d\phi = \frac{\omega_c dz}{v_p} ,$$

where v_p is the phase velocity. For a lossless plasma, the phase velocity is given as,

$$v_p = \frac{c}{\sqrt{1 - \omega_p^2(z)/\omega_c^2}} ,$$

where ω_p^2 is the square of the plasma critical frequency and c is the speed of light in a vacuum. The plasma critical frequency, determined by the free electron density of the plasma, is the frequency at which the dielectric constant of the plasma reaches zero. Substituting equations produces the following expression for the incremental phase:

$$d\phi = \frac{\omega_c dz}{c} \sqrt{1 - \omega_p^2(z)/\omega_c^2} = \frac{dz}{c} \sqrt{\omega_c^2 - \omega_p^2(z)} .$$

Integrating this expression over the distance from 0 to R gives the total phase shift,

$$\phi = \int_0^R \frac{1}{c} \sqrt{\omega_c^2 - \omega_p^2(z)} dz .$$

Substituting the above expression into the definition for group delay, the total group delay is found to be:

$$\tau_{group} = \frac{\omega_c}{c} \int_0^R \frac{1}{\sqrt{\omega_c^2 - \omega_p^2(z)}} dz .$$

For this study, a linear plasma density profile is assumed. This means that at the starting point of the plasma, $z=0$, ω_p^2 is equal to some arbitrary value of ω_b^2 (ω_b^2 is assumed to be less than ω_c^2). The plasma critical frequency, ω_p^2 , then increases linearly in the z direction until, at a distance $z=R$, ω_p^2 equals ω_c^2 . At this point, the traveling wave is totally reflected by the plasma. This linear plasma density profile gives rise to the following expression for ω_p^2 :

$$\omega_p^2(z) = \frac{\omega_c^2 - \omega_b^2}{R} z + \omega_b^2 .$$

Substituting this expression into the expression for group delay gives

$$\tau_{group} = \frac{2\omega_c R}{c} \frac{1}{\sqrt{\omega_c^2 - \omega_b^2}} = \frac{2R}{c} \frac{1}{\sqrt{1 - \omega_b^2/\omega_c^2}}$$

or

$$\tau_{group} = \frac{2R}{c} \frac{1}{\sqrt{\epsilon_b}} ,$$

where ϵ_b is the dielectric constant of the plasma at $z=0$.

For the case where $\omega_b^2 = 0$,

$$\tau_{group} = \frac{2R}{c}$$

or twice the delay of free space.

The above analysis was used for various linear density profiles to determine what the measured time delay to the reflection should be. The MRIS operation was then

simulated in MATLAB and the reflection was determined from the resulting time plot. Results were obtained from the simulation for three cases: no correction, vector error subtraction, and vector error correction. These results were compared to the anticipated result based on the analysis above.

MRIS AND PLASMA SIMULATION

The MRIS is modeled in MATLAB as a stepped-frequency system. For each transmit frequency, the reflection coefficient of the medium (TPS and plasma) is calculated and stored. The reflection coefficient array is then transformed to the time domain with an FFT to provide reflection versus range information. For the simulations contained in this section, no error sources were introduced; the aim is to investigate the general effects of the plasma on MRIS operation.

The plasma modeling process consists of calculating the dielectric constant as a function of frequency and offset distance. This calculation is based on the plasma density profile. The program then starts at the maximum range and steps in towards the sensor until the dielectric constant goes above zero. At this point, the program takes the reflection coefficient for the reflecting layer, -1, and starts transforming it through transmission line sections to obtain the reflection coefficient at the beginning of the plasma (closest to the sensor). The impedance of the transmission line sections is calculated from the dielectric constant of the plasma. After the reflection coefficient at the beginning of the plasma is calculated, the reflection coefficient that the sensor sees through the TPS is calculated. This process is done for all the frequencies that are being analyzed.

The first simulations show the general effects of the plasma on system operation. All of these runs are for a 20 GHz center frequency with 32 steps of 128 MHz. A rectangular window is used before FFT processing. Figure B2-1 shows the magnitude of the reflected signal versus range (cm) with no plasma. The reflection coefficient is slightly less than one and the nulls in the waveform do not reach zero because of the interference from the TPS. Figure B2-2 shows the same situation except that the reflection is due to a plasma with linear density profile. The maximum free electron density is 6×10^{12} . The response is very similar to the first case. Note that the peak is at a different location, because the first case had a reflector at some arbitrary distance

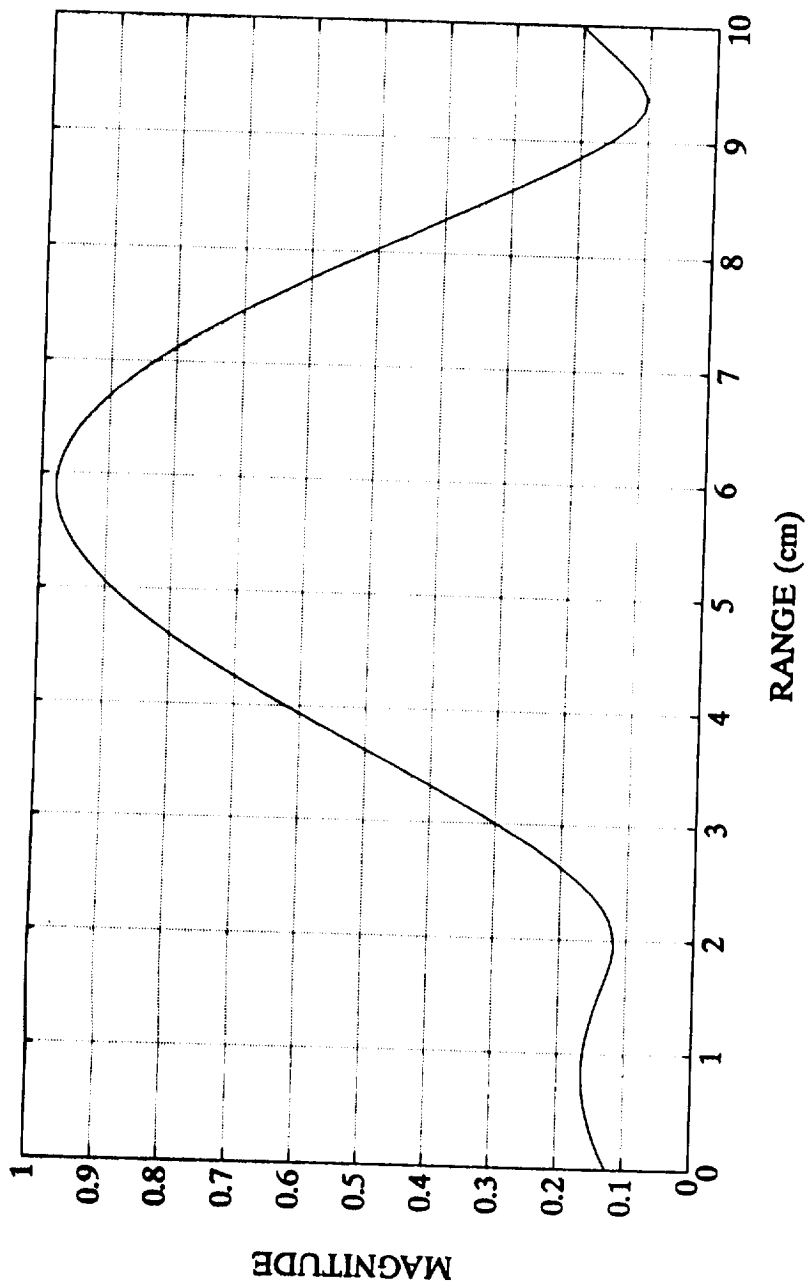


Figure B2-1. Response versus range for the no-plasma case.

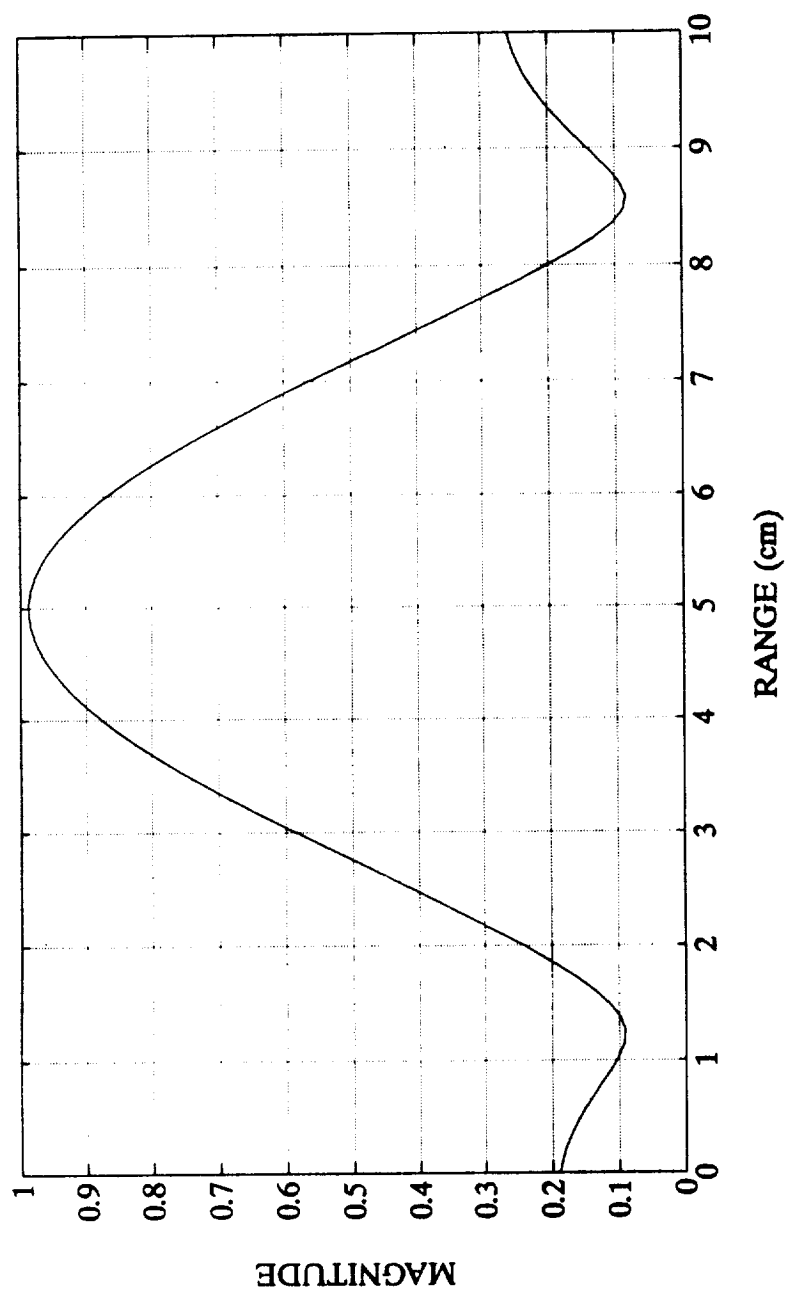


Figure B2-2. Response versus range for the plasma case (linear profile, 0 to $6 \times 10^{12} \text{ cm}^{-3}$).

and was not related to the plasma case. The resolution, indicated by the width of the peak, is about the same for the two cases, so the dispersion due to the plasma had little effect. When the plasma starts with a significant density next to the TPS, though, there is a large effect on the response as seen in Figure B2-3. Here, the first peak (magnitude of approximately 0.4) is due to the interface between the TPS and the plasma. The reflecting layer of the plasma has a smaller magnitude and the peak is broadened. Similar results were obtained for the other MRIS bands.

The general plasma effects can be summarized as follows. The plasma dispersion appears to have little effect on system operation. This is reasonable, since the system bandwidth is not a large percentage of the center frequency. An abrupt change in the plasma density (and dielectric constant) over the transmission path can cause another reflection appearing before the critical density layer in range. If the density change is small over the space of the transmit wavelength, then, intermediate reflections will be insignificant. A possible circumstance for an abrupt change in dielectric constant is when the plasma has a significant density next to the TPS.

The previous simulations were uncorrected data. Two types of error correction were studied: Vector Error Subtraction (VES) and Vector Error Correction (VEC). VES is a procedure where the response without any plasma is stored as a reference. Further simulations, then, subtract this reference from the response. The VEC technique used here assumes that the dielectric constant is the same on either side of the TPS and then takes the multiple reflections between the TPS and plasma into account. Again, these techniques are used in the TEM simulations; the usefulness of these techniques for a near-field plasma case has not been established.

Figure B2-4 is a plot of the plasma dielectric constant versus range for the lowest frequency, F1, and the highest frequency, F32. The parameters are those listed in the MATLAB listing below, except that "dstart" was set to zero. The average point where the dielectric constant crosses zero is at 1.33 cm range. The expected range for the return in the time domain can be found by multiplying this average range by two and adding the thickness of the TPS, 2 cm, giving a result of 4.66 cm. The time domain results are shown in Figure B2-5 for the cases of no correction, VES, and VEC. The peak of the return is closest to the expected value, 4.66 cm, for the VEC case and worst for the uncorrected case.

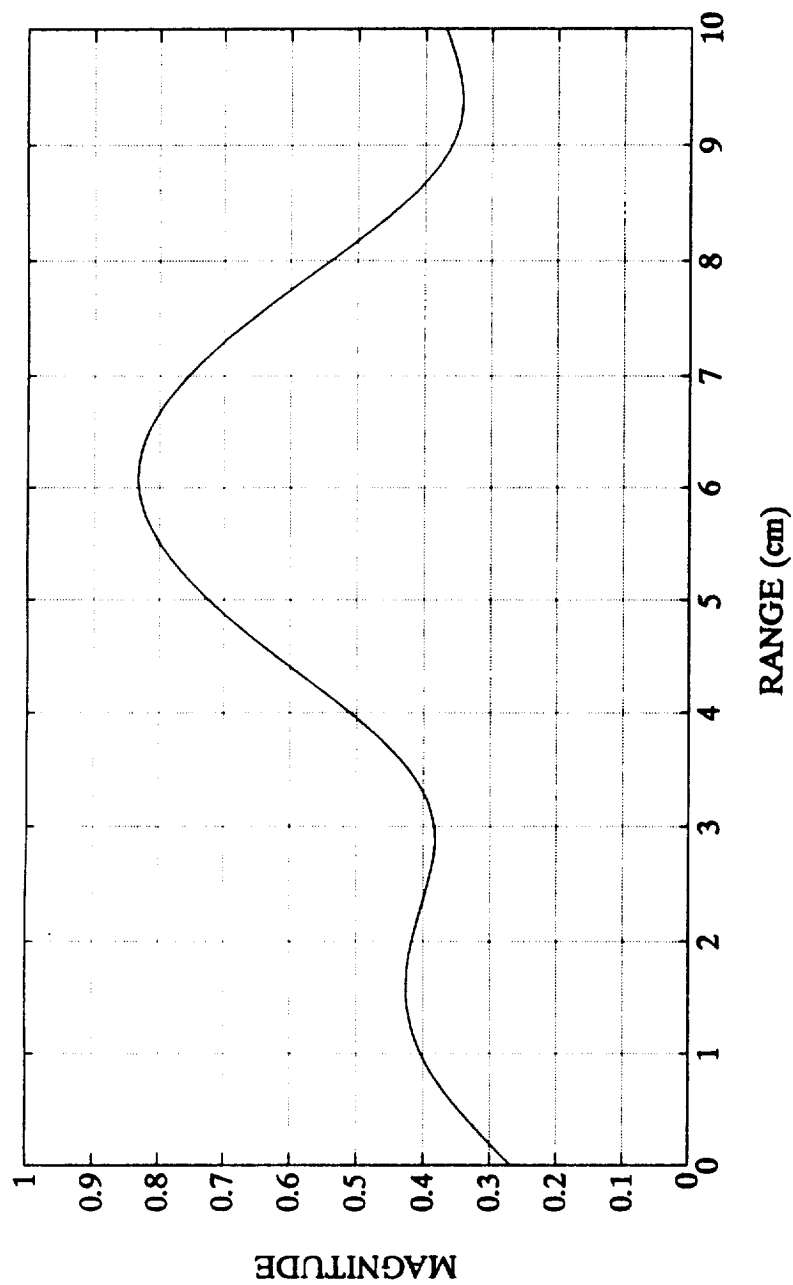


Figure B2-3. Response versus range for the plasma case (linear profile, $3 \times 10^{12} \text{ cm}^{-3}$ to $6 \times 10^{12} \text{ cm}^{-3}$).

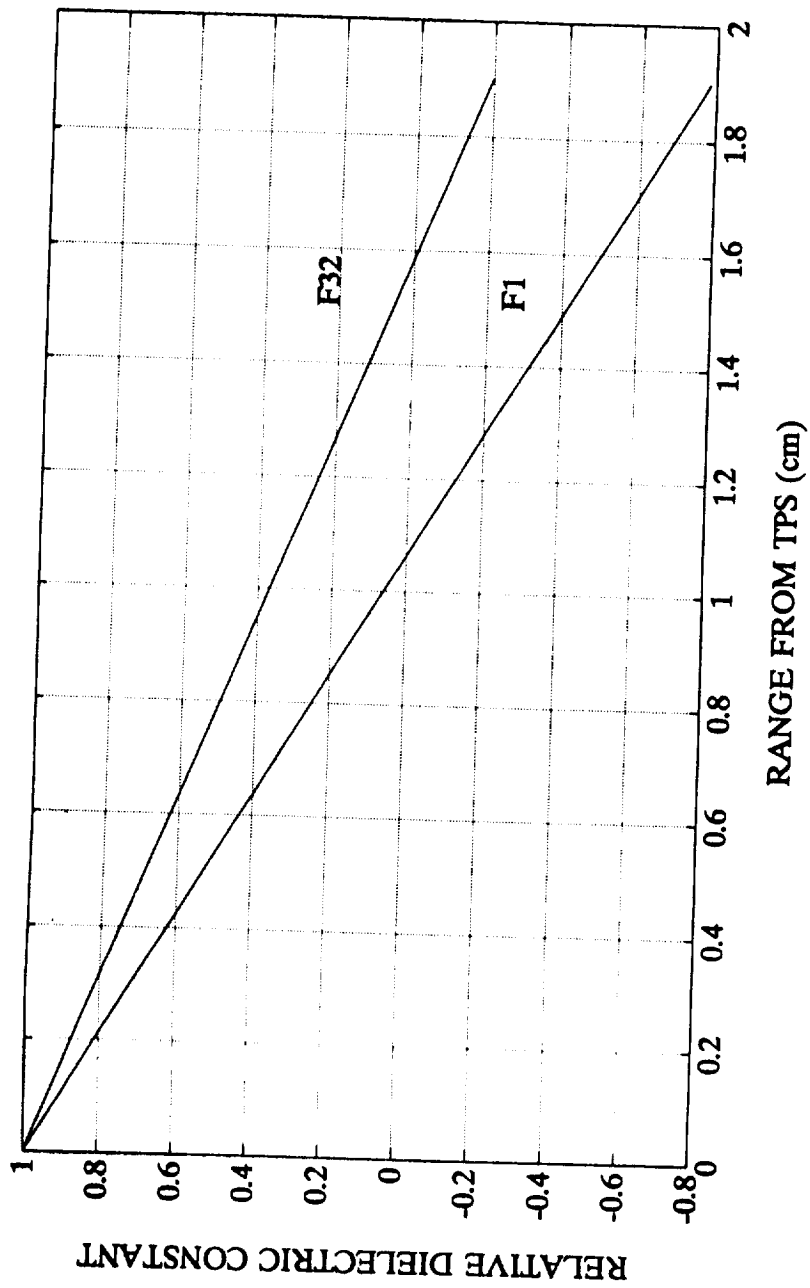


Figure B2-4. Relative dielectric constant versus range for the plasma case.

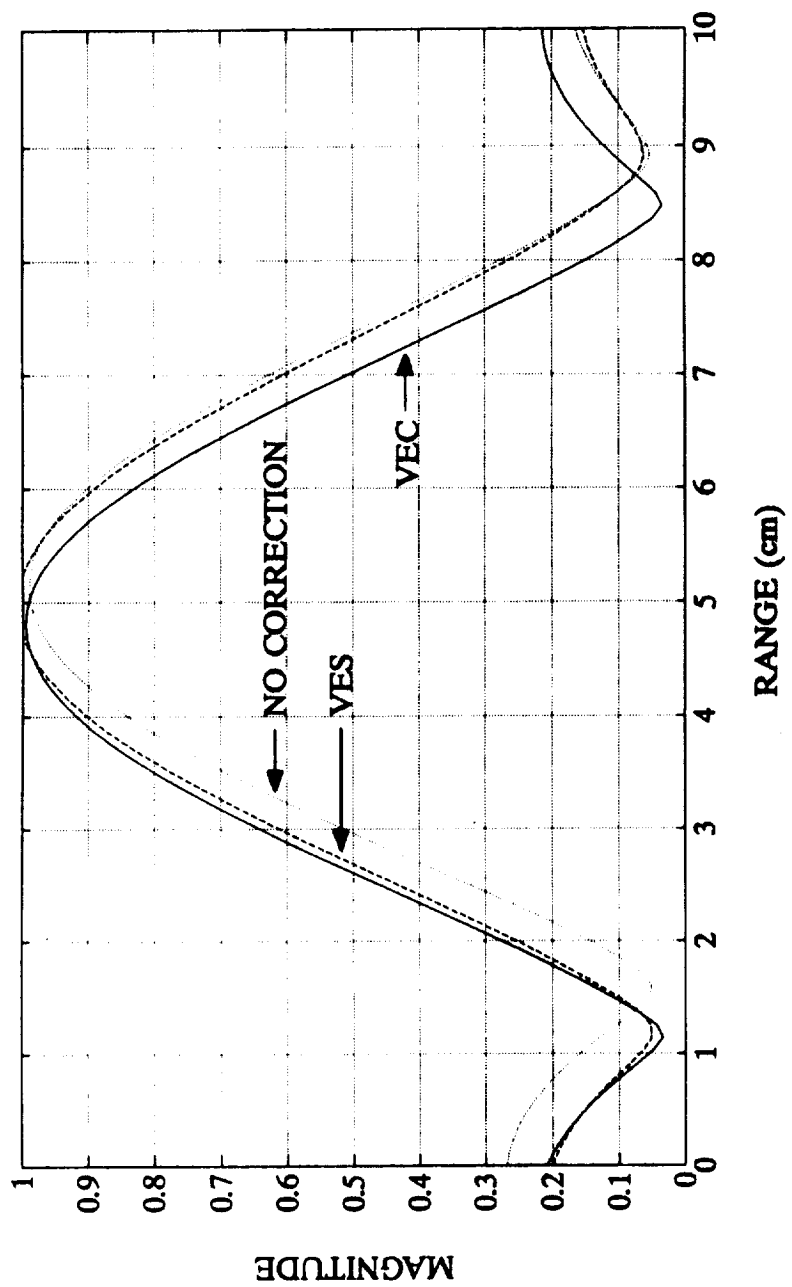


Figure B2-5. Response versus range for different correction techniques (plasma from Figure B2-4).

Another result from the above simulation shows the variation in indicated range as the plasma is offset from the TPS. The indicated range is the range of the peak of the time domain response, while the offset of the plasma is accomplished by inserting a section of transmission medium with relative dielectric constant of unity. As shown in Figure B2-6, the worst variation is the case with no correction, while the smallest variation occurs for the VEC case.

A second simulation uses a plasma having a relative dielectric constant less than unity immediately outside the TPS. The relative dielectric constant is plotted in Figure B2-7 for F1 and F32. The average zero-crossing for this case is at 1.27 cm, while the average dielectric constant at zero range is 0.38. From the analysis above, the expected range can be calculated as,

$$2\left(1.27\frac{1}{\sqrt{0.38}}\right)+2=6.12$$

Figure B2-8 shows the resulting time domain plots for this case. In these cases, all of the peaks lie close to the expected range. Note that there is a significant peak in the 1 to 2 cm range due to the TPS plasma interface. Figure B2-9 shows the indicated range versus the plasma offset distance (similar to the case of Figure B2-6). The variation is, again, least for the VEC case and worst for the no correction case.

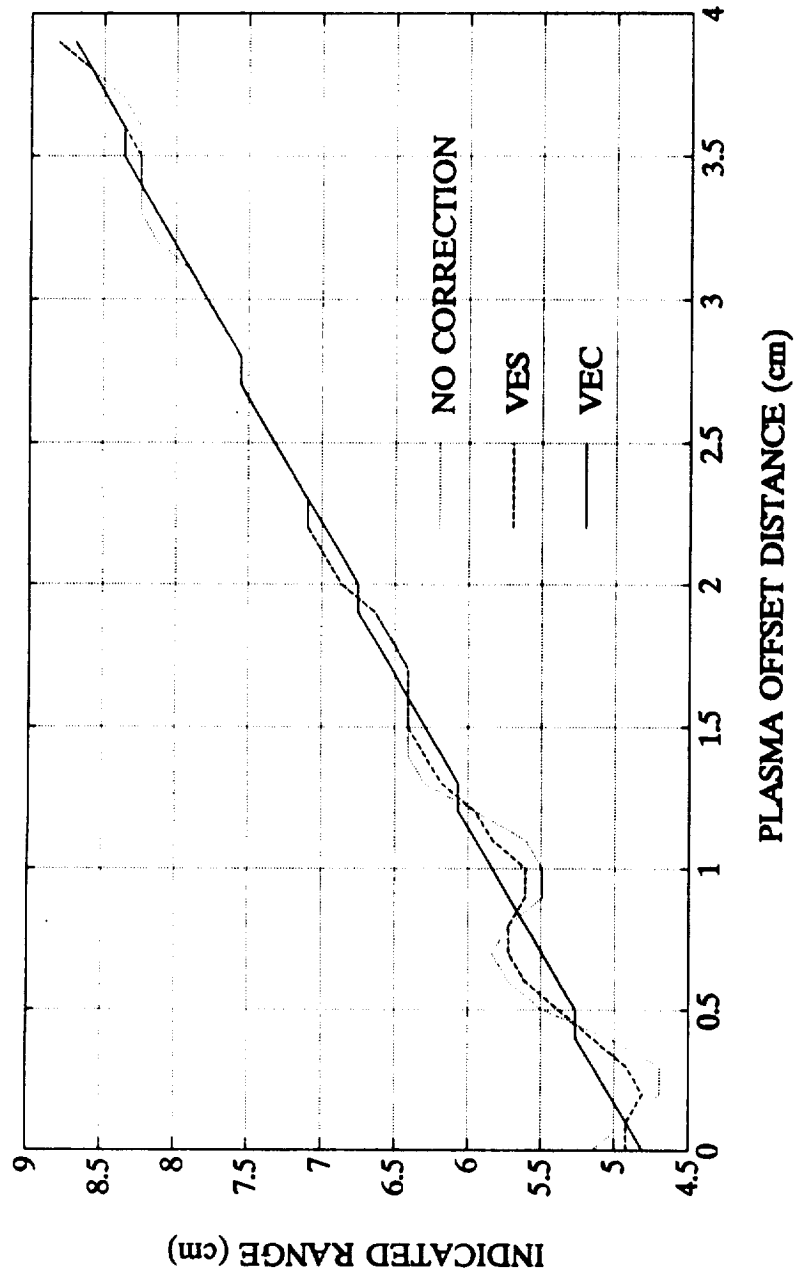


Figure B2-6. Indicated range versus plasma offset range for different correction techniques (plasma from Figure B2-4).

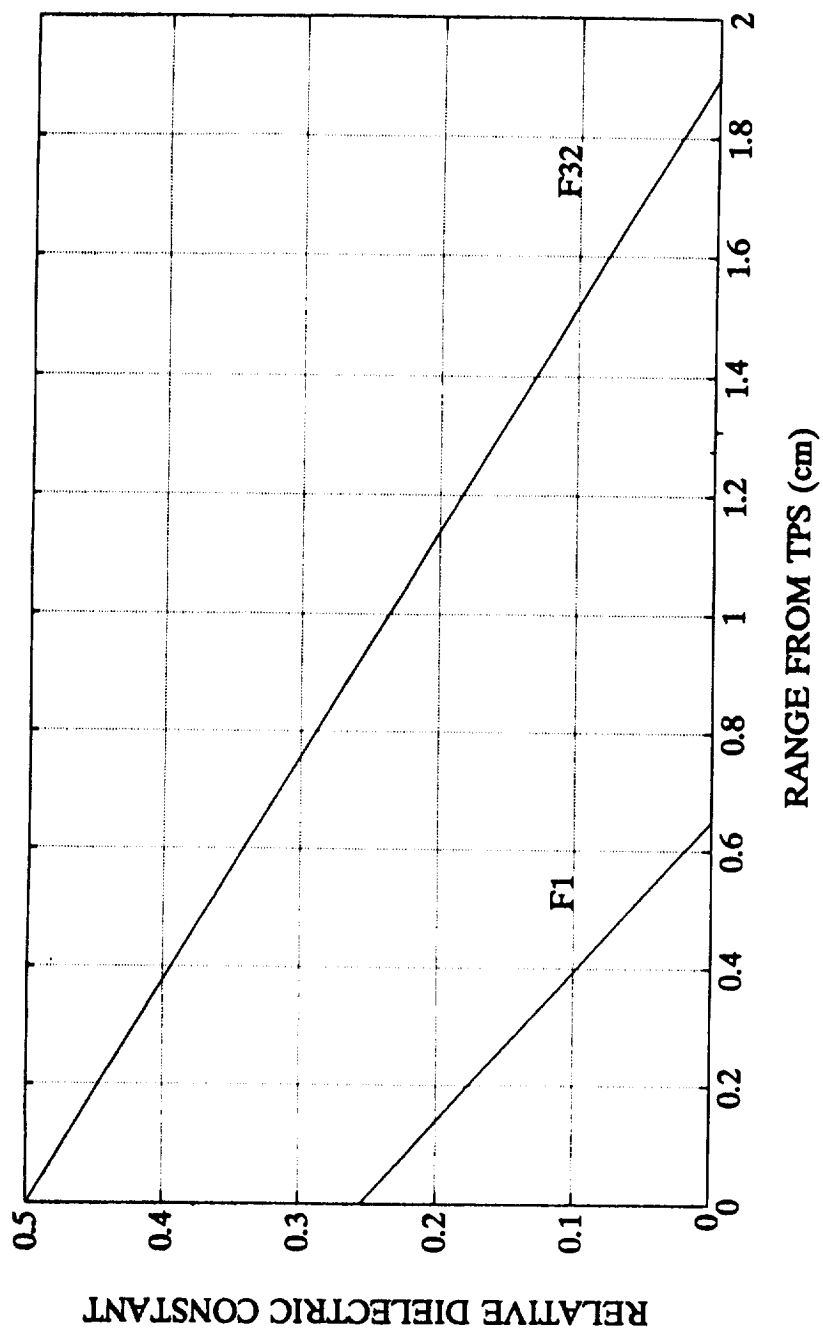


Figure B2-7. Relative dielectric constant versus range for the plasma case (linear profile, $3 \times 10^{12} \text{ cm}^{-3}$ to $6 \times 10^{12} \text{ cm}^{-3}$).

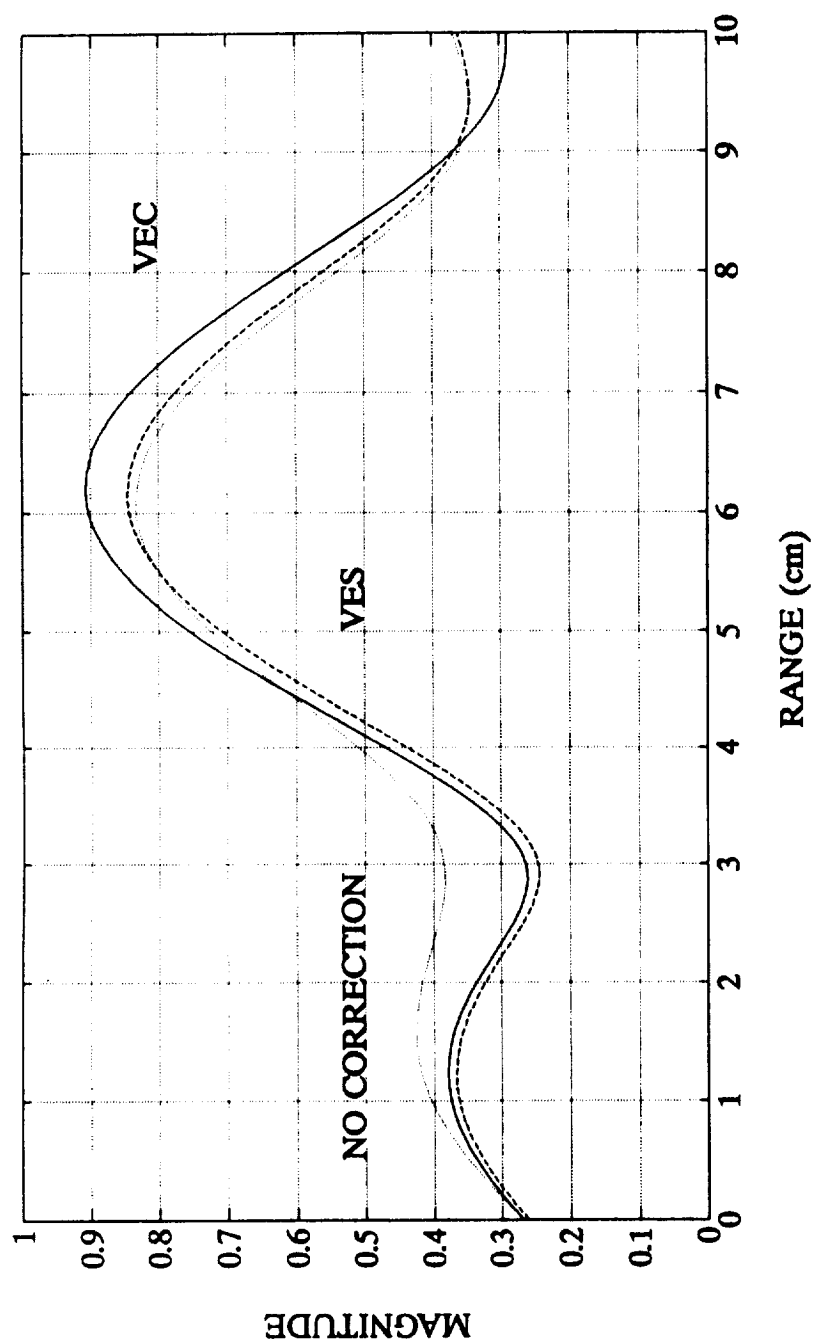


Figure B2-8. Response versus range for different correction techniques (plasma from Figure B2-7).

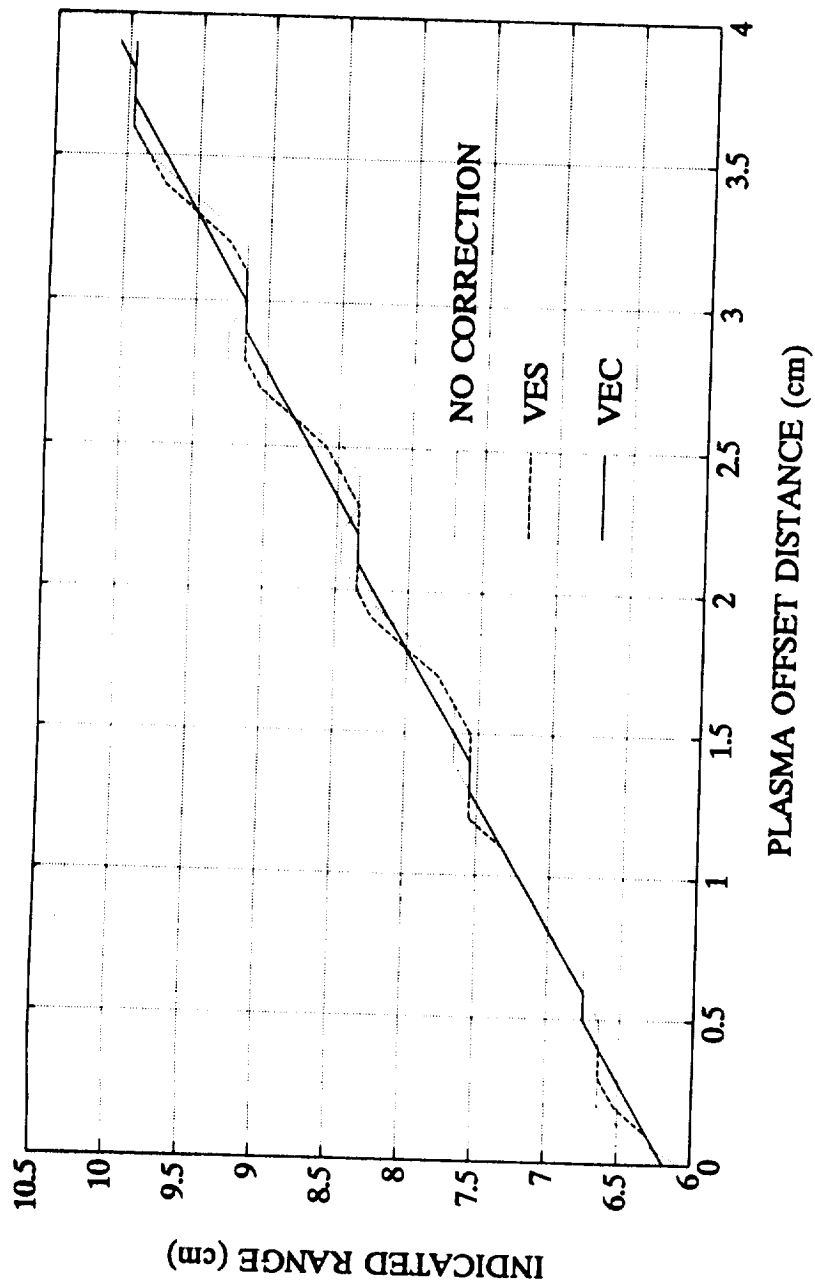


Figure B2-9. Indicated range versus plasma offset range for different correction techniques (plasma from Figure B2-7).

MATLAB CALSEALP.M PROGRAM LISTING

```
% CALSEALP.M
echo on
meter=1;
sec=1e6;
mhz=1;
khz=.001;
c=3e8*meter/sec;
fillfactor=32;    % zero-filling factor for FFTs
n=32;             % number of frequencies
fstart=18000*mhz; % start frequency
fstep=128*mhz;    % frequency step size
lengtha=.02*meter;% thickness of bulk tile
lengthb=.000254*meter; % thickness of RCG
lossb=0;          % loss in RCG (dB/meter)
lossc=0;          % loss in free space offset of plasma (dB/meter)
etile=1;          % dielectric constant of bulk tile
ercg=4;           % dielectric constant of RCG
zinc=.001;        % size of increment for plasma offset from outside of
TPS
ninc=50;          % number of increments of size zinc
perm=8.854e-12;   % permittivity of free space
q=1.6e-19;        % electron charge
mass=9.1e-31;     % electron mass
rstep=.001*meter; % range increment through plasma
m=20;             % number of rstep
dmax=7.18e12;     % electron density: 1/(cubic cm)
window=ones(1,n); % selected window function for FFT processing
wgain=1;          % 1/(coherent gain of the weighting window)
f=[fstart:fstep:fstart+(n-1)*fstep]; % define frequency array
xvector=100*(c/2)/(fstep*n*fillfactor)*[0:n*fillfactor-1]; % x axis
vector
keyboard
%
% plasma model
%
r=[0:rstep:(m-1)*rstep]'; % meters
```

```

d=dmax*1e6/((m-1)*rstep)*r;
d=d+dmax*1e6/3;
%
fp2=((1/39.478)*q*q/(perm*mass))*d)*ones(1,n);
epsilon=1-fp2./(1e12*(ones(m,1)*f).^2); % range by frequency (row by
column)
clear fp2
%
s=-1*ones(1,n);
for fi=1:n
    for ri=m:-1:2
        if epsilon(ri,fi)>0
            alpha=0;
            beta=2*pi*f(fi)*sqrt(epsilon(ri,fi))/c;
            s(fi)=s(fi)*exp(-2*alpha*rstep)*exp(-i*2*beta*rstep);
            zload=(1/sqrt(epsilon(ri,fi)))*(1+s(fi))/(1-s(fi));
            z0=1/sqrt(epsilon(ri-1,fi));
            s(fi)=(zload-z0)/(zload+z0);
        end
    end
    if epsilon(1,fi)>0
        beta=2*pi*f(fi)*sqrt(epsilon(1,fi))/c;
        s(fi)=s(fi)*exp(-2*alpha*rstep)*exp(-i*2*beta*rstep);
        zload=(1/sqrt(epsilon(1,fi)))*(1+s(fi))/(1-s(fi));
        s(fi)=(zload-1)/(zload+1);
    end
end
clear epsilon
sp=zeros(2,2*n); % plasma reflection coefficient,
sp(1,1:2:2*n-1)=s(1:n); % reformat as a two-port
%
% reflection coefficient for matched load
%
stile=smult(trl(1/sqrt(epsilon)),0,lengtha,f),trl(1/(sqrt(epsilon))),lossb,lengthb,f));
gam1=s11(stile);

```

```

%
% Loop for offsetting plasma
%
for in=1:ninc
    lengthc=zinc*(in-1);
    sm=smult(stile,smult(trl(1,lossc,lengthc,f),sp));
    gamm=s11(sm);          % measured reflection coefficient

    num=gamm-gaml;
    den=1-gamm.*conj(gaml);
    gamcor=num./den;

% no correction
    time0=wgain*fillfactor*ifft(gamm.*window,n*fillfactor);
    [l,m]=max(abs(time0));
    peak0(in)=time0(m);
    xind0(in)=xvector(m);

% simple subtraction of the matched load case (VES)
    time1=wgain*fillfactor*ifft(num.*window,n*fillfactor);
    [l,m]=max(abs(time1));
    peak1(in)=time1(m);
    xind1(in)=xvector(m);

% Joe Seal's correction (VEC)
    time2=wgain*fillfactor*ifft(gamcor.*window,n*fillfactor);
    [l,m]=max(abs(time2));
    peak2(in)=time2(m);
    xind2(in)=xvector(m);
end
xscale=100*((0:zinc:(ninc-1)*zinc)); % xaxis for functions of offset

function z=smult(x,y)
%
% smult(x,y) cascades two 2-port S-parameter matrices, x and y.

```

```

%           The resulting S-matrix consists of port1 of x
%           and port2 of y (port2 of x and port1 of y are
%           connected internally).
%           Matrices x and y should have 2 rows and
%           2*N columns, where N is the number of frequencies
%           contained in the data.

%
% R. G. Pauley 12/08/89
%
[1x,mx]=size(x);
[1y,my]=size(y);
if (1x==2)&(1y==2)&(mx==my) % check size of inputs
    n=mx/2; % n is the number of frequencies
    index1=[1:2:mx-1]; % set up the indices
    index2=[2:2:mx];
    det=ones(1,n)-x(2,index2).*y(1,index1); % determinant from Mason's
Rule
%
    z(1,index1)=x(1,index1)+x(1,index2).*x(2,index1).*y(1,index1)./det;
    z(2,index2)=y(2,index2)+y(1,index2).*y(2,index1).*x(2,index2)./det;
    z(2,index1)=x(2,index1).*y(2,index1)./det;
    z(1,index2)=x(1,index2).*y(1,index2)./det;
elseif (1x==2)&(1y==1)&(mx==2*my)
    n=my;
    index1=[1:2:mx-1];
    index2=[2:2:mx];
    det=ones(1,n)-x(2,index2).*y(1:n);
    z(1:n)=x(1,index1)+x(1,index2).*x(2,index1).*y(1:n)./det;
elseif (1x==1)&(1y==2)&(mx*2==my)
    n=mx;
    index1=[1:2:my-1];
    index2=[2:2:my];
    det=ones(1,n)-x(1:n).*y(1,index1);
    z(1:n)=y(2,index2)+y(1,index2).*y(2,index1).*x(1:n)./det;
else

```

```

disp('ERROR in input arguments')
end
function s=trl(zn,ln,length,f)
%
% trl(zn,ln,length,f) produces the S-parameter matrix for a
transmission line.
%
% 'zn' is the normalized characteristic impedance.
It
%
% may be a constant or function of frequency
%
% 'ln' is the loss in dB/meter. It may be a
constant
%
% or a function of frequency.
%
% 'length' is the length in meters. It may be a
constant
%
% or a function of frequency.
%
% 'f' is an array containing the frequencies (MHz)
where
%
% the transmission line is to be analyzed.

% R. G. Pauley 3/19/90
%
[1,m]=size(f);
[11,m1]=size(zn);
[12,m2]=size(ln);
[13,m3]=size(length);
if (m1==m | m1==1) & (m2==m | m2==1) & (m3==m | m3==1)
    c=300*zn; % relative velocity factor assuming permeability of free
space
    index1=[1:2:2*m-1];
    index2=[2:2:2*m];
    beta=2*pi*f./c;
    alpha=(ln/8.69); % convert from dB to nepers
    gamma=(alpha+i*beta).*length;
    den=2*cosh(gamma)+(zn+ones(1,m1)./zn).*sinh(gamma);
    s(1,index1)=((zn-ones(1,m1)./zn).*sinh(gamma))./(den);
    s(2,index2)=s(1,index1);

```



```
s(2,index1)=2*ones(1,m)./(den);  
s(1,index2)=s(2,index1);  
else  
    disp('ERROR -- matrix sizes in function trl do not agree')  
end
```


APPENDIX B3: VEC ANALYSIS AND DATA SUMMARY

B3.1 INTRODUCTION

In addition to the target reflection, the MRIS instrument receives undesired reflections caused by the TPS tile, the antenna ground plane, and to a lesser degree, moding effects. To aid in suppressing the effects of the undesired reflections, error correction techniques similar to those used in network analyzer measurements and radar cross section measurements were investigated. The approaches investigated involved applying error correction to frequency domain data then transforming the error corrected data to the time domain. The error correction procedures investigated involved performing vector mathematical operations between data collected for the target and data collected for a variety of reference conditions. Hence, the name vector error correction or VEC.

Several different VEC procedures were developed and tested at EMS. When the development effort ended, several effective VEC procedures had been developed. The procedures were based on a monostatic configuration but proved to also be effective for bistatic configurations. The stages of the VEC development are described in the remainder of this Appendix. Further investigation and upgrading of the VEC model was planned. Although these efforts were never initiated, the planned studies would have focused on improving the methods for accounting for the presence of the antenna ground plane.

B3.2 VECTOR SUBTRACTION MODEL (VEC-2)

B3.2.1 Description

The initial VEC procedure investigated is referred to as vector subtraction and is denoted as VEC-2 (no vector error correction is denoted VEC-1). This approach is based on similar techniques used in radar cross section (RCS) measurements. In RCS measurements, the cross section of an unknown target must be measured in the presence of undesired reflections produced by the test chamber (e.g., chamber walls, target stand, etc.). The composite measured

reflected signal, ρ_{MEAS} , is modeled as the sum of the reflection from the target plus reflections produced by the test chamber. That is,

$$\rho_{MEAS} = \rho_{TARGET} + \rho_{ROOM} \quad (B3-1)$$

To determine ρ_{ROOM} , an initial measurement is made with the target removed ($\rho_{TARGET} = 0$). The target is then installed and the composite signal, ρ_{MEAS} , is measured. Finally, the desired target reflection, ρ_{TARGET} , is computed through vector subtraction.

$$\rho_{TARGET} = \rho_{MEAS} - \rho_{ROOM} \quad (B3-2)$$

For the MRIS application, a similar model can be used. In this case reflections produced by the TPS tile in the absence of a target reflection are made analogous to the empty room condition in the RCS measurement example. During testing, this condition was approximated by placing a large piece of low reflectivity microwave absorber in front of the instrument antennas. The reflected signal measured looking into the absorber was defined as ρ_{LOAD} . The composite signal, ρ_{MEAS} , measured with a target in place was defined as the sum of ρ_{LOAD} and the desired target reflection. That is,

$$\rho_{MEAS} = \rho_{LOAD} + \rho_{TARGET} \quad (B3-3)$$

By measuring ρ_{LOAD} , the target reflection can be computed from the measured ρ_{MEAS} value through simple vector subtraction as shown below.

$$\rho_{TARGET} = \rho_{MEAS} - \rho_{LOAD} \quad (B3-4)$$

During MRIS laboratory tests, several tests were made using the vector subtraction model. Results from these tests are discussed in the next section.

B3.2.2 Example Time Domain Data Using Vector Subtraction

The majority of the vector subtraction tests were made for a monostatic 44-GHz test setup using an HP8510 Network Analyzer. The test setup consisted of a ground plane mounted 44 GHz horn antenna that radiated through a TPS tile

sample at a flat metal target. The target plate was positioned parallel to the antenna ground plane and was mounted on a motor drive positioner which allowed the separation between the target and the antenna to be precisely controlled.

The initial step in the test procedure was calibration of the HP8510 for wideband s11 measurements (4 or 10 GHz bandwidth was used in most tests). Calibration was performed at the waveguide port of the HP8510's test set. Following calibration, the antenna was connected to the mmW test set and s11 was measured with the antenna radiating into a sheet of low reflectivity absorber placed in front of the target plate. This provided an array of complex reflection coefficients, $\rho_{LOAD}(f)$, where the variable f denotes the measurement frequency. The $\rho_{LOAD}(f)$ values were stored in the test setup computer.

The absorber was then removed to permit the MRIS instrument to view the target plate. With the target separation set to a known value, s11 was again measured to obtain a second array of complex reflection coefficient values, $\rho_{MEAS}(f)$. These values were also stored in the test setup computer. Software in the computer subtracted the stored $\rho_{LOAD}(f)$ array from the stored $\rho_{MEAS}(f)$ array in accordance to equation (B3-4). The difference array was stored in the computer as the desired target information, $\rho_{TARGET}(f)$.

To determine the target position, the error corrected frequency domain target data is transformed into the time domain. The location of the peak signal in the time domain data set is then used as the target location. To perform the required time domain transformation, the error corrected frequency domain array was loaded back into the HP8510 and the network analyzer's built-in software was used to perform the desired signal processing. This processing included the basic time domain transformation and using the Max-Peak location function to determine the position of the signal peak.

A time domain data set for a $\rho_{LOAD}(f)$ array is shown in Figure B3-1. The waveguide calibration plane is located at zero nanoseconds. The three signal peaks located from 0 to 0.6 ns are due to the waveguide transition used between the circular waveguide antenna and the rectangular waveguide test set.

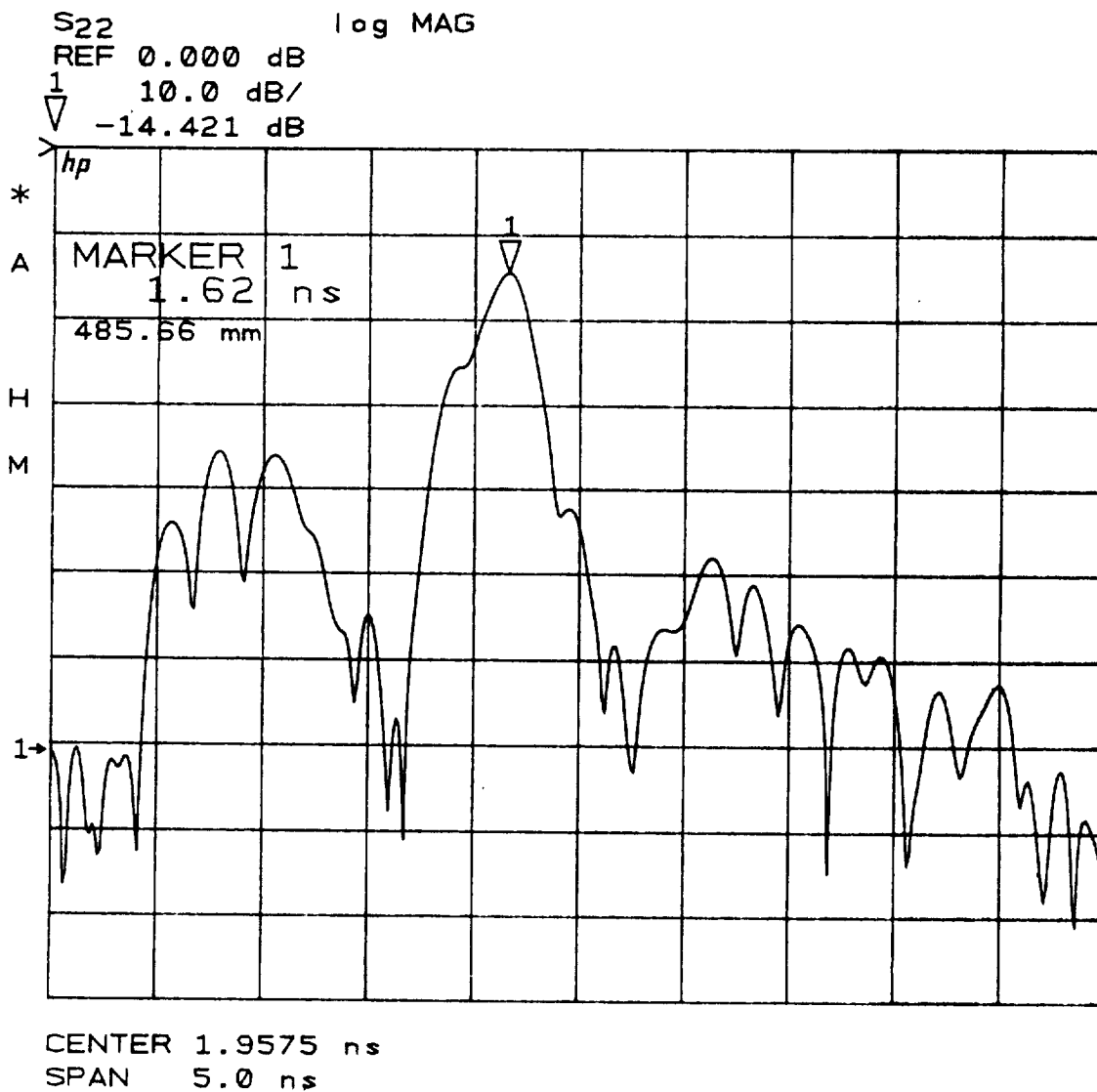


Figure B3-1. Time Domain Plot of ρ_{LOAD} for Monostatic Band-B Tests

The main signal peak at approximately 1.62 ns indicates the presence of the RCG coating of the TPS tile. At approximately 1.38 ns, a slight "shoulder" can be observed on the left side of the main peak. This shoulder appears to be due to the mismatch at the antenna aperture. This would make the electrical distance between the RCG coating and antenna aperture approximately 0.24 ns or 1.42 inches corresponding to a physical distance of approximately 1.24 inches (based on a bulk tile relative dielectric constant of 1.3). This distance is consistent with the known dimensions of the TPS tile and SIP layer.

At approximately 1.92 ns, a second shoulder can be observed on the right side of the main peak. This second shoulder may indicate that a small portion of the tile reflection undergoes a multiple bounce between the RCG surface and the antenna ground plane. Beyond 2.0 ns, the observed reflections are very low (less than -47dB). This confirms that the reflections from the absorber were very low and that the measured absorber data accurately represents the reflections that would be observed in the absence of a target.

The time domain data set for $\rho_{MEAS}(f)$ with a target located two inches from the surface of the TPS tile is shown in Figure B3-2(a). The tile reflection and waveguide transition reflections can still be observed at their previous locations. A large reflection from the target can also be observed at 1.9575 ns. The difference between the tile reflection and the target reflection is 0.3375 ns. This represents the round-trip time delay between the target and the tile surface and corresponds to a one-way distance of 1.99 inches (the target separation was two inches). Beyond 2.0 ns, several additional reflections can be observed. These reflections are multipath reflections mainly due to multiple bounces of the main target signal as it interacts with the TPS tile and the antenna ground plane.

In this example case, the target distance is sufficient to allow the target signal to be easily identified in the presence of the tile interference signal and the multipath signals. As the target is moved closer to the tile surface, the limited system resolution causes the tile reflection, target reflection, and multipath reflections to overlap. The resultant smearing makes it difficult to accurately determine the position of the target reflection. The

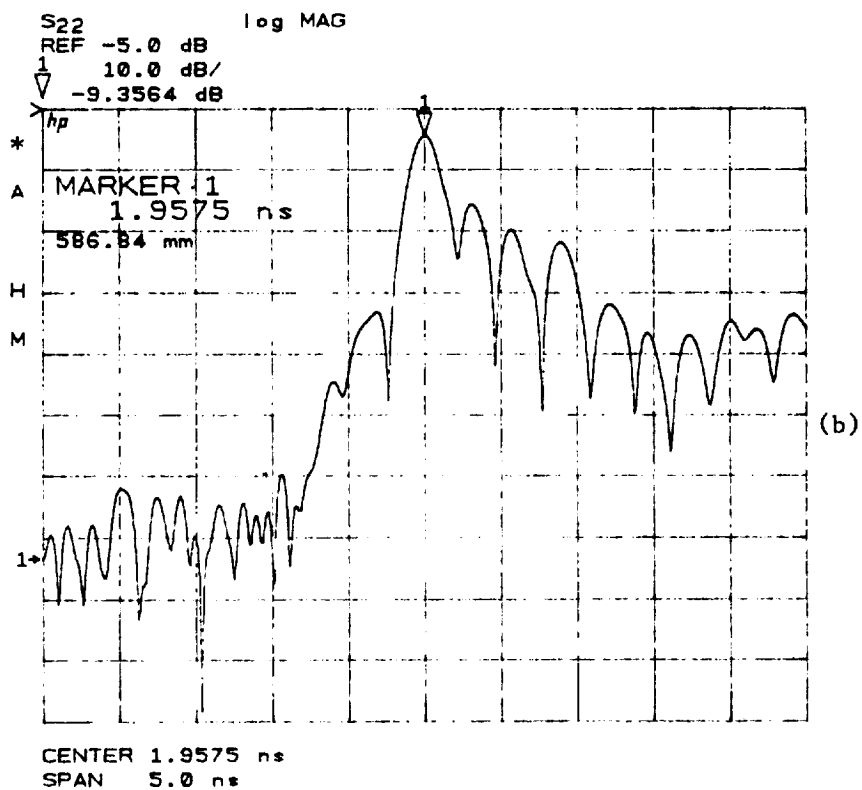
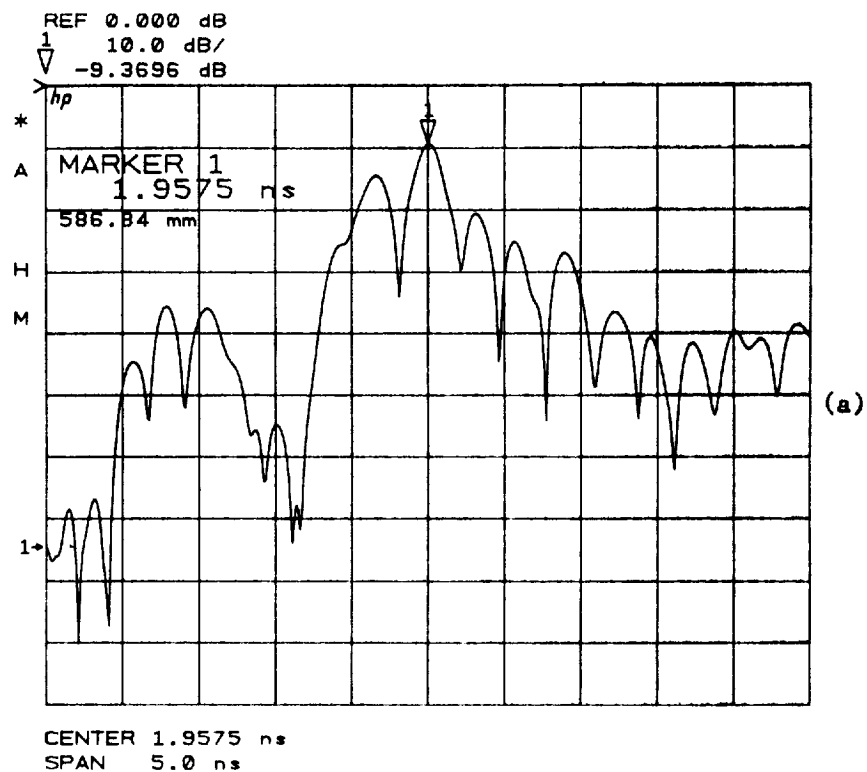


Figure B3-2. Time Domain Plots for Monostatic Band-B Tests With Target Located Two inches from TPS Tile Surface (a) Without Vector Subtraction and (b) With Vector Subtraction

purpose of vector subtraction is to reduce the tile interference reflection, making it easier to locate the desired target reflection.

The time domain data set for the preceding example following vector subtraction is depicted in Figure B3-2(b). The main target reflection can still be observed at 1.9575 ns while the previously observed reflections between 0 and 1.7 ns that were attributed to the tile, antenna, and waveguide transition, have been significantly reduced. As expected, the multiple bounce signals beyond 2.0 ns are essentially unaffected. As will be discussed later, it was the failure of the vector subtraction model to account for these multiple bounce (or multipath) signals that led to the investigation of more sophisticated models.

B3.2.3 System Tests with Vector Subtraction

Using the procedure described above, measurements were made for target separation distances between 0 and 2 inches in 0.025-inch increments. The range was limited to two inches since previous tests had shown the measured time delay errors are small beyond two inches. At each measurement increment, the amplitude and time delay of the largest peak in the time domain data set was determined and stored. The data was processed with and without vector subtraction (i.e., both $\rho_{\text{MEAS}}(f)$ and $\rho_{\text{TARGET}}(f)$ were processed). Ideally, the graph of the measured time delay versus target distance should have been a straight line with a positive slope of $1.693\text{E-}10$ ns/inch. A graph of the measured reflected signal amplitudes should have a maximum value at 0 inches then decay monotonically as the target is moved away from the antenna.

The results of these tests were mixed. With regard to the time delay (distance measurements), vector subtraction provided a significant reduction in the variability observed in the measured data. A comparison is shown in Figure B3-3 for data taken using a monostatic Band-A test setup. For the uncorrected case, the deviations from the ideal straight line correspond to ± 0.035 ns or ± 0.5 cm. With vector subtraction the the observed deviations were reduced to ± 0.02 ns or ± 0.3 cm, a significant improvement. With regard to amplitude measurements, vector subtraction did reduce the variability for distance greater than 0.5 inches as shown in the upper two graphs in Figure

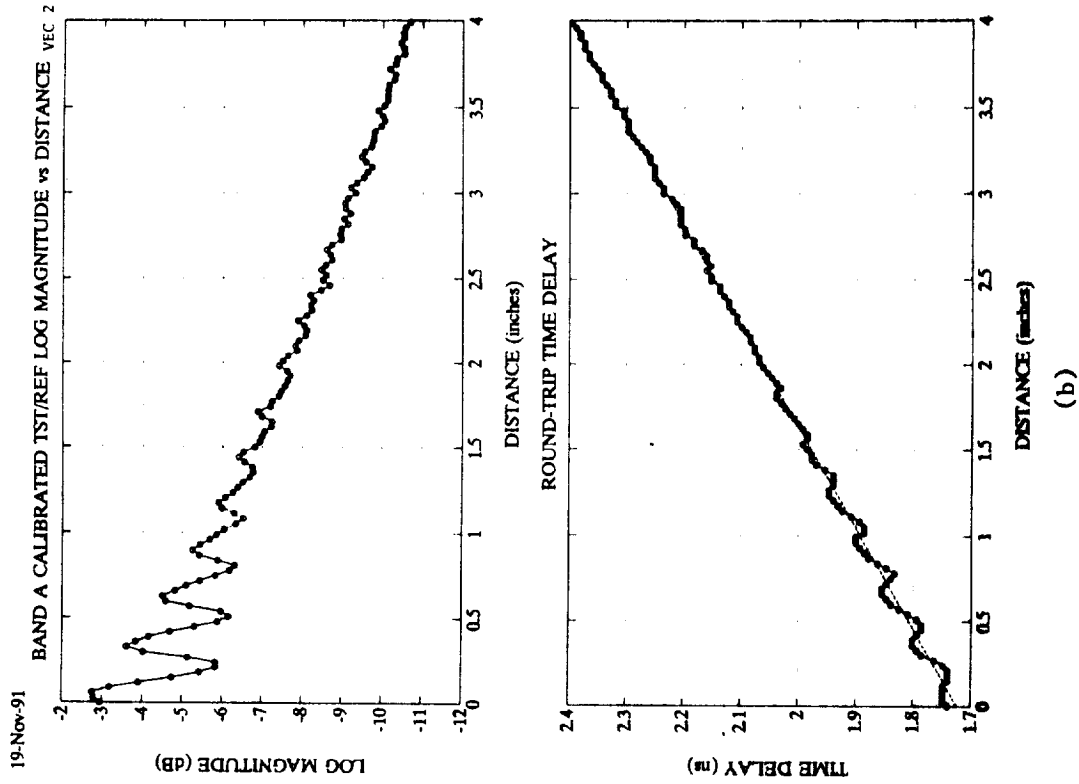
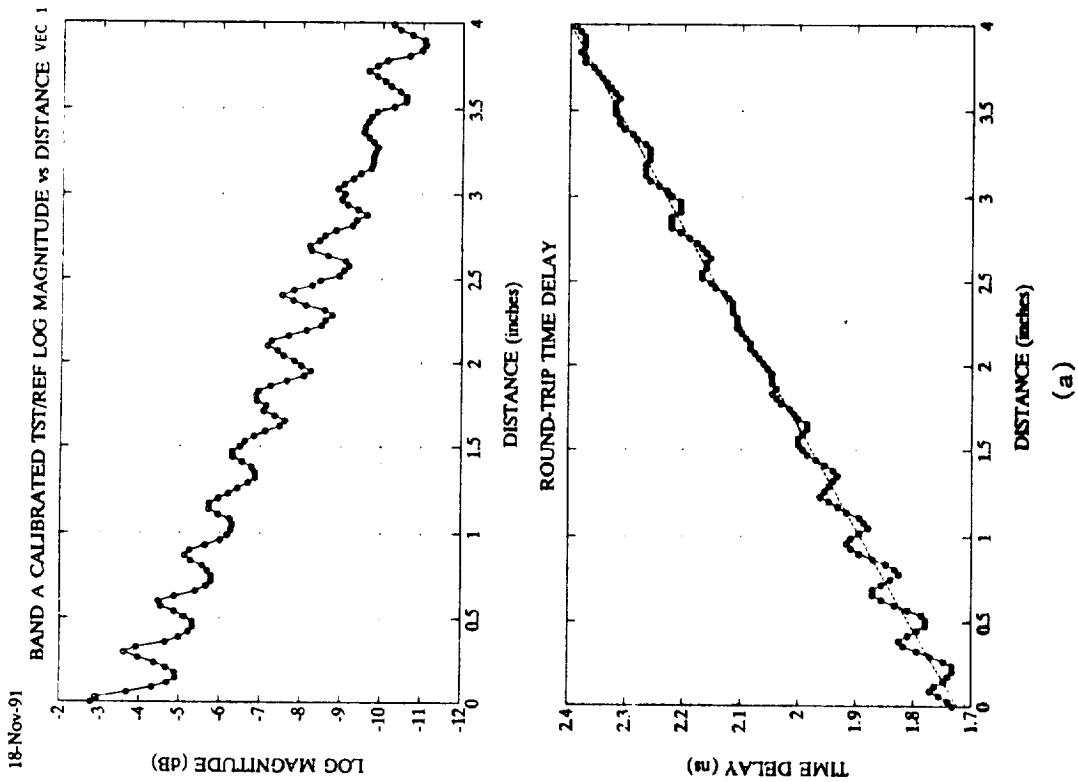


Figure B3-3. Amplitude and Time Delay Versus Distance for Monostatic Band-A Tests Comparing Performance (a) Without Vector Error Correction and (b) With Vector Subtraction

B3-3. However, for distances less than 0.5 inches, vector subtraction caused the amplitude variations to actually increase. It was believed this effect was due to the effects of the multipath reflections which are not accounted for by the vector subtraction model. Therefore, an improved vector error correction model was sought. The results of these efforts are discussed in the next section of this report.

B3.3 BASIC VECTOR ERROR CORRECTION MODEL

B3.3.1 Model Description

In the initial phase of development of a more advanced vector error correction model, a plane-wave, dielectric slab model was used to approximate the interactions of (i) the TPS tile RCG layer, (ii) a flat reflecting target, and (iii) the intervening propagation media (plasma or air). The resultant VEC model accounts for the following items,

- o Interference reflection due to the TPS tile
- o Target reflection (the desired information)
- o Multipath reflections of the target reflection due to the TPS tile

The model does not account for moding effects in the antennas, in the TPS tile, or in the parallel plate waveguide formed between the target surface and the TPS tile surface. The basic vector error correction model also does not include multipath reflections of the target reflection produced by the antenna ground plane.

The basic VEC model was derived from observation of time domain data such as that shown in Figure B3-2. This data shows that the largest reflected signals observed in the uncorrected time domain data are the tile reflection, the target reflection, and a multipath signal due a single multiple bounce of the target reflection between the RCG layer and target surfaces. Each of these terms would be predicted by the plane-wave, dielectric slab model.

The test data also shows several distinct multipath reflections that may be attributable to the antenna ground plane. However, in the example case shown in Figure B3-2, this latter group of reflections is significantly weaker than either the target reflection, tile interference reflection, or the single bounce multipath reflection. Multipath reflections due to the ground plane will also be separated from the target reflection by at least the electrical distance between the ground plane and the tile surface. For the MRIS test setup, this distance is 3.6 cm. Thus, even if the model does not accurately handle multipath reflections due to the ground plane, the inherent range resolution of the FMCW approach used on the MRIS instrument provides immunity against these reflections.

B3.3.2 Plane-Wave Dielectric Slab Model

As noted above, a plane-wave dielectric slab model was used to approximate the interactions between the RCG layer of the TPS tile, a flat reflecting target, and the intervening propagation media. This model is shown in Figure B3-4. When a plane-wave field is incident from the antenna side of the RCG layer, reflected signals are produced at both surfaces of the RCG layer and at the target surface. A composite reflected signal will be produced that consists of an infinite series of individual reflected signals. If the ratio of the composite reflected signal to the incident signal is defined as the complex reflection coefficient, ρ , T-parameter analysis can be used to show that ρ can be represented as,

$$\rho = (\Gamma_1 + \Gamma_A \cdot \Gamma_2^*) / (\Gamma_2 + \Gamma_A \cdot \Gamma_1^*) \quad (\text{B3-5})$$

where,

$$\Gamma_1 = R_1 + R_2 \cdot \exp[-2(\beta_1 d_1)]$$

$$\Gamma_2 = 1 + R_1 \cdot R_2 \cdot \exp[-2(\beta_1 d_1)]$$

$$\Gamma_A = \rho_T \cdot \exp[-2(\beta_1 d_1 + \beta_2 d_2)]$$

DIELECTRIC SLAB VEC MODEL

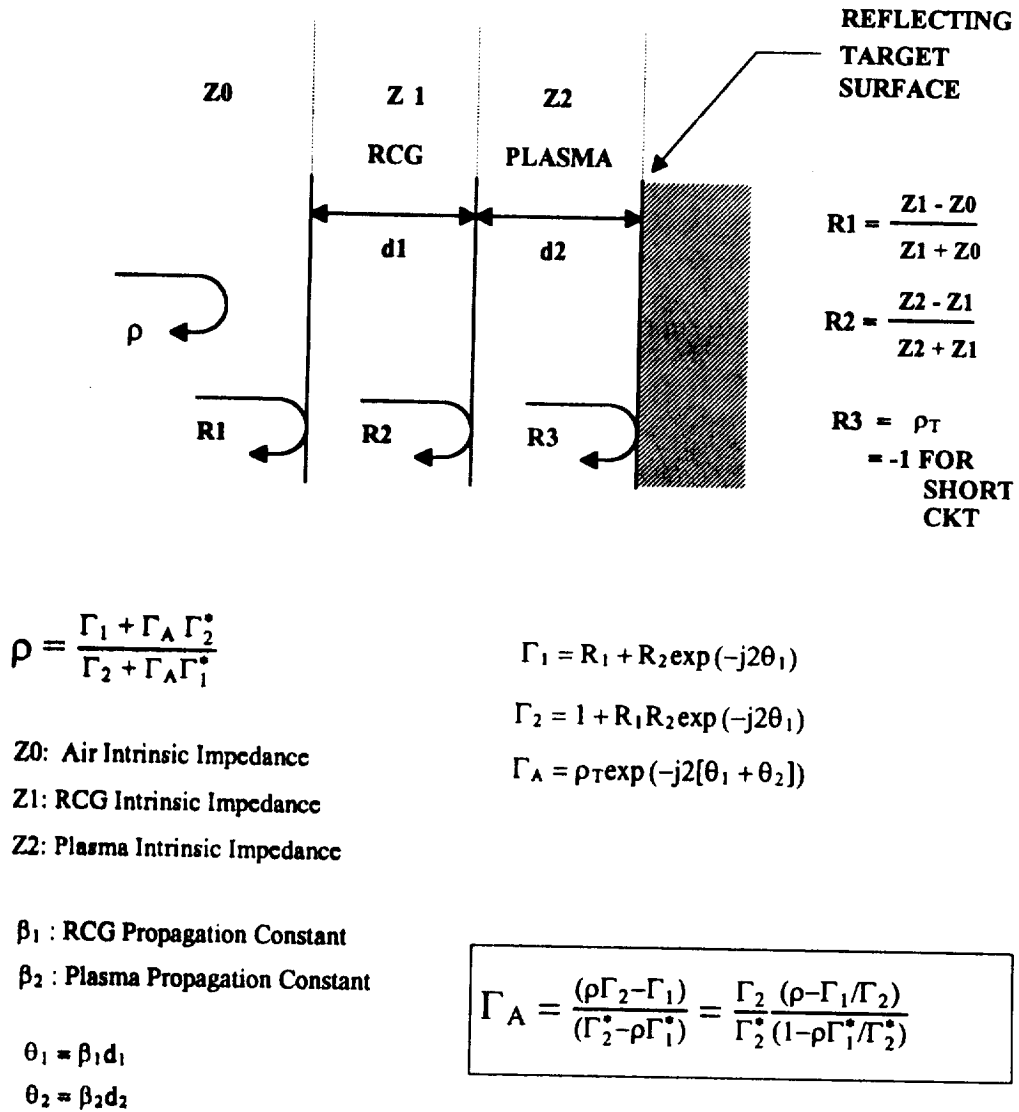


Figure B3-4. Dielectric-slab Model used to Derive Basic Vector Error Correction Model used in MRIS System Tests

The term Γ_A represents a signal that travels through the RCG layer, through the propagation medium (air/plasma region), reflects from the target, then travels back through the propagation medium and the RCG layer. The time-delay of Γ_A represents the desired target distance information. Examination of the above equation for ρ shows that if Γ_1 and Γ_2 can be determined (measured or computed), Γ_A can be computed for a measured ρ value.

For the VEC techniques developed during the MRIS program, initial efforts focused on deriving a technique for determining the values of Γ_1 and Γ_2 through measurements on known standards. It was discovered that the ratio Γ_1/Γ_2 could be determined by performing a measurement for which ρ_T equaled zero. In the laboratory, this condition was approximated by placing a low reflectivity absorber in front of the instrument antennas. In space, this condition could be produced by performing a measurement prior to the aeropass during the time the MRIS instrument was looking into empty space.

If the measured value of ρ for $\rho_T = 0$ is defined as ρ_{LOAD} , it can be seen from equation (B3-5) that,

$$\rho_{LOAD} = \Gamma_1/\Gamma_2 \quad (B3-6)$$

If this result is substituted back into equation (B3-5), which is then solved for the desired target reflection, the following result is obtained (the asterisk denotes the complex conjugate operation),

$$\Gamma_A = (\Gamma_2^*/\Gamma_2)(\rho - \rho_{LOAD})/(1 - \rho \cdot \rho_{LOAD}^*) \quad (B3-7)$$

To simplify the VEC process, the assumption was made that the ratio Γ_2^*/Γ_2 was approximately a constant phase offset. The following definition can then be made,

$$\Gamma_A' = \Gamma_A \cdot (\Gamma_2/\Gamma_2^*) = (\rho - \rho_{LOAD})/(1 - \rho \cdot \rho_{LOAD}^*) \quad (B3-8)$$

The value of Γ_A' can be computed directly from the measured ρ and ρ_{LOAD} values. If an $\Gamma_A'(f)$ array is computed versus frequency using measured $\rho(f)$ and $\rho_{LOAD}(f)$ values, it can be transformed into the time domain to determine

the target reflection location. To test this theory, a simulation was performed using a previously developed dielectric slab computer model. These results are discussed in the next section.

B3.3.3 Simulation Results with Initial VEC Model

A computer model based on TEM cascade model was used to simulate the dielectric slab model shown in Figure B3-4. By setting $\rho_T(f)$ to zero, the values of a $\rho_{LOAD}(f)$ array were computed and stored. The value of $\rho_T(f)$ was then set to -1 to simulate a reflective metal plate and the corresponding values of $\rho(f)$ were computed and stored for a fixed target range. The values of $\Gamma_A'(f)$ were then computed using the error-correction expression derived above. Finally, the $\Gamma_A'(f)$ array was transformed into the time domain to allow the target location to be determined.

The new vector error correction model was found to work flawlessly. It subtracted the effects of both the tile interference and multipath reflections due to multiple bounces between the target and the tile surface. This result is demonstrated in Figure B3-5. In Figure B3-5(a), the result for reflections from a target without error correction are shown. Distinct target, tile interference, and multipath reflections can all be observed. In Figure B3-5(b), the same case is shown using vector subtraction. As expected the tile interference reflection is removed but the multipath reflections are unaffected. Finally, the performance using the vector error procedure is shown in Figure B3-5(c). In this case, the tile interference reflection as well as the multipath reflections have been removed as desired and only the target reflection remains.

The simulation software was then used to evaluate the performance of the vector error correction for sets of $\rho(f)$ taken at different target distances. The results of this test are shown in Figure B3-6. It was found that the error correction procedure reduced the variability observed for uncorrected data to a level equal to that of the range resolution set by the sweep bandwidth. In essence, the error correction worked perfectly for the data generated using a plane-wave, dielectric slab model. With this result achieved, the next goal was to apply the error correction model to experimental data.

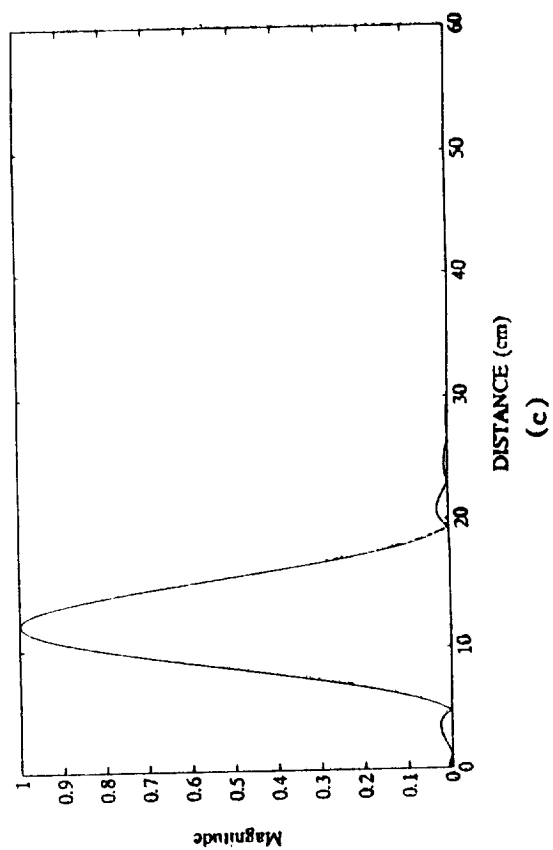
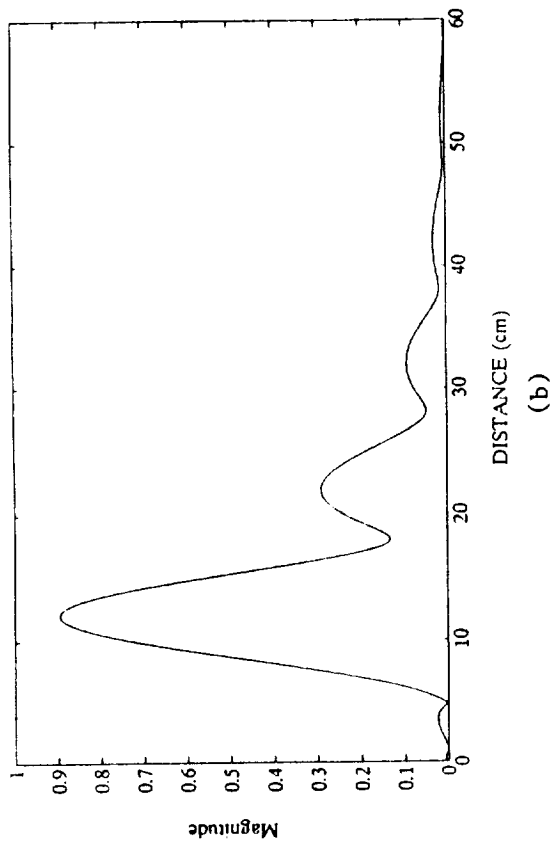
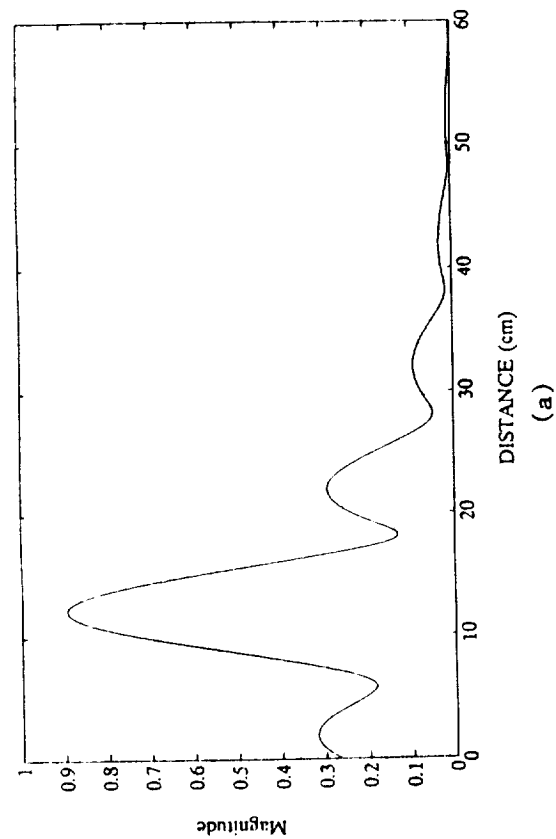


Figure B3-5. Simulated Time Domain Plots using Dielectric Slab Model for Target Located at 10 cm
 (a) Without Vector Error Correction,
 (b) With Vector Subtraction, and
 (c) With Vector Error Correction

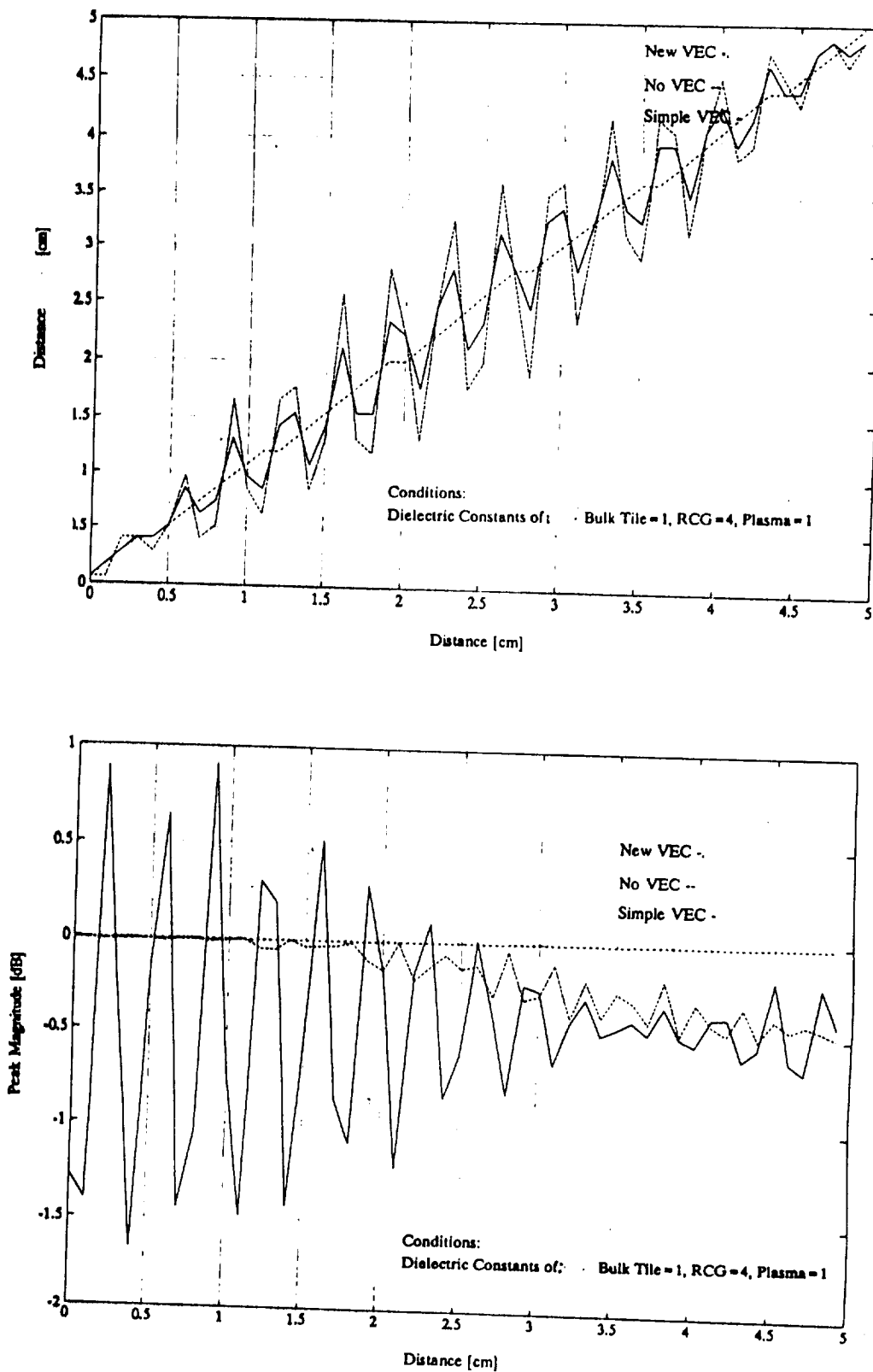


Figure B3-6. Comparison of Measured (Simulated) Target Amplitudes and Standoff Distances Versus Target Distance using Different Error Correction Approaches

To achieve this goal, it was necessary to further evolve the model to include the effects of the antenna and bulk tile.

B3.4 LOSSY DELAY MODEL FOR ANTENNAS AND BULK TILE (VEC-3)

B3.4.1 Derivation of Model

This vector error correction model, denoted as VEC-3, combines the results described in the preceding section with a lossy delay term to account for attenuation due to the antennas, air-gap (between the antenna aperture and bulk tile), and bulk tile. A diagram of the VEC-3 model is shown in Figure B3-7. In this case, the modeled losses are simply expressed as a lossy delay of the form,

$$K = \exp(-\gamma_o d_o) \quad (B3-9)$$

For completeness, a full two-port model could have been used to model the antenna-air-tile cascade. However, no practical methods exist for experimentally determining the terms in the full two-port error model. Since the reflection coefficients of the antenna, air-gap, and bulk tile are small, modeling of the combined cascade as a lossy delay is reasonable. Using the lossy delay model, a simple short-circuit ($\rho = -1$) placed at plane-B on Figure B3-7 can be used to calculate the value of the lossy delay, K.

The VEC-3 model begins with the previously derived result shown below which does not include the lossy delay,

$$\rho_A = (\rho_{MEAS} - \rho_{LOAD}) / (1 - \rho_{MEAS}^* \rho_{LOAD}) \quad (B3-10)$$

To account for the lossy delay, it is noted that the measured reflection coefficients at plane-A in Figure B3-7 can be expressed as the product of the reflection coefficient at plane-B and the lossy delay, D. If a prime symbol is used to denote quantities measured at plane-A and unprimed parameters are used to denote quantities at plane-B, the following definitions can be made,

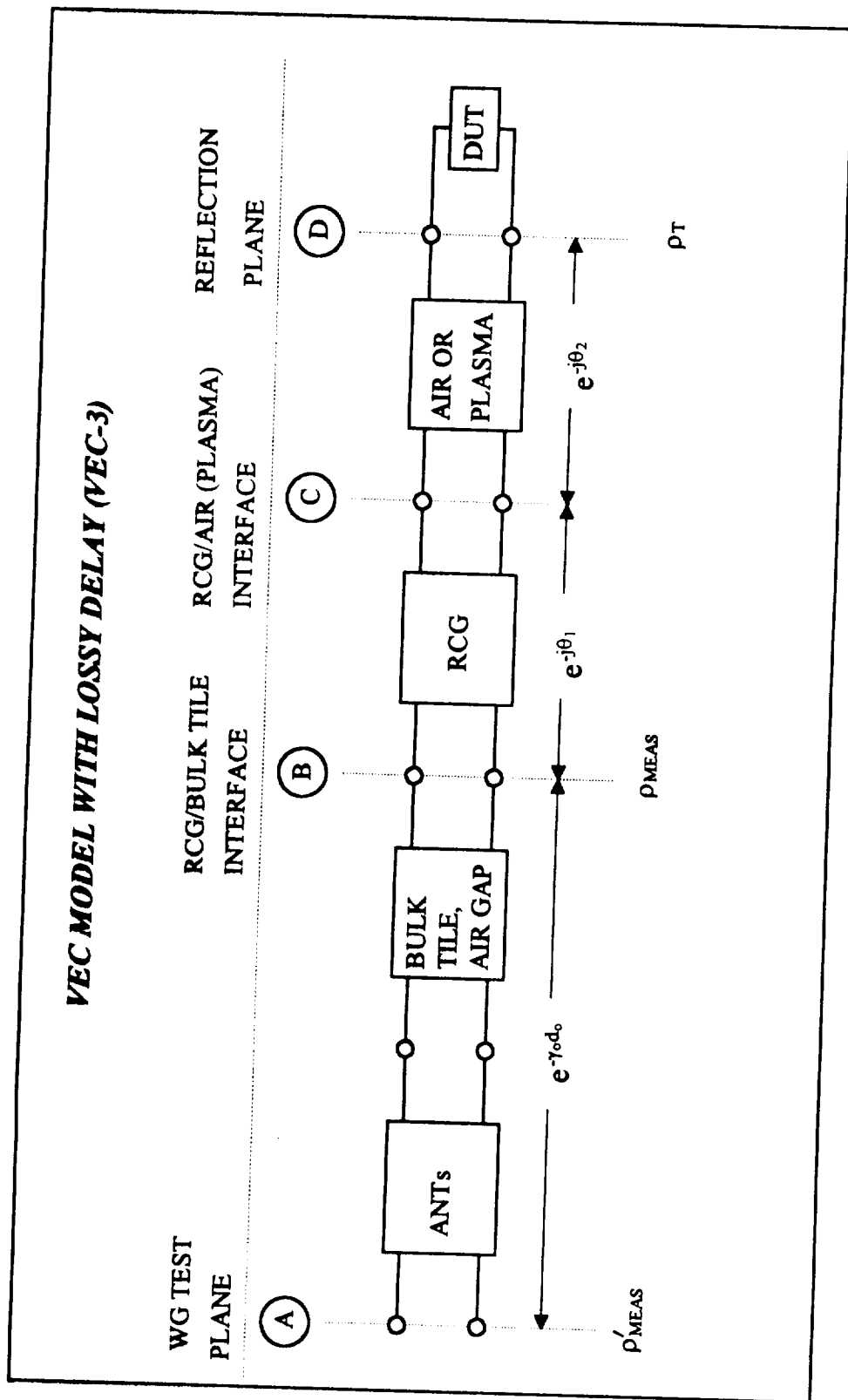


Figure B3-7. Diagram of Updated Vector Error Correction Model Including Lossy Delay Term

$$\rho_{MEAS}' = \rho_{MEAS} \cdot \exp(-2\gamma_0 d_0) \quad (B3-11a)$$

$$\rho_{LOAD}' = \rho_{LOAD} \cdot \exp(-2\gamma_0 d_0) \quad (B3-11b)$$

$$\rho_{SC}' = \rho_{SC} \cdot \exp(-2\gamma_0 d_0) \quad (B3-11c)$$

Using these definitions, the VEC equation can be rewritten as,

$$\rho_A = \frac{(\rho_{MEAS}' \cdot \exp(2\gamma_0 d_0) - \rho_{LOAD}' \cdot \exp(2\gamma_0 d_0))}{(1 - \rho_{MEAS}' \cdot \exp(2\gamma_0 d_0) \cdot \rho_{LOAD}^{*'} \cdot \exp(2\gamma_0 d_0)^*)} \quad (B3-12)$$

Factoring out the $\exp(2\gamma_0 d_0)$ term yields,

$$\rho_A = (\rho_{MEAS}' - \rho_{LOAD}') / (\exp(-2\gamma_0 d_0) - \rho_{MEAS}' \cdot \rho_{LOAD}^{*'} \cdot \exp(2\gamma_0 d_0)^*) \quad (B3-13)$$

If a short-circuit ($\rho = -1$) is placed at plane-B and the measured quantity at plane-A is defined as ρ_{SC}' , the value of the lossy delay can be computed as,

$$\exp(-2\gamma_0 d_0) = -\rho_{SC}' \quad (B3-14)$$

The expression for ρ_A can now be rewritten as

$$\rho_A = (\rho_{MEAS}' - \rho_{LOAD}') / (-\rho_{SC}' - \rho_{MEAS}' \cdot \rho_{LOAD}^{*'} / \rho_{SC}^{*'}) \quad (B3-15)$$

This last result represents the desired vector error equation. This equation accounts for the lossy delay and only includes terms that can be obtained through achievable measurements.

As an initial evaluation of the performance of the VEC-3 model, time domain plots were produced comparing results for three cases, (i) no VEC, (ii) VEC-2 (vector subtraction), and (iii) VEC-3. The tests were performed with mono-static test setup operating in Band-B (44 GHz). Results from this test are shown in Figure B3-8.

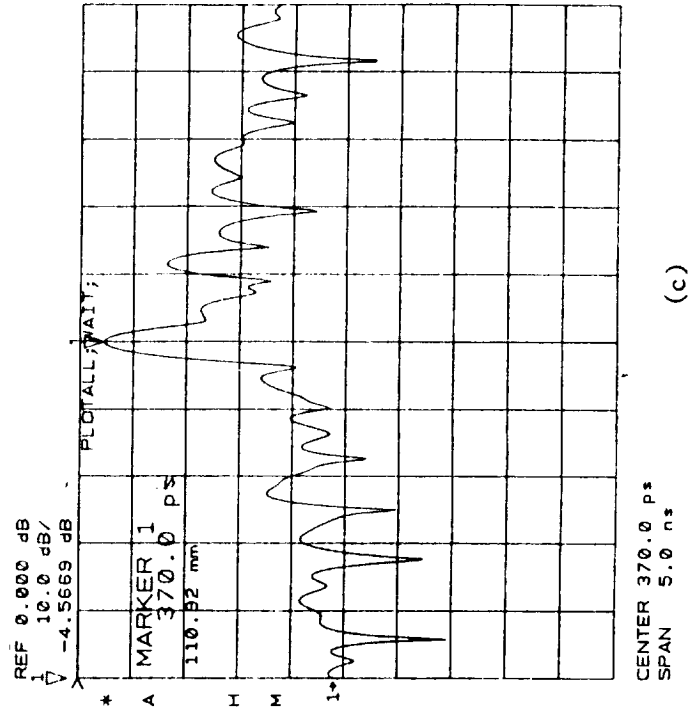
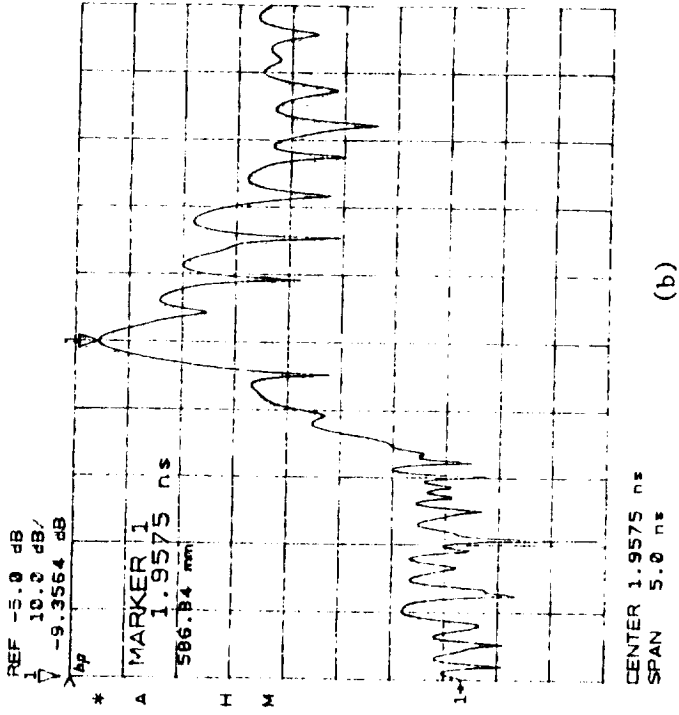
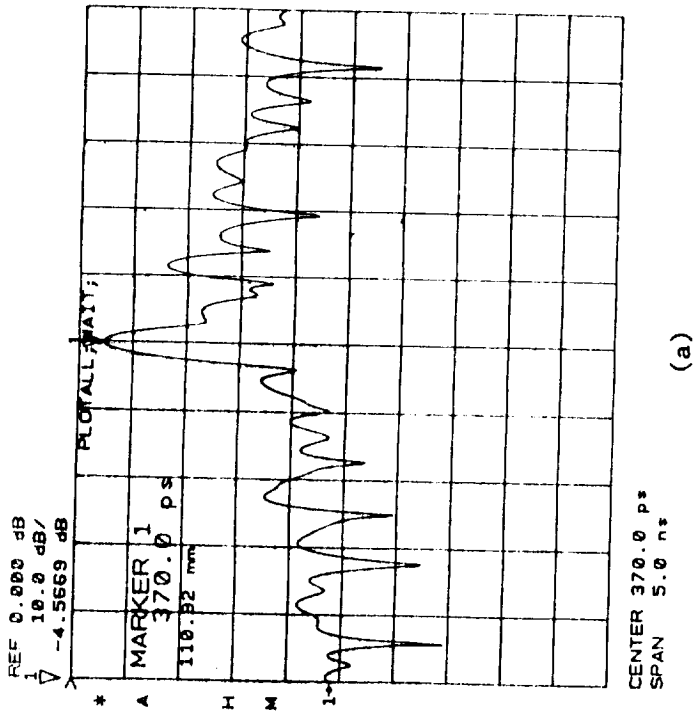


Figure B3-8. Comparison of Time Domain Plots Obtained in Monostatic Band-B Tests using
(a) No Error Correction,
(b) Vector Subtraction, and
(c) VEC-3

For the no-VEC case, reflections can be observed for the antenna, tile, target, and multiple reflections. As noted, reflections due to the antenna, air-gap, and bulk tile appear to be very low as assumed in the VEC-3 derivation. When vector subtraction is applied, the antenna and tile reflections are significantly reduced but as expected, the target and multiple reflections remain unchanged. When the VEC-3 model is used, the antenna and tile reflections are again reduced although not as completely as with vector subtraction. Notably, the multiple reflections, particularly the first multiple reflection following the target reflection, are impacted with VEC-3 applied.

The next goal was to determine if VEC-3 actually improved measurement accuracy and distance measurements were performed on a flat plate target for standoff distances from 0 to 2 inches. The tests were again made with the Band-B monostatic arrangement. The required ρ_{LOAD} value was obtained by using a section of low reflectivity absorber in front of the antenna to simulate a zero reflection target. The required ρ_{SC} value was obtained by placing the metal plate target directly against the surface of the tile.

B3.4.2 Test Results with VEC-3 Model

Results comparing the amplitude measurements for the three different test cases are shown in Figure B3-9. For the no-VEC case, the amplitude deviations from the ideal monotonically decreasing smooth curve, were ± 0.75 dB. For the vector subtraction case, the amplitude deviations were very small near two inches but increased to ± 1.25 at close-in distances. For the VEC-3 case, the amplitude deviations were ± 0.75 dB, comparable to the no-VEC case. In summary, the VEC-3 model worked very well and did not produce as significant close-in accuracy degradation as that observed with vector subtraction.

The comparison of the distance measurement accuracy achieved with the three approaches is shown in Figure B3-10. For the no-VEC case, a worst-case error of ± 0.055 ns (± 0.8 cm) can be observed near a target distance of one-inch. With vector subtraction, the worst case error again occurs near a target distance of one-inch but the maximum error is decreased to ± 0.08 ns (± 0.6 cm). For the VEC-3 case, two notable effects can be observed. The worst case error is very small at ± 0.02 ns (± 0.3 cm) and the error is more randomized in

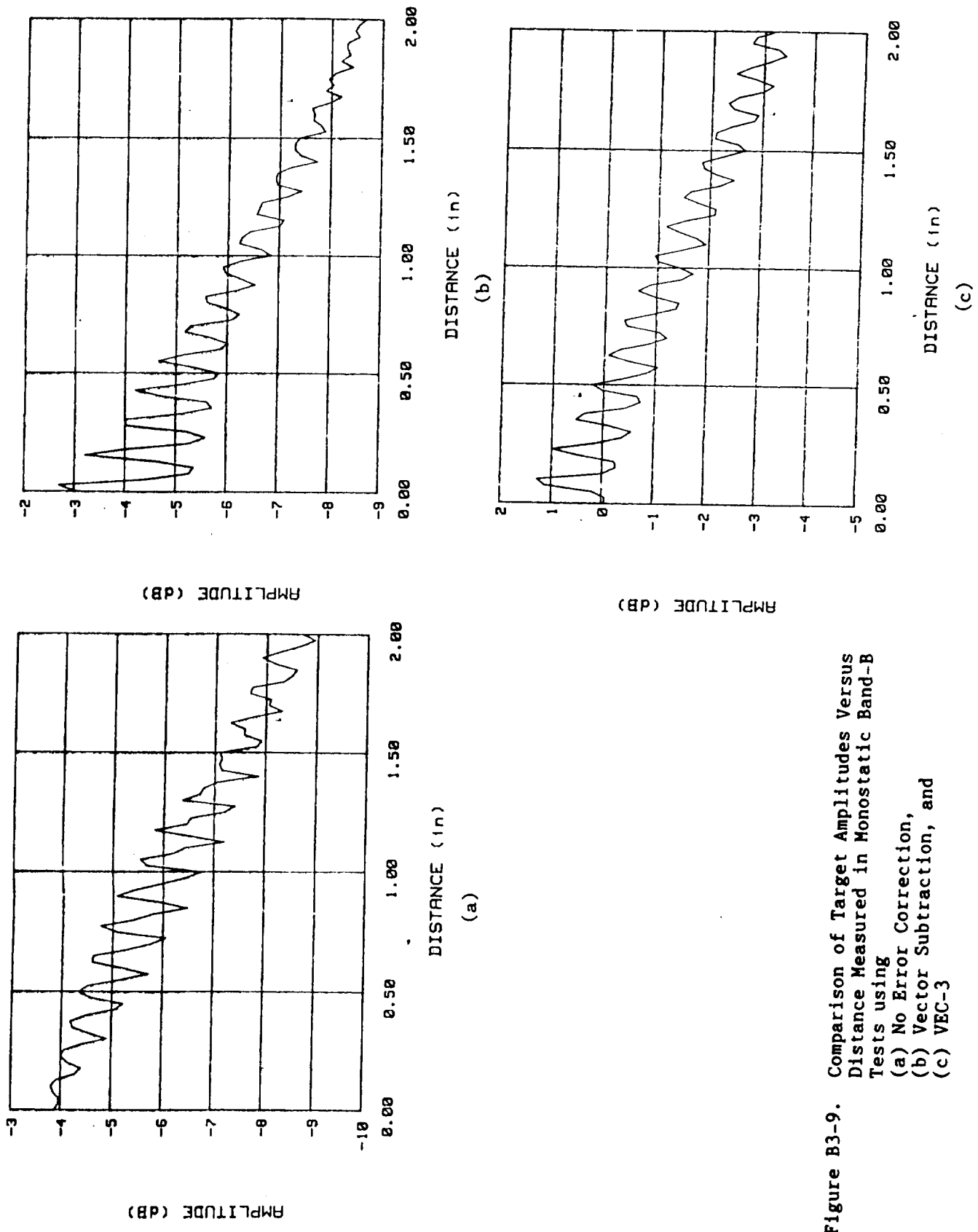
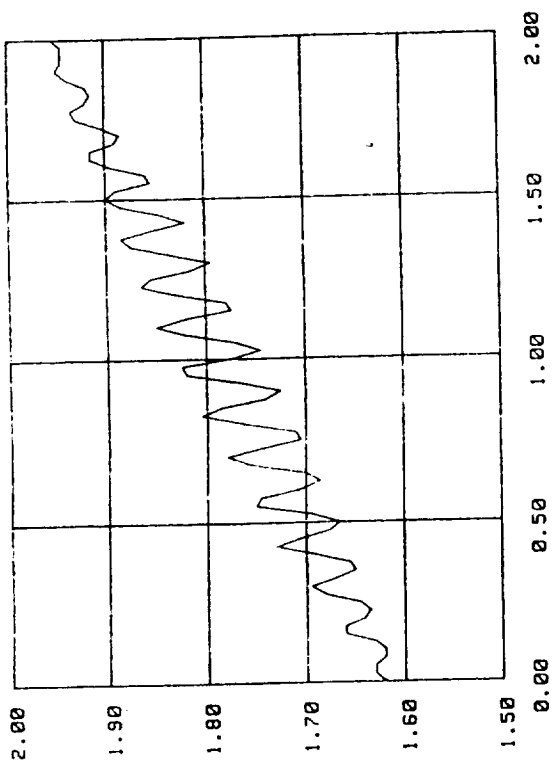


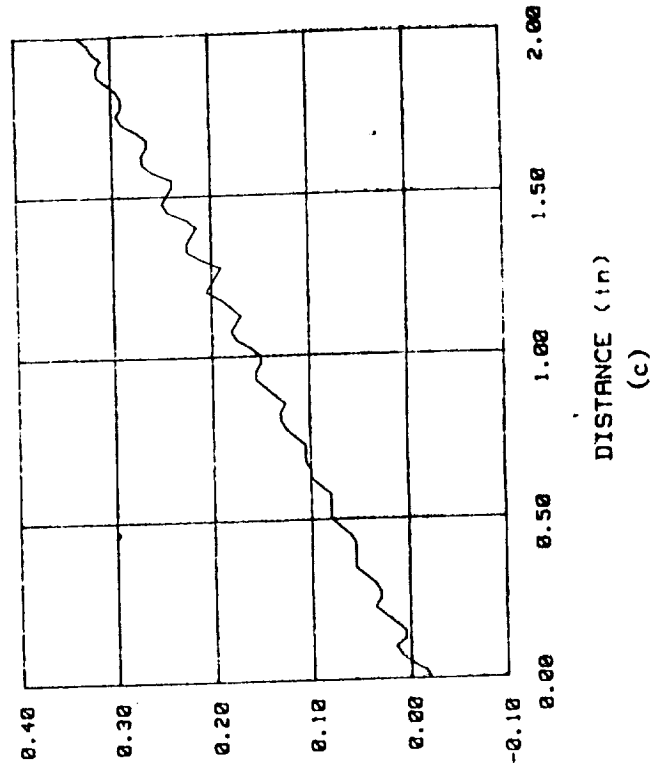
Figure B3-9. Comparison of Target Amplitudes Versus Distance Measured in Monostatic Band-B Tests using
 (a) No Error Correction,
 (b) Vector Subtraction, and
 (c) VEC-3



TIME (ns)

DISTANCE (in)

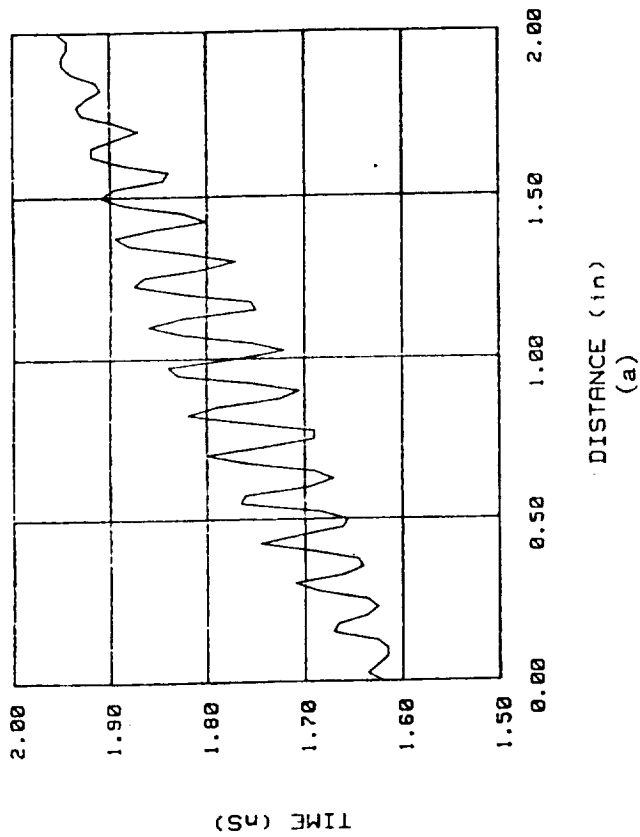
(a)



TIME (ns)

DISTANCE (in)

(b)



TIME (ns)

DISTANCE (in)

(c)

Figure B3-10. Comparison of Target Time Delay Versus Distance Measured in Monostatic Band-B Tests using
(a) No Error Correction,
(b) Vector Subtraction, and
(c) VEC-3

nature. This latter effect implies the accuracy is being influenced by the resolution achievable with the 4-GHz bandwidth used in these tests.

B3.4.3 Conclusions

The VEC-3 model worked extremely well for the monostatic test case. Two factors encouraged further development of the model. One factor was that the VEC-3 model did not include the effects of delays due to the thin RCG layer. A second factor was that the VEC-3 did not work well for similar tests performed with a bistatic equipment arrangement. Several different advanced error models were developed (VEC-4, VEC-5, VEC-6, and VEC-7). However, of these four models, only VEC-7 was thoroughly investigated. This model is discussed in the next section of this report.

B3.5 VEC MODEL THAT INCLUDES TILE RCG LAYER (VEC-7)

B3.5.1 Derivation of VEC-7 Model

Development of the VEC-7 model began by modelling a cascade consisting of the tile RCG layer, the propagation media (air/plasma), and reflecting surface. This initial model was shown in Figure B3-4. The key result obtained from this initial model is an equation of the form

$$\Gamma_M = (\Gamma_1 + \Gamma_A \cdot \Gamma_2^*) / (\Gamma_2 + \Gamma_A \cdot \Gamma_1^*) \quad (B3-16)$$

where Γ_M represents the reflection coefficient at the antenna-side surface of the tile RCG layer and Γ_A represents a signal that has reflected from the target surface and has undergone a total time delay of $2(\theta_1 + \theta_2)$. It may be noted that θ_2 represents the distance between the outer tile RCG surface and the target. Thus, if Γ_A can be determined through appropriate measurements and the delay θ_1 is known or estimated, the target standoff distance, θ_2 can be determined.

In the next development step, the bulk tile, air gap, and antennas were modeled as a lossy delay, $\exp(-2\gamma_o d_o)$, as shown in Figure B3-7. This allows the measured reflection coefficient, ρ_{MEAS} , to be expressed as

$$\rho_{MEAS} = K \cdot \Gamma_M = K \cdot (\Gamma_1 + \Gamma_A \cdot \Gamma_2^*) / (\Gamma_2 + \Gamma_A \cdot \Gamma_1^*) \quad (B3-17)$$

where, $K = \exp(-2\gamma_0 d_0)$.

If a "Load" condition is created for which Γ_A is zero and ρ_{MEAS} is defined as ρ_{LOAD} , the following result is obtained

$$\rho_{LOAD} = K \cdot \Gamma_1 / \Gamma_2 \quad (B3-18)$$

By using the preceding results, the following expression can be derived,

$$\Gamma_A = (\Gamma_2^* / \Gamma_2) (\rho_{MEAS} - \rho_{LOAD}) / (K - \rho_{MEAS} \cdot \rho_{LOAD}^* / K^*) \quad (B3-19)$$

From this result, it may be observed that if the ratio Γ_2^* / Γ_2 and the lossy delay K are known, the value of Γ_A can be computed from measured values of ρ_{MEAS} and ρ_{LOAD} . In previous models, it was assumed that the ratio (Γ_2^* / Γ_2) was a simple phase offset that was constant over the sweep bandwidth. In this new model, the goal is to more completely account for the effects of this ratio.

To accomplish this goal, measurements are performed on an "Offset Short Circuit" for which

$$\rho_{MEAS} = \rho_{OSSC} \quad (B3-20)$$

$$\Gamma_A = -M \cdot \exp(-j2[\theta_1 + \theta_{OSSC}]) \quad (B3-21)$$

where θ_{OSSC} represents the delay due to the known distance to the offset short circuit.

Using the last three equations listed above, the following expression can be derived for the unknown ratio, Γ_2^* / Γ_2 .

$$\Gamma_2/\Gamma_2^* = -M \cdot \exp(-j2[\theta_1 + \theta_{\text{OSSC}}])$$

$$\cdot (K - \rho_{\text{OSSC}} \cdot \rho_{\text{LOAD}}^*/K^*) / (\rho_{\text{OSSC}} - \rho_{\text{LOAD}}) \quad (\text{B3-22})$$

This result can now be substituted into equation (B3-19) to obtain the following result

$$\Gamma_A = -M \cdot \exp(-j2[\theta_1 + \theta_{\text{OSSC}}]) \frac{(|K|^2 - \rho_{\text{OSSC}} \cdot \rho_{\text{LOAD}}^*)(\rho_{\text{MEAS}} - \rho_{\text{LOAD}})}{(|K|^2 - \rho_{\text{MEAS}} \cdot \rho_{\text{LOAD}}^*)(\rho_{\text{OSSC}} - \rho_{\text{LOAD}})} \quad (\text{B3-23})$$

The goal at this point is to solve the above equation using measured values of ρ_{MEAS} , ρ_{LOAD} , and ρ_{OSSC} and calculated values of θ_{OSSC} . Before this goal can be achieved, it is necessary to account for the unknown parameters M , θ_1 , and $|K|^2$.

To evaluate $|K|^2$, it was determined that measurements should be made for the largest expected reflection and the measured magnitude for this case should be equated to $|K|^2$. From previous monostatic measurements, it was known that the maximum reflection occurred when the metal target was placed directly against the tile RCG surface. For this case, the measured reflection coefficient was defined as ρ_{SC} and the required value of $|K|^2$ was defined as

$$|K|^2 = |\rho_{\text{SC}}|^2 \quad (\text{B3-24})$$

The parameter M represents the two-way attenuation during signal propagation from the short circuit to the offset short circuit position. Since it was intended that this offset would be small, it was reasonably assumed that minimal attenuation would occur and that M would have a value near unity.

The remaining unknown, $2\theta_1$, represents the two-way delay through the RCG layer. Since the goal is to measure the distance between the tile RCG surface and the target, both sides of the preceding equation for Γ_A can be multiplied by $\exp(j2\theta_1)$ to achieve the final result shown below (assumes $M=1$).

$$\Gamma_A \cdot \exp(j2\theta_1) = -\exp(-j2\theta_{\text{OSSC}}) \frac{(|\rho_{\text{SC}}|^2 - \rho_{\text{OSSC}} \rho_{\text{LOAD}}^*)(\rho_{\text{MEAS}} - \rho_{\text{LOAD}})}{(|\rho_{\text{SC}}|^2 - \rho_{\text{MEAS}} \rho_{\text{LOAD}}^*)(\rho_{\text{OSSC}} - \rho_{\text{LOAD}})} \quad (\text{B3-25})$$

This final result was evaluated for both monostatic and bistatic operating modes. For bistatic operation, the ρ_{SC} measurement was made with the target plate actually positioned at a distance that provided a maximum reflected signal amplitude. Generally, this corresponded to a distance of approximately 4 inches. The bistatic offset short circuits were also measured near a distance that provided a maximum reflected signal and were typically offset from the short circuit position 0.25 to 0.6 cm. Results from these measurements are discussed in the next part of this appendix.

B3.5.2 VEC-7 Test Results: Band-A

Initial VEC-7 tests were performed in Band-A. The short circuit condition was produced by placing the target directly against the tile RCG surface. The offset short circuit was produced by moving the target 0.559 cm (0.22 inches) from the short circuit position. Tests were then made for target distances from 0 to 4 inches. Both the amplitude and time delay results were very encouraging as shown in Figure B3-11. In examining the amplitude data, it may be noted that the close-in target amplitudes are now normalized to indicate a zero-dB signal level. This is a direct result of normalizing to a short circuit placed against the tile RCG surface. Also, the measured time-delay at a zero-inch target distance is approximately zero nanoseconds. Thus, the distance measurements have been normalized to the positions of the short circuit and offset short circuit used during calibration.

The worst-case amplitude uncertainties observed in the Band-A VEC-7 data are only ± 0.5 dB, slightly better than the ± 0.8 dB observed without vector error correction and within the instrument specification of ± 1.5 dB. The time delay variations are ± 0.05 ns (± 0.75 cm). This distance measurement accuracy was actually slightly worse than the ± 0.035 ns (± 0.53 cm) accuracy achieved without vector error correction or the ± 0.02 ns (± 0.3 cm) accuracy achieved with vector subtraction. However, the instrument specification of ± 1.0 cm is met.

2-Jan-92

BAND A CALIBRATED TST/REF LOG MAGNITUDE vs DISTANCE vec = 7

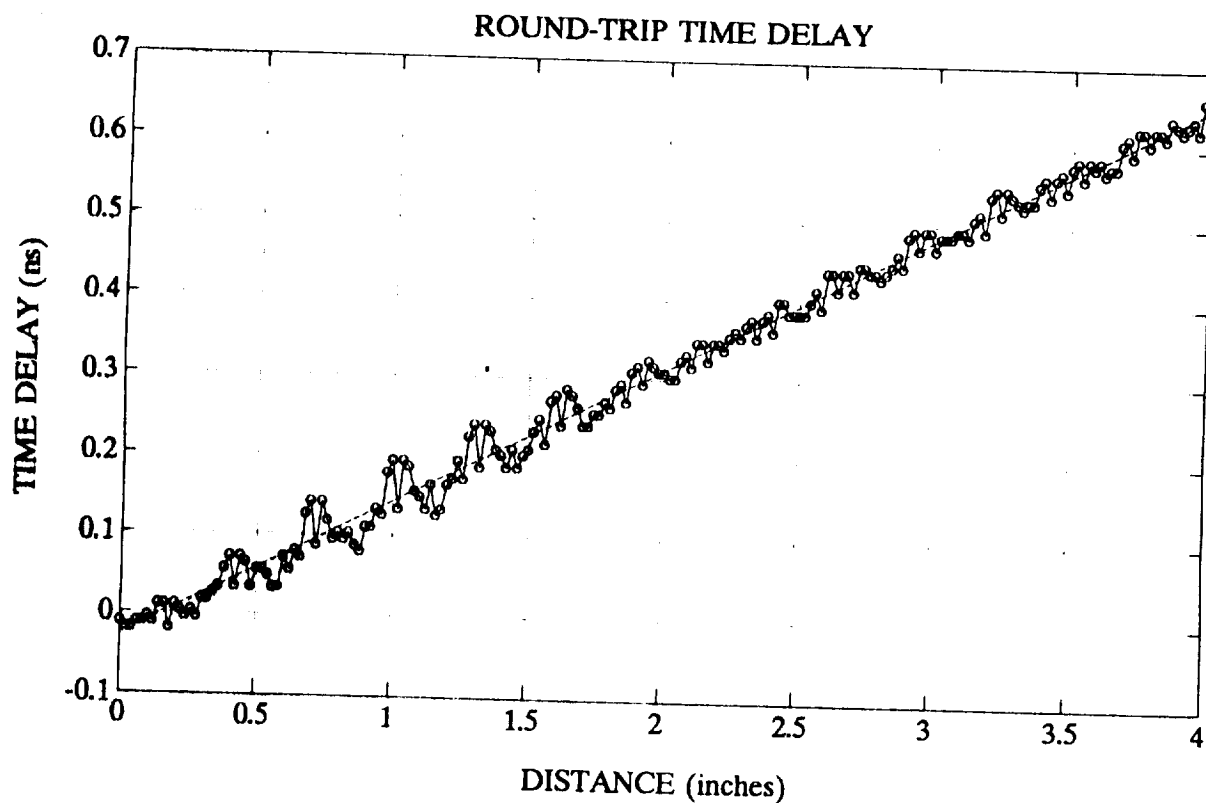
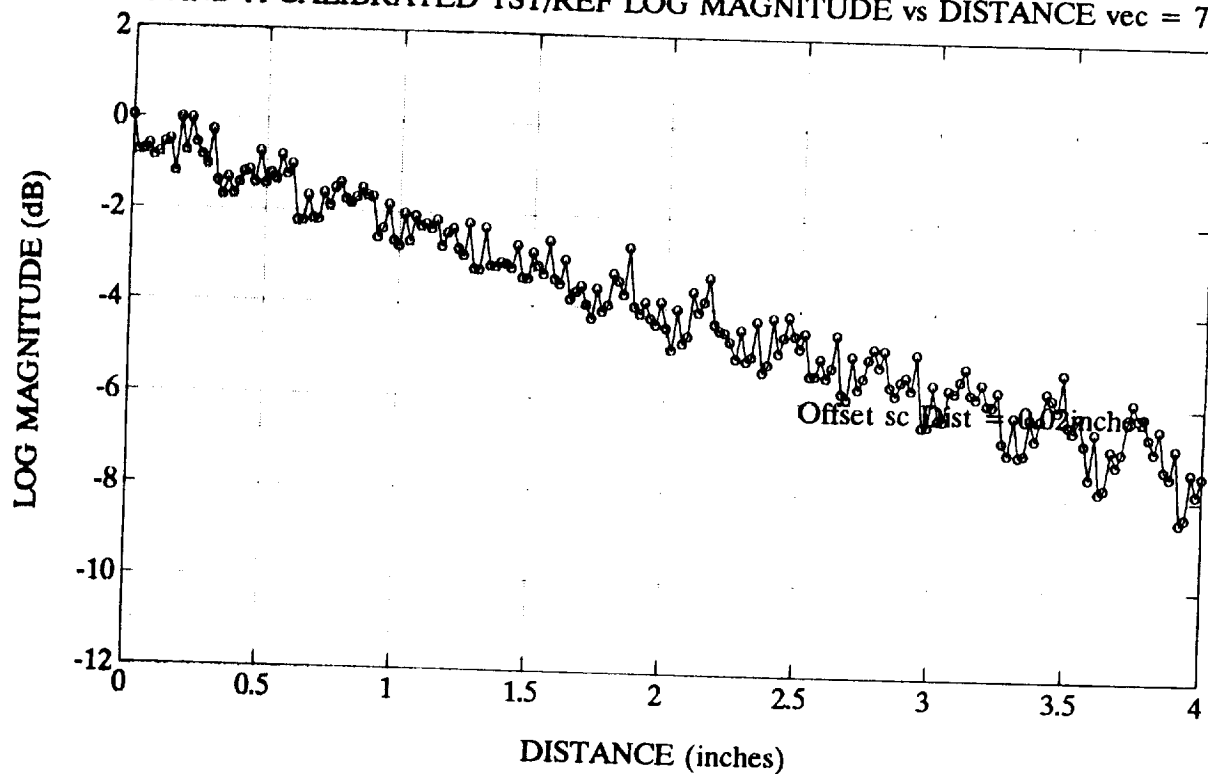


Figure B3-11. Measured Target Amplitude and Time Delay Versus Target Distance for Monostatic Band-A Tests using Full VEC-7 Model

B3.5.3 VEC-7 Test Results: Band-B

Good test results were also obtained with VEC-7 in bistatic Band-B tests. Example test results are shown in Figure B3-12. Because the short circuit used for the calibration was positioned at 4 inches (as discussed above for bistatic operation), the signal amplitude at 4 inches is normalized to 0-dB and the time delay at 4 inches is normalized to 0 ns. The time delay shift is easily correctable in the software. A worst-case amplitude uncertainty of ± 2.5 dB can be observed at target distances below one inch. This is slightly worse than the ± 1.5 dB uncertainty observed without vector error correction but is considerably better than the instrument specification of ± 4.0 dB. The time delay uncertainty observed with VEC-7 is ± 0.035 ns (± 0.53 cm). In comparison to other techniques, the accuracy achieved with VEC-7 in Band-B is better than the ± 0.06 ns (± 0.9 cm) accuracy achieved without vector error correction and nearly identical to that achieved with VEC-2 (vector subtraction).

B3.5.4 VEC-7 Test Results: Band-C

Example test results obtained with VEC-7 in bistatic Band-C tests are shown in Figure B3-13. The short circuit condition required for calibration was again produced by making measurements with the target positioned at a standoff distance of 4 inches. A worst-case amplitude uncertainty of ± 3.5 dB can be observed at target distances below one inch. This is worse than the ± 2.0 dB uncertainty observed without vector error correction but is still better than the instrument specification of ± 4.0 dB. Except for an anomaly at a target distance of 3 inches, the time delay uncertainty observed in Band-C with VEC-7 is ± 0.05 ns (± 0.75 cm). In comparison to other techniques, the accuracy achieved with VEC-7 is better than the ± 0.07 ns (± 1.05 cm) accuracy achieved without vector error correction and the ± 0.06 ns (± 0.90 cm) accuracy achieved with vector subtraction.

B3.5.5 VEC-7 Test Results: Band-D

Example test results obtained with VEC-7 in bistatic Band-D tests are shown in

20-Dec-91

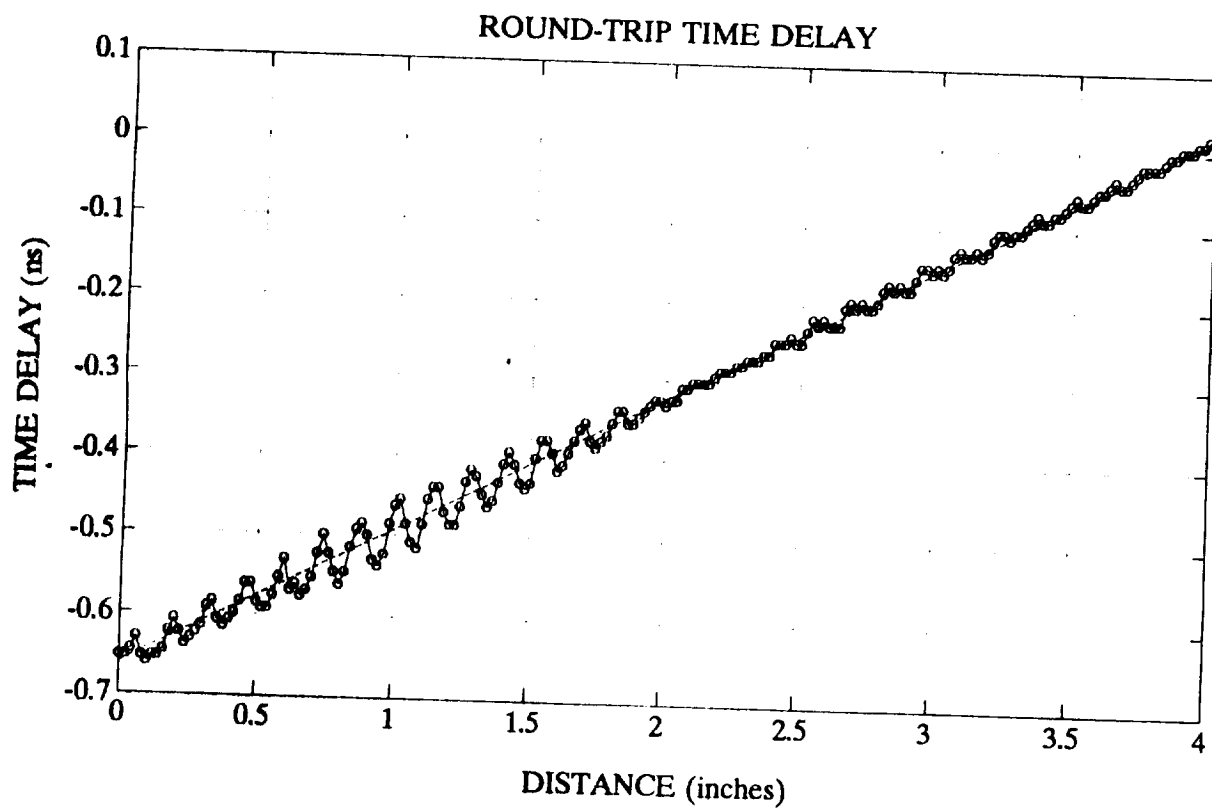
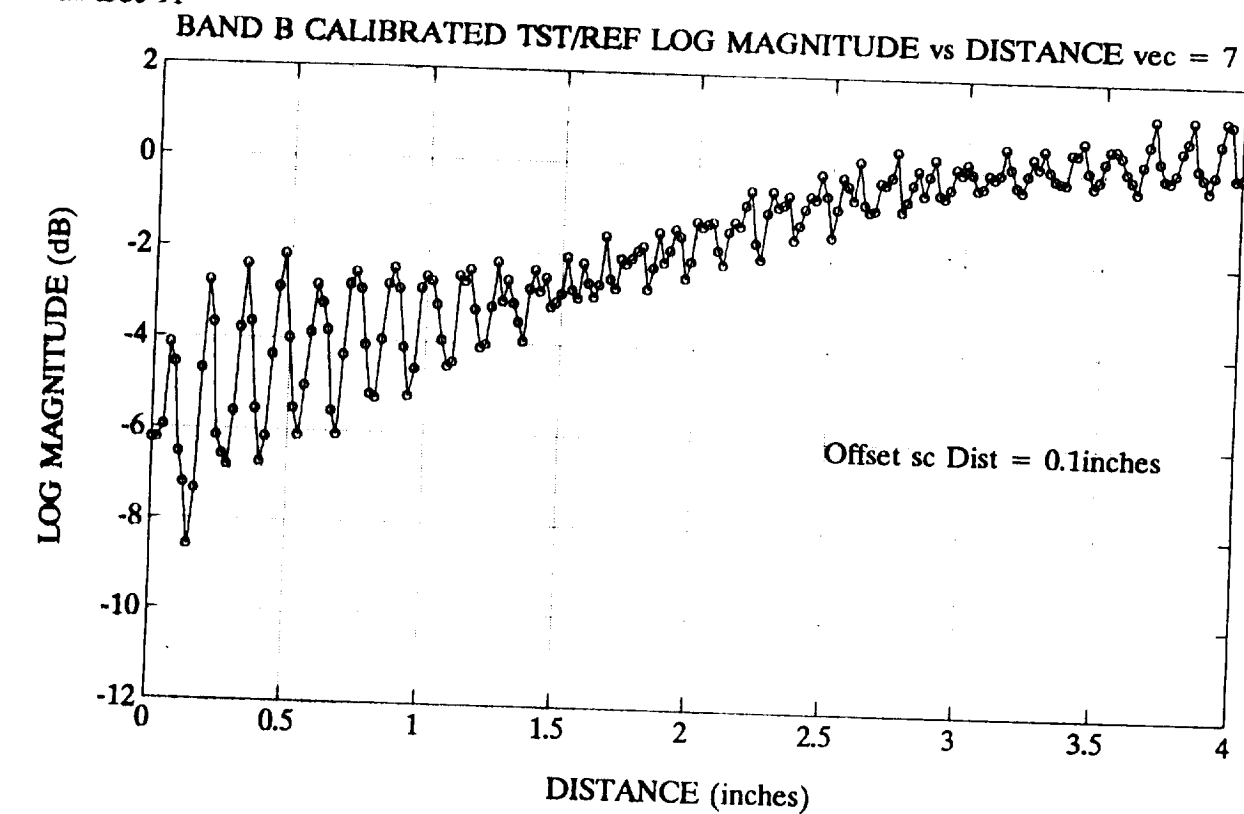


Figure B3-12. Measured Target Amplitude and Time Delay Versus Target Distance for Bistatic Band-B Tests using Full VEC-7 Model

20-Dec-91

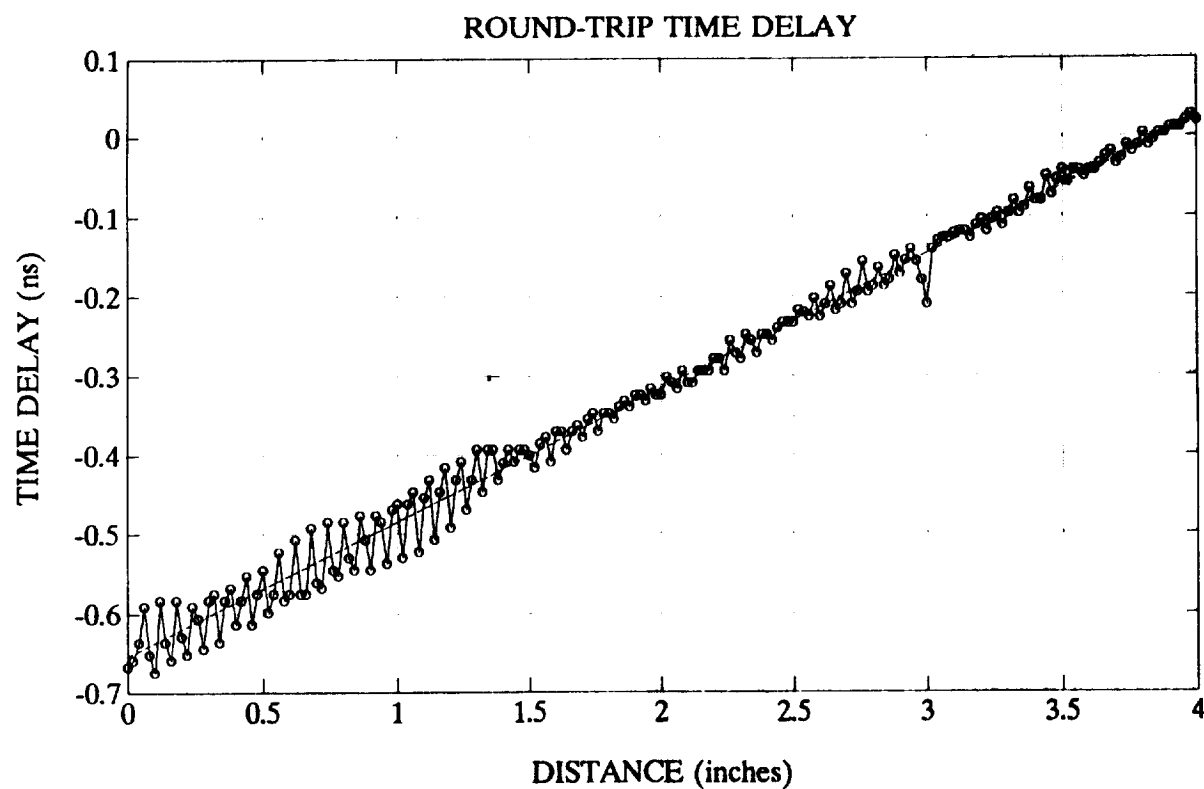
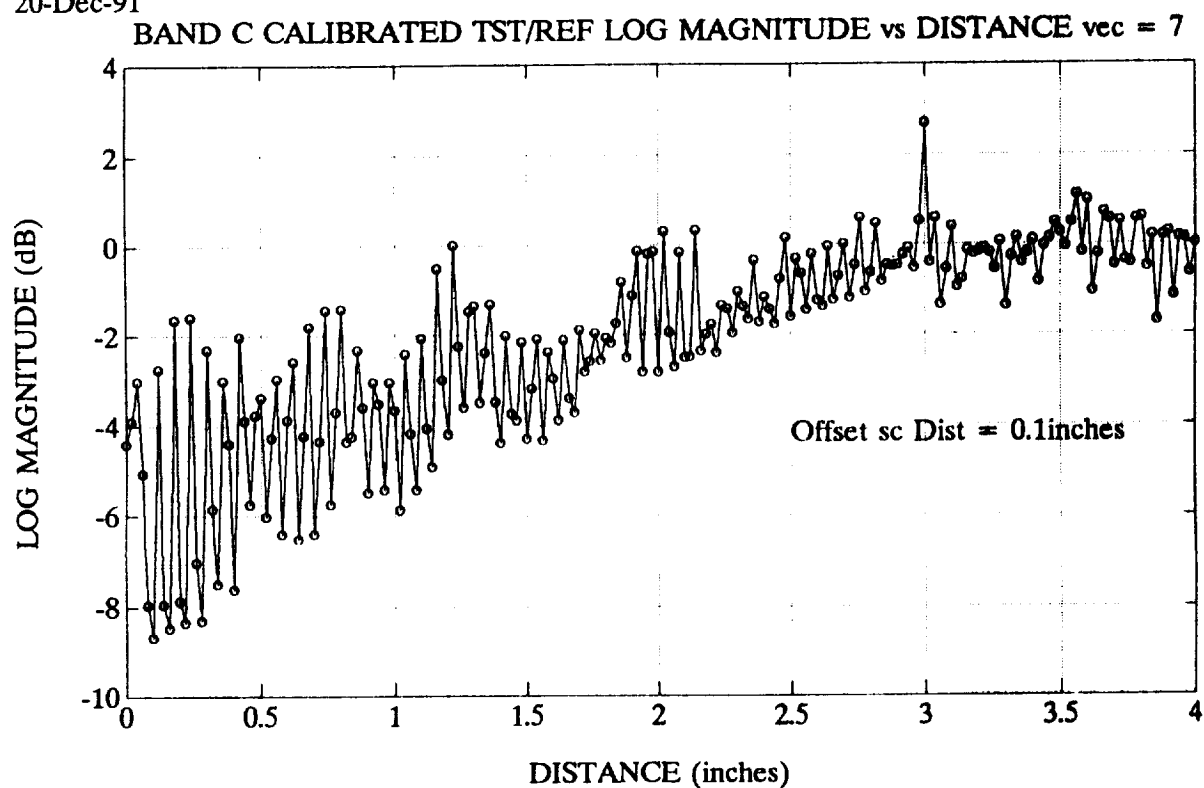


Figure B3-13. Measured Target Amplitude and Time Delay Versus Target Distance for Bistatic Band-C Tests using Full VEC-7 Model

Figure B3-14. In this test, the short circuit condition required for calibration was produced by making measurements with the target positioned at a standoff distance of 0.5 inches due to data availability limitations. A worst-case amplitude uncertainty of ± 2.5 dB can be observed over the 1 to 2 inch target range. This is worse than the ± 1.5 dB uncertainty observed without vector error correction but is still better than the instrument specification of ± 4.0 dB. Except for an unexplained anomaly that appears at a target distance of 0.4 inches, the time delay uncertainty observed in Band-D with VEC-7 is ± 0.05 ns (± 0.75 cm). Compared to other techniques, the accuracy achieved with VEC-7 is better than the ± 1.1 ns (± 1.65 cm) accuracy achieved without vector error correction and the ± 0.08 ns (± 1.2 cm) accuracy achieved with vector subtraction.

B3.5.6 Conclusions on VEC-7

The VEC-7 model attempts to more accurately account for the effects of the RCG tile. Since this model contains more terms than previous models, measurements are required on an offset short circuit in addition to the short circuit and load measurements required with earlier models. In general, the amplitude accuracy achieved with VEC-7 met all instrument specifications and was comparable to that achieved with previous error correction techniques. The time-delay accuracy achieved with VEC-7 also met all instrument specifications and was generally comparable or better than that achieved with other error correction techniques. A unique aspect of the VEC-7 performance was that it simultaneously met all instrument specifications for amplitude and distance measurement accuracy. Conversely, with no vector error correction, good amplitude accuracy but less than optimum time-delay accuracy were achieved. With vector subtraction, good time-delay accuracy but poor close-in amplitude accuracy were achieved.

21-Dec-91

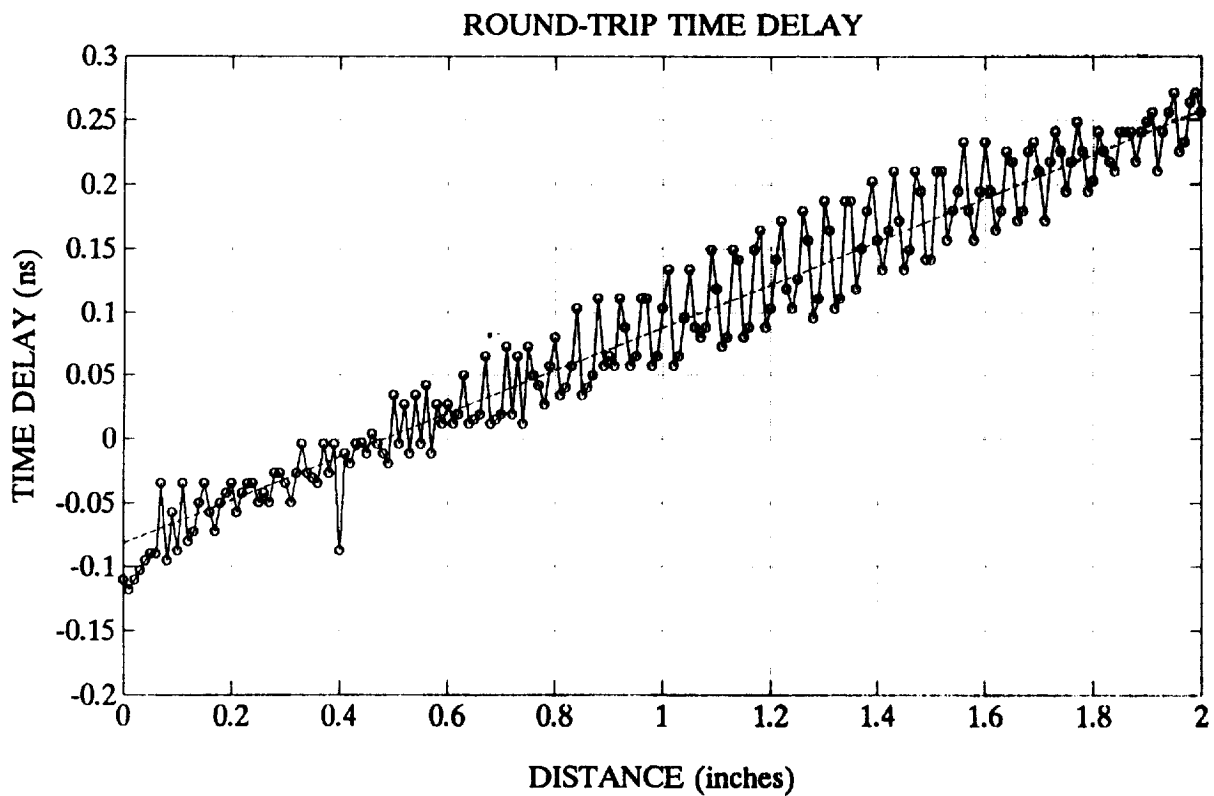
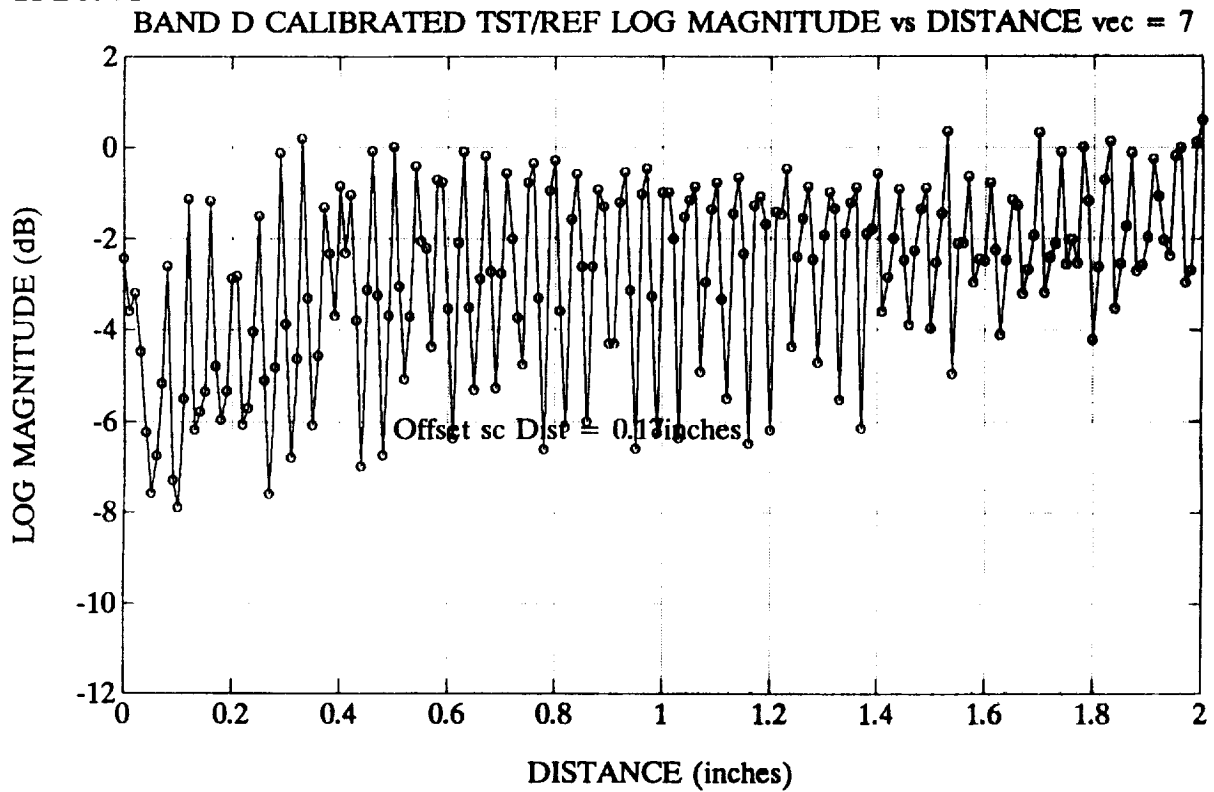
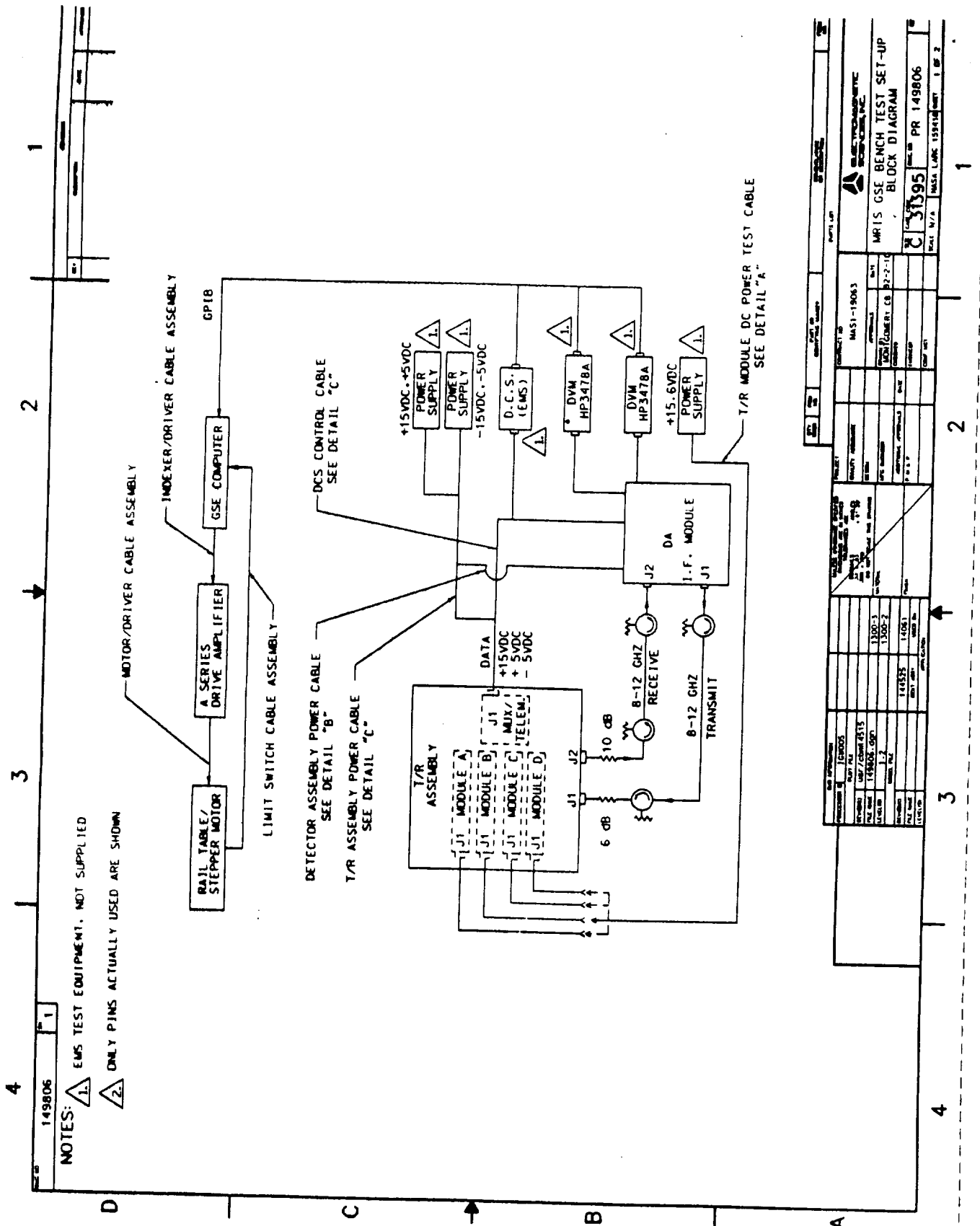
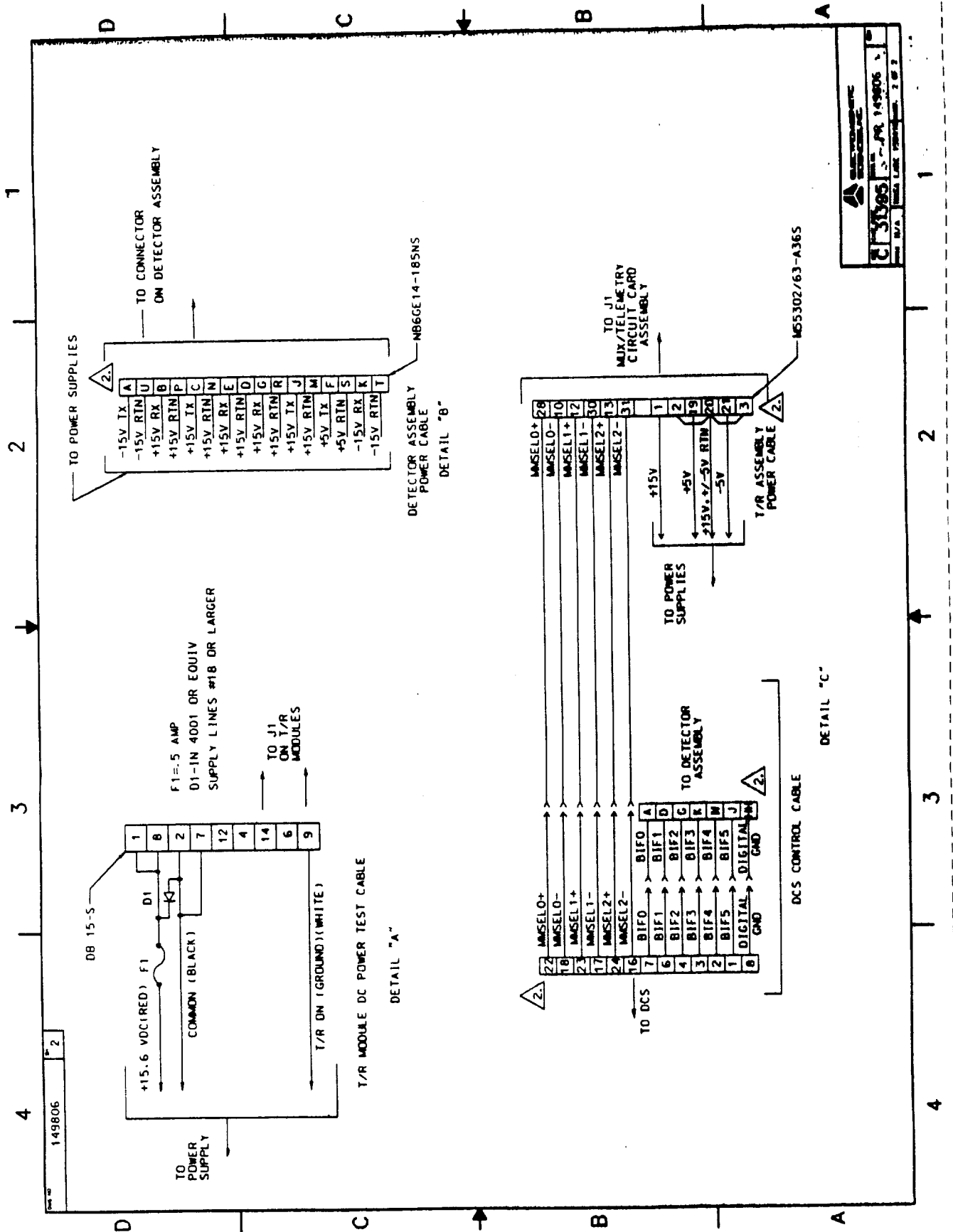


Figure B3-14. Measured Target Amplitude and Time Delay Versus Target Distance for Bistatic Band-D Tests using Full VEC-7 Model

APPENDIX C: TEST SETUP DOCUMENTATION



REV	DATE	BY	CHKD	APP'D	DESCRIPTION
1	10/1/80	W. J. HARRIS			INITIAL DESIGN
2	10/1/80	W. J. HARRIS			REVISED FOR MANUFACTURING
3	10/1/80	W. J. HARRIS			REVISED FOR MANUFACTURING
4	10/1/80	W. J. HARRIS			REVISED FOR MANUFACTURING
5	10/1/80	W. J. HARRIS			REVISED FOR MANUFACTURING
6	10/1/80	W. J. HARRIS			REVISED FOR MANUFACTURING
7	10/1/80	W. J. HARRIS			REVISED FOR MANUFACTURING
8	10/1/80	W. J. HARRIS			REVISED FOR MANUFACTURING
9	10/1/80	W. J. HARRIS			REVISED FOR MANUFACTURING
10	10/1/80	W. J. HARRIS			REVISED FOR MANUFACTURING
11	10/1/80	W. J. HARRIS			REVISED FOR MANUFACTURING
12	10/1/80	W. J. HARRIS			REVISED FOR MANUFACTURING
13	10/1/80	W. J. HARRIS			REVISED FOR MANUFACTURING
14	10/1/80	W. J. HARRIS			REVISED FOR MANUFACTURING
15	10/1/80	W. J. HARRIS			REVISED FOR MANUFACTURING
16	10/1/80	W. J. HARRIS			REVISED FOR MANUFACTURING
17	10/1/80	W. J. HARRIS			REVISED FOR MANUFACTURING
18	10/1/80	W. J. HARRIS			REVISED FOR MANUFACTURING
19	10/1/80	W. J. HARRIS			REVISED FOR MANUFACTURING
20	10/1/80	W. J. HARRIS			REVISED FOR MANUFACTURING
21	10/1/80	W. J. HARRIS			REVISED FOR MANUFACTURING
22	10/1/80	W. J. HARRIS			REVISED FOR MANUFACTURING
23	10/1/80	W. J. HARRIS			REVISED FOR MANUFACTURING
24	10/1/80	W. J. HARRIS			REVISED FOR MANUFACTURING
25	10/1/80	W. J. HARRIS			REVISED FOR MANUFACTURING
26	10/1/80	W. J. HARRIS			REVISED FOR MANUFACTURING
27	10/1/80	W. J. HARRIS			REVISED FOR MANUFACTURING
28	10/1/80	W. J. HARRIS			REVISED FOR MANUFACTURING
29	10/1/80	W. J. HARRIS			REVISED FOR MANUFACTURING
30	10/1/80	W. J. HARRIS			REVISED FOR MANUFACTURING
31	10/1/80	W. J. HARRIS			REVISED FOR MANUFACTURING
32	10/1/80	W. J. HARRIS			REVISED FOR MANUFACTURING
33	10/1/80	W. J. HARRIS			REVISED FOR MANUFACTURING
34	10/1/80	W. J. HARRIS			REVISED FOR MANUFACTURING
35	10/1/80	W. J. HARRIS			REVISED FOR MANUFACTURING
36	10/1/80	W. J. HARRIS			REVISED FOR MANUFACTURING
37	10/1/80	W. J. HARRIS			REVISED FOR MANUFACTURING
38	10/1/80	W. J. HARRIS			REVISED FOR MANUFACTURING
39	10/1/80	W. J. HARRIS			REVISED FOR MANUFACTURING
40	10/1/80	W. J. HARRIS			REVISED FOR MANUFACTURING
41	10/1/80	W. J. HARRIS			REVISED FOR MANUFACTURING
42	10/1/80	W. J. HARRIS			REVISED FOR MANUFACTURING
43	10/1/80	W. J. HARRIS			REVISED FOR MANUFACTURING
44	10/1/80	W. J. HARRIS			REVISED FOR MANUFACTURING
45	10/1/80	W. J. HARRIS			REVISED FOR MANUFACTURING
46	10/1/80	W. J. HARRIS			REVISED FOR MANUFACTURING
47	10/1/80	W. J. HARRIS			REVISED FOR MANUFACTURING
48	10/1/80	W. J. HARRIS			REVISED FOR MANUFACTURING
49	10/1/80	W. J. HARRIS			REVISED FOR MANUFACTURING
50	10/1/80	W. J. HARRIS			REVISED FOR MANUFACTURING
51	10/1/80	W. J. HARRIS			REVISED FOR MANUFACTURING
52	10/1/80	W. J. HARRIS			REVISED FOR MANUFACTURING
53	10/1/80	W. J. HARRIS			REVISED FOR MANUFACTURING
54	10/1/80	W. J. HARRIS			REVISED FOR MANUFACTURING
55	10/1/80	W. J. HARRIS			REVISED FOR MANUFACTURING
56	10/1/80	W. J. HARRIS			REVISED FOR MANUFACTURING
57	10/1/80	W. J. HARRIS			REVISED FOR MANUFACTURING
58	10/1/80	W. J. HARRIS			REVISED FOR MANUFACTURING
59	10/1/80	W. J. HARRIS			REVISED FOR MANUFACTURING
60	10/1/80	W. J. HARRIS			REVISED FOR MANUFACTURING
61	10/1/80	W. J. HARRIS			REVISED FOR MANUFACTURING
62	10/1/80	W. J. HARRIS			REVISED FOR MANUFACTURING
63	10/1/80	W. J. HARRIS			REVISED FOR MANUFACTURING
64	10/1/80	W. J. HARRIS			REVISED FOR MANUFACTURING
65	10/1/80	W. J. HARRIS			REVISED FOR MANUFACTURING
66	10/1/80	W. J. HARRIS			REVISED FOR MANUFACTURING
67	10/1/80	W. J. HARRIS			REVISED FOR MANUFACTURING
68	10/1/80	W. J. HARRIS			REVISED FOR MANUFACTURING
69	10/1/80	W. J. HARRIS			REVISED FOR MANUFACTURING
70	10/1/80	W. J. HARRIS			REVISED FOR MANUFACTURING
71	10/1/80	W. J. HARRIS			REVISED FOR MANUFACTURING
72	10/1/80	W. J. HARRIS			REVISED FOR MANUFACTURING
73	10/1/80	W. J. HARRIS			REVISED FOR MANUFACTURING
74	10/1/80	W. J. HARRIS			REVISED FOR MANUFACTURING
75	10/1/80	W. J. HARRIS			REVISED FOR MANUFACTURING
76	10/1/80	W. J. HARRIS			REVISED FOR MANUFACTURING
77	10/1/80	W. J. HARRIS			REVISED FOR MANUFACTURING
78	10/1/80	W. J. HARRIS			REVISED FOR MANUFACTURING
79	10/1/80	W. J. HARRIS			REVISED FOR MANUFACTURING
80	10/1/80	W. J. HARRIS			REVISED FOR MANUFACTURING
81	10/1/80	W. J. HARRIS			REVISED FOR MANUFACTURING
82	10/1/80	W. J. HARRIS			REVISED FOR MANUFACTURING
83	10/1/80	W. J. HARRIS			REVISED FOR MANUFACTURING
84	10/1/80	W. J. HARRIS			REVISED FOR MANUFACTURING
85	10/1/80	W. J. HARRIS			REVISED FOR MANUFACTURING
86	10/1/80	W. J. HARRIS			REVISED FOR MANUFACTURING
87	10/1/80	W. J. HARRIS			REVISED FOR MANUFACTURING
88	10/1/80	W. J. HARRIS			REVISED FOR MANUFACTURING
89	10/1/80	W. J. HARRIS			REVISED FOR MANUFACTURING
90	10/1/80	W. J. HARRIS			REVISED FOR MANUFACTURING
91	10/1/80	W. J. HARRIS			REVISED FOR MANUFACTURING
92	10/1/80	W. J. HARRIS			REVISED FOR MANUFACTURING
93	10/1/80	W. J. HARRIS			REVISED FOR MANUFACTURING
94	10/1/80	W. J. HARRIS			REVISED FOR MANUFACTURING
95	10/1/80	W. J. HARRIS			REVISED FOR MANUFACTURING
96	10/1/80	W. J. HARRIS			REVISED FOR MANUFACTURING
97	10/1/80	W. J. HARRIS			REVISED FOR MANUFACTURING
98	10/1/80	W. J. HARRIS			REVISED FOR MANUFACTURING
99	10/1/80	W. J. HARRIS			REVISED FOR MANUFACTURING
100	10/1/80	W. J. HARRIS			REVISED FOR MANUFACTURING



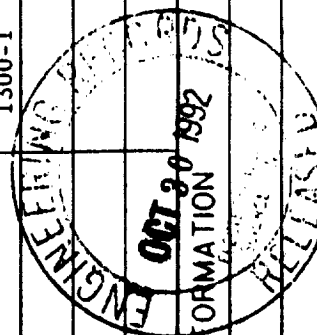
APPENDIX D: LIST OF RELATED DOCUMENTS AND INTERFACE INFORMATION

D1: PARTS LISTS FOR THE DETECTOR ASSEMBLY AND THE TRANSMIT/RECEIVE ASSEMBLY

D2: RELATED DOCUMENTS AND INTERFACE INFORMATION

APPENDIX D1: PARTS LISTS FOR THE DETECTOR ASSEMBLY
AND THE TRANSMIT/RECEIVE ASSEMBLY

PARTS LIST		ELECTROMAGNETIC SCIENCES, INC.		CAGE CODE 31395	DRAWING NO. PL 144564-1 NASA LARC/PL159424-1		REV
TITLE DETECTOR ASSEMBLY UPPER HOUSING (EDM)				CONTRACT NO. NAS1-19063		SHEET 1 OF 5	
REVISIONS				APPROVAL	DATE	APPROVAL	DATE
LTR	DESCRIPTION	DATE	APVD	DRAWN BY Howard Stacy	9/12/15	CHECKED	
				ENGINEER R. W. W. W.	9/24/10	CONF MGT	
				PROJECT		QUALITY	
				MANUFACTURING		P M & P	
<p>NOTE P/L IS FOR THE AS BUILT, AS SHIPPED HARDWARE PER TERMS OF CONTRACT TERMINATION.</p>				APPLICATIONS			
				DASH NUMBER	NEXT ASSY	USED ON	
					144532	Q14061	
						1300-1	
				CAD INFORMATION			
				PROCESSOR ID			
				DEV:IDIRECTORY			
				FILENAME			
				LEVEL(S)			



PRELIMINARY

NOTES:

ELECTROMAGNETIC SCIENCES, INC.

Page 3 of 5

DETECTOR ASSEMBLY, UPPER HOUSING (EDM)

Job Number: Q14061

92/05/28

Model Number: 1300-1

Drawing Number: FL144564-1

Item	Qty	Part Number	Reference Designators	Description	Type	Specification	Manufacturer
19	1	4T-8	ATT1	Attenuator, coaxial, 8 dB			Lucas Weinschel
20	1	4T-5	ATT2	Attenuator, coaxial, 5 dB			Lucas Weinschel
21	1	4T-8	ATT3	Attenuator, coaxial, 8 dB			Lucas Weinschel
22	1	4T-6	ATT4	Attenuator, coaxial, 6 dB			Lucas Weinschel
23							
24	1	89ZEKZEK004.8	CBL1	Coaxial Cable, Flexible	.085"	TBD	W. L. Gore
25	1	89ZEKZEK004.1	CBL2	Coaxial Cable, Flexible	.085"	TBD	W. L. Gore
26	1	89ZEKZ7J007.3	CBL3	Coaxial Cable, Flexible	.085"	TBD	W. L. Gore
27	1	89ZEKZ7G011.5	CBL4	Coaxial Cable, Flexible	.085"	TBD	W. L. Gore
28	1	89ZEKZEK006.2	CBL5	Coaxial Cable, Flexible	.085"	TBD	W. L. Gore
29	1	89Z7GZ7G006.7/270	CBL6	Coaxial Cable, Flexible	.085"	TBD	W. L. Gore
30	1	89ZEKZ7G006.3	CBL7	Coaxial Cable, Flexible	.085"	TBD	W. L. Gore
31	1	89ZEKZ7J006.3	CBL8	Coaxial Cable, Flexible	.085"	TBD	W. L. Gore
32							
33							
34							
35							
36							

ELECTROMAGNETIC SCIENCES, INC.

Page 4 of 5

DETECTOR ASSEMBLY, UPPER HOUSING (EDM)

92/05/28

Job Number: Q14061

Model Number: 1300-1

Drawing Number: PL144564-1

Item	Qty	Part Number	Reference Designators	Description	Type	Specification	Manufacturer
37							
38	2	146351-1		Isolator Shim, I1 & I2			
39	3	147457-1		Isolator Clamp, I1, I2, & I3			
40	1	146352-1		Mixer Shim, M2			
41	1	147456-1		Upconverter Shim M1			
42	3	147522-1		Clamp, Coaxial Cable			
43	1	146353-1		Coupler Shim, DC1			
44	1	146354-1		Oscillator Shim, SO2			
45	1	146355-1		Filter Shim, F1			
46	1	147455-1		Phase Det Clamp, M3			
47	1	147458-1		Filter Shim, F2			
48	1	147459-1		Power Div Shim, PD1			
49	1	147459-2		Amplifier Shim, A2			
50	1	148035-1		Amplifier MTG Bracket			
51	AR			Screw,	4-40		
52	AR			Screw,	2-56		
53	AR			Washer	4-40		
54	AR			Washer	4-40		

D1-4

C-5

ELECTROMAGNETIC SCIENCES, INC.

DETECTOR ASSEMBLY, UPPER HOUSING (EDM)

Job Number: Q14061

Model Number: 1300-1

Drawing Number: PL144564-1

92/05/28

Item	Qty	Part Number	Reference Designators	Description	Type	Specification	Manufacturer
55							
56							
57							
58							
59							
60							
61							
62							
63							
64							
65							
66							
67							
68							
69							
70							
71							
72							

DETECTOR ASSEMBLY, UPPER HOUSING (EDM)

92/05/28

Job Number: Q14061

Model Number: 1300-1

Drawing Number: PL144564-1

Item	Qty	Part Number	Reference Designators	Description	Type	Specification	Manufacturer
1	1	146336		Housing			
2	1	146375		Cover, Top			
3	1	146620-1		IP PC Board Assembly			
4							
5	1	145625-1	F2	70 MHz Bandpass Filter		SCD145625	Integrated Microwave
6	1	ACT5-211-5	A2	Amplifier, RF	10-500 MHz		Avantek
7	1	145627-1	M2	Image Reject Mixer		SCD145627	M/A-COM
8	1	145627-2	M1	Up Converter SSB		SCD145627	M/A-COM
9	1	CSM-10M-10G/67257	DC1	Directional Coupler	10 dB		Merrimac
10	1	WJ-6884-814	A1	Amplifier, Microwave	5-12 GHz		Watkins Johnson
11	1	PDM-26-50	PD1	Power Divider			Merrimac
12	1	145605-1	S02	Crystal Oscillator, 76 MHz		SCD145605	Vectron
13	1	145626-1	F1	Low Pass Filter, 12.4 GHz		SCD145626	Integrated Microwave
14	3	2089261	I1,I2,I3	Isolator, 8-12.4 GHz			TEAK Microwave
15	1	QMK-A315	M3	I/Q Phase Detector		SCD145634	Synergy Microwave
16	1	145535-1	S01	Oscillator, Digital Tuned		SCD145535	General Microwave
17							
18	1	146109		Sleeve, Connector			

ELECTROMAGNETIC SCIENCES, INC.

92/08/28

TOP ASSEMBLY, MRIS T/R MODULE

Job Number: Q14061

Model Number: 1300-1

Drawing Number: PL144531-1

Item	Qty	Part Number	Reference Designators	Description	Type	Specification	Manufacturer
1	X	144531		T/R Assembly			
2	1	145524		Horn Assy, 44 & 95 GHz			
3	1	145274		Horn Assy, 20 & 140 GHz			
4	1	145641		Baseplate			
5	7	171276		Standoff			
6	6	145912		Mainframe			
7	1	145913		Connector Mtg Panel			
8	4	147992		Standoff, 8:1 Switch			
9	1	146280		8:1 Switch Mtg Plate			
10	1	147993		Plate Support SP8Z			
11	1	147601		Waveguide Run, Band A			
12	1	147602		Waveguide Run, Band B/Bec			
13	1	147603		Waveguide Run, Band B/Exit			
14	1	147604		Waveguide Run, Band C/Bec			
15	1	147605		Waveguide Run, Band C/Exit			

* Indicates parts which were not assembled, but shipped to customer as separate piece part.

ELECTROMAGNETIC SCIENCES, INC.

Page 3

92/08/28

TOP ASSEMBLY, MBIS T/R MODULE

Job Number: Q14061

Model Number: 1300-1

Drawing Number: PL144531-1

Item	Qty	Part Number	Reference Designators	Description	Type	Specification	Manufacturer
16	1	147606		Waveguide Run, Band D/Rec			
17	1	147607		Waveguide Run, Band D/Xmit			
* 18	1	147704		W/G Support Brkt, Bottom Band B			
* 19	1	147705		W/G Support Brkt, Top Band B			
* 20	1	147701		W/G Support Brkt, Bottom Band C, Xmit			
* 21	1	147703		W/G Support Brkt, Bottom Band C, Recv			
* 22	2	147702		W/G Support Brkt, Top Band C, Xmit & Recv			
* 23	1	147706		W/G Support Brkt, Bottom Band D, Xmit			
* 24	1	147718		W/G Support Brkt, Bottom Band D, Recv			
* 25	1	147719		W/G Support Brkt, Top, Band D			
* 26	3	147200		W/G Support Brkt, Band A			
* 27	1	147334-1		Waveguide Window, Band A			
* 28	2	147334-2		Waveguide Window, Band B			
* 29	2	147333-1		Waveguide Window, Band C			
* 30	2	147333-2		Waveguide Window, Band D			

TOP ASSEMBLY, MRIS T/R MODULE
 Job Number: Q14061
 Model Number: 1300-1
 Drawing Number: PL144531-1

92/08/28

Item	Qty	Part Number	Reference Designators	Description	Type	Specification	Manufacturer
* 31	12	146986		Thermal Isolator			
* 32	1	148039		Cover, Top			
33	1	147581		Coax Cable SP4T, Band A			
34	1	147582		Coax Cable SP4T, Band D			
35	1	147583		Coax Cable SP4T, Band C			
36	1	147584		Coax Cable SP4T, Band B			
37	1	147585		Coax Cable SP4T, Input			
38	1	147586		Coax Cable SP8T, Band A Ref			
39	1	147587		Coax Cable SP8T, Band A Test			
40	1	147588		Coax Cable SP8T, Band B Test			
41	1	147589		Coaxial Cable SP8T, Band B Ref			
42	1	147590		Coaxial Cable SP8T, Band C Ref			
43	1	147591		Coaxial Cable SP8T, Band C Test			
44	1	147592		Coaxial Cable SP8T, Band D Ref			
45	1	147593		Coaxial Cable SP8T, Band D Test			

ELECTROMAGNETIC SCIENCES, INC.

Page 5

TOP ASSEMBLY, RLIS 7/R MODULE

Job Number: Q14061

Model Number: 1300-I

Drawing Number: PL144531-1

92/08/28

Item	Qty	Part Number	Reference Designators	Description	Type	Specification	Manufacturer
46	1	147594		Coaxial Cable SP8T, Amp			
47	1	147595		Coaxial Cable Amp, Output			
* 48	2	147989		Coax Cable Clamp			
* 49	1	147988		Bracket, Coax Cable			
* 50	2	148013		Bracket, Coax Cable			
* 51	AR	MIL-T-43435		Lacing Cord			Gudebrud
* 52	AR	SS-04		Gasket			Spizal Mfg. Corp. North Hollywood, CA
* 53	1	148366		W/G Support Bkt. Top-Band D, Xmit			
* 54	1	148302		Washer, Bonding			
55	1	145213		Band A Module			
56	1	145604		Band B Module			
57	1	146273		Band C Module			
58	1	146274		Band D Module			
59	1	145629-1		Switch, SP4T			
60	1	145629-3		Switch, SP8T			

ELECTROMAGNETIC SCIENCES, INC.

Page 6

92/08/28

TOP ASSEMBLY, MRIS T/R MODULE

Job Number: Q14061

Model Number: 1300-1

Drawing Number: PL144531-1

Item	Qty	Part Number	Reference Designators	Description	Type	Specification	Manufacturer
61	1	145631-2		Amplifier, 5-12 GHz			
62	1	146248		PC Assy, Mux/Telemetry			
63	1	WB0E14-18PNT		Connector, Power			
64	1	WB0E22-55PNT		Connector, Signal			
65	1	CR42R-3960		Waveguide Transition			Custom Microwave Longmont, CO
66	1	4T-2		Attenuator, Coaxial, 2 dB			Lucas Weinschel
67	1	4T-12		Attenuator, Coaxial, 12 dB			Lucas Weinschel
68	1	4T-4		Attenuator, Coaxial, 4 dB			Lucas Weinschel
69	1	4T-3		Attenuator, Coaxial, 3 dB			Lucas Weinschel
70	1	4T-2		Attenuator, Coaxial, 2 dB			Lucas Weinschel
71	1	4T-3		Attenuator, Coaxial, 3 dB			Lucas Weinschel
72	1	4T-3		Attenuator, Coaxial, 3 dB			Lucas Weinschel
73	1	4T-12		Attenuator, Coaxial, 12 dB			Lucas Weinschel
74	1	147538		Cover, Shipping			
75	4	147562		Stand-Off, Shipping Cover			

ELECTROBIOGENETIC SCIENCES, INC.

Page 7

TOP ASSEMBLY, MBIS T/R MODULE

Job Number: Q14061

Model Number: 1300-1

Drawing Number: PL14531-1

92/08/28

Item	Qty	Part Number	Reference Designators	Description	Type	Specification	Manufacturer
★ 76	1	148037		Cover, Bottom			
77	4	MS		Nut, Hex, .086-56	CRES		
78	4	MS		Nut, Hex, .112-40			
79							
80							
81	1	148581		Bracket, Coax Cable			
82							
83							
84							
85	62			Screw, Soc Head .112-40 x .38 LG			
86	12			Screw, Soc Head .112-40 x .25 LG			
87	7	MS		Bolt, Hex Head, .312-32 UNC-2A x .75 LG			
88	14	MS		Screw, Soc Head, .112-40 UNC-2A x .50 LG			
89	15	MS		Screw, Soc Head, .112-40 UNC-2A x .31 LG			
90	24	MS		Screw, Soc Head, .190-24 UNC-2A x .50 LG			

ELECTROMAGNETIC SCIENCES, INC.

Page 8

92/08/28

TOP ASSEMBLY, MRIS T/R MODULE

Job Number: Q14061

Model Number: 1300-1

Drawing Number: PL144531-1

Item	Qty	Part Number	Reference Designators	Description	Type	Specification	Manufacturer
91	4	MS		Screw, Soc Head, .190-24 UNC-2A X .375			
92	2	MS		Screw, Soc Head, .138-32 UNC-2A X .375			
93	-	MS		Screw, Soc Head, .138-32 UNC-2A X			
94	14	MS		Screw, Soc Head, .164-32 UNC-2A X .375			
95	-	MS		Screw, Soc Head, .164-32 UNC-2A X			
96	12	MS		Screw, Soc Head, .112-40 UNC-2A X .687			
97	4	MS		Screw, Flat Head, .112-40 UNC-2A X .50			
98	5	MS		Screw, Soc Head, .250-20 UNC-2A X .75			
99							
100							
101							
102							
103							
104							
105							

92/08/28

TOP ASSEMBLY, NR15 T/R MODULE

Job Number: Q14061

Model Number: 1300-1

Drawing Number: PL144531-1

Item	Qty	Part Number	Reference Designators	Description	Type	Specification	Manufacturer
106							
107	4	MS15795-802		Washer, Flat #2			
108	16	MS15795-804		Washer, Flat #4			
109	2	MS15795-805		Washer, Flat #6			
110	14	MS15795-807		Washer, Flat #8			
111	26	MS15795-808		Washer, Flat #10			
112	7	MS15795-812		Washer, Flat 5/16			
113	AR			Washer, Flat 1/4			
114							
115							
116				Conformal Coat			
117		22168/A		Adhesive, Scotchweld			
118	AR	SCD114303-2		Adhesive, Epoxy	Scotchweld	114303	3M, AS
119	AR	SCD114304-2		Solothane 113/300		114304	
120							
121	AR	611 WRMA		Flux, Solder	RMA	MIL-F-14256	Alpha

92/08/28

TOP ASSEMBLY, MRIS T/R MODULE

Job Number: Q14061

Model Number: 1300-1

Drawing Number: PL144531-1

Item	Qty	Part Number	Reference Designators	Description	Type	Specification	Manufacturer
122	AR	SM63 WRMAP-2		Solder, Cored	RMA	QQ-S-571	Alpha
123	AR	B43553-II-WHT		Epoxy Ink #9 White	N/A Series	MIL-I-43553	Wornow
124	AR	M22759/18-18-0		Wire, 18AWG, Black		MIL-W-22759/18	
125	AR	M22759/18-18-1		Wire, 18AWG, Brown		MIL-W-22759/18	
126	AR	M22759/18-18-2		Wire, 18AWG, Red		MIL-W-22759/18	
127	AR	M22759/18-18-3		Wire, 18AWG, Orange		MIL-W-22759/18	
128	AR	M22759/18-18-4		Wire, 18AWG, Yellow		MIL-W-22759/18	
129	AR	M22759/18-18-6		Wire, 18AWG, Blue		MIL-W-22759/18	
130	AR	M22759/18-18-7		Wire, 18AWG, Violet		MIL-W-22759/18	
131	AR	M22759/18-18-8		Wire, 18AWG, Grey		MIL-W-22759/18	
132							
133	AR			Wire, Bus, 18AWG			
134	REP			Schematic			
135	AR	M23053/8-002-C		Kynar Sleeving, .063ID		MIL-I-23053/8	
136							

NOTES:

APPENDIX D2: RELATED DOCUMENTS AND INTERFACE INFORMATION

DRL 36: Definition Study Report for Microwave Reflectometer Ionization Sensor, Electromagnetic Sciences, Inc., 22 January 1990.

Equipment Specification Detector Assembly, EMS Drawing #PR146623, 17 February 1992.

Transmit/Receive Assembly Equipment Specification, EMS Drawing #PR146624, 12 October 1992.

Preliminary Thermal Analysis for Transmit/Receive Assembly.

Preliminary Structural Analysis for Transmit/Receive Assembly.

Preliminary Structural and Thermal Analysis for the Detector Assembly.

REPORT DOCUMENTATION PAGE			Form Approved OMB No. 0704-0188	
<small>Public reporting burden for this collection of information is estimated to average 1 hour per response, including the time for reviewing instructions, searching existing data sources, gathering and maintaining the data needed, and completing and reviewing the collection of information. Send comments regarding this burden estimate or any other aspect of this collection of information, including suggestions for reducing this burden, to Washington Headquarters Services, Directorate for Information Operations and Reports, 1215 Jefferson Davis Highway, Suite 1204, Arlington, VA 22202-4302, and to the Office of Management and Budget, Paperwork Reduction Project (0704-0188), Washington, DC 20503</small>				
1. AGENCY USE ONLY (Leave blank)	2. REPORT DATE October 1993	3. REPORT TYPE AND DATES COVERED Contractor Report		
4. TITLE AND SUBTITLE Microwave Reflectometer Ionization Sensor		5. FUNDING NUMBERS C NAS1-19063 WU 505-64-12-04		
6. AUTHOR(S) Joseph Seals, Jeffrey A. Fordham, Robert G. Pauley, and Mario D. Simonutti				
7. PERFORMING ORGANIZATION NAME(S) AND ADDRESS(ES) Electromagnetic Sciences, Inc. PO Box 7700 6600 Engineering Drive Norcross, GA 30091-7700		8. PERFORMING ORGANIZATION REPORT NUMBER		
9. SPONSORING / MONITORING AGENCY NAME(S) AND ADDRESS(ES) National Aeronautics and Space Administration Langley Research Center Hampton, VA 23681-0001		10. SPONSORING / MONITORING AGENCY REPORT NUMBER NASA CR-191464		
11. SUPPLEMENTARY NOTES Langley Technical Monitor: Robert T. Neece - Final Report Seals and Fordham: Electromagnetic Sciences, Inc., Norcross, GA; Pauley: Georgia Tech Research Institute, Atlanta, GA; Simonutti: Millitech Corporation, South Deerfield, MA				
12a. DISTRIBUTION / AVAILABILITY STATEMENT Unclassified-Unlimited Subject Category 19		12b. DISTRIBUTION CODE		
13. ABSTRACT (Maximum 200 words) The development of the Microwave Reflectometer Ionization Sensor (MRIS) instrument for use on the Aeroassist Flight Experiment (AFE) spacecraft is described. The instrument contract was terminated, due to cancellation of the AFE program, subsequent to testing of an engineering develop model. The MRIS, a four-frequency reflectometer, was designed for the detection and location of critical electron density levels in spacecraft reentry plasmas. The instrument would sample the relative magnitude and phase of reflected signals at discrete frequency steps across 4 GHz bandwidths centered at four frequencies: 20, 44, 95, and 140 GHz. The sampled data would be stored for later processing to calculate the distance from the spacecraft surface to the critical electron densities versus time. Four stepped FM CW transmitter/receivers were located behind the thermal protection system of the spacecraft with horn antennas radiating and receiving through an insulating tile. Techniques were developed to deal with interference, including multiple reflections and resonance effects, resulting from the antenna configuration and operating environment.				
14. SUBJECT TERMS Aeroassist Flight Experiment (AFE), Microwave Reflectometer Ionization Sensor (MRIS), FM CW radar, stepped FM CW radar, reentry plasma			15. NUMBER OF PAGES 401	
			16. PRICE CODE A18	
17. SECURITY CLASSIFICATION OF REPORT Unclassified	18. SECURITY CLASSIFICATION OF THIS PAGE Unclassified	19. SECURITY CLASSIFICATION OF ABSTRACT	20. LIMITATION OF ABSTRACT	

